abstracts book
INTERNATIONAL CONFERENCE

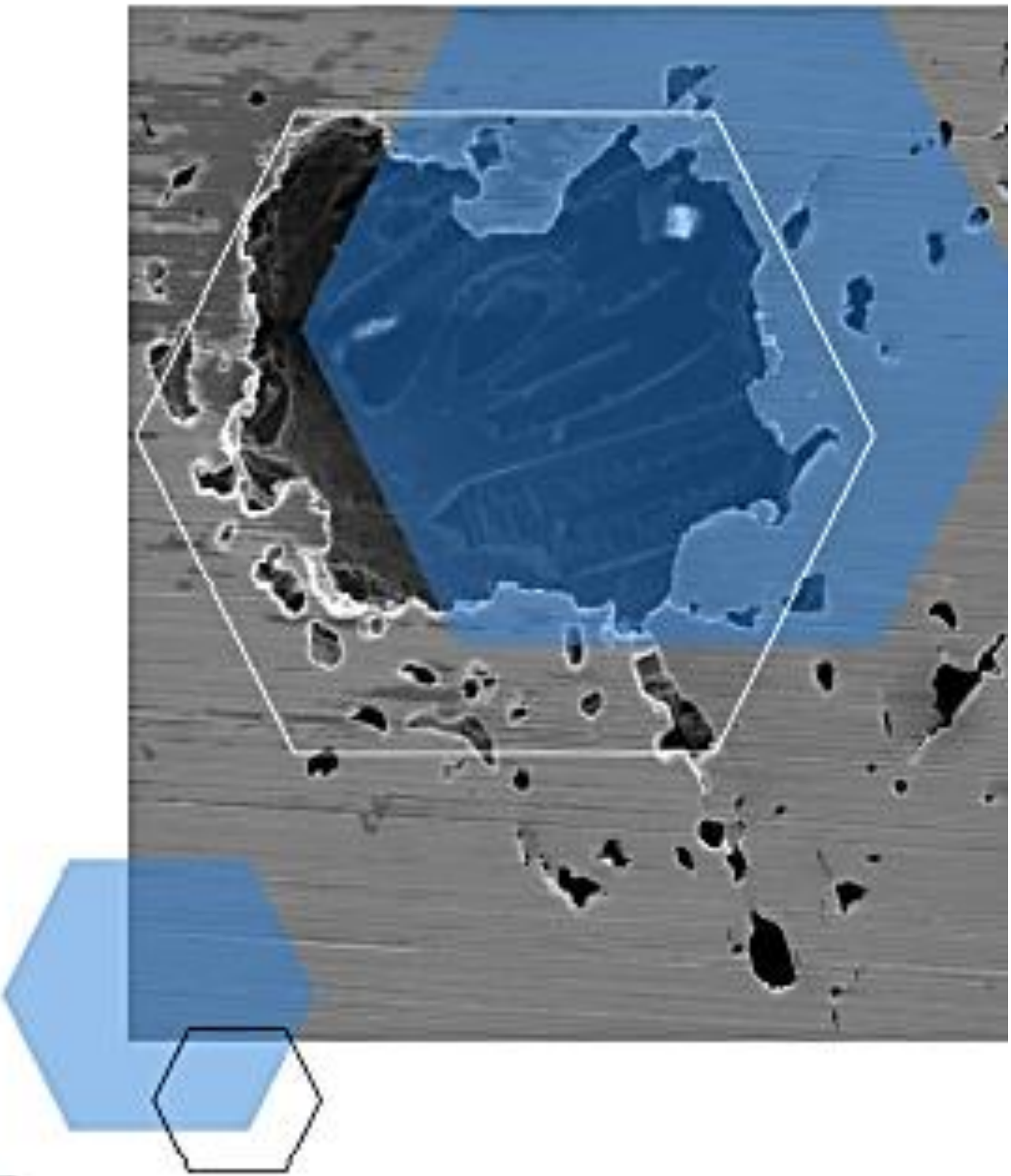

June 27th – 29th, 2018

Vela Luka

Korčula Island

Croatia

MATRIB 2018

MATERIALS/TRIBOLOGY/RECYCLING

Organized by:
Croatian Society for Materials and Tribology
Faculty of Mechanical Engineering and Naval Architecture, University of Zagreb
Faculty of Graphic Arts, University of Zagreb
Polytechnic Pula - College of applied sciences
Dublin Institute for Technology
Institute of Materials and Machine Mechanics, Slovak Academy

MATRIB 2018

MATERIALS/TRIBOLOGY/RECYCLING

June 27th – 29th, 2018
Vela Luka
Korčula Island
Croatia

ORGANIZED BY
Croatian Society for Materials and Tribology

WITH SUPPORT OF
Faculty of Mechanical Engineering and Naval Architecture, University of Zagreb
Faculty of Graphic Arts, University of Zagreb
Polytechnic Pula - College of applied sciences
Dublin Institute for Technology
Institute of Materials and Machine Mechanics, Slovak Academy

IZDAVAČ

PUBLISHER

Hrvatsko društvo za materijale i tribologiju
Croatian Society for Materials and Tribology

c/o FSB, Ivana Lučića 5, 10 000 Zagreb
Tel: 00385 (0)1 6157106
GSM: 00385 (0)91 9092542
Email: hdmt@hdmt.hr

UREDNICI
EDITORS
Mateja Šnajdar Musa, Matija Sakoman

ISSN 1848-5340

Naslovnica
Cover
Mateja Šnajdar Musa

NAKLADA
ISSUE

100 kom

TISAK

PROGRAMSKI ODBOR
PROGRAMME COMMITTEE

Željko Alar (Croatia) / president
Danko Ćorić (Croatia)
Matjaž Godec(Slovenia)
Maurice Grech(Malta)
Krešimir Grilec (Croatia)
Jaroslav Jerz(Slovakia)
David Kennedy (Ireland)
Igor Majnarić (Croatia)
Jan Meneve(Belgium)
Miroslav Mikota(Croatia)
Nikola Mrvac(Croatia)
Bojan Podgornik(Slovenia)
Zdravko Schauperl (Croatia)
Zdenka Zovko Brodarac (Croatia)

ORGANIZACIJSKI ODBOR
ORGANIZING COMMITTEE

Darko Andreis
Natalija Dolić
Tamara Aleksandrov Fabijanić
Vinko Ivušić/ president
Suzana Jakovljević
Davor Mandić
Dinko Prižmić
Jerko Prlić
Denis Prusac
Matija Sakoman
Mateja Šnajdar Musa
Antoneta Tomljenović
Danko Žuvela

RECENZIJSKI ODBOR
REVIEW COMMITTEE

Željko Alar
Danko Ćorić
Krešimir Grilec
Miroslav Mikota
Zdravko Schauperl
Ivan Kumić
Saša Kovačić
Darko Landek
Suzana Jakovljević
Hrvoje Ivanković
Antoneta Tomljenović

Tamara Aleksandrov
Ivan Stojanović
Frankica Kapor
Vesna Alar
Zrinka Švagelj
Marko Katić
Morana MIhaljević
Irena Žmak

SADRŽAJ / CONTENTS

NANOSTRUCTURED HARDMETALS – NEW CHALLENGES FOR POWDER METALLURGY

Tamara Aleksandrov Fabijanić[1], Matija Sakoman[1], Mateja Šnajdar Musa[1], Saša Kovačić[1], Ivan Kumić[1], Vedran Šimunović[1], Marin Kurtela[1]

[1]University of Zagreb, Faculty of Mechanical Engineering and Naval Architecture, Ivana Lučića 5, Zagreb

Pozvano predavanje/Invited lecture

Abstract

The project predicts the development, research and surface engineering of nanostructured hardmetals. At the beginning of the project, the establishment of the Powder Metallurgy Laboratory is foreseen, thus contributing to the strengthening of the Faculty's capacities. The mixtures would be prepared by varying the content and type of binder (Co, Ni, Fe ..), the characteristics of WC powders and grain growth inhibitors (VC, NbC, TiC, TaC and Cr3C2) in order to develop the innovative nanostructured hardmetals with alternative binders and corrosion-resistant nanostructured hardmetals. The consolidation of the mixtures would be performed by sinter-HIP and plasma sintering process at Fraunhofer IKTS, Dresden, Germany, one of the most important institutes in the field. The research and analysis of the consolidated samples would be performed in order to determine the influence of starting mixture characteristics and the consolidation parameters on the final properties. After the development and detailed research predicted in the first three years of the project, the research would be extended to the coating processes of nanostructured hardmetals in the last two years. The plasma assisted chemical vapour deposition PACVD, one of the most advanced surface engineering technologies, would be used. The multilayer gradient coatings by a combination of TiN, TiCN and TiBN are planned for the purpose of creating an innovative coating with enhanced properties on previously consolidated samples. On the basis of the carried research, the applied coating process will be evaluated and the process parameters would be optimized. The conclusions about the applicability of the PACVD process on the nanostructured hardmetals would be brought. The employment of Ph.D, the training of associates, attending the conferences, publishing of scientific papers in the most influential world journals, the procurement of capital equipment and submission of projects to other funding sources are predicted by the project.

***Keywords**: powder metallurgy, nanostructured hardmetals, nano powder, alternative binders, corrosion resistance, PACVD process*

Accknowledgements:

This work has been supported in part by the Croatian Science Foundation under the project number UIP-2017-05-6538.

Corresponding author: Tamara Aleksandrov Fabijanić, tamara.aleksandrov@fsb.hr

BAMBUS, MATERIJAL ZA IZRADU OKVIRA BICIKLA

BAMBOO, BICYCLE FRAME CONSTRACTION MATERIAL

Suzana Jakovljević[1]

[1] Fakultet strojarstva i brodogradnje, Sveučilište u Zagrebu, I. Lučića 1

Pozvano predavanje/Invited lecture

Sažetak: U modernom svijetu sve više se razvija se briga o okolišu. Pretjerana emisija CO_2 u atmosferu te nekontrolirana potrošnja neobnovljivih fosilnih goriva doveli su do neodrživosti sustava. Potreba za održivim rješenjima sve je veća, osobito u sektoru prometa. Bicikl se nameće kao najjeftinije i ekološki najprihvatljviije prijevozno sredstvo.

U radu su ispitana mehanička svojstva (vlačna, tlačna i savojna čvrstoća) dvije vrste bambusa *Pseudosasa amabilis* (ili Tonkin Cane) and *Pleioblastus amarus* (ili Ku Zhu)). Ispitana mehanička svojstva bambusa uspoređena su s ostalim materijalima koji se primjenjuju za izradu okvira bicikla. Svrha ovog rada je prikupiti više znanja o bambusu i dokazati da je moguće primjeniti bambus za izradu okvira bicikla.

Ključne riječi: *bambus, mehanička svojstva, bicikl*

Abstract: In modern world concern for enviroment is increasing. Excessive CO_2 emission and uncontrolled consumption of non renewable fossil fuels have led to unsustainable system. The need for sustainable solutions is increasing especially in the transport sector. The bicycle is imposing itself as the cheapest and enviromentally friendly vehichle.

In this paper, mechanical properties (the tensile, the compressive and the bending strength, the hardness and buckling) of two different bamboos, *Pseudosasa amabilis* (or Tonkin Cane) and *Pleioblastus amarus* (or Ku Zhu) were tested. Mechanical properties of tested bamboos were compared with traditional materials which are used for bicycle frames. The purpose of this study was to gain more knowledge on bamboo and prove his suitability in use as an alternative material for bicycle frame.

Keywords: *bamboo, mechanical properties, bicycle*

Corresponding author: Suzana Jakovljević, suzana.jakovljevic@fsb.hr

TO WHAT EXTENT IS IT NECESSARY TO REVISE THE CURRENT GUIDELINES FOR EVALUATING MEASUREMENT UNCERTAINTY?

U KOJOJ MJERI JE NEOPHODNA POTREBA ZA REVIZIJOM TRENUTNIH SMJERNICA ZA PROCJENU MJERNE NESIGURNOSTI?

Biserka Runje[1], **Amalija Horvatić Novak**[1], **Alen Bošnjaković**[2]

[1]University of Zagreb, Faculty of Mechanical Engineering and Naval Architecture, Zagreb, Ivana Lučića 5, 10000 Zagreb, Croatia
[2]Department for Measurement Standards and Traceability, Augusta Brauna 2, 71000 Sarajevo, Bosnia and Herzegovina

Pozvano predavanje/Invited lecture

Sažetak

U cilju osiguravanja harmoniziranog pristupa procjeni mjerne nesigurnosti prije dvadeset pet godina Vodič za procjenu mjerne nesigurnosti (GUM) utemeljio je opća pravila za proračun i iskazivanje mjerne nesigurnosti. Posljednjih godina dolazi do snažnog razvoja suvremenog mjeriteljstva kao što su dinamička mjerenja, spektroskopija, nanomjeriteljstvo, računalna tomografija, mreže senzora i dr. Ulazne veličinepostaju sve složenijete i same ovise o drugim veličinama što dovodi do složenih funkcijskih odnosa koji se ne mogu uvijek eksplicitno iskazati. U takvim slučajevima primjena GUM metode može dovesti do neprihvatljivih rezultata stoga se zahtijevaju druge analitičke ili numeričke metode. Do danas je Zajednički odbor za upute u mjeriteljstvu (JCGM) izdao četiri dopune Vodiču, a u fazi pripreme su još tri te prijedlog revizije Vodiča. Kroz različite dokumente egzistiraju različiti pristupi procjene mjerne nesigurnosti.Kako bi se prevladali navedeni problemi neophodno je razvijati suvremene modele za procjenu mjerne nesigurnosti kojima će se ostvariti harmonizirana primjena i implementacija principa mjerne nesigurnosti te pouzdano donošenje odluka o sukladnosti rezultata sa specifikacijama.

Ključne riječi: *mjerna nesigurnost, metode procjene mjerne nesigurnosti, suvremeno mjeriteljstvo*

Abstract

In order to ensure a harmonized approach to estimating measurement uncertainty, twenty-five years ago the Guide to the Expression of Uncertainty in Measurement (GUM) has established general rules for calculating and reporting measurement uncertainty. In recent years there has been a strong development of modern metrology such as dynamic measurements, spectroscopy, nanometrology, computed tomography, network sensors etc. Input quantities become more and more complex and dependent on other quantities, leading to complex functional relationships that can not always be explicitly expressed. In such cases the application of the GUM method can lead to unacceptable results, so other analytical or numerical methods are required. Till today, the Joint Committee for Guidance on Metrology has issued four amendments to the Guide, and three more proposals for revising the Guide are being prepared. Various documents exist in different approaches to estimation of measurement uncertainty. In order to overcome these problems it is necessary to develop contemporary models for estimating measurement uncertainty in order to achieve the harmonized application and implementation of the measurement uncertainty principle and to make reliable decisions about the conformity assessment with specifications.

Keywords: *measurement uncertainty, methods for measurement uncertainty evaluation, modern metrology*

Corresponding author: Biserka Runje, biserka.runje@fsb.hr

COPPER EXCHANGE ON NaX IN BAFFLED AND UNBAFFLED BATCH REACTOR STIRRED BY RUSTON TURBINE

Anita Bašić[1], Marija Ćosić[1], Renato Stipišić[1], Sandra Svilović[1]

[1] University of Split, Faculty of Chemistry and Technology, Department of Chemical Engineering, Ruđera Boškovića 35, 21000 Split, Croatia

Abstract

The aim of this work was to determine the influence of hydrodynamic conditions generated by Rushton turbine (RT), in the baffled and unbaffled batch reactor, on just suspended impeller speed (N_{JS}), power consumption (P/m), maximum amount of copper exchanged onto zeolite NaX (q_{e}) and exchange kinetics as well. The amount of exchanged copper at examined conditions was determined using UV/Vis spectrophotometer. Elovich and Blanchard models were used to fit the experimental kinetics data. From the results of the studies of influence of the hydrodynamic conditions generated by Rushton turbine in the reactor with or without baffles can be concluded that the maximum amount of copper exchanged is higher and reaction is faster in the baffled reactor, which is characterized by higher just suspended impeller speed value. But at the same time power consumption per unit mass of suspension is more than three times higher in a baffled reactor. Since the difference in the maximum amount of copper exchanged and the kinetics rate in baffled and unbaffled reactors isn't significant unlike the power consumption, unbaffled reactor stirred by RT may be advisable for studied operation. Analysis of kinetic data show that the process studied follows second order kinetic.

***Keywords**: Zeolite, Rushton turbine, Baffles, Ion exchange kinetics.*

Sažetak

Cilj ovog rada bio je utvrditi utjecaj hidrodinamičkih uvjeta koje generira Rushtonova turbina (RT) u šaržnom reaktoru sa i bez razbijala virova na minimalnu brzinu vrtnje za postizanje potpune suspenzije (N_{JS}), utrošak snage miješanja (P/m), maksimalnu količinu izmjenjenog bakra na zeolitu NaX (q_{e}) te kinetiku izmjene. Količina izmjenjenog bakra određena je korištenjem UV/Vis spektrofotometra. Elovichev i Blanchardov model korišteni su za kinetičku analizu. Iz dobivenih rezultata utjecaja hidrodinamičkih uvjeta koje stvara Rushtonova turbina u reaktoru sa i bez razbijala virova može se zaključiti da je maksimalna količina bakra koja se izmjeni viša te reakcija brža u reaktoru s razbijalima virova, u kojem je i minimalna brzina vrtnje za postizanje potpune suspenzije viša. Međutim u tom istom reaktoru je i utrošak snage čak tri puta viši nego u reakotru bez razbijala virova. S obzirom da razlika u maksimalnoj količini izmjenjenog bakra i brzini izmjene u reakoru sa i bez razbijala virova nije značajna za razliku od utroška snage, za ispitivane uvjete rada preporučljivo je koristiti reaktor bez pregrada. Analizom kinetičkih podataka je utvrđeno da isti slijede reakciju drugog reda.

***Ključne riječi**: Zeolit, Rushtonova turbina, Razbijala virova, Kinetika ionske izmjene.*

1. INTRODUCTION

Zeolites are a large group of natural or synthetic aluminosilicates used primarily in two applications - as sorbents (adsorbents and/or ion exchangers) and catalysts. For sorption applications, zeolites are often used for high sorption capacity for divalent cations. This process seems to be very effective to remove various heavy metals and sorbents can be easily recovered and reused by regeneration operation. [1,2] As microporous materials, zeolites are of great importance for the chemical industry as heterogeneous catalysts with shape/size-selective character in numerous reactions. [3] Zeolites are also used as catalysts in drug (pharmaceutical) production and in the petrochemical industry to break large hydrocarbon molecules into all kinds of products of petroleum.

Sorption on zeolite can be carried out in batch reactor and in fixed bed reactor. Batch sorption is usually conducted in an agitated vessel which is generally widely employed for a variety of chemical processes when particulate solids suspension is involved. In case when solid phase is required to participate in mass-transfer phenomena it is important to provide enough agitation to suspend all particles. Many research efforts have been devoted to the determination of the minimum rotational speed required to attain complete particle suspension, N_{JS}. It was found that it depends on a number of variables such as solid concentration, particle density and mean particle diameter but also of hydrodynamic conditions inside the reactor which depends on geometrical configuration of vessel and impeller used as well. [4,5,6]

Process of ion exchange may potentially also depend on hydrodynamic of the system since its rate may be controlled by film diffusion, particle diffusion or ion exchange itself. However, very little attention has been devoted so far to influence of mixing in the stirred reactors on ion exchange kinetics. For this reason, in this work the influence of hydrodynamic conditions in baffled and unbaffled batch reactor, stirred by Rushton turbine, on maximum amount of copper exchange (q_{e}) onto zeolite NaX and copper exchange kinetics, at the state of its complete suspension, was analyzed. To get a better understanding of the examined process, hydrodynamic of the system was described and various kinetic models were used to test the experimental data. In order to estimate the more viable conditions power consumption per suspension mass was analyzed as well.

2. MATERIALS AND METHODS

2.1. Materials

Zeolite NaX (Sigma-Aldrich) was crushed and sieved to obtain particles smaller than 0,050 mm. Solutions containing 7 mmol L^{-1} Cu^{2+} were prepared dissolving the appropriate weight of $Cu(NO_3)_2{\cdot}3H_2O$ (Kemika) in ultrapure water. The initial concentrations of copper solutions were checked by Perkin Elmer Lambda 25 UV/Vis spectrophotometer.

2.2. Experimental procedure

All experiments were carried out in a glass batch reactor with the internal diameter of d_{T} = 0,12 m (Figure 1a). The solution height, H, was equal to internal vessel diameter ($d_T = H$). Baffled reactor was equipped with four baffles placed at 90° around the vessel periphery. Baffles width, R_{V}, was equal 1/10 d_{T}. The suspension, 1,3 L of copper solution and 6,5 g of zeolite, was stirred using Rushton turbine (Figure 2) Impeller diameter was D = 0,8 m and impeller off-bottom clearance (C/H) was 0,33.

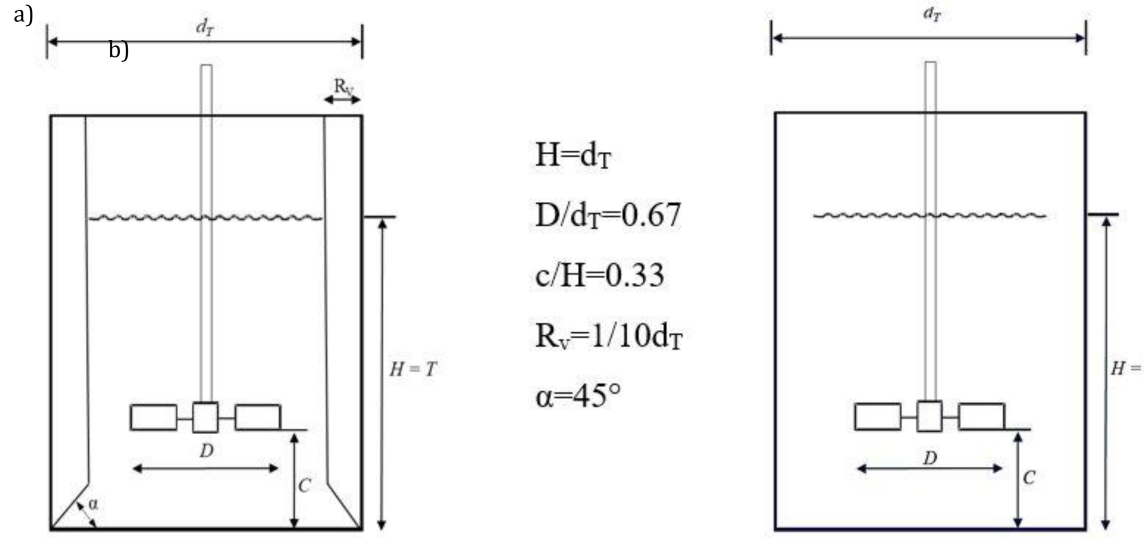

Figure 1. Design details of a) baffled batch reactor, b) unbaffled batch reactor

Mixing was performed by *Lightnin LabMaster LB2* mixer which allowed impeller speed regulation and torque measurement over process time.

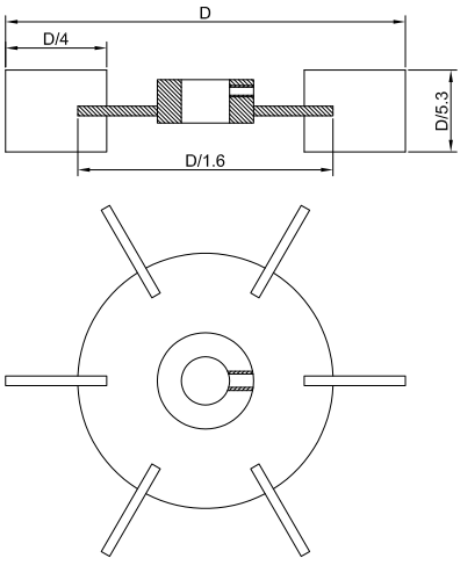

Figure 2. Rushton turbine impeller

In order to enable comparison of obtained results, the initial solution concentration, isothermal conditions (T= 300 K), zeolite mass (6,5 g) and zeolite particle size ($d_P < 0{,}050$ mm) were kept constant. In the first part of the experimental work just suspended impeller speed, N_{JS}, was determined by visual method applying Zweitering criterion 1 s. [4]

While measuring the critical impeller speed, the base of the vessel was illuminated from all directions by placing a mirror below the tank bottom. Impeller speed was gradually increased until all particles of zeolite are in motion and no one remained on the reactor bottom for more than 1 second. Measurements were repeated ten times, and average value was calculated. Upon the N_{JS} were determined in baffled and unbaffled reactor kinetic study was conducted at the state of complete suspension of zeolite. In define process time, samples of slurry were withdrawn from the reactor, centrifuged and filtrated and concentration of the copper in the solution was analyzed by UV/Vis spectrophotometer (Perkin Elmer Lambda 25).

The amount of copper retained on the zeolite, q_t, was calculated as:

$$q_t = \frac{(c_0 - c_t)V}{m} \tag{1}$$

where c_0 is the initial concentration of copper solution (mmol L^{-1}), c_t is the concentration of copper solution at time t (mmol L^{-1}), V is the volume of solution (L) and m is the mass of zeolite (g).

2.3. Kinetic models

By ensuring that particles of zeolite used are small enough to avoid the effect of intraparticle diffusion and assuming that N_{JS} found is sufficient to avoid the impact of film diffusion in this work two reaction based models: Blanchard and Elovich were used.

Blanchard model - second order model – is expressed as: [7]

$$q_t = \frac{q_e^2\, k\, t}{1 + q_e\, k\, t} \tag{2}$$

where q_t is amount of copper ions exchanged after time t (mmol g^{-1}), q_e is maximum amount of copper ions exchanged at equilibrium i.e. equilibrium capacity (mmol g^{-1}), t is time (min) and k is the rate constant of the pseudo second order kinetic model (g mmol^{-1} min^{-1}).

The Elovich model – empirical model - is presented as [8,9]:

$$q_t = \frac{1}{b}\ln(1 + a\, b\, t) \tag{3}$$

where a and b are the constants, a represents the initial sorption rate (g mmol^{-1} min^{-1}) and b is the desorption coefficient (mmol g^{-1} min^{-1}).

3. RESULTS AND DISCUSSION

The results are given in two major sections. First, the baffle presence impact on N_{JS} is presented. Next, analysis of the kinetic experimental data, obtained onto zeolite NaX at the state of complete suspension, in both reactors is made. Finally, the power consumed by the two systems (baffled and unbaffled reactor) is determined and compared.

3.1. N_{JS} results - the state of complete suspension

The state of suspension known as off-bottom or complete suspension is characterized by the complete motion of all particles, with no particle remaining on the base of the vessel for more than 1 to 2 s. Under this condition, the maximum surface area of the particles is exposed to the fluid for chemical reaction or mass or heat transfer in the reactor. [10] N_{JS} is defined as the minimum impeller speed at which all the solids in the vessel are completely suspended.

Fig. 3 shows the N_{JS} results for baffled and unbaffled reactor determined by visual method, applying Zweitering criterion 1s.

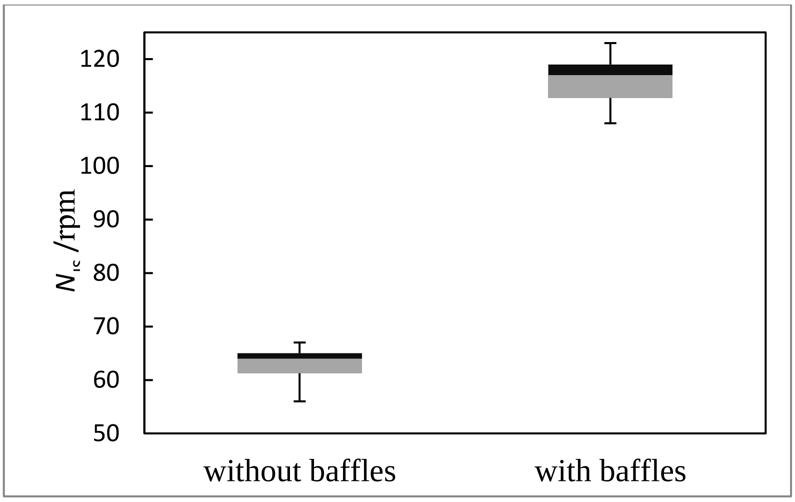

Figure 3. Dependence of N_{JS} on presence of baffles

From the results it is clear that just suspended impeller speed in the baffled reactor is almost double. Since, for solid suspending i turbulent flow field developed inside reactor is responsible, obtained results may be clarified only if fluid flow pattern in both systems is analyzed. Rushton turbine which is applied as impeller in both systems is constructed with six vertical blades on the disk. This turbine was a subject of many researches so its fluid flow pattern in a baffled reactor is well described in literature.[10] In baffled reactor RT generates 100% radial fluid flow pattern as is demonstrated in Figure 4a. As can be seen from the figure, fluid is discharged from the turbine in the radial direction towards the reactor walls where it splits into two loops. One moved towards the vessel bottom and the other towards liquid surface. For suspension of zeolite particles, which are located on the reactor bottom, is responsible the loop near the vessel base. It is important that fluid velocity, i.e. fluid energy, in this loop is high enough for lifting particles from the bottom.

Removing the baffles from the reactor causes transformation of the radial flow pattern to tangential flow pattern. This way, flow created by impeller rotation is two dimensional and causes swirling action, i.e. circular flow (Fig. 4b). [10, 11]. In this case swirling flow which goes towards the vessel bottom lifts zeolite particles at lower impeller speed compared to baffled reactor. This happened because in baffled system, fluid velocity in the lower loop are reduced due to fluid to wall impact, and it will be high enough for particle sweeping only at increased N_{JS}. Although the particles are suspended from the bottom at lower N_{JS} its distribution inside reactor volume may significantly differ from baffled reactor. This difference may be reflected on the ion exchange kinetics.

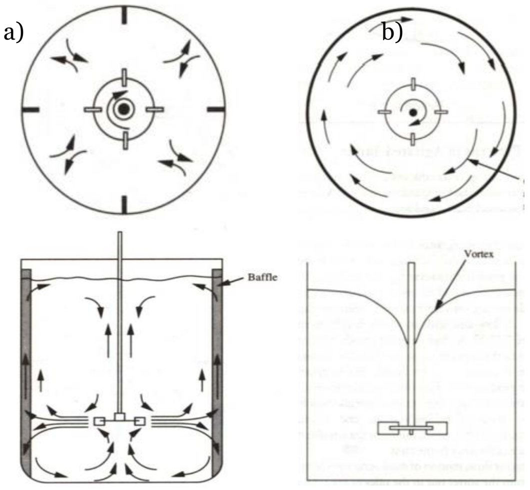

Figure 4. a) Flow pattern produced by a Ruston turbine in a baffled reactor;

b) Circular flow in a unbaffled stirred reactor [11]

3.2. Kinetic experiment results

In the Fig. 5. amount of copper exchanged over time in system with and without baffles, at the state of complete suspension of zeolite, is presented. From the results it is clear that amount of copper exchanged over time has similar trend in both systems. In the beginning it increase significantly and then changes moderately until the process finalization (t = 30 min). By detail analysis it is clear that in the baffled reactor amount of copper exchanged is insignificantly higher over entire process time.

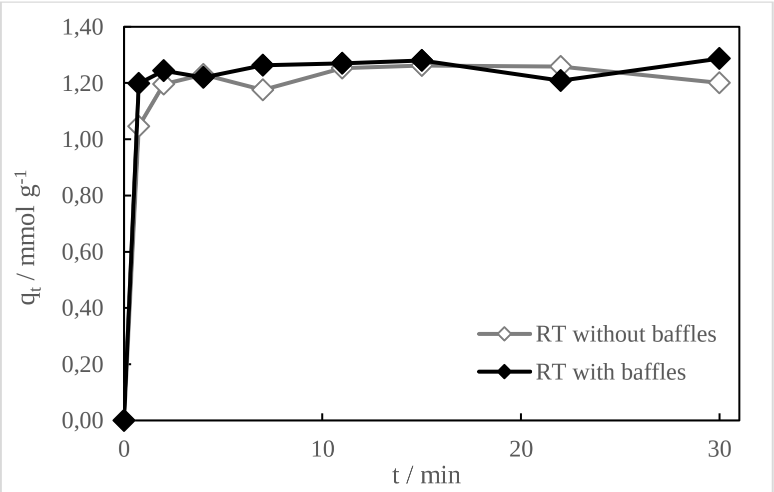

Figure 5. Dependence of ion exchange kinetics on the presence of baffles

Results obtained in this experiment were fit to Elovich and Blanchard kinetic models and the results of kinetic analysis are presented in the Table 1.

Table 1. The parameters of Elovich and Blanchard model in unbaffled and baffled system

Model	**Parameter**	Unbaffled system	Baffled system
Experimental data	$q_{e\ exp}$, mmol g^{-1}	1,2004	1,2869
Elovich	a	5093,9	6761,8
	b	10,716	10,582
	AARD	5,011	6,33
Blanchard model	k g mmol^{-1} min^{-1}	5,910	19,813
	q_e, mmol g^{-1}	1,250	1,262
	AARD	2,192	1,573

The results presented, Table 1., show that the process studied follows the second order kinetic model which means not only that one copper ion exchange two sodium ions but that in all cases N_{JS} applied ensures the effective mixing in order to avoid the effect of film diffusion and to exclude film diffusion as the slowest on-going process.

From the values of rate constant, Table 1, it is clear that the reaction is faster in the baffled reactor, which is characterized by signifincantly higher N_{JS} value. Although in unbaffled system complete suspension state is achieved at lower N_{JS}, in the baffled reactor the top-down motion is ensured. This probably causes more uniform distribution of particles inside suspension what eventually reflected on rate constant.

3.3. Power consumption

Power consumption is defined as quantity of energy input to the liquid phase by stirrer per unit time. Proper choice of hydrodynamic condition in mixing reactor depends on knowledge of the power consumption. In this work power consumption was calculated using equation:

$$P_{JS} = 2\,\pi\,N_{JS}\,\tau \qquad (4)$$

where τ (Nm) presents torque which was measured over process time. Changes of power consumption over process time in the baffled and unbaffled reactor are presented in the Figure 6. as power consumption per unit mass of suspension, $(P/m)_{JS}$ (W kg^{-1}).

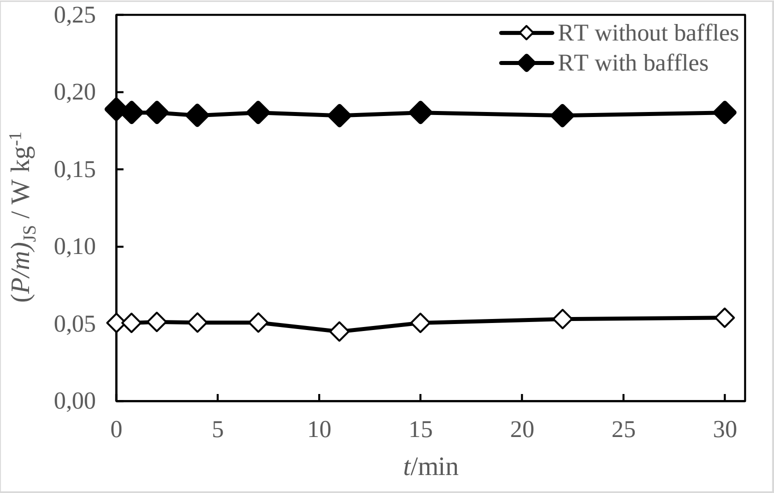

Figure 6. Power consumption per unit mass $(P/m)_{JS}$ in baffled and unbaffled systems

From the presented results it is clear that power consumption is higher more than three times in baffled system. This result could be expected since that power consumption depends on impeller speed (Eq. 4). On the other hand, presence of baffles next to the vessel wall causes resistance to the fluid flow which needs to be overcome by higher power input.

4. CONCLUSION

When copper exchange on complete suspended zeolite NaX is carried out in a batch reactor equipped with Rashton turbine then just suspended impeller speed needs to be twice higher in baffled then in unbaffled reactor. The differences in N_{JS} is consequence of fluid flow pattern generated in those systems. In baffled system fluid velocity in the lower loop is reduced due to fluid to wall impact, and it will be high enough for particle sweeping only at increased N_{JS}. This reflected on the amount of copper exchanged as well, even though the trend is the same in both systems, in the baffled reactor amount of copper exchanged is higher over entire process time. Elovich and Blanchard model were used to fit the experimental kinetics data. Results obtained show that the process studied follows the second order kinetic model. Power consumption per unit mass of suspension is more than three times higher in a baffled system.

Significantly lower $(P/m)_{JS}$ and only slightly lower value of q_e suggests that unbaffled small scale stirred reactor is more viable option when mixing is performed by RT.

Acknowledgement(s):

This work has been fully supported by Croatian Science Foundation under the project HETMIX (**IP-11-2013-8959**)

REFERENCES

[1] Gunatilake S. K., Methods of Removing Heavy Metals from Industrial Wastewater, Journal of Multidisciplinary Engineering Science Studies (JMESS), 1, pp 12-18, (2015).

[2] Yilmaz, B. Müller, U., Catalytic Applications of Zeolites in Chemical Industry, Top in Catal, 52, pp. 888-895, (2009).

[3] Zewail, T.M., Yousef, N.S., Kinetic study of heavy metal ions removal by ion exchange in batch conical air spouted bed, Alex. Eng. J, 54, pp. 83, (2015).

[4] T. N. Zwietering, Suspending of solid particles in liquid by agitatiors, Chem. Eng. Sci, 8, pp. 224-253, (1958).

[5] Nienow, A.W., Suspension of solid particles in turbine agitated baffled vessels. Chem. Eng. Sci. 23, pp. 1453-1459, (1968).

[6] Baldi, G., Conti, R, Alaria, E., Complete suspension of particles in mechanically agitated vessels, Chem. Eng. Sci, 33, pp. 21-25, (1978).

[7] Blanchard G., Maunage M., Martin M. Removal of heavy metals from waters by means of natural zeolites, Water Res. 18, pp. 1501-7, (1984).

[8] Dávilla-Rangel J. I., Solache-Ríos M., Sorption of cobalt by two Mexican clinoptilolite rich tuff zeolitic rocks and kaolinite, J. Radioanal. Nucl. Chem. 270, pp. 465-471, (2006).

[9] Gupta, S. S., Bahattacharyya, K. G., Kinetics of adsorption of metal ions on inorganic materials: A review, Advances in Colloid and Interface Science, 162, pp. 39-58, (2011).

[10] E. L. Paul, V. A. Atiemo-Obeng, S. Kresta, Handbook of Industrial Mixing, John Wiley and Sons, Inc., Hoboken, New Jersey, pp. 1027-1029, (2004)

[11] http://www.dynamixinc.com/baffled-by-baffles, consulted on 27 Apr 2018.

MAGNESIUM SUBSTITUTED HYDROXYAPATITE SCAFFOLDS HYDROTHERMALLY SYNTHESIZED FROM CUTTLEFISH BONE

MAGNEZIJEM SUPSTITUIRANI HIDROKSIAPATITNI NOSAČI HIDROTERMALNO SINTETIZIRANI IZ SIPINE KOSTI

Leonard Bauer, Marica Ivanković, Hrvoje Ivanković

University of Zagreb, Faculty of Chemical Engineering and Technology, Marulićev trg 19, 10000 Zagreb, Croatia

Abstract

Hydroxyapatite (HAp, $Ca_{10}(PO_4)_6(OH)_2$) and magnesium substituted HAp scaffolds were hydrothermally synthesised from the cuttlefish bone. The compositional and morphological properties of the scaffold were studied by means of X-ray powder diffraction, FTIR spectroscopy, thermogravimetric analysis and scanning electron microscopy. Total conversion of aragonite to HAp was confirmed while original highly porous interconnected structure was preserved. The HAp structure was refined with Rietveld refinement and used as initial structure for magnesium substituted samples. As HAp can incorporate only a limited amount of Mg^{2+} into structure, whitlockite (WH, $Ca_{18}Mg_2(HPO_4)_2(PO_4)_{12}$) is formed from the Mg^{2+} excess. As analysis confirmed formation of nonstoichiometric AB-type carbonated HPO_4^{2-} substituted HAp, main component of natural bone, and formation of magnesium rich WH phase, found in human body, synthesised scaffolds should have improved biological properties compared to synthetic stoichiometric HAp.

Keywords: *magnesium substituted hydroxyapatite, X-ray powder diffraction, Rietveld refinement method, whitlockite, scaffold, cuttlefish bone, hydrothermal synthesis ispod sažetka*

Sažetak

Hidroksiapatini (HAp, $Ca_{10}(PO_4)_6(OH)_2$) i magnezijem supstituirani HAp nosači hidrotermalno su sintetizirani iz sipine kosti. Sastav i morfološka svojstva istražena su rendgenskom difrakcijskom analizom praha, FTIR spektroskopijom, termogravimetrijskom analizom i skenirajućim elektronskim mikroskopom. Potvrđena je potpuna konverzija aragonita u HAp uz očuvanje originalne visokoporozne međusobno povezane strukture. Struktura HAp-a utočnjena je Rietveldovom metodom te je korištena kao polazna struktura za analizu Mg^{2+} supstituiranih uzoraka. Budući da HAp u svoju strukturu može primiti ograničenu količinu Mg^{2+}, iz ostatka dodanog Mg^{2+} kristalizira vitlokit ($Ca_{18}Mg_2(HPO_4)_2(PO_4)_{12}$). Kako je analiza potvrdila nastanak nestehiometrijskog AB-tip karbonatnog HPO_4^{2-} supstituiranog HAp-a, glavne komponente prirodne kosti, te nastanak magnezijem bogate faze vitlokita, koja se može naći u ljudskom tijelu, sintetizirani nosači trebali bi imati bolja biološka svojstva nego sintetski stehiometrijski HAp.

***Ključne riječi**: magnezijem supstituirani hidroksiapatit, rendgenska difrakcijska analiza praha, Rietveldova metoda utočnjavanja, vitlokit, sipina kost, hidrotermalna sinteza*

1. INTRODUCTION

One of the main objectives in bone tissue engineering is synthesis of biomaterials that resemble natural bone in structure and composition. Bone mineral has a similar chemical composition to synthetic hydroxyapatite (HAp, $Ca_{10}(PO_4)_6(OH)_2$) [1] but contains several ionic substitutions. HAp has Ca and P in hexagonal crystal structure and it has been demonstrated that strong bonds are generated on the surface between bone and HAp implant due the high bioactivity of HAp.

The mineral part of bone is composed of natural HAp containing various constituents incorporated into the nanoscale crystal lattice or are absorbed onto the crystal structure. Among the substituting ions that are known and reported in bone and tooth mineral are F^-, Cl^-, Na^+, K^+, Fe^{2+}, Zn^{2+}, Sr^{2+}, Mg^{2+}, citrate and carbonate [2-7]. The allowed composition of a mineral is not fixed, but the chemical variations that may occur must fulfil overall charge balance in the mineral and provide a geometric fit of the substituting ions within the crystal lattice. When one ion is replaced by another of the similar size but different charge (e.g. CO_3^{2-} for PO_4^{3-}), coupled ionic substitutions may occur. This means that charge neutrality is maintained either by a second substitution by an ion with dissimilar charge or by vacancies elsewhere in the lattice [8].

Magnesium is one of the predominant substitutes for calcium in biological apatite and plays an important role in bone growth. The effect of magnesium on the formation of apatites and whitlockites was investigated for use in the treatment of osteoporosis due to biocompatibility, bioactivity and other properties that make it an excellent candidate for bone tissue engineering. [9, 10]. The amount of Mg^{2+} that can be incorporated into synthetic apatites has been studied in details and some researchers have found that it is limited to a maximum of 0.4 wt.% unless CO_3^{2-} or F^- is simultaneously incorporated [11]. Bone apatite contains approximately 7 wt. % carbonate and tooth enamel about 3.5 wt.% carbonate [4, 5]. Bone, dentine and enamel contains 0.72 wt.%, 1.23 wt.% and 0.44 wt.% of magnesium [4].

Whitlockite ($Ca_{18}Mg_2(HPO_4)_2(PO_4)_{12}$) has been widely reported in literature as magnesium rich calcium phosphate phase that occurs in biological systems such as dental calculi and young calcifying tissues [10, 12, 13]. Whitlockite can easily incorporate magnesium into structure ensuring better bioresorption under physiological conditions then HAp. Controlling the Mg substitution, the bioactivity and biocompatibility of 3D porous scaffolds based on substituted hydroxyapatite can be improved.

The production of porous scaffolds of HAp is currently the most demanding challenge of biomaterials science and technology. Hydrothermal transformation of aragonitic corals [14], algae [15], cuttlefish bone [16] and similar structure has gained interest because the resultant porous scaffolds featured similar composition and microstructure to the inorganic mineralized structure of natural bones. Several processing routes, reactors and set-ups have been proposed [16, 17]. This article reports the evolution of hydrothermal transformation of aragonite from cuttlefish bone to hydroxyapatite that is carefully studied by our research group [18-20] and continues research focusing on the area of hydroxyapatite ionic substitution.

2. EXPERIMENTAL PROCEDURE

2.1. Materials

Cuttlefish bones (*Sepia Officinalis L.*) from the Adriatic Sea were used as a starting material for the hydrothermal synthesis of hydroxyapatite scaffold. Dorsal shield was mechanically removed from the cuttlefish bones. Lamellae matrix of the bones was cut into pieces (≈ 2 cm^3) and treated with an aqueous solution of sodium hypochlorite ($NaClO$, 13% active chlorine, Gram-mol) at room temperature for 48 h and repeatedly washed with boiling demineralised water to remove the organic component. As prepared pieces of cuttlefish bone were sealed with the required volume of a 0.6 M aqueous solution of ammonium dihydrogenphosphate ($NH_4H_2PO_4$, 99 % Fisher Scientific) in a TEFLON lined stainless steel pressure vessels at 200 °C for 48 h. The self-generated pressure inside the reactor reached up to 20 bars. After hydrothermal treatment the resulting pieces of HAp scaffolds were washed with boiling demineralised water, dried at 105 °C and stored for further analysis.

Magnesium substituted samples were prepared with the same methodology, with addition of Mg^{2+} ions from magnesium chloride hexahydrate ($MgCl_2 \times 6H_2O$, Kemig, Ph.Eur.9.0) into the reactor at the beginning of the reaction with respect to (Ca+Mg)/P=10/6 molar ratio). Required quantity of magnesium was calculated that theoretically 1, 2.5, 5 and 10 percent of calcium ion was substituted with a magnesium and samples named 1-Mg-HAp, 2.5-Mg-HAp, 5-Mg-HAp and 10-Mg-HAp, respectively.

2.2. Characterization

Samples were characterized with XRD Shimadzu 6000 diffractometer (Bragg-Brentano geometry with CuKα source) with scintillation detector and goniometer radius of 185 mm. Used divergence and scattering slit were 1 ° in the primary beam, soller slits were 4.6 °, while 0.30 mm receiving slit and secondary graphite monochromator were in the secondary beam. Samples were scanned in the range of diffraction angles between 5 and 70 °with a 2θ step of 0.02 °/2 s for qualitative analysis and 0.02 °/10 s with the addition of known addition of silicon standard into the pure HAp sample for HAp structure refinement. Identification of the phases was performed by comparing the experimental XRD patterns to standards compiled by the Joint Committee on Powder Diffraction Standards (JCPDS) using the card 41-1475 for aragonite, 09-432 for HAp and 70-2064 for whitlockite.

The Rietveld structure refinement was carried out using a program DIFFRAC.SUITE TOPAS v.5.0 (Bruker) [21, 22]. The background was described by a Chebychev polynomial equation of 5th order. The peak profiles were fitted with pseudo-Voigt function. The structure of Holly Springs HAp was used as a starting model without inclusion of CO_3^{2-} in the structure [22]. Unit cell parameters, positional parameters and occupancies were varied [23]. The structure of synthetic whitlockite, $Ca_{18}Mg_2(HPO_4)_2(PO_4)_{12}$, refined by Gopal [24] and structure of aragonite [25] were used as models for remaining crystal phases.

Fourier transform infrared spectra (FTIR) were performed by attenuated total reflectance (ATR) spectroscopy of solids with a diamond crystal over the spectral range of 400 to 4000 cm^{-1}. Thermogravimetric analysis (TGA) was performed on a Netzsch STA 409 with constant synthetic air flow of 30 cm^3min^{-1} from 40 °C to 1200 °C at a heating rate of

10 °C/min. Microstructure of scaffolds was examined by scanning electron microscopy (SEM Tescan Vega III Easyprobe).

3. RESULTS AND DISCUSSION

The XRD patterns (Fig. 1) confirmed the complete transformation of aragonite cuttlefish bone to hydroxyapatite after hydrothermal reaction at 200 °C for 48 h. Main difference between hydroxyapatite sample and substituted hydroxyapatite samples is the appearance of whitlockite phase – crystal phase that contains more magnesium in structure appears when magnesium is added. Hydroxyapatite can incorporate only a limited amount of magnesium into its structure. Simultaneous incorporation with CO_3^{2-} or HPO_4^{2-} ion can promote magnesium incorporation [8]. Whitlockite is naturally found in the human body [2-4, 11, 13] and can incorporate larger amount of magnesium so it is expected that the addition of more magnesium will increase whitlockite formation. Observing XRD patterns where 5 and 10 percent of magnesium was added a small amount of aragonite can be noticed.

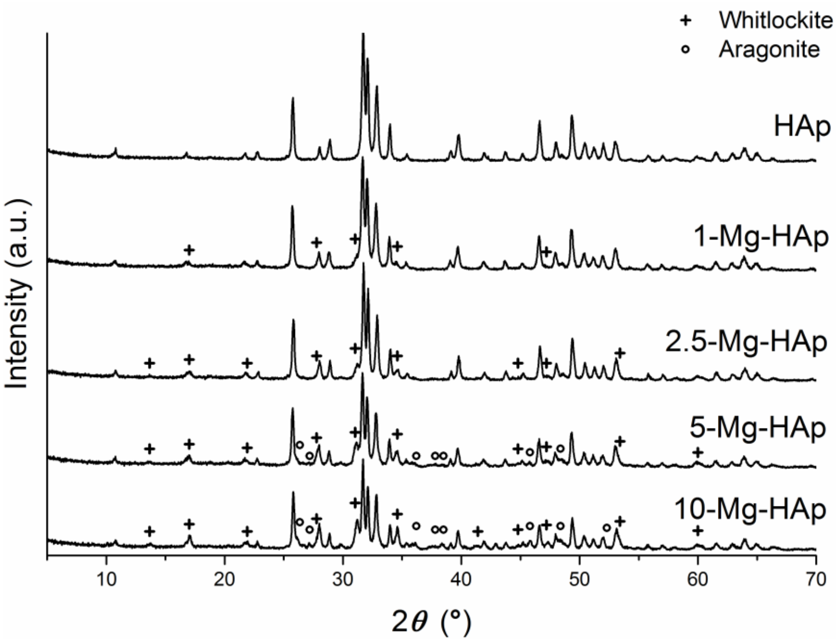

Fig. 1: XRD patterns of hydroxyapatite samples substituted with magnesium from magnesium chloride hexahydrate.

The 2θ positions of whitlockite (JCPDS 70-2064) and aragonite (JCPDS 41-1475) are marked with + and ∘, respectively. The 2θ HAp lines (JCPDS 09-432) were not marked for purposes of clarity.

Initially used Holly Springs hydroxyapatite structure refined by Sudarsannan at all. [22], after refinement of cell parameters only, showed good agreement with experimental data with some clearly visible discrepancy at sites (0 1 0), (0 2 0) and triplet at (2 1 1) – (1 1 2) – (0 3 0) at 2θ (CuKα) 10.82°, 25.81°, 31.73°, 32.12° and 32.86°, respectively. In the next step of Rietveld refinement positional parameters and occupancies were varied too. That refinement converged with smaller error; final Rwp value 6.433 is smaller and better than Rwp=10.230 when only cell parameters were refined. Fig. 2 b) clearly confirms better agreement of the refined hydroxyapatite structure with experimental data. The refined hydroxyapatite structure is further used as initial structure for refinement of samples based on magnesium substituted hydroxyapatite where only unit cell parameters were refined.

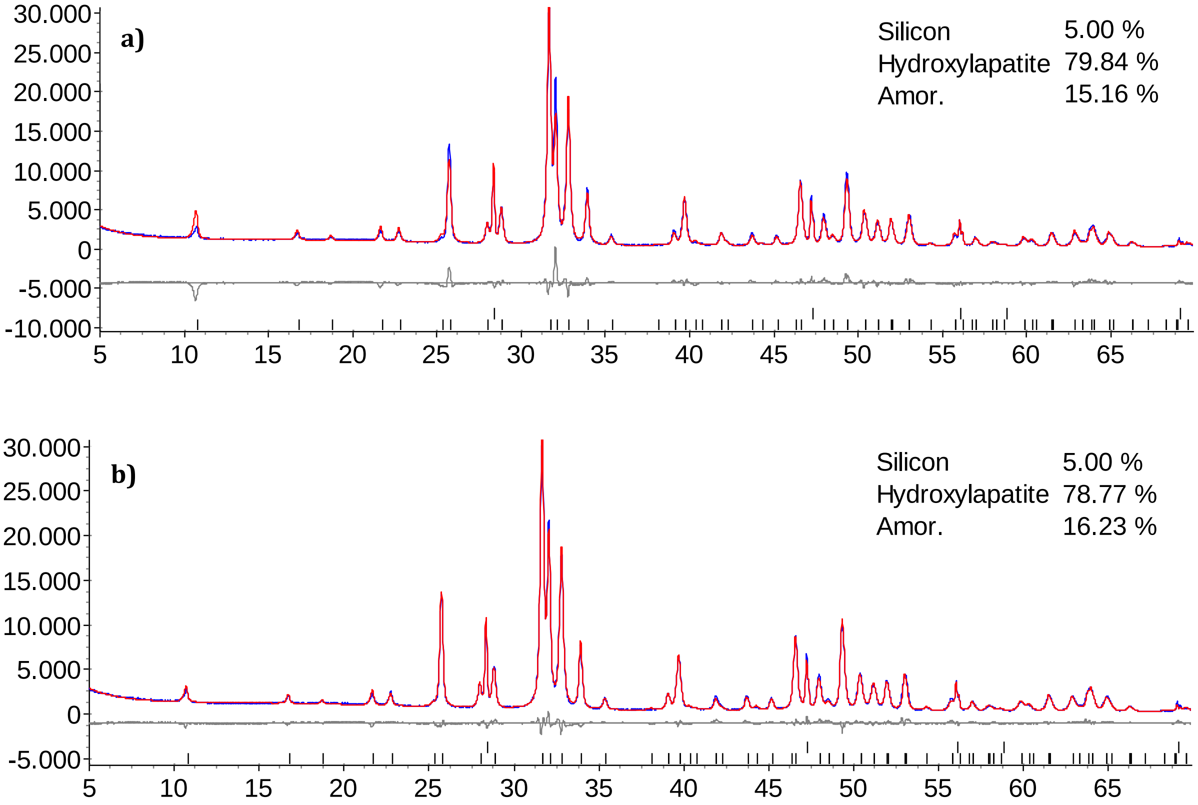

Fig. 2: Rietveld output of X-ray powder diffraction pattern of the hydroxyapatite sample with the addition of 5 wt.% of silicon standard. The red solid line is the best-fit of the profile and blue solid line is the experimental data. The difference between the experimental and fitted patterns is shown under the diffraction pattern. Line markers on the bottom of the figure indicate the position of Bragg reflections for hydroxyapatite (lower line markers) and silicon (higher line markers). Figure 2 a) Holly Springs hydroxyapatite structure [22] with only cell parameters varied and Figure 2 b) with unit cell parameters, positional parameters and occupancies varied.

The Rietveld refinement confirmed appearance of an amorphous phase in the pure hydroxyapatite sample. After 5.00 wt.% of silicon standard as internal standard was added and carefully homogenised into the HAp sample, calculations showed difference between modelled and real silicon content (5.89 wt.% with deviation 0.077°wt.% for non-refined hydroxyapatite structure and 5.97 wt.% with deviation of 0.048 wt.% for refined hydroxyapatite structure). Appearance of amorphous phase in hydroxyapatite samples is known and described in the literature as a consequence of amorphous noncrystalline apatite phases [3, 26].

Refined unit cell parameters of HAp are given in Table 1. Positional parameters and occupancies in initial Holly Springs HAp structure and experimental HAp refined structure are reported in Table 2.

Tab. 1: Values of refined unit cell parameters of hydroxyapatite

Cell parameters	**HAp, refined cell parameters**	**HAp, refined structure**
***a*, Å**	9,43280	9,43246
***c*, Å**	6,89791	6.89785
Cell volume, Å^3	531,532	531,489

Rwp	10,230	6,433

*initial Holly Springs hydroxyapatite unit cell parameters: $a = 9.4240$ Å, $c = 6.8790$ Å

Tab. 2: Values of positional parameters and occupancies in initial Holly Springs HAp structure and experimental HAp refined structure

			Holly springs HAp structure					**Refined HAp structure**			
	Np		x	y	z	occ		x	y	z	occ
Ca1	4		1/3	2/3	0.0013	1		1/3	2/3	0.0007	1.003
Ca2	6		0.2465	0.9931	1/4	1		0.2470	0.9919	1/4	1.026
P1	6		0.3983	0.3683	1/4	1		0.3945	0.3693	1/4	0.931
O1	6		0.3282	0.4846	1/4	1		0.3302	0.4789	1/4	1.051
O2	6		0.5876	0.4652	1/4	1		0.5788	0.4608	1/4	1.043
O3	12		0.3433	0.2579	0.0704	1		0.3340	0.2500	0.0713	0.958
O4	4		0	0	0.1978	0,5		0	0	0.1807	0.594
H1	4		0	0	0.0608	0,5		0	0	0.0608	0.594*

*the H1 occupancy parameter was set to the same value as refined O4 occupancy parameter

The formula given by the unit cell content for hydroxyapatite sample with refined structure is $Ca1_{4.012}Ca2_{6.156}(PO_4)_{5.586}(CO_3)_{0.5148}(OH)_{2.3768}$.

The amount of CO_3^{2-} incorporated in the structure of HAp was calculated under the constraint that the ratio of calcium sites per unit cell to sum of PO_4^{3-} and CO_3^{2-} is ten to six. The calculated molar ratio of Ca/P is 1.8203 which is higher than the stoichiometric value (1.6667) indicating presence of carbonate in the structure, further confirmed by the FTIR spectra (Fig. 3).

Nonstoichiometric carbonated hydroxyapatite is the main component of bone and calculated hydroxyapatite formula indicates that synthesised nonstoichiometric hydroxyapatite should have improved biological properties and bioactivity compared to synthetic stochiometric apatite [4, 6, 8, 27].

Quantitative analysis of samples based on hydroxyapatite substituted with a magnesium shows increase of whitlockite content as more magnesium is added into the initial synthesis solution, Table 3. Additionally, samples 5-Mg-HAp and 10-Mg-HAp have small amount of aragonite which indicate that at our synthesis conditions, where high quantity of magnesium chloride is added, reaction had not fully transformed aragonite to hydroxyapatite and whitlockite.

Tab. 3: Results of quantitative analysis of hydroxyapatite samples substituted with magnesium from magnesium chloride hexahydrate (Mg-HAp)

Content, wt %	**1-Mg-HAp**	**2.5-Mg-HAp**	**5-Mg-HAp**	**10-Mg-HAp**
Hidroksiapatite	90,15	80,81	66,76	58,48
Whitlockite	9,85	19,19	30,37	34,10
Aragonite			2,87	7,42

Unit cell parameters and unit cell volume data, Table 4., show that whitlockite crystal unit cell contracts as more magnesium is added into the initial reaction solution. Those results can be explained and confirmed by considering the fact that magnesium ionic radius is smaller than calcium ionic radius and that whitlockite unit cell can incorporate different amount of magnesium ($Ca_{20-x}Mg_x(HPO_4)_2(PO_4)_{12}$) [10, 28-30]. In literature it is found that changes in hydroxyapatite cell dimensions follow the same principle, but our data showed no dependence on adding magnesium content.

Tab. 4: Unit cell parameters of whitlockite in samples of hydroxyapatite substituted with magnesium from magnesium chloride (Mg-HAp).

	1-Mg-HAp	**2.5-Mg-HAp**	**5-Mg-HAp**	**10-Mg-HAp**
***a*, Å**	10,37207	10,36648	10,36063	10,35369
***c*, Å**	37,24808	37,21525	37,23316	37,18847
Cell volume, Å^3	3470,29	3463,49	3461,25	3452,46

Fourier transform infrared spectra are shown in Fig. 3. The band at 1087 cm^{-1} corresponds to the vibration of the HPO_4^{2-} group present in the HAp sample, meaning that nonstoichiometric HPO_4^{2-} containing hydroxyapatite is formed. At the same wave number, the HPO_4^{2-} band appeared in all Mg-HAp samples, but is losing intensity by increasing magnesium content. According to the literature, the presence of this group suggests that Mg^{2+} ions have been incorporated into HAp structure [31].

PO_4^{3-} groups show a significant reduction in intensity by increasing the magnesium content relative to pure HAp. In the FTIR spectrum of the magnesium-rich samples, 5 and 10% Mg-HAp, spread and deconvolution of the PO_4^{3-} band at the 993 cm^{-1} and about 1062 cm^{-1} is visible, indicating the whitlockite formation. Moreover, appearance of low intensity bands at 922 cm^{-1} and 1134°cm^{-1} are in agreement with the increasing whitlockite content formation [32].

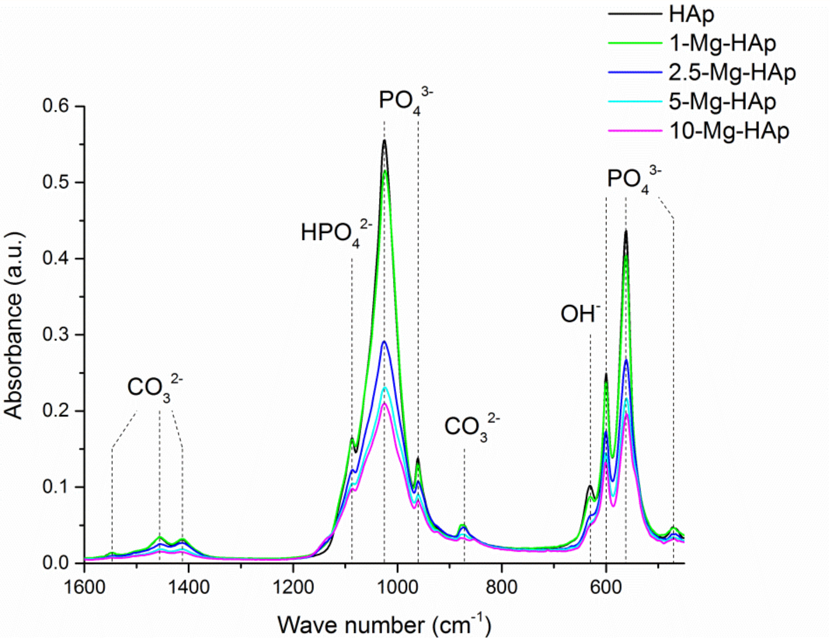

Fig. 3: Infrared spectrum of HAp and samples substituted with magnesium from magnesium chloride hexahydrate (Mg-HAp) over the spectral range of 1600 to 450 cm^{-1}.

From the Fig. 3 it is apparent that the increase in magnesium concentration leads to a reduction of CO_3^{2-} and OH^- groups intensity.

Carbonated HAp is closer to the chemistry of natural human bone than stoichiometrically pure HAp [6, 27] and has been shown experimentally to have enhanced biocompatibility [8, 33]. There are two types of carbonate substitution in HAp. The carbonate substitute either on the phosphate tetrahedral sites (B-type) or on the hydroxyl sites (A-type) or both (AB-type) [8, 31].

Synthetically, A-type carbonated hydroxyapatite, where CO_3^{2-} replaces OH^-, can be produced only at very high temperature (solid-state reactions at 1000 °C), whereas synthetic B-type carbonated apatite precipitates from solutions in the temperature range of 50-100 °C [8, 31]. It is possible to produce mixed A-type/B-type carbonated hydroxyapatite in the laboratory [34]. Based on synthetic samples, it is well documented that this so-called B-type carbonate substitution causes changes in various physical properties in hydroxyapatite, such as decreases in the *a*-axial length, the overall crystallite size, and the thermal stability, and increases in the *c*-axial length, the amount of crystallographic microstrain and the solubility. The higher solubility of carbonate-containing apatite compared to carbonate-free apatite is in part due to the fact that the $Ca–CO_3^{2-}$ bonds are weaker than the $Ca–PO_4^{3-}$ bonds, thus making the carbonated apatite more susceptible to acid dissolution [5].

Bands at 872 cm^{-1}, 1412 cm^{-1} and 1456 cm^{-1} confirm the formation of B-type carbonated hydroxyapatite that is common for biological apatite where CO_3^{2-} dominantly replaces PO_4^{3-} [5, 35]. Further analysis of the spectra indicates the presence of a small amount of the A-type substituted HAp as suggested by CO_3^{2-} band at 1547 cm^{-1} and the very weak band at 879 cm^{-1} [35]. Biological apatites, which constitute bone mineral, feature mixed AB-type substitutions [36]. As this analysis indicates the formation of AB mixed type carbonated HAp after hydrothermal transformation of the cuttlefish bone, therefore the produced scaffolds may have a great potential as bone substitutes.

The observed FTIR spectral changes can be related to a decrease in the relative amount of HAp phase and destabilization of HAp structure by incorporating Mg^{2+}, while simulating the formation of whitlockite phase. These changes are in agreement with results obtained from XRD analysis, thereby Mg^{2+} and CO_3^{2-} incorporated in the HAp structure, a decrease of the sample crystallinity and whitlockite formation are confirmed.

Thermal stability of the HAp is evident from the thermogravimetric curve obtained up to 1200 °C (Fig. 4.). The total weight loss of the HAp sample of about -5.1 wt.% can be attributed to the loss of physically and chemically absorbed water and CO_2 elimination as a result of the decarbonation process in the range 600-1200 °C.

Samples based on magnesium hydroxyapatite substituted materials show a rapid decrease in weight at around 700 °C that is a unique phenomenon of whitlockite phase during thermal treatment. Weight loses of 1, 2.5, 5 and 10 % $MgCl_2$-HAp samples are -5.3, -6.7, -8.8 and -10.7 wt.%, respectively. Whitlockite, ($Ca_{18}Mg_2(HPO_4)_2(PO_4)_{12}$) loses its HPO_4^{2-} group due the dehydration and transforms into the magnesium substituted beta-tricalcium phosphate (β-$Ca_{3-x}Mg_x(PO_4)_2$ [10, 12, 24, 37].

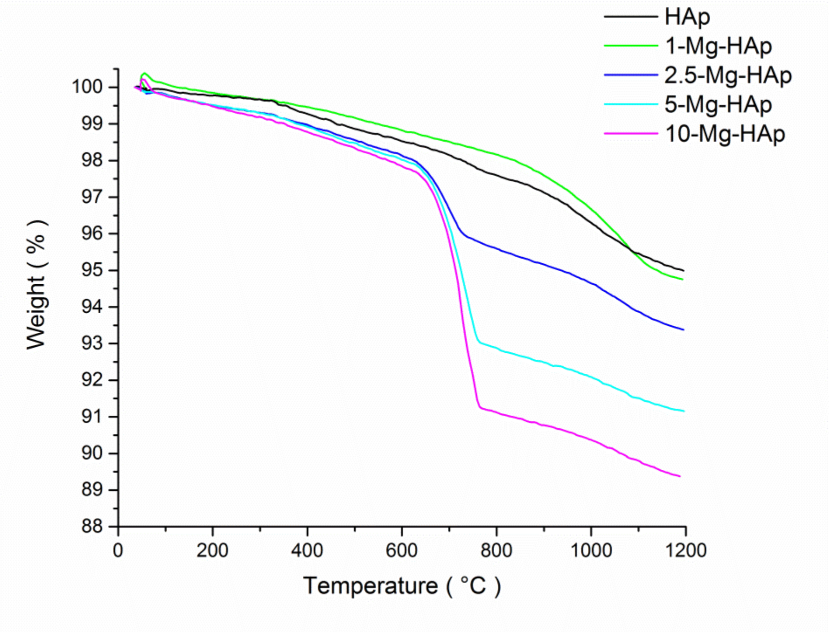

Fig. 4: Thermal decomposition of HAp and samples substituted with magnesium from magnesium chloride hexahydrate (Mg-HAp) heated from 40 to 1200 °C at constant synthetic air flow of 30 $cm^3 min^{-1}$ with a heating rate of 10 °C/min.

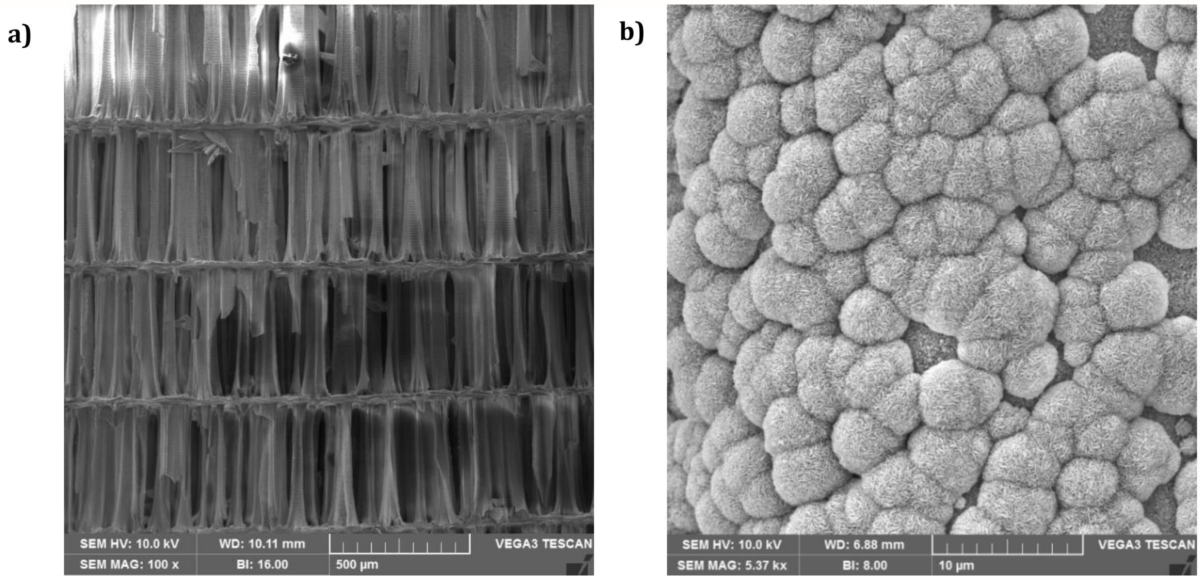

Fig. 5: SEM micrographs of hydroxyapatite sample.

The microstructure of the prepared materials was investigated by SEM analysis (Figs. 5-7). All micrograph images show the inner surface of the material. SEM micrograph of hydroxyapatite sample shows that the original highly porous interconnected structure is completely preserved after the hydrothermal conversion (Fig. 5 a)). At higher magnification it can be seen that HAp crystals form spherical shapes (cauliflower morphology), which cover the surface evenly (Fig. 5 b)).

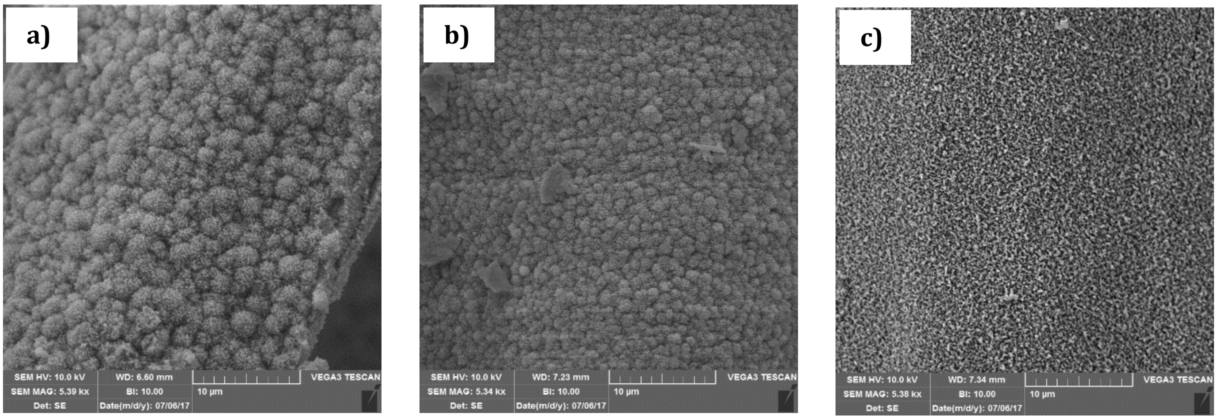

Fig. 6: SEM micrographs of hydroxyapatite samples with different magnesium proportions substituted from magnesium chloride hexahydrate.
Fig. (a) 1-Mg-HAp, Fig. b) 2.5-Mg-HAp and Fig. c) 5-Mg-HAp.

SEM micrographs of hydroxyapatite samples with different magnesium proportions show that the addition of magnesium to the hydrothermal reaction changes the surface morphology with respect to pure HAp. With the increase of magnesium content, HAp still crystallizes in the form of spheres, but smaller than those in the case of pure HAp (Fig. 6 a), b), c)). Similar results were also found in the literature [38].

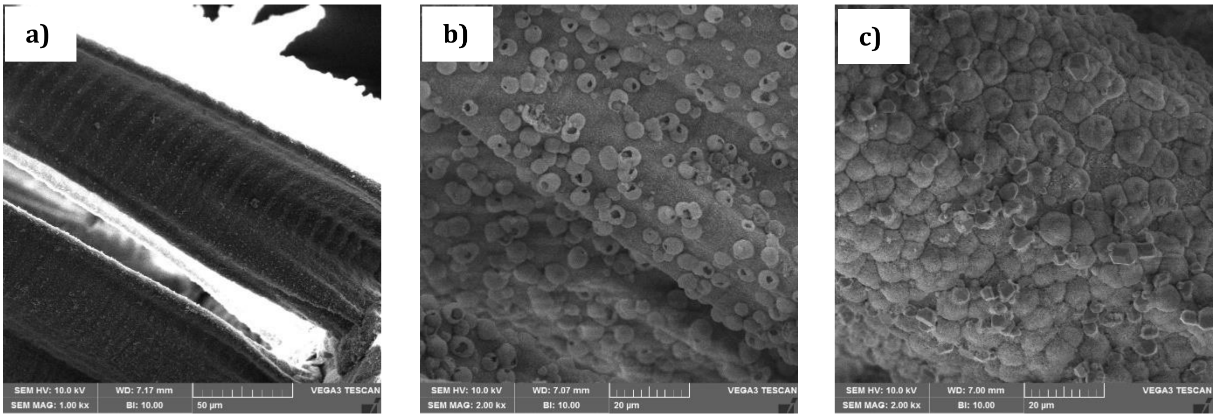

Fig. 7: SEM micrographs of different surface regions of the 10-Mg-HAp sample.

SEM micrographs of 10-Mg-HAp sample show that high magnesium content affect surface homogeneity and that different inhomogeneous regions with different form of agglomerates can be identified. On Fig. 7. c) on the cauliflower like hydroxyapatite surface whitlockite crystals can clearly be identified [39]. High whitlockite content (more than 34 wt.%) and small percent of unreacted aragonite (around 7 wt.%) combined with the fact that skeletal magnesium is located on the surface of hydroxyapatite or in the hydrated layer around the crystal [7] could explain appearance of inhomogeneous surface distribution of crystals.

4. CONCLUSION

The highly porous interconnected cuttlefish bonelike structure is completely preserved after the hydrothermal conversion of cuttlebone. HAp structure is substituted with HPO_4^{2-} and B-type carbonate. The calculated molar ratio of Ca/P=1.8203 confirms the nonstoichiometric hydroxyapatite structure with formula $Ca1_{4.012}Ca2_{6.156}(PO_4)_{5.586}(CO_3)_{0.5148}(OH)_{2.3768}$, given by the unit cell content for refined structure. With the increase of magnesium concentration, more whitlockite phase ($Ca_{10-x}Mg_x(HPO_4)(PO_4)_6$) was formed. Results confirmed that whitlockite crystal unit cell contracts as more magnesium is added into the initial reaction solution. At the highest concentration of magnesium, 10-Mg-HAp, SEM micrographs showed inhomogeneous regions and clearly visible whitlockite crystals. Based on available literature, further investigation and *in vitro* experiments are expected to confirm that synthesised scaffolds based on the magnesium substituted hydroxyapatite should have improved biological properties and bioactivity compared to synthetic stoichiometric hydroxyapatite.

Acknowledgement:
This study is a part of research project HaTEA "Development of Biocompatible Hydroxyapatite Based Materials for Bone Tissue Engineering Applications", **IP-2014-09-3752**, supported by the Croatian Science Foundation. The authors are grateful for this support.

REFERENCES

[1] Posner, A. S., Perloff A., Diorio A. F., Refinement of the hydroxyapatite structure, Acta Cryst., 11, pp. 308-309, (1958).

[2] LeGeros R. Z., Daculsi G., Kijkowska R., Kerebel B., The effect of magnesium on the formation of apatites and whitlockites, in: Itokawa Y., Durlach J. (Eds.), Magnesium in Health and Disease, John Libbey, New York, pp. 11-19, (1989)

[3] Lala S., Ghosh M., Das P. K., Das D., Kar T., Pradhan S. K., Magnesium substitution in carbonated hydroxyapatite: Structural and microstructural characterization by Rietveld's Refinement, Mater. Chem. Phys., 170, pp. 319-329, (2016).

[4] LeGeros R. Z., Kijkowska R., Bautista C., LeGeros J. P., Synergistic effects of magnesium and carbonate on properties of biological and synthetic apatites, Connect. Tissue Res., 33, pp. 203-209, (1995).

[5] Elliott J. C., Calcium phosphate biominerals, Rev. Mineral. Geochem., 48, pp. 427-453, (2002).

[6] Vallet-Regí M., Arcos D., "Biomimetic Nanoceramics in Clinical Use: From Materials to Applications", 2008, R. Soc. Chem. Cambridge

[7] Laskus A., Kolmas J., Ionic substitution in non-apatitic calcium phosphates, Int. J. Mol. Sci., 18, pp. 2542, (2017).

[8] Wopenka B., Pasteris J. D., A mineral perspective on the apatite in bone, Mater. Sci. Eng. C-Mater., 25, pp. 131-143, (2005).

[9] LeGeros R. Z., Mijares D., Yao F., Tannous S., Catig G., Xi Q., Dias R., LeGeros J. P., Synthetic bone mineral (SBM) for osteoporosis therapy: Part 1 - Prevention of bone loss from mineral deficiency, Key. Eng. Mater., 361-363, pp. 43-46, (2008).

[10] Jang H. L., Jin K., Lee J., Kim Y., Nahm S. H., Hong K. S., Nam K. T., Revisiting whitlockite, the second most abundant biomineral in bone: nanocrystal synthesis in physiologically relevant conditions and biocompatibility evaluation, ACS Nano, 8, pp. 634-641, (2014).

[11] Bigi A., Falini G., Foresti E., Gazzano M., Ripamonti A., Roveri N., Magnesium influence on hydroxyapatite crystallization, J. Inorg. Biochem., 49, pp. 69-78, (1993).

[12] Gopal R., Calvo C., Structural relationship of whitlockite and β-$Ca_3(PO_4)_2$, Nat. Phys. Sci., 237, pp. 30-32, (1972).

[13] Lagier R., Baud C. A., Magnesium whitlockite, a calcium phosphate crystal of special interest in pathology, Pathol. Res. Pract., 199, pp. 329-335, (2003).

[14] Sartoris D. J., Gershuni D. H., Akeson W. H., Holmes R. E., Resnick D., Coralline hydroxyapatite bone graft substitutes: preliminary report of radiographic evaluation, Radiology, 159, pp. 133-137, (1986).

[15] Walsh P. J., Buchanan F. J., Dring M., Maggs C., Bell S., Walker G. M., Low-pressure synthesis and characterisation of hydroxyapatite derived from mineralise red algae, Chem. Eng. J., 137, pp. 173-179, (2008).

[16] Rocha J. H. G., Lemos A. F., Kannan S., Agathopoulos S., Ferreira J. M. F., Hydroxyapatite scaffolds hydrothermally grown from aragonitic cuttlefish bones, J. Mater. Chem., 15, pp. 5007-5011, (2005).

[17] Ben-Nissan B., Milev, Vago R., Morphology of sol–gel derived nano-coated coralline hydroxyapatite, Biomaterials, 25, pp. 4971-4975, (2004).

[18] Ivanković H., Tkalčec E., Orlić S., Gallego Ferrer G., Schauperl Z., Hydroxyapatite formation from cuttlefish bones: kinetics, J. Mater. Sci.-Mater. M., 21, pp. 2711-2722, (2010).

[19] Milovac D., Gallego Ferrer G., Ivanković M., Ivanković H., PCL-coated hydroxyapatite scaffold derived from cuttlefish bone: Morphology, mechanical properties and bioactivity, Mater. Sci. Eng. C-Mater., 34 pp. 437-445, (2014).

[20] Rogina A., Ivanković M., Ivanković H., Preparation and characterization of nano-hydroxyapatite within chitosan matrix, Mater. Sci. Eng. C-Mater., 33, pp. 4539-4544, (2013).

[21] TOPAS V4: General profile and structure analysis software for powder diffraction data. - User's Manual, Bruker AXS, Karlsruhe, Germany, (2002).

[22] Sudarsanan K., Young R. A., Significant precision in crystal structural details: Holly Springs hydroxyapatite, Acta Crystallogr. B, 25, pp. 1534-1543, (1969).

[23] Coelho A., Whole profile structure solution from powder diffraction data using simulated annealing, J. Appl. Cryst., 33, pp. 899-908, (2000).

[24] Gopal R., Calvo C., Ito J., Sabine W. K., Crystal structure of synthetic Mg-whitlockite, $Ca_{18}Mg_2H_2(PO_4)_{14}$, Can. J. Chem., 52, 1155-1164, (1974).

[25] Caspi E. N., Pokroy B., Lee P. L., Quintana J. P., Zolotoyabko E., On the structure of aragonite, Acta Crystallogr. B, 61, pp. 129-132, (2005).

[26] Dorozhkin S. V., Amorphous calcium orthophosphates: Nature, chemistry and biomedical applications, Int. J. Mater. Chem., 2, pp. 19-46, (2012).

[27] Bigi A., Cojazzi G., Panzavolta S., Ripamonti A., Roveri N., Romanello M., Suarez K. N., Moro L., Chemical and structural characterization of the mineral phase from cortical and trabecular bone, J. Inorg. Biochem., 68, pp. 45-51, (1997).

[28] Suchanek W. L., Byrappa K., Shuk P., Riman R. E., Janas V. F., TenHuisen K. S., Mechanochemical-hydrothermal synthesis of calcium phosphate powders with coupled magnesium and carbonate substitution, J. Solid State Chem., 177, pp. 793-799, (2004).

[29] Danil'chenko S. N., Kulik A. N., Bugai A. N., Pavlenko P. A., Kalinichenko T. G., Ul'yanchich N. V., Sukhoduba L. F., Determination of the content and localization of magnesium in bioapatite of bone, J. Appl. Spectrosc., 72, pp. 899-905, (2005).

[30] Kannan S., Lemos A. F., Rocha J. H. G., Ferreira J. M. F., Characterization and mechanical performance of the Mg-stabilized β-$Ca_3(PO_4)_2$ prepared from Mg-substituted Ca-deficient apatite, J. Am. Ceram. Soc., 89, pp. 2757-2761, (2006).

[31] LeGeros R. Z., Calcium phosphates in oral biology and medicine, Monogr. Oral Sci., 15, pp. 109-111, (1991).

[32] Aina V., Lusvardi G., Annaz B., Gibson I. R., Imrie F. E., Malvasi G., Menabue L., Cerrato G., Martra G., Magnesium- and strontium-co-substituted hydroxyapatite: the effects of doped-ions on the structure and chemico-physical properties, J. Mater. Sci.-Mater. M., 23, pp. 2867-2879, (2012).

[33] Ellies L. G., Carter J. M., Natiella J. R., Featherstone J. D. B., Nelson D. G. A., Quantitative analysis of early *in vivo* tissue response to synthetic apatite implants, J. Biomed. Mater. Res. A, 22, pp. 137-48, (1988).

[34] Suetsugu Y., Takahashi Y., Okamura F. P., Tanaka J., Structure analysis of A-type carbonate apatite by a single-crystal X-ray diffraction method, J. Solid State Chem., 155, pp. 292-297, (2000).

[35] El Feki H., Rey C., Vignoles M., Carbonate ions in apatites: Infrared investigations in the v4 CO_3 domain, Calcif. Tissue Int., 49, pp. 269-274, (1991).

[36] Elliott J. C., Holcomb D. W., Young R. A., Infrared determination of the degree of substitution of hydroxyl by carbonate ions in human dental enamel, Calcif. Tissue Int., 37, pp. 372-375, (1985).

[37] Calvo C., Gopal R., Crystal-structure of whitlockite from Palermo Quarry, Am. Mineral., 60, pp. 120-133, (1975).

[38] Tampieri A., Celotti G. C., Landi E., Sandri M., Magnesium doped hydroxyapatite: synthesis and characterization, Key Eng. Mater., 264, pp. 2051-2054, (2004).

[39] Rey C., Combes C., Drouet C., Grossin D., Bertrand G., Soulié J., Bioactive calcium phosphate compounds: Physical chemistry, Compr. Biomater. II, pp. 244-290, (2017).

THE EFFECTS OF ECOLOGICAL PROPERTIES ON THE ASSESSMENT OF PAPERBOARD PROPERTIES FOR PACKAGING

Josip Bota, **Maja Brozović**, **Dorotea Kovačević, Jurica Dolić**

Faculty of Graphic Arts University of Zagreb, Department of Graphic Design and Imaging,
Getaldićeva 2, Zagreb, Croatia

Abstract

It is known that consumers choose product based on packaging and its design, but the type of paperboard used is also one of the important factors that can improve visual impressions. This study investigates how consumers perceive packaging paperboard in relation with its composition and how they link paperboards with different types of products. Recycled and non-recycled paperboards were characterized by testing optical and mechanical properties. The same samples were given to participants to assess the price, quality and sustainability of the material and to link the samples to different product types. It was found that even though there is a small difference in optical properties the consumers can easily spot the difference. Also, the study presents how the participants assessed the use of recycled and non-recycled paperboards in correlation with different product types (food, pharmaceuticals, tobacco, cosmetics and hygienic products)

Keywords: *Recycled paperboard, packaging, ecological properties, consumer perception*

1. INTRODUCTION

In recent years paperboard and cardboard production are in constant rise. Statistical data indicates a constant increase in production of paper and cardboard (see Figure 1). The rise of demand is mostly because of the global increase of packaging production. Almost half (40-50%) of cellulose material waste is acquired from packaging [1]. On April 4th 2016 Transparent Market Research announced that the cardboard and paperboard industry is worth $ 122.69 billion, and by 2024 it is projected to be worth $ 227.47 billion [2]. In 2009 Smithers Pira's 2010 report states that 38% of the packaging industry was oriented towards cellulose material [3] and a report from 2014 stated that 42% of luxury packaging were made from paperboards and cardboard[4]. Paperboard packaging is one of the most widely used on the market. Its life-span can be from one day to multiple months or even years. Function of packaging is to protect the product form mechanical damage and decay, safe transportation and distribution, to inform customers and to promote the product through design activity [5]. In order to achieve these goals packaging material needs to meet a wide range of physical, mechanical and optical properties. It should be resistant to temperature oscillations, adapted for print and coatings, resistant to wear and tear and yet suitable for moulding, with an addition of meeting high aesthetic standards [6].

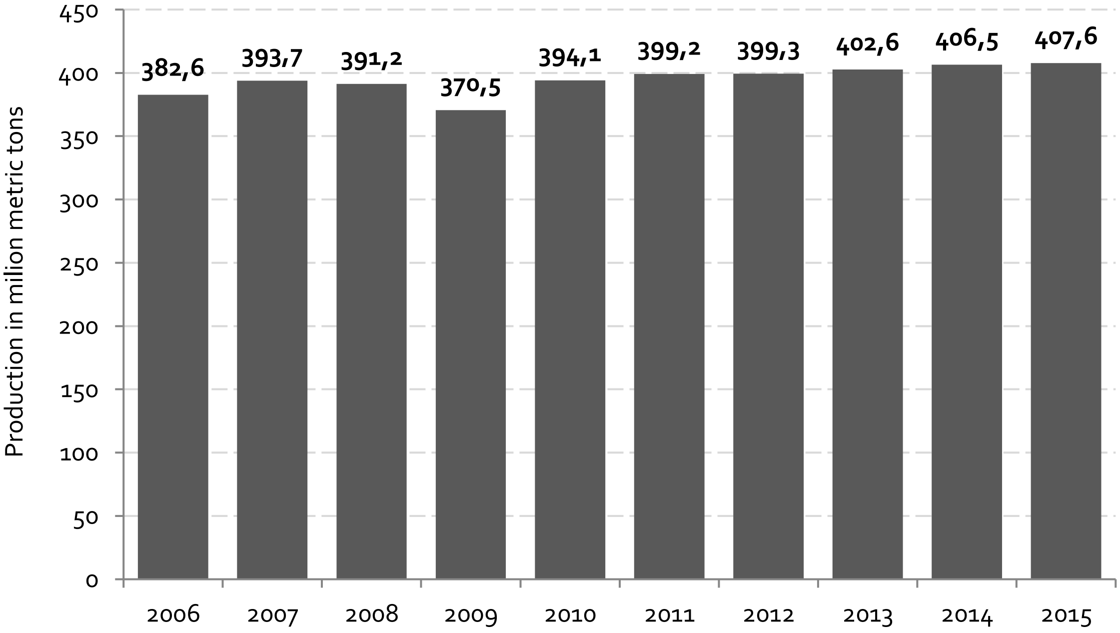

Fig 1: Production volume of paper and cardboard worldwide 2006 to 2015 (in million metric tons) [7]

Today's packaging materials meet most of the requirements. Economic and environmental needs constantly emphasize the necessity to improve and find more efficient and cost-effective packaging materials. There is a constant comparison of recycled and pure cellulose as a packaging material. Recycled cellulose materials are economically viable and environmentally friendly. Paperboards with pure cellulose have a high percentage of primary fibres and the purity of the composition enables better printing properties and excellent features for embossed printing and structural design. The European Parliament and Council Directive 94/62/EC of 20 December 1994 on packaging and packaging waste has a goal on minimizing the effect of packaging and packaging waste on the environment by setting targets for recovery and recycling; encouragement of the use of recycled packaging materials in the manufacturing of packaging and other products; minimization of packaging volume and weight, and to design packaging that allows its reuse or recovery. Recycled cardboard may have some health and technological issues. It may contain contaminants that can cause odour and may not be suitable for packaging sensitive products where it is essential to preserve flavour, taste and/or hygiene. Also it can contain elements of plastics and glue which can lead to problems in the production line of recycled paperboards. On the other hand recycled cellulose help preserving resources which is a important advantage. Today's paperboards are often produced as a combination of recycled and non-recycled cellulose in order to obtain the optimal ratio between quality and savings [1].

One study in New Zealand showed that in conditions of high relative humidity conditions, paperboards with pure cellulose showed better mechanical properties than recycled. In all samples, the non-recycled cardboard had higher compression strength [8]. It is known that the mechanical strength of recycled cellulose material decreases after the first recycle and even more after the second, so sorting of paperboard can also lead to recycled paperboards with better properties [9].

The aim of this paper is to characterise tested paperboard samples and to determine consumer preferences towards recycled and non- recycled packaging material according to their quality, price and sustainability.

Recycled and non-recycled paperboards are independent variables and quality, price and sustainability are dependent variables.

1.1. Hypotheses:

H1 - Non-recycled paperboard leaves an impression of higher quality.

H2 - Non-recycled paperboard leaves an impression of higher cost.

H3 - Recycled paperboard is perceived as more sustainable than non- recycled paperboard.

H4 - Consumers link recycled and non-recycled with certain types of product.

2. METHODOLOGY

2.1. Materials

Two types of paperboard were used in the study. Umka color® 280 g/m2 GD2 paperboard with a high percentage of recycled/secondary fibres and a GC2 paperboard Allyking® 270 g/m2 made from virgin mechanical pulp.

2.2. Methods

Optical and mechanical properties

The paperboard samples were first characterized to confirm the difference in optical and mechanical properties. The Technidyne Color Touch 2® spectrophotometer was used to determine the surface colour and brightness of the paperboard. Dimensions of the tested paperboard samples were 50 x 50 mm. The instrument and the number of test samples are in compliance with the ISO optical and CIE Lab standards [10,11]. Mechanical properties of the samples were defined calculating their Bursting Index (x) as one of the most important properties of paperboard. It was measured using Lorentzen & Wettre Bursting Strength Tester (ISO 2758:2001). Dimensions of the tested paperboard specimen were d=100 mm, measuring range d=50 mm, and the device diaphragm had a diameter d=33,1 mm. The number of samples is determined according to ISO 2758:2001. The index was calculated using the formula:

$$x = \frac{p}{g}$$

x - bursting index (kPa·m2/g)

p - bursting strength (kPa)

g - paper grammage (g/cm2)

Interview

A structured interview was chosen for data collection because it was necessary for the participants to see and feel the prepared paperboard samples. 30 people participated in the study.

There were two paperboard samples cut to the 6 cm x 10 cm dimension. The size of the samples was chosen to simulate the dimension of common packaging size. The samples were divided into two groups according to degree of recyclable material: recycled and non- recycled.

At the beginning of the interview the paperboard samples were given to participants with no explanations. They were allowed to touch and observe the samples but they were not allowed to turn them over so they would assume what type of paperboard was used for the sample production. Then the participants evaluated the sample using a 5 point scale (1 was the lowest and 5 the highest grade) according to tested product characteristics: price, quality and sustainability of products packaged in that type of paperboard.

After the evaluation task, the participants were asked to link a list of product types with the paperboard samples. In this task, they could assign more samples to certain product type or none.

3. RESULTS AND DISCUSSION

3.1. Characterization

As expected characterisations of the paperboard optical properties (Table 1) showed that recycled paperboards have lower lightness values than non-recycled. This is common for recycled paperboards due to the multiple layers of recycled cellulose below the top layer. The positive *CIE b* values of non-recycled paperboard indicate that the tint shift is in the orange hue while recycled paperboard has a blue tint. The blue coloration is usually used to compensate the grey-ish tint that emerges from the lower recycled layers.

Tab 1: CIE Lab values of front and back sides of recycled and non-recycled paperboard

	L	**a**	**b**	**tint**
recycled (GD2)	91,94	0,22	-2,77	1,18
non-recycled (GC2)	93,31	0,04	1,89	-1,13

Table 2 presents that ISO brightness measurements of recycled and non-recycled paperboard show some slight difference in value. Brightness is the percentage of white as a direct reflection, measured in the blue range of the visible spectrum and has an impact on readability and colour intensity so it is important for producers to get similar effects no matter the paperboard used.

Tab 2: ISO brightness of recycled and non-recycled paperboard

	ISO brightness ©
recycled (GD2)	81,34
non-recycled (GC2)	81,42

The mechanical properties were tested defining the bursting index of paperboard samples. This method is the most representative because it stresses the sample using multiple forces simultaneously and is not affected by paper grammage. The results show (Table 3) expected difference between recycled and non-recycled paperboard because recycled paperboards have shorter cellulose fibres which significantly affect the mechanical properties [12].

Tab 3: Burst strength of recycled and non-recycled paperboard

	Burst index (kPa·m2/g)	max	min	st. dev
recycled (GD2)	1,21	1,33	0,98	0,09
non-recycled (GC2)	1,89	2,1	1,7	0,12

3.2. Interview

The results of the assessment (Table 4) showed that participants assessed the products in the non-recycled paperboard as more expensive while linking the recycled paperboard with cheaper products. Similar results were obtained in the assessment of quality. From the obtained results we can assume that attributes of price and quality are linked. As expected the recyclable paperboard was graded as more sustainable.

Tab 4: Assessments of price, quality and sustainability of paperboards (mean grade)

	price	quality	sustainability
recycled (GD2)	1.5	1.3	4,1
non-recycled (GC2)	4.2	4.3	1.3

Even though the characterisation measurements did not show big difference in CIE Lab values and ISO brightness these results show that human perception can identify the difference. But it should be taken into account that there is also a difference in surface texture of GC2 and GD2 paperboard which can also contribute in in quality assessment. It is also important to note that research found that consumer will accept paper with a wider range of colour tint if they are aware that the paper is being recycled [13].

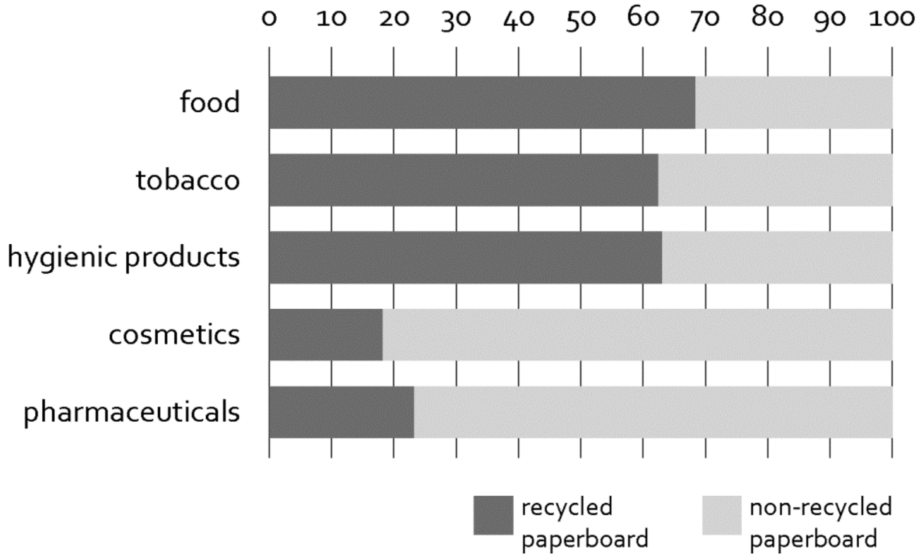

Fig. 2: The results of product type selection according to paperboard sample

From the results of assigning product type (Figure 2) to the type of paperboard sample it is shown that most recyclable paperboard is mostly linked to food produce, a little less with tobacco and hygienic products. Non-recycled samples are mostly connected with cosmetics and pharmaceuticals (food supplements included). The results showed that customers are more inclined to connect non-recycled paperboards with high-end products (higher quality and price range). Recycled paperboards are considered to be more sustainable with lower quality and price. This confirms the first three hypotheses.

The participants are more prone to link food, tobacco and hygienic products with recycled paperboard while relating pharmaceutical and cosmetic products with recycled paperboards. This is an interesting result because tobacco packaging mostly uses paperboards made from virgin cellulose. This lapse in assessment should be investigated more in depth to reveal its connection with recycled paperboard. One explanation can be that consumers perceive tobacco as a natural product, so they connect it with sustainable paperboards.

These findings can help producers to choose materials according to what they want to communicate. It is important to note that materials are not only used for communication or because of their economic factors. Some products, like food and pharmaceutical products need to use non-recycled paperboard to decrease the possibility of contamination.

Also, recycled paper is used in the industry for a longer time and because of that consumers perceive it as a lower functional risk (low probability of bad performance, low cost, and no risk of physical harm to the purchaser or user) [14], so producers should not hesitate to use recyclable materials whenever possible. Further research should try to establish causative factors of why certain paperboards have different impressions on consumers. This would help understand are their assessments based on experience, knowledge or first impressions.

4. CONCLUSION

The characterisation of the paperboard samples showed a small degree of difference in the optical properties of recycled and non-recycled paperboard while a much more notable difference was observed in the mechanical properties.

Through the interview a link was found between the degree of recycled cellulose material in the paperboard and the assessment of product price. If the paperboard of the packaging has pure cellulose fibre the product is perceived as more expensive. The results indicate that when a product is packed in a paperboard with a higher degree of recycled cellulose fibre it is perceived as more sustainable. An unexpected finding showed that the participants assessed that tobacco products are packaged mostly in recycled paperboard.

REFERENCES

[1] D. Petrić, D. Vusić, R. Geček, Cardboards: from the production to the final use, Teh. Glas. 6, 219–227 (2008).

[2] Transparency Market Research, Paperboard Packaging Market to Reach US$227.47 bn by 2024, Growth Attributable to Strong Demand from F&B Industry, (2017) http://www.transparencymarketresearch.com/pressrelease/paperboard-market.htm.

[3] WPO, Market Statistics and Future Trends in Global Packaging, J. Chem. Inf. Model. 53, 1689–1699 (2013).

[4] Smithers Pira, Luxury packaging market forecast to grow by 4.4% to 2019,(2015). http://www.smitherspira.com/news/2015/march/luxury-packaging-market-forecast.

[5] S. Horvatić, Grafika: papiri i kartoni, 2009, Grafička škola,.

[6] M.J. Kirwan, Handbook of Paper and Paperboard Packaging Technology: Second Edition, 2012, Wiley-Blackwell

[7] VDP, Production volume of paper and cardboard worldwide 2006 to 2015, (2017).

[8] N. Navaranjan, A. Dickson, J. Paltakari, K. Ilmonen, Humidity effect on compressive deformation and failure of recycled and virgin layered corrugated paperboard structures, Compos. Part B Eng. 45 965–971 (2013).

[9] N. Wistara, R.A. Young, Properties and treatments of pulps from recycled paper. Part I. Physical and chemical properties of pulps, Cellulose. 6, 291–324, (1999).

[10] ISO 2470-2:2008 -- Paper, board and pulps -- Measurement of diffuse blue reflectance factor.

[11] ISO/CIE 11664-6:2014 -- Colorimetry --.

[12] M.J. Kirwan, Paper and Paperboard Packaging Technology, 2007, Wiley-Blackwell.

[13] H. Jung, H.J. Suk, S. Kitaguchi, T. Sato, K. Kajiwara, Color tolerance prediction for recycled paper based on consumers' awareness, in: Color Res. Appl., 272–280, (2012).

[14] L. Hamzaoui Essoussi, J.D. Linton, New or recycled products: how much are consumers willing to pay?, J. Consum. Mark. 27, 458–468, (2010).

PRIPRAVA NANOCELULOZE IZ MIKROCELULOZE

PREPARATION OF NANOCELLULOSE FROM MICROCELLULOSE

Martina Budimir, bacc. ing. chem. [1], Roko Blažic, mag. ing. cheming. [1]

[1]University of Zagreb, Faculty of chemical engineering and technology, Petroleum and Petrochemical Department, Savska street 16, Zagreb, Croatia

SAŽETAK

Celulozu se može pronaći svuda u okolini. Zbog svoje biorazgradivosti zadnjih godina se sve više provode ispitivanja i modifikacije koje bi omogućile njenu upotrebu u kompozitnim materijalima. Izuzetno zanimljiva modifikacija je u nanocelulozu. Naime, duge lance celuloze se skraćuje raznim metodama do nanodimenzija. Takve molekule se još bolje mogu iskoristiti u kompozitnim materijalima, zbog poboljšanih svojstava. Istu celulozu i nanocelulozu se može i funkcionalizirati za poboljšanje drugih svojstava. U ovome radu proučene su metode dobivanja nanoceluloze kiselinskom hidrolizom koristeći sulfatnu kiselinu i uspoređena svojstva produkata. Utvrđeno je da metoda priprave nanoceluloze utječe na veličinu čestica i poroznost strukture. Dokazano je da je u strukturi doista prisutan sumpor vezan na ugljikovodični spoj, što upućuje da je uistinu došlo do hidrolize.

ABSTRACT

Cellulose can be find all around us. It is biodegradable so for the past few years there are a lot of analysis and modifications to allow its use in composite materials. Very interesting modification is nanocellulose. These molecules can be used in composites, because of the better features. These same cellulose and nanocellulose can be functionalized to improve different properties. In this research the different methods of synthesis by sulfuric acid hydrolysis and the properties of the product were compared. It is found that the method of nanocellulose synthesis affects final particle size and the porosity of the structure. It's also found that there really is sulfur connected to the hydrocarbon, which is demonstrated by the hydrolysis reaction.

KLJUČNE RIJEČI

celuloza, nanoceluloza, hidroliza, ester, kompozitni materijali, biorazgradivost

KEY WORDS

cellulose, nanocellulose, hydrolysis, ester, composite materials, biodegradable

1. UVOD

Celuloza je prirodni polimer kojeg ima u izobilju, a koristi se već oko 150 godina za proizvodnju razih materijala i proizvoda. Tek nedavno je došlo do saznanja o djelovanju hidrolize kiselinom. Naime, u tom slučaju dobiva se produkt u obliku kristalnih štapića, bez defekata i nanometarskih dimenzija. Nanoceluloza je zbog toga, a posljedično i zbog odličnih fizikalnih i kemijskih svojstava, uz činjenicu da je obnovljiv materijal, pridobila veliku pažnju u inženjerstvu materijala, pogotovo kompozita. Celuloze je vlaknasta, čvrsta, netopiva tvar od iznimne važnosti za staničnu stjenku biljaka. Polimer je visoke molekulske mase, točnije homopolimer s jedinicama β-1,4-anhidro-D-glukoze, gdje se svaka jedinica spaja na prethodnu pod kutem od 180°. Ovaj ponavljajući segment se često postavlja za dimer glukoze – celobioza. Svaki lanac posjeduje usmjerenu asimetriju s obzirom na kraj lanca. Tako jedan kraj lanca sadrži reducirane funkcionalne grupe, dok drugi kraj lanca sadrži nereducirane. Broj jedinica (stupanj polimerizacije) je do 10000. Struktura se dodatno stabilizira vodikovim vezama unutar molekule, a kemijska struktura celuloze je prikazana na slici 1 [1].

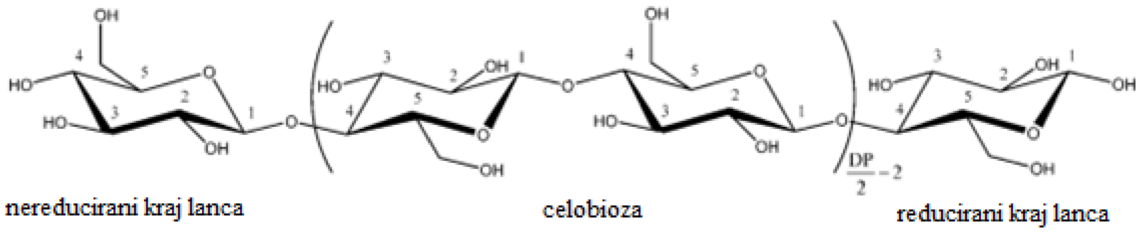

Slika 1. Kemijska struktura celuloze [1]

U prirodi se celuloza ne nalazi kao individualna molekula, već kao skupina molekula tvoreći vlakna – fibrile. Dalje ta vlakna uslijed stvaranja van der Waalsovih i intra- i intermolekuskih vodikovih sila tvore nakupine zvane mikrofibrili (2-20 nm), koji tvore celulozna vlakna. Većinom nastaje struktura rozete promjera 30 nm [1].

Iz strukture i kristalne prirode celuloze je jasno da je moguće odvojiti nanočestice koristeći metodu odozgo prema dolje [2]. Metode odozgo prema dolje se temelje na uklanjanju agregata molekula s površine ili rastavljanju veće molekule do manje u svrhu postizanja željene strukture [3]. Nanoceluloza se obzirom na načine dobivanja može podijeliti na tri tipa materijala: celulozni nanokristali (ili nanokristalinična celuloza, celulozni nanoviskeri), celulozna nanovlakna i bakterijska celuloza [4]. Nanokristalinična celuloza je tvar koja se sastoji od štapićastih čestica. Dimenzije čestica nanokristalne celuloze su uglavnom: širina 10-50 nm i dužina 100-500 nm. Glavna metoda dobivanja je blaga kiselinska hidroliza jakim kiselinama. Celulozna nanovlakna se mogu dobiti i postupkom mehaničke destrukcije i enzimatskom obradom, iako se još razvijaju nove i brze metode dobivanja. To su čestice nanoceluloze širine 2-60 nm i dužine par mikrometara. Bakterijska nanoceluloza je dobila svoj naziv zbog toga što se dobiva obradom bakterijama. Može imati morfologiju mreže ili vrpce, a još veće je kristalnosti i čistoće (do 100 % celuloze) [5].

Svojstva dobivene nanoceluloze ovise o određenim faktorima procesa dobivanja (temperatura, vrijeme i brzina miješanja reakcijske smjese) i sirovinama (jakost kiseline te omjer kiseline i celuloze) pa se mogu dosta razlikovati [1]. Zapreka u korištenju nanoceluloze za nanokompozitne materijale je postizanje homogene disperzije u polimernoj matrici jer čestice nanodimenzija imaju veću specifičnu površinu, pa zbog toga lakše aglomeriraju u polimernoj matici. Kod nanoceluloze aglomeraciji pridonose i reaktivne hidroksilne skupine sa površine čestica zbog intramolekulskh interakcija, pa je izuzetno bitna kontrola agregacije. Ipak, hidroksilne skupine u određenim uvjetima djeluju pozitivno na povećanje čvrstoće celuloze (papir) [2].

1.1. NAČINI PRIPRAVE CELULOZNIH NANOKRISTALA

Glavni postupak izolacije nanoceluloze iz celuloznih vlakana je hidroliza kiselinom (slika 2.). Deformirane i polikristalne faze celuloze se preferencijalno hidroliziraju, dok su kristalne faze otpornije na djelovanje kiseline te ostaju netaknute. Tako se hidrolizom celuloze odvajaju mikrofibrili zbog defekata, pa se dobivaju igličasti nanokristali. Morfologija nanoceluloze je slična onoj izvornih celuloznih vlakana. Cijepanje samo dijelova celuloze pod djelovanjem kiseline je posljedica razlike u kinetici hidrolize amorfne i kristalne faze. Kiselina lakše prodire u slabije uređene amorfne dijelove nego u visokouređene kristalne, pa najprije dolazi do hidrolize amorfnih dijelova nanoceluloze. Ostatak kiseline hidrolizira zatim neke kristalne djelove nanoceluloze. Za polikristalne faze se pretpostavlja da su statistički jednoliko raspoređenene u mikrofibrilima i zbog svoje strukture podložnije hidrolizi kiselinom, nakon čega nastaju homogeni kristaliti. To je potvrđeno rendgenskom difrakcijskom analizom i elektronskom mikroskopijom. Proizvodnja nanoceluloze se danas sastoji od podvrgavanja celuloznih materijala (pamuk, konoplja, lan, pšenična slama, palma) jakoj kiselinskoj hidrolizi (uglavnom sulfatna i kloridna kiselina) pod strogo kontroliranim uvjetima temperature, vremena i brzine miješanja. Među bitnim parametrima je i omjer kiseline naspram celuloznih vlakana. Ovaj pristup je klasičan, ali se sve češće kombinira s enzimatskom hidrolizom, hidrolizom plinovitim kiselinama i ionskim tekućinama [1,2].

Pristup mehaničke destrukcije podrazumjeva da se raznim mehaničkim postupcima obrađuju celulozna vlakna i odvajaju individualni mikrofibrili. Dobiveni materijal se naziva mikroceluloza. Postupci se većinom sastoje od visokotlačne homogenizacije, ultrazvučnih postupaka, kriodrobljenja i/ili mljevenja, koji zahtjevaju veliku potrošnju električne energije za odvajanje mikrofibrila. Zato se predlaže predobrada mehaničkim rezanjem, kiselinskom hidrolizom, enzimatskom predobradom ili uvođenjem nabijenih skupina karboksimetilacijom. Nakon odvajanja mikrofibrili se većinom suspendiraju u tekućini, najčešće vodi. Viskoznost se homogenizacijom suspenzije povećava, pa se uglavnom pripremaju suspenzije sa masenim udjelom vlakana do w=0,02. Ove suspenzije pokazuju svojstva slična gelovima [2,6].

2. MATERIJALI I METODE:

Nanoceluloza je pripravljena kiselinskom hidrolizom sa sulfatnom kiselinom pomoću dvije različite metode.

Prva metoda je provedena tako da je usitnjenom filter papiru dodano 50 ml ultračiste vode. Pripravila se pulpa homogenizatorom tokom 5 minuta na 7000 min^{-1}. Zatim je stavljena na sušenje dok sva voda ne ispari (100°C tokom par sati, vaganje za provjeru gubitka vode). Pri kraju otparivanja viška vode iz pulpe, pripremljena je sulfatna kiselina w=0,64, (iz sulfatne kiseline SigmaAldrich, 95-98 vol. %, p.a., gustoće 1,840 g/mL na 25 °C). Odvagano je 1,0092 g osušene pulpe u staklenu čašu i postavljeno u ledenu kupelj. Polagano se dodavala sulfatna kiselina $w = 0,64$ kap po kap uz miješanje (10 ml H_2SO_4 na 1 g celulozne pulpe). Reakcijska smjesa je prebačena u reaktor, koji je postavljen u uljnu kupelj na 47±1°C tokom jednog sata. Reaktor je zatim uklonjen iz uljne kupelji. Dodano je 50 ml ultračiste vode ohlađene na 4°C u svrhu zaustavljanja reakcije.

Dobivena suspenzija je zatim je centrifugirana, gdje je zaključeno da se iz suspenzije dovoljno dobroodvoje dvije faze (nanoceluloza i otapalo) tek centrifugiranjem tokom 13 min brzinom od 3500 min^{-1}. Dekantirano je otapalo, a zaostali talog nanoceluloze u malo otapala ispirao se tri puta ultračistom vodom. Postupak centrifugiranja i ispiranja je proveden 3 puta. Nakon zadnjeg dekantiranja uzorci su postavljeni na dijalizu, koja je provedena do nepromijenjene vrijednosti električne provodnosti uzoraka (1,29 µS/cm na 22 °C, izmjereno konduktometrom MettlerToledo F3 - LE703 IP67). Za dijalizu je upotrijebljena polupropusna membrana Spectra/Por 4 Dialysis Membrane, Standard RC Tubing, širina izravnate membrane: 75 mm, promjer: 48 mm, volumen/duljina: 18 ml/cm, dužina: 15 m, broj: 132709. Odrezana je potrebna količina membrane iz role, namočena u ultračistu vodu da se odvoje stijenke membrane od folije koja štiti membranu od isušivanja. Plastičnim štipaljkama su zatvoreni krajevi membrane, koja je zatim postaveljan u posudu s ultračistom vodom i na magnetsku miješalicu (**Pogreška! Izvor reference nije pronađen.**). Dijaliza je trajala 2 tjedna uz svakodnevnu izmjenu ultračiste vode u posudi.

Celulozna pulpa se sušila u sušioniku do otklanjanja cijele količine vode, pa je dodano još 40 ml ultračiste vode, homogenizatorom ujednačeno i sušeno do količine vode potrebne za razrjeđenje 95 vol.% H_2SO_4 (5,08g vode), što je potvrđeno vaganjem. Koncentracija sulfatne kiseline je $\gamma = 1,5421$ g/ml ($w = 0,64$) kao u prvoj metodi. Nakon toga je dodana 95 vol.% H_2SO_4 kap po kap uz konstantno miješanje u ledenoj kupelji. Nakon toga je opet reakcijska smjesa prebačena u reaktor u uljnoj kupelji na temperaturi 46±1 °C, a ostatak postupka je identičan prvome. Iz dobivene nanoceluloze pripravljeni su uzorci nanoceluloze osušeni izmjenom otapala (ohlađenim etanolom). Također su pripravljeni i nanocelulozni filmovi. Početna celulozna pulpa je korištena za usporedbu. Osušena je na dva načina: u sušioniku i izmjenom otapala.

Uzorci su karakterizirani rendgenskom difrakcijskom analizom praha na Shimadzu XRD 6000 difraktometru s CuKα (λ=1,54059 Å) zračenjem uz napon od 40 kV i jakost struje od 30 mA. Podaci su prikupljeni između 7° i 70 °2θ sa korakom od 0,02 ° i zadržavanjem od 0,6 s po koraku.Obavljena je i analiza FTIR-om (ATR – prigušena totalna refleksija), na uređaju Perkin Elmer Spectrum One, raspona valnih brojeva 0-4000 cm^{-1}, s korakom 1,000. Karakterizirani su i pomoću pretražnog elektronskog mikroskopa (SEM) – SEM TescanVegaIII Easyprobe, pri različitim uvećanjima. Za ovu analizu je bilo potrebno najprije uzorke napariti vodljivom legurom Au/Pd.

3. REZULTATI I RASPRAVA:

SEDIMENTACIJSKI TEST

Na slici 2 prikazani su uzorci nanoceluloze nakon što su odstajali 10 dana. Naime, pod učinkom gravitacije lijevi uzorak (prva metoda) se lagano sedimentirao. U desnom uzorku (druga metoda) nije došlo do sedimentacije. Prvi uzorak, dakle, je uzorak u kojem su prisutne veće čestice, veličine dovoljne da dođe do sedimentacije. Oba uzorka su mliječno bijele do lagano plavičaste boje, što znači da su čestice dovoljno velike da dolazi do raspršivanja svjetlosti. To ukazuje da jedna dimenzija čestica mora biti veća od 500 nm.

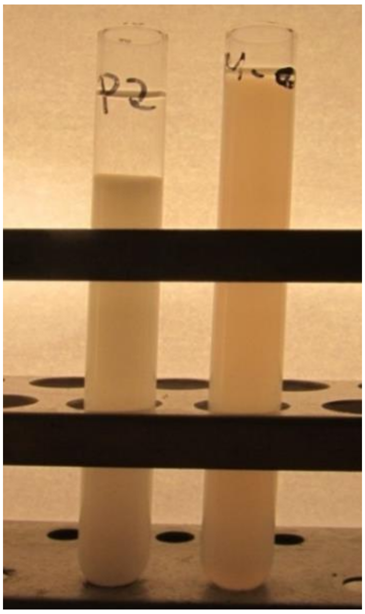

Slika 2. Sedimentacijski test uzoraka nanoceluloze dobivenih metodama 1 i 2

RENDGENSKA DIFRAKCIJSKA ANALIZA

Slika 3. prikazuje rezultate analize rendgenske difrakcije celuloze i nanoceluloze. Kod uzoraka celuloze i nanoceluloze jasno su izraženi određeni i isti difrakcijski maksimumi (15, 17, 23, i 34 °2θ). To ukazuje da tijekom kemijske reakcije nije došlo do promjene kristalnosti. Također, preferirano je došlo do hidrolize samo amorfne faze celuloze.

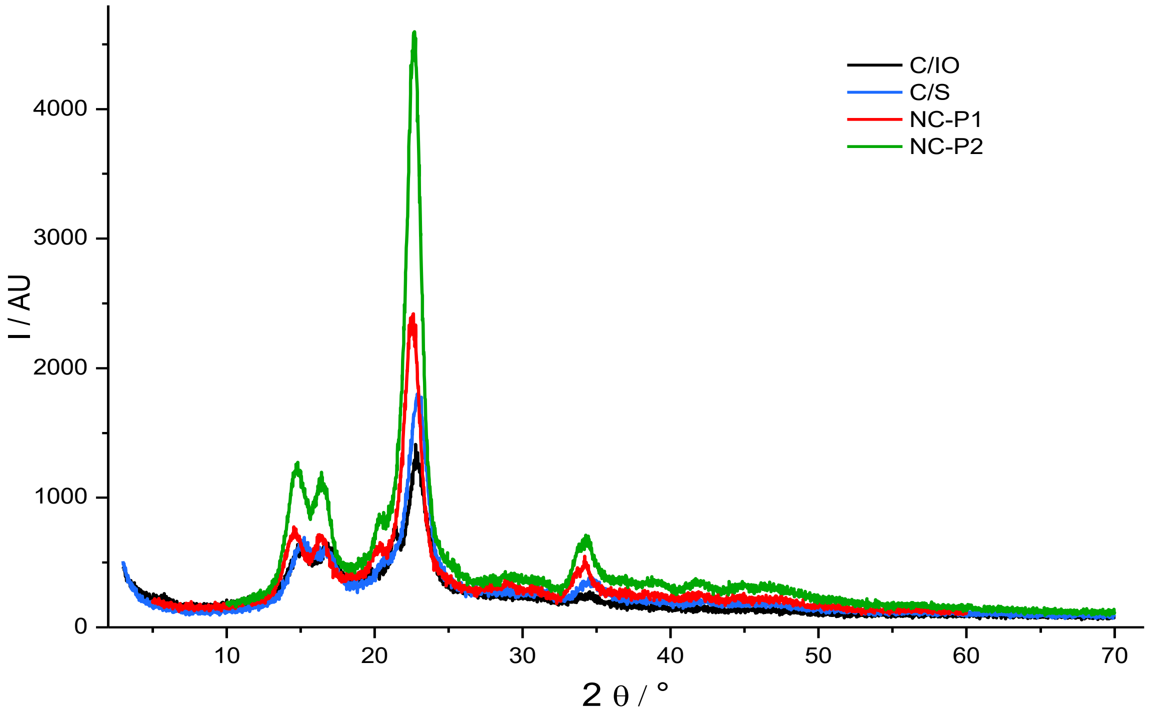

Slika 3. Rezultati rendgenske difrakcije celuloze sušene izmjenom otapala (C/IO), celuloze sušene u sušioniku (C/S), nanoceluloze dobivene prvim postupkom (NC-P1) i nanoceluloze dobivene drugim postupkom (NC-P2)

ATR

Slika 4. Rezultati ATR analize Slika 4 prikazuje rezultate FTIR analize. Ispod je Tablica 1, s pripadajućim značajnim vibracijama kemijskih veza. Svi uzorci sadržavaju odzive na valnim brojevima karakterističnim za celulozu (1160, 1050, 1030 cm^{-1}). Jasno je vidljivo da su na nanocelulozi prisutni maksimumi koji označavaju vibracije veza C-S (odziv na 672 cm^{-1}) i S=O (odziv na 1016 cm^{-1}). Do toga je došlo jer je nanoceluloza dobivena kiselinskom hidrolizom koristeći sulfatnu kiselinu, koja se pritom i vezala na površinu nanoceluloze. Mehanizam ove reakcije je prikazan ranije (**Pogreška! Izvor reference nije pronađen.**). To ukazuje da je uistinu došlo do kiselinske hidrolize celuloze.

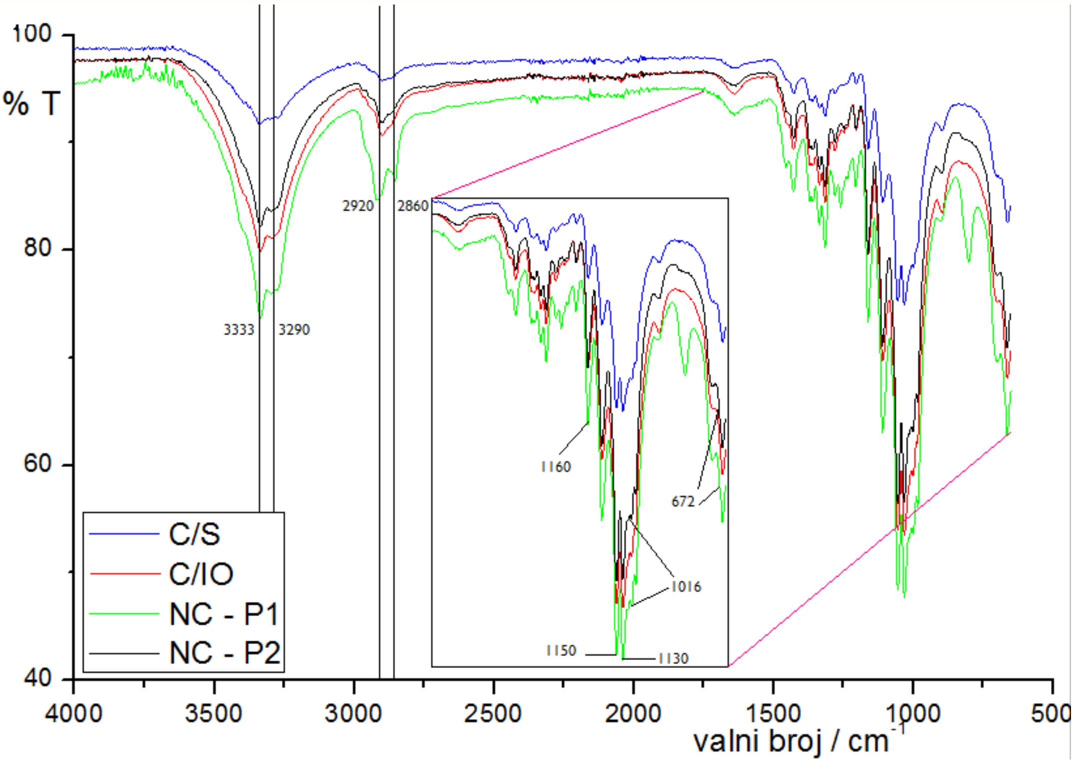

Slika 4. Rezultati ATR analize celuloze sušene izmjenom otapala (C/IO), celuloze sušene u sušioniku (C/S), nanoceluloze dobivene prvim postupkom (NC-P1) i nanoceluloze dobivene drugim postupkom (NC-P2)

Tablica 1. Prikaz valnih brojeva koji ukazuju na vibraciju određenih kemijskih veza, za uzorke celuloze i nanoceluloze (metode 1 i 2) ispitane ATR-om [8]

valni broj / cm^{-1}	**pripadajuća vibracija veze**
2920, 2860	vodikova veza (-OH skupine)
3333, 3290	vodikova veza (-OH skupine)
1160	tri najvažnije skupine karakteristične za celulozu
1050	
1030	
672	C-S
1016	S=O

SEM

Fotografije površine celuloze iz celulozne pulpe snimljene SEM-om (Slika 6) ukazuju na to da je morfologija površine jako hrapava i jako porozna. Vidljivo je jako puno velikih celuloznih vlakana. Vidljiva je mreža celuloznih vlakana koja su ipak do određene mjere usmjerena u istom smjeru. Celuloza sa slike 5 je sušena izmjenom otapala, zbog čega je zadržala svoju poroznu strukturu. Širina čestica je 20-30 µm. Slika 6.a SEM fotografije nanoceluloze dobivene prvom metodom ukazuje da je površina jako glatka i nije porozna. Građena je od čestica dimenzija manjih i od 2 µm. Fotografija strugotina nanoceluloze dobivene prvom metodom pokazuje linije pravca struganja. Ovdje je ipak vidljivo da postoji određena poroznost ovog uzorka, a površina je relativno glatka.

Nanoceluloza pripravljena drugim postupkom je promatrana u dva uzorka. Prvi uzorak ima glatku površinu i poroznu strukturu. Vidi se malo dužih vlakana nego u slučaju nanoceluloze pripravljene prvom metodom. To ukazuje na veći raspon veličine čestica nego kod tog uzorka. Površina je poroznija od NC dobivene prvom metodom, ali manje porozna od celuloze. Drugi uzorak ima manje poroznu i manje hrapavu površinu od prvog uzorka pripravljenog također drugom metodom. Ipak ima veću poroznost i hrapavost nego nanoceluloza pripravljena prvom metodom. Malo je manja raspodjela veličine čestica nego kod prvog uzorka dobivenog ovom metodom, jer su vlakna malo manja. Raspodjela veličine čestica u drugom uzorku dobivenom drugom metodom je između RVČ prvog uzorka i nanoceluloze dobivene prvom metodom. Širina velikih vlakana promatranih na fotografiji, s obzirom na naznačenu skalu od 50 µm, u oba je uzorka u prosjeku 15 µm. SEM fotografije potvrđuju sedimentacijski test. Pretpostavlja se da su glatki dijelovi na svim slikama nakupine manjih čestica.

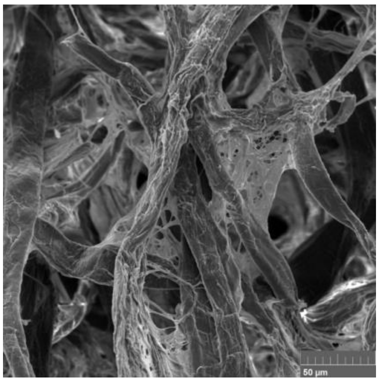

Slika 5. SEM fotografija celuloze prije hidrolize

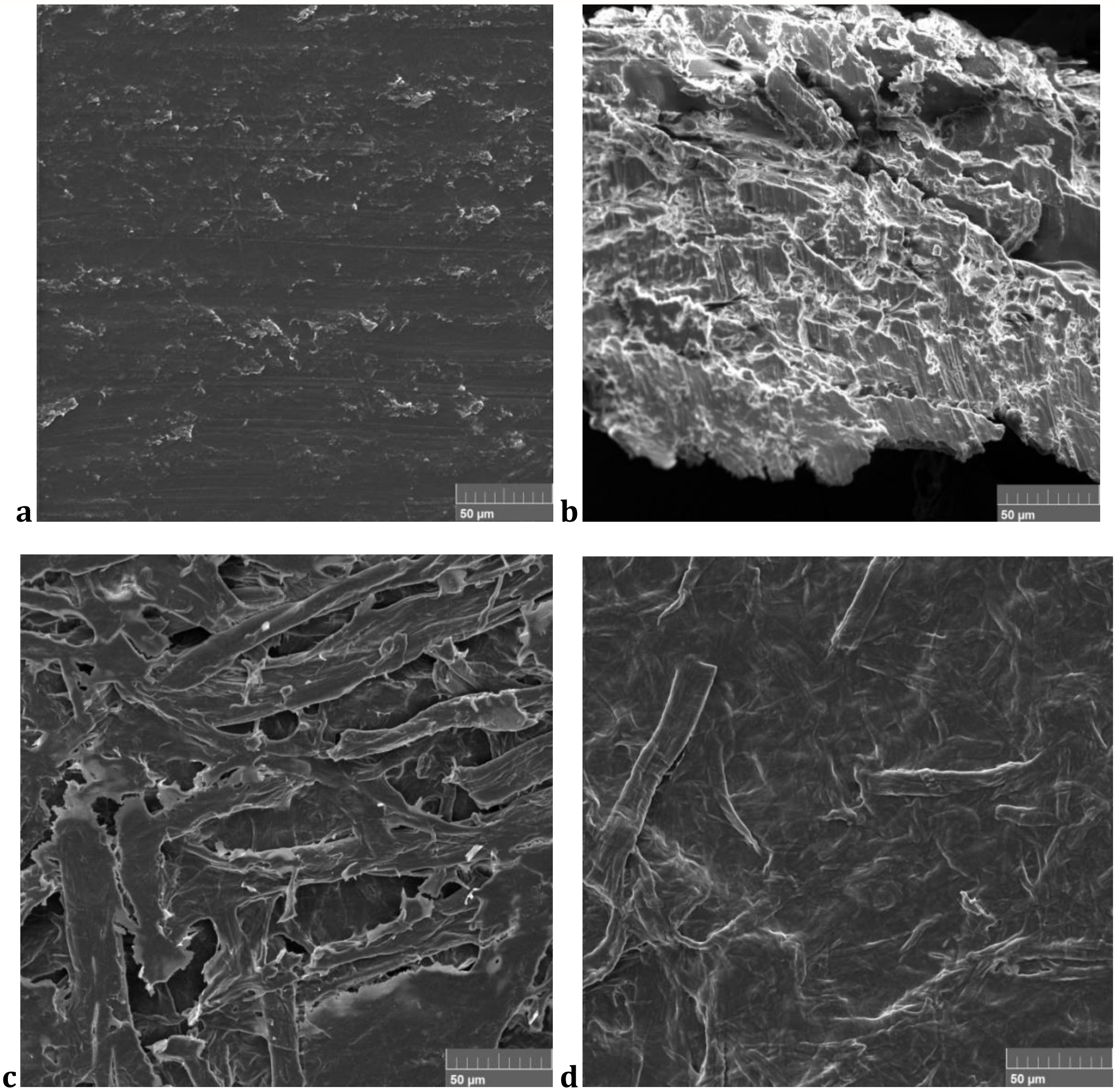

Slika 6. Prikaz SEM fotografija redom: a) nanoceluloze dobivene prvom metodom, b) strugotina nanoceluloze dobivene prvom metodom, c,d) nanoceluloze dobivene drugom metodom (prvi i drugi uzorak)

Uzorci su ispitani da se odredenjihova fizikalna svojstva, što je provedeno pomoću sedimentacijskog testa (veličina čestica) i pretražnog elektronskog mikroskopa (veličina čestica i poroznost). Jednako važno je i dokazati da je uistinu došlo do hidrolize uz zadržavanje kristalnosti, što je potvrđeno pomoću rengdenske difrakcijske analize (ispitana kristalnost uzorka). U tome je pomogla i spektrometrija pomoću ATR-a, kojom se dobio uvid u skupine pristune u uzorku.

5. ZAKLJUČAK

Sedimentacijskim testom je utvrđeno da jedna dimenzija čestica mora biti veća od 500nm. Kod difraktograma uzoraka celuloze i nanoceluloze jasno su izraženi određeni i isti difrakcijski maksimumi. Dakle, tokom hidrolize nije došlo do promjene kristalnosti.

Prigušenom totalnom refleksijom infracrvenog zračenja (ATR) su dobiveni rezultati koji upućuju na postojanje nove funkcionalne skupine u strukturi. Usporedbom valnog broja pri kojem se javlja refleksija, dokazana je prisutnost atoma sumpora povezanog dvostrukom vezom s kisikom i jednostrukom vezom s ugljikom. Hidrolizom je zadržan dio strukture celuloze jer su na uzorcima nanoceluloze jasno vidljivi isti odzivi karakteristični za celulozu.

Pretražnim elektronskom mikroskopom se pokazalo da je dobivena nanoceluloza porozna. Poroznost ovisi o metodi priprave, pa može biti više ili manje izražena. Na fotografijama su vidljiva vlakna – veće čestice, ali i glatki dijelovi koji se sastoje od manjih čestica nanoceluloze. Raspodjela veličine dobivenih čestica varira ovisno o metodi priprave.

Ovim analizama je utvrđeno da metoda priprave nanoceluloze utječe na veličinu dobivenih čestica i poroznost dobivene strukture. Dokazano je da je u strukturi doista prisutan sumpor vezan na ugljikovodični spoj, što upućuje da je došlo do hidrolize. Neke od dobivenih čestica su u nanodimenzijama, ali se uglavnom radi o nanovlaknima. Dobivene su i manje čestice, čija je veličina dosta manja od 10 µm, koliko je bilo moguće vidjeti SEM-om.

6. LITERATURA:

[1] Habibi, Y., Lucia, L.A., Rojas, O.J. Cellulose nanocrystals: Chemistry, self-assembly, and applications. Chemical Reviews. 9. lipanj 2010., str. 3479-3500.

[2] Dufresne, A. Nanocellulose: A new ageless bionanomaterial. Materials Today. lipanj 2013., str. 220-227.

[3] S. Kurajica, S. Lučić Blagojević. Uvod u nanotehnologiju - predavanja iz kolegija. 4. Pristup odozgo prema dolje. [Mrežno] https://www.fkit.unizg.hr/_download/repository/UvodUNano4OdozgoPremaDolje%5B9%5D.pdf.

[4] Abitbol, T., Rivkin, A., Cao, Y., Nevo, Y., Abraham, E., Ben-Shalom, T., Lapidot, S., Shoseyov, O. Nanocellulose, a tiny fiber with huge applications. Current opinion in biotechnology , **39**, 76-88, 1. lipanj 2016.

[5] Development and applications of transparent conductive nanocellulose paper. Shaouhi Li, Pooi See Lee. 1, s.l. : Science and Technology of Advanced Materials, 30.. kolovoza 2017., **18**, str. 620-633. https://doi.org/10.1080/14686996.2017.1364976.

[6] George, J. Cellulose nanocrystals: Synthesis, functional properties, and applications. Nanotechnology, Science and Applications. 4. studeni 2015., str. 45-54. https://www.ncbi.nlm.nih.gov/pmc/articles/PMC4639556/.

[7] P. Lu, Y.-L. Hsieh. Preparation and properties of cellulose nanocrystals: Rods, spheres, and network. Carbohydrate Polymers. rujan 2010., **82**, 2, str. 329-336. https://doi.org/10.1016/j.carbpol.2010.04.073.

[8] Stuart, B. Infrared spectroscopy: fundamentals and applications. Chichester, Engleska : Wiley, 2004. ISBN: 9780470011140.

[9] Camarero Espinosa, S., Kuhnt, T., Foster, E.J. Isolation of Thermally Stable Cellulose Nanocrystals by Phosphoric Acid Hydrolysis . [Mrežno] 8. travanj 2013. http://sci-hub.cc/10.1021/bm400219u.

[10] Ćirić-Marjanović, Gordana. Fizička hemija II . s.l. : http://helix.chem.bg.ac.rs/~saska/Fizicka_hemija_2--1022A/FH%20II%20-%20materijal/PREDAVANJA/Predavanja%20-%20fizicka%20hemija%202.pdf.

[11] Buffiere, Jean., Balogh-Michels, Zolt´an., Borrega, Marc., Geiger,Thomas., Zimmermann,Tanja., & Sixta, Herbert. The chemical-free production of nanocelluloses from microcrystalline cellulose and their use as Pickering emulsion stabilizer. [Mrežno] 9.rujan 2017. Carbohydrate Polymers. http://dx.doi.org/10.1016/j.carbpol.2017.09.028.

[12] Schmidt, W. Microporous and Mesoporous Materials. The Official Journal of the International Zeolite Association. ISSN: 1387-1811.

[13] Helmenstine, A.M. Tyndall Effect Definition and Examples. 2017. https://www.thoughtco.com/definition-of-tyndall-effect-605756.

[14] Chaplin, M. Water structure and science. http://www1.lsbu.ac.uk/water/supercritical_water.html. [Mrežno] studeni 2017.

[15] W. Bai, J. Holbery, K. Li. A technique for production of nanocrystalline cellulose with a narrow size distribution. Cellulose. 2009, **16**, 3, str. 455-465.

[16] Jan P F Lagerwall i suradnici. Cellulose nanocrystal-based materials: from liquid crystal self-assembly and glass formation to multifunctional thin films. NPG Asia Materials. siječanj 2014., **80.**

USPOREDBA *IN VIVO* REAKCIJA S *IN VITRO* BIOAKTIVNIM TESTIRANJIMA U SBF-U

CORRELATING *IN VIVO* REACTIONS WITH SBF *IN VITRO* BIOACTIVITY TESTING

Matej Gojanović-Rakić, Mateo Carević, Ivan Kumić[1]

[1] Sveučilište u Zagrebu, Fakultet strojarstva i brodogradnje, Ivana Lučića 5, 10000 Zagreb, Hrvatska
[1] University of Zagreb, Faculty of Mechanical Engineering and Naval Architecture, Ivana Lučića 5, 10000 Zagreb, Croatia

Sažetak

Biokompatibilni materijali su grupa materijala pretežito korištenih u obnavljanju koštanog tkiva. Od bioaktivnih materijala, kao potkategorije biokompatibilnih materijala, se očekuje da reagiraju sa tjelesnim tekućinama na poseban način, olakšavajući stvaranje slojeva apatita sličnog kostima, na njihovim površinama. Na taj način, bioaktivne površine mogu ubrzati zarastanje u kost kao trajno učvršćeni implantat. Testiranje takvih materijala i iniciranih bioloških i biokemijskih odziva se može napraviti ili *in vivo* (neizvedivim, štetnim, etički upitnim) ili *in vitro* načinom, korištenjem simulacije tjelesne tekućine (eng. SBF). Cilj ovog rada je predstaviti trenutne pronalaske u ovom vrlo sprecifičnom području istraživanja i dati određene smjernice kako približiti *in vivo* i *in vitro* SBF ispitivanja sa različitim kemijskim sastavima spomenuth tekučina, i ostalih mogućih utjecajnih čimbenika.

Ključne riječi: *Bioaktivnost, SBF, apatit, koštana integracija.*

Abstract

Biocompatible materials are a group of materials used extensively in bone tissue regeneration. Bioactive materials, as a subcategory of biocompatible materials, are expected to react with bodily fluids in a specific way, facilitating the formation of bone-like apatite layers on their surfaces. By doing so, bioactive surfaces may expedite bone integration as a means of permanent implant fixation. Testing of such materials and initiated biological or biochemical responses can be done either *in vivo* (not feasible, harmful, ethically complicated) or *in vitro* using Simulated Body Fluids (SBF). The goal of this paper is to present current findings in this very sprecific field of research and give certain guidelines on how to approximate *in vivo* and *in vitro* SBF testing with various chemical compositions of mentioned fluids, and other possible influental factors.

Keywords: *Bioactivity, SBF, apatite, osseointegration.*

1. INTRODUCTION

The desire for biocompatible materials has been growing steadily since their discovery. Given that there is only a small number of biocompatible materials, there was always a need to test their biocompatibility *in vitro*. As a response, a Simulated Body Fluid (SBF), that has similar physical and chemical properties to human blood plasma, was invented. When a biocompatible material is immersed into the SBF with the similiar surrounding conditions as those of the human blood plasma, hydroxyapatite (a natural ingredient that makes up 70% of bone mass) is formed on the surface of the material. The goal of this paper is to examine why SBF is even used, the apatite formation process on variuos titanium forms in SBF, as well as the validity of the whole process.

2. HISTORY

When a material is implanted into the bone tissue, human body has an immunological reaction to encapsulate the material in a fibrous tissue, isolating the material from the rest of the bone. That was a general rule for all materials up until 1972, when it was discovered that certain glasses, as well as some ceramics (bioglasses and bioceramics respectively), integrate themselves into the bone tissue without the response of fibrous tissue formation. Nevertheless, those ceramics and glasses, while biocompatible, are not mechanically compatible, meaning that they do not provide the necessary mechanical properties during exploitation. This led to a massive need for materials that are up to the task, which in turn led to two big questions: What makes a material bind to the bone, i.e. why do bioceramics and bioglasses bind to the bone; and is there a more feasible way of testing such materials in a laboratory environment?

In order to reduce *in vivo* experiments, there was a need for creating a solution that would simulate body fluid to perform *in vitro* tests. In order to create a fluid as similar as possible to a body fluid, researchers developed a couple of Simulated Body Fluids throughout the years. Here are a few SBFs, that are often used in various experiments, known as original SBF (SBF), corrected, i.e. conventional SBF (c-SBF), revised SBF (r-SBF) and Newly improved SBF (n-SBF). Their ion concentrations are given in Table 1. In 1990 Kokubo et al. showed that the apatite foremed *in vivo* can be reproduced in a SBF with ion concentrartions very similar to those of the human blood plasma. After tests and detailed analysis, the conclusion was given that the *in vivo* bone bioactivity of materials can be predicted by examining a formation of apatite on a surface in SBF. From Table 1 it can be seen that c-SBF is richer in Cl^- ion and poorer in HCO_3^- ion than human blood plasma. This difference was tried to be corrected in r-SBF which has decreased and increased concentrations of Cl^- and HCO_3^- ions in relation to the levels of human blood plasma. In 2004 it was proposed that n-SBF with decreased Cl^- ion concentration to the level of human blood plasma should be compared to c-SBF in its stabilitiy and reproducibility of apatite formation and it was confirmed that they do not differ [1].

Tab. 1: Ion concentrations of SBFs and human blood plasma. [1]

Ion concentration (mM)								
	Na^+	K^+	Mg^{2+}	Ca^{2+}	Cl^-	HCO_3^-	HPO_4^{2-}	SO_4^{2-}
Human blood plasma	142.0	5.0	1.5	2.5	103.0	27.0	1.0	0.5
Original SBF	142.0	5.0	1.5	2.5	148.8	4.2	1.0	0
c-SBF	142.0	5.0	1.5	2.5	147.8	4.2	1.0	0.5
r-SBF	142.0	5.0	1.5	2.5	103.0	27.0	1.0	0.5
n-SBF	142.0	5.0	1.5	2.5	103.0	4.2	1.0	0.5

3. CRYSTALLIZATION PROCESS

3.1 Crystallization theory

Crystallization is a natural process in which atoms and molecules of a solid form a highly organized structure known as a crystal. In order for a crystal to form, two events have to happen: crystal nucleation and crystal growth. Thermodynamics teaches us that, for apatite to form, both our serum and SBF have to be supersaturated towards apatite crystals, meaning that the system is metastable until apatite crystals form, when it becomes thermodynamically stable [2]. These factors that affect crystal nucleation and growth are key to understanding how apatite forms in SBF.

3.1.1 Crystal nucleation

Crystal nucleation happens when atoms or molecules of a solid achieve an energy state called the crystalliaztion activation energy. This is the first step of the crystallization, also known as primary nucleation. An important thing to note here is the difference between homogenous and heterogenous crystallization. Homogenous crystallization happens when a crystal comes to form exclusively from a liquid. This crystallization happens rarely due to high energies needed for its realization. Heterogenous crystallization happens when a solid initates the crystallization process, and is much more frequent in practice. This primary nucleation can be mathematically modelled via the following equation (works for both homogenous and heterogenous crystallization) [3]:

$$B = \frac{dN}{dt} = k_n(c - c*)^n, \quad (1)$$

where:

- B is the nuber of nuclei formed per unit volume per unit time,

- N is the number of nuclei per unit volume,

- k_n is a rate constant,

- c is the instanteneous solute concentration,

- c* is the solute concentration at saturation,

- n is an empirical exponent that usually varies between 3 and 4.

3.1.2 Crystal growth

Once the initial phase has begun, a secondary phase known as crystal growth, also known as secondary nucleation has to take place. Secondary nucleation is the formation of nuclei attributable to the influence of the existing microscopic crystals. Simply put, secondary nucleation is when crystal growth is initiated with contact of other existing crystals or "seeds." [4] Secondary nucleation is often modelled by the following, somewhat simplified equation [3]:

$$B = \frac{dN}{dt} = k_1 M_T^j (c - c*)^b \quad (2)$$

where:

- k_1 is a rate constant,

- M_T is the suspension density,

- j is an empirical exponent that is usually 1,

- b is an empirical exponent that is usually 2.

3.2 Crystallization theory and apatite

Material which accelerates heterogenous apatite crystallization in a solution that is supersaturated towards hydroxyapatite is clearly a bioactive material. This can be deduced from the established correlation between crystallization theory and apatite formation process in SBF [2]. In doing so, several strategies can be employed:

The first strategy is to provide apatite nuclei [2] in such a manner to allow for heterogenous primary crystallization. This explains why hydroxyapatite is rapidly covered with new apatite crystals[5].

The second strategy is to provide a low interfacial surface with apatite [2], which explains why apatite forms on CP β-Ti surfaces [6].

The third strategy is to change the local supersaturation towards apatite precipitation [2], which explains why bioglasses and bioceramics are quickly covered with an apatite layer upon their imersion in SBF.

4. APATITE FORMATION ON PURE TITANIUM

In 1999, it was discovered that titanium can induce apatite formation, both *in vivo* and *in vitro*, which meant that titanium and its alloys could potentially be regarded as a bioactive material.

The most used treatment reagents are sodium hydroxide and hydrogen peroxide solution. Hydrochloric and sulfuric acid are also used to etch titanium before alkaline treatment. Sodium hydroxide solution treatment produces a sodium titanate gel layer on surface of titanium samples while hydrogen peroxide treatment produces a titania gel layer. Both of the stated gel layers have the ability to induce formation of bone-like apatite while they are immersed in SBF and are also considered as bioactive. The gel layers can initiate apatite nucleation on itself. Apatite spontaneously grows by taking calcium and phosphate ions from the SBF after nucleation is done [7].

The proposed mechanism of apatite formation goes as follows. First, the sodium titanate layer releases Na^+ ions into the SBF during an ion exchange with hydronium from the fluid to form a titanium hydroxide layer. The layer reacts with the calcium present in the fluid to form calcium titanate, which then incorporates both calcium and phosphate ions-resulting in a formation of apatite nuclei inside the SBF. Once the apatite nuclei are present, hydroxiapatite crystal grows following the two aforementioned principles of crystallization [8].

Kokubo et al. (2010.) showed that the most probable reason for apatite formation on titanium surfaces is their positive surface charge. After heat treating the metal at 600 °C followed by acid etching, the XPS spectrography revealed that the surface firstly adsorbs a large amount of phosphate ions, followed by calcium ions. This finding shows that positively charged titanium oxide induces the formation of apatite on its surface, as shown by figure 1. The negatively charged phosphate ions get selectively absorbed by the already positively charged titanium oxide on its surface. The build up of phosphate ions leads to negative surface charge, therefore they combine with the calcium ions to form calcium phosphate. The formation of calcium phosphate eventually leads to stable crystalline apatite transformation [9].

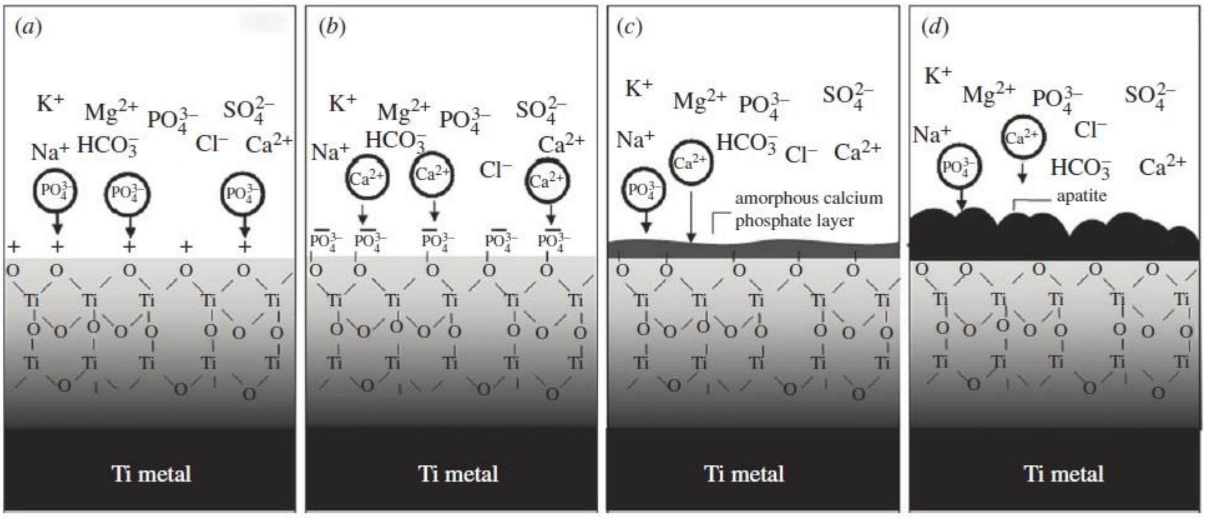

Fig. 1: Process of formation of apatite on positively charged Ti metal in SBF. Apatite is formed by the process shown in (a–d) [9]

Zhao et al. (2005, 2008) reported that an acid solution(such as sulfuric and nitric acid) treatment of a plasmasprayed titanium oxide layer with a rutile phase showed a high apatite-forming ability in an SBF [10].

Kokubo et al. (2008) reported that coating polyethylene terephtalate (sol-gel method) with a titania gel layer formed apatite on its surface in an SBF, provided that it was treated with a hydrochloric acid solution at 80 °C for an 8-day period. The most probable cause is the formation of a titanium oxide layer that contains a positive surface charge in an SBF due to adsorbed acid groups on its surface [11].

5. CONCLUSION

After thoroughly reviewing all the referenced work, we come to the following set of conclusions:

- Testing of biocompatiblity is best done in a Simulated Body Fluid for a variety of reasons, the main ones being feasibility and reproductibility.
- The only possible setback of Simulated Body Fluid testing could be the different chemical compositions and their chemical incompatiblity with actual human blood plasma.
- Due to its mix of properties, be it mechanical, technological or chemical, and its biocompatibility, surface treated titanium is, without a doubt, the material for manufacturing bone implants.
- To achieve titanium biocompatibility, apatite nucleation must be enabled through surface engineering, which is traditionally done by employing various surface treatments such as acid etching [12] or plasma spraying, but other surface engineering methods are also to be assesed.
- Different bones require different attributes (Young's modulus, surface area, etc.) which allows for use of other materials to be coated with biocompatible titanium or its compounds.

All in all, a combination of SBF testing and surface engineering shows very promising results in the field of bone-tissue engineering. However, in some cases where dental titanium implants were used, some inflammations were reported, which were later found out to be due to corrosion and/or pathogen biofilm formation [12, 13]. Issues such as these keep us aware that no material is perfect, no test method covers all the variables, and that the conditions within the human body are everchanging, making our search for complete insight far from over.

REFERENCES

[1] Kokubo, T., Takadama, H., How useful is SBF in predicting in vivo bone bioactivity? *Biomaterials* **27** (2009),2907-2915.

[2] Bohner, M., Lemaitre, J.,Can bioactivity be tested in vitro with SBF solution? *Biomaterials* **30** (2009),2175–2179.

[3] Tavare, N.S. (1995), *Industrial Crystallization*, Plenum Press, New York.

[4] "Crystallization"; www.reciprocalnet.org,Archived from the original on 2016-11-27. Retrieved 2017-01-03.

[5] Kim, H.M., Himeno, T., Kawashita, M., Kokubo, T., Nakamura, T., The mechanism of biomineralization of bone-like apatite on synthetic hydroxyapatite: an in vitro assessment. *J Royal Soc Interface* **1** (2004),17–22.

[6] Juhasz, J.A., Best, S.M., Auffret, A.D., Bonfield, W., Biological control of apatite growth in simulated body fluid and human blood serum. *J Mater Sci Mater Med* **19** (2008),1823–9.

[7] Wang, C.X., Zhou, X., Wang, M., Mechanism of apatite formation on pure titanium treated with alkaline solution. *Bio-Medical Materials and Engineering* **14** (2004),5–11.

[8] Takadama, H., Kim, H.M., Kokubo, T., Nakamura, T., An X-ray photoelectron spectroscopy study of the process of apatite formation on bioactive titanium metal, *J. Biomed. Mater. Res.* **55** (2001), 185–193.

[9] Kokubo, T., Pattanayak, D.K., Yamaguchi, S., Takadama, H., Matshushita, T., Kawai, T., Takemoto, M., Fujibajashi, S., Nakamura, T., Positively charged bioactive Ti metal prepared by simple chemical and heat treatments, *J. R. Soc. Interface* (2010).

[10] Lu, X., Zhao, Z. & Leng, Y. Biomimetic calcium phosphate coatings on nitric acid treated titanium surfaces. *Material Science Engineering* (2009).

[11] Kokubo, T., Ueda, T., Kawashita, M., Ikuhara, Y., Takaoka, G. H., Nakamura, T. PET fiber fabrics modified with bioactive titanium oxide for bone substitutes. *J. Mater. Sci.* (2008) **19**, 695–702.

[12] Kim, H. M., Miyaji, F., Kokubo, T., Nakamura, T. Preparation of bioactive Ti and its alloy via simple chemical surface treatment. *J. Biomed. Mater. Res.* (1996) **32**, 409– 417.

[13] https://www.ncbi.nlm.nih.gov/pmc/articles/PMC4307950/

HYBRID WOODEN BEAMS: A NUMERICAL MODEL

Gorazd Fajdiga[1], **Barbara Šubic**[2] **and Aljaž Kovačič**[1]

[1] University of Ljubljana, Biotechnical Faculty, Department of Wood Science and Technology, Jamnikarjeva 101, 1000 Ljubljana, Slovenia
[2] M Sora d.d., Trg Svobode 2, 4226 Žiri, Slovenia

Abstract

A specific problem from practice is analysed. Slender wooden beams, used in industry for manufacturing windows of larger dimensions (height above 2.5 m), can be deformed under wind load to such an extent that they do not seal anymore; in worst cases they do not even provide basic functions of windows (it is not possible to close the windows). A model of hybrid wooden beams is presented. Based on computer simulations it must enable forecasting and analysis of the mechanical behaviour of a beam, assembled from several interconnected components made from various basic materials. The model includes material and geometrical properties of joints that connect components; it makes it possible to change material parameters, geometrical parameters and boundary conditions. For different boundary conditions and parameters, the model of hybrid wooden beams provides correct data about the strength, primarily about the bending strength, and stresses related to it, deformations and shifts.

Keywords*: hybrid beams, wooden windows, numerical analysis.*

1. INTRODUCTION

In civil engineering, there are many different combinations of boundary conditions of load capacity, applicability and climate influences; consequently, materials used must satisfy many requirements and, therefore, rapid growth in searching for hybrid materials that would satisfy as many project requirements as possible with the combination of two or more materials can be observed. In addition, the objective of the search for new combinations is to optimize solutions and, consequently, to reduce the materials used, which is directly encouraged also by sustainable building. In our research, the main characteristics constantly dealt with are the bending strength and stiffness of a hybrid support in comparison to reference wooden supports without reinforcements. In the past, hybrid supports with improved bending load capacity and/or stiffness were made by means of concrete [1], [2], steel [3]–[5], and glass [6]–[8], carbon [9]–[11] or basalt [12], [13] fibres. Fibre-reinforced-polymers (FRP) that are most frequently used are as follows: glass-fibre-reinforced polymer (GFRP) and carbon-fibre-reinforced polymer (CFRP). The history of the development of hybrid supports with FRP reinforcements goes back to 1992 [14]. It is proved that reinforcements have a significantly greater impact upon the increase in the bending load capacity of supports than upon the stiffness [6]. It makes sense to increase the proportion of reinforcements in the support if the L/h ratio (ratio between length and height) is large (long supports of small heights), otherwise the stiffness is not improved with the increased proportion of reinforcements [6]. By adding 1–2% of FRP material, the bending load capacity is improved by 56% and stiffness by 37% [15]. The special characteristic of hybrid supports researched is that reinforcements must not be visible in the external appearance of windows. A lot of research was carried out about the bending load capacity of supports, whereas not much research was done about it for cases when reinforcements are hidden in the support [16].

1. PROBLEM DESCRIPTION

Modern architecture dictates trends with windows stretching over the entire storey, sometimes even over two storeys, thus, the desired element height is over 2.5 m (also up to 6.5 m). At the same time, wooden elements must be as narrow as possible from aesthetic reasons and in order not to veil the view to residents. Consequently, the element height is getting larger and the profile width is getting narrower; both parameters have an unfavourable impact upon the bending load capacity and stiffness of elements. Slender wooden supports used for the production of windows of larger dimensions (height above 2.5 m) can be deformed under wind loads to the extent that they no longer ensure sealing, in worst cases they do not even ensure basic functionalities of windows (it is not possible to close the window). The development of windows was based on testing new ideas, on the basis of many years of experience and of knowledge gathered in many years, however, the principle of the development was more or less to fulfil an idea by direct tests carried out in practice – i.e. with numerous successful and unsuccessful tests and without in-depth analyses why some ideas were good and some were not. These time-consuming tests can be replaced by the use of numeric simulations that can make it possible to quickly and effectively test various variations of ideas that you wish to integrate into a product without the need to physically produce each of the variations. The influence of variations on the final product can be noticed quickly and its contribution can be evaluated quickly. To use numerical models to obtain precise results that are reliable also in the absolute sense, these models must be validated and verified on the basis of reliable experimental data. As a hybrid support is only a part of the entire window, the influence of reinforcements and of the improvement of the bending stiffness upon the entire window is of interest. In relation to this, the proportion of influences of other parameters that also have an impact upon the bending stiffness of wooden profiles must be defined, i.e. gluing of glass, connecting of a window wing with a window frame by means of fittings and, last but not least, the impact of fixing the window frame into the opening. The problem is thus significantly more complex. The choice, position and placing of reinforcements must be monitored also from the aspect of thermal characteristics of cross-sections as products manufactured for the market must be sustainable; in addition to this, the improvement of the bending stiffness must not reduce the thermal comfort near the windows and increase the energy losses of the building.

Figure 7: Example of modern architecture with large transparent areas along the entire two sides of the building without supporting pillars of the concrete plate. Source: M SORA d.d.

1.1 Purpose and requirements of the model

The dealt with wooden window supports are produced from three glued lamellas made from massive spruce (Picea Abies) wood. In the glued elements, lamellas, as a rule, oriented in such a way that the wind load has an impact upon them in tangential direction. With such orientation, a smaller bending strength is ensured, but the appearance of the final, wooden surface of the window with evenly and parallelly distributed annual growth rings is beautiful from the aesthetic point of view. In the research, orthotropic wood properties were taken into consideration.

Purpose and requirements of the model:

- The model based on computer simulations makes it possible to foresee and analyse mechanical behaviour of a hybrid composite, composed of several interlinked components made of various basic materials.
- The model must include also material and geometrical properties of joints that join the connected components.
- The model must make it possible to change material parameters, geometrical parameters and boundary conditions.
- For different boundary conditions and parameters, the model must provide correct data about stiffness, primarily about bending stiffness, and stresses, deformations and shifts related to it and data on exceeding the permitted values of loading the materials.

2.0 NUMERICAL MODEL

The produced model, based on the finite element method (FEM) [17], was developed in the Abaqus computer program [18]. Its description includes constitutive material models with recommended values of material data, foreseen characteristics of the acquisition of the geometry, of establishing interactions, of defining boundary conditions and producing a mesh. In the numerical model, material models do not change, variations can include material parameters, geometry, interactions, boundary conditions and a mesh of finite elements. All constitutive material models, used in our work so far, are limited to elastic properties and boundaries of irreversible changes (plastification, damage initialization).

2.1 Model development

The developed model allows the variability of geometry (with the mesh and interactions) for searching for an optimal structure of a hybrid composite in regard to boundary conditions that are also variable. Below there are some recommendations that refer to modelling the geometry, defining the mesh, and determining interactions and boundary conditions in the presented numerical model.

2.1.1 Geometry

In order to be able to use the model for searching for an optimal geometry structure, the model makes it possible to change geometry for all the components integrated in the composite. They can be modelled in the Abaqus 3D modeller. Also it is possible to compound individual components into a composite by using the Abaqus graphic interface; in relation to this it is required to ensure a mechanical connection between the components of the composite.

Each component of the hybrid support is modelled separately (wooden battens, reinforcement elements, gluing layers), then the entire composite is made from individual elements as presented in Fig. 1. Virtual geometry must simulate reality as closely as possible, however, some details are simplified on the basis of the judgement of the numerical expert. For the given geometries it is required to prescribe the orientation of material properties. In the framework of boundary conditions of a test, also other components (supports, analytically stiff objects) can be modelled, however, they are not a part of the general description of the hybrid composite model.

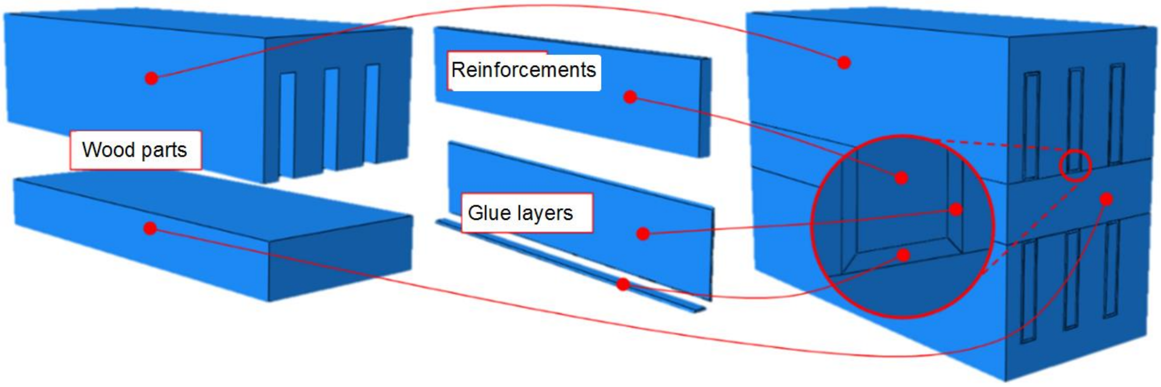

Figure 1: Example of a geometry structure with components for a wooden hybrid composite model with glued reinforcements.

2.1.2 Mesh

The geometries of components are put in structured meshes of finite elements. Domains with isotropic and orthotropic material models are put in a mesh with hexaedric finite elements with quadratic interpolation and reduced integration (C3D20R type). Domains with cohesive material models (thick joints) are meshed with cohesive elements (COH3D8 type). In comparison with a non-structured mesh, a structured mesh gives more reliable results, also it makes it possible to thin the mesh in the directions of a monotone building, which can significantly reduce the time required for calculation. The mesh thickness is defined along all the edges of geometrical properties based on convergence analysis, by means of which its negligible impact upon model results is proved. An example is presented in Fig. 2, where due to insignificant convergencies a negligible impact upon the model results is established for all checked mesh densities.

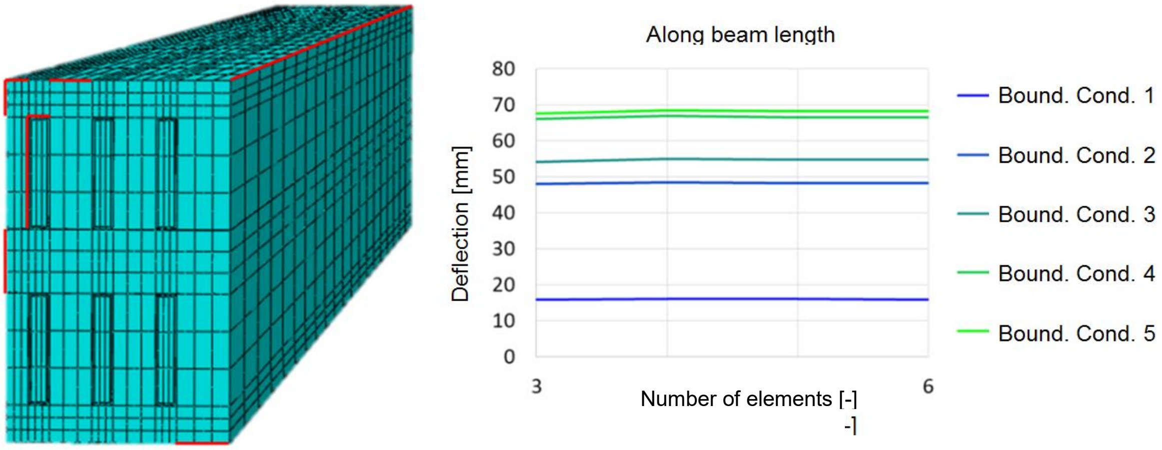

Figure 8: An example of a model with reinforced edges of geometrical properties, where the mesh density was checked with convergence analysis (left) and an example of convergence analysis results for the mesh density along the reinforcement width (right).

2.1.3 Interactions

Interactions link models of different components into a physical whole. The following interaction types are foreseen: i) connected surfaces, ii) ideally stiff contact, iii) very thin glued joint and iv) friction in case of boundary conditions. It is necessary to connect surfaces on the common surfaces of domains that lie next to each other and have to remain like that if they do not share common nodes. Such a phenomenon appears at the transition between the domain of isotropic and orthotropic materials and the cohesive domain with a thick joint. Although in this case, the cohesive elements used prevent the domains from overlapping, it is recommended to prescribe also the ideally stiff contact for connected surfaces of non-cohesive domains. For very thin glued joints, the cohesive behaviour is prescribed in the form of contact between the joined surfaces. The requirement of the ideally stiff contact and friction between the surfaces can be used in some case of requesting boundary conditions of an analysis, which no longer belongs to the description of a hybrid composite model.

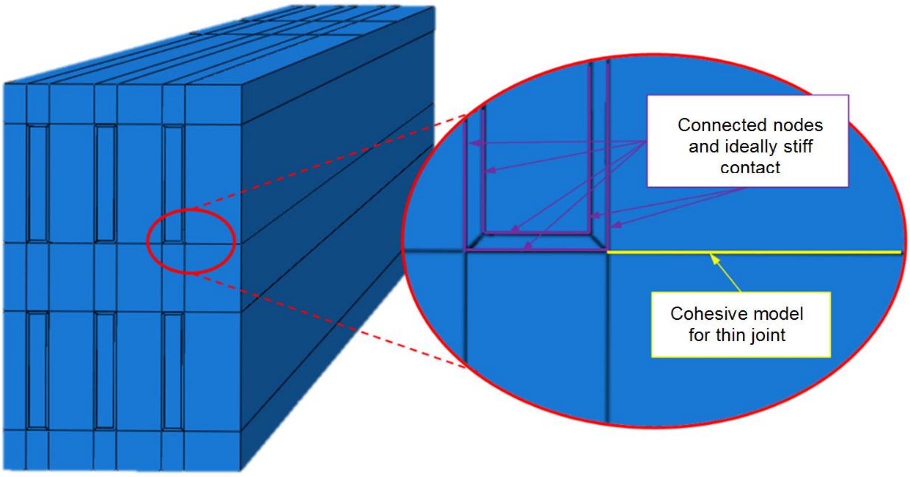

Figure 9: Places in an example of a wooden hybrid composite model with glued reinforcements, as shown in Fig. 1.

2.1.4 Boundary conditions

Due to its universal applicability, the numerical model is made in such a way that it makes it possible to change boundary conditions. The foreseen boundary conditions include local presriptions of shifts and loads. In some cases, due to a more precise physical description, they can be prescribed by means of additional deformable domains or analytically stiff objects. The use of symmetry boundary conditions is recommended to reduce the size of the calculation problem (Fig. 4).

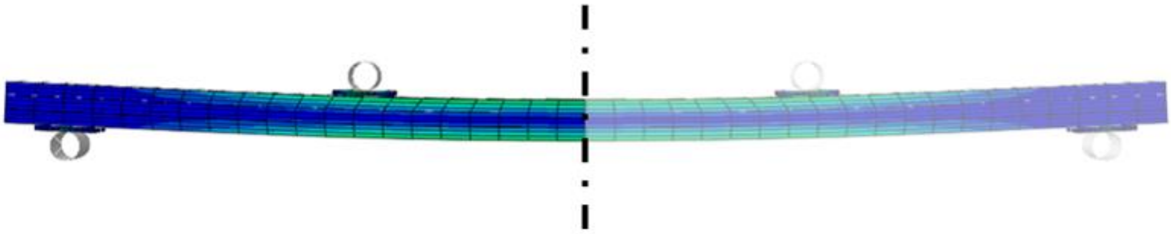

Figure 10: An example of a wooden hybrid composite support model with glued reinforcements and prescribed boundary conditions (4-point bending test) and boundary conditions of symmetry.

2.1.5 Automatized model development

The use of a model is significantly limited if it is necessary to change model parameters manually. These parameters can be material (less time is required to change material parameters) or geometrical (more time is required to change geometrical parameters as geometry of other components, their meshes, interactions and required boundary conditions must be refreshed as well). It is therefore sensible to automatize the most time-consuming variation steps of model parameters.

The automatization process depends on a specific example of use and it must be adjusted to each specific example of use of the model with changes in only a limited number of parameters. In the automatization process, it is necessary first to adjust the model in such a way that it is uniformly defined with the foreseen number of changeable parameters. In addition to this, extreme values of changeable parameters for which the model still gives good results must be defined.

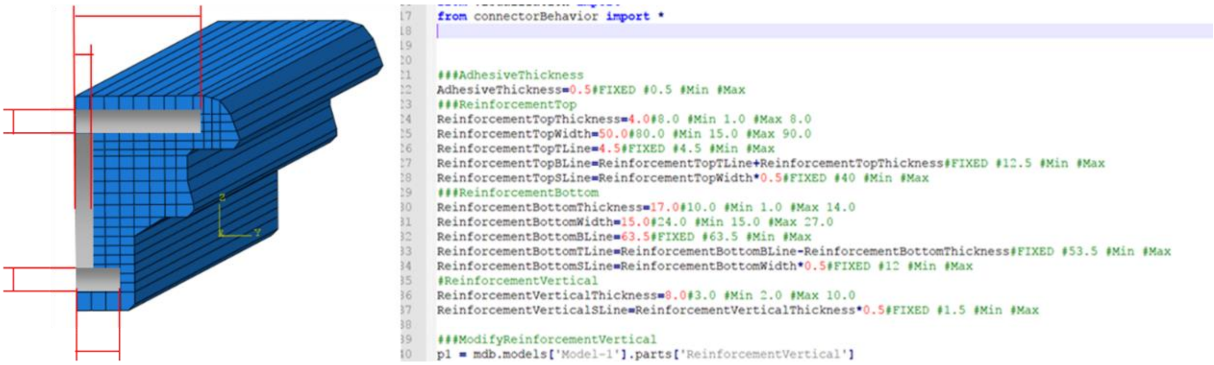

```
from connectorBehavior import *



###AdhesiveThickness
AdhesiveThickness=0.5#FIXED #0.5 #Min #Max
###ReinforcementTop
ReinforcementTopThickness=4.0#8.0 #Min 1.0 #Max 8.0
ReinforcementTopWidth=50.0#80.0 #Min 15.0 #Max 90.0
ReinforcementTopTLine=4.5#FIXED #4.5 #Min #Max
ReinforcementTopBLine=ReinforcementTopTLine+ReinforcementTopThickness#FIXED #12.5 #Min #Max
ReinforcementTopSLine=ReinforcementTopWidth*0.5#FIXED #40 #Min #Max
###ReinforcementBottom
ReinforcementBottomThickness=17.0#10.0 #Min 1.0 #Max 14.0
ReinforcementBottomWidth=15.0#24.0 #Min 15.0 #Max 27.0
ReinforcementBottomBLine=63.5#FIXED #63.5 #Min #Max
ReinforcementBottomTLine=ReinforcementBottomBLine-ReinforcementBottomThickness#FIXED #53.5 #Min #Max
ReinforcementBottomSLine=ReinforcementBottomWidth*0.5#FIXED #12 #Min #Max
#ReinforcementVertical
ReinforcementVerticalThickness=8.0#3.0 #Min 2.0 #Max 10.0
ReinforcementVerticalSLine=ReinforcementVerticalThickness*0.5#FIXED #1.5 #Min #Max

###ModifyReinforcementVertical
p1 = mdb.models['Model-1'].parts['ReinforcementVertical']
```

Fig. 11: The display of changeable parameters of a model based on an example of a wooden hybrid composite with glued reinforcements (left) and scripts in Abaqus adjusted for this purpose (right).

Afterwards, the script in Python is made (Fig. 5), on the basis of which Abaqus independently builds and changes a numerical model and also updates all the model properties related to the change (Fig. 6). Automatic development and automatic changes of the model enable much faster parametric studies and searches for the optimal composite structure if compared to changes of model parameters carried out manually.

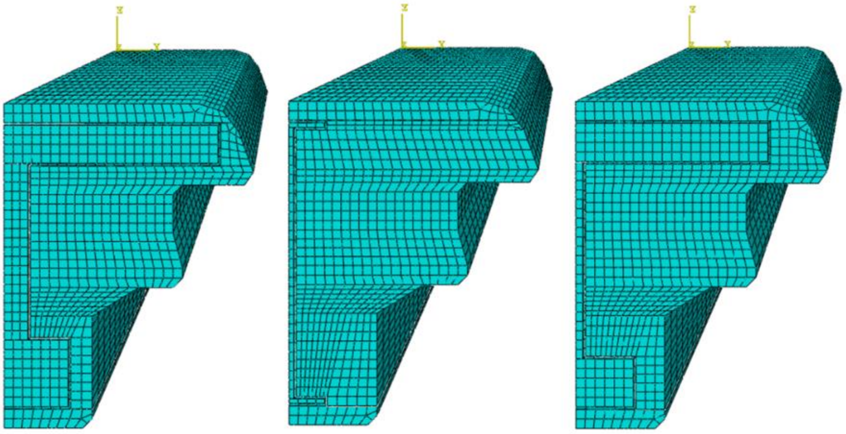

Fig. 12: Automatically generated geometries of a wooden hybrid composite with glued reinforcements: a model with the largest portion of reinforcements (left), with the smallest portion of reinforcements (in the middle) and with the medium portion of reinforcements (left).

2.2 Verification and validation of the numerical model

The model was validated on the basis of previously obtained experimental results. The numerical simulation fully simulates the experimentally carried out 4-point bending test (Fig. 7), regarding composite material properties, its geometry, interactions of domains and boundary conditions of supports and loading. In the numerical analysis, material data for wood, aluminium and glue were used. Geometrically, 4 cross-sections were made (1 without reinforcements and 3 with reinforcements, Fig. 8) that precisely simulated the cross-sections of experimentally tested supports, of experiments carried out in previous research.

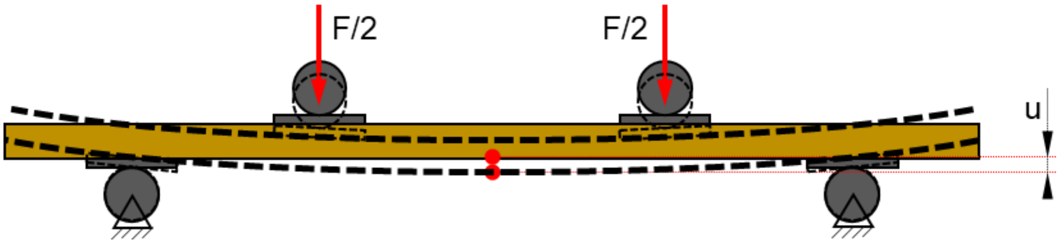

Figure 13: Schematic presentation of a mechanical experiment (4-point bending test) with used boundary conditions and observed values.

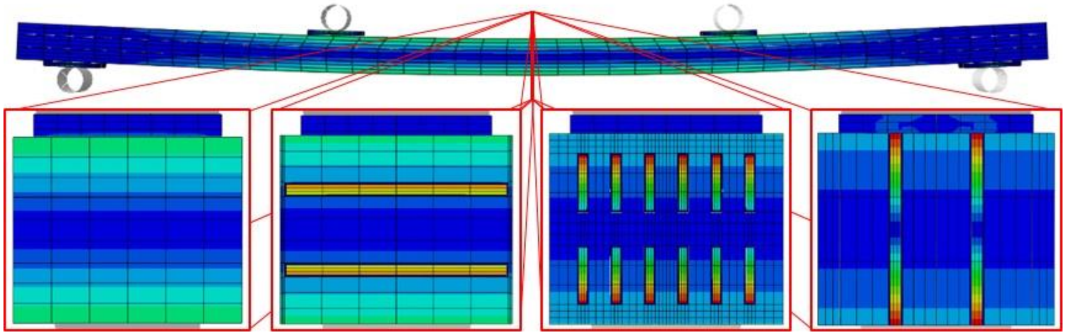

Fig. 14: Visualised simulation results for numerical models of hybrid composite supports with four different geometries of cross-section (from left to right: A, B, C and D).

During the experiment and also during simulation, the largest deformation of the hybrid composite support was observed. Fig. 9 presents the comparison between numerical and experimental results; the results match very well. Consequently, the model was validated to be used in comparable analyses.

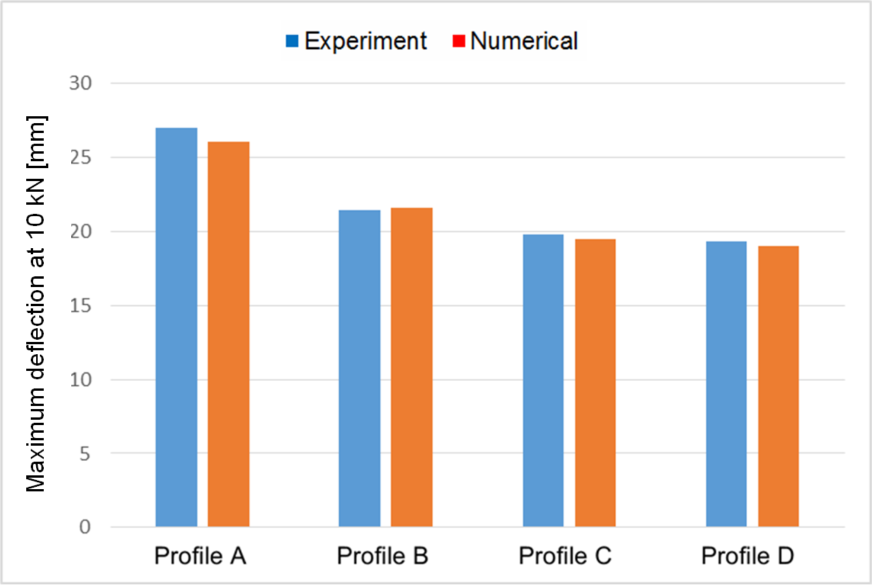

Fig. 15: Comparison of numerical and experimental results for a 4-point bending test of a reinforced composite support.

For the area of the established linear dependency of bendings of a hybrid support on the load, the bending stiffness of the support (ratio load/bending) was calculated on the basis of numerical results and also analytically on the basis of adding the products between elasticity modules and the torque of single component domains in cross-section.

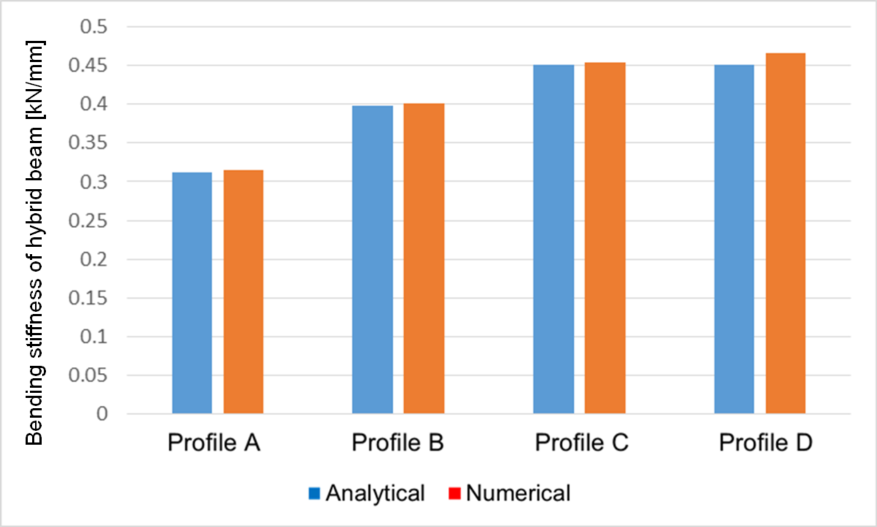

Figure 16: Comparison of numerically and analytically determined bending stiffnesses of a reinforced composite support.

Fig. 10 presents the comparison between numerically and analytically determined bending stiffnesses of the composite support with four different reinforced cross-sections. It is possible to establish very good matching of numerical and analytical results, consequently, the numerical model of the composite support is verified for the use in comparable analyses.

3.0 CONCLUSION

The paper presents the computer models based on the finite element method (FEM) implemented in the commercially available code Abaqus [6]. The model allows for variation of mechanical and geometrical properties, and enables observation of irreversible change initiation in the window frame member. It was used in parametrical simulations to find the optimal layout of reinforcements in the member, as well as for estimations of maximum performance for a certain design. All results presented here are making the platform for decisions of choosing proper orientation, number of reinforcements and their position in real-life window profiles (Figure 5). While searching for optimal hybrid beams, manufacturing limitations will be considered; avoiding contacts of reinforcements with machinery blades, having enough space for corner joints with dowels. Validity of the model was confirmed with good agreement between computational and experimental results.

Acknowledgement(s):
This work was supported by Ministry of Education, Science and Sport of the Republic of Slovenia, and by the European Regional Development Fund, European Commission, project: "**TIGR4smart/5441-1/2016/116**".

REFERENCES

[1] Bardella L., Paterlini L., Leronni A., Accurate modelling of the linear elastic flexure of composite beams warped by midlayer slip, with emphasis on concrete-timber systems, Int. J. Mech. Sci., 87, pp. 268–280, (2014).

[2] Auclair S. C., Sorelli L., Salenikovich A., A new composite connector for timber-concrete composite structures, Constr. Build. Mater., 112, pp. 84–92, (2016).

[3] Jasieńko J., Nowak T. P., Solid timber beams strengthened with steel plates – Experimental studies, Constr. Build. Mater., 63, pp. 81–88, (2014).

[4] Negrão J. H., Prestressing systms for timber beams, World conference on timber engineering, Auckland New Zealand, (2012).

[5] Winter W., Tavoussi K., Pixner T., Parada F. R., Timber-steel-hybrid beams for multi-storey buildings, World conference on timber engineering, Auckland New Zealand, (2012).

[6] Alhayek H., Svecova D., Flexural Stiffness and Strength of GFRP-Reinforced Timber Beams, J. Compos. Constr., 16-3, pp. 245–252, (2012).

[7] Fiorelli J., Dias A. A., Analysis of the strength and stiffness of timber beams reinforced with carbon fiber and glass fiber, Mater. Res., 6-2, pp. 193–202, (2003).

[8] Yang Y., Liu J., Xiong G., Flexural behavior of wood beams strengthened with HFRP, Constr. Build. Mater., 43, pp. 118–124, (2013).

[9] Nadir Y., Nagarajan P., Ameen M., Arif M., Flexural stiffness and strength enhancement of horizontally glued laminated wood beams with GFRP and CFRP composite sheets, Constr. Build. Mater., 112, pp. 547–555, (2016).

[10] Premrov M., Dobrila P., Experimental analysis of timber–concrete composite beam strengthened with carbon fibres, Constr. Build. Mater., 37, pp. 499–506, (2012).

[11] Nowak T. P., Jasieńko J., Czepiżak D., Experimental tests and numerical analysis of historic bent timber elements reinforced with CFRP strips, Constr. Build. Mater., 40, pp. 197–206, (2013).

[12] De la Rosa García P., Escamilla A. C., Nieves González García M., Bending reinforcement of timber beams with composite carbon fiber and basalt fiber materials, Compos. Part B Eng., 55, pp. 528–536, (2013).

[13] Borri A., Corradi M., Speranzini E., Reinforcement of wood with natural fibers, Compos. Part B Eng., 53, pp. 1–8, (2013).

[14] Plevris N., Triantafillou T. C., FRP-Reinforced Wood as Structural Material, J. Mater. Civ. Eng., 4-3, pp. 300–317, (1992).

[15] Ferrier E., Agbossou A., Michel L., Mechanical behaviour of ultra-high-performance fibrous-concrete wood panels reinforced by FRP bars, Compos. Part B Eng., 60, pp. 663–672, (2014).

[16] Tomasi R., Parisi M. A., Piazza M., Ductile Design of Glued-Laminated Timber Beams, Pract. Period. Struct. Des. Constr., 14-3, pp. 113–122, (2009).

[17] Zienkiewicz G. C., Taylor R. L., “Finite element method“, Volume 1: The basis., let. 2000, Oxford: Butterworth - Heinemann.

[18] Simulia: Products: Abaqus: FEA, let. 2011. 10.11.

THE HYBRID NATURE-INSPIRED ALGORITHMS APPLIED TO CHARACTERIZE THE HEAT TRANSFER COEFFICIENT FUNCTIONS

Z. Fried[1], G. Pintér[1], S. Szénási[1], I. Felde[1], D.Y.Ju[2]

[1]John von Neumann Faculty of Informatics, Óbuda University, Budapest, Hungary.
[2]Saitama Institute of Technology, Japan

Abstract. A parallelized numerical method based on a hybrid Particle Swarm Optimization (PSO) algorithm has been developed to solve Inverse Heat Transfer Problems. Temperature and space-dependent Heat Transfer Coefficient functions obtained on the surfaces of axisymmetric work pieces are estimated by applying the novel technique. The objective function to be minimized by the hybrid PSO approach is defined by the deviation of the measured and the calculated temperatures. The hybrid PSO algorithm has been parallelized and implemented on a Graphic Processing Unit (GPU) architecture. Numerical results are demonstrated that the determination of Heat Transfer Coefficient functions can be performed by using this hybrid PSO method, as well as, the GPU implementation; providing a less time consuming and more accurate estimation.

Keywords: parallelized numerical method, HTC, PSO, GPU

1. Introduction

The proper design of the heat treatment process requires an accurate knowledge of the thermal boundary conditions, including the Heat Flux (HF) or the Heat Transfer Coefficient (HTC). HTC describes heat exchange between the surface of an object and the surrounding medium. The determination of HTC [1] faces a typical Inverse Heat Conduction Problem (IHCP). The IHCP methods are using the temperature signals recorded and estimated by simulations at given locations of the work-piece. Several IHCP approaches are based on optimization methods, where the objective function has to be minimised is given as the difference of the measured and predicted temperature data [2], [3]. Genetic algorithms [4], [5], [6] are applied successfully for solving many types inverse heat transfer problem. The Particle Swarm Optimization (PSO) algorithm became popular in the recent years due to its ability of maintaining a good balance between the convergence and diversity [7], [8]. The efficiency of PSO technique in inverse heat conduction analysis was analysed by Vakili and Gadala [9] and shown that PSO can reduce the stability problems of the classical methods, for solving the inverse heat conduction problems.

In this work, an IHCP analysis of local coordinate and a time-dependent HTC is presented. Cooling curves recorded at multi-locations in the body of a cylinder have been used to obtain the inverse heat transfer computation. The objective function which is defined by the quadratic residual between the measurements and the calculated temperatures is minimized. The optimization techniques have been parallelized and implemented on a GPU architecture. The numerical results are demonstrated that the determination of Heat Transfer Coefficient functions can be performed by using the proposed approach, as well as, the GPU implementation; provide a less time consuming and accurate estimation.

2. The Inverse Heat Transfer Problem

Assuming that the temperature inside the work piece or on its surface is measured during the heat transfer process, it is possible to solve the inverse heat conduction problem by determining the time or temperature variations of the thermal boundary conditions [1], [2], [3]. The temperature is given by measurements at *p* points in the solid region, located at r_i, and the axial local coordinate z, (i=1…p). On calling T_i^m, the measured temperatures, and T_i^c, the calculated temperature at those points, the solution of the present inverse problem can be obtained by minimizing the following fitness functions

$$S = \sum_{i=1}^{p} (T_i^m - T_i^c)^2 = \min , if |T_i^m - T_i^c| > 1 \tag{1a}$$

$$S = \sum_{i=1}^{p} |(T_i^m - T_i^c)| = \min , if |T_i^m - T_i^c| \leq 1 \tag{1b}$$

The inverse problem is recasted as an optimization problem. A variety of numerical and analytical techniques have been developed to solve the optimization problems.

3. On the Thermal field calculation

A two-dimensional axis-symmetrical heat conduction model is considered to estimate the temperature distribution in a cylindrical work piece (the radius and length of the cylinder is noted by r and z according to Fig 1.). As radius is constant, the cylinder is subjected to a longitudinal local coordinate and time-dependent Heat Transfer Coefficient HTC(z, t) on all its surfaces. Both the thermal conductivity, density and the heat capacity are varying with the temperature, k(T), ρ(T) and C_p(T). The two-dimensional mathematical formulation of this nonlinear transient heat conduction problem can be described as follows:

$$\frac{\partial}{\partial r}\left(k\frac{\partial T}{\partial r}\right) + \frac{k}{r}\frac{\partial T}{\partial r} + \frac{\partial}{\partial z}\left(k\frac{\partial T}{\partial z}\right) + q_v = \rho \cdot C_p \frac{\partial T}{\partial t} \tag{2}$$

with the initial and the boundary conditions are

$$T(r,z,t) = T_0, t = 0 \tag{3}$$

$$k\frac{\partial T}{\partial z} \vee 0 \leq z \leq Z_{r=R} = HTC(z,t)\left[T_q - T(r,z,t)\right] \tag{4}$$

where r and z is the local coordinate, t is the time, T_0 is the initial temperature and T_q is the temperature of the cooling medium and q_v stands for volumetric heat generation . It has to be noted that phase transformations of the materials applied do not occur during the experiments, therefore latent heat generation induced by phase transformations is not considered.

4. Particle Swarm Optimization algorithm

The basic PSO model [10] consists of a swarm of M particles moving in the search space. For a N-dimensional search space, the position of the ith particle is represented as $X_i = (x_{i1},x_{i2}, \ldots ,x_{iN})$. Each particle is a potential solution of the global optimum. In other words, each particle stands for a set of input parameters by its position (X_i) which could give the lowest fitness value (the global optimum) in the search space. At each generation, the new particle position is found by adding a displacement to the current position where the displacement is the particle velocity multiplied by a time step of one as shown in Eq. (5)

$$X_i^{n+1} = X_i^n + V_i^{n+1} \tag{5}$$

In Eq. (5), X_i^n and X_i^{n+1} represent the previous and current positions of particle i, V_i^{n+1} is the current velocity of particle i and it is represented as $V_i^{n+1}= (v_{i1},v_{i2}, \ldots ,v_{iN})$. The velocity of each particle is also updated at each generation as suggested by Clerc [11]

$$V_i^{n+1} = C_3(V_i^n + c_1 r_1(P_{best,i} - X_i^n) + c_2 r_2(G_{best} - X_i^n)) \tag{6}$$

where V_i^n and V_i^{n+1} are the previous and current velocities of the particle i, respectively. Each particle maintains a memory of its previous best position, say $P_{best,i} = (p_{i1}, p_{i2}, \ldots ,p_{iN})$, where the position giving the best fitness function value. The best one among all the particles in the swarm is represented as the global best position, say $G_{best} = (p_{g1},p_{g2}, \ldots ,p_{gN})$. The new velocity in Eq. (6) can be seen as the sum of three parts. The applied c_1 and c_2 constants set to 2.05, while C_3 was set to 0.7298 [11].

5. Hybrid computation procedure for the PSO algorithm

The aim of the inverse analysis is to iteratively estimate the unknown HTCs using a hybrid PSO procedure which results a negligible difference between measurements taken at the given locations of the work piece and temperatures computed from the numerical model. The G_{best} update frequently has been modified by updating the value of the G_{best} every predefined iteration only for speeding up this algorithm. The fitness functions value of each particle at the nth iteration is given by the difference between the measured and calculated temperature curves, Eq (4) at the position X_i^n. The computational steps of the hybrid PSO algorithm described above are given as follows:

- Step 1: Generate the initial particles in a swarm by randomly generating the position and velocity for each particle.
- Step 2: Evaluate the fitness function of each particle.
- Step 3: Update the $P_{best,i}$ for each particle, if its fitness is smaller than the fitness of its previous best position ($P_{best,i}$).
- Step 4: Update the G_{best}, only inside the local thread if the fitness function of a particle is smaller than the fitness of the best position of all particles (G_{best}).

- Step 5: Synchronise all threads and update G_{best} to the real one in every I^{th} iteration. The I update frequently is chosen 500, which is based on some measurements of this algorithm.
- Step 6: Update each particle according to Eqs. (5) and (7).
- Step 7: Repeat the loop from step 2 until the exit criteria or a predefined number of generations is reached.
- Step 8. Repeat the loop from step 1 if the G_{best} is far away from the minima.

The PSO is hybrid because a special exit criteria and restarted functions are created. The exit function is measuring the particles velocities and the G_{best} changing of the particles velocities to identify the best exit point from the algorithm. It is strongly advised to parallelize the computational jobs in Step 2, 3, 4 and 5 due to the fact that there are no interferences between the iterations as well as there are no communication between the particles in the given iterations. Therefore, these parts can be executable in parallel by GPU implementation [12], [13]. We used the following architecture for our tests:

- Graphics Processor Unit: NVIDIA Tesla K40c
- Number of shades: 2880
- SMX Count: 15

6. Case Study

The HTC obtained during immersion quenching of a cylindrical bar have been estimated by using the proposed approach. A cylindrical work piece (diameter 20 mm, lengths 225 mm) have been equipped with eight thermocouples (TC). The material of the rod was an austenitic steel. (chemical composition is in Table 1.The physical properties are summarized in Table 2).

C%	Si%	Mn%	P%	S%	Cr%	N%	Ni%	Cu%
<0.1	<1.0	2.0	0.045	0.2	0.18	0.11	8.0	1.0

Table 1. Chemical composition of X8NiCrS18-9 steel grade

All of the TCs were located various distances from the top surface and 1 mm under the vertical surface of the cylinder (Fig 1.) The rod has been heated up to 880°C and immersed in oil (Isorapid 277) without agitation at 20°C temperature. The signals of the TCs have been recorded during the cooling process.

Temperature, °C	Specific heat, J/kgK	Conductivity, W/mK	Density, Kg/m^3
0	443.3	14.6	7920
200	530.9	17.14	7832
400	568.5	19.68	7865
600	591.5	22.22	7660
800	627.1	24.76	7570
1000	985.3	27.30	7480

Table 2. Physical properties of 1.4305 steel grade

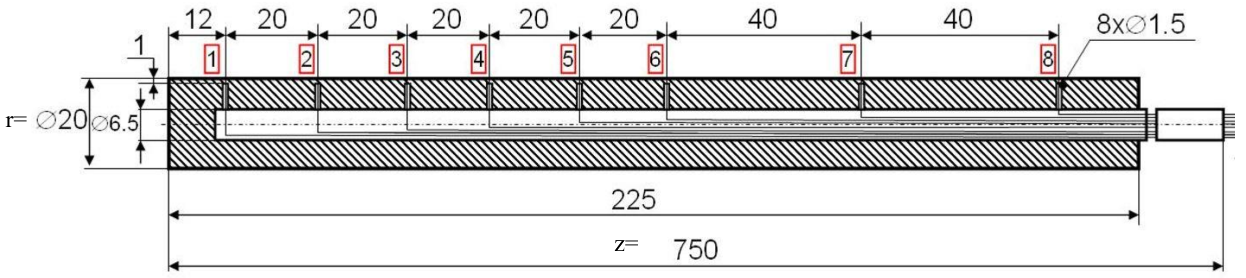

Figure 1. Locations of TCs mounted in the cylindrical work piece

A 2D axisymmetric heat transfer model was applied to calculate the temperature distribution during the cooling process. Inverse computations have been carried out by including PSO algorithm, in order to predict the HTC(z,t) functions. The exact values of the HTC(z,t) function was calculated by the bilinear interpolation procedure. The calculation process in each PSO stopped when the relative deviation of the fitness function between the former and the recent iteration step was less than 10%. The measured T_k^m, and the reconstructed T_k^c cooling curves at the locations of the TCs (i=1,2...8) are shown in Fig 2. Satisfactory agreement of original and predicted cooling curves can be observed. The difference between the measured and estimated samples as a function of time for each TC positions is shown in the charts of Fig. 2.

In order to quantify the magnitude of deviation between the measured and the recovered temperature samples the mean, standard deviation and maximum value of the difference of cooling curves in each positions were calculated (Table 3).

The highest value of temperature difference (22.94°C) was given at the 8th TC at the top of cylinder's length (z = 192 mm). The standard deviation were given in the range of 1.39 to 3.59 while the mean value of the differences was between 1.50 and 3.37. The reason of relatively high maximum deviations could be originated to the fact that the proper time instances needed to reconstruct the Heat Transfer Coefficient have not been found exactly by PSO algorithm. Due to the low value of differences the PSO approach applied to estimate the complex Heat Transfer Coefficient in a two dimensional axisymmetric model seems to be a feasible approach providing an acceptable accuracy.

The predicted Heat Transfer Coefficient function obtained by the PSO technique is shown in Fig. 3.

7. Conclusions

An inverse thermal analysis using a the Particle Swarm Optimization algorithm has been presented to estimate the Heat Transfer Coefficient in a two dimensional heat conduction problem. The HTC obtained on the surfaces of a cylindrical probe was considered as functions of local coordinates and time/temperature. The temperature signals acquisited during immersion quenching experiment have been applied for the inverse method. The obtained results underline the feasibility of the procedure and the capabilities for the PSO technique to predict a complex surface Heat Transfer Coefficients without using any prior information of the unknown transient functions. The PSO algorithm has been carried out in high performance GPU (Graphic Processing Unit) configuration. The GPU implementation of the inverse heat conduction problem provides significant acceleration of the prediction compared to sequential or multi-tier computation used on a personal computer.

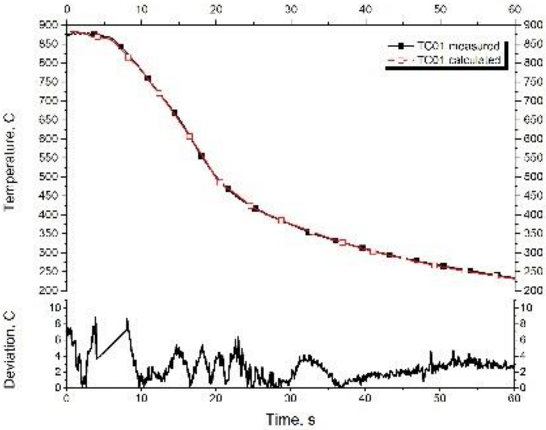

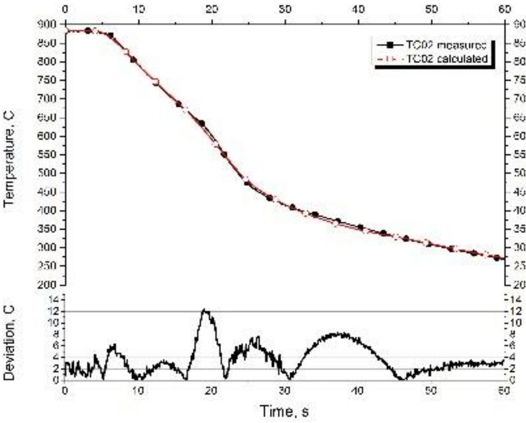

a **b**

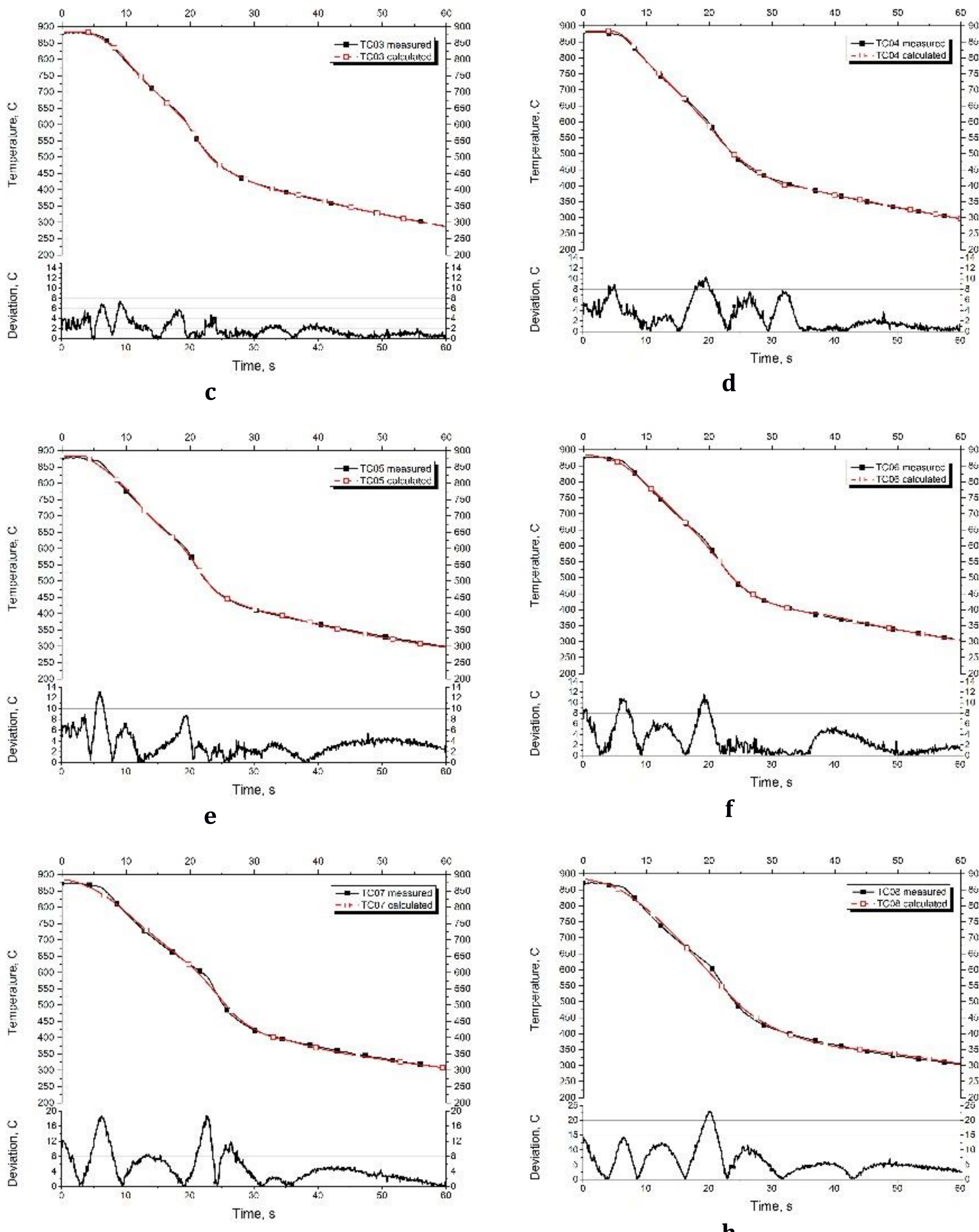

c **d**

e **f**

g **h**

Figure 2. The cooling curves of measured T_k^m, and the predicted T_k^c samples and their deviations at the locations of the TCs (a: TC1, b: TC2, c: TC3, d:TC4, e:TC5, f:TC6, g:TC7, h:TC8)

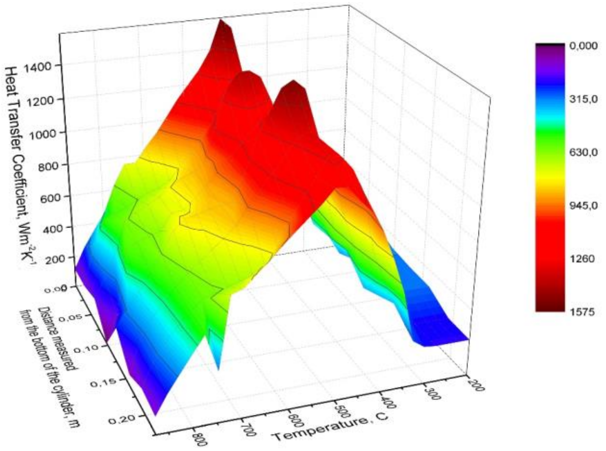

Figure 3. The estimated HTC(z,t) function

TC location, m	Mean, °C	Standard deviation, °C	Maximum deviation, °C
0.012	2.44	1,66	8,83
0.032	2.22	2.12	12.30
0.052	1.97	1.39	7.44
0.072	1.50	1.84	10.38
0.092	1.63	1.73	13.03
0.112	1.80	1.86	11.52
0.152	3.37	2.97	18.79
0.192	2.97	3.59	22.94

Table 3. The statistical information of deviations between measured T_k^m, and the reconstructed T_k^c cooling curves

Acknowledgments

We acknowledge the financial support of this work by the Hungarian State and the European Union under the EFOP-3.6.1-16-2016-00010 project and the Hungarian-Japanese bilateral Scientific and Technological (TÉT_16-1-2016-0190) project. Dr. Szénási acknowledges the support of the grant "ÚNKP-17-4/I. New National Excellence Program of the Ministry of Human Capacities".

References

[1] Beck J. V; Blackwell B; St Clair Jr. C.R: Inverse Heat Conduction, Wiley, New York, 1985. DOI: 10.1002/zamm.19870670331

[2] Alifanov O.M.: Inverse Heat Transfer Problems, Springer, Berlin/Heidelberg, 1994.

[3] Özisik M.N.; Orlande H.R.B.: Inverse Heat Transfer: Fundamentals and Applications, Taylor & Francis, New York, 2000

[4] Verma S.; Balaji C: Multi-parameter estimation in combined conduction radiation from a plane parallel participating medium using genetic algorithms, International Journal of Heat and Mass Transfer 50, 1706-1714., 2007 DOI: 10.1016/j.ijheatmasstransfer.2006.10.045

[5] Kim K.W.; S.W. Baek: Inverse surface radiation analysis in an axisymmetric cylindrical enclosure using a hybrid genetic algorithm, Numerical Heat Transfer Part A e Applications 46 (4) 367-381., 2004 DOI: 10.1080/10407780490478533

[6] Felde I.: Estimation of Thermal Boundary Conditions by Gradient Based and Genetic Algorythms, MATERIALS SCIENCE FORUM 729: pp. 144-149. (2012) DOI: 10.4028/www.scientific.net/MSF.729.144

[7] Ardakani M.D.; Khodadad M.: Identification of thermal conductivity and the shape of an inclusion using the boundary elements method and the particle swarm optimization algorithm, Inverse Problems in Science and Engineering 17 (7), 855-870., 2009 DOI: 10.1080/17415970902884136

[8] Qi H.; Ruan L.M; Shi ; An W.; Tan H.P.: Application of multi-phase particle Swarm Optimization Technique to inverse radiation problem, Journal of Quantitative Spectroscopy & Radiative Heat Transfer 109, 476–493. 2008 DOI: 10.1016/j.jqsrt.2007.07.013

[9] Vakili S.; Gadala M.S.: Effectiveness and efficiency of Particle Swarm Optimization technique in inverse heat conduction analysis, Numerical Heat Transfer Part B: Fundamentals 56 (2), 119–141., 2009 DOI: 10.1080/10407790903116469

[10] Kennedy J.; Eberhart R.C.: Particle Swarm Optimization, in: Proceedings of the IEEE International Conference on Neural Networks, 1942–1948. , 1995 DOI 10.1007/s11721-007-0002-0

[11] Clerc M.: The swarm and the queen: Towards a deterministic and adaptive Particle Swarm Optimization, in: Proceedings of the Congress on Evolutionary Computation, 1951–1957., 1999 DOI: 10.1109/CEC.1999.785513

[12] Szénási S.; Felde I.; Kovács I.: Solving One-dimensional IHCP with Particle Swarm Optimization using Graphics Accelerators, Proceedings of the 10th IEEE International Symposium on Applied Computational Intelligence and Informatics, Timisoara, Románia, 365-369., 2015 DOI: 10.1109/SACI.2015.7208230

[13] Kirk D. B.; Hwu W. W.: Programming Massively Parallel Processors: A Hands-on Approach, 1st ed. San Francisco, CA, USA: Morgan Kaufmann Publishers Inc., 2010.

[14] M.N. Özisik, H.R.B. Orlande: Inverse Heat Transfer: Fundamentals and Applications, Taylor & Francis, New York, 2000

AMINOTRIS(METILEN FOSFONSKA KISELINA) I NATRIJEV GLUKONAT KAO INHIBITORI KOROZIJE UGLJIČNOG ČELIKA U 3.5 % NACL OTOPINI

AMINOTRIS(METHYLENEPHOSPHONIC ACID) AND SODIUM GLUCONATE AS INHIBITORS OF CARBON STEEL CORROSION IN 3.5 % NACL SOLUTION

Franjo Ivušić[1], Vesna Alar[2], Helena Otmačić Ćurković[3]

[1] Croatian Academy of Sciences and Arts, Institute for Corrosion Research and Desalinization, Vlaha Bukovca 14, 20000 Dubrovnik, Croatia
[2] University of Zagreb, Faculty of Mechanical Engineering and Naval Architecture, Ivana Lučića 5, 10000 Zagreb, Croatia
[3] University of Zagreb, Faculty of Chemical Engineering and Technology, Marulićev trg 19, 10000 Zagreb, Croatia

Sažetak

U ovom radu je istraživan utjecaj aminotris(metilen fosfonske kiseline) (ATMP) i natrijevog glukonata (SG) na inhibiciju korozije ugljičnog čelika (RSt 37-2) u 3.5 % NaCl otopini pomoću Tafelove polarizacije i mikroskopije. Rezultati pokazuju da je ostvariva značajna inhibicija korozije primjenom mješavina ATMP-a i natrijevog glukonata (SG) čak i u malim koncentracijama. SG djeluje kao anodni inhibitor, dok ATMP djeluje kao katodni inhibitor. Primjenom mješavine oba inhibitora prevladava mehanizam katodne inhibicije.

Ključne riječi: *ugljični čelik, inhibitori korozije, natrijev glukonat, aminotrismetilen fosfonska kiselina, 3.5 % NaCl*

Abstract

The effect of combined action of aminotris (methylenephosphonic acid) (ATMP) and sodium gluconate (SG) on the corrosion inhibition of carbon steel (RSt 37-2) in 3.5 % NaCl solution has been studied using Tafel polarization and microscopy techniques. The results show that substantial corrosion inhibition using mixtures of ATMP and SG in low concentrations can be obtained. SG acts predominantly as anodic inhibitor whereas ATMP acts as cathodic inhibitor. Using both inhibitors predominant mechanism of cathodic inhibition is observed.

Keywords*: carbon steel, corrosion inhibitors, sodium gluconate, aminotris (methylenephosphonic acid), 3.5 % NaCl*

INTRODUCTION

Seawater and different brines are increasingly used in industrial practice (cooling water systems, desalination plants, injection water, fire fighting, ballast, pressure testing of pipelines) due to the both economic and ecological grounds. Since seawater is complex mixture containing many different salts, dissolved gases, trace elements, suspended solids, decomposed organic matter, and living organisms which composition varies on everyday basis it is not easily simulated in the laboratory for corrosion testing purposes. A 3.5 % NaCl solution is used frequently for this purpose and is known to be more aggressive toward carbon steel than natural seawaters [1, 2].

Carbon and low-alloy steels are low-initial cost alloys and are the most widely used materials for the marine environment, for both structural components and pressure-retaining applications. If appropriate protective measures are not used they have high maintenance and replacement costs [1]. In saline conditions carbon steels are highly susceptible to corrosion attack (general, localized and galvanic corrosion). Their protection is accomplished using protective coatings, corrosion inhibitors, galvanic protection or their combination [1, 3].

Highly toxic substances such as chromates, dichromates and nitrites that were widely and effectively used for corrosion protection are, due to increasingly more stringent environmental regulations, replaced by more environment friendly components [4]. Environmentally acceptable inhibitors are those inhibitors which, in applied concentrations, do not disturb ecological balance or take negative impact on human health. They can be divided in three groups: inorganic substances such as rare-earth metal (REM) salts, borates, silicates, molybdates; organic compounds such as thioglycollates, phosphonates, sulfonates, carboxylic acids and their salts (amino acids, fatty acids, gluconates), vitamins, pigments, antibiotic or antifungal drugs (e.g. imidazole compounds), alkaloids (nicotine, caffeine); and true “green” inhibitors such as various herbal extracts (water, alcohol or acid extracts) [3]. Extracts of natural plants are not expensive, environmentally acceptable and easily biodegradable. However, this biodegradability limits the storage and long-term usage of plant extracts [5]. Since they are complex mixtures of variety of compounds with uncertain exact composition it is not easy to predict their inhibitory action. Therefore, they are still rarely commercially applied in spite their ever growing popularity in numerous scientific researches [2].

Gluconates are environmentally suitable non-toxic compounds having also useful applications in medicine. The efficiency and the mechanism of the corrosion inhibition by gluconates, either as single compound or in a mixture, have been described in a number of recent studies [2, 3, 6-8]. Gluconates are part of the successful commercial corrosion inhibitors and are recommended in mixture with water soluble polymeric dispersant, organophosphonate and silicate [9].

ATMP is an environmentally suitable organic compound, which is mainly used in open water circulation cooling system, petroleum pipelines and boilers as scale and corrosion inhibitor [10]. It can be applied with other inhibitors, most notably Zn^{2+}, in well or saline waters and in those mixtures can have prominent synergistic effect on mild steel corrosion. It is often recognized as mixed type corrosion inhibitor [11].

1. EXPERIMENTAL

The electrochemical experiments were performed using carbon steel EN S235 JRG of following composition: C 0.17 %, P 0.05 %, S 0.058 %, N 0.007 %, Si 0.19 %, Mn 0.42 %. Working electrode area was 1 cm^2. Before measurements the specimen was polished with emery paper (400, 600, 800 and 1200 grade) degreased with ethanol and rinsed with demineralised water. Afterwards the working electrode was immersed in electrochemical cell containing 600 ml of investigated medium. All experiments were performed at ambient temperature (22 ±2 ^{o}C). The electrochemical cell was equipped with graphite auxiliary electrode and a reference saturated calomel electrode which was connected to the working electrode over Luggin capillary. Electrochemical measurements were performed on Potentiostat/Galvanostat EG&G PAR, Model 273 A using software SoftCorr III. The open circuit potential (OCP) was measured as a function of time in order to understand the corrosion behaviour of the sample in the electrolyte. A soon as the sample was immersed into the electrolyte, the initial potential of the sample was noted and monitored as a function of time until the sample attained a constant potential E_{corr} (typically 30–60 min). The method of quasi potentiostatic polarization or the Tafel extrapolation method was carried out recording polarization curves in the range ± 250 mV from the corrosion potential (E_{corr}) with a polarization rate 0.166 mVs^{-1}. From Tafel polarization curves following corrosion parameters were calculated: the corrosion current density (j_{corr}) and the inhibition coefficient (Z) was calculated using equation (1).

$$Z = \frac{j_{ni} - j_{inh}}{j_{ni}} \qquad (1)$$

Z – inhibition coefficient (-)

j_{ni} - corrosion current density of uninhibited experiment (μAcm^{-2})

j_{inh} - corrosion current density of inhibited experiment (μAcm^{-2})

Experiments were performed in 3.5 % NaCl solution. For electrolyte (media) preparation aminotris (methylenephosphonic acid) (p.a. Merck) and sodium gluconate (p.a. Alfa Aesar) were used. Prior to electrochemical measurements, pH of inhibitor solutions was adjusted to 7.00 ±0.02 with 0.1 M (mol L^{-1}) NaOH. After electrochemical measurements, the surface of the steel specimen was observed and photographed using stereomicroscope LeicaMZ6 (low amplification). For weighting of ATMP and SG a Kern ABS 220-4 balance (±0.0002 g) was used.

2. RESULTS AND DISCUSSION

2.1 The effect of SG and ATMP addition on corrosion inhibition in 3.5% NaCl- one inhibitor

In order to separately evaluate corrosion inhibition efficiency of SG and ATMP addition on protective properties of carbon steel in 3.5 % NaCl different concentrations of inhibitors were employed in one inhibitor system. An experiment without inhibitor addition was also performed. Tafel polarization curves are presented in Figs 1 and 2 and corrosion parameters on Tab 1. SG and ATMP were added in small amounts. Concentration range of SG was from 1 mM to 10 mM, and ATMP was added in concentrations from 1 to 8 mM (mmol L^{-1}). All employed SG concentrations had tendency to shift E*corr* value in the positive direction when compared to uninhibited curve. All employed SG concentrations considerably decreased corrosion current notably to similar extent (with exception of 1 mM, Tab. 1).

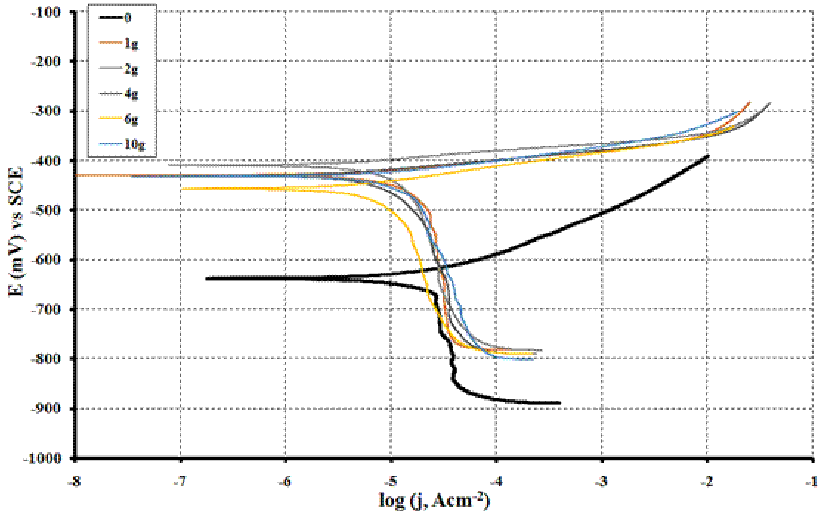

Fig. 1: Tafel polarization curves of carbon steel in 3.5 % NaCl –SG addition (number in legend represents mM of SG (g))

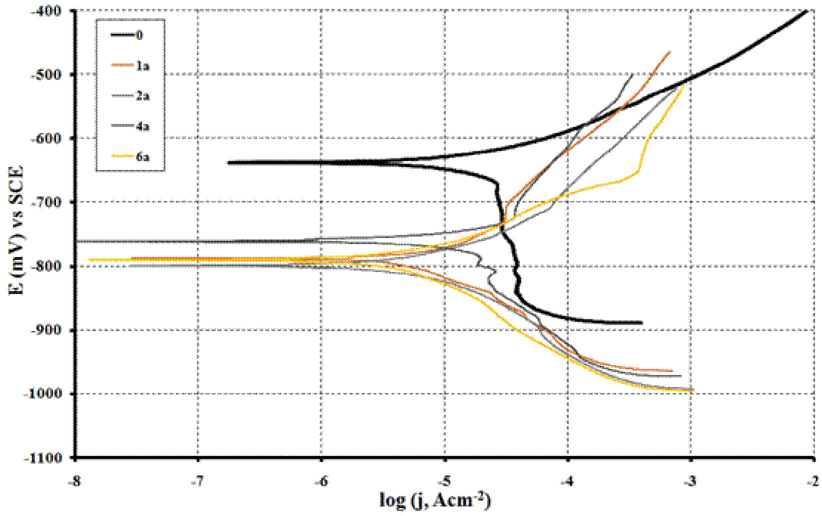

Fig. 2: Tafel polarization curves of carbon steel in 3.5 % NaCl –ATMP addition (number in legend represents mM of ATMP (a))

Opposite to SG experiments, ATMP had tendency to shift E*corr* value in the negative direction when compared to uninhibited curve (Fig 2, Tab 1.). Similar to SG, all employed ATMP concentrations considerably decreased corrosion current to similar extent (75 – 85 %). Despite fairly good corrosion current decrease, after electrochemical measurements the surface of the carbon steel specimens were either showing vast scale and/or oxidation product formation (i.e. Fig. 3, 2 SG, 6 ATMP) or pitting formation (Fig. 3, 6 SG, 1 and 2 ATMP).

Tab. 1: Corrosion parameters of carbon steel in 3.5 % NaCl solution- one inhibitor

Inhibitor concentration		E_{corr}	j_{corr}	Z
mM		mV	μAcm^{-2}	-
-		-631	42.41	0
SG	1	-429	17.42	0.59
SG	2	-409	9.68	0.77
SG	4	-431	8.56	0.80
SG	6	-456	7.94	0.81
SG	10	-432	11.79	0.72
ATMP	1	-788	10.68	0.75
ATMP	2	-799	9.32	0.78
ATMP	4	-761	11.96	0.72
ATMP	6	-790	6.39	0.85

Therefore, giving the fact that surface of the carbon steel specimens after electrochemical research is still not well protected in 3.5 % NaCl medium, exhibiting general or pitting corrosion occurrence, further experiments were performed by mixing SG and ATMP. It can be concluded that SG acts as anodic inhibitor and ATMP as cathodic inhibitor on employed carbon steel in 3.5 % NaCl medium.

Without inhibitor **2 SG** **6 SG**

1 ATMP **2 ATMP** **6 ATMP**

Fig. 3: Surface of the carbon steel specimens after electrochemical measurements in 3.5% NaCl solution- one inhibitor

2.2 The effect of SG and ATMP addition on corrosion inhibition in 3.5% NaCl- two inhibitors mixtures

In order to determine possible synergistic effect on corrosion inhibition, SG was supplemented with ATMP in two inhibitors media (Tab 2.). Tafel polarization curves are presented in Figs 4-7. Surface of the carbon steel specimens after electrochemical measurements is shown in Fig 8. Almost all of the inhibitor combinations showed substantial corrosion rate reduction compared to uninhibited medium. Moreover, all inhibitor combinations had tendency to shift E*corr* value in the negative direction when compared to uninhibited curve, thereby acting as predominately cathodic inhibitors.

a) Experiments with 1 mM of ATMP (Fig 4, Tab 2), which was the lowest employed concentration of ATMP, showed modest corrosion inhibition. In this experimental set the best corrosion inhibition was achieved with medium that contained moderate SG concentration (4 mM) which reached around 80 %. At higher concentrations of ATMP (2 mM; Fig 5, Tab 2) all combinations showed pronounced corrosion inhibition with values greater than 80 %. Likewise all combinations were similar when Tafel curves were compared (Fig 4). The surface of the carbon steel specimens after electrochemical measurements (Fig 8) showed the development of pitting corrosion at lower and higher concentrations of SG. Therefore, combination with 2 mM of both SG and ATMP was chosen as the best combination in this experimental set, given the fact that it displayed both excellent corrosion inhibition and, at the same time, carbon steel specimen surface that was without any signs of general or pitting corrosion after measurement. Moreover, low concentrations of this corrosion inhibitor mixture are favourable regarding the price of consequent inhibitor mixture and also more ecologically beneficial. At higher concentrations of ATMP (4 mM; Fig 6, Tab 2) similar to pevious experimental set, best inhibition was obtained using moderate concentrations. In this case it was combination with 4 mM of both SG and ATMP. Lower and higher concentrations of SG led to the development of pitting corrosion on the steel specimens (Fig 8). In last experimental set with 6 mM of ATMP corrosion inhibitor efficiency decreased significantly when compared to previous experimental sets (Fig 7, Tab2).

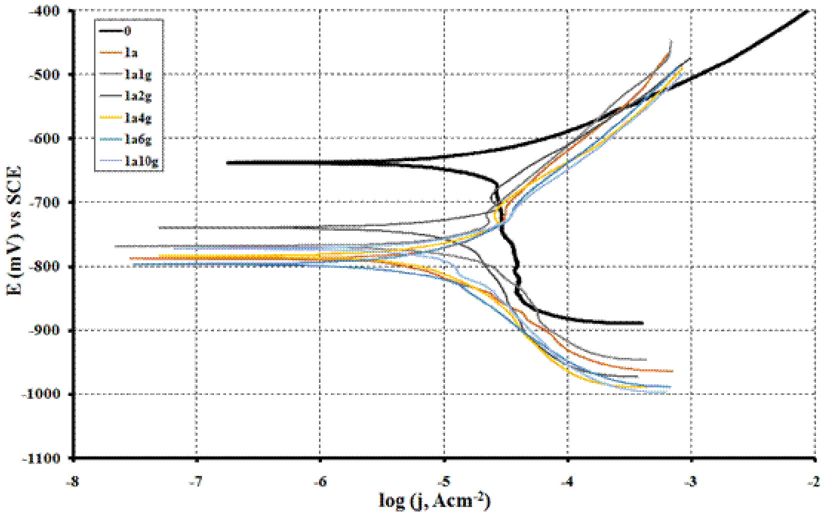

Fig. 4: Tafel polarization curves of carbon steel in 3.5 % NaCl –mixtures with 1 mM ATMP (numbers in legend represents mM; ATMP (a) and SG (g))

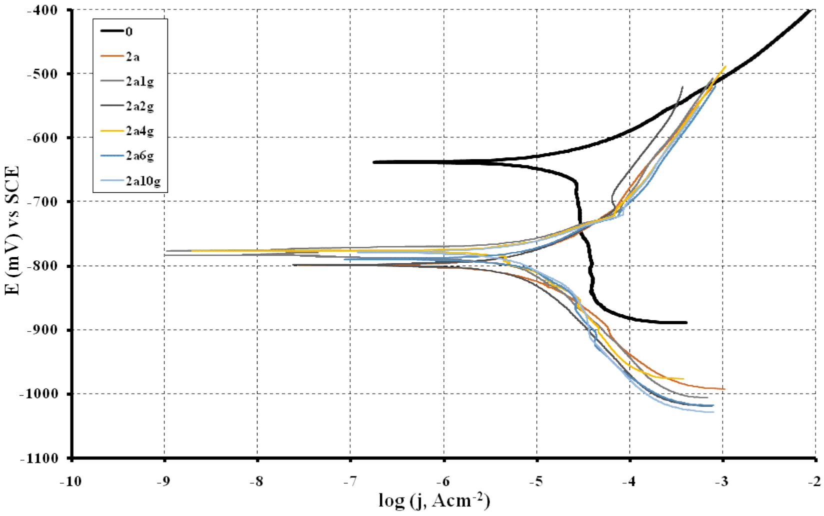

Fig. 5: Tafel polarization curves of carbon steel in 3.5 % NaCl –mixtures with 2 mM ATMP (numbers in legend represents mM; ATMP (a) and SG (g))

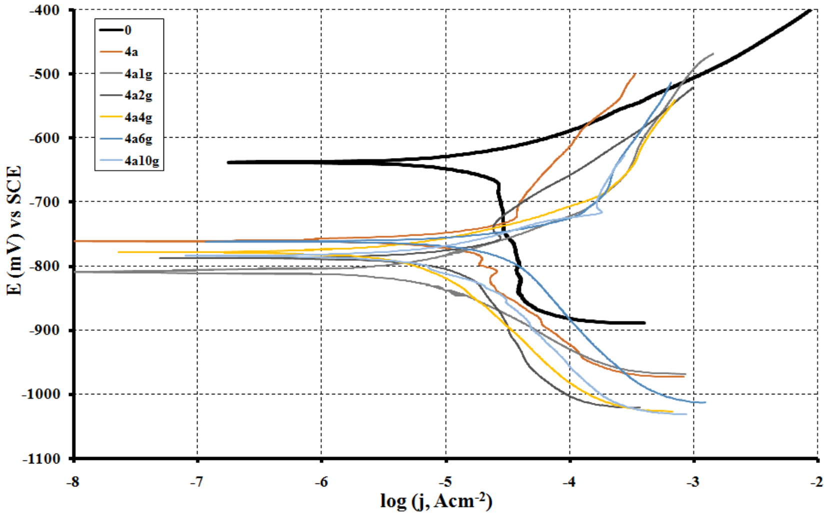

Fig. 6: Tafel polarization curves of carbon steel in 3.5 % NaCl –mixtures with 4 mM ATMP (numbers in legend represents mM; ATMP (a) and SG (g))

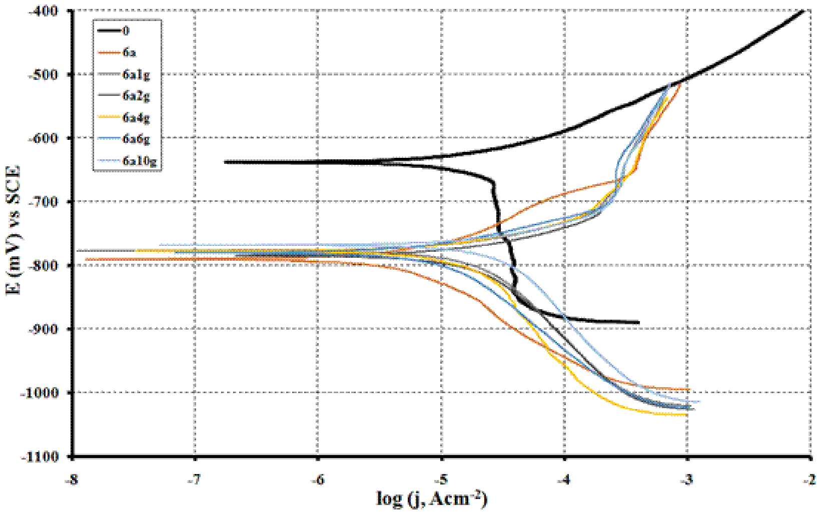

Fig. 7: Tafel polarization curves of carbon steel in 3.5 % NaCl –mixtures with 6 mM ATMP

(numbers in legend represents mM; ATMP (a) and SG (g))

Tab. 2: Corrosion parameters of carbon steel in 3.5 % NaCl solution- two inhibitors mixtures

Inhibitors concentrations		E_{corr}	j_{corr}	Z	Inhibitors concentrations		E_{corr}	j_{corr}	Z
mM		mV	µAcm^{-2}	-	mM		mV	µAcm^{-2}	-
SG	ATMP				SG	ATMP			
1	1	-768	16.37	0.61	1	4	-810	6.71	0.84
2	1	-739	16.78	0.60	2	4	-783	10.82	0.74
4	1	-784	8.81	0.79	4	4	-778	6.17	0.85
6	1	-797	12.05	0.72	6	4	-762	26.44	0.38
10	1	-772	13.83	0.67	10	4	-784	10.84	0.74
1	2	-780	6.02	0.86	1	6	-777	18.61	0.56
2	2	-799	6.76	0.84	2	6	-785	20.23	0.52
4	2	-779	5.62	0.88	4	6	-778	15.55	0.63
6	2	-790	6.31	0.85	6	6	-780	9.82	0.77
10	2	-779	8.2	0.81	10	6	-768	28.72	0.32

1 SG + 2 ATMP **1 SG+ 4 ATMP** **2 SG+ 2 ATMP**

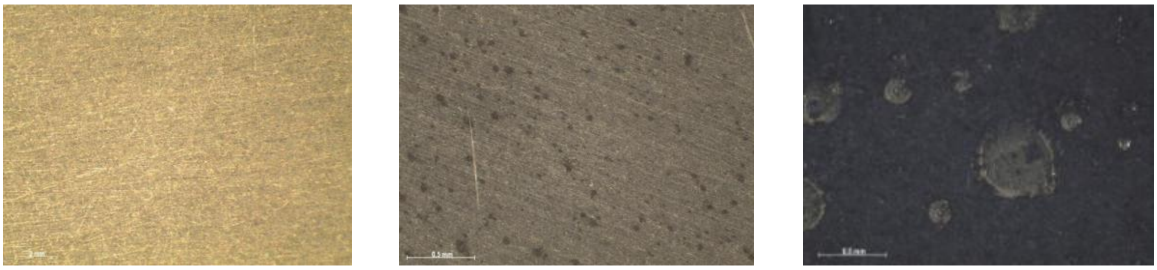

4 SG + 4 ATMP **6 SG+ 2 ATMP** **6 SG + 4 ATMP**

Fig. 8: Surface of the carbon steel specimens after electrochemical measurements in 3.5% NaCl solution (characteristic experiments) - two inhibitors mixtures

3. CONCLUSION

For concluding remarks it can be emphasised that sodium gluconate acts predominately as anodic inhibitor in 3.5 % NaCl on carbon steel. Opposite to sodium gluconate ATMP acts predominately as cathodic inhibitor in 3.5 % NaCl. Its optimal concentration for carbon steel RSt 37-2 was 2 mM. By supplementation with sodium gluconate inhibitory effect was further improved. The mixtures of ATMP and sodium gluconate acted predominately as cathodic inhibitors. Although almost all mixtures decreased corrosion current significantly, combinations of moderate concentrations were more successful. Optimal concentration determined in this work was 2 mM of SG and 2 mM of ATMP. That combination reached efficiency of 84 % without any signs of general or pitting corrosion after measurement.

REFERENCES

[1] Francis R., Powell C., "Corrosion Performance of Metals for the Marine Environment: A Basic Guide", 1st Edition, 2012, Maney Publishing.

[2] Ivušić F., Lahodny-Šarc O., Alar V., Corrosion inhibition of carbon steel in various water types by zinc gluconate, Materialwissenschaft und Werkstofftechnik, 44, pp. 319–329, (2013).

[3] Ivušić F., Lahodny-Šarc O., Otmačić Ćurković H., Alar V., Synergistic inhibition of carbon steel corrosion in seawater by cerium chloride and sodium gluconate, Corrosion science, 98, pp. 88-97, (2015).

[4] Forsyth M., Wilson K., Behrsing T., Forsyth C., Deacon G. B., Phanasgoankar A., Effectiveness of Rare-Earth Metal Compounds as Corrosion Inhibitors for Steel, Corrosion, 58, pp. 953-960, (2002).

[5] Sangeetha M., Rajendran S., Muthumegala T. S., Krishnaveni A., Green corrosion inhibitors-An Overview, Zaštita materijala, 52, pp. 3-19, (2011).

[6] Ivušić F., Lahodny-Šarc O., Stojanović I., Corrosion inhibition of carbon steel in saline solutions by gluconate, zinc sulphate and green clay eluate, Tehnički vjesnik, 21, pp. 107-114, (2013).

[7] Touir R., Cenoui M., El Bakri M., Ebn Touhami M., Sodium Gluconate as Corrosion and Scale Inhibitor of Ordinary Steel in Simulated Cooling Water, Corrosion Science, 50, 1530-1537, (2008).

[8] Shibli S. M. A., Kumary V. A., Inhibitive effect of calcium gluconate and sodium molybdate on carbon steel, Anti-Corrosion Methods and Materials, 51, pp. 277–281, (2004).

[9] Shim S.H., Bakalik D. P., Johnson D. A., Yang B., Lu F. F., Carbon steel corrosion inhibitors, US Patent 5589106, (1996).

[10] Muthumani N., Rajendran S., Pandiarajan M., Lydia Christyd J., Nagalakshmie R., Corrosion Inhibition by Amino Trimethylene Phosphonic Acid (ATMP) - Zn^{2+} System for Carbon Steel in Ground Water, Portugaliae Electrochimica Acta, 30, pp. 307-315, (2012).

[11] Balanaga Karthik B., Selvakumar P., Thangavelu C., Phosphonic Acids used as Corrosion Inhibitors-A Review, Asian Journal of Chemistry, 24, pp. 3303-3308, (2012).

KLIZNO TROŠENJE DENTALNOG POLIMERA OJAČANOG MORSKIM ŠKOLJKAMA

SLIDING WEAR OF DENTAL POLYMERS-SEASHELL BASED BIOCOMPOSITE

Suzana Jakovljević[1] , Krešimir Grilec[1], Ivan Primorac[1], Matija Hržina

[1] Fakultet strojarstva i brodogradnje, Sveučilište u Zagrebu, I-. Lučića 1

Sažetak: U radu je ispitana tvrdoća i otpornost na klizno trošenje poli metilmetakrilata - PMMA ojačanog česticama morskih školjaka u suhom i vlažnom okruženju. PMMA biokompoziti sadržavaju 5%, 10% i 15% masenog udjela čestica morskih školjki, a kao kontrolni uzorak proizveden je uzorak bez čestica. Tvrdoća i otpornost na trošenje u vlažnom okruženju značajno rastu. Najviša vrijednost postignuta je kod biokompozita ojačanog s 10 % čestica morskih školjaka. Zaključeno je da se PMMA biokompozit može uspješno ojačati česticama morskih školjaka te postići bolja svojstva kod sadržaja od 10% čestica morskih školjaka.

Ključne riječi: *biopolimeri, trošenje, morske školjke*

Abstract: A study has been made to evaluate the hardness and sliding properties the Poly (Methyl methacrylate) PMMA based denture composite reinforced with seashell nanopowder in dry and wet condition. The PMMA biocomposites containing 5%, 10% and 15% by weight of seashell nanopowder and an unfilled composite as control specimen were fabricated. The hardness and the wear resistant significantly were increased in wet condition. The highest value was achived in 10% seashell nanopowder reinforced composite. It was concluded that PMMA biocomposite could be successfully reinforced by seashell nanopowder with better properties at 10% seashell nanopowder content.

Keywords: *biopolymers, wear, seashell*

1. UVOD

Kada se govori o stomatološkim materijalima misli se na materijale koji se koriste u različitim stomatološkim zahvatima, bez obzira jesu li određeni za stalnu ili privremenu primjenu u ustima pacijenta ili se, pak, koriste u zubotehničkom laboratoriju tijekom izradbe nadomjestaka. U svrhu uspješnog rukovanja stomatološkim materijalima, u kliničkoj i laboratorijskoj stomatologiji, neophodno je poznavati njihova mehanička, fizikalna, kemijska i biološka svojstva, kao i tehnološki postupak primjene pojedinog materijala. [1] Poželjna svojstva biomaterijala definiraju se pojmom biokompatibilnosti, tj. sposobnošću materijala da pobudi prikladan biološki odgovor na mjestu primjene.

U stomatološkoj protetici primjenjuje se oko 95% akrilata i ojačanih akrilnih polimera. Mobilne, djelomične i potpune proteze najčešće se izrađuju iz polimera za bazu proteze, uglavnom poli (metil-metakrilata), ukratko PMMA. Iako s brojnim dobrim i klinički prihvatljivim svojstvima, ovaj materijal ima i nedostataka, tj. krhak je. Žvačni sustav „proizvodi" naprezanja protezne baze stotine tisuća puta godišnje, uz učestali lom protezne baze, što predstavlja klinički nedostatak, neugodu i dodatne troškove korisnicima mobilnih proteza [2].

Kod kompozita s disperzijom, povišena čvrstoća postiže se ekstremno malim česticama disperzirane faze koje usporavaju gibanje dislokacija. Razmatranje ovog mehanizma očvršćivanja je na nivou atoma. Male čestice disperzirane su u matrici, a dimenzije su im od 10 nm do 250 nm. Svojom prisutnošću male čestice ometaju gibanje dislokacija matrice, te je na taj način ojačavaju. Kompoziti s dodanim malim česticama se zbog toga nazivaju disperzijski ojačanim kompozitima. Za učinkovito ometanje gibanja dislokacija matrice, disperzirane male čestice moraju biti tvrde, a učinak ojačanja osim o tvrdoći ovisi i o veličinama, oblicima, količinama i raspodjelama disperziranih čestica. U materijalu matrice se disperzirane čestice ne smiju otapati niti s njom kemijski reagirati. S druge strane male čestice moraju biti čvrsto povezane s materijalom matrice [3].

2. EKSPERIMENTALNI DIO

2.1. Priprema čestica morskih školjaka i kompozita ojačanog morskim školjkama

U svrhu stvaranja biokompozita školjke su četkicom očišćene od stranih tvari i prljavštine, potom isprane u čistoj, slatkoj vodi te ostavljene da se osuše. Nakon sušenja školjke su grubo, mehanički usitnjavane - prvo čekićem pa potom dodatno usitnjene korištenjem tučka i tarionika. Nakon grubog mehaničkog usitnjavanja školjke su prebačene u posudu planetarnog kugličnog mlina, Retsch PM100. Materijal stijenke posude i kuglica je aluminij oksidna keramika α-Al_2O_3. Brzina okretaja je 300 rpm i vrijeme trajanja usitnjavanja kuglicama je 2h. Postupak usitnjavanja školjki se ponovio 2x kako bi se dobile čestice 50 µm ili manje. Dobiveni prah je sušen u peći na temperaturi 100 °C u trajanju tri sata kako bi se uklonila vlaga. Slika 1 prikazuje postupak dobivanja praha.

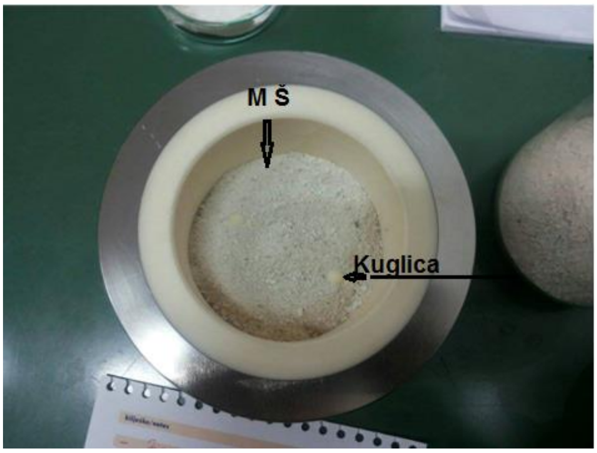

Slika 1. Grubo usitnjene morske školjke s Al_2O_3 kuglicama u mlinu [4]

S ciljem dobivanja čestica < 50 μm, usitnjene školjke prosijane su na uređaju za prosijavanje Retsch AS 200. Postupak je proveden dva puta zbog čestica koje su zatvarale otvore sita. Čestice školjaka i prah PMMA miješani su u mlinu PM 100, Retsch u različitim postocima. Vrijeme trajanja pojedinog postupka iznosi 10 minuta, a broj okretaja 500 min^{-1}. Sastav suhog dijela biokompozita sadržavao je PMMA s 5%, 10% te 15% čestica morskih školjaka.

Prilikom lijevanja korišten je ProBase Cold, samotvrdnjavajući materijal za temelje proteze. ProBase Cold ima odlične osobine slijevanja i oblikovanja. Lagan je i pouzdan za upotrebu s tehnikom lijevanja ili brtvljenja, čak i kad postoje dva ili više kalupa. Prašak i tekućina se mogu dozirati po želji unutar uobičajenih granica, pa zato postoji mogućnost različitog vremena rada sa postojećim materijalom [5].

Omjer miješanja komponenti je 15 g kompozita (prašak; PMMA + morske školjke) : 10 ml monomera (tekućina). Lopaticom je dobro izmiješan polimer s monomerom, te je ostavljen 15 sekundi da izađe višak zraka kako ne bi ostale šupljine. Nakon toga se kompozit lijeva u kalup i pokriva gornjom pločom kako bi se kalup zatvorio te materijal poprimio dimenzije kalupa. Zatvoreni kalup se stavlja u prešu na temperaturu 40°C i tlak 2 bara u trajanju 15 minuta. Nakon hlađenja uzorci su izvađeni iz kalupa, slika 2, te izrezani na odgovarajuće dimenzije definirane zahtjevima ispitivanja [4].

Slika 2. Uzorci s 0 % i s 15% čestica [4]

Ispitivanja su provedena na uzorcima u suhom stanju te na uzorcima koji su bili 24sata uronjeni u NaCl.

2.2. Ispitivanje tvrdoće uzoraka

Tvrdoća uzoraka je izmjerena Rockwellovom metodom, na tvrdomjeru za mjerenje tvrdoće polimera. Tvrdoća je mjerena utiskivanjem kuglice promjera 5mm prema standardu DIN53456. Kuglica je utiskivana silom od 358 N. Tvrdoća je ispitana u vremenskim intervalima od 10, 30 i 60 sekundi na svim uzorcima. Na svakom ispitnom uzorku izvršeno je 5 mjerenja, 2 u suhom stanju i 3 u mokrom. Od izmjerenih vrijednosti je oduzeta vrijednost korekcije koja iznosi 0,02 mm. Nakon korekcije vrijednosti prodora izračunate su vrijednosti prema jednadžbi [4]:

$$H = \frac{F}{D \cdot \pi \cdot h} \tag{1}$$

gdje je:
H – tvrdoća, N/mm^2
F – sila utiskivanja kuglice, N
D – promjer kuglice, mm
h – dubina prodiranja kuglice, mm

Rezultati tvrdoće navedeni su u tablicama:

Tablica 1. Rezultati izmjerene tvrdoće

Stanje uzorka	Tvrdoća 10 s, N/mm^2	Tvrdoća 30 s, N/mm^2	Tvrdoća 60 s, N/mm^2
0% školjaka			
suho	143,18	136,80	132,83
vlažno	144,72	134,75	130,9
5% školjaka			
suho	132,83	134,75	127,27
vlažno	152,72	149,43	144,72
10% školjaka			
suho	143,18	134,75	130,90
vlažno	165,65	156,23	152,72
15% školjaka			
suho	132,83	129,09	127,27
vlažno	146,25	141,73	137,48

.

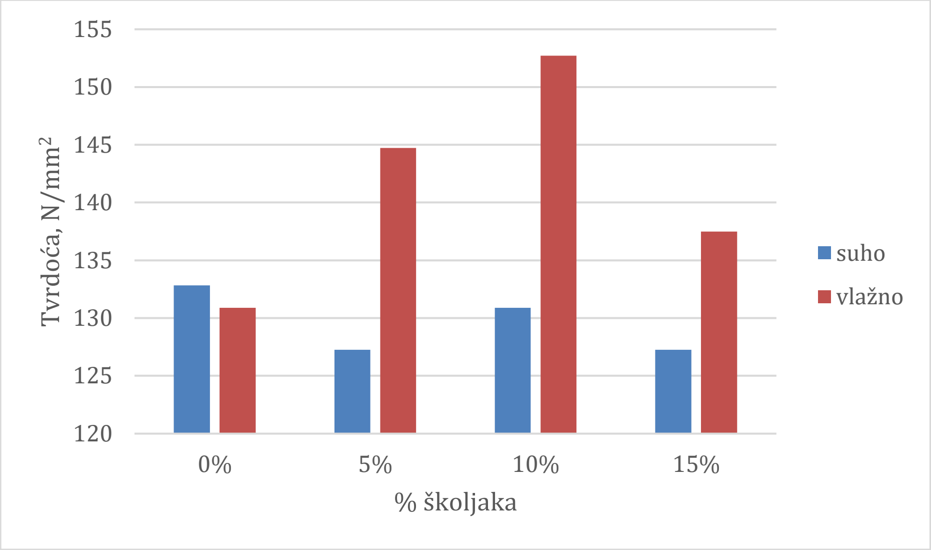

Slika 3. Tvrdoća nakon 60s u vlažnom i suhom stanju

Rezultati prikazani tablicom 1 i histogramom na slici 3 pokazuju da vrijednosti tvrdoća padaju nakon povećanja vremena ispitivanja kod svih biokompozitnih uzoraka u oba stanja, suhom i vlažnom. Vrijednosti tvrdoće uzoraka vlažnog stanja veće su od vrijednosti u suhom što se može objasniti upijanjem tekućine čestica školjaka. Rast tvrdoće nije veći s većim udjelom postotka čestica školjaka već pada nakon dostignute najviše vrijednosti tvrdoće kod uzoraka s 10% udjela čestica školjaka. Vrijednost tvrdoće uzoraka s 5% školjaka u vlažnom stanju više su od vlažnih uzoraka s 15% čestica školjaka što se može objasniti aglomeracijom čestica unutra kompozita [6].

2.3. Klizno trošenje

Ispitivanja na klizno trošenje provedena su na uređaju za ispitivanje kliznog trošenja, slika 4, u Laboratoriju za tribologiju, Fakultet strojarstva i brodogradnje – Zagreb.
Uređaj je pokretan elektromotorom. Tribo par za ispitivanje kliznog trošenja je keramika Al_2O_3 prikazana na slici 5 i polimer PMMA s česticama MŠ. Prizma Al_2O_3 učvrsti se u gornju čeljust uređaja, a ispitivani biokomopozitni uzorak u donju čeljust. Nakon opterećenja uzorka utegom preko poluge, uzorci dolaze u međusobni dodir. Uključivanjem elektromotora gornji uzorak klizi o površinu donjeg [4].

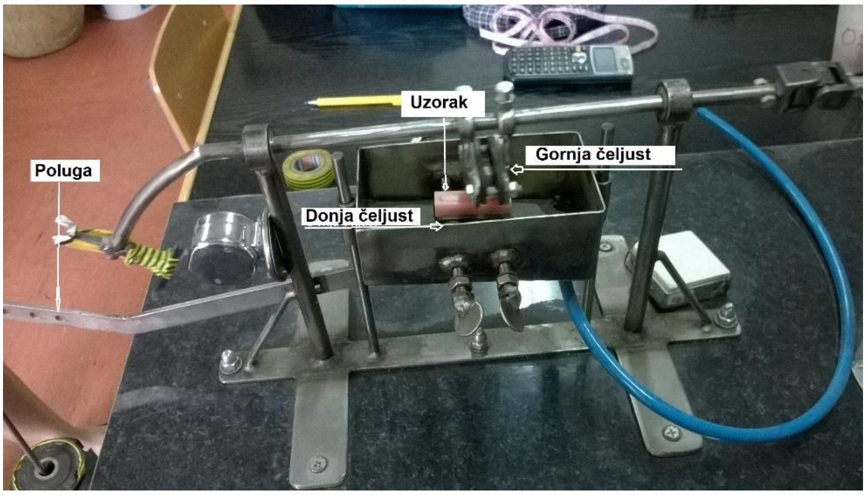

Slika 4.: Uređaj za ispitivanje kliznog trošenja [4]

Slika 5.: Keramika Al_2O_3 [4]

Broj ciklusa ponavljanja iznosio je 2000, a opterećenje je bilo 20 N. Ispitivani su uzorci u suhom i vlažnom stanju, broj uzoraka po stanju je 3. Dimenzije uzoraka iznosile su 85x10x10 mm, a prikazani su slikom 6.

Slika 6. Uzorak prije trošenja [4]

Na početku ispitivanja svim biokompozitnim uzorcima izmjerena je masa. Nakon završenog ciklusa ispitivanja uzorci su obrisani, očišćeni od čestica trošenja te im je izmjerena masa. U tablici 2 su prikazani rezultati mjerenja gubitka mase.

Tablica 2. Izmjerene vrijednosti mase uzoraka

Stanje uzorka	**Prije ispitivanja, *m* (g)**	**Nakon ispitivanja, *m* (g)**	**Gubitak mase, *m* (g)**
0% školjaka			
Suho	7,7251	7,7224	0,0027
Vlažno	8,0236	8,0204	0,0032
5% školjaka			
Suho	8,3644	8,3612	0,0032
Vlažno	8,5831	8,5804	0,0027
10% školjaka			
Suho	8,0934	8,0903	0,0031
Vlažno	8,1473	8,1449	0,0024
15% školjaka			
Suho	8,4448	8,4410	0,0038
Vlažno	8,4441	8,4408	0,0033

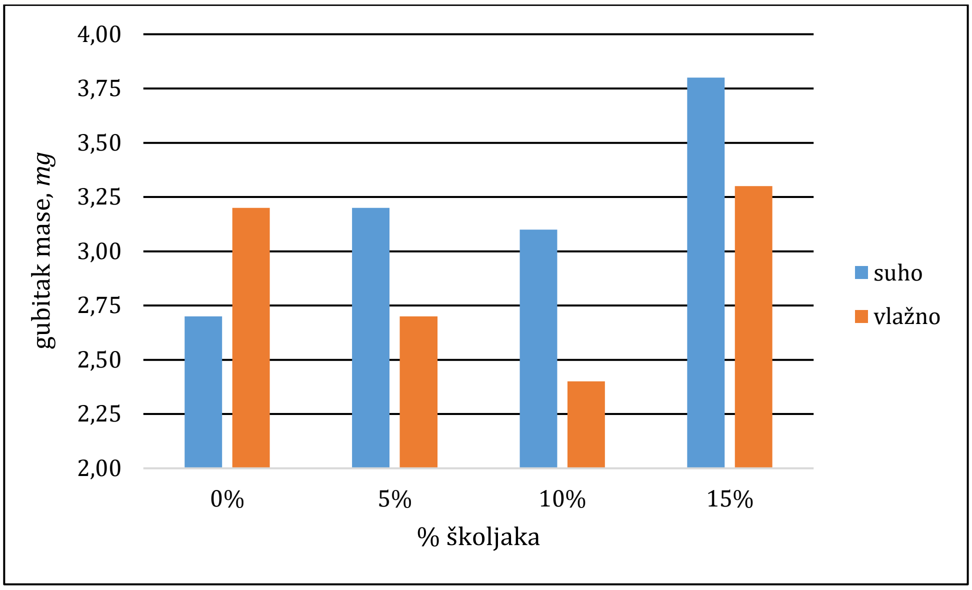

Slika 7. Prikaz gubitka mase za uzorke u vlažnom i suhom stanju

Iz tablice 2 i histograma na slici 7 vidljivo je da svi uzorci ojačani česticama školjaka pokazuju veću otpornost na klizno trošnje u vlažnom okruženju.

Najmanji gubitak mase u suhom stanju pokazuje uzorak koji ne sadrži čestice školjki, a uzorak s 10% čestica školjki ima veću otpornost trošenju od uzoraka s 5% i 15% čestica. Najmanji gubitak mase u vlažnom stanju pokazuje uzorak koji sadrži 10% čestica morskih školjaka. U vlažnom stanju uzorak s 10% školjaka ima 25%, a uzorak s 5% čestica 16% bolju otpornost na klizno trošenje od uzorka koji sadrži 0% čestica školjki. Uzorak sa 15% čestica ima 3% manju otpornost na trošenje od uzorka sa 0% čestica. Ispitivanjem kliznog trošenja utvrđeno je da čestice utječu na gubitak mase te da čestice povećavaju otpornost na trošenje u vlažnom stanju. Uzorak sa 0% MŠ pokazuje lošije vrijednosti u vlažnom stanju nego li u suhom stanju. Vrijednosti gubitka mase u vlažnom stanju su niže što pokazuje da je biokompozit otporniji na klizno trošenje u vlažnim uvjetima. Manja otpornost na klizno trošenje kod uzoraka s 15% čestica objašnjava se aglomeracijom čestica kako je navedeno u literaturi [6]. Jednako ponašanje uzoraka je prikazano i pri ispitivanjima tvrdoće gdje su najviše vrijednosti bile kod uzoraka s 10% morskih čestica.

3. ZAKLJUČAK

U radu su ispitivani biokompozitni materijali PMMA ojačani morskim česticama u različitim postotcima. Uzorak s 10% čestica morskih školjaka pokazuje najvišu vrijednost tvrdoće u vlažnom stanju dok uzorak s 0% čestica morskih školjaka ima najnižu vrijednost tvrdoće. Najveću otpornost na trošenje pokazuju uzorci s 10% čestica morskih školjaka u vlažnom stanju. U oba stanja uzorci s 15% čestica morskih školjaka pokazuju najnižu otpornost na trošenje.

Najboljim se pokazao biokompozit s 10% čestica morskih školjaka. Zaključuje se da čestice morskih školjaka poboljšavaju ispitivana svojstva, tvrdoće i otpornosti kliznom trošenju biokompozita ojačanog česticama

LITERATURA

[1] The Biomedical Engineering Handbook, Second Edition - Section 04, Biomaterials, 1999, Taylor&Frances Group

[2] Jerolimov, V. i suradnici.: Osnove stomatoloških materijala, 2005.,Stomatološki fakultet Sveučilišta u Zagrebu.

[3] Filetin T., Kovačiček F., Indof J.: Svojstva i primjena materijala, Sveučilišni udžbenik, 2002, Fakultet strojarstva i brodogradnje, Zagreb

[4] Hržina M, diplomski rad.: Ispitivanje tribomehaničkih svojstava dentalnog polimera ojačanog morskim školjkama, 2017, Fakultet strojarstva i brodogradnje, Zagreb.

[5] http://www.ivoclarvivadent.com.hr/hr/productcategories/zavrsi/probase-cold, 19.11.2015.

[6] Karthick R., Sirishab P., Ravi Sankarc M. Mechanical and Tribological Properties of PMMA-Sea Shell based Biocomposite for Dental application, Procedia Materials Science, 1989 – 2000, 6 (2014).

CENTRIPHONE IMAGING TECHNIQUE OPTIMISATION BY ADITIVE SUPPPORT PRODUCTION

Anna Maria Hackenberger Kutuzović[1], Trpimir Jeronim Ježić[1]

[1]Sveučilište u Zagrebu Grafički Fakultet, Getaldićeva 2, Zagreb, Hrvatska

SAŽETAK

3D tisak svojim razvojem postaje važan produkt za stvaranje novih ideja u različitim poljima industrija. 3D ispis se može koristiti za stvaranje novih idejnih multimedijskih, odnosno grafičkih rješenja, tj. proizvoda. Ovaj rad predstavlja izradu prototipa 3D kućišta za centriphone tehniku snimanja pomoću GoPro kamere. Korištenjem centripetalne sile centriphone tehnika snimanja stvara 360° video koji se naknadnom montažom vremenski određuju određeni kadrovi pomoću sporog ili brzog upravljanja slika u sekundi. Rad obuhvaća izradu kućišta za centriphone tehniku snimanja i primjenu centriphone tehnike snimanja za multimedijalni i fotografski prikaz. Centriphone tehnika snimanja je nova i neuobičajena tehnika snimanja koja se može koristiti za razni sadržaj poput reklamnih, filmskih, dokumentacijskih, marketinških i promo video materijala. Za razliku od fotoaparata i kamera gdje se kontrolira kadar koji će se snimiti, centriphone tehnikom snimanja se nagađaju određene željene scene, te kasnijim odabirom određuju određeni kadrovi videa odnosno scene. Uloga 3D tiska kod centriphone tehnike snimanja video sadržaja ima bitan utjecaj za stvaranje novih ideja, te pruža novi spektar ideja koji se mogu primijeniti u budućnosti. 3D tisak nudi promjenu i doradu određenih ideja i prototipa za upotrebu drugih i izradu novih multimedijskih produkata.

KLJUČNE RIJEČI: *3d ispis, centriphone, 360 snimanje, multimedija, video produkcija*

ABSTRACT:

3D print with it's development becomes an important product for creating new ideas in various industries. 3D print can be used to create new conceptual multimedia or graphic solutions, ie products. This paper presents the development of a prototype 3D case for centriphone recording technology using the GoPro camera. Using centripetal force, the centriphone image technique generates 360 ° video footage, which is subsequently determined by certain frames with slow or fast image control for a few seconds. Work includes the development of centriphone casing design and centriphone technique for capturing multimedia and photographic displays. The Centriphone recording technology is a new and unusual recording technique that can be used for various content such as advertising, film, documentary, marketing and promotional video. Unlike photo and video cameras where the captured camera is being controlled, centriphone recording techniques speculate on certain desired scenes, and later selects certain video or scenes. The role of 3D printing on centriphone video recording techniques has a major impact on creating new ideas and provides a new set of ideas that can be applied in the future. 3D printing offers changing and refinement of certain ideas and prototypes for the use of others and the creation of new multimedia products.

KEYWORDS: *3D Printing, centriphone, 360 recording, multimedia, video production*

FOTOGRAFSKI EFEKTI PARALAKSNOG POMAKA U SUVREMENOM MULTIMEDIALNOM I WEB OKRUŽENJU

PHOTOGRAPHIC PARALLAX EFFECTS IN CONTEMPORARY MULTIMEDIA AND WEB CONTEXT

Anna Maria Hackenberger Kutuzović[1], **Trpimir Jeronim Ježić**[2]

[1] Sveučilište u Zagrebu, Grafički fakultet , Getaldićeva 2, Zagreb, Hrvatska
[2] Sveučilište u Zagrebu, Grafički fakultet , Getaldićeva 2, Zagreb, Hrvatska

Sažetak

Pokret je jedno od obilježja svijeta kojemu je naš perceptivni sustav iznimno prilagođen i kojemu naša zamjedba pripisuje veliku važnost. Kao takav, pokret se u vizualnim komunikacijama pokazao kao iznimno potentno sintaktičko sredstvo u prijenosu informacija i pri usmjeravanju pažnje primatelja poruke. Premda je fotografija izvorno smatrana statičnom umjetnošću, ona je, uklapajući se u nove multimedijalne tehnologije, velikim korakom zašla i u sferu dinamičnih medija. Brojne nove digitalne tehnologije dodatno su zamutile granicu između same fotografije i medija poput filma, interaktivnih aplikacija, web stranica pa čak i računalnih igrica. Ovaj će rad proučiti prirodu pokreta u slici nazvanog efektom paralaksnog pomaka, a do kojeg prirodno dolazi pomicanjem položaja 'oka promatrača' u odnosu na promatranu scenu. Rad će izložiti sustavnu kategorizaciju načina reprodukcije efekta paralaksnog pomaka koji su u posljednjih nekoliko godina preplavili područja video prezentacije i web produkcije. On će pratiti razvoj tehnika izvorno poteklih iz područja animacije i pokretnog filma sve do znatnog proširenja njihovih mogućnosti pojavom interaktivnih medija poput suvremenih računalnih (web) aplikacija i računalnih igara. Cilj rada je sintezom pregleda tehnika rabljenih za postizanje efekta paralaksnog pomaka predložiti načine pojednostavljenja njihove izvedbe ili proširenja mogućnosti njihove primjene, bilo da je riječ o obradi samostalne fotografije ili pak njihove serije.

Ključne riječi: *efekt paralaksnog pomaka, računalna fotografija, interaktivna fotografija, piksel grafika, web dizajn.*

Abstract

Motion is one of the characteristics of our world that our perceptive system is exceptionally adapted to and to which our cognition attaches a great importance. As such, the motion has presented itself as an extremely potent syntactical tool for transmitting visual information and for focusing the attention of the recipient of the message. Although the photograph was originally considered as a static form of art, it has lately made, by incorporating itself into new multimedia technologies, a big step into the sphere of dynamic media. Numerous new digital technologies contributed to blurring the boundaries between photography and media such as movies, interactive applications, websites, and even computer games. This paper will present a principal study of the nature of the *parallax effect*, that comes about naturally by moving the position of the 'eye of the observer' in relation to the observed scene. The paper will outline the systematic categorization of the techniques used for achieving the *parallax effect* that has over the last few years flooded the fields of video presentations and web production. It will showcase the development of these techniques originally derived from the animation and motion pictures and greatly expanded with the emergence of interactive media such as modern computer (web) applications and computer games. The aim of the paper is to suggest ways of increasing their efficiency or broadening the possibilities of their application by synthesizing the scope of contemporary techniques used to achieve the *parallax effect*, whether it is derived by manipulating a standalone photograph or their series.

Keywords*: Parallax effect, Computational photography, Interactive photography, Pixel graphics, Web design.*

UTJECA DODATKA TROSKE VISOKE PEĆI NA MEHANIČKA SVOJSTVA CEMENTIH MORTOVA

INFLUENCE OF ADDITION OF GGBFS ON MECHANICAL PROPERTIES OF CEMENT MORTARS

Dražan Jozić[a,*],Andrija Petrović[a], Goran Baloević[c], Branimir Ljubičić[b]

[a] University of Split, Faculty of Chemistry and Technology, R. Boškovića 35, Split, Croatia
[b]CEMEX Hrvatska d.d., F. Tuđmana 45, 21212 Kaštel Sućurac, Croatia
[c] University of Split, Faculty of Civil Engineering, Architecture and Geodesy, Matice Hrvatske 15, Split, Croatia

Sažetak

Granulirana troska visoke peći (GBFS) je nusproizvod u procesu proizvodnje željeza koja se dobiva naglim hlađenjem troske u vodi kako bi se zadržala amorfna struktura u granuliranom proizvodu. Ova studija ima za cilj utvrditi utjecaj samljevene granulirane troske visoke peći (GGBFS) koja se koristi kao zamjenski dodatak u količinama od 0-40 mas.% na masu portland cement (OPC) (tipa CEM I 42,5R) na vrijeme vezanja i na razvoj tlačne čvrstoće u sustavu cementnih mortova. U ovoj radu OPC je proizveden na polu industrijskom kugličnom mlinu. Sirovine OPC i GGBFS analizirane su pomoću XRF, XRD i mikroskopije. U svrhu određivanja utjecaja GGBFS pripremljene su cementne paste i cementni mortovi s zamjenskim dodatkom u iznosu od 5, 15, 20, 25, 30 i 40% masenog udjela GGBFS. Uzorci cementnog morta njegovani su u vodi pri 20 ± 1°C u razdoblju od 3, 7, 14, 28, 70 i 90 dana hidratacije. Rezultati pokazuju da uloga GGBFS u cementnim pastama ovisi o njegovom masenom udjelu. Superplastifikator korišten u pripravi mortova ima ulogu reducensa vode i značajno utječe na povećanje tlačne čvrstoće. Pripremljeni cementni mortovi nakon 70 dana hidratacije, čak i sustav s 40% masenog udjela zamjene GGBFS pokazuje veću vrijednost tlačne čvrstoće u odnosu na referentni mort.

Keywords: *Cement, Mort, Superplastifikator, granulirana troska visoke peći, XRD*

Abstract

Granulated blast-furnace slag (GBFS) is byproduct in the factory for iron production where it is produced by quenching molten iron slag in the water or steam. This study has goal to determine the effect of ground-granulated blast-furnace slag (GGBFS) used as replacement addition (0-40 mass %) to the Ordinary Portland cement (OPC) (type CEM I 42,5R) on the setting time and on the development of compressive strength in the system of cement mortars. In this study OPC were produced at the semi-industrial ball mill. Raw materials OPC and GGBFS were analyzed by using XRF, XRD and microscopy. In the purpose to determine the influence of GGBFS, cement paste and mortars were prepared with replacement addition of GGBFS in the amounts of 5, 15, 20, 25, 30 and 40 mass %. Samples of the cements mortar were kept in a thermostated water at 20 ± 1°C in the period of the 3, 7, 14, 28, 70 and 90 days of hydration. The results show that the role of the GGBFS into cement paste depends on its content. Used super plasticizing admixture in preparation of the mortars has a role of water reduction agent and it significantly influences an increase in the developed compressive strength. In the system of the prepared mortar after 70 days of hydration, even the system with 40 mass % of replacement addition of GGBFS shows higher value of the developed compressive strength relative to the reference mortar.

Keywords: *Cement, Mortar, Superplasticizer, Granulated blast furnance slag, XRD*

1. INTRODUCTION

Currently trends in the all industry and their policy of development are based on the eco-friendly and low-carbon emission products which are being actively developed and more efforts are being made to improve their manufacturing processes by involving new innovate. In the construction industry cement is an essential binder which is used for manufacturing concrete and mortar for different application. Since the Portland cement production requires a large amount of energy, the process itself is burdened with a high greenhouse gas emission, primarily carbon dioxide (CO_2) which has a significant impact on global warming. Cement industry emits approximately 5% to global anthropogenic CO_2 emissions, and therefore, more efforts have been made by the industry to reduce carbon emissions by implementation innovation in the process of production and by using materials with the low content of carbon [1]. For a very long time, the scientific community research the application of different materials as substitute cement additives in production processes [2]. All attempts actually lead to global sustainable development and the lowest possible impact of cement industry on the environment. Many years cement industry use different waste material which arise from the different industry where they present by-product such as granulated furnace slag (GFS), ground granulated blast furnace slag (GGBFS), fly ash (FA) and silica fume (SF) they are reused as mineral admixture in the process of production of the Portland cement and/or production Portland cement concrete [3][4][5]. Application those waste materials in the process of recycling and utilization in the cement industry and in the production of the cement composite have a great economic and ecological benefit on industry, society and environment. From the ecological aspect reusing waste materials especially in the cement industry have a greater influence on decrease of the waste materials, decrease of CO_2 emission and it keep the natural raw materials which a usually have to be used in the process of the production Portland cement. Ground-granulated blast-furnace slag is widely used many years in cement industry, as a clinker replacement material in the quantity form 35-95 mass % production cement according to the European norm product belong to the CEM III type A-C of cement [6][7][8]. Main characteristic of produced CEM III/A-C type of cement are low hydration heat, low compressive strength in the early stage of hydration and very good resistance on aggressive sulphate environment [9][10]. Cement type CEM III/A-C is suitable to be used for preparation of concrete works in warm climate, structures in humid and aggressive environment rich in sulfates, bridge base, maritime and littoral objects, road works, irrigation systems, sewage and drainage systems.

This paper concerns the study of influence GGBFS as replacement addition up to 40 mass % for the OPC on the setting time in the system of cement paste. In the systems of the cement mortars was study the influence of the GGBFS on developed mechanical properties up to the 90 days of hydration of cement mortar which were prepared with and without of addition of the super plasticizing admixture.

2. 2. EXPERIMENTAL

2.1. Materials and testing methods

2.1.1. Clinker

The clinker used in this experimental work was produced at CEMEX Hrvatska d.d., factory St. Juraj, Kaštel Sućurac. Fresh industrial prepared clinker was taken from the clinker cooler. The granulometric composition of the clinker was determined on the mass of 6,940 kg the clinker by using set of sieves deployed from above to the bottom with the sieve size as follows: 31,5 mm; 22,4 mm, 16 mm, 11,2 mm, 8 mm, 5,6 mm, 4 mm, 2 mm, 1 mm and 0,5 mm.

Table 1. Particle size distribution of the clinker

Sieve (mm)	Mass retained (g)	Mass passed (g)	% Passing
31,5	230	6710	96,7
22,4	430	6280	90,0
16,0	400	5880	85,0
11,2	770	5110	73,6
8,0	900	4210	60,0
5,6	1000	3210	46,3
4,0	880	2330	33,6
2,0	1360	970	14,0
1,0	720	250	3,6
0,5	170	80	1,15
< 0,5 mm	80	-	-

Chemical composition of the clinker was analyzed by using X-Ray Fluorescence (XRF, Thermo Scientific, model ARL 9900-74). Samples for thus analysis were prepared in accordance with HRN EN 196-2:2013 in the form of the melted tablets and as such were used for analysis. The melting process of samples was carried out to eliminate the possibility of interfering binder material used in preparation of tablets as well as moisture, sulphates or potentially carbonates with the components which arise from the sample to prevent effect on qualitative and quantitative analysis. Its mineralogical phases, were determined by X-ray diffraction (XRD) analysis by using a Shimatzu 6000 diffractometer with nickel filtered Cu Kα1 radiation (λ= 1.5405Å, 40 kV and 30mA). The clinker microstructure was examined by using optical microscopy. Sample has been prepared by selecting 3-4 clinker grains (with the size between 4-10 mm) which was placed into silicon mould and in the next step of preparation sample was covered by epoxy resin. The brushed and polished sample was treated with solution of the ammonium nitrate (NH_4NO_3), washed with ethanol and sample was dried in the oven. The prepared sample in the next step of preparation was exposed to the influence of the salicylic acid ($C_6H_4(OH)COOH$) in duration of the 6 seconds and then rinsed with ethanol and in the finally stage sample was the dried. The microscopic observation of the polished and etched samples of the clinker achieved by using a Olympus Gx 51 optical microscope in darkfield of the reflected light.

2.1.2. Ground-granulated blast-furnace slag

The ground-granulated blast-furnace slag used in this paper originates from the iron production plant located at Zenica, Federation of Bosnia and Herzegovina. The granulated blast-furnace slag is by-product in the process of production of iron, where the granulated blast-furnace slag as by-produced in production iron is produced by cooling the blast furnace slag into large volumes of water [1]. The ground-granulated blast-furnace slag in this experimental work is prepared by milling granulated blast furnace slag into semi-industrial ball mill (same is used in preparation of cement). Chemical composition of the GGBFS is determined by X-ray fluorescence (XRF) (Table 3.) as well as structural characterization by using X-ray diffraction (XRD) (Figure 3.) and Fourier Transform Infrared Spectroscopy (FTIR) (Figure 4.).

2.1.3. Preparing of the cement CEM I 42,5R

A sample of ordinary Portland cement type CEM I 42,5R (OPC) was prepared at a semi-industrial laboratory ball mill at CEMEX Hrvatska d.d. Laboratory located at the factory Sv. Kajo, Kaštel Sućurac. The grinding media in the ball mill were steel balls with different sizes (from 20-90 mm) and different mass portion of them into mill (Table 2.) and rotation speed of the mill body was optimized at 50 rpm. Samples of the clinker were crushed and grinding on a semi-industrial laboratory ball mill of 6 kg capacity. In the phase of cement preparation (type of CEM I 42,5R) and in the purpose to achieve suitable specific surface area (target value was above 3600 Blain) in the reasonable time in the raw mixture was added additive for improving clinker milling.

Mineral mixture used in the preparation cement were composed from the mixture of the industrially produced clinker, gypsum and additives to improve the milling properties. Additive was commercially available under trade name HEA 213 HEA2®, product of the GCP Applied Technologies Inc, dosing on the mass of the clinker in amount of the 0,032 mass %. Gypsum has been also added into raw mixture, but addition was limited on total amount of the SO_3 into cement which was limited at maximum value of the 3 mass %. In this purpose to properly dosing gypsum content of the SO_3 in the clinker was measured before addition of gypsum, and after producing cement, into cement content of the SO_3 also was measured.

Table 2. Steel ball size, numbers of each size them and mass of each fraction

Size, mm	Number of balls	Mass, kg
90	2	5,958
60	7	6,218
70	3	4,062
60	4	3,500
50	4	2,066
40	10	2,490
30	50	6,200
25	156	9,760
20	920	29,226
	Total	69,480

2.1.4. Preparation cement paste

In order to determinate influence on the setting time and heat of hydration were prepared cement paste. Cement paste were prepared without and with the replacement addition of Ground-granulated blast-furnace slag in the amounts of 5, 15, 20, 25, 30, and 40 mass % of the cement mass (CEM I 42,5R). Samples were marked as it follows: PB0, PB5, PB15, PB20, PB25, PB30, and PB40. Sample made without any replacement addition, a reference sample, was marked as PB0. Distilled water was used in preparation of paste samples. Normal consistence, start and the end of binding were determinate on prepared samples by means of the Vicat method. In order to determined influence Ground-granulated blast-furnace slag on the heat released by process of the hydration cement testing has been provided into differential microcalorimetry, by using method described in preview paper [11]. Sample for calorimetry was prepared by using mass of blended cement of 4g (separately for each mixture) placed into calorimetric cell on the cooling together with the injection filled with 2 ml distilled water (water/cement ration have to be 0,5 (w/c=0,5)). After 24 hours, samples of cement and water are cooled on 20 ± 0,01 ^{o}C, and adding water into cement process of hydration are started and during 48 hours is measured thermo voltage (mV) which are collected and saved by using a data logger.

Heat released by process of hydration can be calculated by using equation:

$$Q(t) = \frac{Cp}{gm}\left(\Delta U(t) + \beta \int_{t_0}^{t} \Delta U(t)dt\right) \cdot 1000 \qquad (1)$$

Where is Cp-thermal capacity of the microcalorimeter, (43.4368 J/^{o}C), g- constant of proportionality (303 μV/^{o}C), β-cooling constant (0.022·60 s^{-1}), m-mass of the sample (4.0000 g) and ΔU difference in the voltage between referent and sample cell into differential micro calorimetry (mV)-.

2.1.5. Preparation cement mortars

The cement mortar was prepared according to the standard HRN EN 196-1:2005. The standard quartz sand was used as aggregate. The aggregate/binder (cement + GGBFS) ratio was constant in all mixtures and was 3:1. The quantity of water needed in mortar preparation was differed, so the mortar samples were prepared in such a way that they had the same consistency, measured by mortar spreading on a flow bed within the limits of 197±20 mm. Mortars containing GGBFS were prepared by replacing cement with 5, 15, 20, 25, 30, and 40 mass % GGBFS and with addition of super plasticizing admixture based on polycarboxylic ether producer BASF available at market under trade name MasterGlenium ACE 430 in amount of 0,87 mass % (3,9 g) on the mass of the produced cement (cement + GGBFS). Addition of super plasticizing admixture in the case of adding mineral addition such as GGBFS have a role to prevent agglomeration of GGBFS into developed microstructure and increase a homogeneity. Mortars were marked as it follows: PB0S, PBT5S, PBT15S, PBT20S, PBT25S, PBT30S and PBT40S (Table 3.).

Table 3. Composition of the mixture and denotations of samples of prepared cement mortars.

Sample	Sand, g	Cement, g	GGBFS, g	Consistency, mm	Water, ml	w/c	w/(GGBFS+c)
PB0	1350	450	0	207	225	0,500	0,500
PB0S	1350	450	0	200	175	0,389	0,389
PBT5S	1350	427,5	22,5	190	175	0,409	0,389
PBT15S	1350	382,5	67,5	195	175	0,458	0,389
PBT20S	1350	360	90	210	175	0,486	0,389
PBT25S	1350	337,5	112,5	190	165	0,489	0,367
PBT30S	1350	315	135	182	167	0,530	0,371
PBT40S	1350	270	180	200	165	0,611	0,367

A sample prepared without of addition GGBFS was marked as PB0 and with addition of superpastificator is marked as PB0S. Prepared mortars, with the dimensions of 4×4×16 cm, were cured for 24 hours in a conditioned chamber at a temperature of 20°C and relative humidity (RH) higher than 95 %, after which samples were taken from the mould and cured in thermostated pools filled with tap water (RH = 100 %, T = 20 ± 1°C) until examination of mechanical properties. Examinations of mechanical properties (compressive strengths) of mortars were carried out on the Zwick Roell system of hydraulic presses. The rate of increase of compressive load was 1.50 Nmm^{-2}s^{-1}.

3. RESULTS AND DISCUSSION

In the purpose to produce cement type of CEM I 42,5 R at the semi-industrial ball mill were used industrial produced clinker. Clinker was analyzed by using optical microscopy and X-ray florescence (XRF). Sample of the clinker were prepared according to the chapter 2.1.1. and obtained microscopic picture are shown at Figure 1.

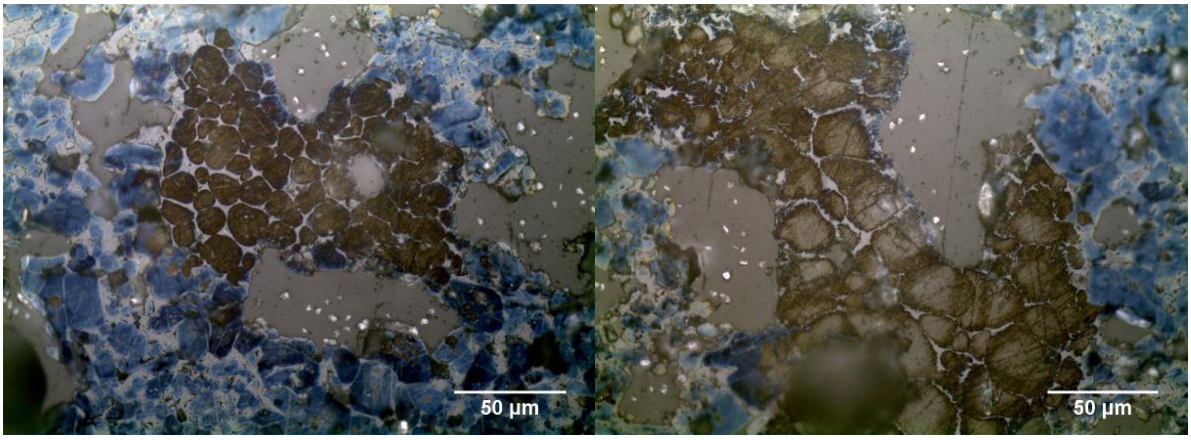

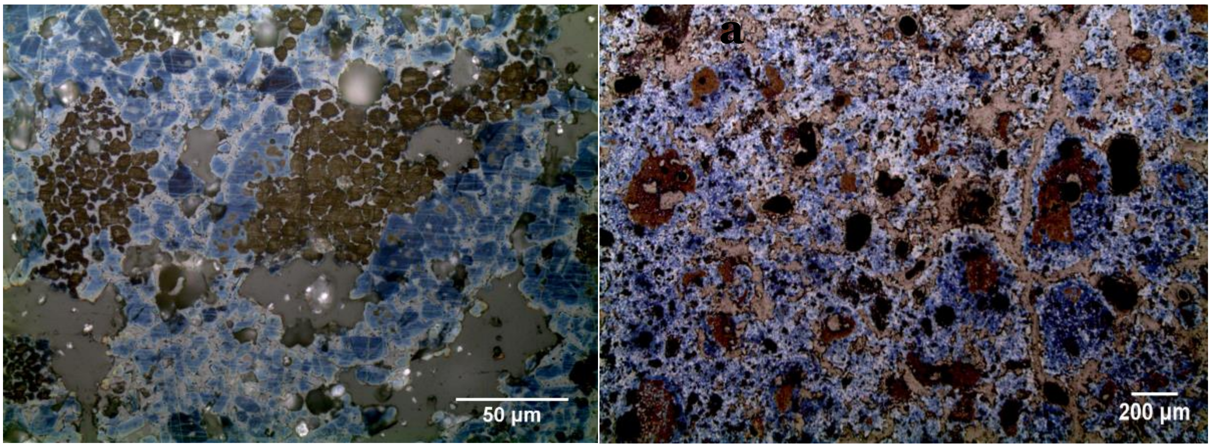

Figure 1. Microstructure of Portland cement clinker well formed alite crystals and Brownish rounded belite crystals

Using mineralogical characteristics, different optical properties of minerals which are characteristic for particular minerals it enables the qualitative identification of clinker minerals and the quantitative mineral size analysis clinker, whereby a range of 14 to 73 µm alite (C_3S) was established with a mean value of 32 µm grain size or a range of 14 to 29 µm in diameter for belite (C_2S). The size of the produced clinker minerals within the clinker grain is related to the potential reactivity of the minerals, and this information are mostly connected with the conditions of thermal treatment of raw materials into rotary kiln and the with the cooling rate of the produced clinker. Sizes of clusters in the sample mean the mean value of the size is 231 µm while the grain size of the free lime is 102 µm.

The pre-fabricated cement was characterized by XRF and the results of this analysis are shown in Table 4.

Table 4. Physical and Chemical composition of the CEM I 42,5 R and GGBFS

Chemical and mineralogical composition		
	Cement, mas.%	**GGBFS, mas.%**
SiO_2	19,68	38,95
Al_2O_3	4,92	9,79
Fe_2O_3	3,12	0,68
CaO	63,86	39,83
MgO	2,09	4,60
SO_3	3,14	2,24
Na_2O	0,20	0,33
K_2O	1,40	0,86
Total	1,19	0,77
C_3S	66,80	-
C_2S	15,13	-
C_3A	2,5	-
C_4AF	13,4	-
Loss of ignition (LOI), %	0,18	0,77
Physical characteristic		
Specific mass, kg/m^3	3,13	2,8
Specific surface area, Blain, m^2/kg	368,9	398,56
Consistency, %	26	-
Start setting	2 h 20 min	-
End setting	4 h 0 min	-

The content of the of Cr^{6+} and Cl^- was made in according to standard HRN EN 196-10:2016 and according to standard HRN EN 196-2:2013. Results show that content of the Cr^{6+} is 16,35 ppm and Cl^- is 0,007 mass %. Mineralogical analysis of the prepared cement CEMI 42,5R has been analyzed by using XRD. The result of the analysis of the XRD powder pattern of the polycrystalline cement sample is shown in Figure 2.

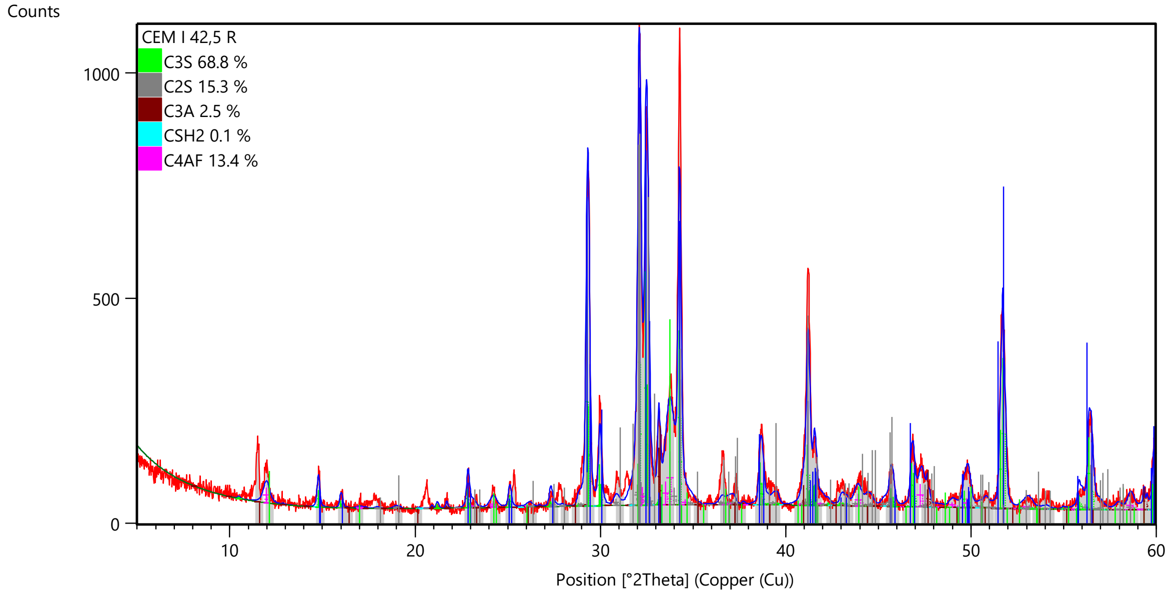

Figure 2. X-ray diffraction pattern of the Portland cement type CEM I42,5R and its mineralogical composition

The crystalline phase presence into sample of cement belong to the major minerals of clinker, alit (C_3S), belite (C_2S), aluminate (C_3A) and aluminate-ferrite phase (C_4AF). Quantitative analysis of the presence each mineralogical phase in the sample of produced cement has been obtain by using Rietveld method of analysis of diffraction pattern. According to the analysis content of each mineral fraction are shown at Figure 2. For prepared cement type of CEM I 42,5R has been determined setting time by using standard method by using Vicat apparat under cement paste with standard consistency. Start of setting time after 140 min. and end of setting is after 240 minutes after adding the water into cement.

The X-Ray powder pattern of the GGBFS is shown at the Figure 3. From the very diffuse diffraction maximum which appear in the range of the 2Theta from 20 up to the 38^o it's obviously that the GGBFS is material with the amorphous structure. Requirement for quality of the GGBFS which can be used in the preparation of cement mortars are described by EN 197-1:2012 and for application it in the concrete is described by EN 15167-1:2006 which they are same and the mass of the oxide sum of CaO + MgO + SiO_2 should be greater than 2/3 of the total mass and ratio ((CaO + MgO) / SiO_2)>1. For the GGBFS used in this experimental part the sum of the oxide (CaO + MgO + SiO_2) is 83,38% means greater than 2/3 while the ratio of ((CaO + MgO) / SiO_2) = 1,14 which suggest the GGBFS is suitable to be used in the preparation of the cement composite. Mineral admixture based on the chemical composition of aluminum silicate and with the amorphous structure is suitable for preparation cement or concrete/mortar.

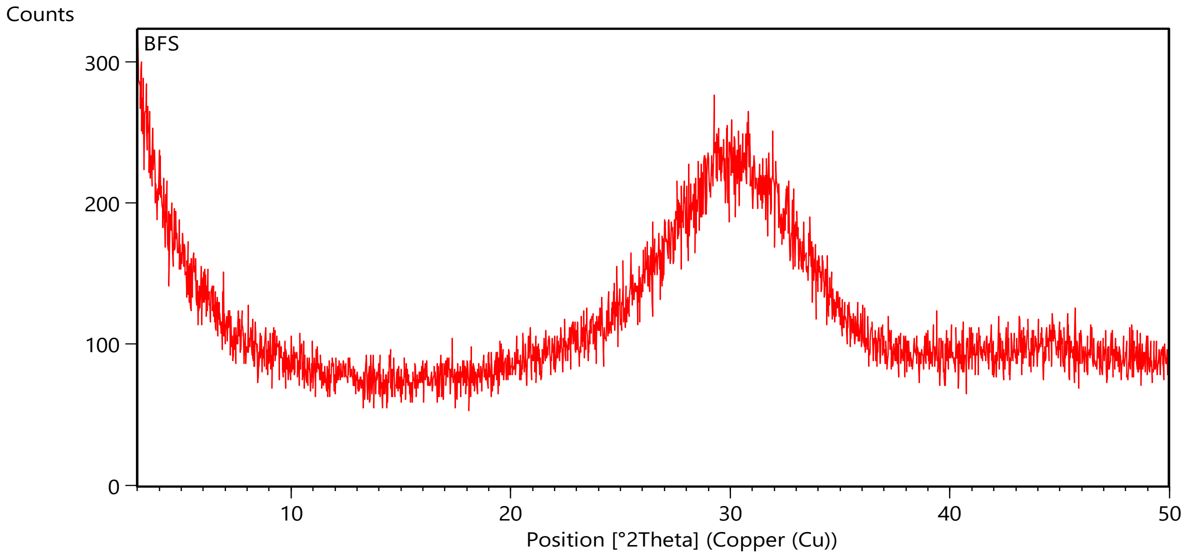

Figure 3. XRD powder pattern of the GGBFS

In the FTIR spectrum (Figure 4.) is obvious that in the range of the wave numbers of 3000-4000 cm^{-1}, a very weak and wide absorption band centered at 3413 cm^{-1} this band suggest on the presence of very low content of the absorbed water.

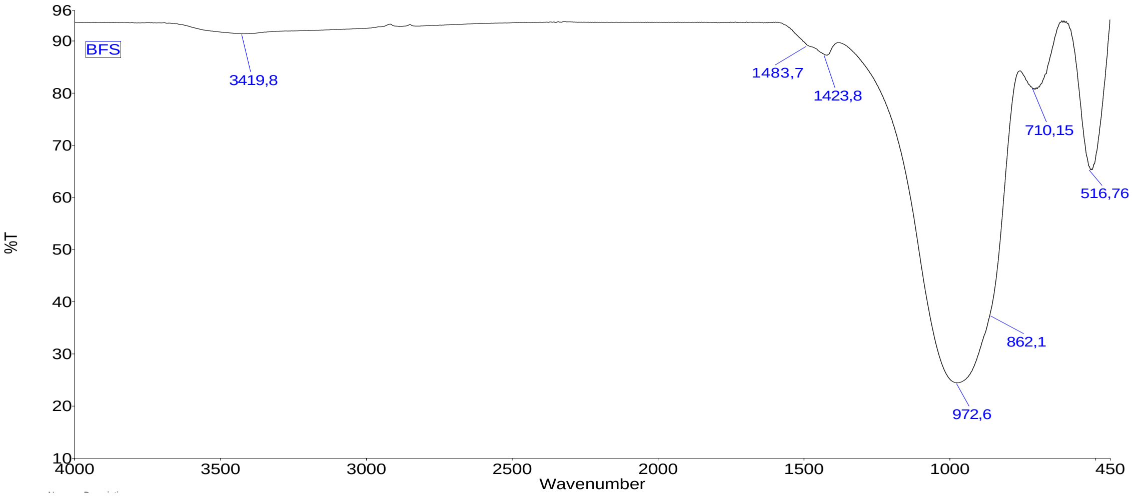

Figure 4. FTIR spectrum of the GGBFS

In the low-wavenumber region, for the spectrum the bands around 516 and 710 cm^{-1} are assigned to the T-O (T = tetrahedral Al or Si) bending modes in the TO_4 tetrahedral. The band at 710 cm^{-1} indicates on of Al^{IV} as the main Al environment. The presence of the carbonate functional group is observed through a very clearly absorption band at the wavenumber 1428-1483 cm^{-1} (ν3) while the other absorption bands characteristic for carbonates at wave numbers 1030 cm^{-1} (ν1) and 880 cm^{-1} (ν2) are convoluted with the principal very strong absorption band which appear at the 972,6 cm^{-1} which arise from the Si-O-Si vibration of the oxygen linkages between the tetrahedral SiO_4.

3.1. Influence of GGBFS on the setting time and heat realized during process of hydration

Influence of the replacement addition of GGBFS on the setting time into system of the cement paste are shown at the Figure 5. Cement paste were prepared with addition water in amount that cement paste satisfies normal consistency. From the results it is obviously that replacement addition of the GGBFS in range of the amount between 5-15 mass % postpone the start and end of setting to the longer period of hydration on which way GGBFS play a role as retarder of setting time. Increasing replacement addition in the range between the 20-40 mass % GGBFS shift the start and end of setting time at the earlier time of hydration and GGBFS have a role as accelerator of the setting time.

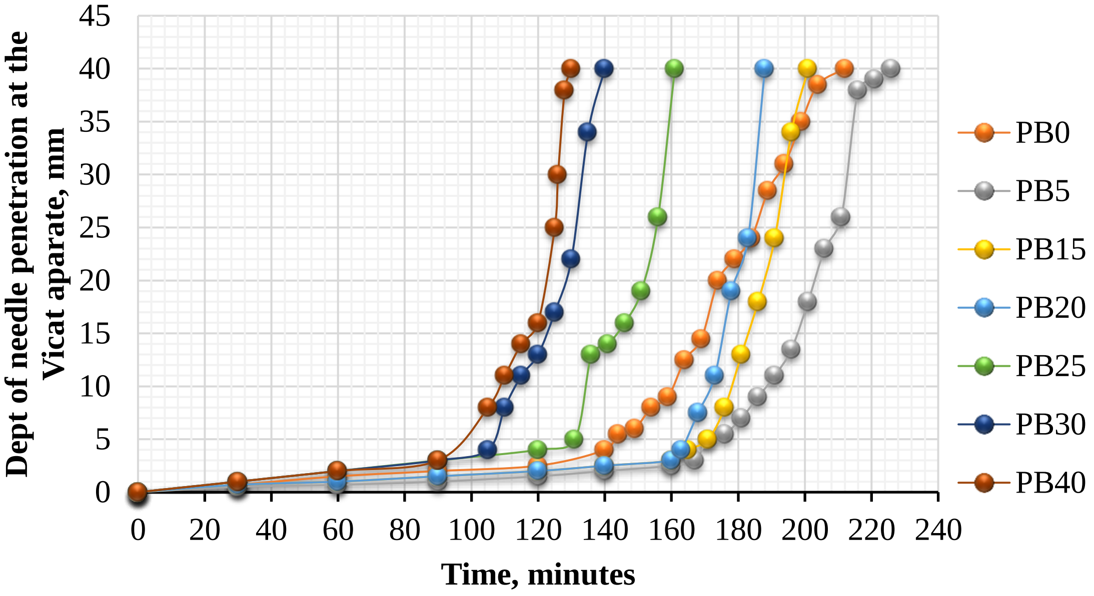

Figure 5. Influence of replacement addition of the GGBFS on the setting time of the OPC in the system of the cement paste prepared to satisfy normal consistency

Results of testing heat released during process of hydration blended cement prepared by replacing cement CEM I 42,5R with ground-granulated blast-furnace slag in amount of 0, 5, 15, 20, 25 and 30 mass % (sample are denoted as PBO, PB5, PB15, PB20, PB25, PB30 and PB40) are shown in the table 4. Calculated value of heat released during process of hydration in the period of 48 hours of hydration for the ordinary Portland cement show the highest value of released heat (173,84 J/g). Smallest addition of the GGBFS in amount of the 5 mass % have an influence on decrease of heat released (149,10

J/g) which is 14,23 %. lower than it's measured for the sample PB0. Results show also that with increasing addition of GGBFS have an influence on decrease value of heat released during the process of hydration from the 149,10 (PB5) up to the lowest measured value of 138,69 J/g (PB40) which is less for 20,21 % than in the sample PB0.

Table 4. Values of heat released during the process of hydration in the cement paste prepared with the v/c = 0.5 and t = 20.0 ± 0.1 ° C in the first 48 hours

Sample	Heat release during the first 48 hours, J/g
PBO	173,84
PB5	149,10
PB15	157,28
PB20	130,60
PB25	130,16
PB30	128,01
PB40	138,69

3.2. Mechanical properties of cement mortars

The compressive strength of prepared cement mortars was examined after 3, 7, 14, 28, 70, and 90 days of hydration. The results (Figure 6) show that the developed compressive strengths increase with time for all the samples.

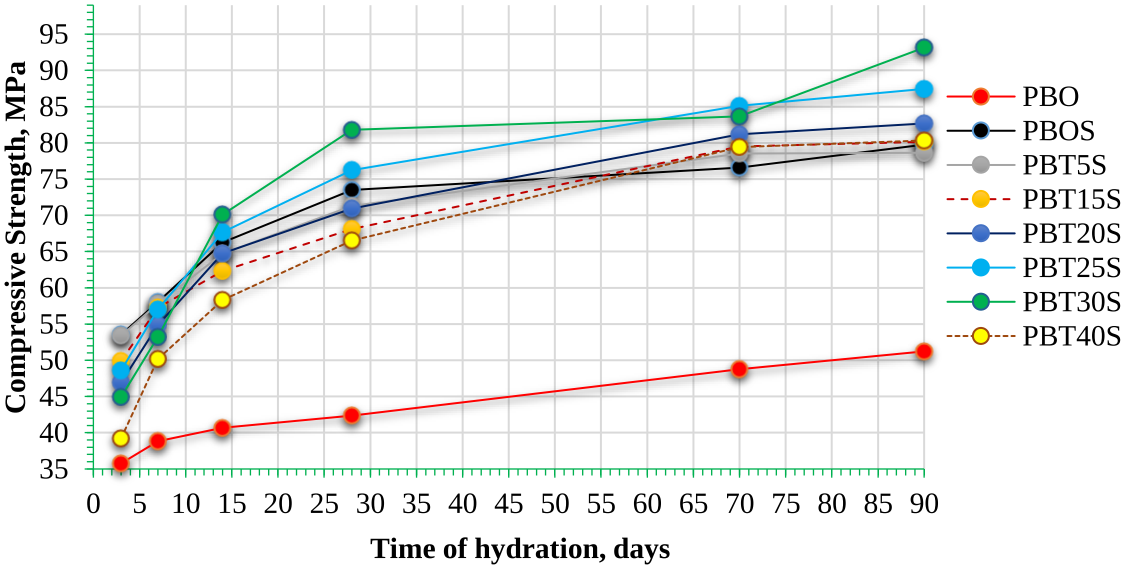

Figure 6. Development of compressive strength in mortars with GGBFS replacement addition (0-40 mass %) relative to hydration duration (3-90 days of hydration).

The comparison of developed compressive strength in mortar samples denoted as PB0, sample which was prepared without of addition of GGBFS and without addition of super plasticizing admixture it shows lowest value of the compressive strength in comparisons with the all other samples. Effect of addition super plasticizing admixture on the compressive strength on the OPC is visible through the developed compressive strength into sample PB0S. Sample PB0S is prepared with addition of the super plasticizing admixture (without of addition of GGBFS), the developed compressive strength in comparisons with the series PB0 achieves a higher compressive strength even after 3 days of hydration where the measured compressive strength was 35,77 MPa for PB0 and 53,54 MPa for the sample PB0S and after 90 days similar difference is measured. Here it is of utmost importance to emphasize that the addition of superplasticizer type additives has a significant impact on the values of developed compressive strengths in cement mortar systems. At the stage of mortar-making, the additive acts as a water reducer, which is often a condition that substantially contributes to the development of mortar mechanical properties. For any further comparison between the prepared mortars as well as the influence GGBFS on the compressive strength in cement mortars, the PB0S mortars are a reference sample. From the measured values of the compressive strength in the mortar systems prepared with replacement addition of GGBFS (PBT5S, PBT15S, PBT20S, PBT25S, PBT30S and PBT40S) after 3 days of hydration is visible that the measured values of compressive strength decrease with the increasing of the amount replacement addition of GGBFS in comparison with the reference sample (PB0S). The measured compressive strength of the PBT5S sample is almost equal to the value of the compressive strength of the reference sample, PB0S, while the other samples achieve lower values of developed compressive strengths relative to the reference sample. Compared to the reference sample, the smallest decrease in the 0,28 % compressive strength value shows the PBT5S sample, while the lowest value of the compressive strengths measured for the sample with the highest amount of replacement addition of GGBFS (PBT40S) show lower compressive strength for 26,73 % compared to the reference sample.

In later period of hydration, after 14 days of hydration, a higher value of the compressive strength than into the reference sample are measured for the samples PBT25S (higher for 2,11 %) and PBT30S (higher for 5,8 %). For other samples with replacement addition of GGBFS in the amount of 5, 15, 20 and 40 mass % the developed compressive strength is lower than into the reference sample, the lowest values are measured for the sample PBT40S (12 % lower than PB0S). By comparing the values of the compressive strength of the samples PBT25S and PBT30S after 28 days of the hydration they are still higher for 3,69% and 11,25 % than into a reference sample PB0S. For other samples, the values of developed compressive strength are lower than the reference sample. The lowest values of compressive strength were measured for the sample with the highest amount of replacement addition of GGBFS, PBT40S, which is lower by 9,49% than the reference sample. Already after 70 and 90 days of hydration from the measured data, it is apparent that all mortar samples prepared with the replacement addition of GGBFS in the amount of 5-40 mass % show higher developed compressive strength than into reference sample. The highest increase in the value of the compressive strength compared to the reference sample after 70 days of hydration was measured at the PBT25S sample, where the measured value of compressive strength compared to the reference sample increase for 11,14 %, whereas after 90 days of hydration the highest increase in the value of developed compressive strength relative to the reference sample measured at the sample PBT30S in the amount of 16,78 %.

4. CONCLUSION

GGBFS according to the chemical composition and structural properties as amorphous materials represent a suitable material for preparation cement and its composite. Testing provided into cement paste prepared with the replacement addition of GGBFS in amount 5-40 mass % show that GGBFS has a role as retarder of the setting time in the system of the cement paste prepared to satisfy normal consistency on the way that the start and end of stetting time is shifted at the later time of hydration, while his role is changed if it is added in the higher amount (20-40 mass %) where it influences on acceleration of setting time. Addition of GGBFS as replacement mineral admixture influence on decrease of the heat realized by the process of the cement hydration up to the 20,21 % than in the pure OPC. In the system of the cement mortar prepared with the OPC and without and with addition of the super plasticizing admixture, MasterGlenium ACE 430 (added in the amount of 0,87 mass % on the mass of used OPC) in the phase of preparation of cement mortars mixture it shows role as water reducers. Results obtained at early phase of cement mortar hydration show on signified influence of it on the developed compressive strength which is much more visible at the later phase of cement mortar hydration. In the system of the prepared cement mortars with the addition of the GGBFS together with addition of the same chemical admixture show similar effect as in the OPC mortars. Namely, in this preparation is visible that addition of GGBFS as well as admixture a MasterGlenium ACE 430 have additionally influence on the reduction of water which is necessary for the achieve normal consistency. Developed compressive strength for the all mixture are compared with the reference sample (PB0S) at the all measured values and for the all mortars. At the later time of hydration (above 14 days) measured value of the compressive strength show that mortars prepared with high addition of the GGBFS (PBT25S and PBT30S) shows the greater value of developed compressive strength than it is measured into reference sample, and after 90 days even the sample prepared with the highest amount of the GGBFS (PBT40S) show the greater value of the compressive strength. Results suggest on positive effect of additions, on the way that the increase of the amount of GGBFS and chemical admixture influence on water reduction with the rheology which satisfy normal consistency and on the time of setting. Influence GGBFS used with chemical admixture on the developed compressive strength probably it is consequence of the at least two effects. One effect is role of the GGBFS as nucleation place for hydration product of cement (which influence on degree of the OPC hydration) and second is participation amorphous aluminous silicate from the GGBFS into pozzolanic reaction which produce new C-S-H phase into developed microstructure of cement mortar.

REFERENCES

[1] M. Shariq, J. Prasad, A. Masood, Effect of GGBFS on time dependent compressive

strength of concrete, Constr. Build. Mater., 24, 1469–1478 (2010). doi:10.1016/j.conbuildmat.2010.01.007.

[2] Y. Ueki, History and Utilization of Portland Blast Furnace Slag Cement, Nippon Steel & Sumitomo Metal Technical Report No. 109, pp. 109–113 (2015).

[3] D. Jozić, J. Zelić, The effect of fly ash on cement hydration in aqueous suspensions, Ceram. - Silikaty,. 50, pp. 98-105 (2006).

[4] J. Zelić, I. Radovanović, D. Jozić, The effect of silica fume additions on the durability of Portland cement mortars exposed to magnesium sulfate attack, Mater. Tehnol. ,41, pp. 91-94 (2007).

[5] D. Jozić, J. Zelić, I. Janjatović, Influence of the coarse fly ash on the mechanical properties of the cement mortars, Ceram. - Silikaty. 54, pp.144-151 (2010).

[6] V. Václavík, V. Dirner, T. Dvorský, J. Daxner, The Use of Blast Furnace Slag., Metalurgija. 51, pp.461-464 (2012).

[7] P.E. Tsakiridis, G.D. Papadimitriou, S. Tsivilis, C. Koroneos, Utilization of steel slag for Portland cement clinker production, J. Hazard. Mater. 152, pp.805-811 (2008). doi:10.1016/j.jhazmat.2007.07.093.

[8] X. Huang, Z. Wang, Y. Liu, W. Hu, W. Ni, On the use of blast furnace slag and steel slag in the preparation of green artificial reef concrete, Constr. Build. Mater. 112, pp. 241-246 (2016). doi:10.1016/j.conbuildmat.2016.02.088.

[9] B.S. Divsholi, D.T.Y. Lim, S. Teng, Evaluation of Heat of Hydration for High Performance Concrete Incorporating Normal and Ultra Fine Ground Granulated Blast Furnace Slag, Proceedings, 37th Conference on Our World in Concrete & Structures, Singapore, 29-31 August 2012, pp.1-13 (2012).

[10] S. Ogawa, H. Hyodo, H. Hirao, K. Yamada, A. Matsui, D. Hooton, Sulfate Resistance Improvement of Blended Cement Based on Ground Granulated Blast Furnace Slag, 3rd ACF Int. Conf., pp. 499–506 (2008).

[11] P. Dabić, R. Krstulović, D. Rušić, New approach in mathematical modelling of cement hydration development, Cem. Concr. Res., 30, pp. 1017–1021 (2000). doi:10.1016/S0008-8846(00)00293-3.

UTJECAJ SNAGE PLAZME NA POSTUPAK NITRIRANJA U PLAZMI

THE EFFECTS OF PLASMA POWER IN PLASMA NITRIDING PROCESS

Ivan Kumić[1], Ljerka Juroš[1], Martina Kesner[1]

[1]Sveučilište u Zagrebu, Fakultet strojarstva i brodogradnje, Ivana Lučića 5, Zagreb, Hrvatska

Sažetak

U radu je istražen utjecaj parametra snage plazme na uspješnost nitriranja u plazmi. Ispitni uzorci legure Ti6Al4V ELI nitrirani su u neovisnim postupcima na sličnim temperaturama, atmosferi, trajanju i drugim parametrima osim parametra snage plazme koji je bio znantno različit. Po provedenom nitriranju u plazmi, uzorci su analizirani optičkom emisijskom spektrometrijom uz tinjajuće pražnjenje (GDOES) i energijskom disperzivnom spektroskopijom (EDS) u sklopu skenirajućeg elektronskog mikroskopa. Istražena je promjena hrapavosti ispitnih uzoraka kroz analizu amplitudnih parametara površinske hrapavosti (Ra, Rp i Rv). Usporedbom kemijskog sastava uzoraka prije i nakon nitriranja u plazmi kao i hrapavosti, doneseni su zaključci o postojanju utjecaja snage plazme na efekte nitriranja u plazmi.

Ključne riječi: *Nitriranje u plazmi, ionsko nitriranje, snaga plazme, Ti6Al4V, hrapavost*

Abstract

In this paper a research on the influence of plasma power in plasma nitriding process is presented. Test samples of alloy Ti6Al4V ELI were nitrided in independent processes at similar temperatures, atmosphere compositions, duration and other parameters except for plasma power which was considerably varied. After plasma nitriding, samples were analysed by the means of glow discharge optical emission spectrometry method (GDOES) and energy-dispersive detector (EDS) incorporated within scanning electron microscope. Roughness of test samples was investigated through analysis of amplitude roughness parameters (Ra, Rp and Rv). Comparison of chemical composition and roughness of test samples, before and after plasma nitriding, allowed for conclusions on the influence of plasma power in plasma nitriding process to be drawn.

Keywords*: Plasma nitriding, ion nitriding, plasma power, Ti6Al4V, roughness*

1. INTRODUCTION

Nitriding is a heat treatment where nitrogen is diffused into the surface of a metal. Nitriding is used on all sorts of steels, titanium, aluminium and molybdenum. There are three main processes named after medium which brings nitrogen onto surface, and they are: gas nitriding, salt bath nitriding and plasma nitriding. Nitriding temperatures are different based on a medium in which is happening and for plasma nitriding is between 450 and 660 °C. Nitrided parts are showing significant increase in surface hardness and wear resistance [1].

In this research medical grade titanium alloy Ti6Al4V ELI was used. To improve this alloy's surface properties in some specific direction, surface modification and/or coating techniques have been successfully implemented. Coating is basically adding or applying additional layer of material onto a pre-existing surface, and modification stands for modifying existing surface by a variety of techniques – primarily by introducing additional elements into the surface of material which in return changes its properties. Materials which are modified don't necessarily exhibit better properties than materials which are coated, but, because coatings don't usually diffuse well into the material itself, they pose a risk of delamination. One of the most common ways of modifying surfaces is nitriding. Best process of nitriding to be used on this alloy is plasma nitriding because it has a wide range of adjustable parameters, like: time, temperature, gas composition, plasma parameters, power etc. Plasma is one of four fundamental states of matter which is generated by subjecting electrically neutral gas to a strong electromagnetic field. Gases usually used in plasma nitriding are: N_2, H_2, Ar and their mixtures. Plasma nitrided parts do not need any additional machining nor polishing after nitriding because the process may be conducted without formation of white layer. It uses less energy than gas nitriding and it is ecologically more advanced than salt bath nitriding.

2. MATERIALS AND METHODS

2.1. Ti6Al4V ELI alloy samples

Because of two-phase structure and its purity, Ti6Al4V ELI alloy has a wide range of applications with great significance in biomedical implants. The alloy contains levels of oxygen, nitrogen, carbon and iron reduced to undetectable levels. ELI stands for Extra Low Interstitial which means that alloy is provided with better ductility and fracture toughness [2]. Because of its properties, this alloy is the most common titanium alloy and interesting for research and improvements with modification processes like plasma nitriding. In following table, guaranteed composition of samples is presented.

Tab. 1: Guaranteed composition of Ti6Al4V ELI alloy (AZ STEEL srl.) [3]

%	N	C	H	Fe	O	Al	V	Ti
Min.	-	-	-	-	-	5,5	2,5	Residual
Max.	0,05	0,08	0,0125	0,25	0,13	6,5	4,5	

In this research, samples of Ti6Al4V ELI alloy were divided into three groups and prepared: they were successively ground, polished, cleaned in alcohol, rinsed-off with demineralized water and dried.

2.2. Plasma nitriding

Plasma nitriding or Ion Nitriding is one of nitriding processes which requires introducing active nitrogen into treated surface. This modern thermochemical treatment improves wear resistance, surface hardness and fatigue strength. The process is suitable for all ferrous materials, sintered steels, cast iron and alloyed steels, as well as for other conductive materials. [4]

To achieve successful plasma nitriding it is necessary to set up the parameters correctly: temperature, duration, flow of hydrogen, nitrogen and argon gas, composition of gas mixture, plasma power, voltage and pressure.

In table 2, parameters of each plasma nitriding process are presented. Samples from first two processes are nitrided with similar parameters, but samples from third process significantly differs with plasma power parameter. Samples were nitrided by means of MICROPULS PACVD PC 70/90 (Rübig GmbH&Co KG) in the Laboratory for surface engineering at Faculty of Mechanical Engineering and Naval Architecture, University of Zagreb.

Tab. 2: Parameters of plasma nitriding processes

	Process 1	**Process 2**	**Process 3**
Temperature	500°C	600°C	500°C
Duration	6 h	9 h	6 h
H_2 flow	190 l/h	120 l/h	180 l/h
N_2 flow	10 l/h	60 l/h	20 l/h
Ar flow	10 l/h	10 l/h	10 l/h
Plasma power	1000 W	1000 W	1800 W
Voltage	560 V	560 V	560 V
Pressure	2 mbar	2 mbar	2 mbar

Process number 1 was performed as a preliminary experimental run in order to confirm that applied or similar parameters will result in successful adsorption (and diffusion) of nitrogen into the surface of Ti6Al4V ELI samples. Other tests, such as roughness analysis, haven't been conducted on those specific samples. Prior to all nitriding processes, *sputtering* step was performed within the vacuum chamber, under same conditions (same parameters) each time. *Sputtering* comprises of repetitive bombardment of treated surfaces with charged particles (energetic ions). The role of this step is to additionally clean surfaces and free them of oxides as much as possible.

2.3. Chemical composition analysis

Composition of samples after nitriding was analysed by means of Glow-Discharge Optical Emission Spectroscopy (GDOES) and Energy Dispersive Spectroscopy (EDS).

GDOES is a method of quantitative analysis with which were analysed samples from processes 1 and 2. GDOES provides direct elemental composition and depth profiling analysis of solids. Samples from process 3 were analysed with EDS which is microanalysis technique incorporated within scanning electron microscope (SEM). Both methods present quantitative compositions of samples. GDOES analysis was carried out on LECO SPECTRUMAT 850 GDS device in Laboratory for metal analysis while EDS analysis took place in Laboratory for materialography on TESCAN VEGA 5136MM microscope, both of which are situated at the Faculty of Mechanical Engineering and Naval Architecture, University of Zagreb.

2.4. Roughness

Surface roughness is one of the means of quantifying surface texture, and it is defined as a vertical deviation of surface from its mean profile line. Roughness measurement is widely used and important for complete insight into surface characteristics. In this research, parameters Ra, Rp and Rv were investigated. Parameter Ra is an arithmetic mean deviation of the assessed profile and one of the most often used dimensional roughness parameter. Rp is easily explained as a maximum peak height, while Rv is a maximum valley depth on a sampling length [5].

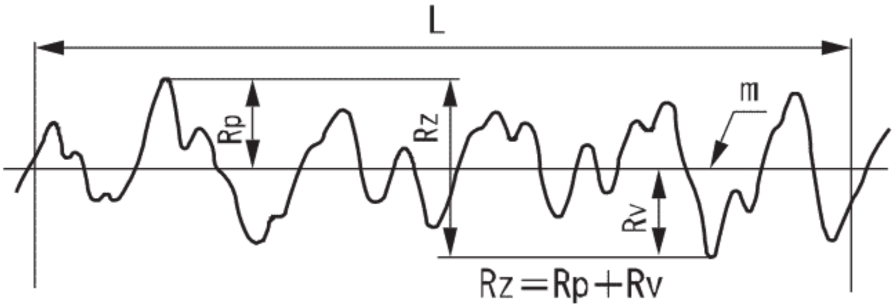

Fig. 1: Correlation between R_p, R_v and R_z [5]

Parameters were measured with surface roughness tester Time TR220 in compliance with ISO 4288:1996, ISO 4287:1997 and ISO 3274:1996 in Laboratory for precise measurements at the Faculty of Mechanical Engineering and Naval Architecture, University of Zagreb.

Surface roughness analysis was conducted on samples treated with process 2 (which was rather similar to process 1) and 3, prior and post treatment. In each case (for each process), roughness changes were determined on the same sample to exclude any other influence except for the treatment. Parameters of individual tests done are given in detail in table 3, with remark that Gauss filter was employed.

Tab. 3: Parameters of roughness testing

	Sample treated with process 2		**Sample treated with process 3**	
	Before	**After**	**Before**	**After**
Stylus tip radius, r [μm]	5	5	5	5
Number of traces: N	6	6	5	5
Tracing length: Lt [mm]	1.75	1.75	1.75	0.56
Evaluation length: Ln [mm]	1.25	1.25	1.25	0.40
Sampling length (*Cut-Off*, λc): Lr [mm]	0.25	0.25	0.25	0.08

3. RESULTS AND DISCUSSION

3.1. GDOES and EDS analysis results

Results of GDOES analysis of samples treated under parameters of processes 1 and 2 are shown with figures 2 and 3.

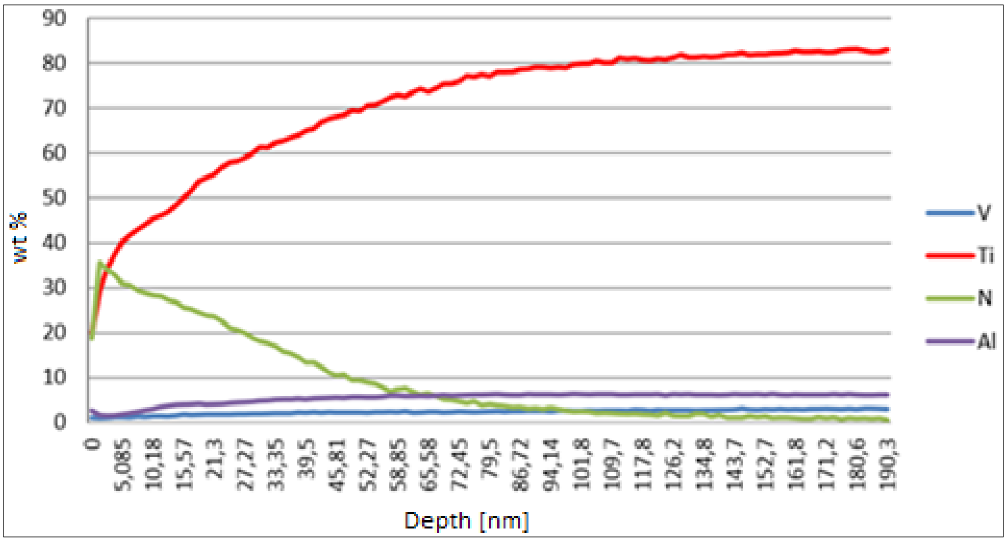

Fig. 2: GDOES analysis of samples from process 1 [2]

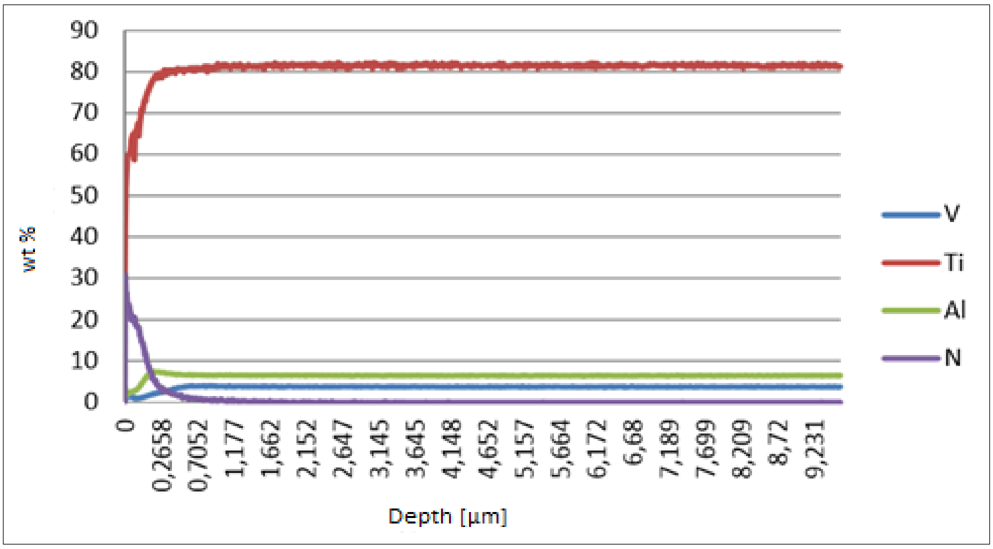

Fig. 3: GDOES analysis of samples from process 2 [2]

On both figures 2 and 3 it can be noticed that both sets of process parameters of plasma nitriding resulted in nitrogen adsorption within the samples' surfaces, and even more so, diffusion of nitrogen is noticeable. The depth of diffusion and the maximum content of

nitrogen on the samples' surfaces does not differ significantly between these two processes.
However, significant difference is noticable when effects of process number 3 are taken into account. Figure 4 shows results of EDS composition analysis conducted on the surface of sample treated with the process number 3.

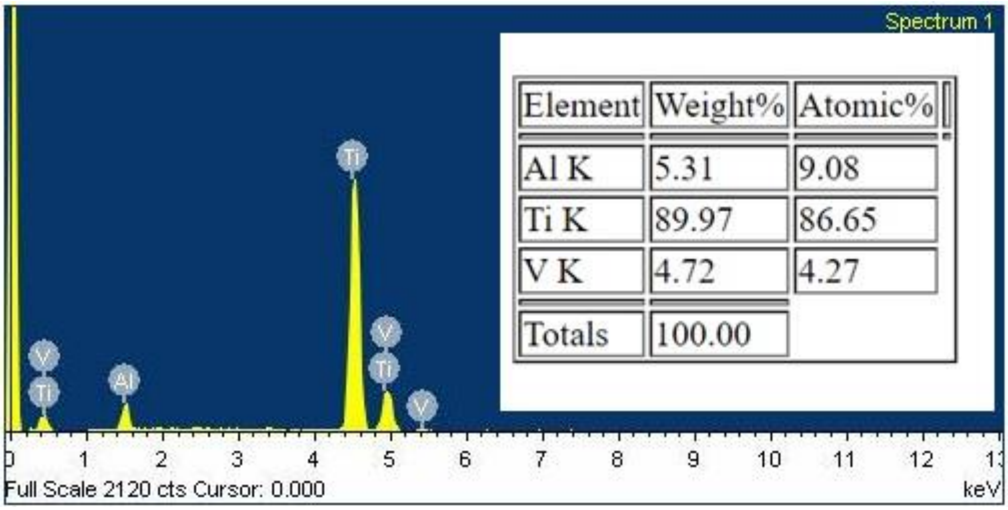

Element	Weight%	Atomic%
Al K	5.31	9.08
Ti K	89.97	86.65
V K	4.72	4.27
Totals	100.00	

Fig. 4: EDS analysis of samples treated with process 3

Samples treated with the third processes, clearly, didn't adsorb any amount of nitrogen, and further in-depth analysis of elemental distribution (via GDOES, for example) simply wasn't indicated.

3.2. Roughness analysis results

Roughness parameters were measured according to conditions explained earlier. Since parameter which is commonly taken as definitive indication of surface roughness changes, Ra, doesn't give enough information, Rp and Rv parameters were also measured. Results of each surface roughness analysis are given in tables in a form of mean values.

Tab. 4: Roughness analysis of process 2 [2]

	Before nitriding	After nitriding	Change
R_a [µm]	0.073	0,073	0,000
R_p [µm]	0,289	0,310	0,021
R_v [µm]	0,251	0,251	0,000

Tab. 5: Roughness analysis of process 3

	Before nitriding	**After nitriding**	**Change**
R_a [μm]	0.021	0.006	-0.015
R_p [μm]	0.094	0.032	-0.062
R_v [μm]	0.035	0.004	-0.031

First what can be observed from tables 4 and 5 is that initial values differ. That is because they were not prepared as attentive in both cases. Surface topography is not something that may influence its susceptibility towards nitrogen diffusion or the adsorption of the element. Also, in the case of roughness parameters analysis, the influence of different surface initial quality is annulled by measuring the change of parameters' values on the same sample – before, and after the nitriding process.

Process number 2 resulted in close to none changes in surface roughness parameters – surface roughness was preserved by the parameters of the process applied. The only change is a small increase in Rp value (of approximately 0.02 μm) but since it is not accompanied with any other change in general roughness indicator (Ra), it can be disregarded as a result of some local extreme on sampling length.

What clearly stands out is the magnitude of change in values of roughness parameters in the case of sample treated with process number 3. Ra parameter indicated significant enough change, and analysed parameters Rv and Rp revealed a bit more due to what that roughness really changed. Decrease in Rv value suggests that overall depth of profile decreased – valleys have been filled with material (debris) which became loose during the process. The source of that material may be identified as the excess of the peaks that have been removed (shaved off) by the same process, lowering the overall peak height (Rp) within the profile. Exactly that (Rp) is the parameter that changed the most, which, in combination with the change in Rv value, resulted in general smoothening of the profile (Ra).

4. CONCLUSION

Due to analyses carried out in this research, following conclusions may be drawn:

- The parameters, of processes 1 and 2 diferred significantly in temperature, duration and gas composition but the plasma power remained the same. Although mentioned process parameters were changed from process 1 to process 2, both of them resulted in successeful nitriding of the Ti6Al4V ELI alloy. Parameters of the third process were set within the range of previously confirmed (process 1 and 2) values, with a single significant difference – plasma power has been ramped up almost twofold. The third process resulted in no detectable nitrogen within the specimens' surfaces post the treatment. At this point, this effect may only be attributed to massive plasma power increase. Surface roughness before and after nitriding on sample treated with process 2 changed negligibly, while sample treated with process 3 shows significantly lower values of all measured surface roughness parameters.

- Higher plasma power, meaning higher amount of energy carried into process, could have resulted in ejection of any potentially adsorbed nitrogen. This, also, might be recognized as a mechanism of significant changes in topography and displacement of material around arithmetical mean deviation of the assessed profile.
- Selective variations of the process parameters (one at a time) for each treated material and detailed analysis of achieved effects is the only way to a complete insight and understanding of a process as complex as plasma nitriding.

5. REFERENCES

[1] M. Stupišnek, F. Cajner: Osnove toplinske obradbe metala, Faculty of Mechanical Engineering and Naval Architecture, Zagreb, 2001.

[2] http://www.arcam.com/wp-content/uploads/Arcam-Ti6Al4V-ELI-Titanium-Alloy.pdf/

[3] Ivan Kumić: New surface diffusion modification process for endoprosthetic bone implants titanium alloy, Faculty of Mechanical Engineering and Naval Architecture, Zagreb, 2016.

[4] http://www.bodycote.com/en/services/heat-treatment/case-hardening-without-subseque nt-hardening-operation/plasma-nitriding.aspx

[5] https://www.ns-tool.com/en/technology/technical_data/surface_roughness/

KOROZIJSKA POSTOJANOST PACVD PREVLAKA NA ALATNIM ČELICIMA ZA TOPLI RAD

CORROSION RESISTANCE OF PACVD COATINGS DEPOSITED ON HOT WORK TOOL STEEL

Vladimir Macura[1], **Darko Landek**[2]

[1] Sveučilište u Zagrebu, Fakultet strojarstva i brodogradnje ,Ivana Lučića 5, Zagreb,Hrvatska
[2] University of Zagreb, Facullty of mechanical engineering and naval architecture, Ivana Lučića 5, Zagreb, Hrvatska

Sažetak

Eksploatacijska svojstva alatnih čelika mogu biti poboljšana nanošenjem površinskih slojeva dobivenih postupkom plazma potpomognutog kemijskog prevlačenja iz parne faze (PACVD) .U radu su navedena osnovna mehanička i tribološka svojstvima tvrdih prevlaka TiN,TiN/TiCN i TiN /TiBN nanešenih PACVD postupkom na alatne čelike za topli rad. Provedena su korozijska ispitivanja na alatnim čelicima za topli rad EN DIN X38CrMoV5-3 i EN DIN X 37CrMoV5-1 u kaljenom i popuštenom stanju , nitriranom u plazmi te zaštićenom prevlakom TiN/TiCN i TiN/TiBN. Ispitan je korozijski potencijal, polarizacijski otpor i brzina korozije navedenih stanja i gubitak mase u slanoj komori. Iz rezultata provedenih ispitivanja uočava se povećanje otpornosti na koroziju primjenom obje PACVD prevlake.

Ključne riječi: *EN DIN X38CrMoV5-3 , EN DIN X 37CrMoV5-1,PACV, D TiN/TiCN, TiN/TiBN, korozijska postojanost*

Abstract

Exploitation properties of tool steels can be improved by deposition of layers in plasma assisted chemical vapour deposition process (PACVD). The paper describes mechanical and tribological properties of hard metal coatings TiN,TiN/TiCN i TiN /TiBN deposited by PACVD process on hot work tool steels .Corrosion measurments were performed on hot work tool steels ; EN DIN X38CrMoV5-3 i EN DIN X 37CrMoV5-1 in these states ; tempered , tempered and nitred in plasma , tempered and nitred in plasma with PACVD coating (TiN/TiCN i TiN/TiBN) .Corrosion potential , polarization resistnace ,corrosion speed and weigth loss in salt spray chamber were determined .From results we can conclude that both PACVD coatings improve corrosion resistance on hot work tool steel .

Ključne riječi: *EN DIN X38CrMoV5-3 , EN DIN X 37CrMoV5-1,PACV, D TiN/TiCN, TiN/TiBN*

1.Uvod

Postupak kemijskog prevlačenja iz parne faze potpomognut plazmom (eng. *Plasma Assisted Chemical Vapour Deposition, PACVD*) pripada skupini suvremenih postupaka prevlačenja površina koji se provode na temperaturi od 450 °C do 650°C uz prednosti visokotemperaturnog postupka CVD i mogućnost nanošenja višeslojnih i gradijentnih tvrdih prevlaka [1, 2, 3]. Dodatna prednost PACVD uređaja korištenog u ovom radu je mogućnost prethodnog nitriranja površine u plazmi, prije prevlačenja, čime se proizvode dupleks slojevi. Primjena dupleks slojeva s nitriranom difuzijskom zonom kao potpornim slojem i tvrdom PACVD prevlakom svoju primjenu nalazi u zaštiti površina alata za preradu polimera, obradu defromacijom u toplim stanju te površina kalupa za tlačni lijev [4, 5]. Na alatne čelike za topli rad koji će se ispitivati u radu uobičajeno se nanose tvrde PACVD prevlake TiN, TiCN i TiBN [1, 3, 4].

Utjecajni čimbenici na otpornost na koroziju navedenih tvrdih prevlaka nisu još dovoljno istraženi. Stoga će se u radu istražiti otpornost na koroziju dupleks slojeva proizvedenih nitriranjem u plazmi bez stvaranja zone spojeva i nanošenjem PACVD višeslojne PACVD prevlake TiN/TiCN, odnosno TiN/TiBN/TiN/TiBN

2. Materijali i metode

Tvrde PACVD prevlake nanešene su na podloge od kaljenih i popuštenih alatnih čelika ta topli rad: EN DIN X38CrMoV5-3 i EN DIN X37CrMoV5-1 kemijskog sastava prikazanog u tablici 1. Oba čelika isporučena suu obliku šipki dimenzija 220x50x260 mm iz kojih su strojnom obradom izrađeni ispitni uzroci za korozijska ispitivanja u slanoj komori i elektrokemijskoj radnoj ćeliji (slika 1)

Tablica 2 Kemijski sastav ispitivanih čelika

Oznaka čelika	Oznaka uzorka	C	Cr	Mo	V	Si	Mn
W.No. 1.2367 EN DIN X38CrMoV5-3	**A**	0,38	5,00	3,00	0,50	0,40	0,40
W.No.1.2343 EN DIN X37CrMoV5-1	**B**	0,38	5,00	1,30	0,40	1,00	0,40

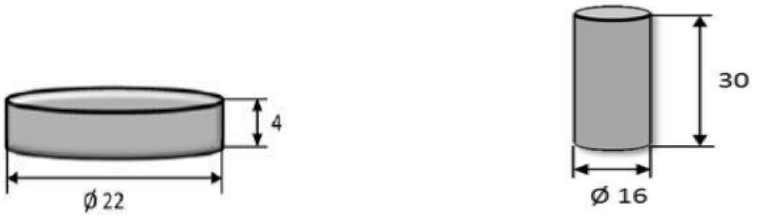

a) b)

Slika 1 Uzorci: a) za ispitivanje u slanoj komori, b) za ispitivanje elektrokemijske korozije

Osnovna toplinska obrada ispitnih uzorka se sastojala od kaljenja u vakuumskoj peći VFC proizvođača Ipsen GmbH i dva visokotemperaturna popuštanja u električnoj peći (slika 2). Izabrani optimalni parametri visokotemperaturnog popuštanja čelika EN DIN X38CrMoV5-3 bili 620°C/2h i 570°C/2h. Čelik EN DIN X37CrMoV5-1 je popušten na nešto niže temperature (500°C/2h za 1. popuštanje i 570°C/2h za 2. popuštanje) nego prethodno navedeni čelik. Nakon osonove toplinske obrade svi ispitni uzorci su brušeni i polirani. Zavrna gradacija vodootpornog brusnog papira bila je #1200. Parametri dupleks postupka navedeni su u tablici 2. Pri tom slovo u oznaci predstavlja vrstu čelika (prema tablici 1) a pripadajući broj vrstu naknadne toplinske obrade: nitriranje u plazmi (1), PACVD prevlačenja prevakom TiN/TiCN (2) te prevlačenje prevlakom TiN/TiBN/TiN/.TiBN (3). Nitriranje u plazmi i nanošenje PA CVD prevlaka proveno je u uređaju Rubig PC 70/90 instaliranom u Laboratoriju za inženjertsvo površina na Fakultetu strojarstva i brodogradnje u Zagrebu.

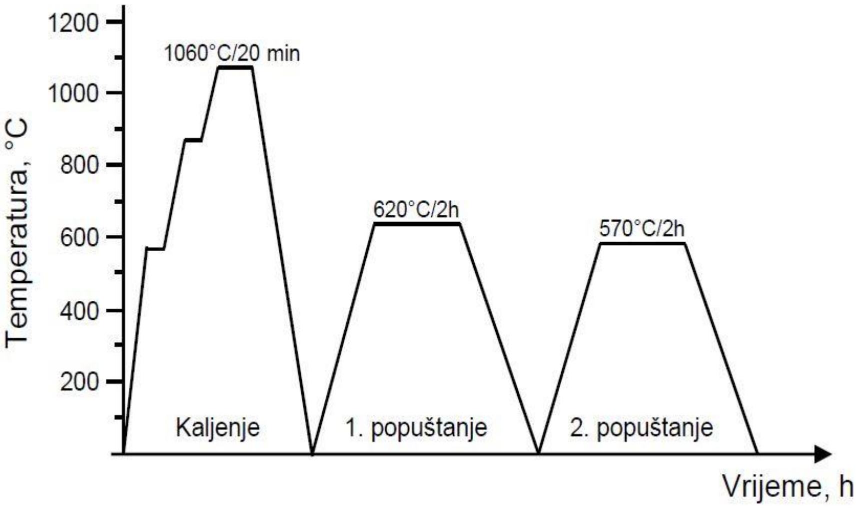

Slika 3. Dijagram postupka toplinske obrade alatnog čelika za topli rad EN DIN X38CrMoV5-3

Tablica 3. Parametri dupleks postupaka nitriranja u plazmi i PACVD prevlačenja

Oznaka	Toplinska obrada		Tip prevlake i parametri nanošenja
A0, B0	0. 1060°C/20 min/N_2 1. 620°C/2h 2. 570°C /2h	0. 1060°C/20 min/N_2 1.ϑ_p=500°C 2.ϑ_p=570°C	———
A1, B1	osnovna toplinska obrada + nitrirano u plazmi		TiN 500°C / 6h / 5% N_2
A2, B2	osnovna toplinska obrada+ nitrirano u plazmi + PACVD prevučeno		TiN + TiCN 1,5h TiN + 0,5h prijelaza zona iz TiN u TiCN + TiCN prevlaka 500°C/6 h
A3, B3	osnovna toplinska obrada + nitrirano u plazmi + PACVD prevučeno		TiN + TiB_2 (TiN + višeslojna TiBN (TiN + TiB_2), debljine 3-4 μm): TiN/2h + TiBN (43 sloja TiN–TiB_2)/7,5h

Nakon modificiranja i prevlačenja površina uzorci su ispitani u slanoj komori uz određivanje gubitka mase te u elektrokemijskoj ćeliji s ispitivanjem otpornosti na koroziju istosmjernom strujom. Ispitivanja otpornosti na elektrokemijsku koroziju obuhvatila su određivanje korozijskog potencijala, provedbu linearne polarizacija i Tafelova ekstrapolacije.

Ispitivanje u slanoj komori u trajanju od 24 h provedeno je sukladno normi HRN ISO 9227:2012. u slanoj komori *Ascott*, model S450 s maglom 5%-tne vodene otopine NaCl na temperaturi 35 ºC. Masa ispitnih uzoraka prije izlaganja slanoj magli i i nakon skidanja korozijskih produkata mjedenom četkom izmjerena je na preciznoj vagi Mettler Tolledo.

Elektrokemijska ispitivanja su provedena na uređaju *Potenciostat /Galvanostat 273A,* prema normi ASTM G5-94 u Laboratoriju za zaštitu materijala Fakulteta strojarstva i brodogradnje u Zagrebu. Na potenciostatu je proveden je polarizacija tijekom koje je uspostavljen određeni potencijal na mjernoj elektrodi, a potom je izmjerena struja odziva elektrokemijskog sustava *radna elektroda (ispitni uzorak) – protuelektroda (jedna ili dvije) - kalomel elektroda*. Mjerenja su provedena sa zasićenom kalomel elektrodom (ZKE) potencijala +0,242 V u odnosu na standardnu vodikovu elektrodu (E = 0 V). Kao protuelektroda, kojom se zatvario strujni krug korištena je elektroda izrađena od grafita. Radna elektroda se tijekom ispitivanja nalazila između dvije grafitne protuelektrode [6]. Elektrokemijskoj koroziji bila je izložena površina ispitnog uzorka od 1 cm^2. U svim elektrokemijskim ispitivanjima u korozijskoj ćeliji elektrolit je bila 3,5 % -tna otopina NaCl u deioniziranoj vodi, a ispitivanja su provedena na sobnoj temperaturi (20°C do 24°C). U računalnom programu *SoftCorr* određeni su parametri opće korozije: korozijski potencijal E_{kor}, polarizacijski otpor R_p, brzina korozije V_{kor} i gustoća korozijske struje I_{kor}. Izgled korodirane površine je snimljen stereomikroskopom Leica MZ6 s povećanjem od 25 puta.

3. Rezultati i diskusija

3.1. Ispitivanje otpornosti na koroziju u slanoj komori

Gubitak mase ispitnih uzoraka nakon 24 h ispitivanja u slanoj komori naveden je u tablici 3, a izgled površina je prikazan na slici 4. Iz slike 4 uočava se vrlo malo tragova korozije na prevlaci TiN/TiBN (A3, B3) kod oba ispitivana čelika, što se također podudara s rezultatima mjerenja gubitka mase navedenim u tablici 3. Općenito neprevučeni i prevučeni ispitni uzroci na čeliku EN DIN X37CrMoV5-1 korodirali su manje od uzroaka izrađenih od čelika EN DIN X38CrMoV5-3.

Tablica 4 Gubitak mase nakon slane komore

Stanje površine prije ispitivanja u slanoj komori	Gubitak mase, mg	
	EN DIN X38CrMoV5-3 (A)	EN DIN X37CrMoV5-1 (B)
Neprevučeno (0)	0,0218	0,0147
Nitrirano u plazmi (1)	0,0189	0,0230
Prevučeno PACVD TiN/TICN (2)	0,0142	0,0134
Prevučeno PACVD TiN/TIBN (3)	0,0139	-0,0039

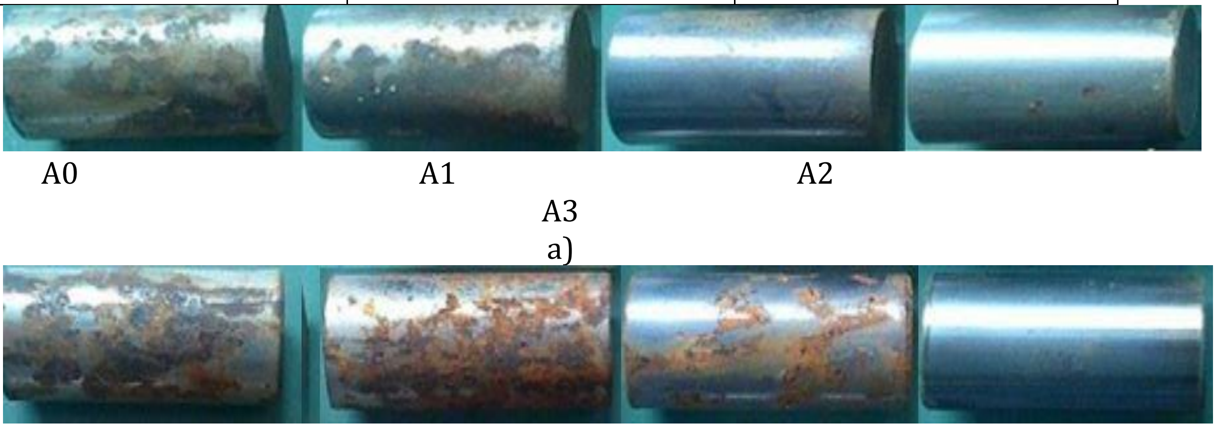

A0 A1 A2
A3
a)

B0 B1 B2
B3
b)

Slika 17. Izgled površina nakon 24 h korozije u slanoj komori ispitnih uzoraka izrađenih od čelika: a) EN DIN X38CrMoV5-3, b) EN DIN X37CrMoV5-1

3.2. Ispitivanja otpornosti na elektrokemijsku koroziju

Otpornost na elektrokemijsku kroziju ispitana je usporedbom krozijskog potencijala, polarizacijskog otpora i gustoće korozijske struje određene Tafelovom ekstrapolacijom.

Korozijski potencijal E_{kor} određen je nakon uranjanja ispitnog uzorka (radne elektrode) u 3,5 %-tnu otopinu NaCl u vodi pri čemu je izmjerena razlika potencijala između referentne i radne elektrode koja se ustalila nakon određenog vremena. Rezultati određivanja E_{kor} ispitnih uzoraka navedeni su u tablici 4. Negativne vrijednosti E_{kor} ukazuju na sklonost površine svih ispitnih uzoraka otapanju u elektrolitu, odnosno pojavi korozije [6] .

Tablica 5 Izmjerene vrijednosti korozijskog potencijala ispitnih uzoraka

Oznaka uzorka	A0	A1	A2	A3	B0	B1	B2	B3
E_{kor}vs ZKE(mV)	-554	-503	-336	-470	-553	-572	-419	-471

Polarizacijski otpor (R_{p}) ili otpor Faradayevoj reakciji elektrolize definira se kao otpor prolazu elektroaktivnih cestica iz jedne faze (metala ili legure) u drugu (elektrolit). On se uobičajeno odreduje u odnosu na potencijal otvorenog strujnog kruga oko područja polarizacije (±20 mV), gdje se prema Mansfieldu nalazi približno linearan omjer jakosti struje i potencijala. Veće vrijednosti polarizacijskog otpora ukazuju na bolju otpornost površine ispitivanog uzorka na koroziju u elektrolitu u koji je uronjen [3]

Tablica 6 Izmjerene vrijednosti polarizacijskog otpora ispitnih uzoraka

Oznaka uzorka	A0	A1	A2	A3	B0	B1	B2	B3
R_{p}(kΩcm^2)	1,665	1,958	24,000	21,000	2,311	1,363	8,371	112,1

Gustoća korozijske struje i iz nje izvedena brzina korozije određuju se iz Tafelove ekstrapolacije. Ova metoda se temelji se na Butler-Volmerovoj jednadžbi kojom je opisana ukupna struja koja prolazi kroz granicu faza ispitni uzorak - elektrolit. Nakon anodne i katodne polarizacijom ispitnog uzorka (radne elektrode) u širokom području vrijednosti korozijskog potencijala ($E = E_{\mathrm{kor}} \pm 250$ mV) ovisnost promjene korozijskog potencijala o gustoći korozijske struje prikazuje se grafički u linearno-logaritamskom obliku (E – log j) [3] Na slici 5 prikazane su Tafelove krivulje za sve ispitne uzorke. Rezultati određivanja gustoće korozijske struje, brzine korozije i koeficijenata u Butler-Volmerovoj jednadžbi za čelik EN DIN X38CrMoV5-3 navedeni u tablici 6, dok su rezultati za čelik EN DIN X37CrMoV5-1 navedeni u tablici 7.

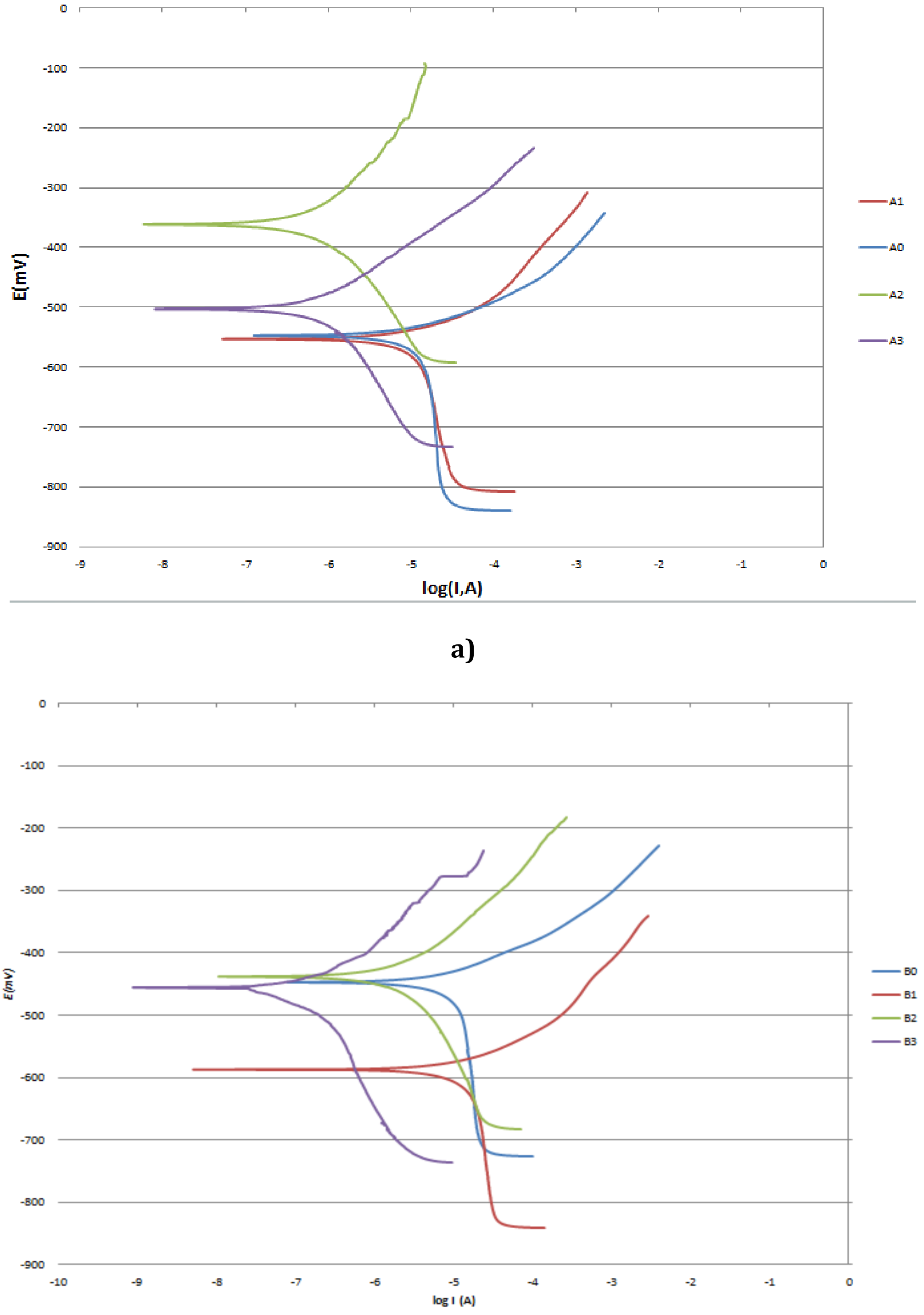

a)

b)

Slika 18 Tafelove krivulje za ispitne uzorke od čelika: a) EN DIN X38CrMoV5-3, b) EN DIN X37CrMoV5-1

Tablica 7 Korozijski parametri na temelju Tafelovih krivulja za čelik EN DIN X38CrMoV5-3

Oznaka uzorka	I_{cor} (µA)	V_{cor} (mm/god)	b_a (V/dek)	b_c (V/dek)
A0	16,87	0,191	73	1756
A1	16,45	0,188	83	1029
A2	1,205	0,013	209	204
A3	1,033	0,011	105	211

Iz rezultata ispitivanja elektrokemijske korozije ispitnih uzoraka izrađenih od čelika EN DIN X38CrMoV5-3 navedenih u tablici 6 očekivano se uočava se da prevučeni uzorci A2 i A3 imaju značajno manju brzinu korozije u odnosu na neprevučene uzorke A0 i A1. Također ispitni uzorak A3 s višeslojnom prevlakom PACVD TiN/TiB_2 se je korozijski najpostojaniji te je vrijednost njegove brzine korozije 17,36 puta manja u odnosu na neprevučeni čelik X38CrMoV5-3.

Tablica 8 Korozijski parametri na temelju Tafelovih krivulja za čelik EN DIN X37CrMoV5-1

Oznaka uzorka	I_{cor} (µA)	V_{cor} (mm/god)	b_a (V/dek)	b_c (V/dek)
B0	13,09	0,148	72	1209
B1	22,53	0,255	85	1776
B2	3,316	0,037	127	250
B3	0,208	0,002	109	267

Rezultati ispitivanja elektrokemijske korozije ispitnih uzoraka izrađenih od čelika EN DIN X37CrMoV5-1 pokazali su slične kvalitativne odnose prametara korozije između prevučenih i neprevučenih površina. Posebno se ističe mala brzina korozije ispitnog uzorka B3 koja je 74 puta manja u odnosu na neprevučeno stanje B0.

Izgled površine ispitnih uzoraka nakon provedbe elektrokemijskih ispitivanja Tafelovom metodom prikazan je na slici 7.

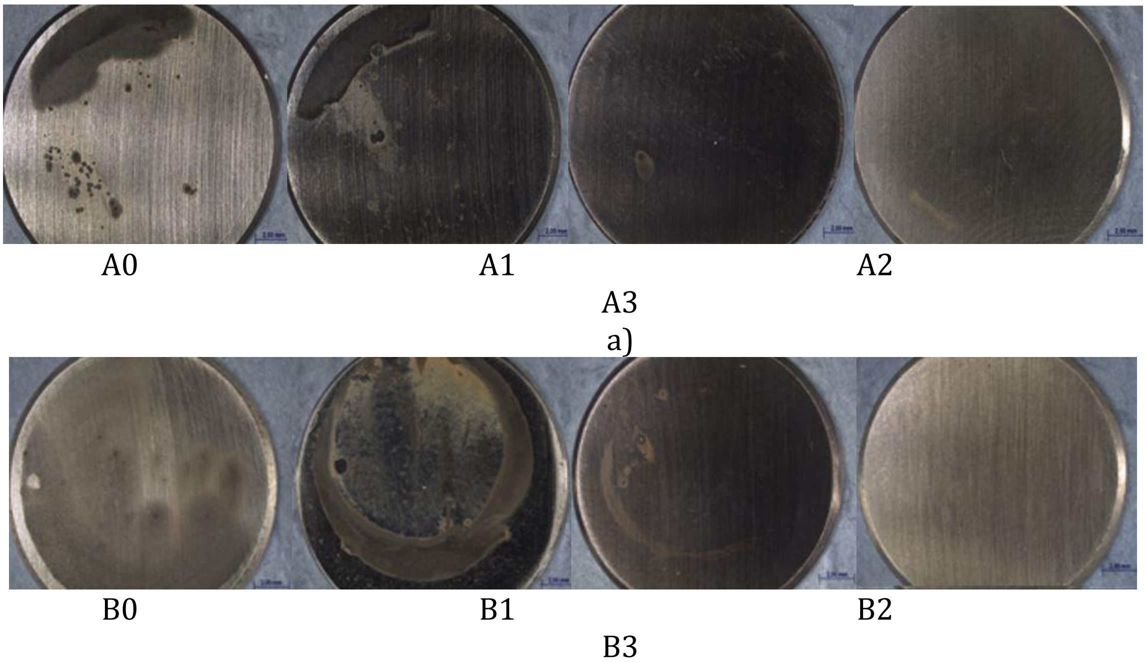

a)

b)

Slika 19. Izgled korodirane površine nakon elektrokemijskih ispitivanja ispitnih uzoraka izrađenih od čelika: a) EN DIN X38CrMoV5-3, b) EN DIN X37CrMoV5-1

Izgled površina ispitnih uzoraka prikazanih na slici 7 potvrđuje utvrđene odnose korozijskih parametara navedenih u tablici 6 i tablici 7. Uzorci u polaznom stanju i nitriranom stanju (bez zone spojeva) korozijski su oštećeni na sličnom udjelu površine. Na ispitnim uzorcima s prevlakom PACVD TiN/TiCN uočava se pojava lokalne i točkaste korozije. Ispitni uzorci s višeslojnom prevlakom PACVD TiN/TiB_2 pokazuju vrlo mala korozijska oštećenja točastom korozijom.

4. Zaključak

Iz elektrokemijskih ispitivanja provedenih u 3,5 % NaCl na sobnoj temperaturi te ispitivanja u slanoj komori zaključuje se značajno povećanje otpornosti na elektrokemijsku koroziju primjenom prevlaka PACVD TiN/TiCN i PACVD TiN/TiB_2 na obje ispitane podloge od čelika EN DIN X38CrMoV5-3 i EN DIN X37CrMoV5-1.

Nitranje u plazmi bez zone spojeva nije moglo omogućiti značajnije povećanje otpornost na elektrokemijsku koroziju u odnosu na polazno stanje, što je očekivano jer je difuzijska zona na nitriranim uzorcima samo nosiva podloga za tvrdu PACVD prevlaku.

Primjenom dvoslojne PACVD TiN/TiCN prevlake brzina korozije je smanjena za 14,69 puta kod uzoraka od čelika EN DIN X38CrMoV5-3 te 4 puta kod uzoraka od čelika EN DIN X37CrMoV5-1. Primjenom višeslojne PACVD TiN/TiB_2 prevlaka se ostvarilo smanjenje brzine korozije kod uzoraka od čelika EN DIN X38CrMoV5-3 za 17,36 puta, a kod uzorka od čelika EN DIN X37CrMoV5-1 za 74 puta u odnosu na brzinu korozije ne prevučenih uzorka.

Analiza izgleda korodirane površine ukazala je na sklonost PACVD prevlaka na altatnim čelicima za topli rad pojavi lokalne i točkaste korozije.

Literatura

[1] C. Mitterer, et. al.: "Industrial applications of PACVD hard coatings, Surface and Coatings Technology 163 –164 (2003) 716–722

[2] B. Podgornik, S. Hogmark: „Surface modification to improve friction and galling properties of forming tools“, Journal of Materials Processing Technology, Vol. 174, Issue 1-3, (2006), 334-341.

[3] Stoiber, S. Perlot, C. Mitterer, M. Beschliesser, C. Lugmair, R. Kullmer, PACVD TiN/Ti-B-N multilayers: from micro-to nano-scale, Surf. Coatings Technol. 177–178 (2004) 348–354

[4] K. Gammer, M. Stoiber, J. Wagner, H. Hutter, R. Kullmer, C. Mitterer, Investigations on the effects of plasma-assisted pre-treatment for plasma-assisted chemical vapour deposition TiN coatings on tool steel, Thin Solid Films, 461 (2004) 277-281.

[5] S. Kovačić: Utjecaj nitriranja i prevlačenja na svojstva alatnih čelika za topli rad, doktorski rad, Sveučilište u Zagrebu, Fakultet strojarstva i brodogradnje, 2015

I. Juraga, V. Alar, I. Stojanović: Korozija i zaštita premazima, Sveučilište u Zagrebu, Fakultet strojarstva I brodogradnje, 2016

ALUMINA COMBUSTION SYNTHESIS

SINTEZA ALUMINIJEVOG OKSIDA SAGORIJEVANJEM

Katarina Mužina, Vilko Mandić, Filip Brleković, Emina Ema Alić, Stanislav Kurajica

University of Zagreb, Faculty of Chemical Engineering and Technology, Marulićev trg 19, Zagreb, Croatia
Sveučilište u Zagrebu, Fakultet kemijskog inženjerstva i tehnologije, Marulićev trg 19, Zagreb, Republika Hrvatska

Abstract

Combustion synthesis is a process that uses a highly exothermic redox reaction between fuel and oxidizer to produce metal oxides of desired properties. In this work, combustion synthesis of aluminium oxide from aluminium nitrate as oxidizer and alanine as fuel was investigated. The product was thermally treated at various temperatures and characterized using differential thermal and thermo-gravimetric analysis (DTA-TGA), Fourier transformed infrared spectroscopy (FTIR), scanning electron microscopy (SEM), powder X-ray diffraction (XRD) and laser diffraction particle size analysis. The XRD results show that the initially amorphous product shows peaks for γ-alumina after thermal treatment at 800 °C and peaks for α-alumina after treatment at 1000 °C. The FTIR spectra confirm the existence of Al-O bonds. According to the particle size distribution results, the average particle size of the obtained alumina is around 140 μm.

Keywords: *combustion synthesis, alumina, alanine*

Sažetak

Sinteza sagorijevanjem je proces u kojem se koristi egzotermna reakcija između goriva i oksidansa za pripravu metalnih oksida željenih svojstava. U ovom radu istražena je sinteza aluminijevog oksida sagorijevanjem aluminijevog nitrata kao oksidansa te alanina kao goriva. Produkt je termički obrađen na različitim temperaturama te karakteriziran uz pomoć diferencijalne termičke i termogravimetrijske analize (DTA-TGA), infracrvene spektroskopije s Fourierovom transformacijom (FTIR), pretražne elektronske mikroskopije (SEM), rendgenske difrakcije praha (XRD) i analize veličine čestica laserskom difrakcijom. Rezultati XRD analize ukazuju da početno amorfni produkt prelazi u γ-Al_2O_3 pri termičkoj obradi od 800 °C te α-Al_2O_3 pri 1000 °C. FTIR spektri potvrđuju prisutnost Al-O veza. Srednja veličina čestica iznosi oko 140 μm.

Ključne riječi: *sinteza sagorijevanjem, aluminijev oksid, alanin*

1. INTRODUCTION

Alumina (Al_2O_3) is one of the most commonly used inorganic materials, because of its favourable properties such as low cost, good thermal stability, surface acidity and interaction with deposited transition metals. [1] Alumina has a wide variety of applications: as catalyst and catalyst support in heterogeneous catalysis, as adsorbent and in preparation of alumina based ceramics. All these applications are possible due to its complex structure and the ability to exist in a variety of metastable structures known as transition aluminas (β-Al_2O_3, γ-Al_2O_3, δ-Al_2O_3, θ-Al_2O_3, η-Al_2O_3, κ-Al_2O_3, χ-Al_2O_3 and ρ-Al_2O_3) and in a stable α-Al_2O_3 form. [1,2] Among these structures, γ-alumina and α-alumina are most commonly used in practical applications. γ-Al_2O_3 has a large surface area, strong adsorption capacity, good catalytic activity and wear resistance, and therefore has many applications, especially in the refining and petro chemistry. On the other hand, α-Al_2O_3 is extensively used in ceramics, surface protective layer materials, refractory materials, catalyst and catalyst supports due to its good acid, alkali and heat resistances, high hardness and strength. [1,2]

Various methods have been used for the synthesis of alumina powders, such as precipitation, spray pyrolysis, hydrothermal, sol-gel and combustion synthesis. [3] Combustion synthesis (CS) is a technique that uses a highly exothermic redox reaction to produce oxides thus avoiding the use of post-synthesis prolonged thermal treatment. Such synthesis method possesses numerous advantages like simplicity, affordability and good control over composition, homogeneity, purity and particle size. [3,4]

Combustion synthesis can be controlled through various processing parameters, the most important being fuel to oxidizer ratio (F/O). However, both fuel and oxidizer can be composed of oxidizing and reducing elements and therefore fuel to oxidizer ratio is expressed in terms of elemental stoichiometric coefficient as equivalence ratio. The equivalence ratio is expressed as [4]:

$$\varphi = \frac{n_F \sum stoichiometric\ coefficient\ \times valence}{-n_O \sum stoichiometric\ coefficient\ \times valence} \tag{1}$$

In equation 1 n_F is the stoichiometric coefficient of the fuel and n_O the stoichiometric coefficient of the oxidizer. The valences of oxidizing elements are considered as negative, while the valences of reducing elements are considered as positive. Carbon, hydrogen and metal cations are considered as reducing elements, while oxygen is considered as oxidizing element and nitrogen as neutral. Therefore, the valences used in formula are as follows: C: +4, H: +1, M: +1, 2, 3…, O: -2, N: 0.

The mixture is stoichiometric when φ=1, i.e. when the sums of oxidizing and reducing valences in fuel and oxidizer multiplied by its stoichiometric coefficients are equal. When φ<1, the mixture is fuel lean, while when φ>1, the mixture is fuel rich.

Generally, metal nitrates are used as oxidizers, while urea, citric acids, aminoacids etc. are most commonly used as fuels. Besides decomposing to combustible gases such as HNCO and NH_3, which ignite with NO_x, they have to form complexes with the metal ions thus forming an intimate mixture of fuel and oxidizer.

In this work, a stoichiometric mixture of aluminium nitrate as oxidizer and alanine as fuel was used in a combustion synthesis of aluminium oxide. The product was thermally treated at various temperatures and characterized by differential scanning calorimetry and thermo-gravimetric analysis (DSC-TGA), Fourier transformed infrared spectroscopy (FTIR), scanning electron microscopy (SEM), powder X-ray diffraction (XRD) and laser diffraction particle size analyser.

1. EXPERIMENTAL

1.1. Synthesis

Analytical grade aluminium nitrate nonahydrate, $Al(NO_3)_3\times9H_2O$ (Kemika, Croatia) was used as oxidant, while alanine, $C_3H_7NO_2$ (Kemika, Croatia) was used as fuel. For those precursors equation 2 could be written as:

$$\varphi = \frac{n_F(3_C \times 4 + 7_H \times 1 - 2_O \times 2)}{-n_O(1_{Al} \times 3 - 9_O \times 2)} = \frac{n_F 15}{-n_O 15} \tag{2}$$

Thus stoichiometric mixture is achieved when $n_F = -n_O$, i.e. when the molar ratio of alanine and aluminium nitrate equals 1. The synthesis was conducted as follows: Proper amounts of aluminium nitrate nonahydrate (0.05 mol) and alanine (0.05 mol) were weighted in a porcelain bowl and 10 ml of water were added. The mixture was heated to 60 °C and mixed (600 rpm) on a hot plate magnetic stirrer until it became so viscous to stop the magnet. Than the magnet was removed and heating of the hot plate to 380 °C was initiated (but this temperature was not attained). The combustion process was complete in less than 13 min (~12.7 min), while the ignition time was around 9.7 min. The process was flameless, but with red incandescence and a great amount of fumes produced. Produced low specific weight greyish material was collected and stored in a closed glass container.

1.2. Characterization

The temperature of the mixture was monitored using a high temperature IR thermometer (Extech Instruments).

DTA – TGA thermal analysis of the as-prepared sample was conducted using Netsch STA 409C at a heating rate of 10 °C min^{-1} in synthetic air flow of 30 cm^3 min^{-1}. α–alumina was used as a reference.

The as-prepared sample was quenched from temperatures in a range from 600 to 1200 °C. Based on the XRD results of the quenched samples, additional thermal treatment at 600, 800 and 1000 °C for 2 hours was conducted.

All samples were analyzed using powder X–ray diffraction (XRD) on Shimadzu diffractometer XRD 6000 with CuKα radiation. Data were collected between 10 – 70° 2θ, in step scan mode with steps of 0.02 ° and counting time of 0.6 s.

IR spectra were acquired using the Fourier transform infrared spectrometer Bruker Vertex 70 in ATR (attenuated total reflectance) mode. Absorbance data were collected between 400 and 4000 cm^{-1} with the spectral resolution of 1 cm^{-1} and 16 scans.

The morphology of the sample was investigated with Tescan Vega 3 scanning electron microscope operating at 10 kV.

Particle size distribution was determined using Shimadzu SALD-3101 laser diffraction particle size analyser.

2. RESULTS AND DISCUSSION

Figure 1 displays the sample temperature during the combustion process and Figure 2 shows the obtained product. As can be seen, the ignition temperature is ~ 153 °C with the time of ignition being ~ 9.7 min. The peak temperature is 555 °C and the peak is relatively narrow, which indicates that the combustion process is fast, lasting around 3 minutes. The brown colour of the obtained product (Fig. 2) indicates the presence of char in the sample.

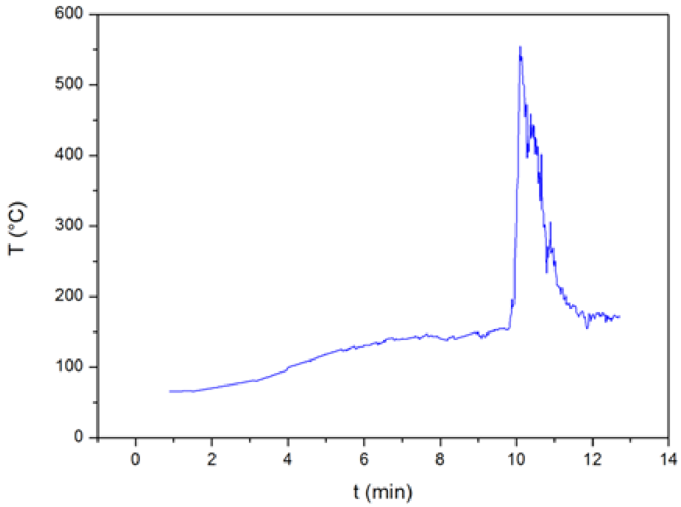

Fig. 1: Sample temperature during combustion process.

Fig. 2: Combustion synthesis product.

The XRD pattern of the as-prepared sample is shown on Figure 3. The pattern indicates the amorphous nature of the sample.

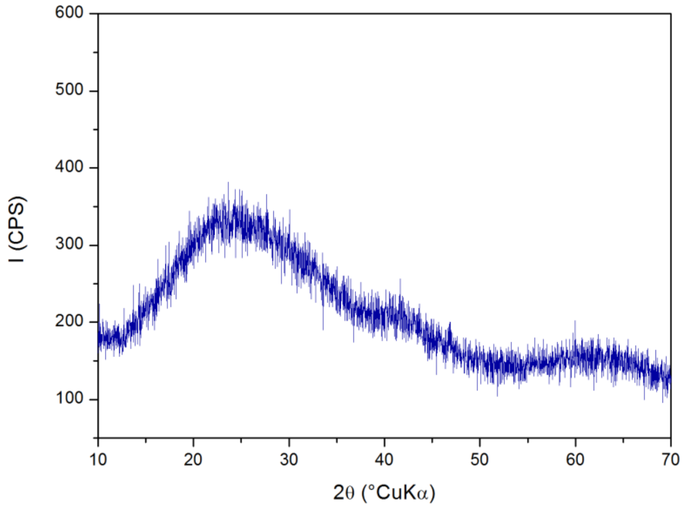

Fig. 3: The XRD pattern of the as-prepared sample.

The as-prepared sample was also subjected to the DTA-TGA analysis and the results are presented in Figure 4.

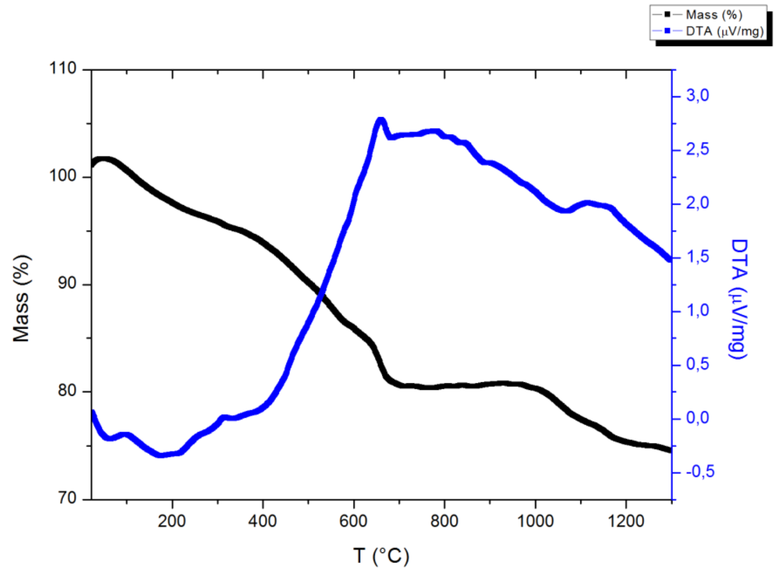

Fig. 4: DTA and TGA curves of the as-prepared sample.

The TG analysis shows a total weight loss of 25.5 %. The first mass loss from room temperature to 300 °C corresponds to the elimination of adsorbed water and carbon dioxide in the sample, accompanied with a few poorly defined peaks on the DTA curve. The second mass loss is most likely due to the burning of residual organic compounds and nitrates from the precursors in the range from 300 to 700°C. The last mass loss from 900 to 1200 °C is accompanied with two exothermal peaks centred at 900 and 1050 °C. These peaks could be associated with the formation of γ-Al2O3 and its transformation to α-Al2O3 [5], while the mass loss is probably due to the burning of residues that remained within the particles and were liberated due to the structural changes.

The as-prepared sample was quenched from 600, 700, 800, 900, 1000, 1100 and 1200 °C in order to gain a deeper insight in its thermal evolution. Figure 5 shows the samples quenched from said temperatures. There is an obvious change in colour from samples quenched from 600, 700 and 800 °C, which are still brown to light brown like the as-prepared sample, over samples quenched from 900 and 1000 °C, which are light grey, to the samples quenched from 1100 and 1200 °C, which are white.

Fig. 5: Samples quenched from different temperatures in a range between 600 and 1200 °C.

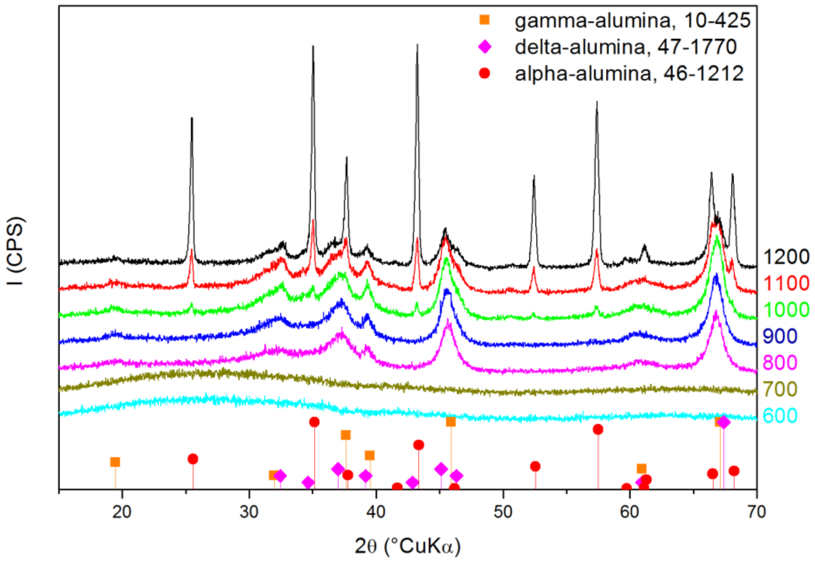

Fig. 6: XRD patterns of samples quenched from different temperatures in a range between 600 and 1200 °C.

The powder XRD patterns of the quenched samples are shown in Figure 6. As can be seen, samples quenched from 600 and 700 °C are amorphous in nature. The XRD patterns of samples quenched from 800 and 900 °C correspond to γ-alumina (ICDD PDF No. 10-425), while in the sample quenched from 1000 °C a split of transition alumina peaks is observed, making them compatible with both γ-alumina and δ-alumina (ICDD PDF No. 47-1770). Furthermore, there are also traces of α-alumina (IDDD PDF No. 46-1212) present in the sample quenched from 1000 °C. The XRD patterns of samples quenched from 1100 and 1200 °C correspond to α-alumina with traces of γ-alumina and δ-alumina, which is in concordance with the fact that during the thermal treatment of γ-alumina a transformation to δ-alumina and finally hexagonal α-alumina occurs. [6]

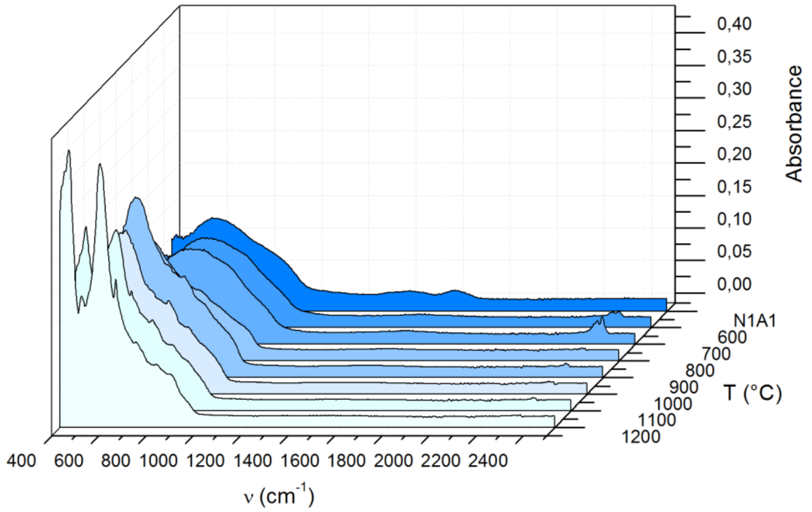

Fig. 7: FTIR spectra of samples quenched from different temperatures in a range between 600 and 1200 °C.

Figure 7 shows FTIR spectra for the as-prepared and quenched samples. The as-prepared sample spectrum shows a flat broad band in the 3500-2700 cm^{-1} region that is attributed to O-H groups caused by the adsorbed water. Bands showing at 1598, 1423 and 1332 cm^{-1} are due to the C-N and N-C-N bonds present in organic residue left after the combustion synthesis. [7,8] After quenching from 600 °C, the bands characteristic for water disappear, as well as organic residue bands, due to their oxidation at higher temperatures. The band observed at 600 and 700 °C in the region around 620 cm^{-1} is characteristic of Al-O bonds in amorphous material created by combustion synthesis. [8] Heating of the sample to 800°C caused the sharpening of the band and its movement to 518 cm^{-1}, which can be connected with the formation of γ-Al_2O_3 and its Al(IV)-O vibrations, while heating the sample to 900 °C makes the band of γ-Al_2O_3 stronger. [7] New sharp bands are visible on the spectrum of the sample heated to 1000 °C at 541 and 447 cm^{-1}, caused by the formation of α-Al_2O_3 and Al-O stretching vibrations of AlO_6 isolated octahedra, while the band due to γ-Al_2O_3 is still, but barely visible. At temperatures higher than 1100 °C the γ-Al_2O_3 band is no longer visible. Sharp bands around 570 and 440 cm^{-1} and weaker bands around 635 and 490 cm^{-1} are now dominant due to the Al-O bonds stretching vibrations in isolated and condensed AlO_6 octahedra from α-Al_2O_3.

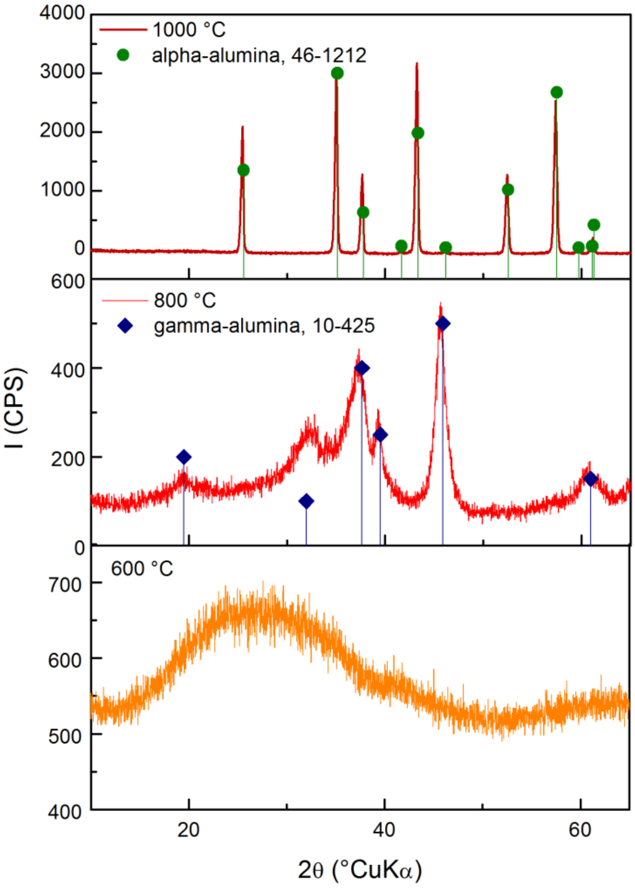

Fig. 8: XRD patterns of samples thermally treated at 600, 800 and 1000 °C.

Three temperatures (600, 800 and 1000 °C) were chosen for thermal treatment of the as-prepared sample based on the results for quenched samples. The as-prepared sample was thermally treated for 2 hours at selected temperatures and then subjected to XRD analysis. The results are presented in Figure 8. The XRD pattern of the sample thermally treated at 600 °C shows an amorphous hump at approximately 28 °2θ, which is similar to the XRD patterns of samples quenched from 600 and 700 °C. The sample thermally treated at 800 °C shows broad peaks which correspond to γ-alumina (ICDD PDF No. 10-425). The XRD pattern of the sample treated at 1000 °C corresponds to pure α-alumina (ICDD PDF No. 46-1212), with no peaks for transition alumina.

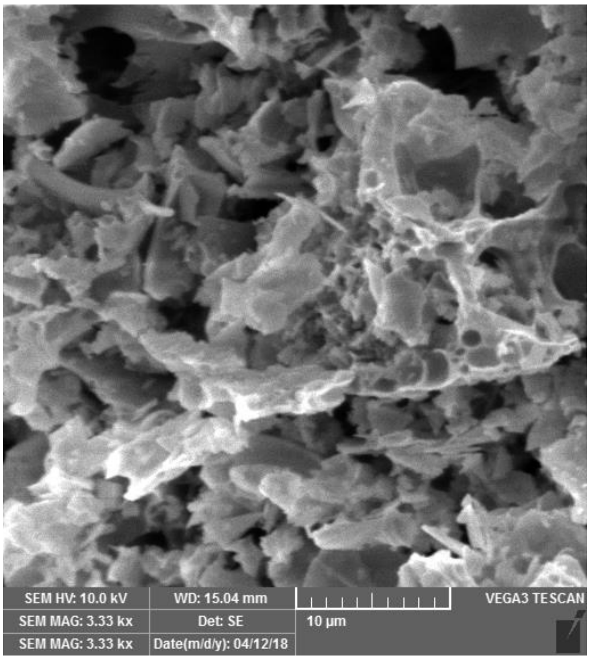

Fig. 9: SEM micrograph of the as-prepared sample.

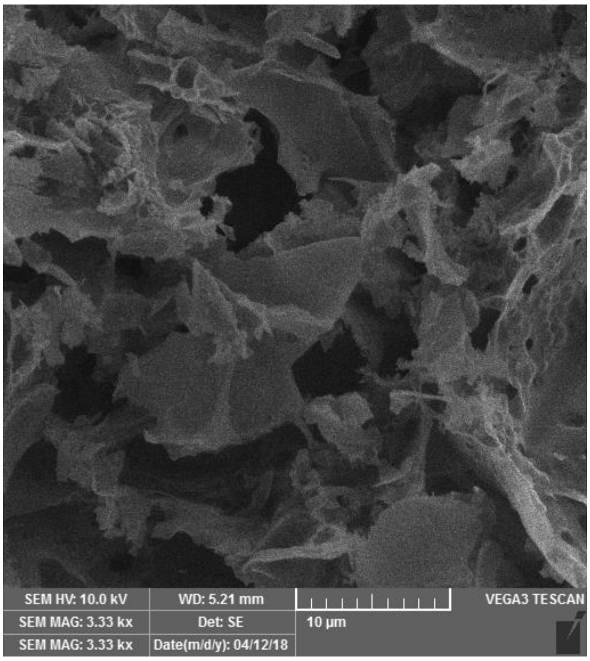

Fig. 10: SEM micrograph of the sample thermally treated at 800 °C for 2 h.

SEM micrographs of the as-prepared sample and sample thermally treated at 800 °C for 2 hours are shown on Figures 9 and 10. As can be seen, the as-prepared sample has a porous flake-like morphology, which is probably a consequence of particles bursting due to gas emissions in the course of the combustion process. The particles are in the size range below a micrometre and several micrometres. The thermally treated sample retains a similar, but more porous flake-like morphology.

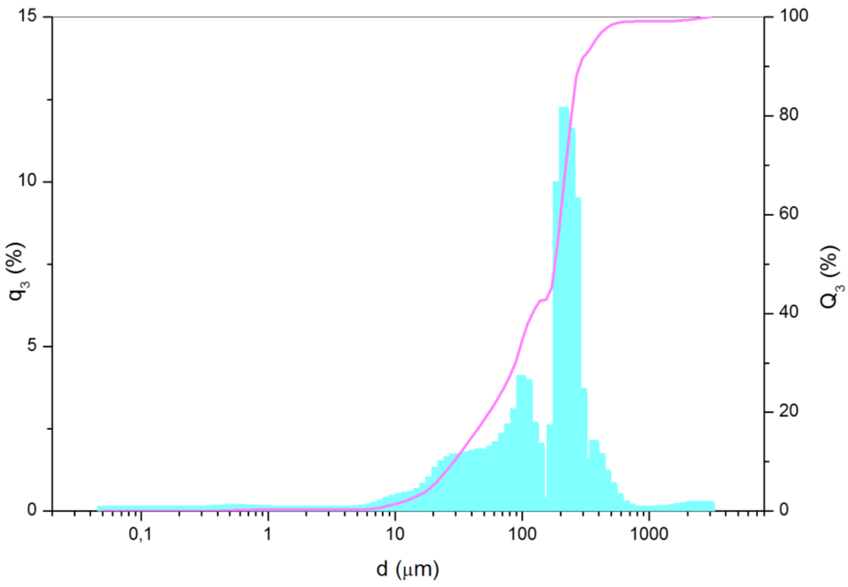

Fig. 11: Particle size distribution for the sample thermally treated at 800 °C for 2 h.

Figure 11 shows particle size distribution results for the sample thermally treated at 800 °C for 2 hours. The results are compatible with SEM micrographs, confirming that the particle sizes are in the range below one micrometre and several micrometres, with the average value being around 140 μm.

3. CONCLUSION

Combustion synthesis of aluminium nitrate and alanine yielded with an amorphous powder product. The amorphous powder crystallises to γ-alumina at around 800 °C, while its slow transformation to α-alumina begins at approximately 1000 °C. During the transformation, traces of δ-alumina were observed. Thermal treatment at 800 °C for 2 hours yields with pure γ-alumina, which has a flake porous morphology and average particle size around 140 μm. After thermal treatment at 1000 °C for 2 hours pure α-alumina has been obtained. Alanine-aluminium nitrate solution combustion synthesis is a simple and economic process which shows a good potential for the production of alumina powders of desired properties.

Acknowledgement:
The support of the University of Zagreb is gratefully acknowledged. Particle size analysis contribution of K. Žižek is much obliged.

REFERENCES

[1] Tafreshi M.J., Khanghah Z.M., Infrared Spectroscopy Studies on Sol-gel Prepared Alumina Powders, Materials Science (Medžiagotyra), 21, pp. 28-31, (2015).

[2] Xie Y., Kocaefe D., Kocaefe Y., Cheng J., Liu W., The Effect of Novel Synthetic Methods and Parameters Control on Morphology of Nano-alumina Particles, Nanoscale Research Letters, 11:259, pp. 1-11, (2016).

[3] Edrissi M., Norouzbeigi R., Synthesis and characterization of alumina nanopowders by combustion of nitrate-amino acid gels, Materials Science-Poland, 25, pp. 1029-1040, (2007).

[4] http://shodhganga.inflibnet.ac.in/bitstream/10603/4952/8/08_chapter%204.pdf, consulted on 15 Apr 2018.

[5] Ji L., Lin J., Tan K.L., Zeng H.C., Synthesis of High-Surface-Area Alumina Using Aluminum Tri-sec-butoxide−2,4-Pentanedione−2-Propanol−Nitric Acid Precursors, Chemistry of Materials, 12, pp. 931-939, (2000).

[6] Yalamaç E., Trapani A., Akkurt S., Sintering and microstructural investigation of gamma and alpha alumina powders, Engineering Science and Technology, 17, pp. 2-7, (2014).

[7] Roque-Ruiz J.H., Reyes-López S.Y., Synthesis of α-Al2O3 Nanopowders at Low Temperature from Aluminum Formate by Combustion Process, Journal of Material Sciences & Engineering, 6, pp. 1-8, (2016).

[8] Lin C.-P., Wen S.-B., Variations in a Boehmite Gel and Oleic Acid Emulsion under Calcination, Journal of the American Ceramic Society, 85, pp. 1467-1472, (2002).

ANALIZA POVRŠINE NANOSTRUKTURIRANIH TVRDIH METALA NAKON PROVEDENIH ELEKTROKEMIJSKIH ISPITIVANJA

SURFACE ANALYSIS OF NANOSTRUCTURED HARDMETALS AFTER ELECTOCHEMICAL MEASUREMENTS

Regina Novak, Tamara Aleksandrov Fabijanić, Matija Sakoman

Sveučilište u Zagrebu, Fakultet strojarstva i brodogradnje, Ivana Lučića 5, Zagreb, Hrvatska
University of Zagreb, Faculty of Mechanical Engineering and Naval Architecture, Ivana Lučića 5, Zagreb

Sažetak

U radu je provedena analiza površine nanostrukturiranih tvrdih metala nakon provedenih elektrokemijskih ispitivanja istosmjernom strujom (DC) i izmjeničnom strujom (AC) u 96 %-tnoj sulfatnoj kiselini H_2SO_4 pri sobnoj temperaturi. Analiza površine provedena je na šest uzoraka nanostrukturiranih tvrdih metala s različitim sadržajem kobalta; 5, 10 i 15 wt.%Co. Uzorke karakterizira 100% gustoća i najniži stupanj poroziteta. Analiza površine provedena je metodom analize slike korištenjem programskog paketa Image J pri različitim povećanjima pri čemu je određen volumni udio površine zahvaćen produktima korozije. Na temelju provedenih ispitivanja ustanovljeno je da su rezultati karakterizacije površine u skladu s vrijednostima brzine korozije određene elektrokemijskim mjerenjima.

Ključne riječi: nanostruktirirani tvrdi metali, analiza površine, metoda analize slike, produkti korozije

Abstract

In this paper, the surface analysis of nanostructured hardmetals after electrochemical measurement performed by direct current (DC) and alternating current (AC) techniques in 96% sulfuric acid H_2SO_4 at room temperature is carried out. The surface analysis was carried out on six different samples of nanostructured hardmetals with different Co content; 5, 10 and 15 wt% Co. The samples are characterised by 100% density and the lowest degree of porosity. The surface analysis was carried out by the image analysis method using the software Image J at different magnifications, whereby the surface volume affected by the corrosion products was determined. Based on the performed research, it was found that the results of the surface analysis are in accordance with the corrosion rate values v_{corr} previously determined by electrochemical measurements.

Keywords**: **nanostructured hardmetals, surface analysis, image analysis, corrosion products

1.UVOD

Tvrdi metali su najrašireniji i najpoznatiji metalni kompoziti dobiveni postupkom metalurgijom praha. Prvi komercijalni tvrdi metali patentirani su od strane njemačkog proizvođača “Krupp“ pod nazivom „WIDIA“, a označava mješavinu volfrsm karbida WC sa 6 wt.% matricom kobalta Co. Trenutno 90% proizvodnje tvrdih metala u svijetu otpada na sustav WC-Co koji sadrži između 3 i 30 wt.% Co [1]. Co ima odličnu oblikovljivost tijekom postupka miješanja i mljevenja te je topivost WC-a u njemu, pri temperaturi sinteriranja, velika. Mikrostruktura tvrdih metala sastoji se od većeg udjela karbida volframa WC međusobno povezanih kobaltom Co koji predstavlja vezivo (slika 1). Co kao vezivo osigurava žilavost, a karbidi predstavljaju nositelje tvrdoće i otpornosti na trošenje. Svojstva tvrdih metala su; visoka tvrdoća, visoka otpornost na trošenje, visoka tlačna čvrstoća, visoki modul elastičnosti, visoko talište, visoka čvrstoća pri povišenim temperaturama, dobra otpornost na toplinske šokove i relativno loša otpornost na koroziju. Korozijskim mehanizmom tvrdih metala dominira otapanje Co u uvjetima otvorenog kruga u neutralnom i kiselom okruženju [1]. U konvencionalnim tvrdim metalima, odvija se selektivno otapanje Co matrice dok čestice WC-a nisu pod utjecajem korozijskog napada. Kod alkalnih pH vrijednosti dolazi do pasivizacije Co matrice i otapanja WC. Prema tome, očekuje se da će brzina korozije porasti povećanjem sadržaja Co u polaznim mješavinama. U posljednjih 20 godina primjenjuju se prahovi sve manje veličine zrna što je dovelo do razvoja tvrdih metala kod kojih se koriste ultrafini (0,2 - 0,5 μm) i nanočestični prahovi (< 0,2 μm). Uporabom prahova s veličinom zrna u nanopodručju postiže se homogena mikrostruktura povišene čvrstoće, otpornosti na trošenje i tvrdoće. Takva mikrostruktura omogućuje duži vijek trajanja reznog alata, njegovu primjenu pri većim brzinama rezanja i manje tolerancije [1].

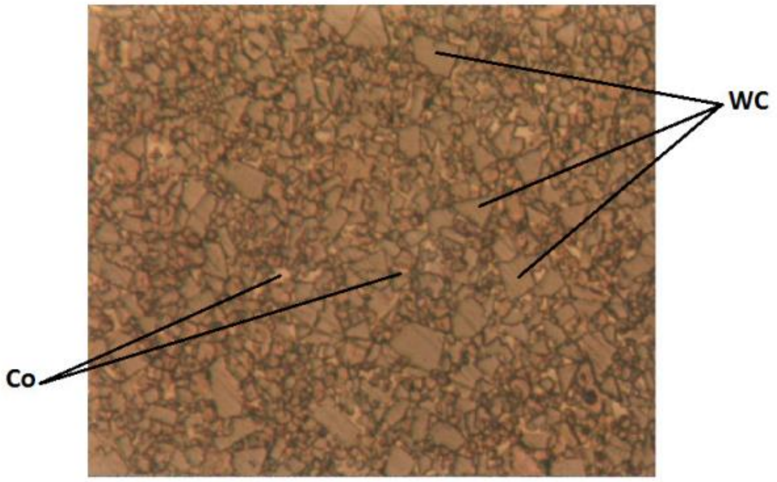

Slika 1. Mikrostruktura WC–Co tvrdog metala [2]

2. MATERIJALI I METODE

2.1. MATERIJAL

Ispitivanja su provedena je na šest uzoraka nanostrukturiranih tvrdih metala s različitim sadržajem kobalta; 5, 10 i 15 wt.%Co. Kao polazni materijal korišten je WC nano prah oznake WC DN 4-0, prozvođača H.C.Starck Tungsten (Goslar, Njemačka). Prah ima prosječnu veličinu zrna d_{BET} = 95 nm i specifičnu površinu (BET) od 3,92 m^2/g. Kao materijal matrice je korišten Co prah s veličinom čestica d_{FSSS} = 770 nm, proizvođača Umicore. Uzorke karakterizira 100% gustoća i najniži stupanj poroziteta. Uzorci su sinterirani sinter-HIP procesom u jednom ciklusu. Karakteristike uzoraka nakon konsolidacije prikazane su u Tablici 1.

Tablica 1: Karakteristike uzoraka prije elektrokemijskih mjerenja [3]

Uzorak	Co, wt.%	GGI, wt.%	C, wt.%	Gustoća, %	Porozitet		
					A	B	C
WC-5Co-1	5	0.41%VC, 0.80% Cr_3C_2	0.150	100	A00	B00	C00
WC-5Co-2		0.39 %VC, 0.76 % Cr_3C_2	0.180	100	A00	B00	C00
WC-10Co-1	10	0.41%VC, 0.80% Cr_3C_2	0.125	100	A00	B00	C00
WC-10Co-2		0.37 %VC, 0.72 % Cr_3C_2	0.225	100	A00	B00	C00
WC-15Co-1	15	0.41%VC, 0.80% Cr_3C_2	0.100	100	A00	B00	C00
WC-15Co-2		0.35 %VC, 0.68 % Cr_3C_2	0.120	100	A00	B00	C00

Iz tablice se može vidjeti da je različiti udio ugljika dodan početnim smjesama, čija je posljedica razlika u vrijednostima magnetske zasićenosti. Na svim uzorcima s nižim vrijednostima magnetske zasićenosti tijekom mikrostrukturne analize primijećena je η-faza [3]. Iz tablice se može iščitati i stupanj poroziteta. Na ispitivanim uzorcima nije uočena pojava poroziteta ili nevezanog ugljika te se navedeno označava kao stupanj poroziteta A00, B00, C00. Mjerenje gustoće provedeno je na svim uzorcima što znači da je postignuta teoretska gustoća 100%.

2.2. ELEKTROKEMIJSKA MJERENJA

Za provođenje elektrokemijskih ispitivanja na uzorcima, primijenjene su tehnike ispitivanja sa istosmjernom strujom (DC) i izmjeničnom strujom (AC) u 96 %-tnoj sulfatnoj kiselini H_2SO_4 pri sobnoj temperaturi. Elektrokemijske tehnike s izmjeničnom strujom, poput korozijskog potencijala (E_{corr}), linearnog polarizacijskog otpora (LPR) i Taffelove metode, provedene su na svakom uzorku u svrhu određivanja brzine korozije. Provedena je i elektrokemijska impedancijska spektroskopija (EIS) kako bi se istražio proces korozije na sučelju između površine uzorka i otopine elektrolita.

2.3. ANALIZA POVRŠINE NAKON PROVEDENIH ELEKTROKEMIJSKIH MJERENJA

Analiza polirane površine nakon provedenih elektrokemijskih mjerenja provedena je u Laboratoriju za materijalografiju Fakulteta strojarstva i brodogradnje na optičkom mikroskopu proizvođača Olympus, Japan, prikazanom na slici 2.

Slika 2. - Optički mikroskop proizvođača Olympus [1]

Za svaki uzorak napravljene su snimke na povećanjima 50x, 100x, 200x, 500x i 1000x. Dodatno su analizirane snimke pri najmanjem povećanju (50x i 100x) na različitim mjestima površine kako bi se izvršila analiza korozije cijele ispitne površine. Fotografije su naknadno obrađene u programu Image J, gdje su prebačene u 8-bitne, crno-bijele fotografije kako bi postojeće pore bile što izraženije te usporedba što lakša i mjerodavnija. U programskom paketu Image J koristila se funkcija „Analyze Particles“ za određivanje udjela korozivnosti [4]. Određen je volumni udio površine zahvaćen produktima korozije.

3. REZULTATI I ANALIZA

Snimke površine uzoraka nakon provedenih elektrokemijskim mjerenja prikazane su na slikama 3-8.

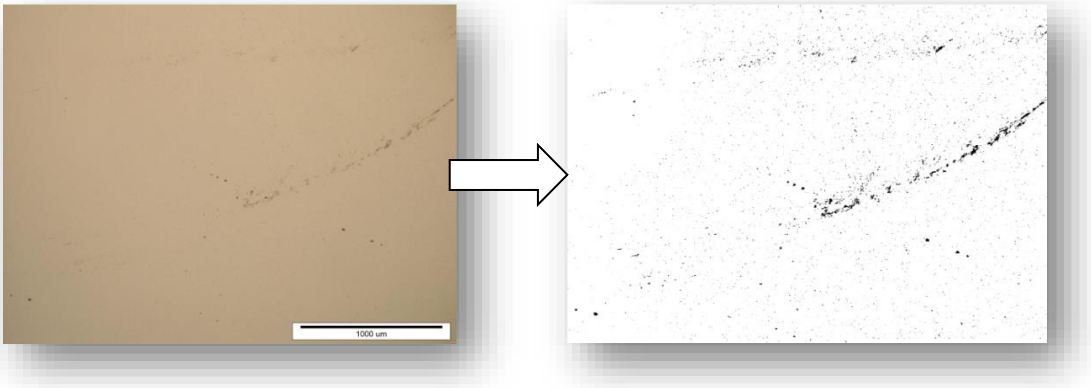

a) **b)**

Slika 3: Uzorak WC-5Co-1
a) Snimka površine pri povećanju 50x b) snimka nakon prebacivanja u ImageJ

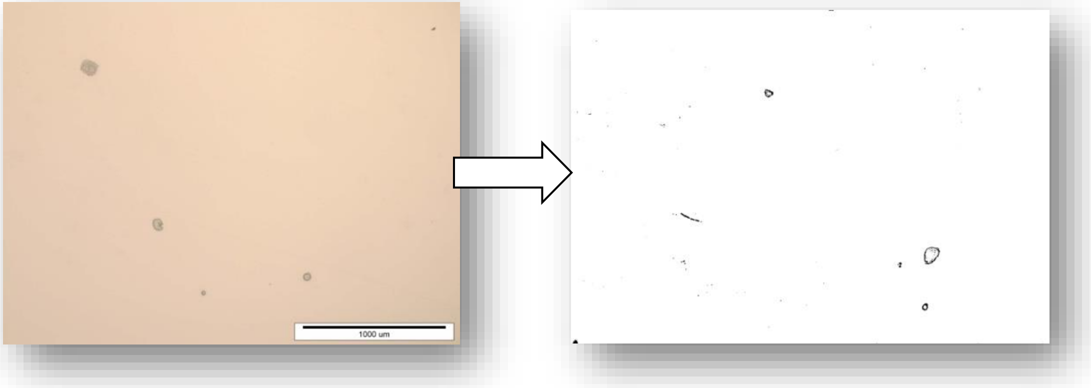

a) **b)**

Slika 4: Uzorak WC-10Co-1
a) Snimka površine pri povećanju 50x b) snimka nakon prebacivanja u ImageJ

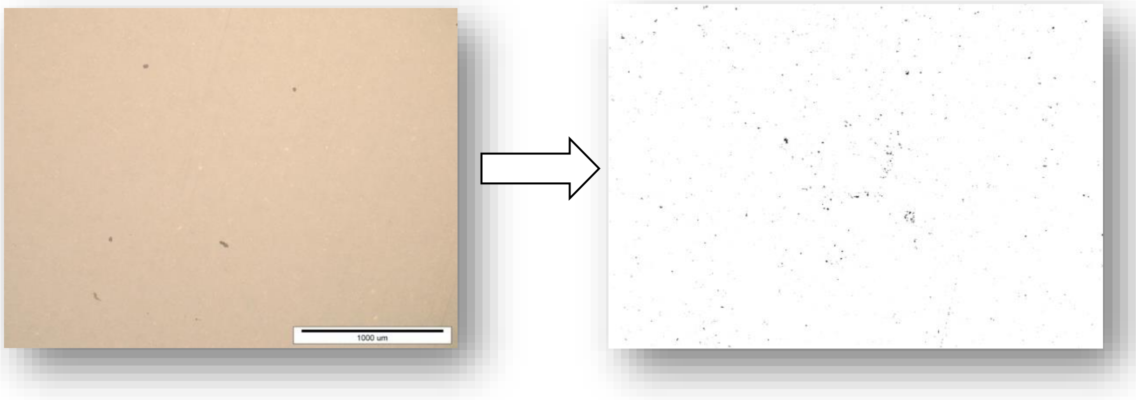

a) b)

Slika 5: Uzorak WC-15Co-1
a) Snimka površine pri povećanju 50x b) snimka nakon prebacivanja u ImageJ

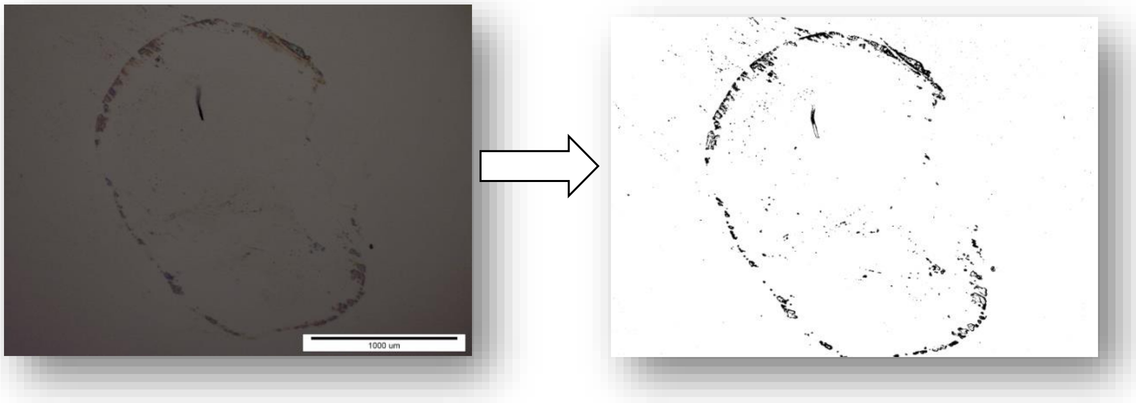

a) b)

Slika 6: Uzorak WC-5Co-2
a) Snimka površine pri povećanju 50x b) snimka nakon prebacivanja u ImageJ

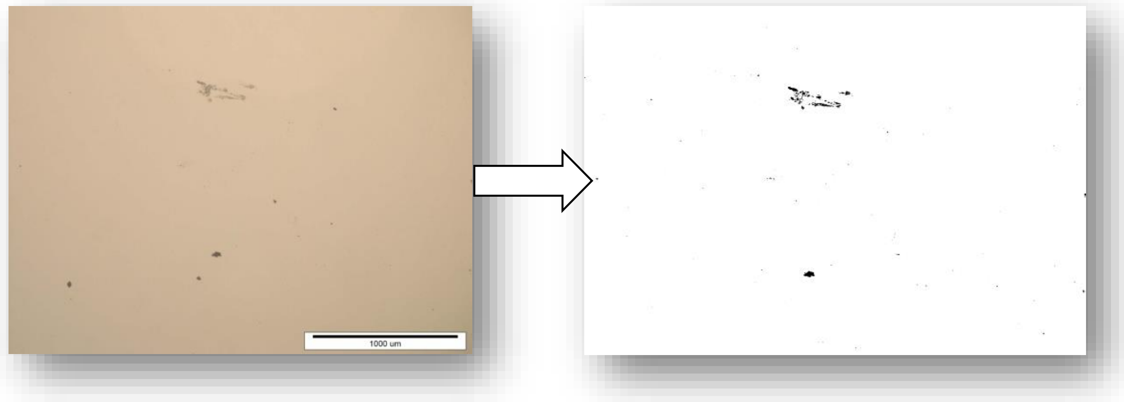

Slika 7: Uzorak WC-10Co-2 a) Snimka površine pri povećanju 50x b) snimka nakon prebacivanja u ImageJ

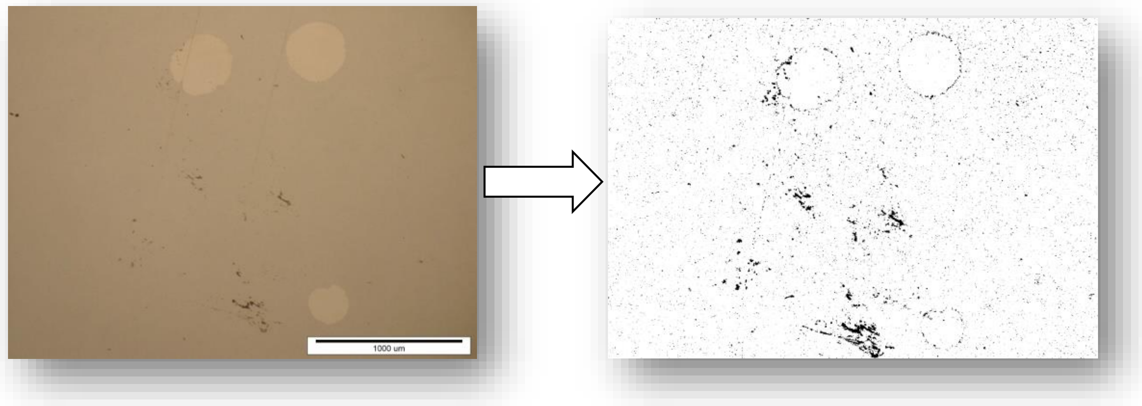

Slika 8: Uzorak WC-15Co-2
a) Snimka površine pri povećanju 50x b) snimka nakon prebacivanja u ImageJ

Rezultati analize površine uzoraka i pripadajuće vrijednosti brzine korozije v_{corr} određene elektrokemijskim mjerenjima prikazani su u Tablici 2.

Tablica 2: Postotak korozije na povećanju 50x i 100x

UZORAK	v_{corr}, **mm/god**	**Volumni udio % pri 50x)**	**Volumni udio % (pri 100x)**
WC-5Co-1	0,32565	0,980	0,404
WC-10Co-1	2,75950	1,608	0,101
WC-15Co-1	1,39580	1,104	0,211
WC-5Co-2	3,78620	1,608	2,085
WC-10Co-2	0,77841	0,240	0,173
WC-15Co-2	0,13279	2,436	1,642

Na temelju rezultata iz Tablice 2 mogu se uočiti vrlo različita očitanja udjela korozije. Elektrokemijskim mjerenjima najveća brzina korozije v_{corr} izmjerena je za uzorak WC-Co-2 dok je najmanja brzina korozije izmjerena za uzorak WC-15Co-2. Usporedimo li uzorke s istim udjelom Co i različitim udjelom C u polaznim mješavinama možemo zaključiti da udio C utječe na korozijsku postojanost. U slučaju uzoraka sa 5 wt. % Co bolju korozijsku postojanost pokazao je uzorak sa nižim udjelom ugljika WC-5Co-1 dok su kod uzoraka sa 10 wt. %Co i 15 wt. %Co bolju korozijsku postojanost pokazali uzorci sa višim sadržajem C; WC-10Co-2 I WC-15Co-2.

Analizom slike pri različitim povećanjima najveći volumni udio površine zahvaćen korozijskim produktima u iznosu od 2,436% određen je za uzorak WC-15Co-2, dok na većem povećanju, tj. 100x, to nije slučaj jer mikroskopom nije zahvaćeno isto područje na površini kao na prethodnom povećanju. Zatim ga slijedi uzorak WC-5Co-2 koji na povećanju 100x ima najveći udio korozije. Poslije njega slijede uzorci WC-10Co-1, te redom WC-15Co-1, WC-10-Co-2 te WC-5Co-1. Udio korozije na uzorku WC-10-Co-2 je određen na dva različita mjesta na površini zbog većih razlika.

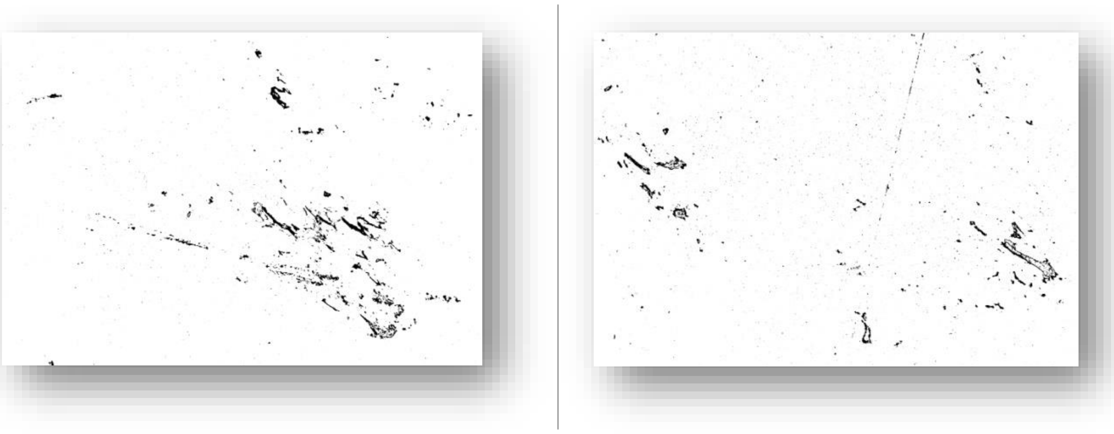

Slika 9: Uzorak WC-15Co-2
a) Snimka površine uzorka WC-15Co-2 na povećanju 200x
b) Snimka površine uzorka WC-15Co-2 na povećanju 50x

Na povećanju 100x rezultati ne prate iste poredak kao kod prethodnog povećanja. Razlog tome su različita mjesta na površini uzorka snimljena optičkim mikroskopom. Općenito, da bi analiza bila što mjerodavnija nužno ju je provesti na minimalno pet različitih pozicija na površini ispitivanih uzoraka pri istim povećanjima kako bih analizom obuhvatili što veći dio površine. Općenito, na temelju analize može se uočiti da najveći udio korozije ima uzorak WC-5Co-2 što je u skladu sa rezultatima elektrokemijskih mjerenja. Površina uzorka WC-5Co-2 pri raznim povećanjima prikazana je na slikama 10 i 11.

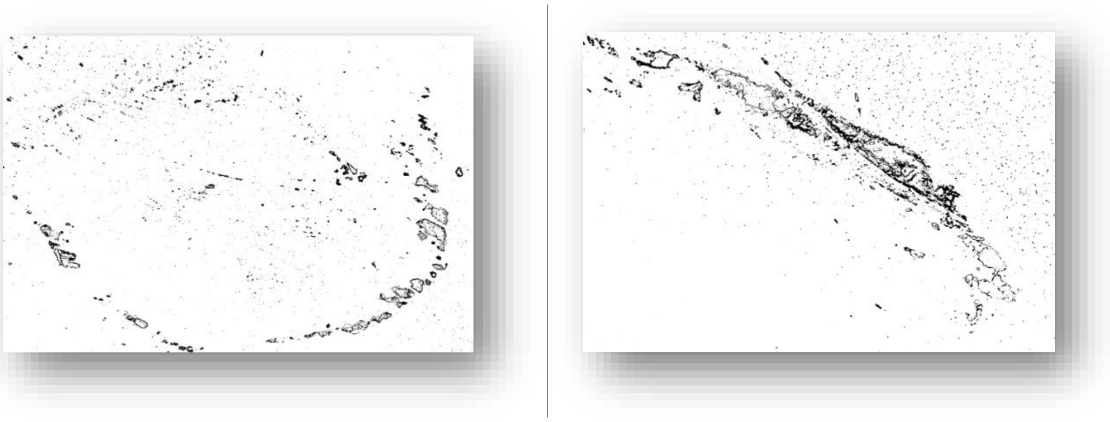

Slika 10: Uzorak WC-5Co-2
a) Snimka površine uzorka WC-5Co-2 na povećanju 200x
b) Snimka površine uzorka WC-5Co-2 na povećanju 100x

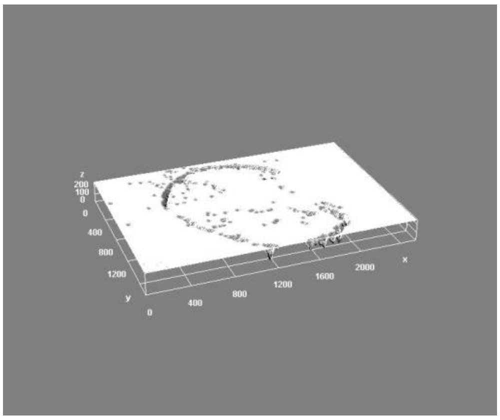

Slika 11: 3D prikaz uzorka WC-5Co-2, 50x

4. ZAKLJUČAK

Na temelju provedenih ispitivanja može se zaključiti sljedeće:

- Sadržaj Co u polaznim mješavinama pokazao je neznatan utjecaj na elektrokemijsku otpornost i analizu površine zahvaćenu korozijskim produktima. Općenito, ne postoji jasan trend povećanja brzine korozije s povećanjem udjela Co što je karakteristika konvencionalnih WC-Co tvrdih metala.
- Udio ugljika u polaznim mješavinama pokazao je značajniji utjecaj na korozijsku postojanost tvrdih nanostrukturiranih tvrdih metala.
- Metodom analize slike može se uspješno odrediti volumni udio površine zahvaćen produktima korozije. U svrhu određivanja udjela korozijskih produkata potrebno je prilikom analize koristiti minimalno pet različitih pozicija na površini ispitivanih uzoraka pri istim povećanjima kako bih analizom obuhvatili što veći dio površine. Rezultati provedenih elektrokemijskih mjerenja u skladu su s rezultatima analize površine izuzev uzoraka WC-15Co.
- U svrhu donošenja točnijih zaključaka o elektrokemijskoj otpornosti nanostrukturiranih tvrdih metala, detaljnije istraživanje korozijskih produkata na većem broju snimki planira se u budućem istraživanju. Važno je istaknuti da su mjerenja provedena samo na jednom uzorku iz svake skupine i potrebno je osigurati ponovljivost prikazanih rezultata kako bi se potvrdili dani zaključci.

LITERATURA

[1] Aleksandrov – Fabijanić, T., Razvoj referentnih pločica tvrdoće po Vickersu postupkom metalurgije praha – Doktorski rad, Fakultet strojarstva i brodogradnje, Zagreb, 2014.

[2] http://repozitorij.fsb.hr/2064/1/06_12_2012_Diplomski_rad_Jure_Burnac.pdf

[3] Aleksandrov Fabijanić T., Sakoman M., Kurtela M.; Electrochemical corrosion resistance of nanostructured hardmetals in acid media, 2017

[4] Introduction for Volume Fraction Measurement in ImageJ: Automatic Threshold Method

Zahvala: Ovaj rad je sufinancirala Hrvatska zaklada za znanost projektom UIP-2017-05-6538 Nanostrukturirani tvrdi metali – Novi izazovi metalurgije praha.

EKSPERIMENTALNO ODREĐIVANJE GRANIČNIH STUPNJEVA DEFORMACIJE U PROCESIMA PROŠIRIVANJA I SUŽAVANJA

EXPERIMENTAL RESEARCH OF LIMIT VALUES OF STRAIN IN PROCESS EXPANDING AND NECKING

Mirna Nožić [1], **Himzo Đukić** [2]

[1] Univerzitet "Džemal Bijedić", Mašinski fakultet, Univerzitetski kampus, 88 000Mostar, Bosna i Hercegovina
[2] Sveučilište u Mostaru, Fakultet strojarstva i računarstva, Matice Hrvatske bb, 88 000Mostar, Bosna i Hercegovina

Sažetak

U radu su predstavljeni teorijski i eksperimentalni rezultati istraživanja graničnih stupnjeva deformacije u procesima proširivanja i sužavanja. Eksperimentalno istraživanje procesa proširivanja je izvedeno u laboratorijskim uvjetima, na vertikalnoj hidrauličnoj preši, sa cijevnim pripremcima od četiri različita materijala (čelika St37.4, mjeda CuZn37, bakra Cu i aluminija Al), različitog vanjskog i unutarnjeg promjera i različitih debljina stijenki. Rezultati eksperimentalnih istraživanja pokazuju da je najveći granični stupanj deformacije postignut kod proširivanja čeličnih cijevi, a najmanji kod proširivanja aluminijskih cijevi. Sve vrijednosti maksimalnih deformacija su manje od teorijske moguće maksimalne deformacije. Eksperimentalno istraživanje procesa sužavanja je izvedeno u laboratorijskim uvjetima, na hidrauličnoj kidalici, sa alatom koji se koristi u proizvodnim uvjetima. Za istraživanje su korišteni cilindrični pripremci različitih dimenzija od dva različita materijala (čelika Č.0148 i mjeda CuZn10).

Ključne riječi: *proširivanje cijevi, sužavanje, granični stupanj deformacije.*

Abstract

Theoretical and experimental results of the boundary degrees research of deformation in the processes of expansion and necking are presented in this paper. Experimental research of the expansion process was performed in laboratory conditions, on a vertical hydraulic press, with tubular preparations of four different materials (steel St37.4, CuZn37 brass, copper Cu and aluminum Al), different outer and inner diameter and different wall thicknesses. The results of experimental research show that the greatest degree of deformation is achieved by expanding the steel tubes, and the smallest one in the expansion of aluminum tubes. All values of maximum deformations are less than theoretically possible maximum deformation. The experimental research of the necking process was carried out in laboratory conditions, on a tensile testing machine, with a tool used in manufacturing conditions. The cylindrical specimens of different sizes for two different materials (steel Č.0148 and CuZn10 brass) were used in the research.

Keywords: *pipe extension, necking, boundary degree of deformation.*

1. UVOD

Procesi proširivanja i sužavanja su međusobno suprotni procesi, koji spadaju u procese specijalnog oblikovanja obrade deformiranjem. U procesu proširivanja cijevnih pripremaka dolazi do povećanja dimenzija vanjskog i unutarnjeg promjera cijevi, koje prati smanjenje debljine stijenke. Proširivanje se najčešće izvodi na hidrauličnim i krivajnim presama sa alatima koji imaju jednodijelne ili segmentne proširivače. Oblik proširivača zavisi od zahtijevanog oblika spajanja cijevi. Istraživanje graničnog stupnja deformacije pri proširivanju cijevi eksperimentalno je izvedeno sa proširivačem u obliku konusa, kako bi se sa jednim alatom proširivale cijevi različitih dimenzija, kako po promjeru, tako i po debljini stjenke. Najveću primjenu ovaj proces ima u automobilskoj i zrakoplovnoj industriji, gdje se javlja potreba za spajanjem više vrsta cijevi ili spajanja cijevi sa različitim konstrukcijskim elementima.
Sužavanje se ostvaruje pomoću tiskača, čiji profil odgovara unutarnjoj strani izratka, i matrice koja ima oblik vanjskog profila izratka. U procesu dolazi do smanjenja promjera i debljine stijenke cilindričnog elementa i do povećanja njegove visine. Radni predmet postepeno mijenja svoj oblik od cilindričnog do konusnog, najčešće u nekoliko operacija sužavanja.
Proces specijalnog sužavanja ima primjenu u vojnoj proizvodnji i u tehnološkom postupku predstavlja jednu od najkomplikovanijih operacija.

2. DEFORMACIJSKA ANALIZA PROCESA PROŠIRIVANJA I SUŽAVANJA

Proširivanje cijevi vrši se sa konusnim tiskačem, čiji je centralni kut 2α, od početnog promjera D=2R do konačne vrijednosti d=2r (Slika 1).

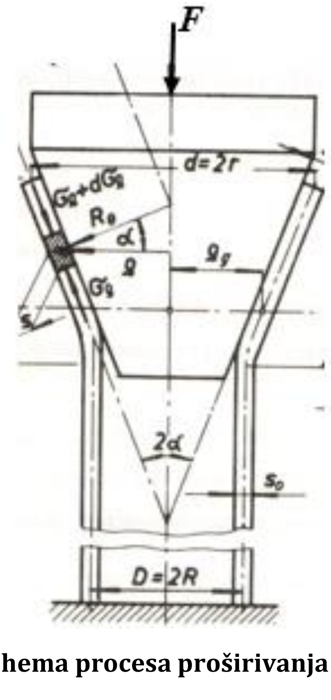

Slika 1: Shema procesa proširivanja [1]

Vrijednost maksimalne jedinične cirkularne deformacije može se odrediti po izrazu:

$$\varepsilon_{max} = \frac{r-R}{R} = \frac{r}{R} - 1 = K - 1$$

(1)

K u izrazu (1) je stupanj proširivanja, a računa se po izrazu:

$$K = \frac{r}{R} = \frac{d}{D} = 1/m$$

(2)

gdje je: m – odnos proširivanja.

Najmanja debljina lima određuje se po izrazu:

$$s_1 = s_0 (\frac{r}{R})^y = s_0 (\frac{r}{R})^{1/2} = s_0 (\frac{R}{r})^{1/2} = s_0 \sqrt{R/r} \tag{3}$$

U realnim uvjetima stupanj proširivanja ne premašuje vrijednost K<1,5, što znači da je uvijek ispunjen uvjet $\rho_g > 0{,}61\ r$, pa u cijelom intervalu deformacije dolazi do smanjenja debljine stijenke.

Odnosi proširivanja po debljini stijenke, vanjskom i unutarnjem promjeru računati su po slijedećim izrazima:

$$m_s = \frac{s_1}{s}; m_{DV} = \frac{D}{D_1}; m_{du} = d/d_1 \tag{4}$$

Logaritamske deformacije računate po debljini stijenke, vanjskom i unutarnjem promjeru računaju se po izrazima:

$$\varphi_s = lns/s_1; \varphi_{DV} = lnD_1/D; \varphi_{du} = \ln d_1/d \tag{5}$$

Oznake u izrazima (4) i (5) predstavljaju: D- vanjski promjer cijevi, d- unutarnji promjer cijevi, s – debljina stijenke, D_1- vanjski promjer proširene cijevi pri maksimalnom stupnju deformacije, d_1- unutarnji promjer proširene cijevi pri maksimalnom stupnju deformacije, s_1 –debljina stijenke proširene cijevi pri maksimalnom stupnju deformacije.

Specijalno sužavanje cilindričnog rotaciono simetričnog komada, dobivenog dubokim vučenjem, vrši se od njegovog dna, u nekoliko operacija, do postizanja konačnog konusnog oblika (Slika 2).

b)

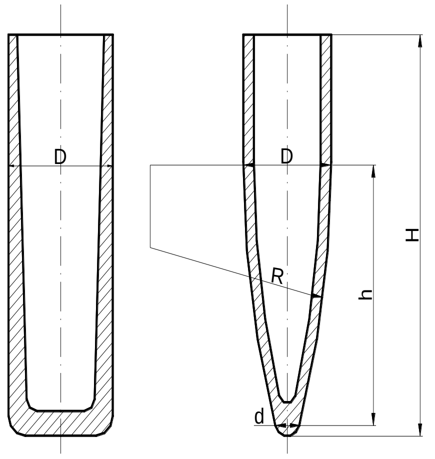

c) **Slika 2: Cilindrični pripremak i radni predmet nakon sužavanja**

Najmanji promjer radnog predmeta nakon zadnje operacije sužavanja računa se prema [2]:

$$\mathrm{d} = \mathrm{D} - 2\left(R - \sqrt{R^2 - h^2}\right) \tag{6}$$

gdje su:
D – promjer pripremka, R – polumjer dijela konusnog oblika, H – rastojanje cilindričnog dijela do najmanjeg promjera konusa (Slika 2).
Deformacije pri sužavanju mogu se izraziti preko ukupnog odnosa sužavanja:

$$m_u = d/D \tag{7}$$

ili preko ukupne logaritamske deformacije:

$$\varphi_u = \log\frac{D}{d} \tag{8}$$

3. REZULTATI EKSPERIMENTALNOG ISTRAŽIVANJA GRANIČNOG STUPNJA DEFORMACIJE ZA PROCES PROŠIRIVANJA

U cilju pronalaženja maksimalnog stupnja deformacije pri proširivanju cijevi provedeni su eksperimenti sa cijevima od četiri vrste materijala i dvanaest različitih dimenzija, kako bi se eksperimentalni rezultati mogli usporediti sa teorijskim.
Sve epruvete su premjerene po promjeru i debljini zida prije i poslije proširivanja. Mjerenja su izvedena pomoću digitalnog pomičnog mjerila. Na osnovu izmjerenih vrijednosti (D- vanjskih promjera cijevi, d- unutarnjih promjera cijevii, s – debljina stijenke, D_1- vanjskih promjera proširene cijevi pri maksimalnom stupnju deformacije, d_1- unutarnjih promjera proširene cijevi pri maksimalnom stupnju deformacije, s_1 – debljina stijenke proširene cijevi pri maksimalnom stupnju deformacije) izračunati su odnosi proširivanja i logaritamske deformacije za sve cijevi (po izrazima 4 i 5), a u Tablici

1 date su srednje vrijednosti maksimalnih deformacija za cijevi od čelika, mjedi, bakra i aluminija.

Tablica 1: Srednje vrijednosti maksimalnih deformacija cijevi

Oznaka materijala	m_s	m_{DV}	m_{du}	φ_s	φ_{DV}	φ_{du}
ST37.4	0,752	0,66	0,58	0,285	0,42	0,54
CuZn37	0,773	0,70	0,64	0,257	0,36	0,44
Cu	0,828	0,75	0,72	0,189	0,29	0,32
Al	0,830	0,83	0,78	0,186	0,18	0,25

Na Slici 3 prikazane su maksimalne vrijednosti logaritamskih deformacija proširivanja: po debljini stijenke, po vanjskom promjeru i po unutarnjem promjeru za ispitivane materijale.

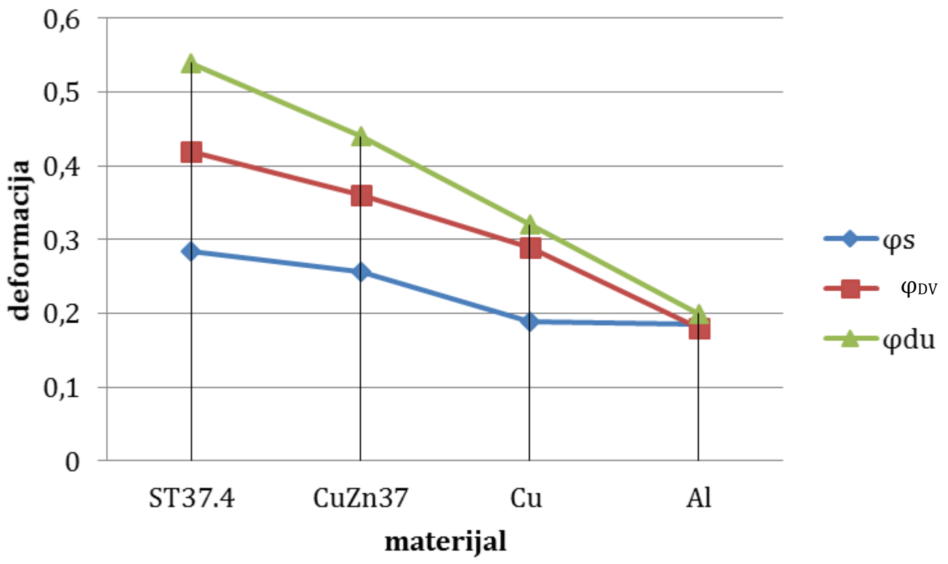

Slika 3: Maksimalne vrijednosti logaritamskih deformacija proširivanja

Utjecaj relativne debljine materijala na stupanj proširivanja i odnos debljine stijenke za čelik St37.4 prikazan je u Tablici 2.

Tablica 2: Utjecaj relativne debljine materijala na granični stupanj deformacije

Oznaka materijala ST37.4	s/D %					
	5,5	**6,6**	**8,3**	**9,3**	**12,5**	**13,3**
m_s	0,78	0,80	0,79	0,75	0,74	0,69
K	1,28	1,25	1,27	1,33	1,35	1,45

Na osnovu rezultata, prikazanih u Tablici 2, vidljivo je da sa porastom relativne debljine materijala raste maksimalni granični stupanj deformacije proširivanja cijevi.
Maksimalna vrijednost graničnog stupnja deformacije iznosi 1,45, što je manje od teorijski mogućeg stupnja deformacije, koji se može postići u realnim uvjetima proširivanja (K<1,5).

4. REZULTATI EKSPERIMENTALNOG ISTRAŽIVANJA GRANIČNOG STUPNJA DEFORMACIJE ZA PROCES SUŽAVANJA

Rezultati eksperimentalnog istraživanja graničnog stupnja deformacije za proces sužavanja dati su za četiri eksperimenta, za pripremke od čelika Č.0148 i mjedi CuZn10 za sve operacije specijalnog sužavanja. Oznake korištene za provedena eksperimente su: 1, 2, 3 i 4. U eksperimentima 1 i 4 korišteni su pripremci od mjedi CuZn10, a u eksperimentima 2 i 3 korišteni su pripremci od čelika Č.0148. U eksperimentima 1 i 2 sužavanje radnog predmeta do konačnih dimenzija se odvijalo u dvije operacije, dok je u eksperimentima 3 i 4 proces oblikovanja obuhvatao tri operacije sužavanja.
Rezultati eksperimentalnih istraživanja su dati preko dijagrama zavisnosti logaritamske deformacije za sve presjeke konusnog dijela radnog predmeta.

Na Slici 4 dat je zajednički dijagram zavisnosti logaritamske deformacije od hoda za prvu i drugu operaciju sužavanja za eksperiment 1, a na Slici 5 zajednički dijagram zavisnosti logaritamske deformacije od hoda za prvu i drugu operaciju sužavanja za eksperiment 2.

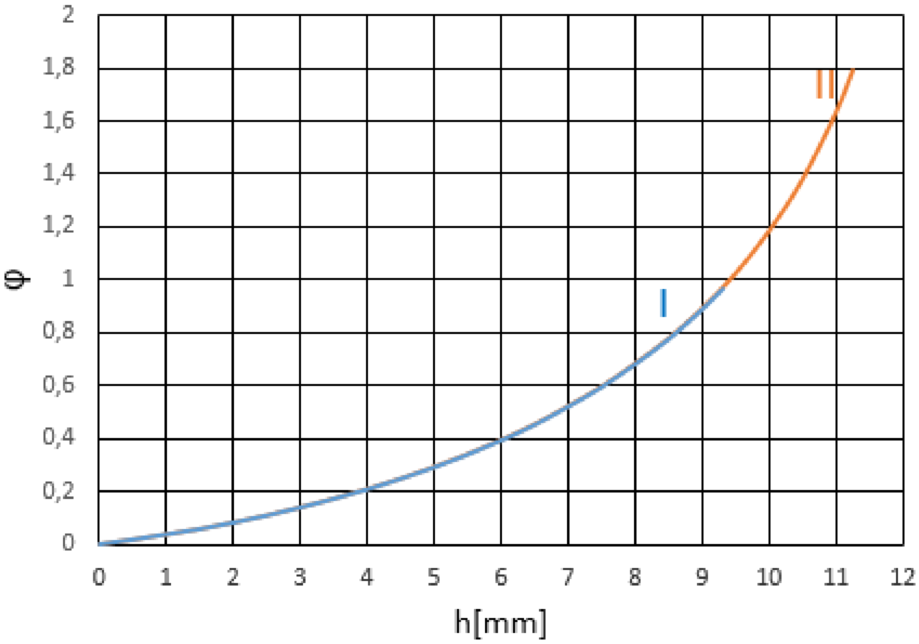

Slika 4: Zajednički dijagram deformacija za I i II sužavanje cilindričnih pripremaka od CuZn10 – eksperiment „1“

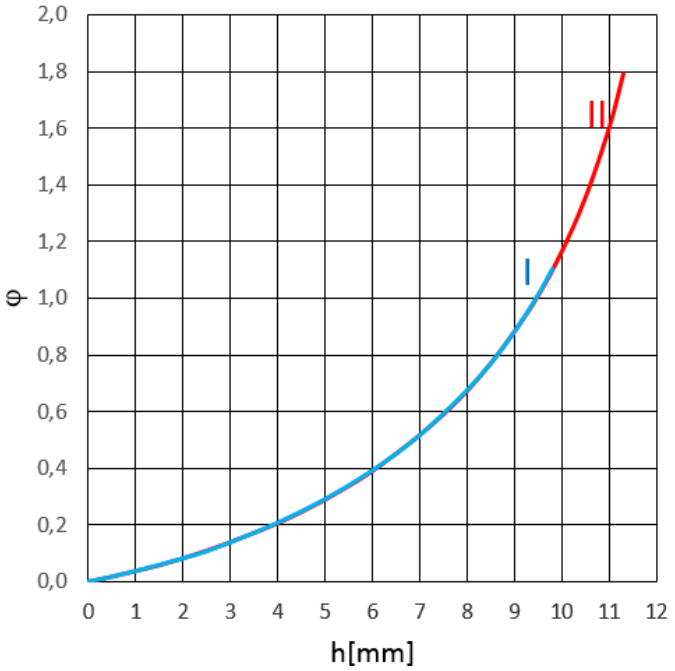

Slika 5. Zajednički dijagram deformacija za I i II sužavanje cilindričnih pripremaka od Č.0148 – eksperiment „2“

U eksperimentima 1 i 2 rabljena je jedna matrica za prvo i drugo sužavanje, što je vidljivo na Slikama 4 i 5, jer se rast logaritamskog stupnja deformacije drugog sužavanja nastavlja na kraj prvog sužavanja.

Na Slici 6 dat je zajednički dijagram zavisnosti logaritamskog stupnja deformacije od hoda za prvu , drugu i treću operaciju sužavanja za eksperiment 3, a na Slici 7 zajednički dijagram zavisnosti logaritamskog stupnja deformacije od hoda za prvu, drugu i treću operaciju sužavanja za eksperiment 4.

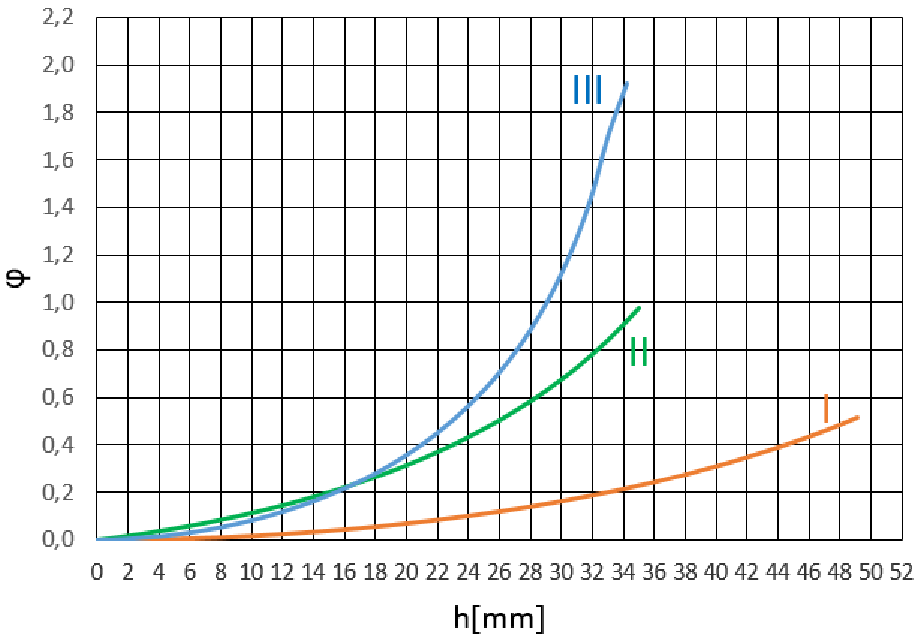

Slika 6. Zajednički dijagram deformacija za I ,II i III sužavanje cilindričnih pripremaka od Č.0148 – eksperiment „3“

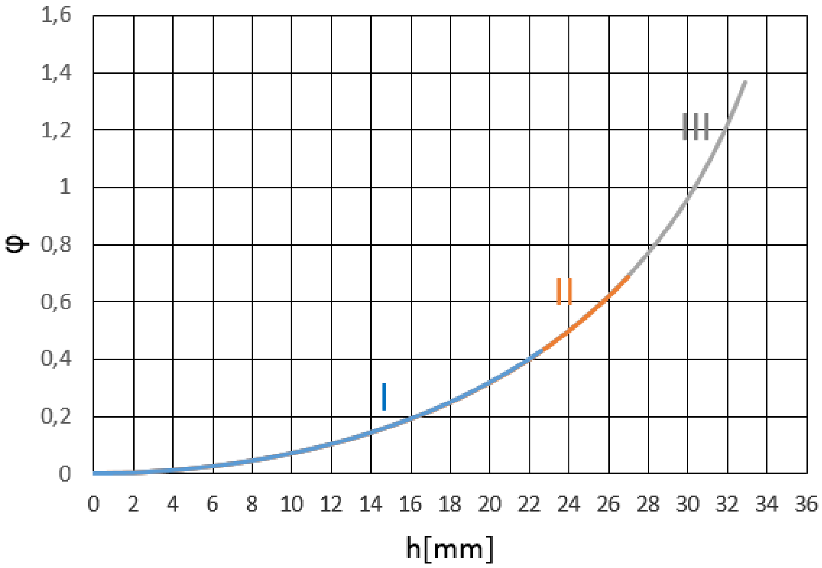

Slika 7. Zajednički dijagram deformacija za I , II i III sužavanje cilindričnih pripremaka od CuZn10 – eksperiment „4“

U eksperimentu 3 rabljene su tri matrice različitih polumjera, za prvo, drugo i treće sužavanje. Sa Slike 6 je vidljiv utjecaj različitih matrica na tok logaritamskog stupnja deformacije.

U eksperimentu 4 je rabljena jedna matrica za sva tri sužavanja, pa je sa Slike 7 vidljivo da je rast logaritamskog stupnja deformacije u prvoj, drugoj i trećoj operaciji predstavljen jednom krivom.

Na osnovu provedenih eksperimentalnih istraživanja u Tablici 3 su date maksimalne vrijednosti logaritamskog stupnja deformacije za sve operacije sužavanja, izvedene u eksperimentima: 1,2,3 i 4.

Tab.: Max. deformacija (φ_{max}) kod I, II, i III operacije sužavanja za eksperimente„1“, „2“, „3“, „4“

	Eksperiment „1“	**Eksperiment „2“**	**Eksperiment „3“**	**Eksperiment „4“**
I operacija sužavanja	0.968	1.10389	0.514	0.430
II operacija sužavanja	1.790	1.792	0.976	0.689
III operacija sužavanja			1.923	1.368

4. ZAKLJUČAK

Na osnovu istraživanja graničnog stupnja deformacije za procese proširivanja i sužavanja mogu se donijeti sljedeći zaključci:

- Maksimalni stupanj proširivanja za teorijske uvjete (μ=0) iznosi K=1,64, odnosno maksimalni odnos proširivanja je 0,61;
- Eksperimentalna vrijednost maksimalnog stupnja proširivanja iznosi K=1,45;
- Sa porastom relativne debljine materijala raste maksimalni granični stupanj deformacije proširivanja cijevi (Tablica 2);
- Maksimalni stupanj sužavanja zavisi od broja operacija sužavanja i od vrste materijala radnog predmeta;
- Dijagrami toka logaritamskog stupnja deformacije zavise od geometrije matrica. Ako je geometrija matrica ista u svim sužavanjima, dijagram toka je pravilan i nastavlja se jedan na drugi (Slike 4, 5 i 7). Ako se za svaku operaciju sužavanja koristi druga geometrija matrice, dijagrami toka logaritamskog stupnja deformacije su bitno različiti (Slika 6).

Poređenjem maksimalnih logaritamskih deformacija procesa proširivanja i sužavanja, može se zaključiti da su maksimalne deformacije kod procesa sužavanja znatno veće. Ova razlika je rezultat različitog stanja naprezanja. Kod procesa proširivanja radni predmet je u zoni deformacije opterećen na istezanje, a kod procesa sužavanja na pritisak.

LITERATURA

[1] Musafija B., “Primjenjena teorija plastičnosti”, 1973, Univerzitet u Sarajevu.

[2] Đukić H., Nožić M., “Obrada deformisanjem”, 2018, Univerzitet “Džemal Bijedić”, Mostar.

[3] Demirović A, Određivanje graničnog stepena deformacije proširivanja cijevi u hladnom stanju, magistarski rad, 2015, Mašinski fakultet Mostar.

[4] Gagula E, Istraživanje uticajnih patrametara izrade košuljice zrna različitih kalibara, magistarski rad, 2017, Mašinski fakultet Mostar.

[5] Đukić H., Nožić M., „Limit values of maximal logarithmics strain in multi-stage cold forming operations“, Journal for Technology of Plasticity, Vol. 40, Number 1, (23-31) (2015).

TANKI FILMOVI CINK OKSIDA DOPIRANOG ALUMINIJEM

ZINC OXIDE THIN FILMS DOPED WITH ALUMINIUM

Ivana Panžić[1], **Jelena Macan**[2], **Krunoslav Juraić**[1], **Krešimir Salamon**[1], **Andreja Gajović**[1]

[1] Ruđer Bošković Institute, Division of Materials Physics, Bijenička 54, Zagreb, Croatia
[2] Faculty of Chemical Engineering and Technology, Department of Physical Chemistry, Marulićev trg 19, Zagreb, Croatia

Abstract

The influence of preparation procedure on the morphological properties of the ZnO thin films doped by aluminium was studied. The ZnO and Al doped ZnO (AZO) films were prepared on glass substrates by sol-gel method using zinc sol doped with 1, 2, or 3 at % of Al with respect to Zn. The films were spin coated layer by layer, and samples with 1,5,10 layers were studied in details. To obtain crystallinity, the films were annealed at different temperatures and different heating rates to investigate the influence of the annealing process on the morphological properties. For the morphological and structural characterization scanning electron microscopy (SEM) techniques, grazing incidence X-ray diffraction (XRD) and Raman spectroscopy were used. For the optical characterization UV/Vis spectroscopy measurements of transmittance were performed. It was observed that the morphology and optical properties of the AZO films can be tailored by varing the temperature applied between deposition of the layers and temperature of post annealing temperature. Therfore, the sol-gel procedure combined with heat and annealing treatment was shown as an easy, fast and low cost method for preparation of AZO films with desired properties.

Keywords: *zinc oxide, spin coating, thin films, SEM*

Sažetak

Ispitan je utjecaj posptupka pripreme na morfološka svojstva tankih filmova ZnO dopiranih aluminijem. ZnO i ZnO dopiran s Al (AZO) filmovi pripravljeni su na staklenim podlogama sol-gel metodom od cinkovog sola dopiranog s 1,2 ili 3 at% Al u odnosu na Zn. Prevlake su pripravljene sloj po sloj rotiranjem, te su uzorci s 1,5,10 slojeva istraženi u detalje. Da bi se postigla kristalnost, filmovi su termički obrađeni na različitim temperaturama uz različite brzine grijanja kako bi se istražio utjecaj toplinskog tretmana na morfološka i strukturna svojstva. Za morfološku i strukturnu karakterizaciju korišteni su skenirajući elektronski mikroskop (SEM), rendgenska difrakcija pod malim kutem i Ramanova spektroskopija. Za optičku karakterizaciju korištena je UV/Vis spektroskopija (mjerenja transmitancije). Opaženo je kako se morfološka i optička svojstva mogu podešavati variranjem temperature primjenjene između depozcije pojedinih slojeva kao i temperature naknadne termičke obrade filmova. Na taj način je pokazano kako je sol-gel jednostavna, brza i jeftina metoda kojom se u kombinaciji s termičkom obradom može lako pripraviti filmove željenih svojstava.

Ključne riječi: *cink oksid, prevlačenje rotiranjem, tani filmovi, SEM*

1. INTRODUCTION

Zinc oxide (ZnO) is a wide-band gap II-VI semiconductor. The un-doped ZnO possesses n-type electrical conductivity due to the presence of oxygen vacancies. It has been studied for decades now and is also currently the subject of numerous studies because of its exceptional properties, chemical and thermal stability, large exciton binding energy of 60 meV at room temperature, non-toxicity and its low price [1], [2], which allows it's use in various applications (electronics, optics, photovoltaic, photocatalysis, etc.) [3]. ZnO thin films can be prepared by various techniques such as thermal evaporation [4], [5], pulsed laser deposition [6], molecular beam epitaxy [7], magnetron sputtering [8], sol-gel [9], chemical vapour deposition [10], spray pyrolysis [11] etc. Among these methods sol-gel in combination with spin coating is an efficient, low cost method that has many advatages like film compositional control and room temperature depostion that can easily be applied even to large substrates [12]. The factors which affect the properties of the films include pre- heat/post-heat temperatures, concentration of the precursor solution, aging of the sol-gel solution, thickness of the grown films, doping etc. All of these factors affect the strucutural, optical and electrical properties of the films.

In the present work the effect of number of layers, pre and post heating treatment and aluminum doping on morphology and strucutre was investigated with the aim to prepare thin films for photovoltaic and photocatalytic applications.

2. EXPERIMENTAL

The sol-gel spin coating method was used to prepare AZO thin films on glass substrates, the detailed optimized procedure for fabrication of ZnO thin films has been described prevouisly [13], and we used a similar mehod for AZO thin films. Precursor solution was prepared by dissolving zinc acetate dihydrate (0.5 M) in isopropanol with the addition of monoethanolamine (molar ratio to zinc 1:1) and aluminum nitrate nonahydrate [(Al/Al+Zn) = 1, 2, 3 at%]. The solutions were aged for 1,2,3,7 days and the spin coated on cleaned glass substrates (30 sec, 3000 rpm), with heating between layers on 150, 200 or 250˚C for 10 min. After the desired amount od layers was achieved (1,5,10) the films were annealed in air on 350, 400, 450˚C for 1 h. During both heating treatment heating rate of 5 °C / min were applied.

The crystalline structure of the films was analyzed by grazing incidence X-ray diffraction (GIXRD). Raman spectra was recored in micro Raman mode (Horiba Jobin-Yvon T64000, 532 nm solid state laser). The Fourier transform infrared (FTIR) transmittance measurements were performed with Bruker VERTEX70, range 4000-40 cm^{-1}, resolution 1 cm^{-1}. The surface morphologies of films were evaluated by field emission scanning electron microscope (FE-SEM, JEOL, JSM-7000F, operating voltage 10.0 kV). For the optical properties measurements, we used a double beam Perkin Elmer Lambda25 UV-Vis spectrophotometer in the wavelength range from 200-800 nm.

3. RESULTS AND DISSCUSION

XRD results show that ZnO and AZO thin films deposited by sol gel spin coating are polycrystalline with hexagonal wurtzite structure (Fig 1). The diffraction peaks are identified as corresponding to (101), (100), and (002) planes of zincite phase. The maxima of Al were not observed indicating that Al was completely inbuilt in the ZnO structure.

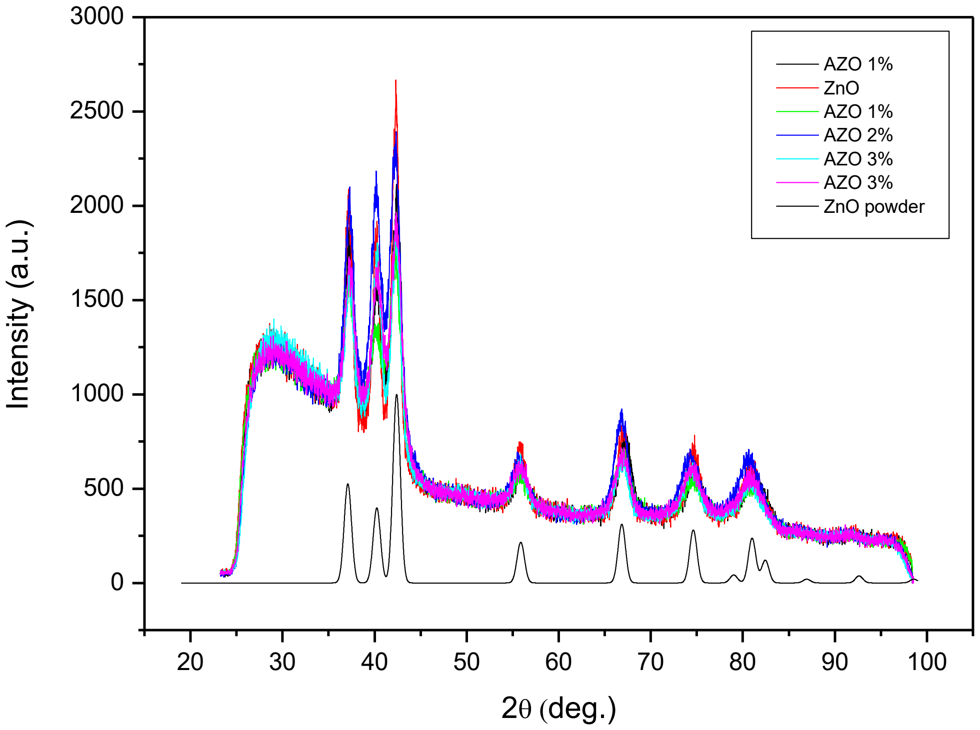

Figure 1. XRD patterns of ZnO and AZO films with different % Al doping.

SEM study show that morphologies of the films were not dependent on number of layers and Al content, as well as finale annealing temperature. Figures 2. to 5. show typical SEM images for the AZO thin films prepared by different heating procedures between application of the layers while all the other parameters where not changed (5 layer, postanealling temperature 400 °C, 3% Al). During the heating between layers, if temperatures below 250°C were used, it was observed that a micro-scaled wrinkle covers the film surface (Fig. 2 and Fig. 3). This result can be explained by the shrinkage of the film arising from the decomposition of the residual organic species during the finale post annealing at 400°C. The organic species remained trapped in the layers of ZnO during formation of the ZnO gel, since the temperature of 100 or 150 °C applied for only 10 min was not sufficient for complete evaporation. Due to the larger amount of residual organic compound after heating on 100°C, the wrinkles were more prominent (Fig. 2) then in the case of heating at 150°C.

By comparison of the SEM images it was observed that heating between layers above 250 °C (Fig. 4 and Fig. 5), a uniform, dense and flat film surface was obtained. The nanoscaled particles are uniformly distributed in the film and no wrinkle was observed on the surface. This indicates that the decomposition of the residual organic species is completely finished during the preheating above 250◦C. The film becomes denser (Fig. 4a) and AZO particles of several nm scale (Fig. 4b) tend to be fomed with increase of the heating temperature between layers. Table 1 shows the data for the EDX measurments for AZO 1% doped film confirming successful doping of ZnO with Al.

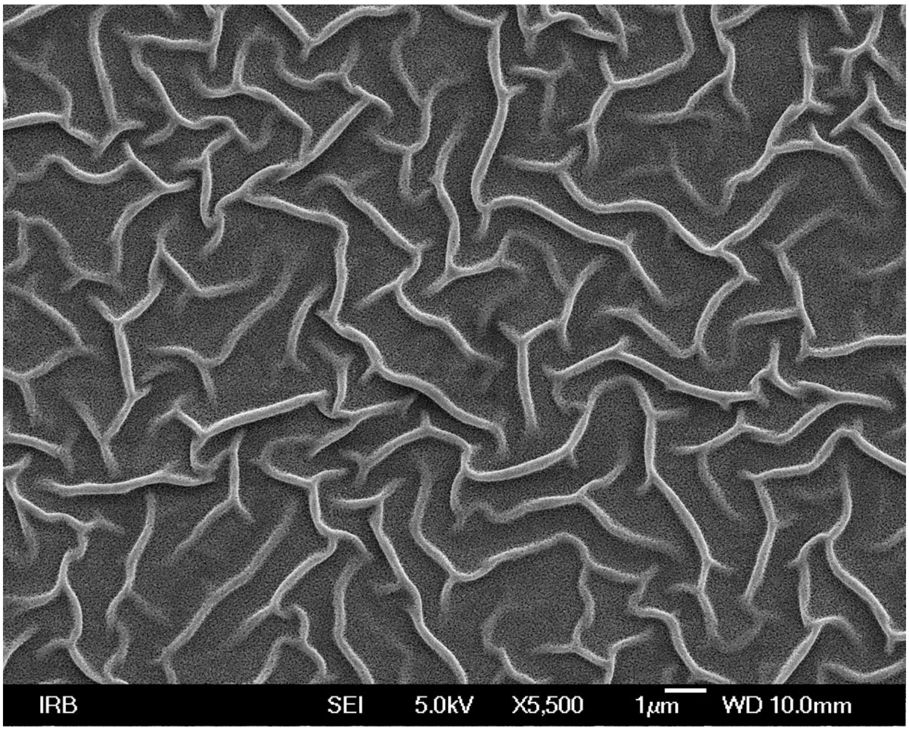

Figure 2. AZO thin films prepared by heating between layers at 100 °C.

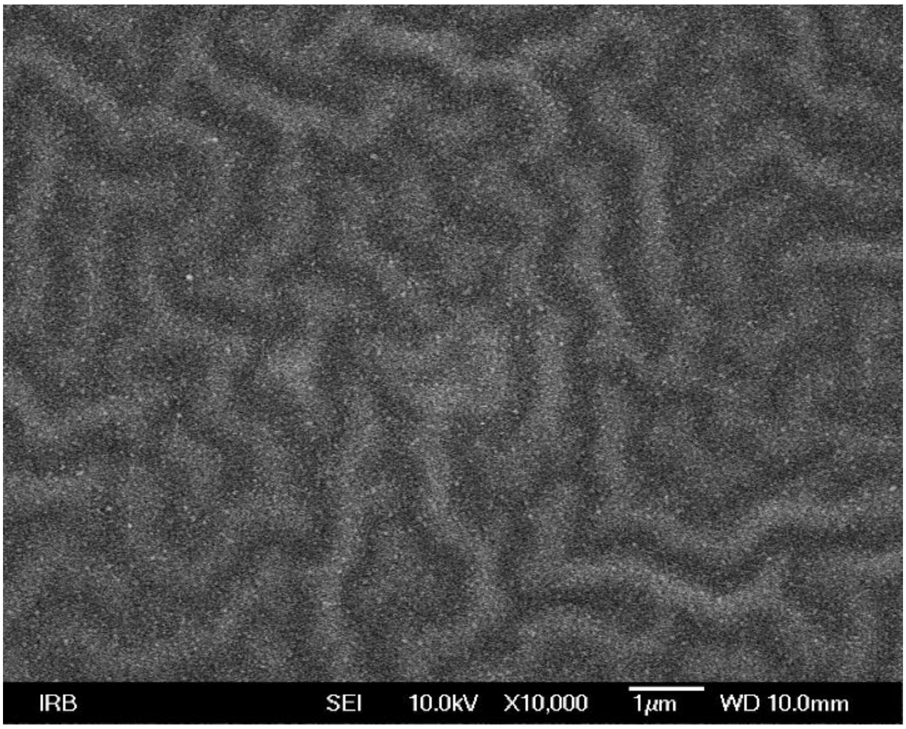

Figure 3. AZO thin films prepared by heating between layers at 150 °C.

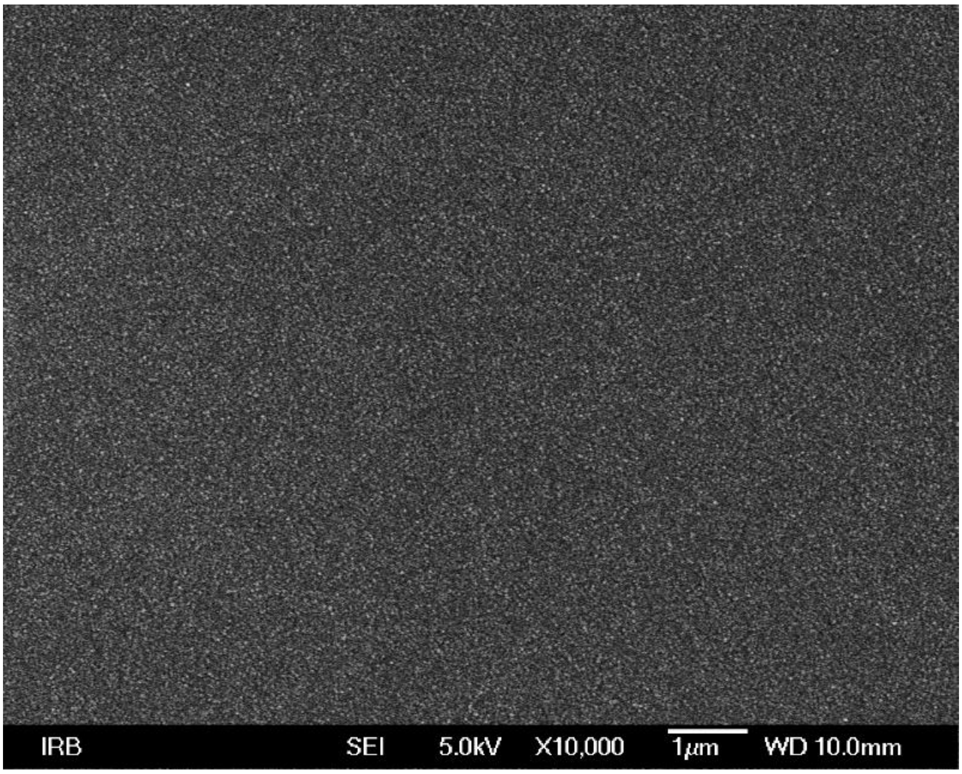

a)

b) 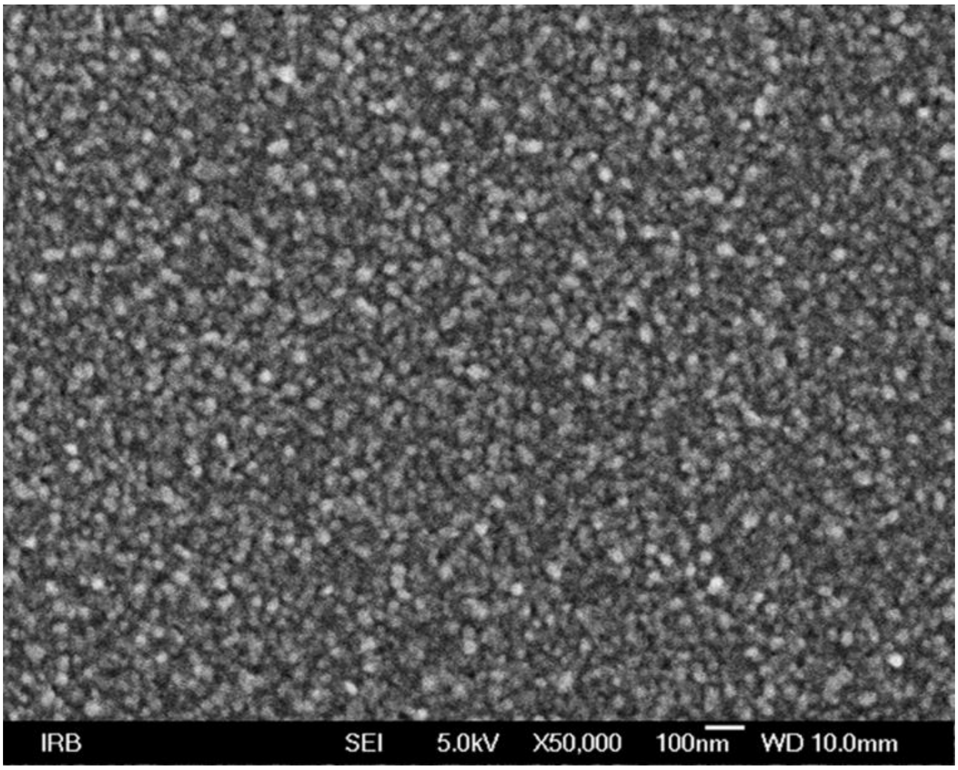

Figure 4. AZO thin films prepared by heating between layers at 250 °C: a) smaller magnification, b) larger magnification.

Table 1: EDX

Element	Weight%	Atomic %
O K	38.69	61.79
Mg K	1.90	1.99
Al K	0.68	0.64
Si K	22.42	20.40
Ca K	3.99	2.54
Zn L	32.32	12.63
Total	100.00	100.00

The SEM images show the morphology of the films can be tailored, so different applications of prepared nanostructured thin films are expected. The films with wrinkled surface would be favoured for photocatalytic or sensing applications due to the larger surface area. On the other side the layer formed by heating between layes at 250 °C show flet surface suitable for application in photovoltaic cells as transparent conductive oxide (TCO). Due that possible application we have done preliminary electrical measurements of the films prepared by heating between layes at 250 °C. It was observed that sample with 3 at. % of Al, finaly annealed at 400 °C showed resistivity much lower than samples annealed at 350 and 500 °C. Also, the samples with lower amount of Al doping in the structure, showed higher resistivity than dopping with 3 at. % of Al.

Raman spectrum of ZnO show six Raman active first order modes [14]. The modes are: A1(TO) = 381, A1(LO) = 574, E1(TO) = 407, E1(LO) = 583, E2(low) = 101 and E2(high) = 437. Figure 6 shows typical Raman spectra of AZO thin film (doped with 3 at. % Al concentration and annealed at temperature of 400˚C for 1 h), while the dried sol gel solution of pure ZnO is shown in comparison. Only the most intensive Raman band at 437(440) cm^{-}1 is observed in thin films, while the Raman bands corresponding to amprohus glass from the substrate were observed at 780 and 1100 cm^{-1}. The spectrum of ZnO powder shows all the Raman active modes. The E2(high) mode is shifted in AZO to 440 cm-1 indicates residual stress, and can used as its measure [15]. Residual stress was introduced in ZnO structure due to the Al doping.

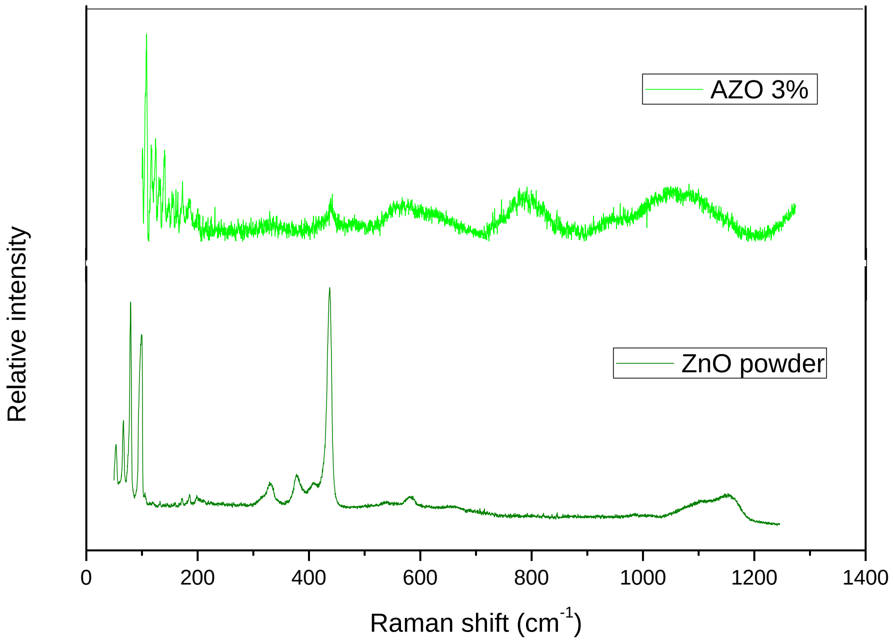

Figure 7. Raman spectra of AZO thin film and ZnO powder prepared by doping with 3 at. % Al concentration and annealed at temperature of 400˚C for 1 h.

The optical measurments (Fig. 8). show that the films are highly transparent with an average transmittance of 85 % in the visible region. The band gap absorption edge is found to be at 370 nm. The band gap was shifted in region around 360 nm due to the blue shift generaly observed in Al doped thin films [16]. With increase of number of layers, a decrease in tranmitance was noticed (Fig.9)

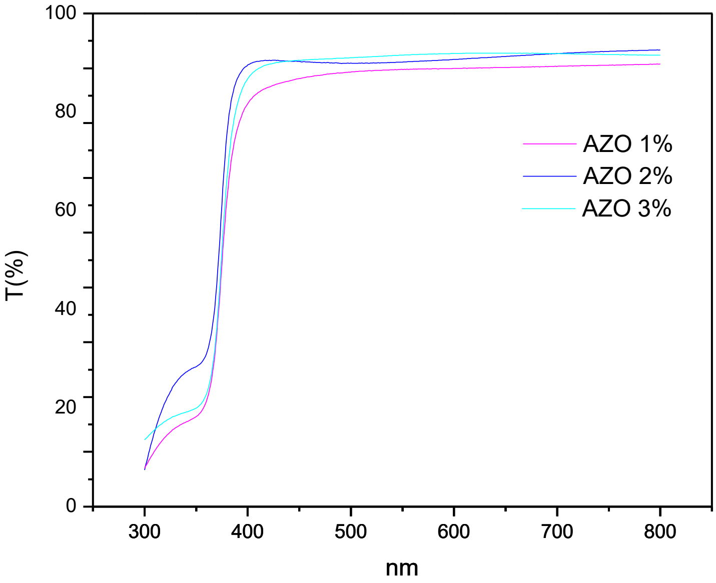

Figure 8. UV/Vis results for one ZnO layer doped with different at. % Al concentration and annealed at temperature of 400°C for 1 h, and heated between layers at 250 °C.

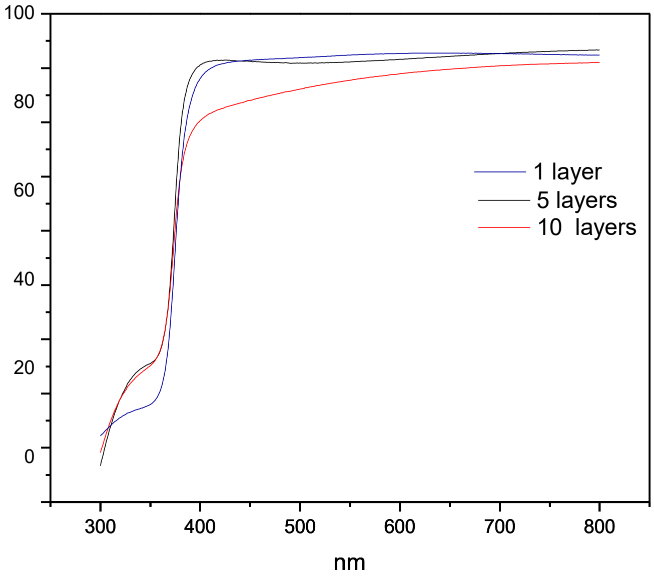

Figure 8. UV/Vis results for ZnO 1,5 and 10 layers, doped with 3 at. % Al and annealed at temperature of 400°C for 1 h, and heated between layers at 250 °C.

4.CONCLUSION

The sol-gel preparation of ZnO thin films was succesfull and different morphology of the films were obtained. The microstructured surface of the ZnO can be obtained by lower temperature of the heating between applications of ZnO layes by spin-coating, while heating at 250 °C favoured the formation of completely flet surface suitable for application for TCO electrode in photovoltaic cells. The transparency of the layer is influenced by number of the applied layers, while the band gap was influenced by the presentage of the Al inbuilt in the ZnO structure. XRD diffraction combined with EDS measurements showed the successful inbuilt of 3 at% of Al in ZnO, while Raman measurement indicated residual stress dou to the dopping. Preliminary electrical measurements show that samples with 3% of Al have the lowest resistivity in samples annealed at 400 °C, which will be the subjest of future work.

Acknowledgement(s):
Present research was financed under the Croatian Science Foundation project HRZZ-IP-2014-09-9419.

REFERENCES

[1] Volkan, S. E., Suat, P., Adan, S., K., Tuna, A., Saliha, E., Soner, O., Naci, E., Zafer, M. B., ZnO thin film synthesis by reactive radio frequency magnetron sputtering. Applied Surface Science. 318, pp. 2-5, (2014)

[2] Mimouni, R., Boubaker, K., Amlouk, M., Investigation of structural and optical properties in Cobalt-Chromium co-doped ZnO thin films within the Lattice Compatibility Theory scope. Journal of Alloys and Compounds. 624, pp.189–194, (2015)

[3] Djurisic, A. B., Ng, A. M. C., Chen, X. Y., ZnO nanostructures for optoelectronics: Material Properties and device applications. Progress in Quantum Electronics. 34, pp.191–259, (2010)

[4] Chrissanthopoulos, A., Baskoutas, S., Bouropoulos, N., Dracopoulos, V., Poulopoulos, P., Yannopoulos, S. N., Synthesis and characterization of ZnO/NiO p–n heterojunctions: ZnO nanorods grown on NiO thin film by thermal evaporation. Photonics and Nanostructures–Fundamentals and Applications. 9, 132–139, (2011)

[5] Feng, L., Liu, A., Mei, L., Yuying, M., Jing, W., Baoyuan, M., Fabrication and characterization of tetrapod-like ZnO nanostructures prepared by catalyst-free thermal evaporation. Materials Characterization. 61, pp.128–133, (2010)

[6] Raied, K. J., Mohammed, A. H., Kadhim, A. A., Optical properties of nanostructured ZnO prepared by pulsed laser deposition technique. Materials Letters. 132, pp.31-33, (2014)

[7] Zhang, T. C., Mei, Z. X., Kuznetsov, A.Y., Du, X. L., Realization of non-polar ZnO (1120) homoepitaxial films with atomically smooth surface by molecular beam epitaxy. Journal of Crystal Growth. 325, pp.93-95, (2011)

[8] Mosbah, A., Aida, M. S., Influence of deposition temperature on structural, optical and electrical properties of sputtered Al doped ZnO thin films. Journal of Alloys and Compounds. 515, pp.149-153, (2012)

[9] Linhua, X., Gaige, Z., Juhong, M., Fenglin, X., Dependence of structural and optical properties of sol–gel derived ZnO thin films on sol concentration. Applied Surface Science. 258, pp.7760–7765, (2012)

[10] Hye, j. J., Seul, G. L., Kim, H., Jin, S. P., Enhanced mobility of Li-doped ZnO thin film transistors fabricatedby mist chemical vapor deposition. Applied Surface Science. 301, pp.358–362, (2014)

[11] Lucio, L. M. A., Luna, A. M. A., Maldonado, A., Olvera, M. L., Acosta, D. R., Preparation of conducting and transparent indium-doped ZnO thin films by chemical spray. Solar Energy Materials& Solar Cells. 90 (6), pp.733-741, (2006)

[12] Kamaruddin, S.A., Chan, K.Y., Yow, H.K., Sahdan, M.Z., Saim, H., Knipp, D., Zinc oxide films prepared by sol–gel spin coating technique. Appl. Phys. A 104, pp263–268 (2011)

[13] Mahrouga, A. Boudjadar, S., Hamrit, S., Guerbous, L., Structural, optical and photocurrent properties of undoped and Al-doped ZnO thin films deposited by sol–gel spin coating technique, Materials Letters 134, pp248–251,(2014)

[14] Birman, J.L., Theory of Crystal Space Group and Lattice Dynamics, Springer Verlag, Berlin, (1984)

[15] Ben Yahia, S., Znaidi, L., Kanaev, A., Petitet, J.P. Raman study of oriented ZnO thin films deposited by sol–gel method, Spectrochimica Acta Part A: Molecular and Biomolecular Spectroscopy, 71, pp.1234-1238, (2008)

[16] Shahzada, M.B., Hong, Y.Q, Wang, L.X., A study on the Al doping behavior with sol aging time and its effect on structural and optical properties of sol–gel prepared ZnO thin films, Thins Solid Films, 534, pp. 242-248, (2013)

REOLOŠKI MODEL ISTEZANJA PAMUČNE TKANINE

RHEOLOGICAL MODEL OF COTTON WOVEN FABRIC STRETCHING

Željko Penava[1], **Diana Šimić Penava**[2], **Lozo Miloš**[1]

[1] Sveučilište u Zagrebu, Tekstilno-tehnološki fakultet, Prilaz b. Filipovića 28a, Zagreb, Hrvatska
[2] Sveučilište u Zagrebu, Građevinski fakultet, Kačićeva 26, Zagreb, Hrvatska

Sažetak

Mehanička svojstva tkanina polazni su parametri pri projektiranju i podešavanju parametara u tekstilnoj industriji. Pri djelovanju vlačnih opterećenja dolazi do kidanja tkanine ili pojave nepoželjnih viskoelastičnih ili plastičnih deformacija. Takve deformacije su nepoželjne jer uzrokuju lošu kvalitetu gotovog proizvoda, npr. tkanine, a mogu se uočiti tek u završnim fazama prerade. Da bi se izbjegla pojava plastičnih deformacija u tkanini treba unaprijed znati pri kojem vlačnom opterećenju će doći do takvih deformacija. Treba postaviti odgovarajući reološki model koji dobro opisuje ponašanje tkanine ovisno o njezinim strukturnim i konstrukcijskim parametrima pri vlačnom naprezanju, krivulja (F-ε). Za potrebe ispitivanja reoloških svojstava tkanina otkane su različite vrste sirovih pamučnih tkanina u platnenom vezu s istom gustoćom osnove i različitim gustoćama potke. Na temelju eksperimentalnih rezultata dobivenih za istezanje uzoraka tkanina postavljen je reološki model prema Lethersichu. Izvedene su i riješene odgovarajuće diferencijalne jednadžbe za ispitivane uzorke tkanina, čime je dobivena ovisnost između vlačne sile (naprezanja) i relativnog istezanja. Reološki model prema Lethersichu dobro opisuje proces istezanja pamučne tkanine u statičkim uvjetima ispitivanja.

Ključne riječi: *tkanina, istezanje, reologija, Lethersichov model, diferencijalne jednadžbe istezanja*

Abstract

The mechanical properties of the woven fabric are starting parameters in design and adjustment of parameters in the textile industry. When tensile loads occur, comes to tearing fabric or unwanted viscoelastic or plastic deformations occur. In order to avoid the appearance of plastic deformations in the fabric, it is necessary to know in advance which tensile force will cause such deformations. An appropriate rheological model that describes the behavior of fabric, depending on its structural and structural parameters in the tensile stress, curve (F-ε), should be set. For this purpose of testing the rheological properties of fabric, various types of raw cotton fabrics have been deposited in the plain weave with same warp density and different weft densities. Based on the experimental results obtained to stretch the fabric samples, a rheological Lethersich's model was introduced. Appropriate differential equations for the tested sample patterns were made and resolved, resulting in the dependence between tensile force and relative strain.

Keywords*: fabric, stretching, rheology, Lethersich's model, differential equations of stretching*

1. UVOD

Primjena tekstilnih materijala u različitim industrijskim granama sve više raste, posebno kao kompozitnih materijala, te je poznavanje njihovih fizikalno-mehaničkih svojstava jako važno. Prilikom mjerenja, na mehanička svojstva tkanina utječu nelinearna visokoelastičnost, trenje između vlakana, pređe, gustoća tkanine, geometrijske promjene veza za vrijeme djelovanja vanjskih sila, te promjena temperature i vlažnosti.

Pri djelovanju vlačnih sila dolazi do kidanja tkanine ili pojave viskoelastičnih ili plastičnih deformacija [1]. Takve deformacije su nepoželjne jer se nepoželjni efekti, loša kvaliteta gotovog proizvoda, npr. tkanine, mogu uočiti tek u završnim fazama prerade, odnosno nakon oplemenjivanja i bojadisanja. Zbog toga se dobra kvaliteta gotovog proizvoda postiže ako se tijekom uporabe tkanine osiguraju takvi uvjeti u kojima će deformacije biti u granicama elastičnog područja.

Za opis ponašanja tkanine pod opterećenjem uglavnom se usvaja da je tkanina (tijelo) neprekidna sredina pa se govori o Mehanici kontinuuma [2, 3]. Geometrijski gledano, deformacije i naprezanja mogu se odredit bez obzira na strukturu i fizikalna svojstva tkanine koje je izloženo deformaciji. Međutim, za potpuno rješavanje problema treba uspostaviti veze između naprezanja i veličina kojima je opisana deformacija u okolini proizvoljne točke tkanine. Ove veze ovise od nekih svojstava promatranog tijela (tkanine) koja nazivamo mehaničke karakteristike materijala. Znanost koja se time bavi naziva se reologija [4, 5].

Da bi se izbjegla pojava plastičnih deformacija u tkanini treba unaprijed znati pri kojem vlačnom opterećenju će doći do takvih deformacija. Treba postaviti odgovarajući reološki model koji dobro opisuje ponašanje tkanine. Reologija je znanost koja se bavi fizikom deformacija i osnovni joj je cilj uspostavljanje veze između sila, odnosno, naprezanja i njihovih derivacija po vremenu, s nastalim deformacijama uslijed djelovanja tih sila i njihovih derivacija po vremenu [6]. Osnovna reološka svojstva su elastičnost, viskoznost i plastičnost. Ako deformacije tijela pod djelovanjem konačnih sila rastu neprekinuto i neograničeno, kažemo da materijal teče.

Viskoznost je svojstvo materijala da trpi neku trajnu deformaciju ukoliko je ona dovoljno spora. Viskozno tečenje može nastati pod djelovanjem bilo kakve sile, ako se brzina deformacija umanjuje pri umanjenju sile, a pri iščezavanju teži prema nuli. Ovdje očito u račun mora ući tenzor brzine deformacije $\dot{\varepsilon}_{ij}$ koji ovisi samo o trenutnoj konfiguraciji.

Plastičnost je svojstvo materijala da pri određenim stanjima naprezanja trpi trajnu (plastičnu) deformaciju. Plastično tečenje nastaje kad sila prelazi neku granicu, nazvanu granicom tečenja za dani materijal.

Elastičnost je svojstvo tijela da se nakon prestanka djelovanja vanjskih sila vraća u svoj prvobitni oblik. Za opisivanje ovog svojstva koristimo tenzor deformacija ε_{ij} koji daje mjeru deformacije neovisno o njenom putu i brzini. Dio deformacije može biti povratni po djelovanju sile. To je elastični dio deformacije. Iz toga slijedi da iz samo jednog dijagrama opterećenja koji predstavlja opću deformaciju ne možemo naći elastičnu deformaciju, već samo nakon rasterećenja možemo utvrditi kolika je povratna deformacija. Ako nema naprezanja, nema ni elastične deformacije, dok viskozne i plastične deformacije postoje i bez naprezanja. Istraživanje ovisnosti različitih oblika deformacije od pripadnih naprezanja predstavlja zadaću reologije.

Zahvaljujući ispitivanju mehaničkih svojstava tkanina, postavljanju odgovarajućih reoloških modela i dobroj analizi promjene opterećenja u različitim procesima proizvodnje tkanina, dozvoljene vrijednosti sile naprezanja tkanina trebaju se kretati u granicama pojave elastičnih deformacija, i na temelju te vrijednosti sile vrši se optimizacija i potpuna automatizacija odgovarajućih procesa.

Cilj ovog rada je postaviti reološki model koji relativno dobro opisuje ponašanje pamučne tkanine ovisno o njezinim strukturnim i konstrukcijskim parametrima pri vlačnom naprezanju, krivulja (F-ε).

2. TEORIJSKI DIO

2.1. Veze između naprezanja i deformacija

Funkcionalnu vezu između sila (naprezanja) i deformacija ne možemo odrediti teorijski, već samo eksperimentalno ispitivanjem uzoraka tkanina. Pokusom utvrđujemo vezu između sila (naprezanja) i deformacija u obliku karakterističnog dijagrama pri određenim uvjetima. Provode se pokusi na rastezanje uzoraka tkanine, a eksperimentalno izmjereni podaci sile F i relativnog istezanja ε prikazuju se u obliku karakterističnog dijagrama istezanja (F-ε) za tkaninu, slika 1.

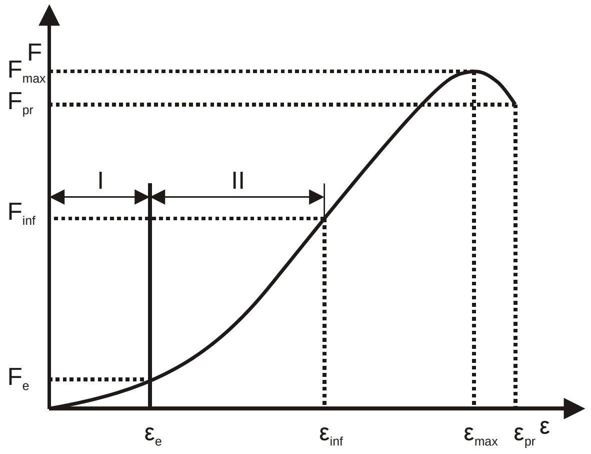

Slika 1. Karakteristični oblik dijagrama sila – relativno istezanje (F-ε) za tkaninu

F_{max}- maksimalna sila primijenjena na uzorak tkanine

F_{pr}- krajnja sila neposredno prije prekida uzorka tkanine

F_{inf}- sila u točki infleksije

F_e- sila na granici elastičnosti, pravci opterećenja i rasterećenja se poklapaju (vrijedi Hook-ov zakon)

ε_{max}- maksimalno istezanje uzorka tkanine pri djelovanju maksimalne sile

ε_{pr} - istezanje uzorka tkanine do prekida

ε_{inf} – istezanje u točki infleksije

ε_{e} – elastično istezanje (deformacija) koje nakon rasterećenja isčezava

A_{max}- površina (rad) ispod krivulje do maksimalne sile

A_{pr} - površina (rad) ispod krivulje do sile prekida

A_{inf} - povrišna (rad) ispod krivulje do sile u točki infleksije

Područje I je do granice elastičnosti (F_e, ε_e) i naziva se elastično područje koje se može predstaviti reološkim Maxwellovim modelom. Područje II je od granice elastičnosti (F_e, ε_e) do točke infleksije (F_{inf}, ε_{inf}) i predstavlja viskoelastično područje koje se može opisati Burgersovim modelom koji nastaje serijskom vezom Maxwellovog i Kelvinovog modela.

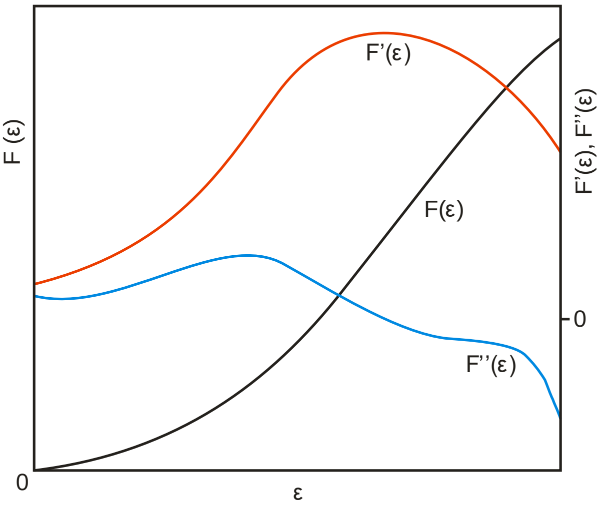

Slika 2. Dijagram ovisnost sila-istezanje funkcije $F(\varepsilon)$, prva $F'(\varepsilon)$ i druga $F''(\varepsilon)$ derivacija funkcije

Granice elastičnosti tkanina određene su na osnovu dijagrama ovisnosti sila-istezanje $F(\epsilon)$ kao i na osnovu $F'(\epsilon)$ i $F''(\epsilon)$. Slika 2 predstavlja funkciju sila-istezanje, kao i njezinu prvu derivaciju i drugu derivaciju. Maksimum prve derivacije ukazuje na dozvoljeno opterećenje do čije granice tkanina pokazuje elastična svojstva. Do ove točke, tkanina pokazuje veću otpornost na djelovanje vlačne sile ($F(\varepsilon)$ funkcija raste). Kada funkcija prve derivacije dostigne maksimum, u toj točki je druga derivacija jednaka 0. Zatim nastupa brža deformacija tkanine sve do destrukcije materijala (funkcija $F'(\epsilon)$ opada).

2.2. Osnovne postavke reologije

Reološko ponašanje materijala određeno je nekim odnosom koji sadrži naprezanja, deformacije i njihove derivacije po vremenu:

$$f\left(\sigma_{ij},\dot{\sigma}_{ij},\varepsilon_{kl},\dot{\varepsilon}_{kl}\right)=0. \tag{1}$$

Taj odnos nazivamo reološkom jednadžbom stanja materijala ili reološkim jednadžbama stanja materijala. Reološke jednadžbe sadrže neke skalarne veličine (parametre - konstante) koje karakteriziraju reološka svojstva materijala i nazivaju se reološkim konstantama, koeficijentima ili modulima, npr. modul elastičnosti ili koeficijent viskoznosti. Naprezanja i deformacije nazivaju se reološkim promjenjivim veličinama. Reološke jednadžbe sadrže promjenljive veličine: naprezanja, deformacije, brzinu deformacija i brzinu promjene naprezanja [7, 8].

Osnovni reološki modeli (tijela) su Hookeov, Newtonov, St. Venantov model. Realna tijela imaju istodobno svojstva elastičnosti, viskoznosti i plastičnosti u različitom obliku i odnosu. Kombinacijom jednostavnih elemenata može se složiti model tijela koji opisuje ponašanje realnih materijala [9 -11].

Hookeov model tj. linearno elastično tijelo „H“ predstavlja vezu između devijatora naprezanja S_{ij} i devijatora deformacija e_{ij} i ta veza je linearna. Idealan elastičan Hookeov materijal, prikazan je elastičnom oprugom, slika 3a. Za taj model vrijedi relacija $S_{ij} = 2 \cdot E \cdot e_{ij}$.

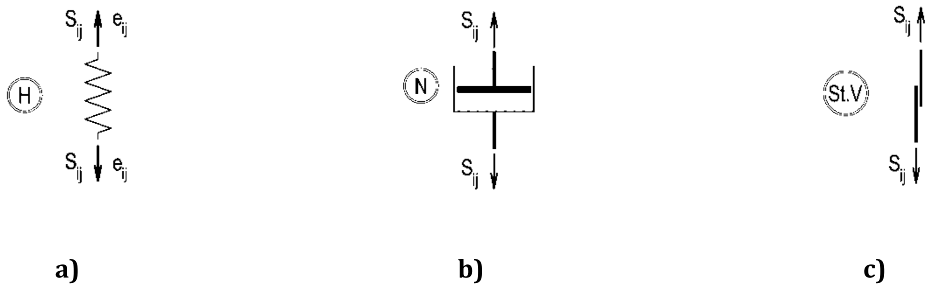

Slika 3. Osnovni reološki modeli: a) Hookeov model, b) Newtonov model, c) Saint Venantov model

Newtonov model „N“, slika 3b, je viskozni prigušivač i predstavlja model viskozne tekućine. Za jednoosno stanje naprezanja je $\sigma = \eta \dot{\varepsilon}$, gdje su η Newtonov koeficijent viskoznosti, $\dot{\varepsilon}_{ij}$ brzina deformacije. Saint Venant-ov model „St.V“, slika 3c, opisuje plastičnu deformaciju materijala. Za jednoosno stanje naprezanja vrijedi $\sigma = \sigma_T$.

2.3. Složeni reološki modeli (materijali)

Modele osnovnih materijala H, N i St.V možemo međusobno spajati na različite načine i tako dobiti modele nekih složenih materijala koji imaju složena reološka svojstva.

Maxwellov model je serijski spoj između Hookeova i Newtonova elementa naziva se još i elastoviskozni fluid koji ima reološku formulu M = H—N, slika 4a. U slučaju jednoosnog stanja naprezanja vrijedi sljedeći izraz:

$$\dot{\varepsilon} = \frac{1}{E}\dot{\sigma} + \frac{1}{\eta}\sigma \tag{2}$$

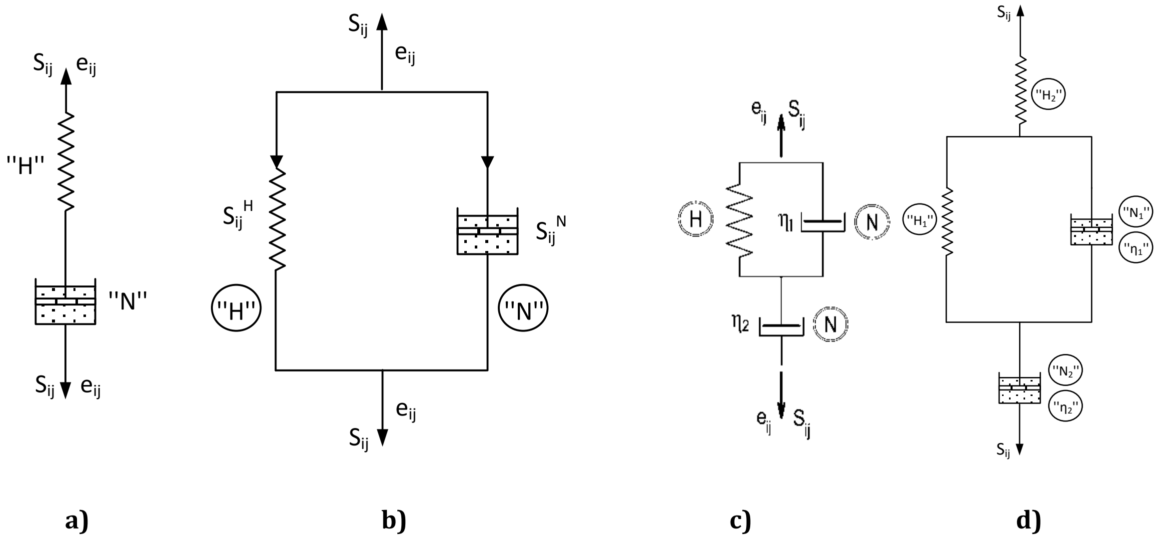

Slika 4. Složeni reološki modeli: a) Maxwellov model, b) Kelvinov model, c) Lethersichov model, d) Burgersov model

Kelvinov/Voightov model materijala nastaje paralelnim spajanjem Hooke-ovog i Newton-ovog materijala, odnosno simbolički K = H I N, slika 4b. To je viskoelastičan materijal koji polagano dostiže konačnu deformaciju, zadržava ju dulje vrijeme bez daljnjeg primjetnog povećanja, a prilikom rasterećenja ta deformacija se polagano gubi i tijelo se vraća u prvobitni oblik. Za jednoosno stanja naprezanja vrijedi izraz:

$$\sigma = E\varepsilon + \eta\dot{\varepsilon} \tag{3}$$

Lethersichov model je pogodan za ispitivanje reoloških svojstava pri istezanju pamučnih pređa, pamučnih tkanina različitih vrsta vezova i gustoća, opisivanje ponašanja geotekstila, slika 4c. Ovaj materijal je prikazan modelom kao serijska veza Kelvinovog i Newton-ovog elementa, pa mu je reološka formula L = K — N. Izraz za brzinu deformacije tijela prema modelu Lethersicha možemo zapisati i u sljedećem obliku:

$$\dot{\varepsilon} = \frac{\sigma}{\eta_N} + \frac{\sigma}{\eta_K} - \frac{\sigma}{\eta_K} \cdot \exp\left(-\frac{E_K}{\eta_K} \cdot t\right) \cdot \left[\varepsilon_0 + \frac{1}{\eta_K} \cdot \int \sigma \cdot \exp\left(\frac{E_K}{\eta_K} \cdot t\right)\right] dt$$

(4)

gdje su: η_N koeficijent viskoznosti Newtonovog tijela, η_K koeficijent viskoznosti Kelvinovog modela, E_K koeficijent elastičnosti Kelvinovog modela, ε_0 početno relativno istezanje. Derivacijom po vremenu i sređivanjem izraza (4) dobiva se diferencijalna jednadžba reološkog modela pamučne tkanine u obliku:

$$\ddot{\varepsilon}\cdot\eta_K+\dot{\varepsilon}\cdot E_K\cdot\eta_K=\dot{\sigma}\cdot(\eta_N+\eta_K)+\sigma\cdot E_K \tag{5}$$

Kako je u ovom slučaju $\dot{\varepsilon}=konst.$ i ε=0, jednadžba (5) poprima sljedeći oblik:

$$\dot{\sigma}\cdot(\eta_N+\eta_K)+\sigma\cdot E_K=\dot{\varepsilon}\cdot E_K\cdot\eta_K \tag{6}$$

Rješenje diferencijalne jednadžbe (6) može se prikazati izrazom (7):

$$\sigma=-C\cdot\exp\left(-\frac{E_K}{\eta_N+\eta_K}\cdot t\right)+\eta_N\cdot\dot{\varepsilon} \tag{7}$$

Konstanta integracije C određuje se iz početnih uvjeta, za t = 0, σ = 0. Ovisnost naprezanja o vremenu nakon određivanja konstante integracije može se prikazati izrazom (8):

$$\sigma=\eta_N\cdot\dot{\varepsilon}\cdot\left[1-\exp\left(\frac{l_0}{100\cdot v\cdot\tau_r}\cdot\varepsilon\right)\right] \tag{8}$$

gdje je:

$\tau_r=(\eta_N+\eta_K)/E_K$ - vrijeme relaksacije, l_0 – početna duljina uzorka, v – brzina testa, ε – relativno istezanje.

Burgersov model se primjenjuje za tekstilne materijale koji imaju znatniju plastičnu deformaciju, slika 4d. Taj model je komponiran kao serijska veza između Maxwellovog i Kelvinovog materijala, a po svojim svojstvima donekle odgovara viskoelastičnom ponašanju materijala. Reološka mu je formula: B = M — K=(H – N) – (H I N). Za jednoosno stanje naprezanja dobiva se jednadžba:

$$\left(\eta_1\frac{\partial^2}{\partial t^2}+E_1\frac{\partial}{\partial t}\right)\varepsilon=\left[\frac{\eta_1}{E_2}\frac{\partial^2}{\partial t^2}+\left(1+\frac{\eta_1}{\eta_2}+\frac{E_1}{E_2}\right)\frac{\partial}{\partial t}+\frac{E_1}{\eta_2}\right]\sigma \tag{9}$$

3. EKSPERIMENTALNI DIO

U eksperimentalnom dijelu rada provedeni su pokusi na rastezanje uzoraka pamučne tkanine u platnenom vezu s istom gustoćom osnove i različitim gustoćama potke. Krivulje sila-deformacija (F-ε) dobivene su ispitivanjem uzoraka u laboratoriju na računalno vođenom dinamometru tvrtke Textechno, koji registrira podatke u obliku dijagrama. Vlačna svojstva svih uzoraka ispitivana su prema standardu HRN EN ISO 13934-1:2013 metodom ispitne trake na uređaju za mjerenje čvrstoće tkanine tj. na dinamometru. Uzorci su rezani duljom dimenzijom u smjeru potke i u smjeru osnove. Smjer djelovanja vlačne sile tijekom izvođenja pokusa je uvijek jednak. Za svaki navedeni smjer rezanja uzorka, provedeno je pet ispitivanja. Izrezani su standardni uzorci (epruvete) dimenzija 350 x 50 mm, uklliješteni u stezaljke uređaja na razmaku od l_0=200 mm, te izloženi jednoosnom vlačnom opterećenju. Stezaljke dinamometra kreću konstantnom brzinom od 100 mm/min, te se može ustvrditi da je brzina deformacije konstantna. Vrijeme prekida uzorka 20 s. Ispitivanja su izvedena u standardnoj atmosferi pri temperaturi 20±2 °C i relativnoj vlažnosti 65±2%. Da bi se postigla uravnotežena vlažnost, tkanina je prije ispitivanja stajala 24 h u standardnim uvjetima.

3.1. Uzorci za ispitivanje

Za potrebe ispitivanja reoloških svojstava tkanina otkane su sirove pamučne tkanine. Uzorci tkanina navedenih konstrukcijskih karakteristika (tablica 1) otkani su na zračno-mlaznom tkalačkom stroju OMNIplus 800 tt. Picanol u tvornici Čateks d.d.. U realnim uvjetima proizvodnje, tkanine na tkalačkom stroju podložne su promjeni, naročito u konkretnim slučajevima kada se mijenjaju pojedini parametri strukture, kao što je ovdje slučaj promjenom gustoće niti potke. U tablici 1 nalaze se realne (izmjerene) vrijednosti strukturnih parametara sirovih tkanina. Finoća pređe određena je gravimetrijskom metodom prema normi HRN EN ISO 2060:2008. Gustoća tkanine ispitivana je prema normi ISO 7211-2:1984. Određivanje debljina tkanine je definirano normom HRN EN ISO 5084:2015. Pređa za potku je ista kao i za osnovu tj. korištena je ista pamučna pređa nazivne finoće 30 tex.

Tablica 1. Rezultati ispitivanja osnovnih parametara tkanina

Naziv tkanine	Oznaka tkanine	Gustoća osnove (niti/cm)	Gustoća potke (niti/cm)	Finoća osnove (tex)	Finoća potke (tex)	Površinska masa (g/m²)	Debljina (mm)
Platno	P12	24,1	12,1	30,3	30,3	115,23	0,362
	P18	24,2	18,2	30,3	30,3	135,48	0,363
	P24	24,3	24,2	30,3	30,3	157,89	0,365

Određivanje gustoće osnovinih i potkinih niti izvedeno je pomoću računalno upravljanog (stereo) mikroskopa DinoLite.

3.2. Rezultati ispitivanja

Uzorci se ispituju kada vlačna sila djeluje u smjeru osnove i u smjeru potke. Zbog toga se u oznake tkanina uvodi još jedno slovo. Prvo slovo u oznaci tkanine označava vrstu veza, drugo slovo smjer djelovanja sile, a broj označava gustoću potke, npr. PP18 – platneni vez, sila u smjeru potke, gustoća potke 18,2 niti/cm.

Dijagrami srednjih vrijednosti dobivenih rezultata ispitivanja djelovanja vlačne sile F i pripadne uzdužne deformacije (istezanja) ε na uzorcima tkanina, prva derivacija funkcije F'(Ɛ) i druga derivacija funkcije F''(Ɛ) kada sila djeluje u smjeru osnove i u smjeru potke prikazani su na slikama 5 -7.

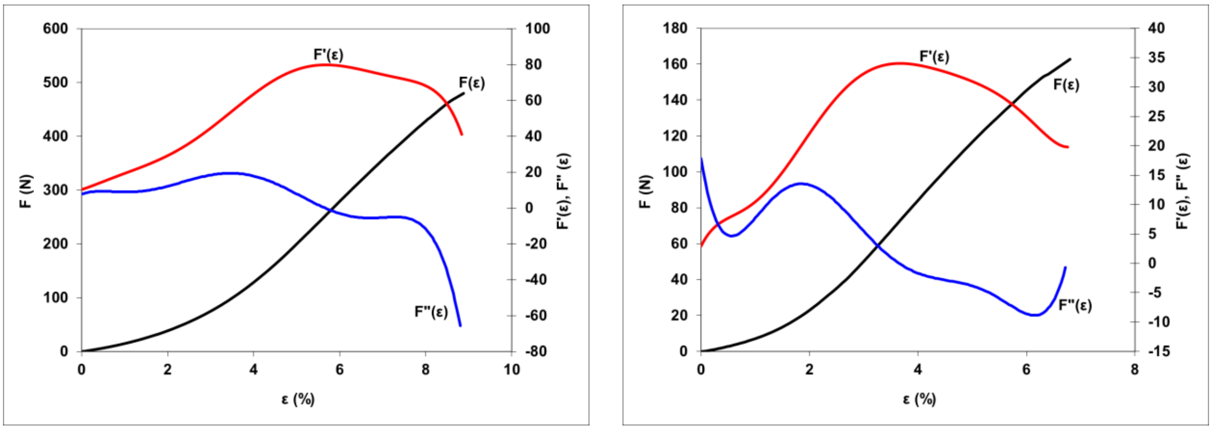

a) **b)**

Slika 5. Dijagram sila – relativno istezanje (F-ε), prva derivacija funkcije F'(Ɛ), druga derivacija funkcije F''(Ɛ): a) za uzorak PO12, b) za uzorak PP12

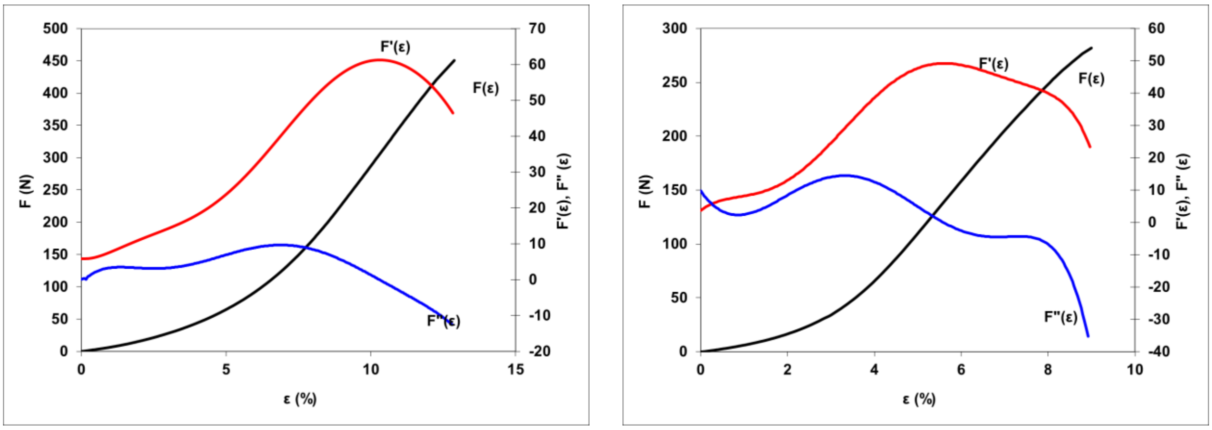

a) **b)**

Slika 6. Dijagram sila – relativno istezanje (F-ε), prva derivacija funkcije F'(Ɛ), druga derivacija funkcije F''(Ɛ): a) za uzorak PO18, b) za uzorak PP18

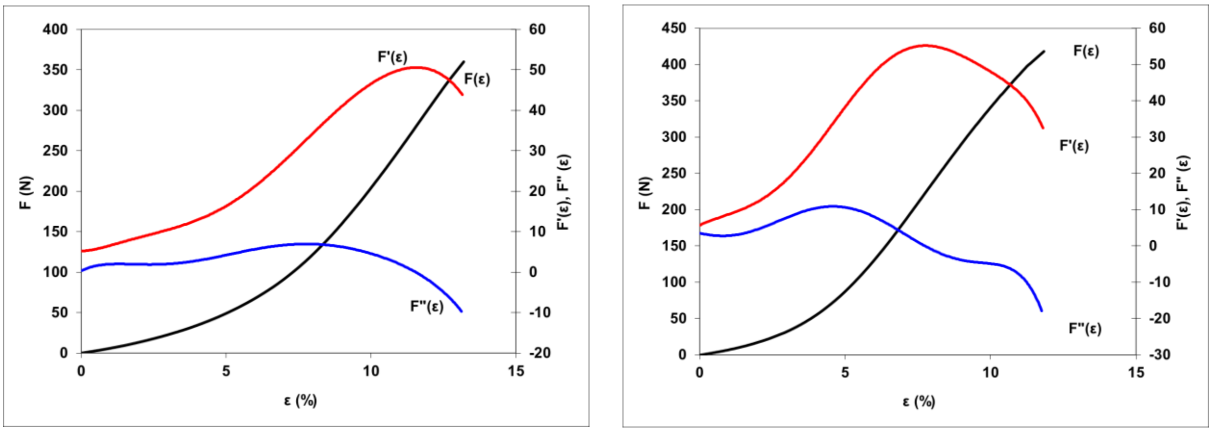

a) **b)**

Slika 7. Dijagram sila – relativno istezanje (F-ε), prva derivacija funkcije F'(Ɛ), druga derivacija funkcije F''(Ɛ): a) za uzorak PO24, b) za uzorak PP24

U tablici 2 prikazane su srednje vrijednosti rezultata ispitivanja maksimalne sile F_{max}, maksimalnog istezanja ε_{max}, rada do maksimalne sile W_{max}, prekidne sile F_{pr}, pripadnog prekidnog istezanja ε_{pr}, rada do prekida W_{pr}, sile u točki ifleksije F_{inf}, istezanja u točki infleksije ε_{inf} i rada do točke infleksije W_{inf}.

Tablica 2. Srednje vrijednosti F_{max}, ε_{max}, W_{max}, F_{pr}, ε_{pr}, W_{pr}, F_{inf}, ε_{inf}, W_{inf}

Ozn.tk.	F_{max} (N)	ε_{max} (%)	W_{max} (Ncm)	F_{pr} (N)	ε_{pr} (%)	W_{pr} (Ncm)	F_{inf} (N)	ε_{inf} (%)	W_{inf} (Ncm)
PO12	479,5	8,88	340,3	479,5	8,88	340,3	81,6	5,60	96,9
PP12	162,9	6,80	95,2	162,9	6,80	95,2	35,8	3,48	16,2
PO18	451,0	12,88	398,6	451,0	12,88	398,6	65,9	10,72	228,5
PP18	281,7	9,00	196,7	281,7	9,00	196,7	49,7	5,88	58,0
PO24	359,9	13,20	313,6	359,9	13,20	313,6	52,5	11,44	201,6
PP24	418,3	11,84	381,7	418,3	11,84	381,7	58,2	8,52	151,3

3.3. Postavljanje reološkog modela tkanine do točke infleksije

Predviđanje ponašanja pamučnih tkanina do točke infleksije pri istezanju kada djeluje vlačna sila može se predstaviti reološkim materijalom prema modelu Lethersich. Pri istezanju na dinamometru, brzina deformacije ima konstantnu vrijednost. Početna duljina epruvete je 0,2 m. Brzina kretanja stezaljke dinamometra je 100 mm/min. Uvođenjem ovih podataka u jednadžbu (8) i uz pretpostavku da su koeficijenti viskoznosti jednaki ($\eta_N = \eta_K$), dobiva se jednadžba (10):

$$\sigma = a \cdot \left[1 - e^{-b\cdot\varepsilon}\right] \tag{10}$$

Fitovanjem eksperimentalno dobivenih podataka u obliku jednadžbe (10), određene su vrijednosti koeficijenata „a“ i „b“ [14, 15]. U tablici 3 nalaze se vrijednosti koeficijenata modela „a“ i „b“ dobivenih na osnovu reološkog modela koji je postavljen na bazi eksperimentalnih podataka za tkanine koji su dobiveni na temelju istezanja uzoraka tkanina.

Tablica 3. Koeficijenti modela do točke infleksije

Naziv tkanine	a	b	Koeficijent determinacije R^2	Korijen srednje kvadratne pogreške RMSE (cN)
PO12	-3856,6	-0,36259	0,99888	243,8
PP12	-1034,5	-0,58509	0,99817	84,8
PO18	-3101,8	-0,23300	0,99831	398,5
PP18	-1411,1	-0,42837	0,99684	255,5
PO24	-2623,9	-0,21569	0,99920	223,1
PP24	-2990,1	-0,27465	0,99614	495,3

Dijagrami srednjih vrijednosti rezultata F-ε dobivenih eksperimentalno i prema Lethersich modelu prikazani su na slikama 8-10.

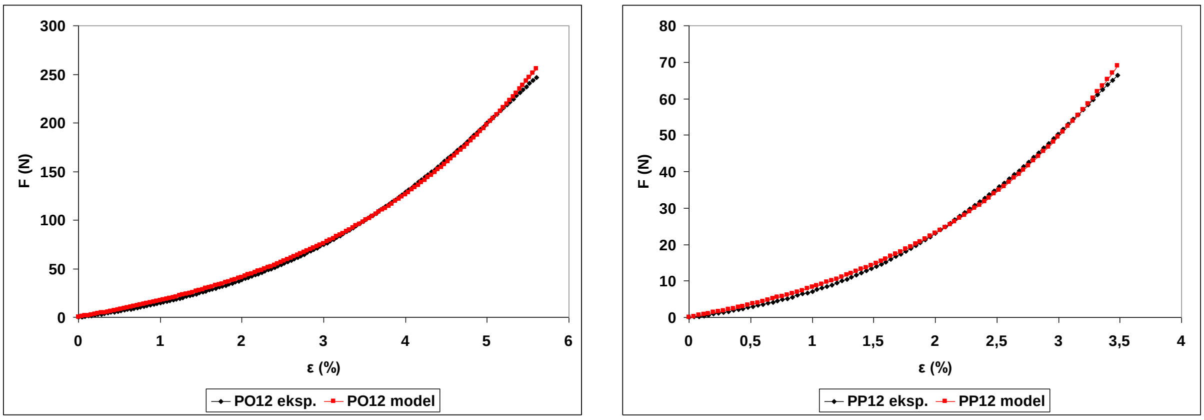

a) b)

Slika 8. Dijagram ovisnosti sila-istezanje (F-ε) dobiven eksperimentalno i po modelu: a) za uzorak PO12, b) za uzorak PP12

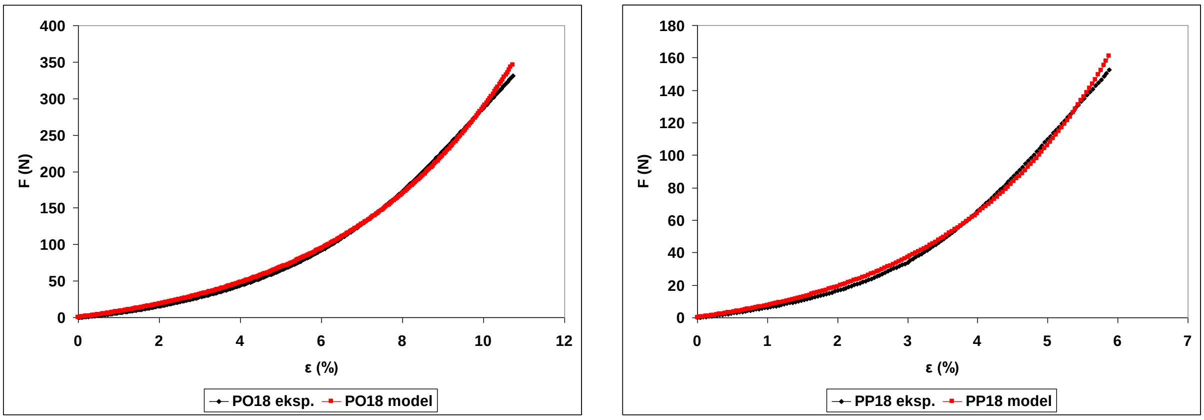

a) b)

Slika 9. Dijagram ovisnosti sila-istezanje (F-ε) dobiven eksperimentalno i po modelu: a) za uzorak PO18, b) za uzorak PP18

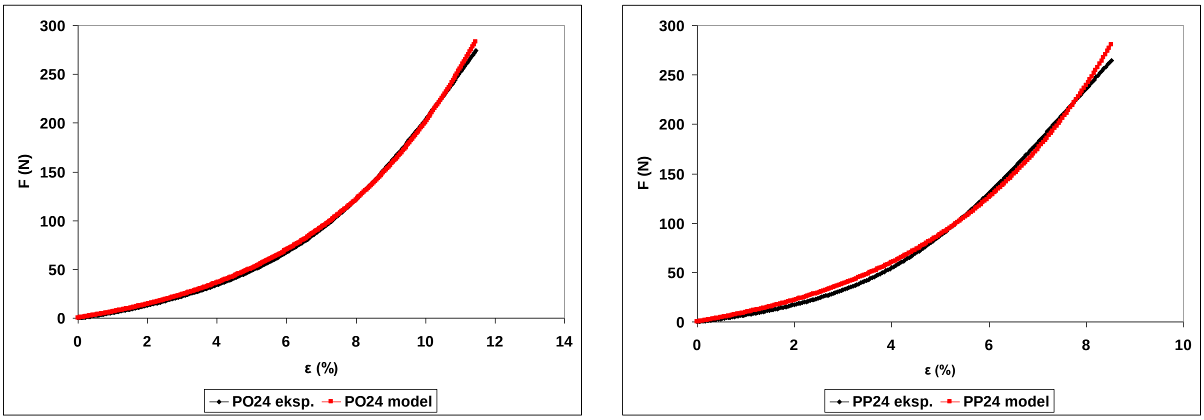

a) b)

Slika 10. Dijagram ovisnosti sila-istezanje (F-ε) dobiven eksperimentalno i po modelu: a) za uzorak PO24, b) za uzorak PP24

Pregledom dijagrama, od slike 8 do slike 10, formiranih na osnovu eksperimentalnih rezultata (crna boja) i rezultata dobivenih pomoću modela (crvena boja) uočava se da one nemaju linearan oblik, što potvrđuje da se tkanine ne ponašaju idealno elastično čak ni pri manjim naprezanjima. Na osnovu eksperimentalnih rezultata i oblika krivulja sila-istezanje može se konstatirati da se kod tkanina uočava viskoelastično ponašanje u analiziranom području. Granica elastičnosti je u suštini granica do koje dominiraju elastične deformacije u materijalu. Poslije granice elastičnosti nastaje veća brzina deformacije materijala i narušavanje strukture tkanina. Zbog toga granica elastičnosti tkanina predstavlja granično opterećenje pri kome nastale deformacije u tkanini neće značajno utjecati na stabilnost strukture i trajnost tkanine. Analizom dijagrama može se utvrditi da Lethersichov model, slika 4c, korektno opisuje ponašanje pamučnih tkanina platnenog veza u zoni elastičnih deformacija.

4. ZAKLJUČAK

Tkanina je tekstilni plošni proizvod s unaprijed projektiranim konstrukcijskim elementima. Mehanička svojstva tkanina polazni su parametri pri projektiranju i podešavanju parametara u tekstilnoj industriji. Definiranjem granice elastičnosti tkanina dolazi se do saznanja o graničnim intenzitetima sila kojima se mogu podvrgnuti tkanine, a da se pri tome ne naruši njihova kvaliteta. Anizotropna struktura tkanina doprinosi različitim, nekada teško objašnjivim, ponašanjima tkanina tijekom istezanja. Pojam „granica elastičnosti“ definira granicu do koje dominiraju elastične deformacije u tkanini. To je granica kada se materijal počinje brže deformirati pri naprezanju, te se zbog toga treba smatrati granicom dozvoljenih opterećenja.

Mehanička svojstva tkanina mogu se predvidjeti primjenom reoloških modela. Time se svaki tip deformacije realnih materijala opisuje osnovnim modelom ili se ponašanje tkanine predstavlja složenim modelima koji su nastali kombinacijom osnovnih modela. Osnovni modeli koji služe za opisivanje elastične, viskoelastične i plastične deformacije su modeli koji definiraju svojstva idealnih materijala kojih nema u prirodi ali čija svojstva, pod određenim uvjetima opterećenja i ostalih vanjskih utjecaja, približno opisuju ponašanje realnih materijala.

Na temelju eksperimentalnih rezultata dobivenih za istezanje uzoraka tkanina u standardnim uvjetima ispitivanja, kombinacijom poznatih elementarnih reoloških modela, postavljenih reoloških modela istezanja tkanine, izvedene su i riješene odgovarajuće diferencijalne jednadžbe za ispitivane uzorke tkanina, čime je dobivena ovisnost između vlačne sile (naprezanja) i relativnog istezanja. Reološki modeli relativno dobro opisuju proces istezanja pamučne tkanine u statičkim uvjetima ispitivanja.

Za opisivanje ponašanja pamučnih tkanina u platnenom vezu koristio se Lethersichov model. Taj model može opisati ponašanje pamučne tkanine podvrgnute djelovanju vlačne sile u zoni gdje dominiraju elastične deformacije. U zoni elastičnih deformacija, tj. do točke infleksije, definirana je veza sila-istezanje za pamučne tkanine. Pogreška procijene između modela i eksperimentalno dobivenih vrijednosti je vrlo niska, pa se može zaključiti da razvijena metoda može poslužiti za predviđanje ponašanja pamučnih tkanina u zoni elastičnih deformacija. Iz dobivenih koeficijenata determinacije (R^2) vidljiva je visoka povezanost ($R^2 > 0,99$) između odnosa modela i eksperimentalno dobivenih rezultata te da se neznatno razlikuju (tek u trećoj decimali).

Pogreška procijene krivulje sila-istezanje iskazana kroz korijen srednje kvadratne pogreške (RMSE) najmanja je za model tkanine u platnenom vezu (PP12) s najnižom gustoćom i iznosi (84,8 cN), a najveća za model tkanine u platnenom vezu (PP24) s najvišom gustoćom i iznosi (495,3 cN). Jedan od razloga je taj što platneni vez doseže veći raspon prekidnih sila i prekidnih istezanja pa je i mogućnost pogreške procjene veća. Mehaničke karakteristike tkanina ovise o njihovim strukturnim rješenjima, kao i o tehnološkim uvjetima izrade. Pri tome, najznačajniju ulogu imaju strukturne i fizičko-mehaničke karakteristike tkanina, površinska masa tkanina i parametri procesa tkanja. Poznavanjem uzajamne povezanosti mehaničkih karakteristika tkanina pruža se mogućnost njihovog pravilnog projektiranja u ovisnosti o budućoj namjene, što može doprinijeti uštedi sirovine i energije. Razvijeni Lethersichov model može poslužiti za predviđanje graničnih opterećenja pamučnih tkanina poslije kojih nastaju nepovratne deformacije ovih materijala.

LITERATURA

[1] Kostrenčić Z., Teorija elastičnosti, 1982, Školska knjiga, Zagreb.

[2] Šuklje L., Rheological aspects of soil mechanics, 1969, John Wiley, London.

[3] Ivković M., Radojčić T., Reologija i opšta teorija loma betona, 1987, Naučna knjiga, Beograd.

[4] Frgić L., Hudec M., Mehanika kontinuuma i reologija, skripta, 2006, Rudarsko-geološko-naftni fakultet u Zagrebu.

[5] Brčić V., Uvod u reologiju i teoriju plastičnosti, skripta, 1978, Građevinski fakultet u Zagrebu.

[6] Dmitriev O. U., Osmin N. A., Koefficient uskorenia ekspressnogo metoda ocenki obryvnosti prazi, Tehnologia tekstilnoj promyslennosti, 2, str. 28-30, (1990).

[7] Dmitriev O.U., Opredelenie parametrov cetyrehelementnoj modeli mehaniceskih svojstv v tekstilnyh materialah, Tehnologia tekstilnoj promyslennosti, 2, str. 17-19, (2002).

[8] Koblyakov A., Laboratory Practice in the Study of Textile Materials, 1989, Mir Publishers, Moscow.

[9] Postle R., de Jong S., The Rheology of Woven and Knitted Fabrics, Part 1: Fabric Geometry and Force Methods of Analysis Applied to Fabric Mechanics, Sen'i Kikai Gakkaishi (Journal of the Textile Machinery Society of Japan), 5, P264-P273, (1981).

[10] Postle R., de Jong S., The Rheology of Woven and Knitted Fabrics, Part 2 : Energy Minimization Techniques Applied to Elastic Mechanism of Fabric Deformation, Sen'i Kikai Gakkaishi (Journal of the Textile Machinery Society of Japan), 7, P344-P353, (1981).

[11] Postle R., de Jong S., The Rheology of Woven and Knitted Fabrics, Part3 : Objective Specification of Fabric Mechanical Behaviour and Inelastic Mechanisms of Deformation and Recovery, Sen'i Kikai Gakkaishi (Journal of the Textile Machinery Society of Japan), 10, P442-P460, (1981).

[12] Lasić V., Srdjak M., Stupica I., Reološki modeli dvoosnovinih pletiva, Tekstil 11, str. 656-660, (1990).

[13] Kukin G.N., Solovjev A.N., Kobjanakov A.I., Tekstilnoje materijalovedenie (volokna i niti), Moskva, 1989, Legprombitizdat.

[14] Zhang X., Bagging of Woven Fabrics: The Rheological Mechanism and Predictions, Journal of the Textile Institute, 3, 235-255, (2001).

[15]Tarfaoui M., Drean J., Akesbi S., Predicting the Stress-Strain Behavior of Woven Fabrics Using the Finite Element Method, Textile Research Journal, 9, 790-795, (2001)

POVIŠENJE OTPORNOSTI NA TROŠENJE PRSTENA KLIZNOG LEŽAJA NITRIRANJEM

INCREASING IN WEAR RESISTANCE OF PLAIN BEARING RING BY NITRIDING

Antonio Petrak[1], **Darko Landek**[1]

[1] Sveučilište u Zagrebu, Fakultet strojarstva i brodogradnje, Ivana Lučića 5, 10002 Zagreb, Hrvatska
[1] University of Zagreb, Faculty of Mechanical Engineering and Naval Architecture, Ivana Lučića 5, 10002 Zagreb, Croatia

Sažetak

U radu je ispitano povišenje otpornosti na adhezijsko trošenje prstena kliznog ležaja od čelika EN DIN 100Cr6 nakon modificiranja površine nitriranjem u plazmi i nitrokarburiranjem u solnoj kupci TENIFER. Provedena su ispitivanja faktora trenja, mikrotvrdoće, mikrostrukture i otpornosti na adhezijsko trošenje nitriranog sloja. Ispitivanja faktora trenja uz manje opterećenje normalnom silom od 60 N pokazala su veću vrijednost faktor trenja na ne nitriranom prstenu u odnosu na nitriranu u plazmi i nitrokarburiranu površinu. Najmanje vrijednosti faktora trenja ostvarene su na prstenu nitrokarburiranom u solnoj kupci TENIFER. U drugom slučaju, kod opterećenja normalnom silom od 120 N, utvrđena je veća vrijednost faktora trenja na nitrokarburiranom u odnosu na ostale uzorke. Ovdje je najmanja vrijednost faktora trenja utvrđena na prstenu nitriranom u plazmi.

Ključne riječi: *klizni ležaj, nitriranje u plazmi, nitrokarburiranje TENIFER, EN DIN 100Cr6, otpornost na adhezijsko trošenje.*

Abstract

This paper examines the increase in adhesive wear resistance of plain bearing ring made of EN DIN 100Cr6 steel after surface modification including plasma nitriding and nitrocarburizing in the TENIFER solvents procedures. The following properties were tested: the microhardness and microstructure of the nitride layer, the adhesive wear resistance and the friction factor of the nitrided and non-nitrided surface. The examination of the friction factor showed that, when 60N normal force is applied, the ring in the initial state has the biggest friction factor, while the ring nitrocarburized in the TENIFER solvents has the smallest friction factor. In the second examination, in which 120N normal force was applied, the biggest friction factor was found in the ring nitrocarburized in the TENIFER solvents, while the smallest friction factor was found in the plasma nitride ring.

Keywords*:* *plain bearing, plasma nitriding, nitrocarburizing in the TENIFER solvents, EN DIN 100Cr6, adhesive wear resistance.*

1. UVOD

Klizni ležajevi su strojni elementi koji služe kao oslonci rukavca osovina ili vratila. Rukavci rotiraju u blazinicama ležaja, te su zbog toga ležaji izloženi trenju klizanja, kontaktnim pritiscima i trošenju te visokim dinamičkim naprezanjima [1]. Klizni ležaji se uobičajeno troše mehanizmom adhezije ili kombinacijom adhezije i abrazije. To trošenje karakterizira prijelaz materijala s jedne klizne plohe na drugu pri relativnom gibanju uz pojavu zavarivanja i raskidanja mikro zavara. Otpornost na adhezijsko trošenje ovisi o sklonosti stvaranju mikrozavarenih spojeva kliznog para i jakosti uspostavljenih adhezijskih veza. Postupcima modificiranja i prevlačenja površine kliznog ležaja moguće je značajno poboljšati svojstva i otpornost na trošenje [2].

U radu će se provesti nitrokarburiranje u solnoj kupci TENIFER i nitriranje u plazmi na prstenima kliznog ležaja od čelika EN DIN 100Cr6. Na temelju provedenih ispitivanja hrapavosti, mikrotvrdoće i otpornosti na adhezijsko trošenje površine metodom Blok na prstenu (eng. Block on Ring) usporedit će se otpornost na adhezijsko trošenje neprevučenih i prevučenih prstena.

2. MATERIJALI I METODE

2.1. Ispitivani čelik

Ispitni uzorci korišteni u radu su tržišno dostupni prsteni ležaja oznake NTN-1R30X35X16 dimenzija ∅ 35/30x16 mm izrađeni od poboljšanog čelika EN DIN 100Cr6. Ovaj čelik pripada skupini niskolegiranih alatnih čelika za hladni rad, odnosno podskupini niskolegiranih Cr čelika dobre otpornosti na trošenje i otpornosti na specifične pritiske do 500 MPa [3]. Kemijski sastav čelika EN DIN 100Cr6 prema normi EN ISO 683–17 naveden je u tablici 1.

Tablica 9. Kemijski sastav čelika EN DIN 100Cr6 prema normi EN ISO 683–17 [4].

Udio elemenata	C%	Si%	Mn%	Cr%	Ostali
Čelik EN DIN 100Cr6	1,00	0,25	0,35	1,50	-

2.2. Nitriranje ispitnih uzoraka

Prema [5], nitrokarburiranje je postupak termokemijske obrade kojim se postiže obogaćivanje površinskih slojeva predmeta dušikom i ugljikom uz stvaranje zone spojeva. Ispod zone spojeva nalazi se difuzijska zona obogaćena dušikom. Nitrokarburiranje u solnim kupkama izvodi se uranjanjem i držanjem predmeta u solima koje sadrže cijanide (NaCN) uz dodatak kalijeva cijanata (KCNO). Svojstva nastalog sloja su: bolja svojstva klizanja, manja sklonost zaribavanju, veća otpornost na trošenje, povišena duktilnost, dinamička čvrstoća i otpornost koroziji te povišena tvrdoća na povišenim temperaturama. Dijagram postupka nitrokarburiranja u solnoj kupci TENIFER koji je proveden na ispitnom prstenu prikazan je na slici 1. a. Nitriranje u plazmi provedeno je na uređaju Rubig PC 70/90 (Sveučilište u Zagrebu, Fakultet strojarstva i brodogradnje, Laboratorij za inženjerstvo površina). Dijagram postupka nitriranja u plazmi prikazan je na slici 1. b, dok su parametri postupka navedeni u tablici 2. Nitriranje u plazmi provedeno je bez stvaranja zone spojeva.

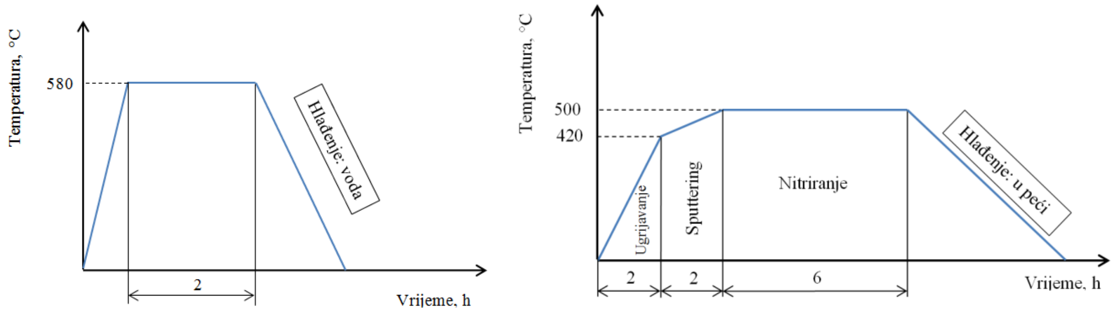

a) b)

Slika 1. Toplinska obrada ispitnih uzoraka. a) nitrokarburiranje u solnoj kupci TENIFER, b) nitriranje u plazmi

Tablica 2. Parametri nitriranja u plazmi

Korak procesa	Ugrijavanje	Sputtering (čišćenje) u plazmi	Nitriranje
Temperatura, °C	20 → 420	420 → 500	500
Vrijeme, h	2 h	2 h	6 h
Tlak, mbar	2	2	2
Sastav plinova	100% H_2	5% N_2, 5% Ar, 90% H_2	10% N_2, 5% Ar, 85% H_2
Napon, V	-	420 V	560 V
Snaga, W	-	1000 W	1800 W

2.3. Ispitivanje hrpavosti i otpornosti na trošenje

Ispitivanje hrapavosti provedeno je u Nacionalnom laboratoriju za duljinu RH na Fakultetu strojarstva i brodogradnje Sveučilišta u Zagrebu, u skladu sa normama: ISO 4287:1997, ISO 4288:1996 i ISO 3274:1996. Ispitivanje je provedeno na uređaju Perthometer S8P (Feinprüf Perthen GmbH) na 5 slučajno odabranih mjesta na vanjskoj površini prstena. Ispitana je hrapavost površine prstena u polaznom stanju te nakon nitrokarburiranja postupkom TENIFER.

Otpornost na adhezijsko trošenje ispitana je metodom Blok na prstenu (eng Block on ring) prema normi ASTM G77 [2]. Sustav se sastoji od nepomičnog kontra para (bloka) koji zadanom normalnom silom (F_N, N) opterećuje rotirajući ispitni prsten (slika 2.). U provedenim ispitivanjima blok dimenzija 7x7x10 mm bio je izrađen od nehrđajućeg čelika

EN X5CrNi18-10 s tankom PACVD prevlakom TiCN. Tijekom rotacije pojavljuje se sila trenja (F_T, N) na kontaktnoj površini bloka i ispitnog prstena koja se odrađuje indirektno na temelju otklona savojne opruge. Određivanje sile trenja provedeno je tijekom 180 s rotacije prstena tijekom kojih je ostvaren put trošenja od 10 m. Faktor trenja određen je iz omjera $\mu = F_T/F_N$ za ispitivanje s normalnom silom od 60 N i 120 N.

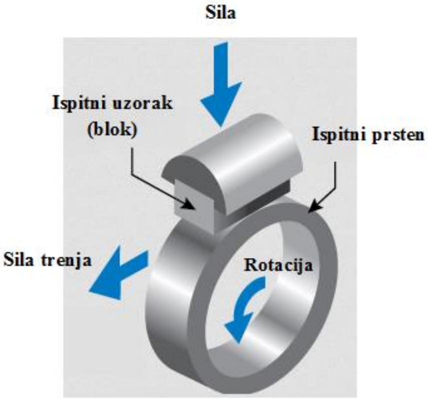

Slika 2. Prikaz ispitivanja otpornosti na adhezijsko trošenje metodom „Blok na prstenu“ [6]

3. REZULTATI I DISKUSIJA

3.1. Ispitivanje hrapavosti i mikrotvrdoće površine

Najveća hrapavost površine prstena u polaznom stanju iznosila je Rmax=0,506±0,039 µm uz profil hrapavosti prikazan na slici 4.a. Nakon nitrokarburiranja u solnoj kupci TENIFER najveća hrapavost je porasla do 3,5 puta na vrijednost Rmax=1,819±0,461 µm, što je posljedica stvaranja zone spojeva uobičajene za ovaj postupka. Također je izmijenjen izgled profila hrapavosti prikazan na slici 4.b. Stvaranje zone spojeva s mikroporama na površini nakon nitrokarburiranja uzrokuje pojavu niza dodatnih brjegova i dolova na profilu hrapavosti u odnosu na profil polaznog ne nitriranog uzorka.

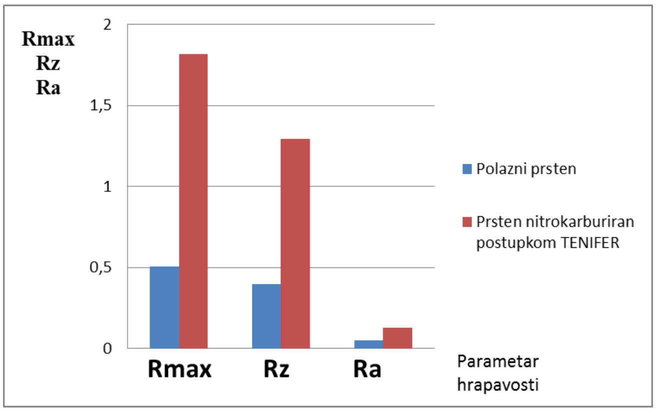

Slika 3. Parametri hrapavosti ispitivanih prstena ležaja

Tablica 3. Vrijednost parametara hrapavosti ispitivanih prstena ležaja

Parametri hrapavosti	Polazni prsten	Prsten nitrokarburiran postupkom TENIFER
R_{max}, [µm]	0,506 ± 0,039	1,819 ± 0,461
R_z, [µm]	0,397 ± 0,026	1,291 ± 0,208
R_a, [µm]	0,050 ± 0,005	0,129 ± 0,016

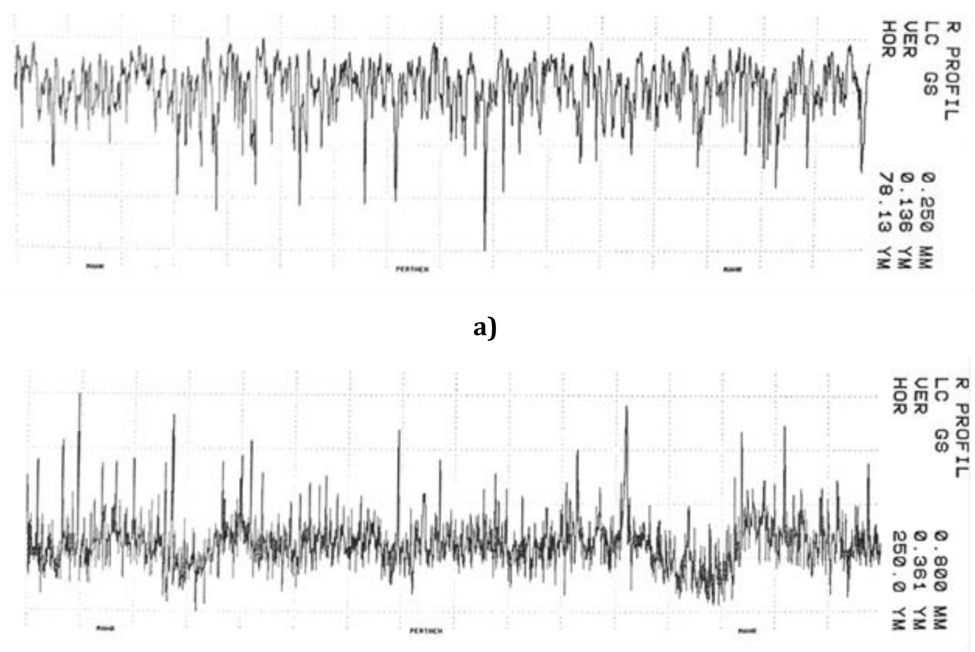

a)

b)

Slika 4. Izgled profila hrapavosti: a) za polazno stanje prstena kliznog ležaja, b) za prsten nitrokarburiran postupkom TENIFER

Mikrotvrdoća jezgre i površine ispitnih uzorka određena je na tvrdomjeru „Wilson – Wolpert Tukon 2100B“, metodom Vickers HV 0,5. U provedenim ispitivanjima dobivene su sljedeće vrijednosti tvrdoće:

- mikrotvrdoća jezgre ispitnih uzoraka iznosi 360 ± 10 HV0,5
- mikrotvrdoća nitrokarburirane površine iznosi 796 ± 16 HV0,5
- mikrotvrdoća površine nitrirane u plazmi iznosi 790 ± 55 HV0,5

3.3. Ispitivanje otpornosti na adhezijsko trošenje

Rezultati ispitivanja faktora trenja prikazani su na slici 5. za sva ispitana tri tribo sustava. Iz rezultata ispitivanja s manjom normalnom silom od F_N = 60 N (slika 5.a) uočava se period uhodavanja tribo para na putu trošenje do 4,0 m. Nakon toga prsten nitriran u plazmi se troši slično kao i prsten nitrokarburiran u solnoj kupci TENIFER. Kod nitriranja u plazmi nije nastala zona spojeva te su vrijednosti faktora trenja slične vrijednostima ne nitriranog uzorka. Nitrokarburirani prsten u početku trošenja ima nešto veću vrijednost faktora trenja nego u uznapredovaloj fazi trošenja kada se formirala klizna staza.

Na slici 5.b prikazana je promjena faktora trenja kod opterećenja normalnom silom od F_N = 120 N. Ovdje odmah na početku trošenja dolazi do uhodavanja tribopara odnosno stvaranja klizne staze te svi ispitivani prsteni pokazuju slične vrijednosti faktora trenja.

Iz usporedbe vrijednosti faktora trenja za oba normalna opterećenja uočava se da prsten nitrokarburiran u solnoj kupci TENIFER ima sličnu vrijednost faktora trenja za oba normalna opterećenja, od 60 i 120 N. Analizom izgleda trošene površine prstena prikazane na slici 6. uočava se da je kod ne nitriranog prstena bilo značajno više vibracija tijekom ispitivanja u odnosu na ostala dva uzorka, što objašnjava i rasipanje rezultata na dijagramu ovisnosti faktora trenja o putu trošenja (slika 5.a). Na nitrokarburiranom uzorku (slika 6.b) ostala je očuvana zona spojeva kod oba normalna opterećenja te su i vrijednosti faktora trenja slične. Kod prstena nitriranog u plazmi uočavaju se poprečna klizanja bloka po prstenu pri manjem opterećenju F_N = 60 N (slika 6.c) slično kao kod ne nitriranog prstena. Kod većeg normalnog opterećenja F_N = 120 N trag trošenja na prstenu nitriranom u plazmi postaje uži u odnosu na trag ostvaren pri manjem normalnom opterećenju, uz zanemarivo male oscilacije vrijednosti faktora trenja.

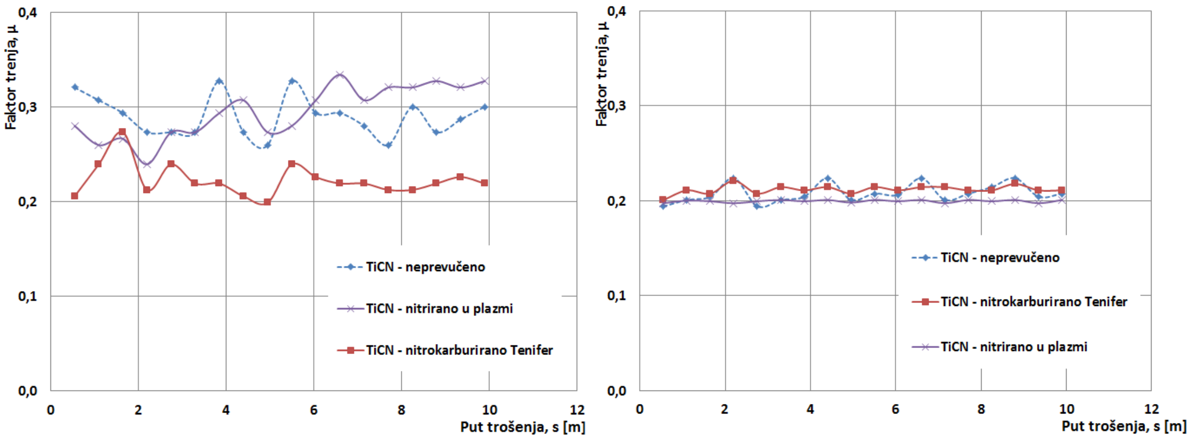

a) **b)**

Slika 5. Ovisnost faktora trenja o putu trošenja za ispitivanje nitriranog sloj s normalnom silom:

a) F_N=60 N i b) F_N=120 N

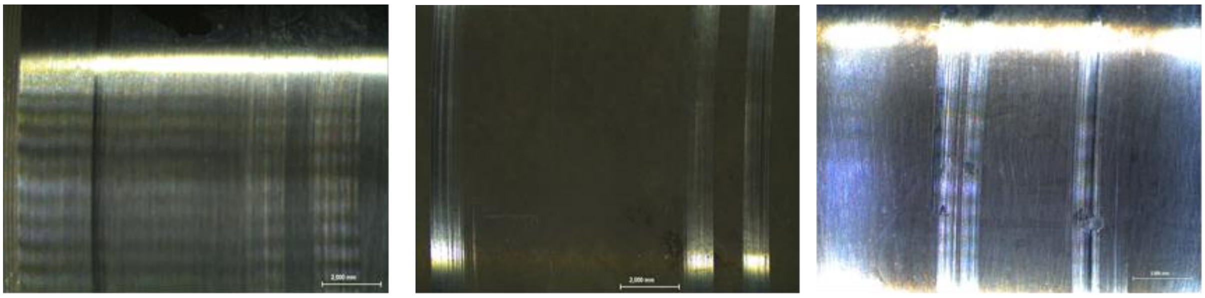

a) b) c)

Slika 6. Prikazi tragova trošenja snimljenih stereo mikroskopom Leica MZ6 (trag trošenja lijevo na slikama nastao je uz F_N = 60 N, trag trošenja desno na slikama nastao je uz F_N = 120 N): a) prsten u polaznom stanju, b) prsten nitrokarburiran postupkom TENIFER, c) prsten nitriran u plazmi

4. ZAKLJUČAK

Iz provedenih ispitivanja hrapavosti i mikrotvrdoće površine te otpornosti na adhezijsko trošenje na toplinski obrađenim uzorcima prstena kliznog ležaja od čelika EN DIN 100Cr6 nitrokarburiranih u solnoj kupci TENIFER i nitriranih u plazmi zaključuje se slijedeće:

Iz rezultata ispitivanja hrapavosti površine uočava se očekivano povišenje hrapavosti nakon nitrokarburiranja u solnoj kupci TENIFER

Iz rezultata ispitivanja površinske tvrdoće utvrđena je srednja vrijednost od 790±55 HV0,5 na površini nitriranoj u plazmi, 796±16 HV0,5 na površini nitrokarburiranoj u solnoj kupci TENIFER te mikrotvrdoća od 360 ± 10 HV0,5 u jezgi.

Iz rezultata ispitivanja faktora trenja tribopara bloka prevučenog PAVCD prevlakom TiCN i različito površinski modificiranih ispitnih prstena uočava se najmanja vrijednost faktora trenja μ = 0,20 kod ispitnog prstena nitrokarburiranog u solnoj kupci TENIFER, bez obzira na normalno opterećenja (F_N = 60 N , 120 N). Sličnu vrijednost faktora trenja postiže i prsten nitriran u plazmi te ne nitrirani prsten kod povišenog normalnog opterećenja F_N = 120 N.

Iz navedenog slijedi da je primjena nitriranja u plazmi za prstene kliznih ležajeva opravdana za slučajeve povišenog normalnog naprezanja kod kojih uz sniženi faktor trenja dolazi do izražaja i povišena otpornost na kontaktne pritiske. Nitrokarburiranje prstena ležaja u solnoj kupci TENIFER prikladno je za širi raspon normalnog opterećenja u odnosu na ne nitrirani prsten, kao i onaj nitriran u plazmi. Ovdje će stvaranje zone spojeva dodatno doprinijeti boljem podmazivanju ležaja i zaštiti od korozije.

LITERATURA

[1] Decker K. H., Elementi strojeva, Golden marketing – Tehniška knjiga, Zagreb, 2000.

[2] Grilec K., Jakovljević S., Marić G., Tribologija u strojarstvu, Fakultet strojarstva i brodogradnje, Zagreb, 2017.

[3] Novosel M., Cajner F., Krumes D., Alatni materijali, Strojarski fakultet u Slavonskom Brodu, Slavonski Brod, 1996.

[4] https://www.saarstahl.com/sag/downloads/download/11609 preuzeto (1.6.2018.)

[5] Krumes D., Toplinska obradba, Strojarski fakultet u Slavonskom Brodu, Slavonski Brod, 2000.

[6] http://extremecoatings.net/resources/test-results/adhesive-wear-test-astm-g77.html - preuzeto (13.2.2018.)

PONAŠANJE TVRDIH METALA U OBRADI ODVAJANJEM ČESTICA POD KRIOGENIM UVJETIMA

BEHAVIOUR OF HARD METALS IN MACHINING UNDER CRYOGENIC CONDITIONS

Matija Pisk, Ivan Kumić, Božidar Matijević

[1] Fakultet strojarstva i brodogradnje, Ivana Lučića 5, Zagreb, Hrvatska
Faculty of mechanical engineering and naval architecture, Ivana Lucica 5, Zagreb, Croatia

Sažetak

Kao alati, tvrdi metali svojim iznimnim omjerom tvrdoće i žilavosti, postaju neizostavni dio svake proizvodnje koja se oslanja na obradu dijelova odvajanjem čestica. U ovom su radu prikazani ključni aspekti uporabe tekućeg dušika umjesto, ili u kombinaciji, s klasičnim sredstvom za hlađenje i podmazivanje. Ovaj rad predstavlja pregled trenutnog stanja u području istraživanja te ističe najvažnije recentne spoznaje o utjecaju snižene radne temperature na alate načinjene od tvrdog metala, poput mikrostrukturnih promjena, promjena u vidu mehaničkih svojstava te, posljedično, promjena u pogledu parametara same obrade te trajnosti alata.

Ključne riječi: *Tvrdi metali, obrada odvajanjem čestica, kriogeno hlađenje*

Abstract

Cemented carbides, used as tools, with exceptional ratio of hardness and toughness, became invaluable in any machining dominant production line. This paper presents all significant aspects of using liquid nitrogen cryogenic coolant instead of or in conjunction with additional, commonly used cooling medium. Within this paper, current observations in the field of research are summerized and concisely evaluated with focus being set mostly on any microstructural changes and changes in physical properties of tool material which, consequently, may result in better optimisation of cutting speeds and in longer tool life.

Keywords: *Cemented carbides, machining, turning, cutting, milling, cryogenic cooling*

1. UVOD

Tvrdi metali nalaze se u skupini metalnih kompozita (neokisdne keramike), koji se sastoje od barem jedne tvrde faze (karbida), nositelja tvrdoće i vezivne metalne matrice, najčešće kobalta, koja je žilavija i otpornija na udarna opterećenja. Najčešći karbidi koji se koriste u tvrdim metalima su volfram-karbid (WC), titan-karbid (TiC) i tantal-karbid (TaC) [1].

Za razliku od ostalih neoksidnih keramičkih materijala, kod tvrdih metala su izraženija metalna svojstva poput kombinacije tvrdoće, duktilnosti, otpornosti na popuštanje, toplinske vodljivosti i magnetičnosti. Udio tvrdog metala kao reznog materijala u tehnologijama obrade je oko 33 %, a istovremeno, tvrdim metalom skinuta odvojena čestica čini oko 68 % od ukupne količine skinute odvojene čestice. Poseban segment u razvoju reznih materijala koji zauzima veoma značajno mjesto je razvoj tehnike nanošenja površinskih prevlaka na tvrdi metal.

Sva navedena svojstva i potencijali u obradi postupcima inženjerstva površina čine tvrde metale neizostavnim materijalom u izradi alata za obradu odvajanjem čestica te se koriste u izradi:

- Reznih alata
- Alata za probijanje, duboko vučenje i provlačenje žice
- Dijelova strojeva.

1.1. Vrste tvrdih metala

Najčešće korištene tvrde metale dijelimo prema sastavu i udjelu komponenata na [2]:

- Tvrde metale na bazi WC – Co
- Tvrde metale na bazi WC – TiC – Co

U industriji su određene serije tvrdih metala poznate po nazivu određenim standardom ISO 4499, prema kojemu je klasificirano 5 grupa:

1.) P 01 – P 40 – namijenjen za finu, srednju i grubu obradu željeza, čelika, legiranih čelika i temper lijeva,

2.) K 01 – K 40 – namijenjen za finu, srednju i grubu obradu sivog lijeva, temper lijeva, manganskog čelika, obojenih metala, plastike i drva,

3.) M 10 – M40 – namijenjen za tokarenje, glodanje, blanjanje; srednja brzina rezanja velikom dubinom reza,

4.) G 10 – G 60 – namijenjen za kovanje, provlačenje, duboko izvlačenje, štancanje,

5.) B 06 – B 40 – namijenjen za sve vrste obrade kamena, betona, granita.

1.2. GENERIRANJE I PRIJENOS TOPLINE – OPĆE SPOZNAJE

Alati na bazi tvrdog metala redovito se koriste u industrijskoj proizvodnji. Njihova dugotrajnost i isplativost u postupku obrade odvajanjem čestica uvelike ovisi o generiranju i disipaciji topline na sučelju alat/obradak, kao i karakteristici (svojstvu) materijala alata za provođenjem i disipacijom topline. Generirana toplina ovisi o parametrima postupka, materijalu obratka i materijalu alata, dok disipacija topline najviše ovisi o načinu hlađenja sučelja alat/obradak.

Obradni centri koji kao sredstvo hlađenja, ispiranja i podmazivanja (u nastavku SHIP) koriste vodenu emulziju ulja, najčešći su u industrijskoj primjeni. Takva emulzija omogućuje adekvatno inicijalno hlađenje sustava, no u zahtjevnim primjenama, poput obrade tvrdih obradaka, predstavlja problem zbog malog koeficijenta provodnosti te toplinskog kapaciteta emulzije.

Kroz dulji period rada obradnog centra, akumulirana toplina u recirkulirajućoj emulziji smanjuje temperaturni gradijent te mogućnost odvođenja topline. Rijetko se primijenjuju zatvoreni sustavi s izmjenjivačem topline sredstva za hlađenje te u nekim slučajevima ovaj sustav hlađenja predstavlja usko grlo u proizvodnji. Također, takva emulzija predstavlja problem zbrinjavanja nakon iskorištenja.

Rješenje ovog ali i niza drugih problema, dolazi u obliku primjene sredstva za hlađenje koje je temperaturom ispod sobne temeprature, poput tekućeg ugljikovog dioksida, ili još bolje, tekućeg dušika.

Hlađenje u struji tekućeg dušika omogućuje veliki temperaturni gradijent te efikasnije odvođenje topline sa sučelja alata/obradak, u usporedbi s vodenom emulzijom, uljem i sličnim sredstvima za hlađenje. Tekući dušik pritom isparava u atmosferu, bez tragova i potrebe za zbrinjavanjem i potpuno je neškodljiv za ljude i okoliš.

Eventualni logistički problem proizlazi iz nemogućnosti primjene hlađenja tekućim dušikom u zatvorenom sustavu s recirkulacijom čime potencijalno rastu inicijalni investicijski troškovi u smjeru uspostave postrojenja za proizvodnju samog medija na licu mjesta. Logički se nameće zaključak kako je takvo rješenje isplativije što je veći broj obradnih centara unutar pogona prilagođen radu sa kriogenim hlađenjem.

Smanjenje akumulirane topline u alatu sprječava bilo kakva temperaturna naprezanja (dilatacije i kontrakcije) zbog nehomogenosti faza (kobalta i karbida), osigurava postojanu geometriju alata na mikroskopskoj razini, što kao povoljni faktor osigurava i preduvjete za dimenzijsku točnost i kontinuitet kvalitete površine obratka. Naknadno, smanjuje se toplinski umor, kao i trošenje alata uslijed oksidacije ili temepraturne razgradnje, umora površine itd.

Slijedom navedenih činjenica omogućene su veće brzine rezanja (eng. *material removal rate* ili MRR), iz razloga što je alat pri zahtjevnijim parametrima obrade (posmak, broj okretaja, brzina) toplinski i dimenzijski stabilan, a povećana brzina rotacije obratka smanjuje mogućnost pojave naljepka (eng. *build-up-edge* ili BUE), te prijevremenog trošenja alata.

2. ANALIZA TRENUTNOG STANJA U PODRUČJU ISTRAŽIVANJA

U nastavku je predstavljen presjek rezultata niza različitih istraživanja implementacije kriogenog hlađenja u obradi odvajanjem čestica. U općem smislu, fokus analiziranih istraživanja bazira se na analizi sljedećih pokazatelja: **količina odvojenog materijala (eng. *Material Removale Rate* ili MRR)**, **primijenjena sila prilikom rezanja**, **faktor trenja**, **smična sila**, **parametar hrapavosti Ra**, **analiza trošenja alata**.

U znanstvenim člancima su korišteni obratci legura na bazi volframa, nehrđajućeg čelika, te legiranog ugljičnog čelika.

U istraživanju utjecaja kriogenog hlađenja, autora Srinivasa Rao Nandam *et al.*, obrađivane su legure na bazi volframa sljedećih kemijskih sastava:

1. 90W-7Ni-2Fe-1Co
2. 93W-4,9Ni-1,4Fe-0,7Co
3. 95W-3,5Ni-1Fe-0,5Co.

Obrada odvajanjem čestica vršila se oštricama izrađenim od tvrdog metala, oznake K20 (ISO 6 R 2525). Volframove legure 1 i 2 su duktilnije, dok legura 3 pokazuje sklonost krkom lomu [3].

2.1. Efikasnost obrade

Na slici 1, iz prethodno navedenog istraživanja, prikazana je razlika brzina odnošenja materijala (eng. *Material Removal Rate* ili MRR) u procesima gdje se kao sredstvo hlađenja, ispiranja i podmazivanja (u nastavku SHIP) koristi emulzija naspram onih u kojima se koristi tekući dušik.

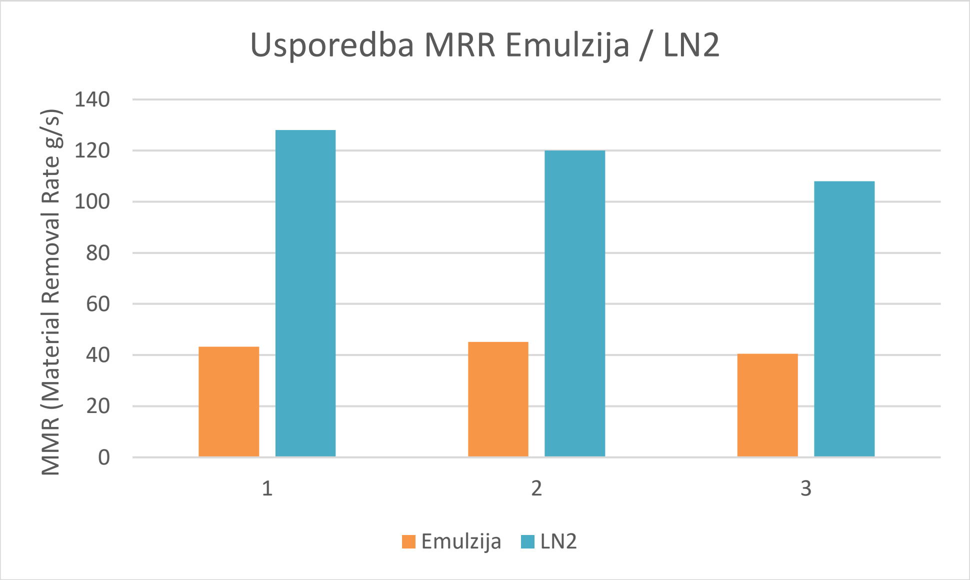

Slika 1: Usporedba brzine odnošenja materijala u ovisnosti o SHIP-u triju volframovih legura [3]

U pogledu sila kojima je potrebno pristupiti uklanjanju čestica zahvatom oštrice alata i obratka, nekoliko istraživanja donosi vrlo pozitivne rezultate uslijed primjene kriogenog hlađenja. Na slici 2 prikazana je razlika iznosa rezultantne sile zahvata alata i obratka u ovisnosti o primjeni različitih sredstava za hlađenje i podmazivanje: emulzije i tekućeg dušika (LN2).

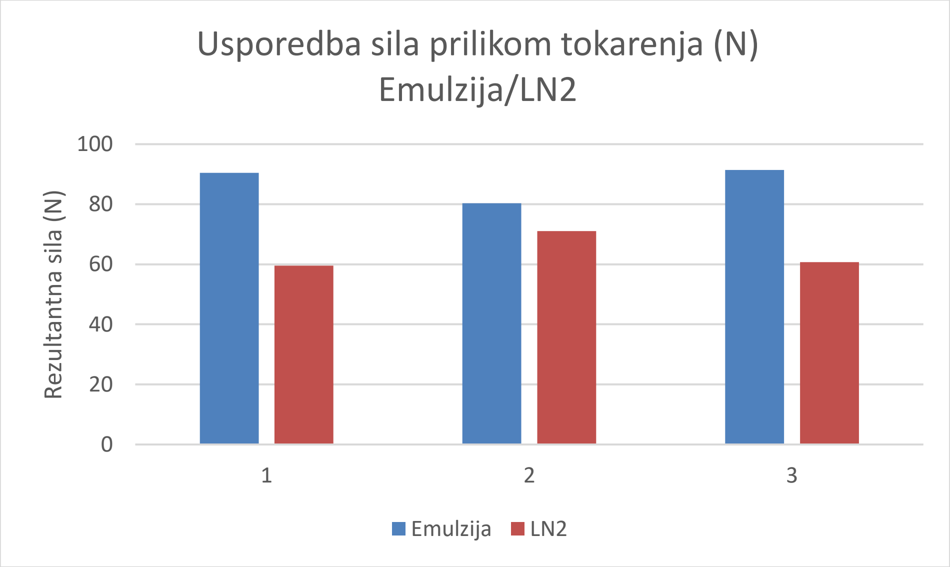

Slika 2: Usporedba sila rezanja u ovisnosti o SHIP-u triju volframovih legura [3]

Slika 2 prikazuje smanjenje potrebne sile rezanja (ovdje prikazane rezultantnom silom) za sve 3 legure na bazi volframa, u slučaju kada se kao sredstvo hlađenja i podmazivanja koristi tekući dušik, u odnosu na sve slučajeve kada je korištena emulzija. U nekim slučajevima sile su reducirane i za 30 %.

Sličan trend zabilježen je i u istraživanju S.Arun Kumar *et al.*, što je i prikazano slikom 3, prilikom obrade čelika (AISI: 4340; IS: 40Ni2Cr1Mo28) [4].

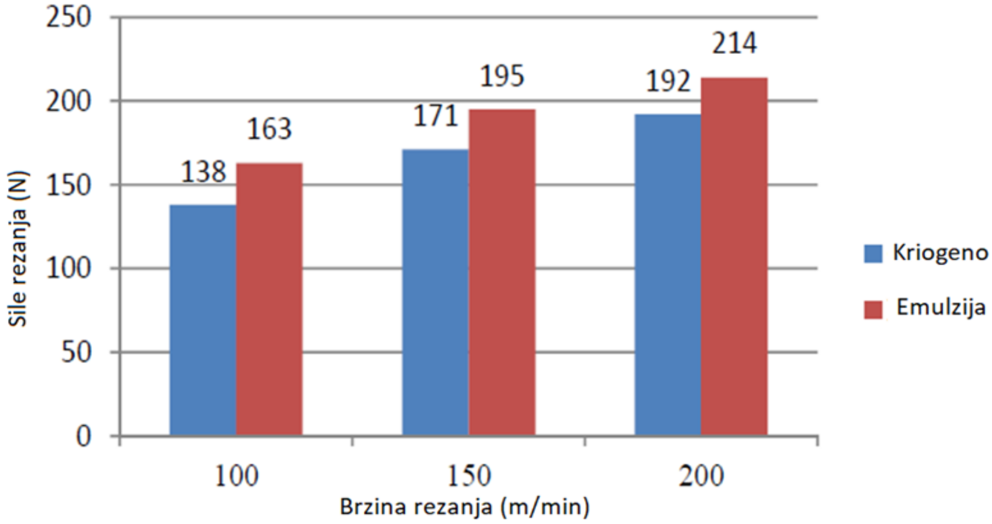

Slika 3: Usporedba sila rezanja u ovisnosti o brzini rezanja i SHIP-u čelika [4]

Na slici 3 primjetno je smanjenje sila rezanja spomenute vrste čelika u slučaju primjene kriogenog hlađenja tekućim dušikom, neovisno o brzinama rezanja. Smanjenje sile rezanja primjenom kriogenog hlađenja u nekim slučajevima doseže gotovo i do 20 % u odnosu na hlađenje emulzijom. Važan aspekt u primjeni tekućeg dušika jest i činjenica da, u najmanju ruku, ne narušava faktor trenja, a u nizu slučajeva ga uvelike i reducira – što je prikazano na slici 4.

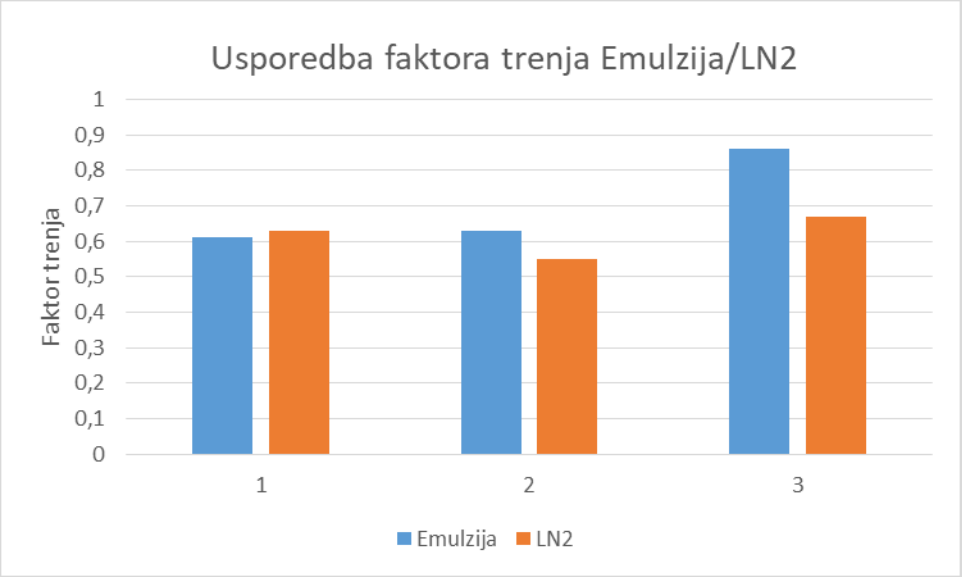

Slika 4: Ovisnost faktora trenja o SHIP-u pri obradi triju volframovih legura [3]

Slikom 4 prikazano je kako faktor trenja ovisi o sredstvu za hlađenje, koje je ujedno i sredstvo za podmazivanje, ali i o materijalu obratka u zahvatu. Ispitivanje je provedeno na već spomenute tri legure na bazi volframa. Primjetno je da za istu leguru, faktor trenja niti u jednom slučaju ne doživljava signifikantan porast s primjenom tekućeg dušika, već se u većem broju slučajeva čak i smanjuje u odnosu na primjenu emulzije.

Intenzivno hlađenje omogućuje postojanu geometriju oštrice na mikroskopskoj razini, dok tekući dušik ujedino djeluje kao mazivo na sučelju alat/obradak, smanjujući faktor trenja. Tekući dušik stvara površinski mikrofilm te hidrodinamički podmazuje površine u kontaktu. Ovisno o materijalu alata i obratka, taj efekt može biti i izraženiji [6].

Ovo je dodatno potkrijepljeno i posredno, efektom generiranja topline kojega su u svom istraživanju u obradi nehrđajučeg čelika dokumentirali P. Sivaiah *et al.*, a što je prikazano dijagramom na slici 5 [5].

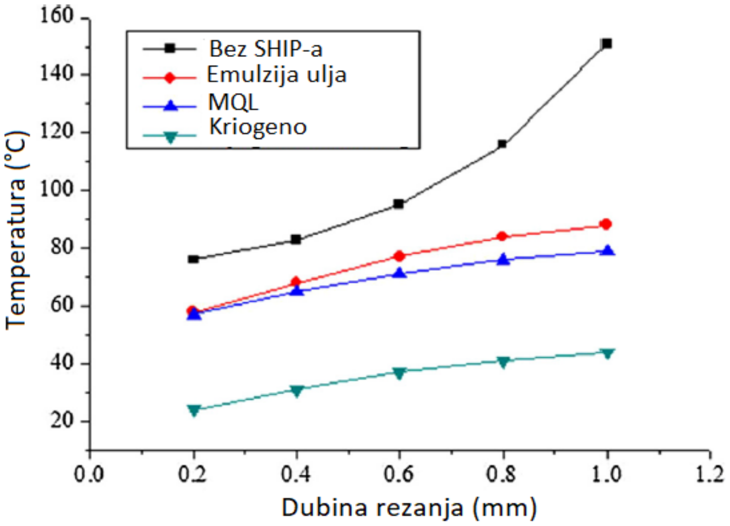

Slika 5: Promjena temperature s dubinom rezanja u ovisnosti o primijenjenom SHIP-u [5]

Smanjenjem faktora trenja primjenom kriogenog hlađenja, osiguravaju se uvjeti za najmanji razvoj topline u usporedbi s drugim sredstvima za hlađenje i podmazivanje, čak i uz kontinuirani porast dubine rezanja (slika 5).

2.2. Kvaliteta površine obratka

U nastavku su prikazane postignute kvalitete površina obradaka iskazane amplitudnim parametrom Ra, odnosno srednjim aritmetičkim odstupanjem profila. Prikazani rezultati proizašli su iz nekolicine istraživanja koja sva redom u korelaciju dovode primijenjeni SHIP i promjenu hrapavosti površine (Ra) [3-5], korištenjem tekućeg dušika kao SHIP-a, u slučajevima obrade volframovih legura [3] te dviju vrsta čelika (martenzitni nehrđajući 17%Cr i 4%Ni [4] i čelik oznake 40Ni2Cr1Mo28 [5]).

Ranije spomenuto bolje odvođenje topline ima za posljedicu zadržavanje geometrije rezne oštrice, tj. onemogućuje prijevremeno otupljivanje oštrice, koje za sobom nosi pogoršanje stanja površinske hrapavosti. U slučaju volframovih legura te nehrđajućeg i legiranog čelika, otkrivena su značajna poboljšanja kvalitete površine.

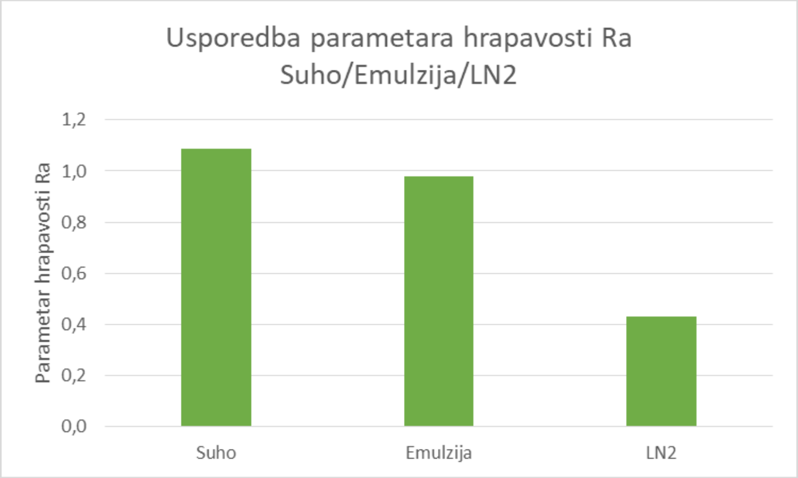

Slika 5: Ovisnost hrapavosti površine obratka nehrđajućeg martenzitnog čelika o primijenjenom SHIP-u [4]

Autori Srinivasa Rao Nandama *et al.* u svom su radu predočili najjednostavniji prikaz prednosti primjene tekućeg dušika u pogledu osiguranja visoke kvalitete površine obradaka na bazi volframa. Na slici 6 jasno je prikazano koliko je hrapavost obrađene površine manja ukoliko se kao SHIP koristi tekući dušik, u odnosu na suhu obradu ili primjenu emulzije [3].

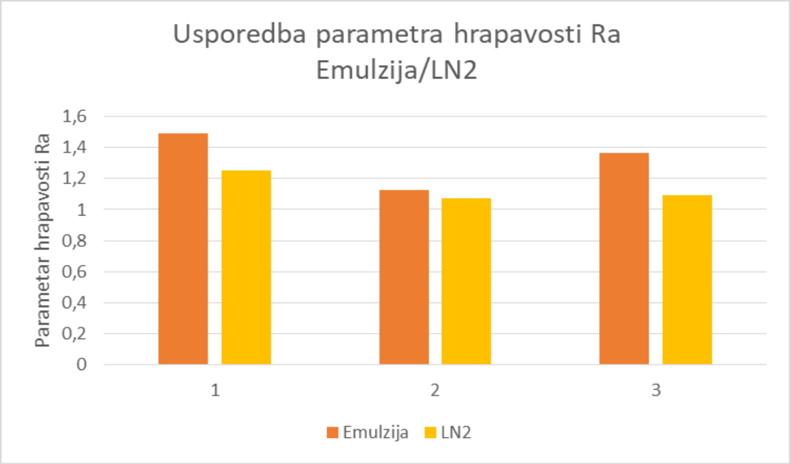

Slika 6: Ovisnost hrapavosti površine obratka (Ra) o primijenjenom SHIP-u pri obradi triju volframovih legura [3]

Slika 6 ukazuje kako je u provedenom istraživanju u svakom od slučajeva konačna kvaliteta površine obradaka bila bolja ukoliko se kao SHIP koristio tekući dušik, u odnosu na klasičnu obradu uz primjenu emulzije. Legure obradaka (označene s 1, 2 i 3) ranije su spomenute legure na bazi volframa.

Autori P. Sivaiah *et al.* na slici 7 demonstriraju sličan efekt na čeliku oznake 40Ni2Cr1Mo28 [5].

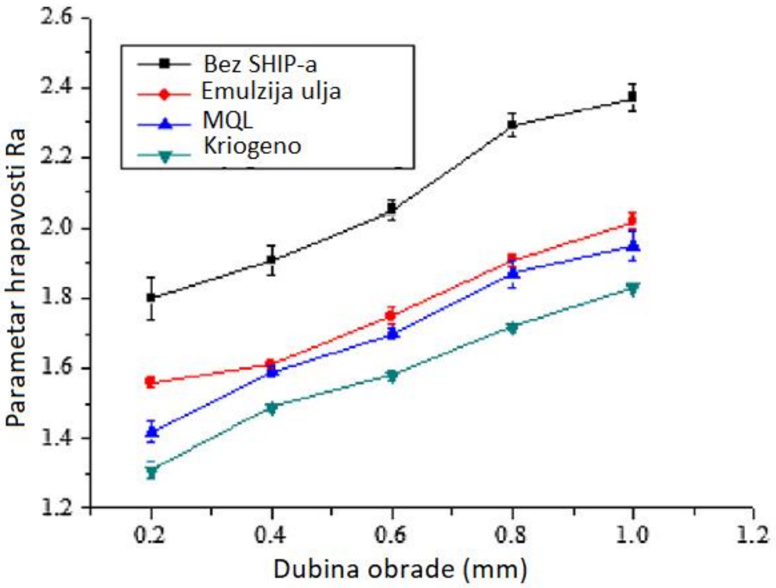

Slika 7: Promjena hrapavosti s dubinom obrade u ovisnosti o primijenjenom SHIP-u [5]

Iz dijagrama na slici 7 vidljivo je kako se, neovisno o primijenjenom SHIP-u, povećava hrapavost površine čeličnih obradaka (čelika oznake 40Ni2Cr1Mo28) s povećanjem dubine obrade. Međutim, vrijednost istraživanja provedenog od strane navedenog autora jest upravo u usporedbi utjecaja primijenjenog SHIP-a na incijalnu hrapavost te na trend njenog povećanja s povećanjem dubine rezanja. U pogledu analize kriogenog hlađenja, posebno je interesantno što su za sve dubine rezanja površine obradaka zadržale najvišu razinu kvalitete (izraženo najmanjim vrijednostima Ra) u usporedbi sa svim drugim opcijama.

Slika 8 potvrđuje tezu o smanjenju hrapavosti primjenom tekućeg dušika kod nešto duktilnijih volframovih legura 1 i 2 u odnosu na leguru 3, čija je krhkost više izražena.

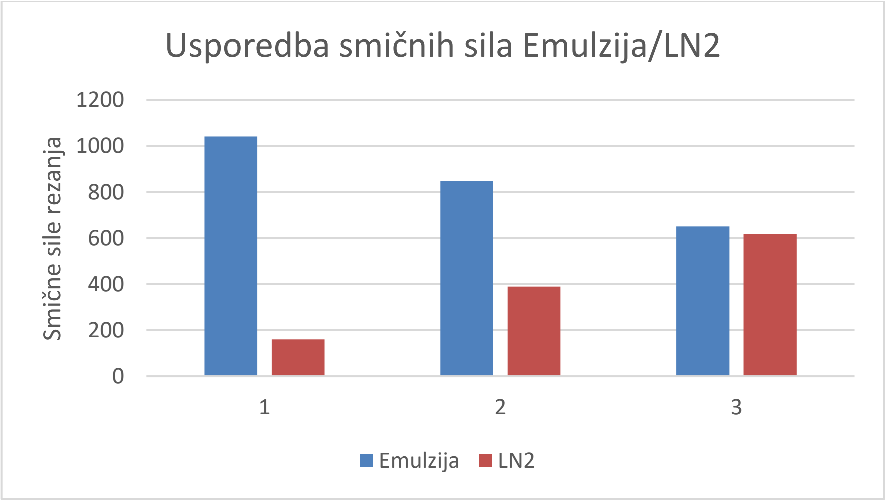

Slika 8: Ovisnost smičnih sila o primijenjenom SHIP-u pri obradi triju volframovih legura [3]

Tekući dušik omogućuje višestruko smanjenje smičnog naprezanja na sučelju alat/obradak, koje se smatra nepoželjnim [3]. Spomenuto smično naprezanje svojom pojavom smanjuje efikasnost alata na način da alat u svom radu ne reže nego deformira površinu, stvarajući mogućnost pojave *build-up-edge*, lokalne nepravilne geometrije oštrice te prijevremenog trošenja alata.

2.3. Trošenje alata

Jednako značajano, a u pogonima s velikosersijskom prozvodnjom možda i najznačajniji pozitivan efekt primjene kriogenog hlađenja, odnosno tekućeg dušika kao SHIP-a, jest smanjenje trošenja alata. Time se osim troškova za sam alat, smanjuju i indirektni troškovi zaustavljanja proizvodnje te obradnih centara i radnika *u praznom hodu.*

Prikaz trošenja prednje i stražnje površine rezne oštrice u obradi nehrđajućeg čelika dan je slikom 9, nastale rezultatom istraživanja P. Sivaiah e*t al.* [5].

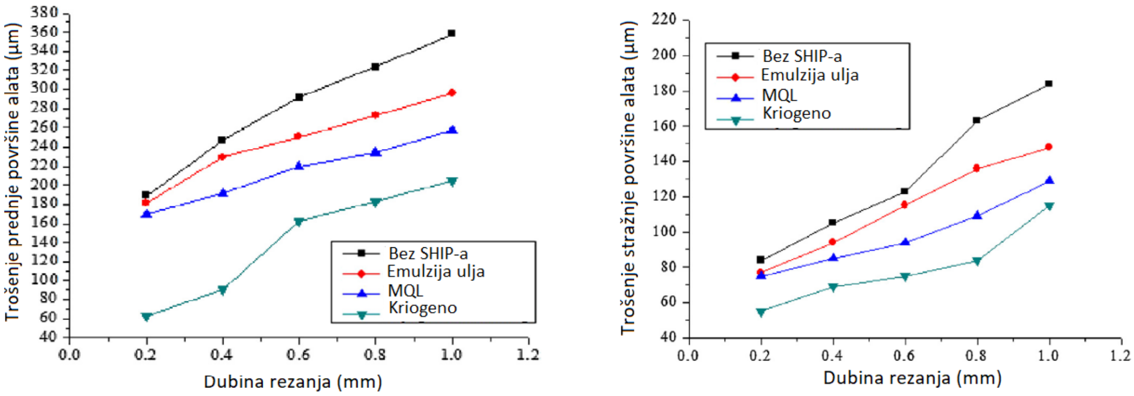

Slika 9: Ovinosti trošenja alata o primijenjenom SHIP-u i dubini rezanja [5]

Slika 9, na primjeru prednje i stražnje strane rezne oštrice od prevučenog tvrdog metala (prevlaka TiAlN), prikazuje koliko gubitak materijala može biti reduciran primjenom kriogenog hlađenja u odnosu na neki drugi SHIP, i to u slučaju svih ispitivanih dubina rezanja. Gubitak materijala oštrice, ovisno o promatranoj površini alata i parametrima rezanja, može biti i dvostruko manji ukoliko se emulzija zamijeni kriogenim hlađenjem.

Na slici 10 prikazane su snimke oštrice alata snimljene skenirajućim elektronskim mirkoskopom, nakon 30 minutne eksploatacije alata. Vidljivo je značajno manje trošenje oštrice prilikom uporabe tekućeg dušika kao SHIP. Niže radne temperature smanjuju pojave adhezijskog naljepljivanja te otkidanja komada prilikom procesa obrade. Odsutstvo naljepka, odnosno *build-up-edge*, također povoljno utječe na trajnost oštrice, dodatno smanjujući adhezijsko i abrazijsko trošenje [5].

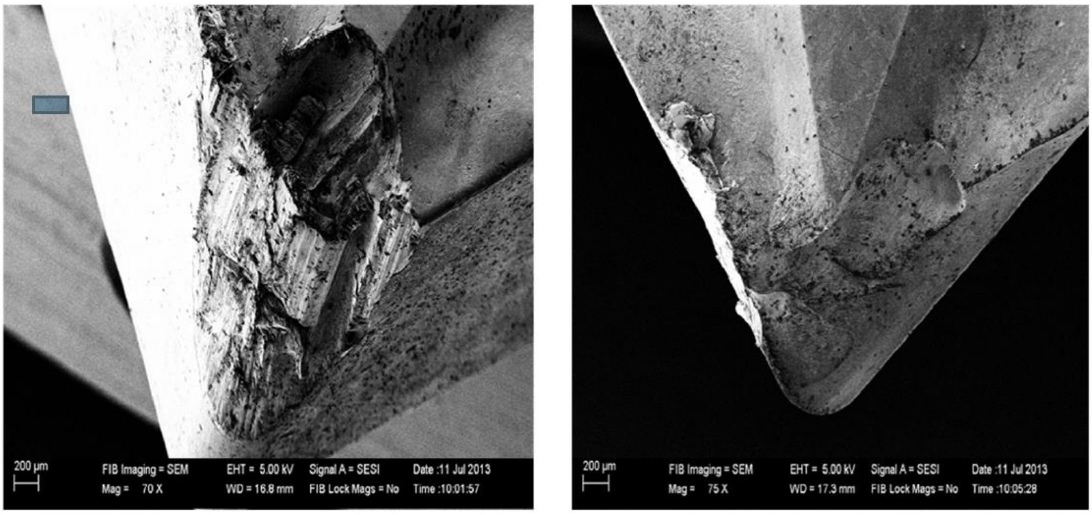

Slika 10: SEM snimke rezne oštrice nakon eksploatacije: emulzija (lijevo) i tekući dušik (desno) [5]

Bitna stavka u pogledu trošenja alata, potencijalnog oštećenja strojeva, opreme i radnika, svakako je i geometrija srha koji nastaje tijekom obrade. Dimenzije, geometrija, a uvelike i volumen nastalog srha, mogu biti odgovorni za značajne troškove indirektnog karaktera. Na izgled generiranog srha utječe cijeli niz faktora poput parametara obrade, materijala obratka, ali i primijenjenog SHIP-a. Slika 11 prikazuje izgled generirane odvojene čestice (srha), prilikom procesa obrade odvajanjem čestica – tokarenjem. Parametri postupka u analiziranom istraživanju provedenom od strane P. Sivaiah *et al.* bili su sljedeći: brzina rezanja = 78,5 m/min, posmak = 0,143 mm/okr, dubina = 0,2 mm [5].

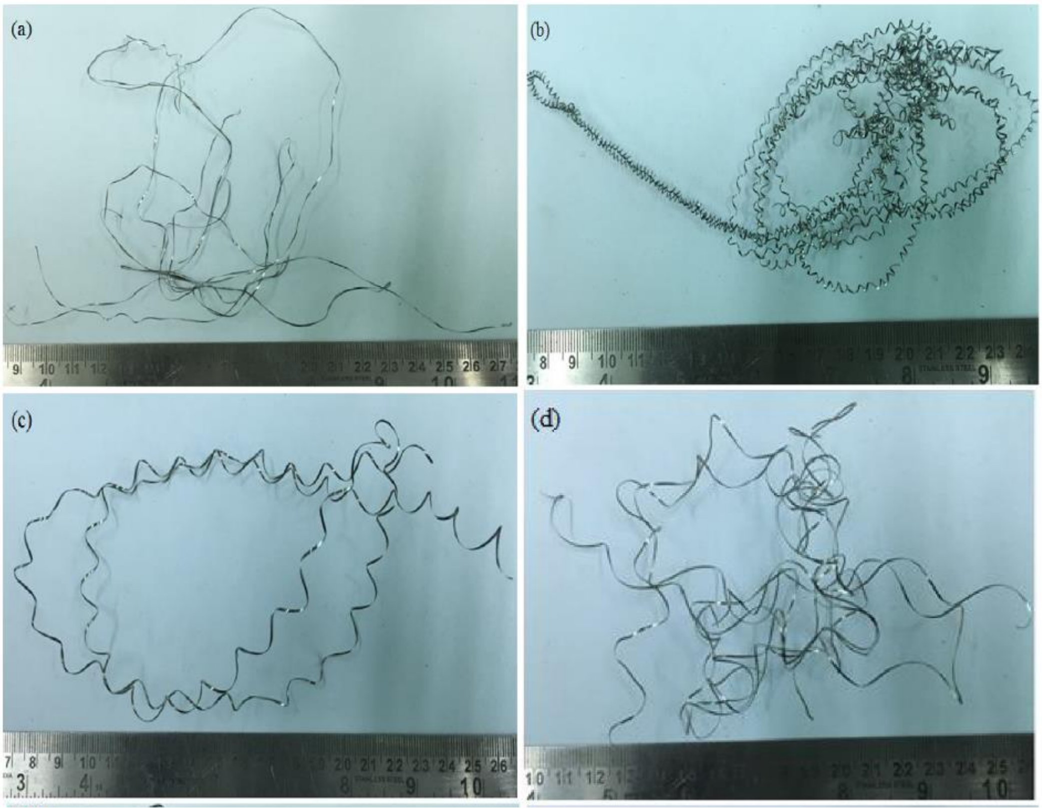

Slika 11: Izgled odvojene čestice (srha): a) Kriogeno hlađenje, b) MQL hlađenje, c) Hlađenje emulzijom, d) Suho tokarenje – bez SHIP-a [5]

Vidljivo je kako je čestica (a) najpovoljnija sa stajališta usmjerenosti i volumena kojega zauzima. Putanja takve čestice unutar obradnog centra je lakše predvidiva i lakše se kontrolira, ne zapliće se oko pokretnih dijelova alata i ne predstavlja veliki rizik po zdravlje radnika. Takva čestica se ujedno i lakše skladišti i jeftinija je za transport.

2.4. Ušteda energije

Slika 12 prikazuje potrošnju električne energije obradnog centra prilikom hlađenja sučelja alat/obradak u slučajevima korištenja emulzije i tekućeg dušika [5].

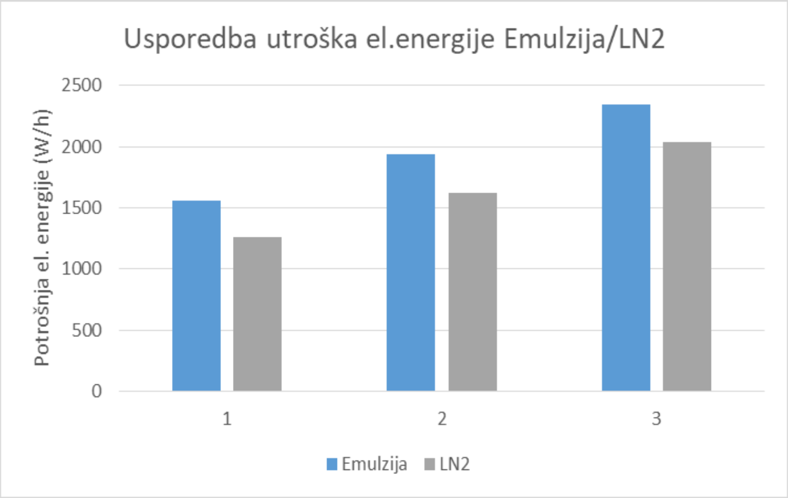

Slika 12: Usporedba potrošnje el. energije pri brzinama obrade: 1) 100 m/min, 2) 150 m/min, 3) 200 m/min [5]

Rezultati prikazani histogramom na slici 12 ukazuju na ujednačeno smanjenje potrošnje energije prilikom obrade čelika, primjenom tekućeg dušika pri sljedećim brzinama obrade: 100 m/min, 150 m/min i 200 m/min. Uštede energije kreću se između 300 i 320 W/h, odnosno između 10-20 %, u korist hlađenja tekućim dušikom, u usporedbi sa hlađenjem emulzijom vode i ulja.

3. ZAKLJUČAK

Unosom topline u obradni sustav, ovisno o vrsti i svojstvima materijala i gustoći toplinskog toka, dolazi do slabljenja ključnih svojstva materijala rezne oštrice, poput tvrdoće i, posljedično, otpornosti na abrazijsko trošenje, čvrstoće te dimenzijske stabilnosti alata.

Zbog negativne promjene mehaničkih svojstava, dolazi do bržeg trošenja ili potpunog otkazivanja alata, lošije površinske kvalitete (hrapavost) obratka kao i poskupljenja procesa zbog češće nabave alata, potrebe za dodatnim naknadnim obradama i zaustavljanja proizvodne linije.

U zahtjevnim postupcima obrade odvajanjem čestica, struja tekućeg dušika primijenjena na hlađenje sučelja obradak/alat odvodi toplinu te na taj način onemogućuje bilo kakve negativne promjene koje se javljaju zbog utjecaja povećanog toplinskog toka te povišenja temperature.

Sniženjem radne temperature sučelja alat/obradak moguća su i poboljšanja parametara prozvodnje poput povećanja brzine odnošenja materijala (MRR), smanjenja primijenjene sile zbog smanjenja faktora trenja, posljedičnog smanjenja zagrijavanja alata i obratka te ukupnog poboljšanja stanja obrađivane površine (parametar hrapavosti).

Također, povećanjem brzine odnošenja materijala, kao i brzinom posmaka, pozitivno se utječe i na generiranu odvojenu česticu te se smanjuje mogućnost kontinuiteta odvojene čestice. Čestica se, poželjno, razlama na manje komade, koji povoljno utječu na smanjenje trošenja stražnje površine alata, uz manje rizike za oštećenja obradnih centara i ozljede radnika te su jednostavnije za skladištenje i odvoz.

Zbog duljeg trajanja oštrica alata, bolje završne obrade, nedostatka čišćenja obradaka, manje potrošnje el. energije obradnih centara, moguće je amortizirati početne investicijske troškove nastale kupovinom postrojenja za proizvodnju i dobavu tekućeg dušika. Primjenom tekućeg dušika kao SHIP-a, odnosno kriogenog hlađenja, povoljno se utječe na ekološki otisak proizvodnog pogona zbog uklanjanja potrebe za zbrinjavanjem SHIP-a te zbog uštede električne energije.

REFERENCE

[1] Filetin T., Kovačićek F., Indof J., Svojstva i primjena materijala, FSB, 2013., Zagreb.

[2] Tehnologija proizvodnje nemetalnog i klasičnog tvrdog metala, SinterMAK d.o.o.

[3] Srinivasa Rao Nandama, U. Ravikiran and A. Anand Rao, Machining of Tungsten Heavy Alloy under Cryogenic Environment, Procedia Materials Science 6 (2014) 296 – 303.

[4] S.Arun Kumara, V.G.Yoganath, Prasad Krishna, Machinability of Hardened Alloy Steel using Cryogenic Machining, Materials Today: Proceedings 5 (2018) 8159–8167.

[5] P. Sivaiah, D. Chakradhar, Effect of cryogenic coolant on turning performance characteristics during machining of 17-4 PH stainless steel: A comparison with MQL, wet, dry machining, CIRP Journal of Manufacturing Science and Technology (2018).

[6] Shane Y. Hong, Lubrication mechanisms of LN2 in ecological cryogenic machining, Science and Technology, 10:133–155.

SILICON-SUBSTITUTED CALCIUM PHOSPHATES FOR BONE TISSUE ENGINEERING APPLICATIONS

SILICIJEM SUPSTITUIRANI KALCIJEVI FOSFATI ZA PRIMJENE U INŽENJERSTVU KOŠTANOG TKIVA

Antonia Ressler, Marica Ivanković, Hrvoje Ivanković

University of Zagreb, Faculty of Chemical Engineering and Technology, Marulićev trg 19, HR-10000 Zagreb, Croatia

Abstract

Silicon-substituted calcium phosphate (CP) powders were prepared by wet precipitation method, at 50°C, using $CaCO_3$, $(NH_2)_2CO-H_3PO_4$), and $Si(OCH_2CH_3)_4$ as reagents. Fourier transform infrared spectroscopy (FTIR), X-ray diffraction (XRD) and Rietveld refinement were used to characterize the samples. The raw precipitated powders were composed of carbonated hydroxyapatite and octacalcium phosphate. After heat treatment at 1200°C well crystalline phases of β-tricalcium phosphate (β-TCP, $Ca_3(PO_4)_2$) and α-tricalcium phosphate (α-TCP) were detected.

Keywords: *hydroxyapatite, octacalcium phosphate, tricalcium phosphates, silicon*

Sažetak

Silicijem supstituirani kalcijevi fosfati pripravljeni su mokrim precipitacijskim postupkom, pri 50°C, korištenjem reagensa: $CaCO_3$, $(NH_2)_2CO-H_3PO_4$), i $Si(OCH_2CH_3)_4$. Karakterizacija materijala provedena je pomoću infracrvene spektroskopije s Fourierovim transformacijama (FTIR), rendgenske difrakcijske analize (XRD) i Rietveldovog utočnjavanja. Sirovi precipitirani prašci sadržavali su karbonatni hidroksiapatit i oktakalcijev fosfat. Nakon toplinske obrade pri 1200°C detektirane su kristalne faze β-trikalcijevog fosfata (β-TCP, $Ca_3(PO_4)_2$) i α-trikalcijevog fosfata (α-TCP).

Ključne riječi: *hidroksiapatit, oktakalcijev fosfat, trikalcijevi fosfati, silicij*

1. INTRODUCTION

The development of novel materials as bone tissue substitutes is an attractive research area where calcium phosphate (CP)-based ceramics play a leading role. Synthetic hydroxyapatite (HAp), $Ca_{10}(PO_4)_6(OH)_2$), is the most widely used CaP for hard tissue applications due to its compositional similarity to biological apatite, excellent biocompatibility and bioactivity [1]. In addition to HAp, other CaPs, more resorbable than HAp, such as octacalcium phosphate (OCP), and tricalcium phosphates (TCP), are gaining increasing attention.

There have been many studies demonstrating the importance of trace elements in bone formation [2, 3]. Today, one of the most widely used approach to improve the biological and physicochemical properties of CaPs is ionic substitution with trace ions. Silicon has been noted to be an important trace element in osteogenesis, with a strong stimulatory effect on cellular activities such as proliferation, differentiation, and mineralization of osteoblast cells as well as facilitating osteogenic differentiation of mesenchymal stem cells [4, 5].

The aim of this study was to synthesize silicon doped calcium phosphates, with varying silicon dopant content, by an aqueous precipitation method, and to study the effect of the doping on phase composition and crystal structure of synthesized materials.

2. EXPERIMENTAL

To prepare a silicon-free, stoichiometric hydroxyapatite (denoted as CP_Si_0), as a reference material, and silicon-doped calcium phosphates a wet precipitation method was used, with $CaCO_3$, urea phosphate (UPH), $(NH_2)_2CO\text{-}H_3PO_4$), and $Si(OCH_2CH_3)_4$ (TEOS) as calcium, phosphorus and silicon precursors, respectively. The amount of reagents was calculated on the assumption that SiO_4^{4-} would substitute $PO_4^{\ 3-}$ in hydroxyapatite, keeping the Ca/(P+Si) ratio of 1.67. $CaCO_3$ was obtained from natural source (cuttlefish bone) as previously described [6]. $CaCO_3$ was dissolved in acetic aqueous solution (pH = 4.60) and then urea phosphate was added. Stirring was continued for 5 days at 50 °C followed by overnight aging at room temperature.

To prepare Si-doped samples with different doping level three different concentrations of TEOS were used (1, 5 and 10 mol%) and the prepared samples are denoted as CP_Si_1, CP_Si_5 and CP_Si_10, respectively. All prepared powders were heat-treated at 1200 °C for 2 h.

The Fourier transform infrared spectra (FTIR) of as-prepared powders were recorded by attenuated total reflectance (ATR) spectrometer for solids with diamond crystal (Bruker Vertex 70) at 20 °C, over the spectral range of 4000 – 400 cm^{-1}, with 32 scans and 4 cm^{-1} of resolution.

Mineralogical composition of the as-prepared powders and the heat-treated powders were determined using X-ray diffraction analysis (Shimadzu XRD-6000) with Cu K_α radiation operated at 40 kV and 30 mA, in the range of $3° < 2\theta > 60°$, at a step size of 0.02°

and a count time of 5 s. Identification of phases was achieved by comparing the experimental diffraction patterns with reference spectra compiled by the international Centre for Diffraction Data (ICDD) . The lattice parameters, the cell volume *V* and phase composition of prepared powders were determined by Rietveld refinement of the XRD data using software DIFFRAC.SUITE TOPAS V.5.0. (Bruker).

3. RESULTS AND DISCUSSION

The FTIR spectra of four raw precipitated materials were found to be very similar (Fig.1). There was no noticeable change of the peak intensities and widths with increasing silicon content. All FTIR spectra show characteristic pattern of a carbonated hydroxyapatite. The bands at 1077, 1020 and 962 cm^{-1} correspond to P–O stretching vibration. The doublet at 600 and 560 cm^{-1} and the band at 465 cm^{-1} correspond to O–P–O bending vibrations. The band at 874 and two bands at 1450 and 1420 cm^{-1} were assigned the vibrations of carbonate groups located in the B site of the apatite (CO_3^{2-} substituting PO_4^{3-})[7, 8, 9]. Absorption bands at 522 cm^{-1} could be associated with HPO_4^{2-} groups that can indicate precipitation of other calcium phosphate phases [10, 11].

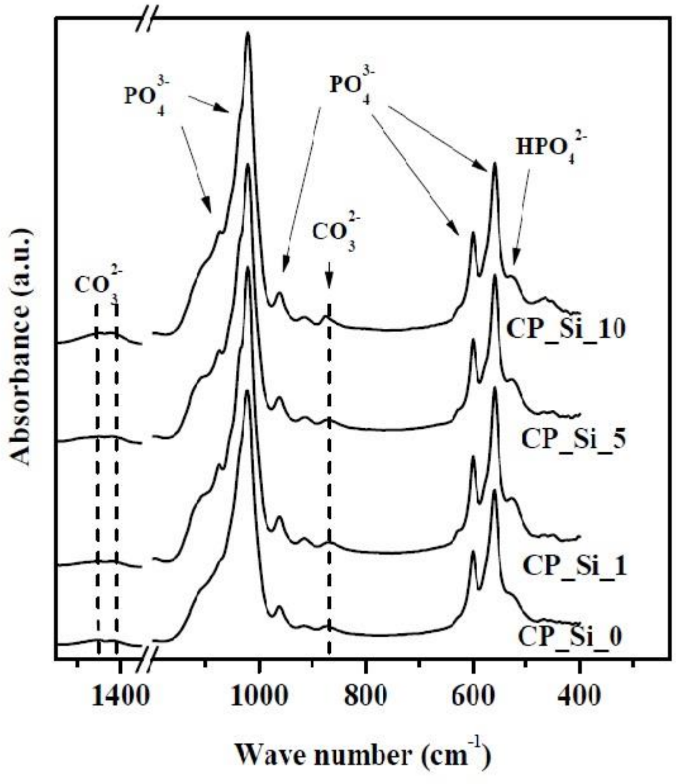

Fig. 1. FTIR spectra of raw precipitated powders.

XRD patterns of as-prepared powders are shown in Fig. 2.

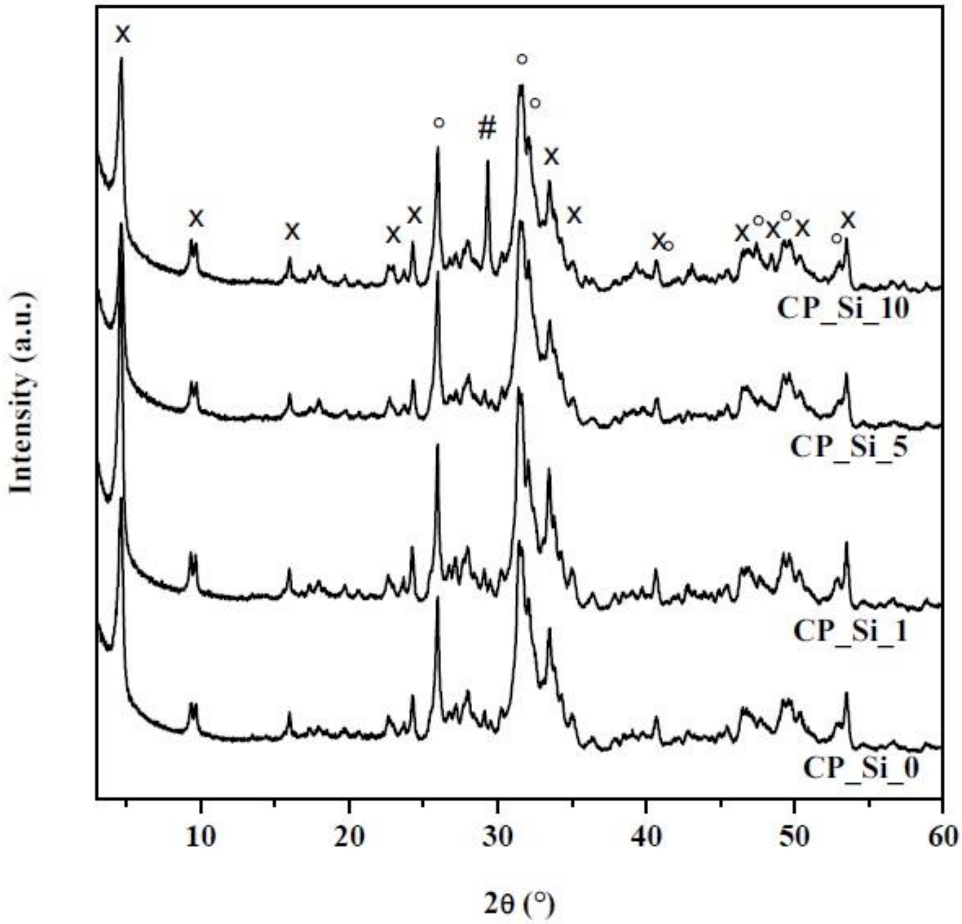

Fig. 2. XRD patterns of as-prepared powders. Phases are marked as follows: hydroxyapatite, HAp (°); octacalcium phosphate, OCP (ˣ); calcium carbonate, $CaCO_3$ (#).

The silicon doping does not appear to affect the diffraction pattern of raw precipitated powders. The qualitative analysis of XRD data indicated the presence of two calcium phosphate phases: hydroxyapatite and OCP. In the powder CP_Si_10 a small quantity of $CaCO_3$ was detected as well. The OCP phase is considered to be the important one as it participates in bone formation and also because it is a precursor of the HAp phase [12].

Results of quantitative phase analysis and the lattice parameters of HAp and OCP phase in as prepared powders, determined by Rietveld refinement of the XRD data, are shown in Table 1 and 2, respectively.

Tab. 1. Quantitative analysis of calcium phosphate phases in the as-prepared powders performed by Rietveld refinement of the XRD data

	HAp phase	OCP phase	$CaCO_3$
Sample		**Wt. %**	
CP_Si_0	63.68	36.32	
CP_Si_1	60.27	39.73	
CP_Si_5	50.63	49.37	
CP_Si_10	53.13	43.91	2.96

Tab. 2. Unit cell parameters of HAp and OCP phase in the as prepared powders

	HAp phase				
Sample	**V (Å^3)**	**a (Å)**	**b (Å)**	**c (Å)**	**Density (g/cm^3)**
CP_Si_0	533.508(4)	9,467446	-	6,872977	3.121
CP_Si_1	533.782(4)	9,467446	-	6,873088	3.119
CP_Si_5	536.203(4)	9,496011	-	6,866201	3.105
CP_Si_10	532.493(2)	9,448159	-	6,887934	3.127
	OCP phase				
	V (Å^3)	**a (Å)**	**b (Å)**	**c (Å)**	**Density (g/cm^3)**
CP_Si_0	1222.354(2)	19.707654	9.532881	6,859621	2.670
CP_Si_1	1221.907(3)	19.714513	9.531926	6,856358	2.671
CP_Si_5	1221.700(6)	19.700521	9.534793	6,855265	2.671
CP_Si_10	1223.355(9)	19.713604	9.538213	6,856065	2.667

It is noteworthy that the relative weight fractions of crystalline phases given in Table 1 may be overestimated if amorphous phases are present in samples. The Rietveld method assumes that all phases are crystalline. To get more accurate results, a quantitative analysis, with an internal standard, needs to be made.

As seen from Table 2 no systematic variations in lattice parameters and unit cell volumes of HAp and OCP phase occurred with increasing silicon content. Similar results are reported by Arcos and Leventouri [13, 14].

It is fair to say that FTIR and XRD do not directly reveal the substitution of P by Si in the apatite structure. The FTIR characterizations showed that all raw precipitates were carbonated. As the carbonate groups were in the B site of the apatite structure, all the initial silicon could not be in the apatite cell after precipitation. On the hypothesis that the B site must be fully occupied, i.e. containing six ionic groups, and that all the initial phosphate (i.e. 6-x mol) is in this site, the real composition for the B site of the apatite is as follows:
$(PO_4)_{6-x}(CO_3)_y(SiO_4)_z$
In this case the amount of silicate incorporated in the apatite is only
$z = x - y$
where *y* represents the molar number of carbonate. Thus, a part of the initial silicon, equivalent to the *y* mole of carbonate must be in a crystalline or amorphous silicate, as a separate phase. No crystalline silicate phase was detected by XRD. But, due to the measurements precision, traces of a silicate phase in amount below or around the detection limit could not be excluded.

The small quantity of $CaCO_3$ detected in the powder CP_Si_10 indicates that the silicon had not entered completely into the HAp lattice. In this case, the resulting material has a Ca/P+Si molar ratio greater than the stoichiometric value of 1.67; that is, it is calcium rich, resulting in a secondary ($CaCO_3$) phase being observed in the diffraction pattern.

XRD patterns of heat treated powders (Fig.3), at 1200°C, indicated that the samples are composed of different amounts (Table 3) of well crystalline β-tricalcium phosphate (β-TCP, $Ca_3(PO_4)_2$) and α-tricalcium phosphate (α-TCP).

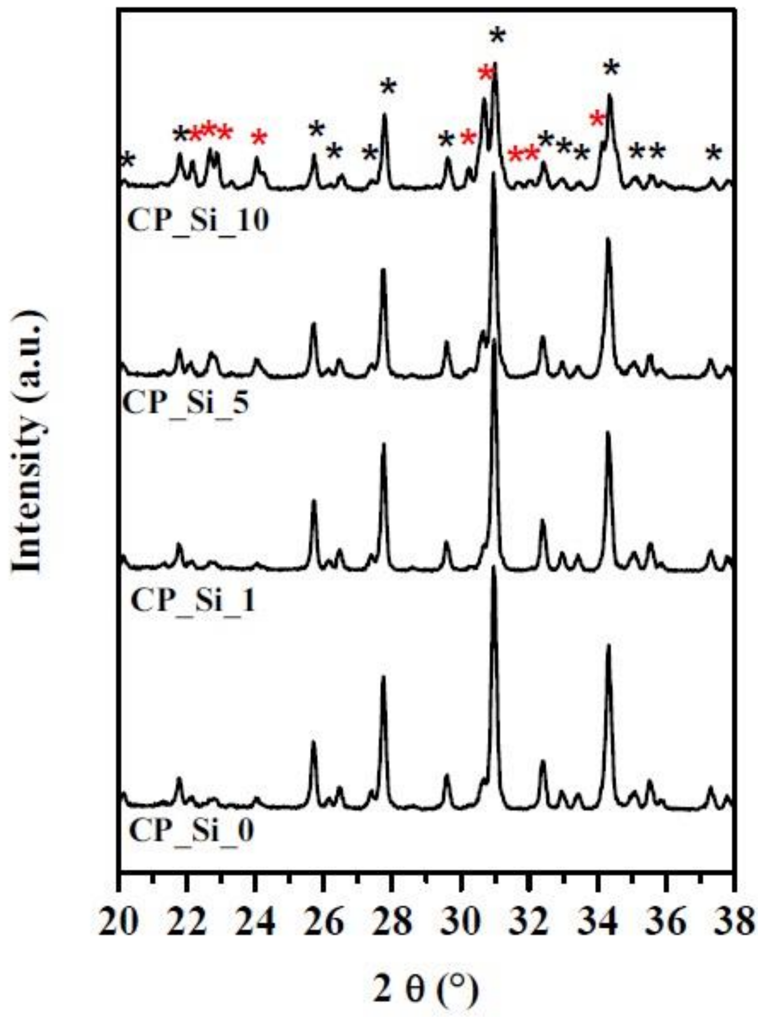

Fig. 3. XRD patterns of the heat-treated samples. Phases are marked as follows: β-tricalcium phosphate, β-TCP (*); α-tricalcium phosphate, α-TCP (*).

Tab. 3. Quantitative analysis of calcium phosphate phases in heat treated powders

	β-TCP	α-TCP	CaO
Sample		**Wt. %**	
CP_Si_0	90.14	9,86	
CP_Si_1	91.85	8,15	
CP_Si_5	78.05	21,95	
CP_Si_10	52.93	49,11	2.96

The formation of α-TCP is expected to occur at higher temperatures (about 1300°C). Sayer et al. [15] have demonstrated that this phase is stabilized by the Si presence and can crystallize from HAp at lower temperatures. Results shown in Table 2 also confirm that silicon act as a stabilizer of the high temperature polymorph α-TCP that is metastable at room temperature. If it is cooled slowly β-TCP becomes the principal phase. As seen from Table 2 by increasing the Si loading the β-α transformation is more inhibited. The α-TCP phase is as biocompatible as β-TCP, but more soluble, and hydrolyses rapidly to calcium-deficient hydroxyapatite, which makes α-TCP a useful component for preparing self-setting osteotransductive bone cements and biodegradable bioceramics and composites for bone repairing [16].

It should be noted that heat treated CP_Si_0 powder also contain α-TCP phase. It could be due to the fact that CP_Si_0 powder is probably not "silicon-free" since $CaCO_3$, obtained from natural source (cuttlefish bone) probably contains a low quantity of silicon, as well.

Acknowledgement(s):
This work has been supported by the Croatian Science Foundation under the project **IP-2014-09-3752.**

REFERENCES

[1] Sadat-Shojai M., Khorasani M. T., Dinpanah-Khoshdargi E, Jamshidi A., Synthesis methods for nanosized hydroxyapatite with diverse structures, Acta Biomaterialia, 9, pp. 7591-7621, (2013).

[2] Boanini E., Gazzano M., Bigi A., Ionic substitutions in calcium phosphates synthesized at low temperature, Acta Biomaterialia, 6, pp. 1882-1894, (2010).

[3] Ran J., Jiang P., Sun G., Ma Z., Hu J., Shen X, Tong H., Comparisons among Mg, Zn, Sr, and Si doped nano-hydroxyapatite/chitosan composites for load-bearing bone tissue engineering applications, Materials chemistry frontiers, 1, pp. 900-910, (2017).

[4] Carlisle E. M., Silicon: a possible factor in bone calcification, Science, 16, pp. 279-280, (1970).

[5] Carlisle E. M., Silicon: A Requirement in Bone Formation Independent of Vitamin D_1, Calcified Tissue International, 33, pp. 27-34, (1981).

[6] Milovac D., Gallego Ferrer G., Ivanković M., Ivanković H., PCL-coated hydroxyapatite scaffold derived from cuttlefish bone: Morphology, mechanical properties and bioactivity, Materials Science and Engineering C, 34, pp. 437-445, (2014).

[7] Bianco A., Cacciotti I., Lombardi M., Montanaro I., Si-substituted hydroxyapatite nanopowders: Synthesis, thermal stability and sinterability, Materials Research Bulletin, 44, pp. 345-354, (2009).

[8] Lafon J. P:, Champion E., Bernache-Assollant D., Processing of AB-type carbonated hydroxyapatite $Ca_{10-x}(PO_4)_{6-x}(CO_3)_x(OH)_{2-x-2y}(CO_3)_y$ ceramics with controlled composition, Journal of the European Ceramic Society, 28, pp. 139-147, (2008).

[9] Ren F., Leng Y., Carbonated Apatite, Type-A or Type-B?, Key Engineering Materials, 493-494, pp. 293-297, (2012).

[10] Qiu Z. Y., Li G., Zhang Y. Q., Liu J., Hu W., Ma J., Zhang S. M., Fine structure analysis and sintering properties of Si-doped hydroxyapatite, Biomedical materials ,7, pp. 1-10, (2012).

[11] Rogina A., Rico P., Gallego Ferrer G., Ivanković M., Ivanković H., Effect of in situ formed hydroxyapatite on microstructure of freeze-gelled chitosan-based biocomposite scaffolds, European Polymer Journal, 68, pp. 278-287, (2015).

[12] Assis C. M., Vercik L. C. O., Santos M. L., Fook M. V. L., Guastaldi A. C., Comparison of crystallinity between natural hydroxyapatite and synthetic cp-Ti/HA coatings , Materials Research, 8 (2), pp. 207-211, (2005).

[13] Arcos D., Rodriguez-Carvajal J., Vallet-Regi M. The effect of the silicon incorporation on the hydroxylapatite structure. A neutron diffraction study, Solid State Sciences, 6 (9), pp. 987-996, (2004).

[14] Leventouri T., Bunaciu C. E., Perdikatsis V., Neutron powder diffraction studiesof silicon-substituted hydroxyapatite, Biomaterials, 24 (23), pp. 4205-4211, (2003).

[15] Sayer M., Stratilatov A. D., Reid J., Calderin L., Stott M. J., Yin X. ,MacKenzie M., Smith T. J. N., Hendry J. A., Langstaff S. D.. Structure and composition of silicon-stabilized tricalcium phosphate, Biomaterials, 24, pp. 369 –382, (2003).

[16] Carrodeguas R. G., De Aza S., α-Tricalcium phosphate:synthesis,properties and biomedical applications. Acta Biomaterialia, 7 (10), pp. 3536-3546, (2011).

Vela Luka, Croatia
International Conference
MATRIB 2018
MATERIALS, TRIBOLOGY, RECYCLING

INFLUENCE OF SURFACE DETERMINATION ON CT MEASUREMENT RESULTS

Biserka Runje[1], **Amalija Horvatić Novak**[1], **Marko Orošnjak**[2], **Andrija Belošević**[1]

[1]University of Zagreb, Faculty of Mechanical Engineering and Naval Architecture, Zagreb, Ivana Lučića 5, 10000 Zagreb, Croatia
[2]University of Novi Sad, Faculty of technical science, Trg Dositeja Obradovića 6, 21101 Novi Sad, Serbia

Sažetak

Računalna tomografija relativno je nova metoda u području dimenzionalnog mjeriteljstva. Metoda omogućava provedbu nerazornih mjerenja i analiza unutarnje i vanjske geometrije predmeta mjerenja. Računalnom tomografijom omogućena je provedba većeg broja različitih analiza na istom modelu dobivenom skeniranjem rendgenskim zrakama, što metodu čini interesantnom u širem području primjene. Međutim, mjeriteljska sljedivost i mjerna nesigurnost rezultata mjerenja još uvijek nisu osigurane i uspostavljene. S obzirom na to da je procjena mjerne nesigurnosti rezultata mjerenja jedan od preduvjeta šire implementacije metode u području dimenzionalnih mjerenja, velik broj istraživanja usmjeren je prema rješavanju tog pitanja. U cilju osiguravanja mjeriteljske sljedivosti potrebno je identificirati parametre prisutne u procesu mjerenja te odrediti njihov utjecaj na rezultate mjerenja. Jedan od značajnijih parametara jest odabir granične vrijednosti sive skale. U ovom radu razmatran je i istražen utjecaj odabira granične vrijednosti sive skale na rezultate mjerenja aluminijskih cilindara različitih površinskih hrapavosti dobivenih računalnom tomografijom.

Ključne riječi: *računalna tomografija, granična vrijednost sive skale, dimenzionalna mjerenja*

Abstract

Computed tomography is a relatively new method in a field of dimensional measurement. The method allows non-destructive measurements and inspections of both inner and outer objects geometries. Also, the method allows conduction of different analysis on the same model obtained by one CT scanning which makes it very desirable in wide range of use. However, metrological traceability and measurement uncertainty are still not assessed and achieved. Since the prerequisite for wider implementation and use of the method for purposes of dimensional measurement is assessment of measurement uncertainty, many researches are focused to address this matter. In order to achieve metrological traceability, influence parameters as well as their impact on measurement results need to be defined. One of the main parameter is threshold determination. This paper deals with influence of threshold determination on CT measurement results of aluminium cylinders with different surface roughness.

Keywords: *computed tomography, threshold determination, dimensional measurements*

1. INTRODUCTION

Requirements in production nowadays include production of more complex inner and outer object geometries. Problem which arises is how to non-destructively inspect and measure inner geometry accurately [1]. Since additive technologies are increasingly used in production, this also requires a suitable measurement method. One of the promising solutions is measuring with computed tomography. The method enables inspection of both inner and outer geometry on the same model, as well as, conduction of many different analyses such as pore/inclusion inspection, wall thickness analysis, comparison with CAD model etc [2,3]. Use of computed tomography for purposes of dimensional measurement started in beginning of 2000 when first industrial CT scanner was presented at Control fair in Germany [3]. Since then, applications of the method in industrial field significantly rose. The method is an answer to new production technologies and approaches, such as rapid prototyping and reverse engineering. It is a method that allows non-destructive 3D measurements either by nominal/actual comparison or by fitting objects of simple geometry [4]. Dimensional measurement with computed tomography can be divided in three separate sub processes; CT scanning, model reconstruction and dimensional measurement. Each sub process is defined by many factors that influence measurement process and measurement results [5]. Since the exact influence of factors on measurement results is not known, metrological traceability is still not achieved [6-8]. One of the biggest problems is how to accurately define the border between material and background, when measuring mono-material objects, and how to define borders between different materials and background when measuring multi-material objects. In ideal case, when measuring mono-material objects, there will be two different gray values, one representing background and one representing material. However, due to different influence parameters either in scanning or reconstruction process, different phenomena appears at the voxel model that complicate surface determination process. These phenomena are systematic errors named CT artifacts. According to ISO 15708-1 CT artifacts are described as discrepancies between the actual value of some physical property of an object and the map of that property generated by a CT imaging process [9]. Artifacts cause different gray values along objects' edges which can lead to incorrect edge determination and later incorrect measurement results. Defining a correct and accurate threshold value is one of important steps in metrological traceability achievement. At the moment there are a few approaches in surface determination process. This article analyses and compares results obtained by measuring aluminium cylinder using different surface determination approaches using VG Studio MAX software.

2. MATERIALS AND METHODS

2.1. Aluminium cylinders

Influence of different methods used to define threshold value of 3D voxel models, obtained by computed tomography, was evaluated on six aluminium cylinders with different surface roughness. All cylinders were made from the same material, aluminium, at the same CNC turning machine by the same operator. Cylinders are given in Figure 1.

Fig. 1: Aluminium cylinders

Surface roughness was measured using Taylor Hobson Surtronic25 roughness tester according to ISO 4288:1966 and ISO 4287:1997. Surface roughness was observed by measuring two amplitude parameters *Ra* (arithmetic mean deviation of the assessed profile) and *Rz* (maximum height of the profile), and one spatial parameter *RSm* (mean spacing of profile elements). Results are given in Table 1.

Tab 1: Measured surface roughness parameters of aluminium cylinders

	1	2	3	4	5	6
***Ra*, μm**	1,45	2,05	3,77	5,57	6,98	10,2
***Rz*, μm**	6,8	10,3	16,9	21,3	27,8	41,0
***RSm*, μm**	112	168	214	320	350	469

2.2. Reference measurements

Reference measurements of outer diameters were conducted in repeatability conditions using TESA Micro Hite 3D CMM. Each cylinder was measured five times with reference method. Results of reference measurements are given in Table 2.

Tab 2: Reference measurements obtained by CMM

Cylinder	Outer diameter, mm
1	11,958
2	11,966
3	11,995
4	11,955
5	11,964
6	12,024

2.3. CT measurements

CT measurements were conducted using industrial CT scanner. All samples were scanned using the same X-ray source setups. Objects were placed at the polystyrene basis in a slightly tilted orientation. All cylinders were scanned at the same geometrical magnification together with calibration rod, which was later used for voxel size correction.

After reconstruction process was done, all cylinders were analyzed using VG Studio MAX 3.0 software. Before making measurements or performing any analysis of a model, the border between object and background has to be determined. Since in observed case only mono-material objects were inspected, two gray values need to be defined, one for material (aluminium), and one for background. Software which was applied for conduction of measurements offers several approaches for surface determination. Here, three approaches were used and analyzed in case when measuring objects with significantly different surface roughness. Firstly, global threshold method was used. The method is suitable in cases when scanning homogenous materials such as aluminium where, under ideal conditions, it would be possible to define the component surface simply by determining the grey value threshold [10]. Threshold could be calculated as the mean value from the material grey value and the image background grey value [10]. The result of global threshold method is a material boundary defined alongside whole object by one gray value, so called threshold value.

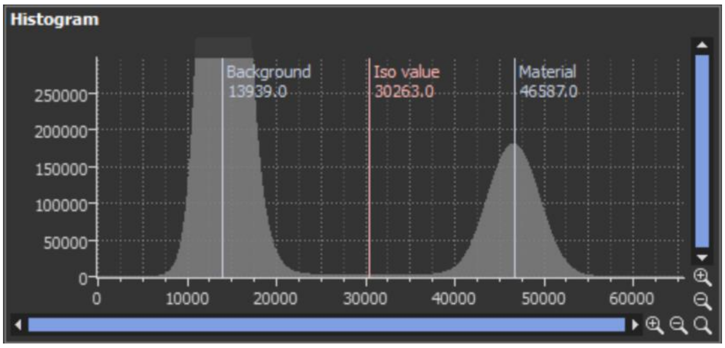

Fig. 2: Histogram: global threshold surface determination method applied on cylinder 1

Second approach was the local adaptive approach, which defines locally adapted gray values. This approach is well suited and used in cases with big variations in gray level due to presence of image artifacts. The same grey value, which can be determined by using global threshold method, will be interpreted differently depending on the surrounding voxels [11].

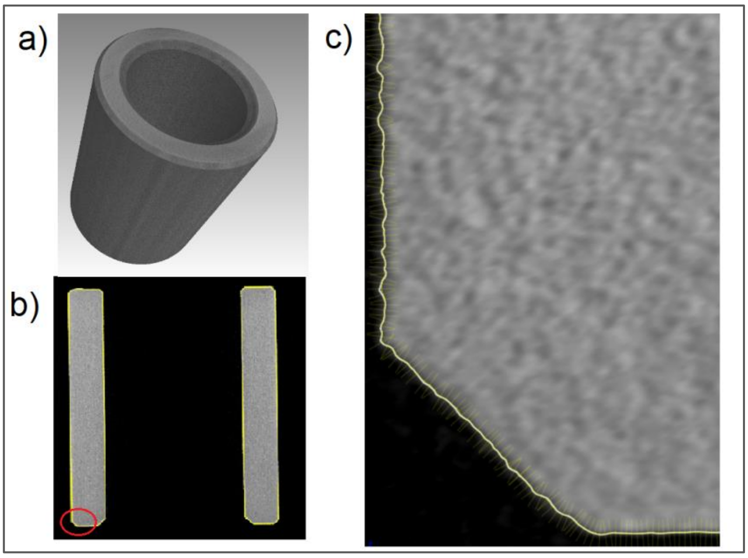

Fig. 3: Local adaptive surface determination method: a) CT model of cylinder 1, b) 2D slice image, c) magnified border on 2D slice image

Third applied and analyzed approach was manual surface determination conducted by using sample area on CT data scans. The procedure implies determination of grey values by selecting sample area that belongs to material, respectively to background.

After the surface was determined, measurement of outer diameters was carried out. Used measuring approach considered fitting simple geometry objects, in observed case fitted were cylinders. In total 1000 points was used to describe simple geometry, using Gaussian method.

3. RESULTS AND DISCUSSION

Measurement results of six aluminium cylinders were analyzed in dependence of applied surface determination method and object surface roughness. All results were compared to reference values obtained by using CMM method. The results are given graphically as deviations from reference values. Outer diameters were observed.

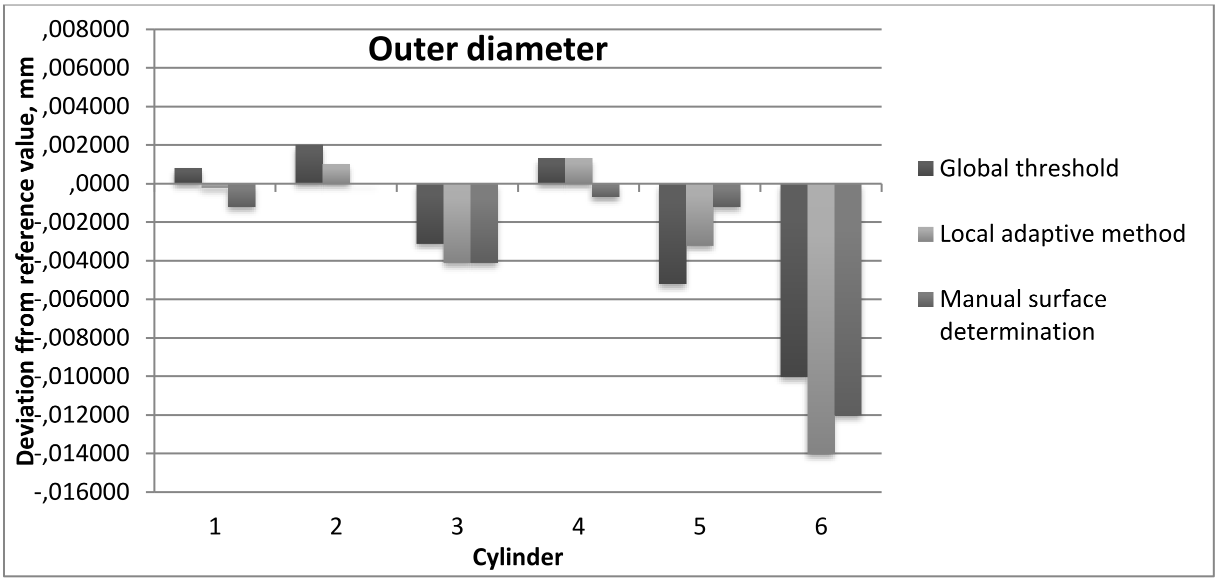

Fig. 4: Measurement results for surface determination approaches on aluminium cylinders

By comparing deviations from reference values both depending on surface roughness and applied surface determination method in cases with lower surface roughness the best results were obtained when using local adaptive surface determination method. Contrary to that, when measuring diameter on cylinder with the highest observed surface roughness, cylinder number 6, the lowest deviation is obtained when using global threshold method. In the case of measuring outer diameters of cylinders 1, 2, 3 and 4, analysis of variance was performed. Obtained *p*-value was larger than alpha risk, which means that there is no significant difference between results. Deviation in results which are still present cannot be attributed to the choice of surface determination method. When measuring objects with higher surface roughness, here cylinders 5 and 6, more significant differences in measurement results with regard to the chosen method were observed.

4. CONCLUSION

In this research influence of surface determination on CT measurement results was observed. Six aluminium cylinders with significantly different surface roughness were measured using computed tomography method where three different approaches in surface determination were used. Measured were outer diameters and results were compared to reference values measured by coordinate measuring machine. Obtained results indicates that there is no significant difference between results obtained by using different surface determination approaches on observed cylinders with lower surface roughness. Deviation in results which are still present cannot be attributed to the choice of surface determination method. Opposite to that, when measuring objects with higher surface roughness, lower deviations can be observed when applying local adaptive method.

REFERENCES

[1] Schmitt R., Niggemann C., Uncertainty in measurement for x-ray-computed tomography using calibrated work pieces. Measurement Science & Technology, 21, (2010).

[2] Angel J., De Chiffre L., Comparison on Computed Tomography using industrial items. CIRP Annals, 63, pp. 473-476, (2014).

[3] Kruth J.P., Bartscher M., Carmignato S., Schmitt R., De Chiffre L., Weckenmann A., Computed tomography for dimensional metrology. Cirp Annals-Manufacturing Technology, 60, pp. 821-842, (2011).

d) [4] Horvatić Novak A., Runje B., Stepanić J., Capabilities of industrial computed tomography in the field of dimensional measurements. Advances in Production Engineering & Management, 12, pp. 245-253, (2017).

[5] Horvatić Novak A., Runje B., Influence of object surface roughness in CT dimensional measurements. Proceedings of iCT 2017. Leuven: Katholieke Universiteit Leuven, iCT 2017, pp. 159-160, (2017).

[6] Carmignato S., Pierobon A., Rampazzo P., Parisatto M. , Savio E., CT for Industrial Metrology – Accuracy and Structural Resolution of CT Dimensional Measurements. Proceedings of iCT 2012. Wels: University of applied sciences Upper Austria, iCT 2012, pp. 161-172, (2012).

[7] Horvatić A., Runje B., Alar V., Degiuli N., Computed tomography – a new method in the fields of dimensional metrology and material inspection. Zbornik radova = Proceedings. Zagreb: Hrvatsko društvo za materijale i tribologiju, MATRIB 2015, (2015).

[8] Weckenmann A., Kraemer P., Computed tomography in quality control: chances and challenges. Proceedings of the Institution of Mechanical Engineers Part B-Journal of Engineering Manufacture, 227(B5), pp. 634-642, (2013).

[9] ISO 15708-1:2002, Non-destructive testing – Radiation methods – Computed tomography – Part 1: Principles.

[10] Reinhart C., Industrial Computer Tomography – A Universal Inspection Tool. Proceeding of 17th World Conference on Nondestructive Testing, (2008).

[11] VGStudio MAX 2.2 – Reference Manual. Heidelberg: Volume Graphics GmbH, 2013.

NUMERICAL MODELLING OF WELDED JOINTS PROPERTIES

Božo Smoljan[1], **Dario Iljkić**[2], **Lovro Štic**[2], **Sunčana Smokvina Hanza**[2], **Luciano Gržinić**[3], **Goran Vratović**[4]

[1] Polytechnic of Pula, College of applied sciences, Riva 6, 52100 Pula, Croatia
[2] University of Rijeka - Faculty of Engineering, Vukovarska 58, 51000 Rijeka, Croatia
[3] ULJANIK Mechanical Engineering Diesel JSC, Flaciusova 1, 52100 Pula, Croatia
[4] Plazma tehnika d.o.o., Zona male privrede 12, 52216 Galižana, Croatia

Abstract

The mathematical model for prediction of microstructure composition and mechanical properties of steel welded joint was developed. Finite volume method (FVM), was suitable to create integrated computer program for simulation physical processes during the welding. The computer simulation of hardness of welded joint is based on both, CCT diagrams and the thermo-kinetic expressions using linear alignment with the actual chemical composition. Microstructure and hardness of welded joint has been predicted based on calculated characteristic time of cooling from 800 °C to 500 °C, ($t_{8/5}$). Distribution of hardness of welded joint has been predicted by conversion of calculated cooling times from 800 to 500 °C to the hardness. The algorithm for prediction of hardness in welding joint is based on real chemical composition. Results of steel welding were estimated by taking into account the process of reheating of workpiece during the welding. The established procedure was applied in computer simulation of heat treatable steel welded joint.

Keywords: *Numerical modelling, hardness, microstructure, welded joint, tempering.*

1. INTRODUCTION

Computer simulation of the welding can be done by considering the issues such as achievement of tolerable defects, desired mechanical properties distribution and required microstructure distribution. Many very useful software exist for the calculation of grain structure, porosity, hot tearing, and solid-state transformation. But, there are still questions on which answers should be given to satisfy all industry needs in mathematical modelling and simulation of welding.

During the welding, many different physical processes, such as, melting, solidification, solid state phase transformation, evolution of microstructure, diffusion, heat conduction, and mechanical stressing and distortion are at once taking place inside metal [1, 2]. Simulations of microstructural transformations can be based on the both, CCT diagrams and thermo-kinetic expressions. The first approach is more consistent, but the second approach gives good results using the real chemical composition of the steel.

The input of the simulation is composed of the following categories: geometry, physical characteristics of the steel and, kinematic boundary conditions and thermal boundary conditions. It is necessary to establish the appropriate algorithm which describes heating and cooling processes and to involve appropriate input data in the model. Inverse heat transfer problems should be solved to determine thermal properties for welding material and filler material based on experimentally evaluated results [3].

Proposed numerical model of welding in this work is based on finite volume method (FVM). The finite volume method (FVM) has been established as a very efficient way of solving fluid flow and heat transfer problems. The key feature of the FVM approach is that the FVM is based on flux integration over the control volume surfaces. The method is implemented in a manner that ensures local flux conservation, regardless of the grid structure [4]. FVM is used as a simple and effective tool for the solution of a large range of problems in the analysis of welding processes [5-7].

2. COMPUTER MODELLING OF THERMAL PROCESSES

Numerical simulation of welding gives consideration to both, the melting and solidification processes.

Mathematical formulation of process of welding, i.e., melting, solidification and cooling is based on the following system of differential equations [5, 8]:

- the Navier-Stokes equations

$$\begin{aligned}
&\mu\left(\frac{\partial^2 v_r}{\partial r^2}+\frac{1}{r}\frac{\partial v_r}{\partial r}+\frac{\partial^2 v_r}{\partial z^2}-\frac{v_r}{r^2}\right)-\frac{\partial p}{\partial r}+\rho g_r\beta\left(T-T_\infty\right)=\rho\frac{\mathrm{d}v_r}{\mathrm{d}t}\\
&\mu\left(\frac{\partial^2 v_z}{\partial r^2}+\frac{1}{r}\frac{\partial v_z}{\partial r}+\frac{\partial^2 v_z}{\partial z^2}\right)-\frac{\partial p}{\partial z}+\rho g_z\beta\left(T-T_\infty\right)=\rho\frac{\mathrm{d}v_z}{\mathrm{d}t}
\end{aligned} \tag{1}$$

- the continuity equation

$$\frac{\partial v_r}{\partial r}+\frac{v_r}{r}+\frac{\partial v_z}{\partial z}=0 \tag{2}$$

- the Fourier's heat conduction equation including the convection term

$$\frac{\lambda}{r}\frac{\partial T}{\partial r}+\frac{\partial}{\partial r}\left(\lambda\frac{\partial T}{\partial r}\right)+\frac{\partial}{\partial z}\left(\lambda\frac{\partial T}{\partial z}\right)=\rho c_{\mathrm{ef}}\left(\frac{\partial T}{\partial t}+v_r\frac{\partial T}{\partial r}+v_z\frac{\partial T}{\partial r}\right) \tag{3}$$

Characteristic boundary condition is:

$$-\lambda\frac{\delta T}{\delta n}\bigg|_{\mathrm{s}}=\alpha\left(T_{\mathrm{s}}-T_{\mathrm{a}}\right) \tag{4}$$

$$\frac{\delta\left(c\rho T\right)}{\delta t}=div\lambda\, gradT+q_{\mathrm{s}} \tag{5}$$

Characteristic boundary condition for the top face is:

$$-\lambda\frac{\delta T}{\delta n}\bigg|_{\mathrm{s}}=\alpha_{\mathrm{ef}}\left(T_{\mathrm{s}}-T_{\mathrm{a}}\right)+q_{\mathrm{source}} \tag{6}$$

and for the other faces

$$-\lambda\frac{\delta T}{\delta n}\bigg|_{\mathrm{s}}=\alpha\left(T_{\mathrm{s}}-T_{\mathrm{a}}\right) \tag{7}$$

where T_{s}/K is surface temperature, T_{a}/K is air temperature, q_{s}/Wm^{-3} is volumetric density of heat source, α/Wm^{-2}K^{-1} is heat transfer coefficient of air, α_{ef}/Wm^{-2}K^{-1} is effective heat transfer coefficient by which convection and radiation are taken into account and q_{source}/Wm^{-2} is arc source heat flux.

where T/K is the temperature, t/s is the time, $\rho = \rho(T)$/kgm^{-3} is the density, λ/Wm^{-1}K^{-1} is the thermal conductivity coefficient, T_{s}/K is surface temperature, T_{a}/K is air temperature, α/Wm^{-2}K^{-1} is heat transfer coefficient, v_{r}, v_{z}/ms^{-1} are the r- and z-component of velocity, respectively, $\mu(T)$/Nsm^{-2} is dynamical viscosity coefficient, $c_{\mathrm{ef}} = c + L/(T_{\beta}-T_{\alpha})$/Jkg^{-1}K^{-1} is the effective specific heat of a mushy zone, L/Jkg^{-1} is the latent heat of solidification, c/Jkg^{-1}K^{-1} is the specific heat, p/Nm^{-2} is the pressure, g_{r}, g_{z}/ms^{-2} are the r- and z-component of gravitational acceleration, respectively, β/K^{-1} is the volume coefficient of thermal expansion, r, z/m are the coordinates of the vector of the considered node's position, T_{∞}/K is the reference temperature $T_{\infty} = T_{\mathrm{in}}$, r/m is the radius.

In this model it was presumed that convection term has no relevant role and that liquid metal flow could be neglected after melting.

Quantity of growth of solidified part of welded joint was predicted by calculation of solidification rate in control volume (Fig. 1).

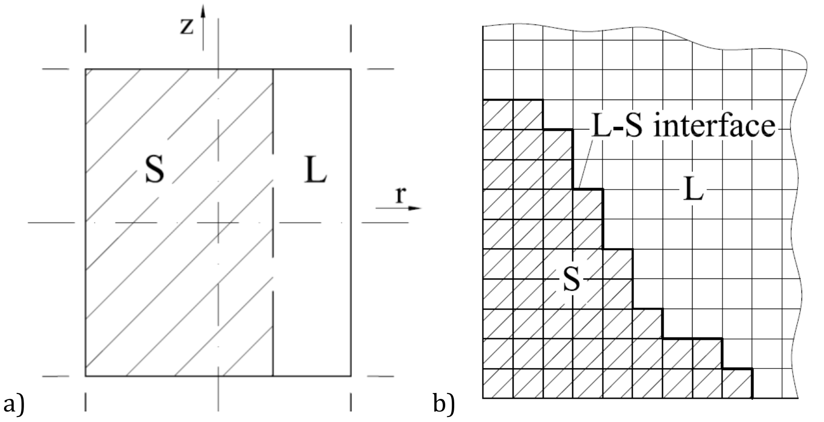

Fig. 1: Liquid-solid interface, a) control volume, b) welding joint

Increment of melted or solidified part, f_{i} in control volume can be calculated by:

$$f_{\mathrm{i}} = \frac{m_{\mathrm{i}}}{m_{\mathrm{vol}}} = \frac{c_{\mathrm{m}}\left(T_1 - T_2\right)}{L} \tag{8}$$

where m_{i}/kg is mass quantity increase of solidified part in control volume, m_{vol}/kg is mass quantity of control volume, c_{m}/Jkg^{-1}K^{-1} is heat capacity of liquid and solid mixture, T_1/K is the temperature at the beginning and T_2/K is the temperature at the end of time step Δt. In proposed model it was presumed that convection term has no relevant role and that liquid metal flow could be neglected after melting [9]. Equations 1 to 3 were found out using the finite volume method. Physical properties included in equations 1 to 8 should be defined [4]. Accuracy of the heat transfer prediction directly influences to the accuracy of both, calculations of phase transformation kinetics and calculations of mechanical properties of steel. Involved variables in model should be additionally adjusted.

Quantity of growth of solidified part of welding joint was predicted by calculation of solidification rate in control volume. When $\Sigma f_i = 1$, the mass of solidified part of welding joint will grow up for mass of control volume.

The temperature field change in an isotropic rigid body with coefficient of heat conductivity, λ/Wm^{-1}K^{-1}, density, ρ/kgm^{-3} and specific heat capacity, c/Jkg^{-1}K^{-1} can be described by Fourier's law of heat conduction:

It is assumed that the arc has a Gaussian distribution on the top face of the workpiece:

$$Q = q_0 \int_0^{\infty} e^{-\frac{d}{r_0^2} r^2} \, 2\pi r dr \tag{9}$$

where Q/W is the total heat input into the workpiece, r_0/m is the radius of the heat input distribution, d is the exponential factor and q_0/Wm^{-2} is the volumetric energy generation rate [5].

Solution of equation 1 can be found out using the finite volume method [4, 6, 7]. If the total volume is divided in N number of control volumes, discretization system has N linear algebraic equations, with N unknown temperatures of control volumes. Time of cooling from T_a to specific temperature in particular point is determined as sum of time steps, and in this way, the diagram of cooling curve in every grid-point of a specimen is possible to find out [5].

Accuracy of the heat transfer prediction directly influences to the accuracy of both, calculations of solidification kinetics, phase transformation kinetics and calculations of mechanical properties of steel. If the variables ρ and c were accepted, variable λ and specially variable α must be estimated, i.e., calibrated according to variables ρ and c [5]. Total heat conductivity coefficients of steel at some temperature T should be calculated in accordance to composition and distribution of microstructure. Heat transfer coefficients of air are given in Table 1 [5].

Tab. 1: Calibrated values of heat transfer coefficient of air

Temperature, T/°C	20	100	200	400	600	800	1000
Heat transfer coefficient, α/Wm^{-2}K^{-1}	12	15	21	33	50	84	113

2. MATHEMATICAL MODELING OF MICROSTRUCTURE COMPOSITION AND HARDNESS

Microstructure composition after the welding depends on chemical composition of steel and nature of cooling process. Kinetics of transformations was calculated by Avrami's isothermal equation. Written in an incremental form the volume fraction Δx of austenite transformed in the time interval Δt_i at temperature T_i can be calculated as follows:

$$\Delta x_{(m)} = nk^{\frac{1}{n}} \left(\ln \frac{1}{1 - x_{(m-1)}} \right)^{1-\frac{1}{n}} \left(1 - x_{(m-1)}\right) \Delta t_{(m)} \tag{10}$$

In accordance to the Scheil's additivity rule, characteristic microstructure transformation can be completed when transformed part of microstructure, $\Sigma\Delta x$ is equal to one [1, 10-12]:

$$\sum_{m=1}^{M} nk^{\frac{1}{n}} \left(\ln \frac{1}{1 - x_{(m-1)}} \right)^{1-\frac{1}{n}} \left(1 - x_{(m-1)}\right) \Delta t_{(m)} = 1 \tag{11}$$

The non-isothermal transformation kinetics can be described as the sum of a series of the small isothermal transformations. The temperature range of cooling is divided into a series of small finite steps. Maintaining the time interval, Δt_i to sufficiently short times permits the assumption that the conditions are isothermal over each time step. It was assumed that each time step produces such a transformation as occurs in the isothermal condition of transformation at the same temperature and microstructure composition. Kinetic parameters *k* and *n* from equation 10 can be determined inversely by using data of time of isothermal transformation.

$$k = \frac{\ln(1 - x)}{t_{\mathrm{T}}^{n}} \tag{12}$$

Characteristic time of isothermal transformation could be calculated by kinetic equations based on chemical composition of steel or could be found out by using IT diagram of steel with standard chemical composition [11]. The IT diagram should be additionally adjusted based on actual chemical composition or based on Jominy test results for applied steel [13].

The martensitic transformation relation is based on the following expression [14]:

$$x_{\mathrm{M}} = \left(1 - x_{\mathrm{F}} - x_{\mathrm{P}} - x_{\mathrm{B}}\right)\left(1 - \exp\left(-0.011\left(M_{\mathrm{S}} - T\right)\right)\right) \tag{13}$$

Increment of martensite is equal to:

$$\Delta x_{\mathrm{M}} = x_{\mathrm{M}}\left(T_{m+1}\right) - x_{\mathrm{M}}\left(T_{m}\right) \tag{14}$$

Between critical temperatures of austenite decomposition and hardenability properties, regression relations are established [12, 15]:

Simulation of as welded hardness at different welding joint points is estimated by the conversion of the calculated equivalent cooling time, $t_{8/5e}$ to the hardness. This conversion is provided using the relationship between the equivalent cooling time $t_{8/5e}$ and distance from the quenched end of the Jominy test specimen, E_d, i.e. by the using the diagram of cooling time $t_{8/5}$ versus distance from the quenched end of the Jominy test specimen. Hardness HRC_q was predicted by using the Jominy curve diagram [1, 12, 16].

Since steel plate is repeatedly heated during the welding processes, influence of reheating of workpiece during welding on microstructure transformation should be taken into account. The reference value of hardness of welded steel plate can be estimated based on hardness at the start of welding H [1, 5, 12, 17, 18]. The algorithm for prediction of hardness of welded steel was established by regression analysis [1, 12, 19]. Since the duration of processes of annealing or tempering at some temperature T_p is equal to Δt, temperature T_{tr} can be expressed by the following equation:

$$T_{\mathrm{tr}} = \frac{T_{\mathrm{p}}(C + a \ln \Delta t)}{C} \tag{15}$$

where a is a constant. Constant C depends on chemical composition and has the same meaning as constant C in Hollomon-Jaffe expression.

3. APPLICATION

The developed method for prediction of hardness and microstructure distribution was applied in computer simulation of welded joints of steel. Welded joints were made of normalized steel EN X15Cr13 [1]. Joint design is shown in Fig. 2. Welding rate was 30 cm/min and heat input was 4.8 kJ/cm. It was accepted that chemical composition of filler metal was the same as was of the base metal. Computer simulation of hardness and microstructure distribution of the welded joint was done using the computer software BS-WELDING.

The distribution of hardness and microstructure of the welding joint made of steel EN X15Cr13 are shown in Fig. 3-5.

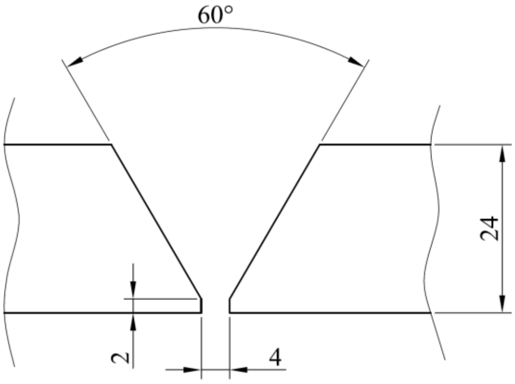

Fig. 2: Joint design

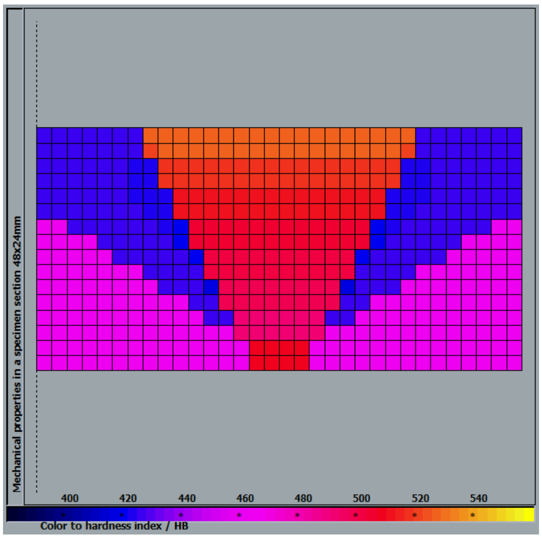

Fig. 3. Distribution of as-welding hardness

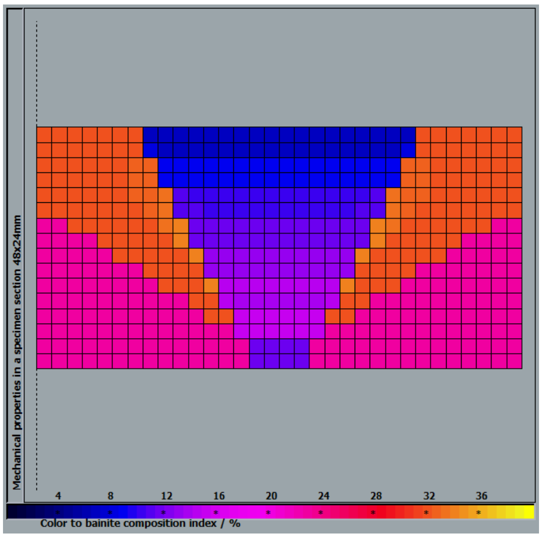

Fig. 4. Distribution of ferrite+cementite

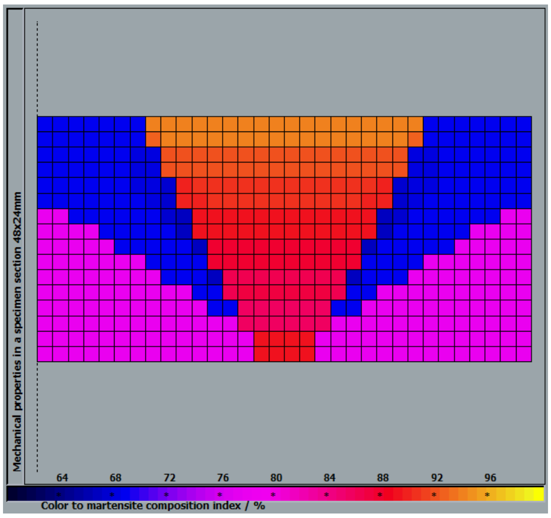

Fig. 5: Distribution of martensite

4. CONCLUSIONS

The numerical simulation of welding is consisted of numerical simulation of transient temperature field of cooling process, numerical simulation of mechanical properties and microstructure transformation in solid state. The model is based on the finite volume method.

Input material data involved in mathematical model of welding, i.e., density and specific heat capacity of steel, heat transfer coefficient and heat conductivity coefficient were accepted from literature and additionally calibrated.

Hardness and microstructure composition in specimen points were calculated by the conversion of calculated time of cooling from 800 to 500 °C, $t_{8/5}$ to hardness and microstructure composition using the CCT diagram and thermo-kinetic expressions. Hardness of steel wildings was estimated by taking into account the process of reheating of workpiece during the welding.

A developed mathematical model has been applied in computer simulation of welding of steel plates. It can be concluded, that hardness and microstructure composition in welded steel can be successfully calculated by proposed method.

Acknowledgements:
This work has been supported in part by Croatian Science Foundation under the project **5371**.
This work has been supported in part by University of Rijeka, Support No **13.09.1.1.02**.

REFERENCES

[1] Smoljan B., Iljkić D., Smokvina Hanza S., Štic L., Jokić M., Numerical modelling of welding of martensitic steel, Proceedings of the The 12th International Seminar "Numerical Analysis of Weldability", 23-26 September 2018, Graz - Castele Seggau, Austria

[2] Telejko I., Adrian H., Skalny K., Pakiet M., Staśko R., The investigation of hardenability of low alloy structural cast steel, Journal of Achievements in Materials and Manufacturing Engineering 37/2 (2009) 480-485.

[3] Gur C. H., Pan J., Handbook of Thermal Process Modelling Steels, CRC Press, 2008

[4] Smoljan B., Iljkić D., Novak H., Estimation of coefficient of heat conductivity and heat transfer coefficient in the numerical model of the steel quenching, Proceedings of the 2nd Mediterranean Conference on Heat Treatment and Surface Engineering, 11-14 June 2013, Dubrovnik - Cavtat, Croatia.

[5] Smoljan B., Iljkić D., Štic L., Tomašić N., Smokvina Hanza S., Mathematical modelling of mechanical properties and microstructure of welded joint, Proceedings of the 41st International Conference WELDING 2016, Modern Joining Processes, Development of Filler Materials and Simulations, 8-11 June 2016, Opatija, Croatia.

[6] Demirdžić I., Application on finite volume method to calculation of temperature fields generated during welding, Zavarivanje, 27/6, 1984, pp 481 – 489, (in Croatian)

[7] Patankar S., Numerical Heat Transfer and Fluid Flow, McGraw Hill Book Company, New York, 1980

[8] Sowa L., Mathematical Model of Solidification of the Axisymmetric Casting While Taking Into Account its Shrinkage, Journal of Applied Mathematics and Computational Mechanics, 13(2014)4, pp. 123-130

[9] Flemings M., Solidification Processing, McGraw-Hill Book Company, 1984.

[10] Heat Treating, ASM Handbook Vol. 4, ASM International, Materials Park, OH, 1991

[11] Smokvina Hanza S., Mathematical Modeling and Computer Simulation of Microstructure Transformations and Mechanical Properties During Steel Quenching, Doctoral Thesis, Department of Materials Science and Engineering, University of Rijeka - Faculty of Engineering, 2011, (in Croatian).

[12] Smoljan B., Iljkić D., Smokvina Hanza S., Jokić M., Štic L., Borić A., Mathematical Modeling and Computer Simulation of Steel Quenching, Materials Performance and Characterization (in print)

[13] Smoljan B., Numerical Simulation of Steel Quenching, Journal of Materials Engineering and Performance, Vol. 11, No. 1, 2002, pp. 75–80.

[14] Koistinen D. P., Marburger R. E., A General Equation Prescribing the Extent of the Austenite-Martensite Transformation in Pure Iron-Carbon Alloys and Plain Carbon Steels, Acta Metall., Vol. 7, 1959, pp. 59–60.

[15] Smoljan B., Iljkić D., Tomašić N., Prediction of Mechanical Properties and Microstructure Composition of Quenched and Tempered Steel, presented at the 28th ASM Heat Treating Society Conference, Heat Treating 2015, Detroit, MI, October 20–22, 2015, ASM International, Materials Park, OH, pp. 266–273.

[16] Smoljan B., Iljkić D., Computer Modeling of Mechanical Properties and Microstructure of Quenched Steel Specimen, presented at the Fifth International Conference on Thermal Process Modeling and Computer Simulation, Orlando, FL, June 16–18, 2014, ASM International, Materials Park, OH, pp. 103–111.

[17] Smoljan B., Iljkić D., Smokvina Hanza S., Computer simulation of working stress of heat treated steel specimen, Journal of Achievements in Materials and Manufacturing Engineering, 34/2, 2009, pp 152 – 156.

[18] Reti T., Felde I., Guerrero M., Sarmiento S., Using Generalized Time-Temperature Parameters for Predicting the Hardness Change Occurring during Tempering, International Conference on New Challenges in Heat Treatment and Surface Engineering (Conference in honour of Prof. Božidar Liščić), B. Smoljan, B. Matijević, Eds., June 9-12, pp 333-342, Dubrovnik-Cavtat, Croatia, 2009.

[19]Iljkić D., A contribution to the development of the mechanical properties prediction of quenched and tempered steel and cast steel, Doctoral Thesis, Department of Materials Science and Engineering, Faculty of Engineering, University of Rijeka, 2010. (in Croatian)

Vela Luka, Croatia
International Conference
MATRIB 2018
MATERIALS, TRIBOLOGY, RECYCLING

LOW-CYCLE FATIGUE LIFE METHODS FOR AUXETIC STRUCTURES

Matjaž Šraml[1], **Janez Kramberger**[2], **Branko Nečemer**[2], **Dušan Gabriel**[3] **and Srečko Glodež**[2]

[1] University of Maribor, Faculty of Civil Eng., Transportation Eng. and Architecture, Smetanova 17, 2000 Maribor, Slovenia
[2] University of Maribor, Faculty of Mech. Engineering, Smetanova 17, 2000 Maribor, Slovenia
[3] Institute of Thermomechanics, ASCR, Dolejškova 5, Prague 8, Czech Republic

Abstract

The objective of this paper is to introduce the fatigue life models (FLM) for auxetic (negative Poisson's ratio) structures, in particular, low-cycle fatigue (LCF) life models. The mechanical properties of open and closed-cell foams can be described in first approximation by considering the density properties of the cellular solids. However, cell shape of foams could provide a significant contribution to the overall mechanical properties of the cellular solids. Auxetic structures are special version of cellular materials. Most of auxetic materials can be classified into three main groups: (i) auxetic honeycombs, (ii) auxetic microporous polymers and (iii) auxetic composites. There is no existed general fatigue life model for auxetic structures, therefore, different "mechanism" must be observed. The present study investigates the properties of existing LCF and its possibilities to be use for fatigue life calculation, considering the auxetic structures properties. Currently, first LCF experiments on potential auxetic materials are ongoing.

Keywords: Fatigue Life Models (FLM), Low-Cycle Fatigue (LCF), Porous structures.

1. INTRODUCTION

The mechanical properties of open and closed-cell foams can be described in first approximation by considering the density properties of the cellular solids [2]. This approach is valid for most conventional foamed materials. However, cell shape of foams could provide a significant contribution to the overall mechanical properties of the cellular solids [2]. When the cells are equiaxed the properties are isotropic, but when the cells become slightly elongated or flattened then the properties will depend on direction, often to a significant extent. Three-dimensional foams, in which the cell walls have random orientations in space, are normally anisotropic, due to the way they are foamed [6]. The cell shape can be modified using special processing techniques to obtain more radical mechanical properties changes, like negative Poisson's ratio (auxetic) characteristics [3].

Since 1987, when isotropic auxetic foam was manufactured for the first time [7], negative Poisson's ratio (ν) materials have created some interest for potential applications in structural integrity compliant structures, sandwich components and, in general, smart passive structural devices [8]. By definition, an auxetic (negative Poisson's ratio) material expands in all directions when pulled in only one, giving therefore a deformation kinematics opposite to that of 'classical' materials (see Fig. 1 [16]).

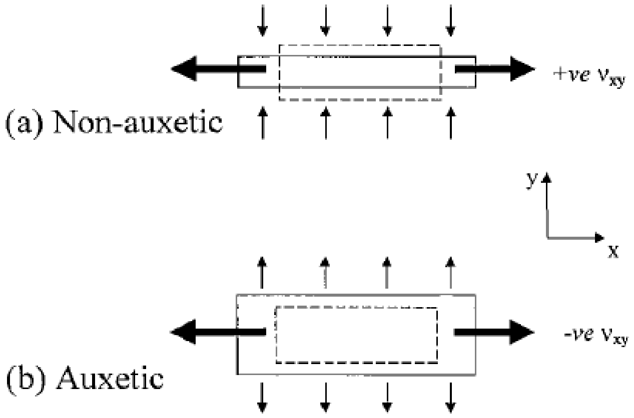

Fig. 1. Schematic diagram of positive and negative Poisson's ratio deformation. [16]

a) Non-auxetic behaviour in which an initially undeformed material (dashed outline) undergoes longitudinal extension and lateral contraction (solid line) for a tensile load applied in the longitudinal (x) direction.

b) Auxetic behaviour in which an initially undeformed material (dashed outline) undergoes longitudinal and lateral extension (solid line) for a tensile load applied in the longitudinal (x) direction.

This behaviour does not contradict the classical theory of elasticity: a homogeneous isotropic thermo-dynamically correct 3D solid has a potential Poisson's ratio range between -1.0 and +0.5, while anisotropic solids can also have larger values in magnitude [9]. A negative Poisson's ratio coefficient for a material could lead to an increase in indentation resistance [10], enhanced bending stiffness in structural elements and shear

resistance [11, 12], optimal passive tuning of structural vibration [13] and enhanced dielectric properties for microwave absorbers [14].
The use of auxetic materials in various field of application can be expected due to following properties [15]:

- Poisson's ratio being negative or zero.
- Large shear resistance.
- Hardness improvement.
- Lower fatigue crack propagation.
- Large toughness and modulus resilience.
- Vibration absorption.

Those features assure to improve mechanical properties, including shear resistance, hardness value (indentation resistance), fracture toughness, fatigue crack propagation, etc., as compared to the conventional materials from which they are made. Table 1 summarizes the applications used in various fields of indutry [15].

Table 1. Summary of the applications of the auxetic materials (in alphabetical order) [15]

Field (Existing and potential)	Application and the rationale
Aerospace	Vanes for gas turbine engine, thermal protection, aircraft nose-cones, wing panel, sounds and vibration absorber, rivet
Automotive	Bumper, cushion, thermal protection, sounds and vibration absorber parts that need shear resistant, fastener
Biomedical	Bandage, wound pressure pad, dental floss, artificial blood vessel (the wall thickness increases when a pulse of blood flows through it), artificial skin, drug release unit, ligament anchors. Surgical implants (similar to that of bone characteristics)
Composite	Fiber reinforcement (because it reduce the cracking between fiber and matrix)
Military (defence)	Helmet, bullet proof vest, knee pad, gloce, protective gear (better impact property)
Sensors/ actuators	Hydrophone, piezoelectric devices, various sensors (the low bulk modulus makes them more sensitive to hydrostatic pressure)
Textile Industry	Fibres, functional fabric, colour-change straps or fabrics, threads

One can find extensive information on auxetic in references [16, 17]. The cyclic stress–strain behaviour of polymer foams and elastomers has attracted recent attention, particularly when energy dissipation is concerned. When samples are loaded under strain control and then unloaded, subsequent extension to the same strain requires a lower force. Further cycling results in continued softening at a progressively slower rate and a steady state may be reached. This softening phenomenon is an important indication of the amount of energy that the material can continue to absorb.
Recently, there has not been yet introduced a unique procedure, that describe fatigue life models for auxetic structures, in general. Some researcher purpose in their investigation methodologies, like polyurethane open cell foam subjected to compressive cyclic until 100 cycles has been investigated by Rehkopf et al. [18]. Shen et al. [19] proposed a model based on the experimental results in [18] which could be applied to express the cyclic stress–strain relationship for conventional polyurethane foam at any given cycle. In

sandwich structures with polymeric foam core and partially with metal-based filler [24], it is expected that the viscoelastic behaviour of the foam play an important role in absorbing and dissipating energy especially during dynamic loading [20, 21]. The dynamic-mechanical viscoelastic behaviour of the core and its effect on the performance of the sandwich is so far relatively unexplored.

Kolsters and Wennhage [22] determined the loss factor ($tan\ \delta$) for a variety of H-grade PVC foams. Recently, Palissery et al. [23] have investigated a PVC foam subjected to a fatigue in tension and compression tests. They describe the static and fatigue properties of auxetic thermoplastic foams made by conventional PU–PE base. The foams have been manufactured following a modification of the manufacturing process route described in [6]. As further comparison, a set of iso-density non-auxetic foams has been manufactured to assess if the overall static and dynamic behaviour is influenced by the density only, and whether the negative Poisson's ratio is playing a role or not. The fatigue tests, in particular, have been carried with varying loading ratios between 0.725 and 0.95, and total number of cycles of 100,000. The auxetic foam shows higher energy absorption characteristics during quasi-static tests and more stable rigidity loss over large number of cycles, compared to the isodensity version [3]. Recently, data on fatigue loading of auxetic and non-auxetic isodensity thermoplastic foams are not present in literature, and a general assessment of the structural integrity of auxetic materials has not been performed yet [3].

The actual paper is upgrade of the work, presented at the last MATRIB conferences, in 2015 and 2016 [4, 5]. Currently, first LCF experiments on auxetic materials are ongoing, performed in the frame of common project of research groups from Maribor and Prague.

2. EXISTING METHODOLOGY

Although, not many procedures exist to examine auxetic structures with the main goal of forecasting fatigue life, using either experiments, numerical methods and/or analytical approach. Furthermore, due to a fact, that many different auxetic structures exist, one cannot expect a unique methodology of FLM for this purpose. Following, (some possible) methodologies will be discussed.

2.1 Static and cyclic FLM of auxetic carbon/epoxy composites [25]

In the following subchapter, the analysis, presented in [25], is focused and discuss. The Hexcel prepreg T300/914 carbon/epoxy is the material, which is frequently in extensive use in aerospace applications, and has, generally, good mechanical characteristics. The prepreg laminate is composed by a thermo hardening epoxy resin reinforced by HR carbon fibres, with a volume fraction approximately equal to 60% [25]. Several stacking sequence laminate plates have been manufactured, for the purpose of static and cyclic experiments [25], and then cut out using a diamonds disc, starting from plates having dimensions 300mm×300mm according to standard ASTM D 790. The final specimens had dimensions h≈1.3 mm, L=100 mm, l=70mm and b=20 mm, which correspond to the thickness, the total length, the distance between supports and the width, respectively. The specimens were subjected to a three-point bending test using a universal testing machine type ZWICK ROELLE Z005; equipped by a cell load of 5 kN and controlled by Testexpert V10.11 software. A statistical data processing has been carried out at the end of each series in order to obtain the median data values. For the static tests, at least five tests were performed for each laminate lay-up with a test speed of 2 mm/min. In analysed work [25] the fatigue tests have been carried out in displacement control with sinusoidal waveform with frequency 1.5 Hz. The specimens were loaded until a mean displacement (d_{mean}) was reached, equal to 50% of the displacement at static failure (d_{fail}), and then different amplitudes were used corresponding to different loading levels r ($r=d_{\mathrm{max}}/d_{\mathrm{fail}}$), where d_{max} is the maximum displacement applied in the fatigue tests.

The mean displacement determines the damage mechanisms activated at the beginning of cycling, whereas the amplitude determines the propagation velocity and the multiplication of these mechanisms. Several loading levels have been considered, ranging between 0.60 and 0.95. The same specimens type used during the static tests have been then employed in the cyclic fatigue loading.

(i) *Static tests*: The static tests were carried out at room temperature and the curves of mechanical behaviour load-displacement of the three types of lay-up $[\pm 20]_{2S}$, $[\pm 25]_{2S}$ and $[\pm 30]_{2S}$ are presented in Fig. 2.

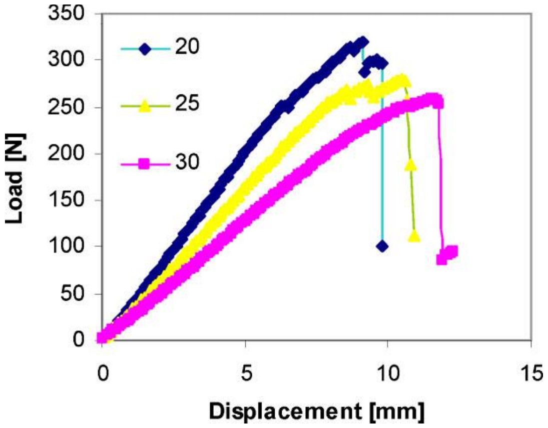

Fig. 2. Load-displacement behaviour of various carbon/epoxy laminates [25]:
$[\pm 20]_{2S}$, $[\pm 25]_{2S}$ and $[\pm 25]_{2S}$.

According to Fig. 2, the laminates $[\pm 20]_{2S}$ are the most rigid ones and feature the highest failure loads, but also show the smallest displacements at failure compared to the laminates $[\pm 25]_{2S}$ and $[\pm 30]_{2S}$. From the damage point of view, the analysis of the failure and damage mechanisms observed after static tests have been made by inspection under optical microscope [25], showing that the dominating damage is the delamination between the layers. This phenomenon is more marked in the layers of the laminate subjected to compression loading at the vicinity of the loading zone.

(ii) *Fatigue tests*: The follow-up of the evolution of the rigidity constitutes one of the most used methods to track the damage progression during the fatigue loading of composite materials. The evolution of the load F compared to its initial load F_0 obtained at the first cycle constitutes an indicator of the damage, which is very useful in laminates design. The monotonic relation between the damage tracer and the number of cycles makes it possible to build a criterion of lifespan (fatigue life) N_x necessary to cause a reduction in x % of the damage parameter. In the case of three-point bending fatigue with imposed displacement, a sudden failure of the specimens is generally not observed.

In order to determine the performance of materials in fatigue, various damage criteria (N_S, N_3, N_5, N_{10}, and N_R) are considered in literature from the curves giving the evolution of the load as a function of the number of cycles. The most severe criterion is the N_S one, which corresponds to the number of cycles at the end of the linear domain. The criteria N_3, N_5, and N_{10} correspond to falls of 3, 5 and 10% of the load (or displacement) in relation to the initial load (or displacement), respectively. The criterion N_R corresponds to the number of cycles at the final failure of the specimen. The choice of the criterion depends on the acceptable tolerance of degradation for the structure element in the application considered. For example, the N_3 criterion is much more penalizing than the N_{10}, and the N_R one is the least severe. Finally, the performances in fatigue can be characterized by the number of cycles necessary to have failure when this number of cycles is reached. In our study, we have chosen the criterion N_5, which is the most frequently used in literature [27, 28, 29], and widely applied to aerospace test cases. Moreover, beyond 10%, different types of failure mechanisms are involved, and their description becomes more difficult. For example, for higher damage rates, the effect of local heating in the specimen cannot be neglected [27].

(i) Hysteresis loops and failure criteria: Figure 3 [25] shows the load-displacement curves with the hysteresis loops for the two laminates and for different loading levels *r*. For a given loading level, the maximum load in the hysteresis loops decreases for increasing numbers of cycles.

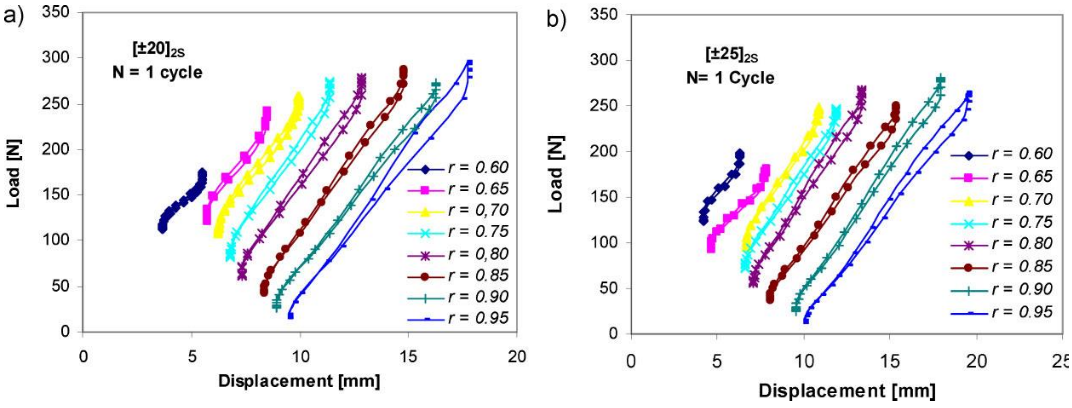

Fig. 3. Hysteresis loops of the first cycle for different loading level of two studied laminates [25].

Fig. 3 also shows the hysteresis loops of the first cycle for different loading levels of the two composite laminates. The maximum load, displacement as well as the air of the cycle augments with the increase in the loading level imposed.

(ii) Dissipated energy: the area under the hysteresis loops represents the energy U dissipated by the laminates during cycling. For any given cycle (N), the dissipated energy can be evaluated by the following relation [30]:

$$U = \int_{\varepsilon_{\min}}^{\varepsilon_{\max}} \sigma \cdot d\varepsilon \qquad (1)$$

where ε_{min} and ε_{max} are the minimum and maximum strain, respectively.

(iii) S–N curves descriptions: The S–N curves obtained on composites with organic matrix are very often described by a linear relation, introduced by Mandell [31] in the case of tension with imposed stress:

$$\sigma = UTS - B\ logN_r \tag{2}$$

where UTS and B are two constants which depend on the material and the test conditions. This formula was adopted in the case of imposed strain flexural tests by Fiore 1988 [27] and also by Salvia et al. [28]:

$$\varepsilon = A - B\ logN_{10} \tag{3}$$

Several studies have shown that this mathematical relation can be applied to a great number of composites [25].

2.2 Thermoplastic polyurethane foams (under compressive cyclic loading) [3]

The cyclic stress–strain behaviour of polymer foams and elastomers has attracted recent attention, particularly when energy dissipation is concerned. When samples are loaded under strain control and then unloaded, subsequent extension to the same strain requires a lower force. Further cycling results in continued softening at a progressively slower rate and a steady state may be reached. This softening phenomenon is an important indication of the amount of energy that the material can continue to absorb.

Static and fatigue test in compressive loading were carried out using a MTS 858 servo-hydraulic testing machine [3]. The load unit is fatigue-rated at 10 kN, and can be operated at frequencies up to 30 Hz. The static tests were carried out on samples having different lengths with a constant strain rate of 0.1 mm/s. The compression was performed to reach the 80% of the initial length.

The fatigue tests have been performed in displacement control for all types of the foams with a sinusoidal waveform with 3 Hz of pulsation. The samples were preloaded at 70% of the maximal displacement obtained during the static tests, and then subjected to a range of different amplitudes (0.6, 1.2, 2.4, 3.6, 4.8 and 6 mm), leading to different loading levels r (0.725, 0.75, 0.80, 0.85, 0.90 and 0.95), where r is defined as the ratio between the maximum displacement and displacement at densification (80% of the initial length).

The static tests showed the peculiar stress–strain behaviour of these foams, departing from the linear-plateau-densification pattern typical of conventional foams. Fatigue failure depends on a series of random processes leading to disperse results due to the heterogeneous nature of the foam, dimension of the samples and their manufacturing. This dispersion is more pronounced in the non-auxetic foams. The cellular solids examined showed a sharp decrease of the rigidity loss with the initial set of loading cycles, showing after a stabilization pattern up to 10^5 cycles. This behaviour was common to the auxetic and non-auxetic iso-density foams. A specific feature that the auxetic showed compared to the other foams was the significant energy dissipated per unit volume at various loading levels, with increase up to 16 times compared to the conventional foam. The iso-density one showed enhanced energy dissipation behaviour versus the conventional parent foam only at loading level 0.95, always scaled down by a factor of 3 compared to the auxetic one. Future work must be performed to assess the influence of the microstructure and the manufacturing process over the fatigue behaviour of these foams for applications like high-performance sandwich panels for energy absorption.

The description and analysis from fatigue tests show that the stiffness degradation (rigidity loss) (F/F_0) of the specimens until 100,000 cycles can be divided in two stages. The first one (Stage I) corresponds to a sharp decrease, while the Stage II is related to a very slow decrease and flat behaviour, corresponding almost to the total fatigue life of the specimen due to stable crack propagation.

A possible explanation on the Stage I behaviour is linked to the manufacturing process of the foams. The crystallization of the buckling of the ribs during the hot forming step of the process could lead to weakening of connectivities and formation of broken ribs during the dynamic loading, with consequent steep decrease of the rigidity loss during the initial loading phase. Once the weakest links have been broken, however, the other cells would preserve their integrity and the relative rigidity loss would show little sensitivity to increasing numbers of cycles.

The stiffness degradation trends show good correlation with a power law function similar to:

$$\frac{F}{F_0} = c \cdot N^k \tag{4}$$

where c is a constant indicating the initial pre-load conditions (~1), k the exponent coefficient and N is the number of cycles applied.

In the case of the conventional foam the curves are fitted from the load versus number of cycles, while the coefficient c represents also the preload F_0 during the first cycle, to highlight close clustering of results for the stiffness ratio F/F_0 in conventional foams. For the iso-density and auxetic foams, the values of the constant c are centred ~ 0.96, with little dependence over the number of cycles [3]. The values of the constant k are ~ 0.04 for the auxetic foams, while the iso-density ones correspond to a 50% value of the auxetic solids. The correlation factor is satisfactory over all the range of results, with an average value of 0.94 [3].

2.3 Tensile fatigue of conventional and auxetic open cell PU foams [26]

The effect of the stiffness degradation and accumulation of energy dissipation versus the number of cycles are discussed for different loading levels r. The results show that the fatigue behaviour until failure, subjected to cyclic loading depends on the loading levels and occur in three stages. Stage I corresponds to a sharp decrease, from the first cycles, of the ratio F/F_0, while the Stage II is related to a very slow decrease and flat behaviour, corresponding almost to the total fatigue life of the specimen due to stable crack propagation. During the Stage III, with a limited number of cycles, one can observe again a sudden growth of damage until the total failure of the specimen.

A useful quantity for the estimation of fatigue behaviour in cellular foams is the energy dissipation [26]. In sandwich structures with polymeric foam core, it is expected that the viscoelastic behaviour of the foam plays an important role in absorbing and dissipating energy especially during dynamic loading.

The load–displacement behaviour observed upon deformation typically includes a significant strain energy contribution, with the area enclosed by the hysteresis loop corresponding to the dissipated energy (E_d) for each cycle. For any given cycle (N), the dissipated energy per unit volume is provided by

$$E_d = \int_{\varepsilon_{min}}^{\varepsilon_{max}} \sigma \cdot d\varepsilon \tag{5}$$

The analysis of tensile fatigue tests shows clearly from the stiffness degradation that the auxetic foam has an improved fatigue resistance compared to the conventional parent phase. The S–N curves demonstrate the endurance of the auxetic foam compared to the positive Poisson's ratio one. The energy dissipation is also substantially increased at various loading levels compared to the conventional open cell foam. While the significant increase in energy absorption for negative Poisson's ratio foams has been also recorded for compressive cyclic loading, the stiffness degradation is decreased in auxetic foams for tensile loading, giving further evidence of the resilience of these peculiar open cell foams. The results obtained in [26] shows, in general, that the auxetic foam have enhanced characteristics under static loading and tensile fatigue compared to the conventional parent phase form.

3. MATERIALS AND TESTING TECHNIQUES

In the following chapter, experimental procedure is discussed. For the purpose of determining material parameters in Direct Cyclic Loading (c_1 and c_2, respectively) [5], which further will be used for determining fatigue life, specimens (Fig. 4) made from Al-alloy AL 5083, which supposed to be basic material for our auxetic structures, are used. Although, mechanical properties of tested Al-alloy AL 5083 can be found in professional literature modulus of elasticity E = 70.000 MPa; yield strength R_e = 150 MPa, ultimate strength R_m = 250 MPa and fracture strain A = 17 %, we will perform static test for this material.

Furthermore, for the purpose of fatigue life determination, the LCF test will be performed.

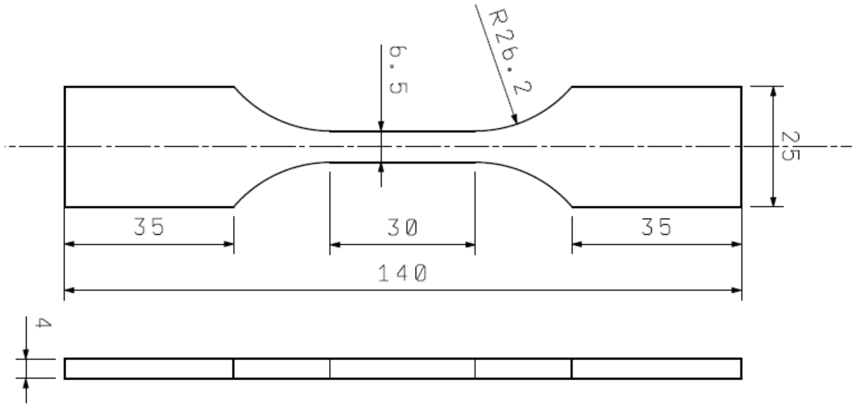

Fig. 4. Specimen Al-alloy AL 5083

3.1 Test conditions

First, static tests to determine the real static mechanical properties and determination the true stress – true strain curve, will be perform on an INSTRON; Second, Low Cycle Fatigue (LCF) tests in the strain control regime using appropriate extensimeter will follow. The following characteristic must be considered during LCF-tests:

- Two loading regimes should be studied: (i) $R_\varepsilon = \varepsilon_{min}/\varepsilon_{max}$= 0.1 and (ii) $R_\varepsilon = \varepsilon_{min}/\varepsilon_{max}$= – 1.
- For each regime, five different strain levels should be considered (at each level 3 tests should be done). It means 30 tests for both regimes (15 tests for R_ε= 0.1 and 15 tests for R_ε= –1).
- In each test, the stable hysteresis loop and also the number of loading cycles until failure should be determined.
- Possible reducing of force after stabilisation of hysteresis loop should also be detected (it is typical for ductile materials what is the case in this study).

4. CONCLUSION

Rather low cases of fatigue life models exist, dealing with porous structures, especially auxetic structures. The main goal of the present paper is to analyse and present some of them. In general, FLM can be based on either experiments, numerical methods and/or analytical approach. However, due to a fact, that many different auxetic structures exist, one cannot expect a unique methodology of FLM for this purpose. Therefore, in present paper, some of most prompt FLM for auxetic structures are discussed. We can conclude, that there is no general FLM of auxetic structures, although some of them presented and discussed in Ch. 2, are of great usefulness and will be used in our further research.

Furthermore, first experimental procedures, which will be obtained for this purpose, is discussed. Since direct cycling loading is one of the possible criteria for damage mechanism, we should determine material constants, i.e. c_1 and c_2, respectively, for this purpose.

Additionally, research should provide, if necessary, new FLM to be use for different auxetic structures, particularly LCF, which is our occupation, recently.

Acknowledgement: Present research work is partially financed by the Slovenian Research Agency "ARRS" in the framework of the Research Programme: "Design of Porous Structures **P2-0063 (B)**" and partially by EU project CeDYNMAT **EF15_003/0000493**, governed by ASCR, the Institute of Thermomechanics, Prague 8, Czech Republic.

REFERENCES

[1] Novak N., Vesenjak M., Ren Z. Auxetic Cellular Materials - a Review. Journal of Mechanical Engineering 62 (2016) 9, pp. 485-493. DOI:10.5545/sv-jme.2016.3656, (2016).

[2] Gibson LJ, Ashby MF. Cellular solids: structure and properties. Cambridge: Cambridge University Press; (1997).

[3] Bezazi A., Scarpa F. Mechanical behaviour of conventional and negative Poisson's ratio thermoplastic polyurethane foams under compressive cyclic loading. International Journal of Fatigue 29 pp. 922–930, (2007).

[4] Šraml M., Kramberger J., Dervarič S., Glodež S. Fatigue behaviour of lotus-type porous structure: numerical approach. *Zbornik radova = Proceedings*. Zagreb: Hrvatsko društvo za materijale i tribologiju, MATRIB 2015, pp. 308-317, (2015).

[5] Šraml M., Kramberger J., Glodež S. Numerical investigation of low-cycle fatigue of lotus-type porous structure subjected to uniaxial/biaxial loading. *Zbornik radova = Proceedings*. Zagreb: Hrvatsko društvo za materijale i tribologiju, MATRIB 2016, pp. 396-407, (2016).

[6] Chan N, Evans KE. Fabrication methods for auxetic foams. Journal Mat.Sci.; 32: pp 5725–36, (1997).

[7] Lakes RS. Foam structures with a negative Poisson's ratio. Science; 253: pp 1038–40. (1987).

[8] Evans Evans KE. Auxetic polymers: a new range of materials. Endeavour New Ser; 15:170–4. (1991).

[9] Alderson KL, Alderson A, Evans KE. The interpretation of straindependent Poisson's ratio in auxetic polyethylene. J. Strain Anal.;32:201–12. (1997).

[10] Lakes RS, Elms K. Indentability of conventional and negative Poisson's ratio foams. J. Compos. Mater.;27:1193–202. (1993).

[11] Lakes RS. Design considerations for negative Poisson's ratio materials. ASME J Mech Des 1993; 115:696–700. (1993).

[12] Scarpa F, Tomlin PJ. On the transverse shear modulus of negative Poisson's ratio honeycomb structures. Fatigue Fract Eng Mater Struct; 23:717–20. (2000).

[13] Scarpa F, Tomlinson G. Theoretical characteristics of the vibration of sandwich plates with in-plane negative Poisson's ratio values. J Sound Vib; 230:45–67. (2000).

[14] Smith FC, Scarpa F, Chambers B. The electromagnetic properties of re-entrant dielectric honeycombs. IEEE Microwave Guided Wave Lett; 10:451–3. (2000).

[15] Prawoto Y. Seeing auxetic materials from the mechanics point of view: A structural review on the negative Poisson's ratio. Computational Materials Science 58 pp 140–153 (2012).

[16] Yang WAY, Li Z-M, Shi W, Xie B-H, Yang M-B. On auxetic materials. J Mat Sci; 39:3269–79. (2004).

[17] Evans KE, Alderson A. Auxetic materials: functional materials and structures from lateral thinking! Adv Mat;12(9):617–27. (2000).

[18] Rehkopf JD, Brodland GW, McNeice GM. Dynamic mechanical analyses and flexural fatigue of PVC foams. Exp Mech;36(1):1–6. (1996).

[19] Shen Y, Golnaraghi F, Plumtree A. Modelling compressive cyclic stress–strain behaviour of structural foam. Int J Fatigue 2001; 23:491–7. (2001).

[20] Kanny K, Mahfuz H, Carlsson LA, Thomas T, Jeelani S. Compos Struct;58:175–83. (2002).

[21] Faughnan P, Bryan C, Gan Y, Aglan H. Correlation between the dynamic mechanical properties and the fatigue behavior of filled and unfilled PTFE materials. J Mat Sci Lett; 17:1743–6. (1998).

[22] Kolsters H, Wennhage P. Density and frequency dependence of loss factor of foam core materials. In: Proceedings of the fifth international conference on sandwich construction, Zurich, 5–7 September; (2000).

[23] Palissery V, Taylor M, Browne M. Fatigue characterization of polymer foam to use as a cancellous bone analog material in the assessment of tothopaedic devices. J Mat Sci Mat Med; 15:61–7. (2004).

[24] Sugimura Y, Rabiei A, Evans AG, Harte AM, Fleck NA. Compression fatigue of a cellular Al alloy. Mat Sci Eng; A269:38–48. (1999).

[25] Bezazi A., Boukharouba W., Scarpa F. Mechanical properties of auxeticcarbon/epoxy composites: static and cyclic fatigue behaviour. Phys. Status Solidi B 246, No. 9, 2102–2110 (2009) / DOI 10.1002/pssb.200982042. (2009).

[26] Bezazi A., Scarpa F. Tensile fatigue of conventional and negative Poisson's ratio open cell PU foams. International Journal of Fatigue 31 pp. 488–494, (2009).

[27] Fiore L. Contribution `a l'´ Etude du Comportement en Fatigue de Mat´eriaux Composites `a Renfort Verre Unidirectionnel, Ph.D. Thesis, Ecole Centrale de Lyon, France (1988).

[28] Salvia M., Fiore L., Fournier P., Vincent L. Flexural fatigue behaviour of UDGFRP experimental approach. Int. J. Fatigue 19(3), 253–262 (1997).

[29] Bezazi A., Mahi A. El, Berthelot J.-M., and Bezzazi B. Strength Mater. 35(2), 149–161 (2003).

[30] Shen Y., Golnaraghi F., Plumtree A. Modelling compressive cyclic stress–strain behaviour of structural foam. Int. J. of Fatigue 23; 491–497 (2001).

[31] Mandell J. F. Fatigue Behavior of Fiber Resin Composites, Developments in Reinforced Plastics, edited by G. Pritchard (Applied Science Publishers, London, New York, 1982), pp. 67–107 (1982).

UPORABNA TRAJNOST MUŠKIH KRATKIH ČARAPA

USAGE DURABILITY OF MALE SOCKS

Antoneta Tomljenović[1], **Ivan Kraljević**[2], **Željana Meral**[1]

[1]Sveučilište u Zagrebu, Tekstilno-tehnološki fakultet, Prilaz baruna Filipovića 28a, 10000 Zagreb, Hrvatska
[2]Jadran Tvornica čarapa d. d., Vinka Žganeca 2, 10000 Zagreb, Hrvatska

Sažetak

Na muške kratke čarape se postavljaju visoki zahtjevi uporabne trajnosti. Zbog toga je, uz ostale proizvodne zahtjeve, veoma značajno međusobno uskladiti i odabrati pređe za njihovu izradu. Činjenica da je broj europskih normi vezanih uz ispitivanje i karakterizaciju pletiva, kao i od njih izrađenih čarapa mali, ukazuje na potrebu proširenja istraživanja u području razvoja metodologije vrjednovanja njihove uporabne trajnosti u uvjetima primjene. Stoga su u radu ispitana i uspoređena uporabna svojstva finih muških kratkih čarapa, izrađenih s najvećim udjelom pamuka u potpunom platiranju različitim pređama, primjenom predložene metodike vrjednovanja uporabne kvalitete prema normiranim metodama. Provedeno je ispitivanje dimenzijske stabilnosti čarapa nakon jednog i pet uzastopnih ciklusa pranja i sušenja, postojanosti obojenja na pranje, djelovanje alkalnog i kiselog znoja te suho i mokro trljanje nakon 10, 25 i 50 ciklusa otiranja površine, sklonosti pilingu nakon 125, 500, 1000, 2000, 5000 i 7000 habajućih ciklusa te otpornosti na habanje metodom prohabavanja, a u svrhu analize utjecaja primijenjene pređe za platiranje na uporabnu trajnost čarapa i potvrde primjenjivosti predložene metodike.

Ključne riječi: *muške kratke čarape, pletiva, uporabna trajnost, ispitivanje materijala.*

Abstract

On male socks are placed high demands of usage durability. In addition to other production requirements, it is very important to harmonize and select yarns for their production. The number of European standards related to testing of knitted fabrics and socks are low. It is necessary to expand the research in the field of evaluation of their usage durability in the conditions of use. The paper examined and compared usage properties of fine male socks, made with the highest share of cotton in full plating by different yarns, applying the proposed methodology for evaluation of usage quality according to the standardised methods. It was carried out the testing of dimensional stability of socks after five repeated washing and drying cycles; colour fastness to washing, alkaline and acid perspiration, dry and wet rubbing after 10, 25 and 50 rubbing cycles; propensity to surface pilling after 125, 500, 1000, 2000, 5000 and 7000 rubbing cycles; and abrasion resistance, with the purpose of analysing the influence of the applied plating yarn on the usage durability of socks and confirmation of the applicability of the proposed methodology.

Keywords*: male socks, knitted fabrics, usage durability, materials testing.*

1. UVOD

Čarape su pleteni tekstilni proizvodi namijenjeni odijevanju nogu. Njima se prekriva odgovarajuća površina nogu, a ovisno o vrsti i duljini ih dijelimo na stopalice, kratke čarape, duge čarape (ili natkoljenice) i čarape s gaćicama. Kratke čarape, uz stopalo, prekrivaju i dio potkoljenice dijelom koji nazivamo tijelom čarape. Tijelo kratke čarape je u pravilu dulje od duljine donjeg stopalnog dijela čarape, a ovisno o njegovoj duljini razlikujemo sokne (čarape koje dosežu polovicu potkoljeničnog dijela noge) i čarape do koljena ili dokoljenice (slika 1). Kratke čarape su primjenjive za sve dobne skupine, a nose se tijekom svakodnevnih slobodnih i poslovnih aktivnosti. Trebale bi zadovoljiti visoke zahtjeve uporabne trajnosti, a ukoliko se radi o čarapama dizajniranim za specifičnu namjenu (sport, zaštitna odjeća i sl.) i definirane funkcionalnosti.

a) b)

Sl. 1: Muške kratke čarape: a) sokne, b) dokoljenice [1, 2]

Uporabna trajnost čarapa ovisi o njihovoj konstrukciji te vrsti i sirovinskom sastavu pređa od kojih su izrađene, a ogleda se u dobrom prilijeganju čarape uz nogu, stabilnosti veličine i strukture po višestrukom pranju, visokoj postojanosti obojenja, manjoj sklonosti pojave površinskog pilinga te dobroj otpornosti na habanje. Zbog toga je, uz ostale proizvodne zahtjeve, veoma značajno, a u svrhu dobivanja proizvoda visoke uporabne kvalitete, međusobno uskladiti i odabrati pređe za izradu čarapa. Kratka čarapa je jedan od rijetkih tekstilnih odjevnih proizvoda koji se u pravilu izrađuje iz najmanje tri bitno različite sirovine, npr. pamuka, poliamida i elastana. Ovisno o namjeni, umjesto pamuka mogu se koristiti vuna ili neka druga vlakna. Glavnina se čarape izrađuje pamučnom jednonitnom ili dvonitnom predenom pređom. Za elastičnost čarape, osim temeljne pređe, uplići se najčešće poliamidna teksturirana multifilamentna pređa. Pri izradi čarapa pređa se u pletaći stroj dovodi iglama u istegnutom stanju. Nakon izrade, pređe se skupljaju vraćajući se u prvotno stanje, a pletivo koje oblikuje čarapu se skuplja 30 do 50 %. U tom slučaju, skupljanje pletiva omogućuje upravo elastičnost poliamidne multifilamentne pređe. U gornjem okrajku tijela čarape (često nazivanim render čarape) potrebna je veća elastičnost pa se u ovaj dio u pravilu uplići elastanska nit (tzv. gumica) čija je svrha pridržavanje čarape u samostojećem položaju uz nogu. Sve tri upletene niti pređe imaju svoju funkciju koja se ogleda u kvalitetnoj čarapi [3-5]. U novije vrijeme se uz temeljnu nit u pletenju za platiranje primjenjuju inovativne pređe iz mješavina – primjerice poliamida i elastana ili pamuka i elastana.

Pritom valja istaknuti da je broj europskih normi vezanih uz ispitivanje i karakterizaciju pletiva, kao i od njih izrađenih čarapa mali. To ukazuje na potrebu proširenja istraživanja u području razvoja metodologije vrjednovanja njihove kvalitete te uporabne i funkcionalne trajnosti u uvjetima primjene [6]. Stoga su u radu ispitana i uspoređena uporabna svojstva finih muških kratkih čarapa, izrađenih s najvećim udjelom pamuka u potpunom platiranju različitim pređama, primjenom predložene metodike vrjednovanja kvalitete prema normiranim metodama prilagođenih specifičnostima ispitivanih odjevnih predmeta i uvjetima njihove uporabe. Provedeno je ispitivanje dimenzijske stabilnosti čarapa, postojanosti obojenja na pranje, znoj i trljanje, sklonosti pilingu i otpornosti na habanje, a u svrhu analize utjecaja primijenjene pređe za platiranje na uporabnu trajnost čarapa i potvrde primjenjivosti predložene metodike.

4.1. Postupak izrade muške kratke čarape

Proizvodnja muških kratkih čarapa pripada u tzv. deblji čaraparski program. Pri izradi istih slijedno se provode sljedeće radne operacije:

- pletenje – ponajprije okrajka (odn. rendera) potom tijela čarape, pete, stopalnog dijela čarape i na posljetku prstiju (slika 2a);
- mehanička dorada – okretanje čarape i šivanje prstiju (slika 2b i c);
- termička dorada – glačanje i termofiksiranje odn. stabiliziranje dimenzija (slika 2d i f) te
- završna kontrola, razredba i pakiranje [5].

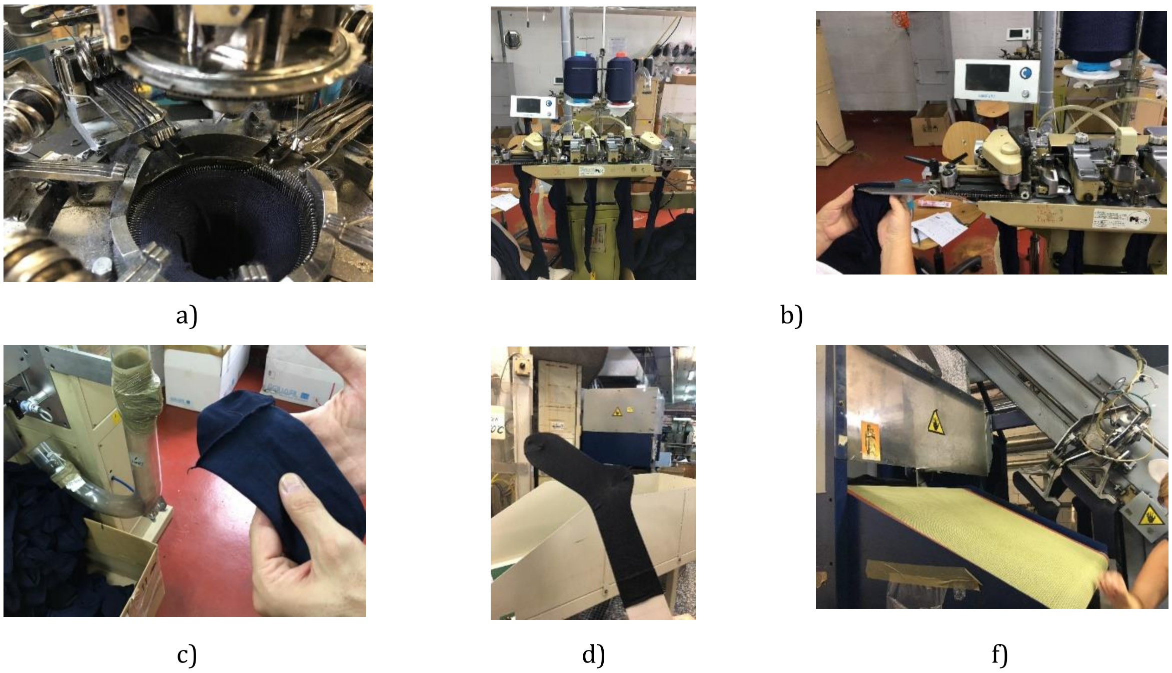
a) b)
c) d) f)

Sl. 2: Proizvodnja muških kratkih čarapa u Jadran Tvornici čarapa d. d: a) pletenje, b) šivanje prstiju, c) čarapa prošivenih prstiju na naličju, d) čarapa pripremljena za glačanje, f) termofiksiranje

Pletenje muških kratkih čarapa provodi se na jednocilindričnim čaraparskim strojevima koji su potpuno automatizirani i elektronski programirani. Strojevi imaju sljedeće tehničke karakteristike: promjer cilindra ležišta od 3'' do 4'', broj okretaja od 500 do 1500 min^{-1}, uz vrijeme izrade jedne kratke čarape do 1 min i 15 s. Optimalna brzina pletenja, odnosno broj okretaja cilindra ležišta kod okrajka je 500 min^{-1}, pletenja tijela čarape i stopala 1200 min^{-1}, a pri završavanju čarape 500 min^{-1}. **Okretanje** čarapa provodi se ručno, pri čemu se čarape okreću na naličje (unutarnju stranu) zbog provedbe prošivanja prstiju čarapa. **Šivanje** prstiju se provodi na automatu za šivanje prstiju koji poslužuje jedan radnik, a radna operacija za jednu čarapu iznosi svega nekoliko sekundi. **Vizualna kontrola** čarapa je potpuna i provodi se na način da se čarape okreću na pravu stranu i dijele po veličinama i razredu kvalitete. Posebna se pozornost posvećuje kvaliteti šavova koji se ispituju istezanjem u poprečnom smjeru. **Glačanje** i **termofiksiranje** čarapa provodi se na aluminijskim kalupima u obliku noge koji stoje okomito na određenom razmaku, pričvršćeni na kružnoj ploči u skupinama od 5 do 10 komada, ovisno o vremenu i temperaturi termičke obrade u komori. **Pakiranje** čarapa u kartonske kutije ili vrećice provodi se ručno ili strojno. Ručno se mogu pakirati sve vrste čarapa, a strojno na automatima samo izglačane čarape.

2. EKSPRIMENTALNI DIO

2.1 Primijenjeni materijali

U radu su primijenjeni uzorci finih muških kratkih čarapa crne boje u veličini 42/43 izrađeni u Jadran Tvornici čarapa d.d. na čaraparskom automatu finoće E14 tt. Lonati promjera cilindra 95 mm, (3 ¾'') koji je pleo sa 168 igala. Po šivanju prstiju čarape su tvornički izglačane na metalnim kalupima propisane veličine i termofiksirane pri temperaturi od 120 °C na stroju tt. Cortese. Izrađene su tri skupine čarapa u desno-lijevom kulirnom potpuno platirnom prepletu s najvećim udjelom pamuka, ali različitog sirovinskog sastava uvjetovanog primjenom različitih pređa za platiranje. Sve čarape izrađene su iz jednonitne pamučne pređe od nemerceriziranog pamuka finoće Nm 34/1 odnosno 29,4 tex uz uplitanje pređe za platiranje u svakom redu pletiva čarape kako slijedi:

- Čarape **skupine 1** (uzorak 1) su u okrajku platirane elastanskom pređom oznake 130 dtex/78 dtex f23/1, a u preostalom dijelu poliamidnom pređom oznake PA 6.6 44 dtex f13 x 2. Odnosno, okrajak čarape je ojačan pređom koja se sastoji od elastanske niti obavijene multifilamentnom teksturiranom pređom iz poliamida 6.6 (PA 6.6). Pritom finoća elastanske niti iznosi 130 dtex, a finoća poliamidne pređe izrađene iz 23 monofilamentne niti iznosi 78 dtex. Ostatak čarape je platiran s pređom iz PA 6.6 odn. multifilamentnom teksturiranom pređom iz dviju međusobno uvijenih multifilamentnih pređa finoće 44 dtex izgrađenih od 13 monofilamentnih niti. Ukupna finoća pređe za platiranje tijela i stopalnog dijela čarape (uključujući petu i prste) iznosi oko 10 tex.
- Čarape **skupine 2** (uzorak 2) su platirane u okrajku elastanskom pređom oznake 130 dtex/78 dtex f23/1, dok su peta i prsti platirani primjenom poliamidne pređe oznake PA

6.6 44 dtex f13 x 2 kao i u prve skupine čarapa. Tijelo i stopalni dio čarape platiran je pređom iz elastanske niti obavijene jednonitnom predenom pamučnom pređom ukupne finoće Nm 100/1 odnosno 10 tex.

- Čarape **skupine 3** (uzorak 3) su platirane u okrajku elastanskom pređom oznake 130 dtex/78 dtex f23/1, u tijelu i stopalnom dijelu čarape primjenom elastanske pređe oznake 22 dtex/78 dtex f23/1, a peta i prsti primjenom poliamidne pređe oznake PA 6.6 44 dtex f13 x 2. Platiranje je u okrajku čarape te na prstima i peti provedeno na način kao i u prve dvije skupine čarapa, dok je tijelo čarape i stopalni dio platiran pređom koja se sastoji od elastanske niti obavijene multifilamentnom teksturiranom pređom iz PA 6.6. Finoća elastanske niti je 22 dtex, finoća teksturirane PA pređe je 78 dtex uz broj monofilamentnih niti od 23, a ukupna finoća pređe iznosi 10 tex.

Primjenom pređa za platiranje tijela i stopalnog dijela čarape jednake finoće osigurana je približno jednaka masa svih ispitivanih uzoraka čarapa. U tablici 1 prikazane su temeljne karakteristike čarapa primijenjenih za ispitivanje.

Tab. 1: Karakteristike triju skupina čarapa primijenjenih za ispitivanje

Uzorak	Lice čarape	Platiranje okrajka	Platiranje čarape		Sirovinski sastav čarape			Masa čarape (g)
			Tijelo čarape i stopalo	Peta i prsti čarape	Pamuk (%)	PA 6.6 (%)	Elastan (%)	
1	pamuk	elastan/PA 6.6	PA 6.6		78	21	1	19,9
2	pamuk	elastan/PA 6.6	elastan/pamuk	PA 6.6	91	6	3	19,8
3	pamuk	elastan/PA 6.6	elastan/PA 6.6	PA 6.6	78	19	3	19,9

2.2 Metodika vrjednovanja uporabne trajnosti čarapa

Za ispitivanja kod kojih je bilo potrebno izrezivati uzorke, čarape su razrezane sredinom prednjeg dijela do šava prstiju i poprečno zarezane sa svrhom izravnavanja pete (slika 3).

Sl. 3: Uzorkovanje čarape: 1 - izglačana čarapa, 2 - rezanje čarape po prednjoj sredini čarape, 3- prorezivanje čarape do šava prstiju, 4 - otvorena čarapa, 5 - poprečno zarezivanje čarape sa svrhom izravnavanja pete (ostavljajući minimalnu širinu od 40 mm), 6 – čarapa pripremljena za uzorkovanje

Kondicioniranje i ispitivanje čarapa provedeno je u uvjetima standardne atmosfere (temperature: 20 ± 2 °C i relativne vlažnosti zraka: 65 ± 4%). U svrhu karakterizacije pletiva temeljnog dijela čarape (tijela i stopalnog dijela) utvrđena je:

- **plošna masa pletiva** čarapa prema HRN EN 12127:2003 [7] iskazana u g/m^2,
- **gustoća pletiva** odn. broj nizova i redova očica na duljini jednog centimetra izbrojavanjem prema HRN EN 14971:2008 [8] te
- **sposobnost vezanja vlage pletiva** u skladu s ASTM D 2654-89a [9] metodom sušenja, a rezultat iskazan u postocima u odnosu na apsolutno suhu masu uzorka.

U svrhu definiranja uporabne trajnosti čarapa primjenom normiranih metoda, prilagođenih specifičnostima ispitivanih odjevnih predmeta i uvjetima njihove uporabe, utvrđena je:

- **Dimenzijska stabilnost čarapa** po pranju i sušenju. Čarape su označene na način kojim je omogućeno praćenje promjena specifičnih izmjera po duljini i širini čarape (slika 4). Mjerenje udaljenosti između naznačenih oznaka na čarapi je provedeno na početnim izglačanim uzorcima čarapa te nakon jednog i pet uzastopnih ciklusa pranja i sušenja. Simulacija od strane proizvođača preporučene njege provedena je prema HRN EN ISO 6330:2012 [10] na temperaturi od 40 °C uz normalnu mehaniku pranja (postupak 4N) i primjenu standardnog deterdženta ECE bez fosfata i optičkih bjelila (br. 3) te sušenje na zraku (postupak A). Razlika u dimenzijama po provedenoj obradi u odnosu na početnu utvrđena je na tri uzorka istovrsnih čarapa i iskazana u postocima.

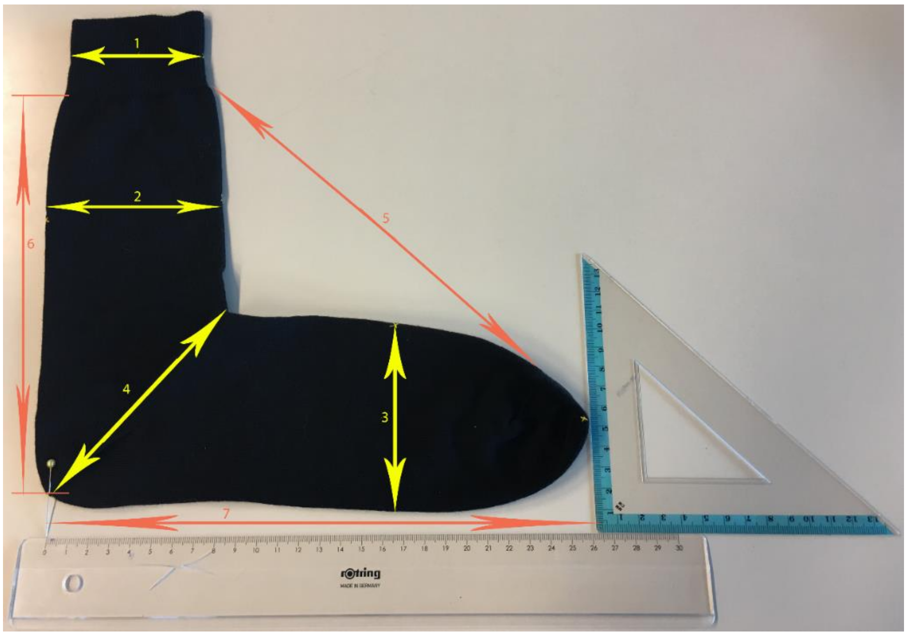

Sl. 4: Prikaz izmjera za ispitivanje dimenzijske stabilnosti: 1- širina okrajka, 2- širina tijela čarape, 3 - širina stopalnog dijela čarape, 4 - polovica opsega u visini gležnja, 5 - duljina od vrha tijela čarape (bez okrajka) do šava prstiju, 6 – duljina od vrha tijela čarape (bez okrajka) do izbočene točke pete čarape odn. mjera visine čarape, 7 - duljina od izbočenog dijela pete čarape do izbočenog dijela prstiju odn. duljina stopalnog dijela čarape

- **Postojanost obojenja čarapa** u pranju, na djelovanje znoja i trljanje. **Postojanost obojenja na pranje** utvrđena je po provedenoj simulaciji kućanskog pranja prema HRN EN ISO 105-C06:2010 [11] na temperaturi 40 °C uz primjenu standardnog deterdženta ECE s dodatkom fosfata bez optičkog bjelila (postupak A1S), ispiranju i sušenju. U tu svrhu pripremljen je kombinirani uzorak na način da je na lice uzorka pletiva čarape dimenzija 100 x 40 mm našivena DW bijela standardna višekomponentna popratna tkanina s 6 utkanih vrpci različitog sirovinskih sastava (celulozni acetat, nemercerizirani pamuk, poliamid 6.6, poliester, akril i vuna). Po provedenoj obradi vizualno je primjenom sivih skala ocijenjena promjena obojenja ispitivanog pletiva (HRN EN 20105-A02:2003 [12]) i prijelaz bojila na svaki dio popratne tkanine (HRN EN 20105-A03:2003 [13]) ocjenama od 1 (najlošija) do 5 (najbolja). **Postojanost obojenja na znoj** utvrđena je prema HRN EN ISO 105-E04:2013 [12], pri čemu se dva kombinirana uzorka zasebno namoče u lužnatoj otopini (pH 8) i kiseloj otopini (pH 5,5) znoja na sobnoj temperaturi uz omjer kupelji 1:50 u vremenu od 30 min te potom stješnjeni između staklenih pločica (dimenzija: cca 60 mm x 115 mm x 1,5 mm) 4 sata obrađuju u sušioniku na temperaturi 37 °C u dva zasebna perspirometra uz opterećenje od 12,5 kPa (5 kg). Po provedenom sušenju u raširenom stanju daju se ocjene promjene obojenja pletiva i prijelaza bojila na popratnu tkaninu za svaki uzorak zasebno primjenom sivih skala. Pri **ispitivanju postojanosti obojenja na trljanje prema** HRN EN ISO 105-X12:2016 [15], ispitivani uzorak čarape se tare suhom odnosno vlažnom bijelom pamučnom standardnom popratnom tkaninom veličine 50 x 50 mm o pletivo čarape na krokmetru, a potom vizualno ocjenjuje prijelaz bojila na popratnu tkaninu primjenom sive skale. U radu je postupak suhog i mokrog trljanja (uz efekt cijeđenja oko 100 %) zaobljenim klipom krokmetra presvučenim bijelom pamučnom tkaninom proveden na duljini od 10 cm u smjeru duljine čarape, 3 puta na različitom dijelu površine stopalnog dijela čarape u intervalima od 10, 25 i 50 ravnocrtnih ciklusa i opterećenje od 9N.
- **Sklonost nastanku pilinga pletiva čarapa** odn. sklonost izvlačenju vlakana i njihovo zamrsivanje na površini pletiva koje umanjuje estetsku vrijednost gotovog proizvoda metodom habanja prema preinačenoj metodi po Martindale-u (HRN EN ISO 12945-2:2000 [16]). Ispitivanje je provedeno plošnim habanjem ispitivanog pletiva učvršćenog na habajuću glavu o standardnu vunenu tkaninu na podlozi instrumenta slijedeći Lissajous-ovu krivulju uz opterećenje od 415 g. Ocjena sklonosti pilingu (1 - 5) daje se vizualno usporedbom s početnim uzorkom i odgovarajućim etalonima nakon definiranog broja habajućih ciklusa (koji za pletiva iznosi 125, 500, 1000, 2000, 5000 i 7000).
- **Ispitivanje otpornosti pletiva čarapa na habanje** primjenom habalice prema Martindale-u. Proveden je postupak prohabavanja, a otpornost na habanje utvrđena prema HRN EN 13770:2008, modificiranom metodom 1 [17]. Ispitivanje se provodi habanjem pletiva čarape o habajuće sredstvo - standardnu vunenu tkaninu. Pomoću kružnog rezača promjera 38 mm izrežu se 4 istovrsna uzorka (dva iz pete čarape i dva iz donjeg dijela stopala od. tabanskog dijela čarape). Prethodno se kao podložak na radno mjesto aparata postavi filc promjera 140 mm, a na habajuću glavu odnosno gornji nosač uzorka spužva promjera 38 mm. Nakon što se uzorci pričvrste, gornji nosači uzorka se opterete pripadajućim utegom od 795 ± 7g (kojim se uz masu nosača ostvaruje pritisak

od 12 kPa). Potreban broj kontrolnih ciklusa do prohabavanja definiran je normom i prikazan u tablici 2.

Tab. 2: Kontrolni periodi tijekom ispitivanja otpornosti na habanje

Očekivani broj habajućih ciklusa pri kojem dolazi do prohabavanja	Kontrolni period
do 10000	svakih 1000 habajućih ciklusa
više od 10000 do 15000	svakih 2000 habajućih ciklusa
više od 15000 do 30000	svakih 5000 habajućih ciklusa
više od 30000	svakih 10000 habajućih ciklusa

Po provedbi definiranog broja habajućih ciklusa valja odrezati grudice zamršenih vlakana na površini ispitivanog pletiva nastale habanjem škarama svinutog vrha. Postupak habanja se završava po pojavi rupice (odn. prekida niti u pletenoj strukturi) ili vidljivog stanjenja pletiva odn. odhabavanja predene pamučne pređe i pojave zaostale sintetske podloge iz niti pređe za platiranje.

3. REZULTATI I RASPRAVA

U tablici 3 prikazani su rezultati utvrđene plošne mase, sadržaja vlage u pletivu te gustoće pletiva odn. broja nizova i redova očica pletiva tijela i stopalnog dijela čarapa na jediničnoj duljini (prije i nakon pet opetovanih ciklusa pranja i sušenja).

Tab. 3: Rezultati plošne mase, gustoće i sadržaja vlage u pletivu tijela i stopalnog dijela čarape

Uzorak	Plošna masa (g/m^2)	Vlaga (%)	Broj nizova/cm		Broj redova/cm	
			Početni	Nakon 5 pranja	Početni	Nakon 5 pranja
1	189,87	6,30	9,5	10	11	12
2	199,9	6,96	9,5	10,5	12	13
3	237,62	6,63	10	10	13	14

Udio vlage u pletivu je gotovo jednak kod svih uzoraka čarapa. Neznatno je veći u uzorku čarapa 2 koji sadrži i najveći udio pamuka boljih sorpcijskih svojstva u odnosu na druge materijale (poliamid 6.6 i elastan) primijenjenih za izradu čarapa. Kod uzorka 3 utvrđena je najveća gustoća pletiva odn. broj nizova/cm i redova očica/cm što se može povezati s većom elastičnosti pređe primijenjene za platiranje tijela i stopalnog dijela čarape, a samim tim i najvećom utvrđenom plošnom masom pletiva. Kod svih uzoraka čarapa utvrđeno je skupljanje pletiva nakon provedenih pet ciklusa pranja i sušenja po širini (veći broj nizova očica/cm) i po duljini (veći broj redova očica/cm) što potvrđuju i rezultati prikazani u tablici 4.

U tablici 4 prikazani su rezultati dimenzijskih promjena čarapa nakon jednog i pet uzastopnih ciklusa pranja i sušenja utvrđeni na mjestima karakterističnih izmjera prikazanih na slici 4, a iskazani u postocima.

Tab. 4: Rezultati dimenzijskih promjena čarapa nakon jednog i pet uzastopnih ciklusa pranja i sušenja u smjeru duljine (*Sd*) i smjeru širine (*Sš*)

Uzorak	Izmjera	Promjene dimenzija nakon 1 pranja		Promjene dimenzija nakon 5 pranja	
		Sd (%)	*Sš* (%)	*Sd* (%)	*Sš* (%)
1	1	/	-5	/	-5
	2	/	-7	/	-8
	3	/	-5	/	-6
	4	/	-6	/	-12
	5	-4	/	-6	/
	6	-7	/	-7	/
	7	-7	/	-8	/
2	1	/	-5	/	-6
	2	/	-11	/	-12
	3	/	-10	/	-13
	4	/	-5	/	-15
	5	-8	/	-12	/
	6	-9	/	-12	/
	7	-10	/	-13	/
3	1	/	-4	/	-6
	2	/	-11	/	-11
	3	/	-9	/	-11
	4	/	-6	/	-8
	5	-3	/	-6	/
	6	-2	/	-7	/
	7	-5	/	-5	/

Kod svih ispitivanih čarapa je po provedenom pranju utvrđeno skupljanje te stoga i rezultati prikazani u tablici 4 nose negativni predznak. S povećanjem broja ciklusa pranja i sušenja povećava se i skupljanje u svih ispitivanih uzoraka čarapa. Uzorci čarapa iz skupine 2 koji sadrže najveći udio pamuka se u odnosu na ostale ispitivane uzorke čarapa više skupljaju što je posebice uočljivo kod izmjera načinjenih u smjeru duljine. Sukladno očekivanom, zbog različite strukture, skupljanje pletiva u okrajku je manje od skupljanja pletiva u tijelu i stopalnom dijelu čarape u smjeru širine u svih uzoraka.

Ispitivanje postojanosti obojenja čarapa na specifične utjecaje u simuliranim uvjetima uporabe i njege provedeno je u svrhu definiranja kvalitete obojenja odn. zadovoljavajućeg fiksiranja bojila na pređi pletiva. U tablici 5 prikazani su rezultati ispitivanja postojanosti obojenja pletiva tijela i stopalnog dijela čarapa u pranju i na djelovanje znoja.

Tab. 5: Ocjene promjene obojenja pletiva i prijelaza bojila na popratnu bijelu višekomponentnu popratnu tkaninu po pranju i djelovanju alkalne i kisele otopine znoja

Prijelaz bojila na popratnu tkaninu	Pranje			Alkalni znoj			Kiseli znoj		
	Uzorak 1	Uzorak 2	Uzorak 3	Uzorak 1	Uzorak 2	Uzorak 3	Uzorak 1	Uzorak 2	Uzorak 3
Acetat	5	5	5	5	5	4/5	5	5	4/5
Pamuk	4/5	4/5	4/5	4/5	4/5	3	4/5	4/5	4
Poliamid 6.6	4/5	4/5	5	4/5	4/5	4	4	4	4/5
Poliester	5	5	4/5	5	4/5	4/5	4/5	4/5	4/5
Akril	5	5	5	5	5	4/5	5	5	5
Vuna	4/5	5	5	4/5	4/5	4/5	4/5	4	4
Promjena obojenja pletiva	4/5	4/5	4/5	4/5	4/5	4/5	4/5	4/5	4/5

Kod svih ispitivanih uzoraka čarapa utvrđena je visoka postojanost obojenja u pranju i na djelovanje znoja te ocijenjena ocjenom 4/5. Jedva primjetna razlika je prisutna u ocjenama prijelaza bojila na popratnu tkaninu odn. referentne dijelove popratne tkanine izrađene od pamuka i vune. Ponešto lošiju postojanost na djelovanje alkalnog znoja bilježi treći uzorak čarapa kod kojeg je prijelaz bojila na pamučni dio popratne tkanine ocijenjen ocjenom 3. Navedeno ukazuje na mogući prijelaz bojila s čarape na kožu korisnika ili podstavne materijale obuće tijekom intenzivnijeg znojenja.

Ispitivanje postojanosti obojenja na trljanje se provodi u svrhu utvrđivanja ponašanja suhe odn. vlažne čarape tijekom nošenja odn. njezina ponašanja u kontaktu s nogom, suhim ili vlažnim materijalima podstave obuće ili unutarnjeg dijela nogavice hlača. U tablici 6 i na slici 5 prikazani su rezultati prijelaza bojila s pletiva čarape na suhu i mokru bijelu pamučnu popratnu tkaninu nakon provedenih 10, 25 i 50 ciklusa otiranja površine. Valja istaknuti da normirana metoda preporuča provesti ocjenu samo nakon 10 ciklusa trljanja, ali je u okviru predložene metodologije vrjednovanja ocjena provedena i nakon većeg broja opetovanih ciklusa trljanja što odgovara realnim uvjetima uporabe. Sukladno očekivanom, s povećanjem broja ciklusa trljanja utvrđene su lošije ocjene postojanosti obojenja pletiva ispitivanih čarapa na trljanje. Kod svih uzoraka čarapa je po provedbi 10 i 25 ciklusa suhog trljanja utvrđena visoka postojanost obojenja (ocijenjena ocjenama 5, 4/5 i 4). Nakon 50 ciklusa trljanja lošija ocjena 3/4 utvrđena je jedino kod uzorka čarapa prve skupine. Kod svih uzoraka čarapa je po provedenih 10 ciklusa trljanja utvrđena lošija postojanost obojenja na mokro trljanje i ocijenjena ocjenom 3. S povećanjem broja ciklusa mokrog otiranja površine prijelaz bojila na popratnu tkaninu se povećava te se sukladno s tim i pripadajuće ocjene smanjuju.

Tab. 6: Ocjene prijelaza bojila pletiva na suhu i mokru popratnu bijelu pamučnu tkaninu nakon 10, 25 i 50 ciklusa trljanja

Broj ciklusa suhog trljanja	Uzorak			Broj ciklusa mokrog trljanja	Uzorak		
	1	2	3		1	2	3
10	4/5	4/5	5	10	3	3	3
25	4	4/5	4/5	25	2/3	2/3	2/3
50	3/4	4	4/5	50	1/2	2	1/2

a) b)

Sl. 5: Prikaz prijelaza bojila s pletiva tri skupine ispitivanih čarapa na pamučnu bijelu popratnu tkaninu nakon provedenih 10, 25 i 50 ciklusa trljanja: a) u suhom i b) u mokrom

U tablici 7 prikazani su rezultati sklonosti nastanka pilinga na površini pletiva tijela i stopalnog dijela čarape tijekom uporabe odn. pripadajuće ocjene utvrđene nakon 125, 500, 1000, 2000, 5000 i 7000 provedenih habajućih ciklusa.

Tab. 7: Ocjene sklonosti nastanka pilinga na površini pletiva tijela i stopalnog dijela čarape

Uzorak		Broj habajućih ciklusa					
		125	500	1000	2000	5000	7000
1	Ocjena	4	3/4	3/4	3	3	2/3
2		4	3/4	3/4	3	2	1/2
3		4	3/4	3/4	3	2/3	2

Iz tablice 7 je vidljivo da se s povećanjem habajućih ciklusa u svih uzoraka čarapa sklonost nastanku površinskog pilinga povećava, a sukladno s tim i ocjene smanjuju. Valja istaknuti da se do 5000 habajućih ciklusa ne uočavaju razlike između ispitivanih uzoraka. Nakon 7000 provedenih habajućih ciklusa najlošije su ocijenjeni uzorci druge skupine čarapa (slika 6) s najvećim udjelom pamuka (ocjena 1/2), dok su pletiva tijela i stopalnog dijela čarapa platiranih s poliamidnom pređom te mješavinom poliamida i elastana ocijenjena neznatno bolje (ocjene 2/3 i 2) što ukazuje na njihove bolje estetske karakteristike i uporabnu trajnost.

Sl. 6: Izgled površine uzoraka pletiva iz tijela druge skupine čarapa nakon provedenog postupka ispitivanja sklonosti pilingu

Po provedbi ispitivanja otpornosti na habanje odn. kontrolnim pregledima ispitivanih uzoraka pletiva izuzetih iz donjeg dijela stopala (odn. tabanskog dijela) čarape i pete čarape nakon definiranog broja habajućih ciklusa (tablica 2) kod uzorka pletiva iz stopalnog dijela čarape 2 izrađenog u potpunom platiranju (pri čemu je u svaki red pletiva upletena jedna jednonitna pamučna pređa i elastanska pređa obavijena jednonitnom pamučnom) utvrđeno je da dolazi do prohabavanja pojavom rupice uvjetovane prekidom niti u pletenoj strukturi pri 30000 habajućih ciklusa (slika 7 a). Otpornijima na habanje su se pokazala pletiva iz stopalnog dijela čarapa 1 i 3 platiranih primjenom sintetske mulifilamentne teksturirane poliamidne pređe (uzorak 1) i elastanske pređe obavijene multifilamentnom teksturiranom poliamidnom pređom (uzorak 3) kod kojih je pri završetku postupka habanja utvrđeno vidljivo stanjenje pletiva odn. odhabavanje predene pamučne pređe i pojava zaostale sintetske podloge iz niti pređe za platiranje (slika 7 b). Pritom je kod uzorka 3 zbog veće elastičnosti elastanske pređe za platiranje, a samim tim i uzorka pletiva, postupak završen pri 45000 habajućih ciklusa, a kod uzorka 1 pri 35000 habajućih ciklusa. Kod pletiva uzorkovanog iz pete čarapa koje je kod svih uzoraka čarapa izrađeno na jednaki način, u potpunom platiranju pri čemu je u svaki red pletiva upletena jednonitna pamučna pređa i poliamidna teksturirana multifilamentna pređa, završetak postupka utvrđen je vidljivim stanjenjem pletiva pri 40000 habajućih ciklusa. U usporedbi s temeljnim pletivom izuzetim iz donjeg dijela stopalnog dijela čarape prve skupine uzoraka platiranog istom pređom, kod pletiva peta utvrđena je veća otpornost pletiva na habanje koju je moguće obrazložiti većom kompaktnosti pletiva u peti čarape uvjetovanu specifičnostima postupka pletenja. Valja istaknuti da je pri provedbi ispitivanja otpornosti na habanje kod svih uzoraka ispitivanih pletiva potvrđena visoka sklonost stvaranju površinskog pilinga (slika 7a).

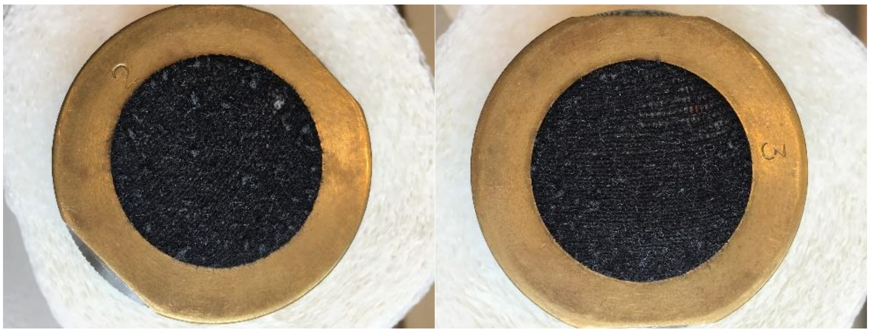

a) b)

Sl. 7: Izgled površine uzoraka pletiva po provedenom postupku prohabavanja: a) pojava rupice, b) vidljivo stanjenje

4. ZALJUČAK

U radu su ispitana i uspoređena uporabna svojstva finih muških kratkih čarapa u desno-lijevom kulirnom potpuno platirnom prepletu s najvećim udjelom pamuka, ali različitog sirovinskog sastava uvjetovanog primjenom različitih pređa za platiranje. Provedbom razrađene metodike vrjednovanja uporabne trajnosti čarapa prema normiranim metodama prilagođenih specifičnostima ispitivanih odjevnih predmeta definiran je utjecaj primijenjene pređe za platiranje na uporabnu trajnost čarapa. Analizom rezultata dobivenim na tri skupine čarapa utvrđena je:

- veća plošna masa pletiva iz tijela i stopalnog dijela kod treće skupine čarapa, a s tim u vezi i veća gustoća pletiva uvjetovana većom elastičnosti pređe primijenjene za platiranje;
- velika sklonost nastanku površinskog pilinga kod svih ispitivanih uzoraka pletiva. Kod čarapa prve i treće skupine valja istaknuti donekle manju sklonost pilingu, ali i veću otpornost na habanje pletiva iz tabanskog dijela čarape;
- zadovoljavajuća postojanost obojenja svih ispitivanih uzoraka na pranje i djelovanje znoja te višestuko suho otiranje. Lošija otpornost na mokro trljanje svih uzoraka čarapa, posebice po povećanju broja ciklusa otiranja može se pojasniti slabije fiksiranim bojilom na primijenjenoj pređi;
- gotovo jednaka količina ravnotežne vlage u svim uzorcima čarapa, no ipak malo veća u drugog uzorka s najvećim udjelom pamuka;
- veće skupljanje po provedenoj simulaciji pranja kod svih uzoraka (nešto izraženije kod uzorka 2) koje se povećava s povećanjem broja ciklusa pranja.

Time je potvrđena primjenjivost razrađene metodike vrjednovanja uporabne kvalitete čarapa i zaključeno da je pri odabiru pređe za platiranje čarapa potrebno voditi računa o cijeni sirovine, njezinoj kvaliteti i sirovinskom sastavu, namjeni gotovog proizvoda, a posebice njegovoj trajnosti u uvjetima uporabe.

Zahvala:
Ovaj rad je financiran sredstvima Hrvatske zaklade za znanost projektom: "Udobnost i antimikrobna svojstva tekstila i obuće, IP-2016-06-5278. Autori se zahvaljuju djelatnicima Jadran tvornici čarapa d.d. iz Zagreba na svesrdnoj pomoći.

LITERATURA

[1] https://www.allergymedicalstore.com.au/products/boody-basic-mens-black-business-socks, posjećeno 10. ožujka 2018.

[2] https://www.amazon.com/JOBST-Knee-8-15-Closed-Black/dp/B009STL6K2, posjećeno 10. ožujka 2018.

[3] Vrljičak Z., Pavlović Ž., Dimenzijska nestabilnost kratkih čarapa, Tekstil, 1-2, pp. 41-48, (2014).

[4] Vrljičak Z., Dodig Z., Utjecaj značajki pređa i strojeva na parametre strukture kulirnih platirnih pletiva, Tekstil, 6, pp. 241-250, (2011).

[5] Vrljičak Z., Kovač A., Projektiranje i izrada kratkih čarapa, Tekstil, 4, pp. 149-159, (2011).

[6] Tomljenović A., Zjakić I., Rolich T., Durability Assessment of Funcionally Printed Knitted Fabrics for T- Shirts, Fibres & Textiles in Eastern Europe, 4, pp. 129-138, (2016).

[7] HRN EN 12127:2003 Tekstil - Plošni tekstil - Određivanje mase po jedinici površine na malim uzorcima.

[8] HRN EN 14971:2008 Tekstilije – Pletiva – Određivanje broja očica po jedinici duljine i jedinici površine.

[9] ASTM D 2654-89a Test Methods for Moisture in Textiles.

[10] HRN EN ISO 6330:2012 Tekstil – Postupci pranja i sušenja u kućanstvu u svrhu ispitivanja tekstila.

[11] HRN EN ISO 105-C06:2010 Tekstil - Ispitivanje postojanosti obojenja – Dio C06: Postojanost obojenja pri pranju u kućanstvu i komercijalnom pranju.

[12] HRN EN 20105-A02:2003 Tekstil – Ispitivanje postojanosti obojenja – Dio A02: Siva skala za ocjenu promjene obojenja.

[13] HRN EN 20105-A03:2003 Tekstil – Ispitivanje postojanosti obojenja – Dio A03: Siva skala za ocjenu prelaska boje.

[14] HRN EN ISO 105-E04:2013 Tekstil – Ispitivanje postojanosti obojenja – Dio E04: Postojanost obojenja na znoj.

[15] HRN EN ISO 105-X12:2016 Tekstil - Ispitivanje postojanosti obojenja - Dio X12: Postojanost obojenja na trljanje.

[16] HRN EN ISO 12945-2:2003 Tekstil – Određivanje sklonosti površinskom stvaranju dlačica i pilingu na plošnom proizvodu – 2. dio: Preinačena metoda po Martindaleu.

[17] HRN EN 13770:2008 Teksilije – Određivanje otpornosti na habanje pletene podstave za obuću.

PRIMJENA KOMPOZITA U AUTOMOBILSKOJ INDUSTRIJI

APPLICATION OF COMPOSITE MATERIALS IN AUTOMOTIVE INDUSTRY

Tomislav Tudek, Zdravko Schauperl

Sveučilište u Zagrebu, Fakultet strojarstva i brodogradnje, Ivana lučića 5, Zagreb, Hrvatska

Sažetak

U ovom radu opisan je razvoj prototipa dijela karoserije električnog vozila. Primarni zadatak je pojednostaviti proizvodnju i uporabu donjeg dijela karoserije vozila. Uz zadovoljavanje tih kriterija, potrebno je i zadovoljiti onaj najvažniji u svijetu automotiva – redukcija mase. Svakoj autokompaniji prilikom razvoja modela glavni cilj je smanjiti masu uz iste ili poboljšane performanse vozila. Tako je i u ovom projektu proveden veći broj testiranja različitih rješenja modela dijela karoserije i konstrukcijskog materijala te modeliranja kako bi se odabrao model optimalnih svojstava. U uvodnom dijelu opisana su svojstva po kojima su polimerni kompoziti toliko superironi nad ostalim materijalima te kratak osvrt na vozilo uz koje je ovaj rad i vezan. U nastavku rada razrađeno je rješenje problema sa krajnjim zaključkom.

Ključne riječi: *Polimerni kompoziti, električno vozilo, karoserija*

Abstract

This paper describes the development of prototype parts of an electric vehicle body. The primary task was to simplify the production and application of the lower part of the car's body. Along with satisfying these requirements, it is necessary to satisfy the one most important in the automotive world – mass reduction. Each car model is designed to reduce the mass with the same or improved vehicle performance as the model develops. To select a model of optimal properties, number of tests on different model design solutions and construction materials have been carried out. The introductory part describes the properties by which the polymer compositions are so superiors over other materials. With the described properties of the composite, in the introduction, there is a brief overview of the vehicle with which this paper and tied. In the course of the paper, a solution to the problem with the ultimate conclusion has been elaborated.

Keywords: *Polymer composite, electric vehicle, car-body*

1. UVOD

Kompozitni materijali zbog svojih specifičnih svojstava u naglom su porastu primjene u razrnovrsnim procesima proizvodnje i granama industrije. Sve veću primjenu stoga bilježe i u automobilskoj industriji. Proizvođači se sve više okreću tim materijalima zbog posebnih svojstava. Svojstva su odraz sastava i mikrostrukture materijala i time sve više potiskuju tradicionalne materijale iz uporabe, u želji za unaprijeđenjem i postignućem što boljih karakteristika. U radu je obrađena tema vezana uz električno vozilo za posebne namjene, čija je karoserija izrađena od posebnih polimernih kompozita s ciljem optimizacije performansi što rezultira boljoj konkurentnosti na tržištu.

1.1. Kompozitni materijali

Polimerni kompoziti relativno su novi materijali čija je proizvodnja započela tek krajem tridesetih godina dvadesetoga stoljeća. Kompozitni materijali zapravo su materijali dobiveni spajanjem dva ili više različitih materijala različitih svojstava. Velika prednost u primjeni kompozitnih materijala uočljiva je zbog uštede na ukupnoj masi proizvoda (posredno se štedi gorivo i ekološki je prihvatljivije), ali i na poboljšanju samih performansi proizvoda. Naime, polimerni kompoziti posebni su po svojoj maloj gustoći uz izuzetno veliku čvrstoću (npr. dijelovi napravljeni od ugljičnih vlakana imaju oko 5 puta veću specifičnu čvrstoću od istih napravljenih od čelika). Uz kombinaciju velike čvrstoće i male mase, polimerni kompoziti odlikuju se i svojom dimenzijskom postojanošću, postojanošću prema atmosferskim utjecajima, postojanosti prema toplini i visokoj dinamičkoj otpornosti. [1]

Slika 1 prikazuje primjenu kompozitnih materijala u različitim granama industrije.

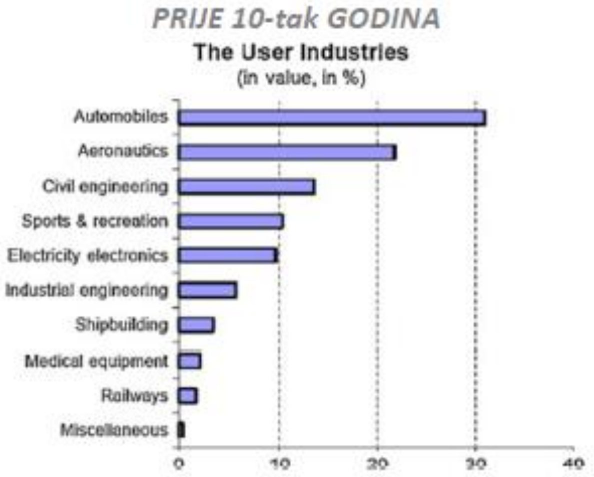

Slika 1. Primjena kompozita u granama industrije [2]

1.2. Električno vozilo

Koncept ovoga električnog vozila prvi je puta predstavljen 2016. godine. Koncept je zamišljen kao multifunkcionalno teretno vozilo. Vozilo je opremljeno sa dva mjesta za sjedenje u kabini, smještenoj na prednjem dijelu vozila. Stražnji dio vozila namijenjen je prijevozu tereta. Kategorija vozila je L7e, teški četverocikl, podkategorija L7e-CU, teški poluzatvoreni četverocikl za prijevoz robe. Na slici 2 prikaz je opisanog električnog vozila. [3]

Slika 2. Prikaz električnog vozila [3]

2. EKSPERIMENTALNI DIO

U početnom modelu karoserija električnog automobila bila je izvedena kao samonoseća konstrukcija sačinjena od jednog dijela. Kako bi se omogućila dimenzijska stabilnost tijekom eksploatacije, potrebna je bila velika debljina stijenke modela. Međutim zbog unapređenja specifikacija vozila dodaje se unutarnje čelično ojačanje. Zbog toga bilo je potrebno reducirati masu karoserije koja u početku iznosi 50 kilograma. Smanjenjem mase postižu se i bolje performanse te se snižuju troškovi proizvodnje. Uz zadatak redukcije mase, bilo je potrebno i postići modularnost dijela karoserije zbog poboljšanja kompaktnosti. Slika 3 prikazuje početni ne modularni model dijela karoserije.

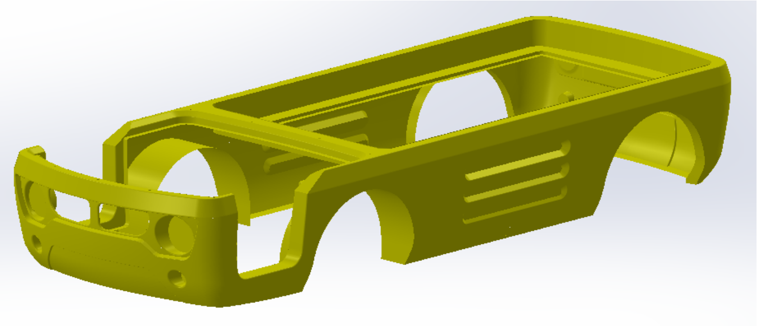

Slika 3. Početni model donjega dijela karoserije električnog vozila

2.1. Oblikovanje dijela karoserije

Prvo je bilo potrebno rastaviti karoseriju na veći broj manjih dijelova kako bi se povećala kompaktnost modela. Samim time indirektno se smanjuje torzijsko opterećenje modela prilikom eksploatacije, što omogućuje smanjenje debljine stijenke. Nakon osmišljanja dolazi se do tri potencijalna modularna modela koji su okarakterizirani svojim manama i prednostima. Ovakav tip konstrukcije omogućuje brzu i učinkovitu zamjenu pojedinog dijela prilikom oštećenja istog, što na prijašnjem modelu nije bilo izvedivo. U tablici 1 prikazani su potencijalni modeli karoserije sa pripadajućim brojem komponenti.

Tablica 1. Prikaz modela karoserija

	PRIKAZ MODELA	BROJ KOMPONENATA
MODEL 1	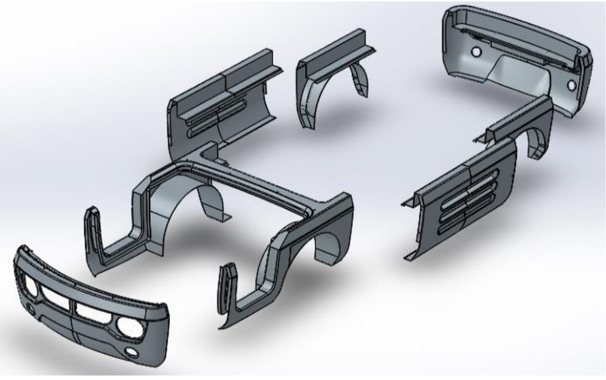	**7**
MODEL 2	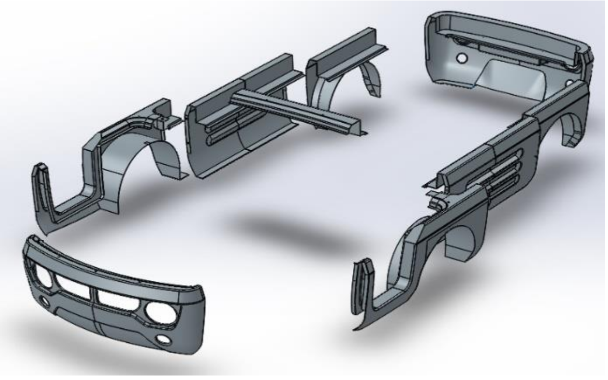	**9**
MODEL 3	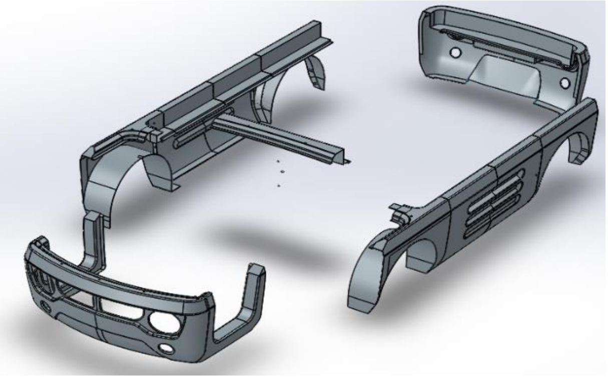	**5**

Nakon modeliranja mogućih načina izvedbe, bilo je potrebno osmisliti način međusobnog spajanja dijelova. Izvedba spojnog mjesta mora omogućiti brzo i učinkovito rastavljanje i sastavljanje pojedinih komponenti. Mora biti lako izvedivo u samom procesu proizvodnje te mora ispuniti zahtjev prostora, koji je ograničen unutarnjim segmentima vozila. Prva moguća solucija vodila se idejom brze i učinkovite izmjene, sa što preciznijim navođenjem kako se ne bih narušavala vanjska estetika koja je jako bitna. Spoj je bio zamišljen u obliku L profila debljine stijenke 3 mm. Takav oblik spoja omogućuje lako navođenje elementa čime bi se izbjegla zračnost. Ovakav ili sličan način spoja široko se primjenjuje u autoindustrijama, a najčešći način spajanja je lijepljenjem ili zakovicama. Indirektno se to i očituje na masi modela, koja je itekako važna u autoindustriji, zbog razlike u masi lijepljenog spoja, odnosno zakovice i čeličnoga vijka. Na slici 4 prikazan je L spoj između dvije komponente karoserije.

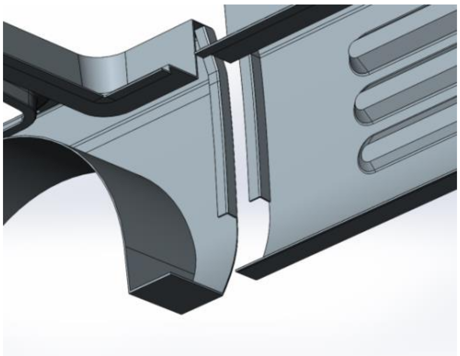

Slika 4. L spoj dvije komponente

Međutim taj način spoja nije se pokazao zadovoljavajućim zbog kompleksnosti izrade te se težilo nečem jednostavnijem sa jednakom učinkovitošću. Tako se došlo do rješenja spoja „stranice uz stranicu“. Ovakav način spajanja pogodan je za brzu izradu bez kompliciranih oblika i brzu i učinkovitu izmjenu pojedinog dijela. Fiksacija između dvije komponente omogućena je zakovicama ili vijcima. Slika 5 prikazuje paralelni spoj između dvije komponente karoserije vozila.

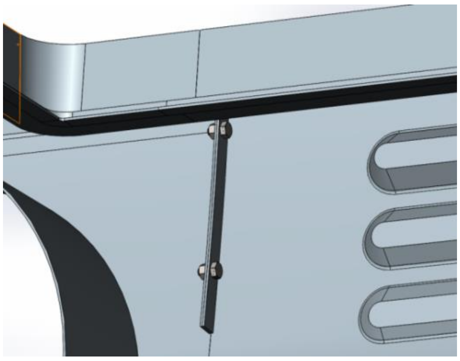

Slika 5. Spoj M12 vijcima dvije komponente

Nakon modificiranja oblika potrebno je riješiti glavni problem u svijetu automotiva. Kako bi se poboljšale performanse vozila, zbog konkurentnosti na tržištu, bilo je potrebno optimirati masu. U ovom slučaju, uz uvjet ostanka istoga materijala, najbolje je smanjenje debljine stijenke. Startni model izrađen je od polimernog kompozita debljine stijenke 5 mm i težio je 50 kilograma. Zbog razlike u gustoći konstrukcijskog materijala postoje velika variranja u masi, stoga je prvi korak bio računanje gustoće. Računanje je provedeno na pločastom uzorku posuđenom od tvrtke koja je i vlasnik ovoga vozila. Nakon provedenih mjerenja dobivena je vrijednost gustoće materijala i iznosi $\rho = 1450\ kg/m^3$.

Dobivenu vrijednost gustoće tada je bilo potrebno unijeti pripadajućem modelu. Kako bi se postigla redukcija početne mase od 50 kilograma, potrebno je bilo smanjiti debljinu stijenke. Negativna nuspojava kod smanjenje debljine stijenke je i smanjenje nosivosti. Prvo testiranje bilo je sa 4,5 mm debljine stijenke gdje je masa karoserije iznosila 48,238 kg. No kako je težnja postići što veće gubitke mase, potrebno je smanjiti debljinu stijenke do krajnje vrijednosti koja osigurava zadovoljavajuće vrijednosti čvrstoće. Optimalna debljina stijenke za ovaj model bila bi 3,5 mm, prema kojoj su i provedena daljnja testiranja. Ovim reduciranje debljine stijenke postiglo se smanjenje mase oko 10,5 kilograma u odnosu na početni model te ona sada iznosi 39,536 kilograma. Naravno, ova masa dolazi sa određenim faktorom sigurnosti zbog same metode izrade i kontinuiranog postizanja iste debljine stijenke niz cijeli model. Smanjenjem mase proporcionalno padaju i troškovi izrade zbog količinski manjeg utroška materijala.

2.2. Prijedlog materijala za izradu

U autoindustriji postoji niz klasičnih materijala koji imaju svoje mane i prednosti i koriste se za izradu pojedinih dijelova. Ista ideja vodilja je i u ovom radu prilikom odabira optimalnog materijala za ovo električno vozilo. Uz već prije upoznati model izrađen od polimernog kompozita ojačanog staklenim vlaknima, idući na redu nametao se polimerni kompozit ojačan ugljičnim vlaknima. Zbog visoke čvrstoće materijala, na modelu je korištena debljina stijenke od svega 2 mm. Iduća slika prikazuje testni model od kompozita ojačanog ugljičnim vlaknima.

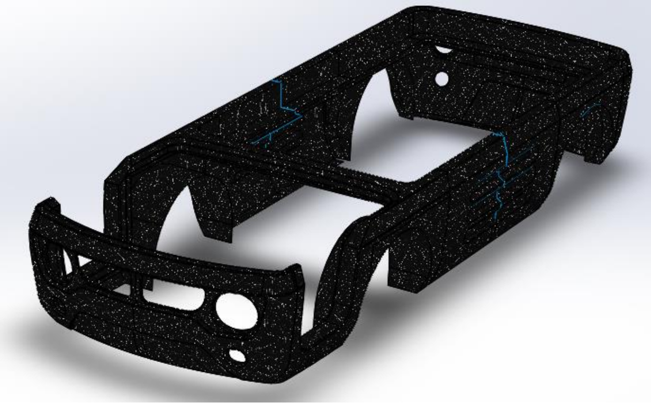

Slika 6. Model izrađen od kompozita ojačanog ugljičnim vlaknima

Ovaj model teži samo 26,35 kilograma, što je 47 % manje nego početni model. Međutim, uza sve prednosti koje ovaj materijal svrstavaju u najčešći materijal u izradi sportskih automobila, ima i velika mana. Najveća mana bila bi visoka cijena samoga materijala, ali i izrade pa zbog toga nije često korišten u proizvodnji „običnih“ automobila.

Idući testirani materijal relativno je novi u autoindustriji, a to je poliuretan. U počecima se ovaj materijal koristio samo za interijere automobila zbog svoje udobnosti i zaštite, no zbog svoje visoke žilavosti i male gustoće, koristi se i za izradu automobilskih karoserijskih dijelova. Ove prednosti rezultiraju manjoj masi i većoj ekonomičnosti vozila. Iduća slika prikazuje testni model izrađen od poliuretana [4].

Na slici 7 prikazan je model karoserije izrađen od poliuretana.

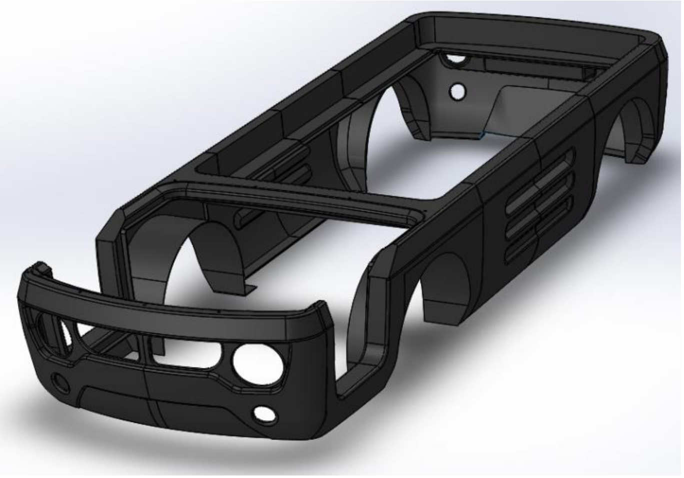

Slika 7. Model izrađen od poliuretana

Korištenjem poliuretana, kao konstrukcijskog materijala, na modelu debljine stijenke 4,5 mm dolazi do redukcije ukupne mase od 13,19 % u odnosu na početni model. Ukupna masa sada iznosi 43,402 kilograma.

2.3. Odabir optimalnog modela

Nakon provedenih testiranja analiza izgleda karoserije i konstrukcijskog materijala, potrebno je odabrati optimalni model i materijal. Prilikom odabira potrebno je voditi se glavnim zahtjevima u autoindustriji, a to su: što manja masa uz što veću vrijednost čvrstoće materijala, visoka dinamička izdržljivost, mogućnost brze i jednostavne izrade, vizualni dojam modela i posljednje i najvažnije, što niža cijena. S obzirom na navedene karakteristike, prvo je potrebno odabrati optimalni model od prethodna tri spomenuta. U tablici 2 nalaze se osnovne prednosti i nedostaci pojedinog modela.

Tablica 2. Usporedba modela karoserije vozila

	MODEL 1	**MODEL 2**	**MODEL 3**
BROJ KOMPONENTI	7	9	5
KOMPLEKSNOST IZRADE	7/10	6/10	5/10
PREDNOSTI	Broj dijelova, isti kalup za bočne stranice, jednostavna izmjena dijelova	Isti kalup za bočne strane, jednostavna izmjena dijelova, poprečna spojnica kao dodatno ojačanje, manja kompleksnost izrade dijelova	Mali broj dijelova, manja kompleksnost izrade dijelova, manji broj spojeva, jednostavna izmjena, poprečna spojnica kao dodatno ojačanje
NEDOSTACI	Kompleksnost izrade	Veliki broj dijelova, veći broj spojeva	Različitost dijelova, otežana izmjena

	POLIMERNI KOMPOZIT OJAČAN STAKLENIM VLAKNIMA	**POLIMERNI KOMPOZIT OJAČAN UGLJIČNIM VLAKNIMA**	**POLIURETAN**
DEBLJINA STIJENKE	3,5mm	2mm	4,5mm
MASA	39,536 kg	26,35 kg	43,42 kg
PREDNOSTI	Mala gustoća, relativno niska cijena materijala i izrade, izrada dimenzijski zahtjevnijih oblika	Mala gustoća, visoka čvrstoća i tvrdoća, izrada dimenzijski zahtjevnijih oblika	Mala gustoća, visoka žilavost, izrada dimenzijski zahtjevnijih oblika, reciklabilan
NEDOSTACI	Krhkost, ekološki neprihvatljiv, slabija mehanička svojstva	Visoka cijena izrade i materijala, ekološki neprihvatljiv	Visoka cijena izrade i materijala

Uzimajući sve kriterije u obzir prilikom rješavanja primarnog problem, kao rezultat dobiven je optimalni model dijela karoserije. Karoserija je zamišljena da se sastoji od 7 dijelova i bila bi izrađena od polimernog kompozita ojačanog staklenim vlaknima. Uz to, model je modificiran u području spojeva, gdje je prihvaćen spoj paralelnog spoja stranice uz stranicu te produženje stijenke u području zadnjih blatobrana. Vanjske dimenzije vozila ostale su nepromijenjene.

3. ZAKLJUČAK

U ovom radu opisan je put razvoja modela karoserije električnoga vozila koji se naizgled činio vrlo jednostavnim, ali zahtjeva niz različitih modela i analiza. Primarni zadatak bila je modifikacija kompletnog modela s ciljem razbijanja cjeline na više dijelova zbog jednostavnije izrade i korištenja. U eksperimentalnom dijelu rada opisan je postupak rješavanja problema. Nailazeći na niz problema i uvjeta koji moraju biti zadovoljeni, formirana su tri konkurentna modela dijela karoserije. Nakon konstruiranja modela, slijedilo je predstavljanje različitih konstrukcijskih materijala. Svaki materijal opisan je kroz svoje prednosti i mane. Uvrštavajući vrijednosti gustoće karakteristične za pojedini materijal u kreirani model karoserije, dolazilo se do vrijednosti masa. Na samom početku nametao se i problem redukcije mase uz zadržavanje traženih mehaničkih svojstava, te kroz provedena testiranja bilo je potrebno dati odgovor na to pitanje. Sumirajući prednosti i nedostatke pojedinih modela i materijala, dolazi se do rješenja kako je model od kompozitnog materijala ojačanog staklenim vlaknima pokazao najbolje rezultate. Za odabir se uzimao i još jedan vrlo bitan podatak – troškovi izrade. Cijena je danas postala glavni čimbenik odabira modela na tržištu. Zbog konkurentnosti potrebno je ponuditi što više uz prihvatljiviju cijenu. Ovaj rad napravljen je u svrhu jačanja konkurentnosti ovog vozila, iako je on mali dio u cjelokupnom razvoju prototipa vozila.

Literatura:

[1] Board Guardian, http://www.boardguardian.hr

[2] H. Chalaye, Composite materials: drive and innovation. Le 4 Pages, des statistiques industrielles, No. 158 – February 2002.

[3] Mück, D.: Tehnička dokumentacija električnog vozila, 2017.

[4] http://polyurethanes.org/en/where-is-it/automotive

Vela Luka, Croatia
International Conference
MATRIB 2018
MATERIALS, TRIBOLOGY, RECYCLING

ISTRAŽIVANJE UZROKA PUKOTINE NA VIJCIMA

CAUSE OF CRACKING ON SCREWS

Karlo Vidić, Andro Raič

Sveučilište u Zagrebu, Fakultet strojarstva i brodogradnje, Ivana Lučića 5, Zagreb, Hrvatska

Sažetak:

Vijčani spoj jedna je od osnovnih vrsta spajanja strojnih elemenata i zastupljen je u svim granama strojarstva. Zbog važne funkcije vijaka (osiguravanje spoja između elemenata) i velike zastupljenosti očito je da njihova izrada mora biti besprijekorna. Tema ovog rada su upravo nesavršenosti, odnosno pukotine koje su se pojavile na tvornički proizvedenim, neeksploatiranim vijcima (klase kvalitete 10.9.). Vijci su izrađeni hladnim kovanjem na višeudarnim strojevima za navedeni postupak. Materijal vijka je čelik za poboljšavanje koji je legiran kromom te prevučen slojem cinka. Cilj je ovog istraživanja bio otkriti uzroke pukotina na temelju usporedbe mikrostrukture te mjerenja tvrdoće vijka bez pukotine i onoga s pukotinom. Nakon izrezivanja ispitnih uzoraka iz vijaka i potrebne pripreme, analizirana je mikrostruktura i kemijski sastav, te izmjerena mikrotvrdoća prema HV0.2 metodi. Na osnovu izvršenih ispitivanja i znanstvenog istraživanja donesen je zaključak o uzroku nastajanja pukotina.

Ključne riječi: *pukotina, čelik za poboljšavanje, hladno kovanje, mikrostruktura, kemijski sastav, tvrdoća*

Abstract:

Screwed joint, the most common joining method in all mechanical engineering branches, is one of the primary joining methods of machine elements. The joint must be faultless since it has extremely important function (ensuring the joint between elements) and huge presence. The paper deals with the imperfections, that is, crackings which appeared on non-exploited, factory made, screws (class quality 10.9.). For the mentioned process, screws are made with cold forging on multishocking machines. Screw material is steel for improving that is alloyed with chromium and coated with a zinc layer. The objective of this research was to detect the causes of cracking based on the comparison of microstructure and measured hardness of screws with no cracking and with the cracking. After cutting the test samples from screws and required preparation, the microstructure and chemical composition were defined by light and electron microscope, and the hardness is measured according to HV-0.2 method. Based on conducted measurements and scientific research, a conclusion was made about the cause of the cracks.

Keywords*: cracking, steel for improving, cold forging, microstructure, chemical composition, hardness*

1.UVOD

Određenu funkciju stroja najčešće nije moguće ostvariti jednim dijelom, pa prema tome svaki kompleksniji stroj može se podijeliti na svoje ugradbene elemente, sklopove i pojedinačne dijelove. Kako bi dobili stroj koji zadovoljava postavljene zahtjeve potrebno je spajati pojedine dijelove prikladnim tehnikama spajanja u cjelinu veće kompleksnosti. Spojevi između elemenata mogu biti rastavljivi (oni koji se mogu više puta razdvojiti bez oštećenja spojnih elemenata) i nerastavljivi. Vijčani spoj, povijesno gledano, prvo je sredstvo za spajanje strojnih elemenata, a trenutno je najkorištenija tehnika spajanja za rastavljive spojeve. [2]

Osnovni dijelovi ove tehnike spajanja su vijak i matica, a po potrebi i podložna pločica. Svaki vijak sastoji se od glave vijka, koja služi za pritezanje vijaka, te od samog tijela na kojem se nalazi navoj. Postoji nekoliko standardnih vrsta navoja, a njihova primjena ovisi o samoj namjeni za koju se vijci koriste. [2]

U samom postupku konstruiranja, proračunavanju vijaka mora se pristupiti pažljivo i s velikim oprezom jer su upravo vijci često puta kritična mjesta na konstrukcijama. Puknuće vijka može oštetiti stroj ili ugroziti sigurnost radnika koji se služe strojem. Budući da se vijcima prenosi opterećenje između spojenih dijelova i da ih moraju držati spojenim, u samom proračunu moraju se poznavati svi parametri materijala vijka (lomna čvrstoća, granica tečenja, dinamička izdržljivost, istezljivost) s visokom točnošću. Uz to, navoji na vijcima većinom se izrađuju tokarenjem, što spada u postupke obrade odvajanjem čestica, pa i nepravilan postupak ovakve obrade može biti uzrokom zaostalih naprezanja u vijcima. Iz navedenog jasno je da je proizvodnja vijaka zahtjevan proces i da vijci na sebi ne smiju imati nikakve pukotine, nehomogenosti u strukturi, ogrebotine ili bilo kakva oštećenja koja bi poticala pojavu pukotina i tako snižavala njihova mehanička svojstva.

Tema ovog rada su pukotine na neeksploatiranim, tvornički proizvedenim vijcima. Ovakvi su vijci neupotrebljivi i iz sigurnosnih razloga ne smiju se slati u prodaju pa tako samo povećavaju financijske troškove proizvođača. Na ispitivanje su poslana 4 vijka, dva na kojima se nalazi pukotina i dva bez pukotine. Vijci s pukotinom razlikovali su se po tome što je kod jednog pukotina bila samo na dijelu tijela, dok je kod drugog pukotina bila i na dijelu glave (3-4 mm), slike 1 i 2.

Slika 1. Vijak bez pukotine

Slika 2. Vijak s pukotinom, crvena crta.

Cilj ovog istraživanja je bio otkriti uzroke nastajanja pukotina koje su nezanemariv problem. Kao što je već navedeno analizirana je mikrostruktura, kemijski sastav i tvrdoća kao jedno od važnijih mehaničkih svojstava.

2. MATERIJAL

Čelik za izradu vijaka spada u klasu čelika za poboljšavanje, koji je legiran kromom. Taj čelik, uz visoku granicu razvlačenja i vlačnu čvrstoću posjeduje i izvrsnu žilavost. Vijci su također pocinčani kako bi se povećala otpornost na koroziju, a izrađeni su hladnim kovanjem tako da je prvo valjanjem izrađeno tijelo vijka na koje se onda udarcem bata oblikuje glava.

Poboljšavanje je postupak koji se sastoji od kaljenja i visokotemperaturnog popuštanja, slika 3. Kaljenje je postupak koji se sastoji od zagrijavanja na temperaturu austenitizacije i podkritičnog hlađenja. Cilj kaljenja je da se što više ugljika koji je otopljen u austenitnoj FCC-rešetki (plošno centrirana kubna rešetka) naglim hlađenjem prisilno zadrži u BCT-martenzitnoj rešetki (volumno centrirana tetragonalna rešetka). Martenzit ima višu tvrdoću od početne feritno-perlitne strukture pa tako povisuje i granicu tečenja, vlačnu čvrstoću, itd. Problem kod materijala koji imaju izrazito visoku tvrdoću (kao što ima martenzit) njihova je krhkost, koja je kod izrade vijaka nepoželjno svojstvo. Zato se vijci nakon kaljenja visokotemperaturno popuštaju. Ovim postupkom materijal se zagrijava na temperature od 400 °C do otprilike 700 °C i sporo hladi, slika 4. Tijekom popuštanja atomi ugljika izlaze iz martenzitne rešetke i zaustavljaju se na mjestima gdje je prisutna manja deformacija rešetke. Zbog toga se smanjuju zaostala naprezanja, povećava se žilavost, a tvrdoća, granica tečenja i vlačna čvrstoća neznatno padaju. [3]

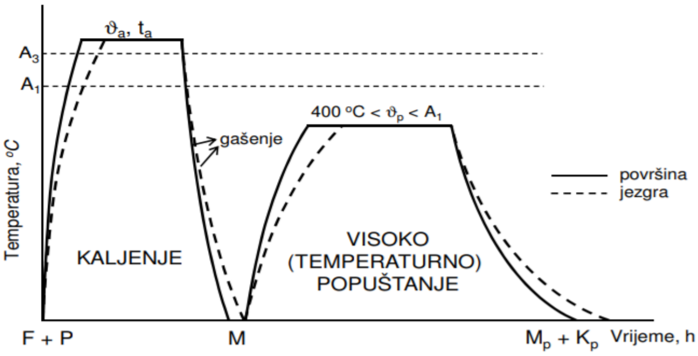

Slika 3. Dijagram postupka poboljšavanja

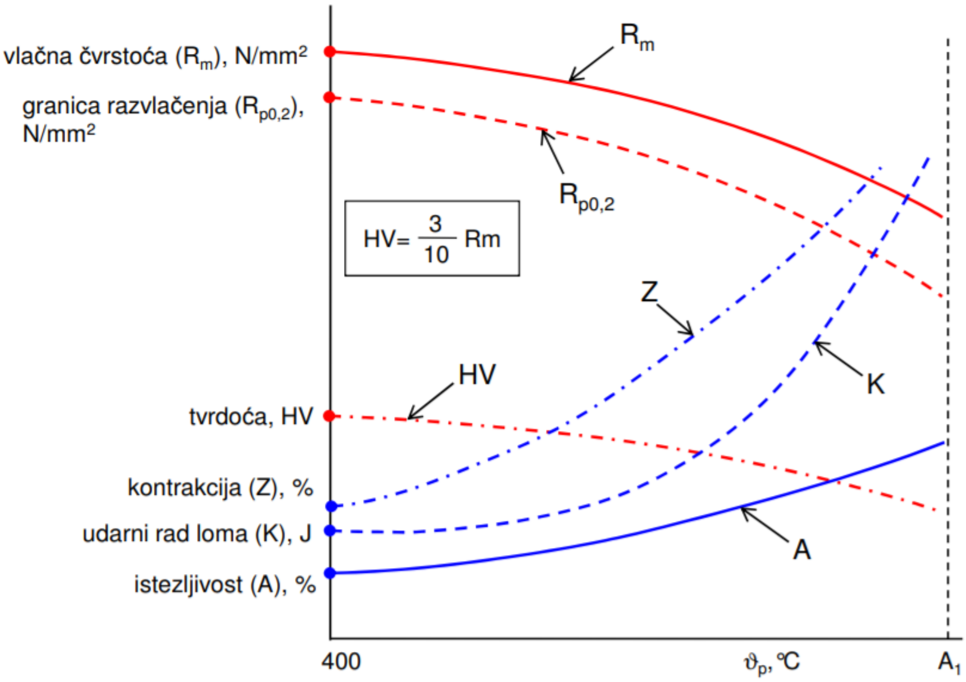

Slika 4. Dijagram promjene svojstava ovisno o temperaturi popuštanja

Postotak ugljika u čelicima za poboljšavanje kreće se od 0,2 % do 0,6 % i obično su čelici nelegirani ili niskolegirani. U ovom slučaju čelik je legiran s kromom koji daje odličnu korozijsku postojanost te povisuje prokaljivost. Krom je također jak karbidotvorac (zajedno s ugljikom stvara karbidne spojeve), pa tako povisuje i tvrdoću. [1]

Pocinčavanje se obavlja uranjanjem vijaka u rastaljeni cink, na temperaturi oko 450 °C (vruće cinčanje). Reakcijom cinka i željeza stvara se njihova legura na površini. Cinkova prevlaka sastoji se od nekoliko slojeva, a postotak željeza u njima pada prema površini. [1]

Oznaka klase 10.9. ispitivanih vijaka znači da maksimalna čvrstoća, odnosno R_m, iznosi 1000 N/mm² (prvi broj u oznaci x 100 = R_m). Drugi broj u oznaci pomnožen s prvim brojem i brojem 10 daje iznos granice elastičnosti, R_e = 10 x 9 x 10 = 900 N/mm². [2]

3. PRIPREMA UZORAKA

Priprema uzoraka za metalografski analizu se izvodi u nekoliko koraka. Postupci pri pripremanju uzoraka su: izrezivanje, ulivanje u polimernu masu, brušenje, poliranje te nagrizanje. Izrezivanje i ulijevanje u polimernu masu početni su koraci kojima se dobije uzorak uniformnog oblika, a također olakšavaju rukovanje te analizu rubova uzoraka. Izrezivanje uzorka može biti problematično jer se trebaju izbjeći negativne poslijedice kao što su lom rezne ploče ili spaljivanje uzorka. [1]

U ovom je radu bilo potrebno pripremiti 3 uzorka. Dva uzorka (jedan s pukotinom, a drugi bez nje) izrezivana su iz tijela vijka pa ih nije bilo potrebno ulijevati u polimernu jer su bili debljine 6 mm i rukovanje njima nije bio problem. Treći uzorak izrezivan je iz glave vijka s pukotinom kako bi se analiziralo do kojeg dijela glave se pukotina širi. Taj uzorak bio je debljine 3 mm pa je bilo potrebno i ulijevanje u polimernu masu.

3.1. Brušenje

Brušenje je najagresivniji postupak odnošenja materijala s površine. Samim se postupkom uklanjaju slojevi prljavštine, apsorbiranih plinova, oksida, te plastično deformirani sloj kako bi se došlo do osnovnog materijala. [1]

Za ispitivanje je korištena brusilica proizvođača Buehler. Postupak je proveden u 6 stupnjeva, odnosno sa 6 vrsta brusnih papira, koji se razlikuju po veličini granulata. Brzina vrtnje je u svim stupnjevima iznosila 300 okretaja/minuti, uz stalni dovod vode za hlađenje i podmazivanje. Za prvi stupanj brušenja korišten je brusni papir P120 gdje 120 označava prosječnu veličinu abraziva u mikrometrima. Uzorak se istosmjerno pomiče po brusnom papiru. Primijenja sila je ručna, a vrijeme određenog stupnja je po potrebi. Za svaki sljedeći stupanj korišteni su finiji brusni papiri prema sljedećem redoslijedu: P320, P500, P1000, P2400, P4000.

Slika 5. Brusilica korištena pri ispitivanju

3.2. Poliranje

Nakon brušenja slijedi postupak poliranja u svrhu dobivanja glatke i sjajne površine uzorka priklade za promatranje pod mikroskopom. Kod poliranja koriste se abrazivi manje veličine pa je ovaj postupak finiji od brušenja. Parametri koji su promatrani u postupku su: podloga, abraziv, hlađenje, brzina, sila i vrijeme poliranja. [1]

Postupak je proveden na uređaju za poliranje Struers DAP-V, slika 6, a podloga je MD-Map. Poliranje se sastojalo od dva stupnja jer su korištena dva različita abrazivna sredstva. U prvom koraku korištena je dijamantna pasta od 3 µm (3 označava prosječni promjer zrna abraziva u mikrometrima) u trajanju od 3 minute. U drugom stupnju korištena je dijamantna pasta od 1 µm u trajanju od 2 minute. U oba slučaja je primijenjena sila ručna. Brzina vrtnje podloge u oba slučaja je 150 okretaja/minuti, a za hlađenje je korištena voda. Nakon poliranja uzorak je ispran u vodi i osušen tkaninom.

Slika 6. Polirka koja je korištena u pripremi uzoraka.

3.3. Nagrizanje

Nagrizanje je postupak selektivnog korodiranja površine materijala s ciljem dobivanja mikrostrukture uzoraka. Postoji nekoliko različitih metoda kako nagristi uzorak (kemijsko, obojeno, elektrolitičko ili termičko nagrizanje), u ovom slučaju primijenjeno je kemijsko nagrizanje jer se ono koristi kod većine metala. [1]

Uzorci su nagriženi s otopinom 3%-tnog nitala. Nital je otopina dušične kiseline (HNO_3) i alkohola (većinom se koristi methanol ili etanol). Uzorci se drže u otopini 5 sekundi, što je dovoljno za otkrivanje mikrostrukture, nakon toga reakcija se prekida, a uzorak se ispire u vodi, te je isti spreman za promatranje pod svjetlosnim mikroskopom Olympus GX51.

4. METODE ISPITIVANJA

4.1. Promatranje pod svjetlosnim mikroskopom

Svjetlosni mikroskop služi za promatranje faza koje su prisutne u pojedinom uzorku. U našem slučaju smo uspoređivali uzorke vijaka sa i bez pukotine kako bi utvrdili da li je došlo do promjene mikrostrukture osnovnog materijala prilikom proizvodnje (toplinskih obrada). Pukotina u poliranom stanju prikazana je na slikama 7 i 8.

Slika 7. Cijela pukotina– uvećanje 50:1

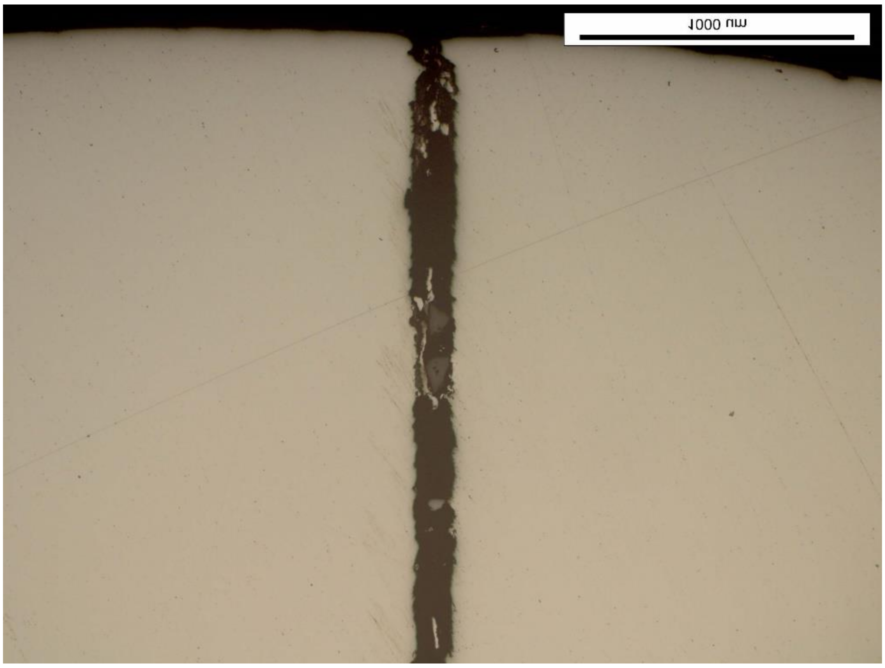

Slika 8. Različite faze u pukotini – uvećanje 50:1.

Usporedbom smo uočili različite boje materijala pukotine i osnovnog materijala, što upućuje na različite faze u pukotini. Na dijelu pukotine koji je bliži rubu širina pukotine je veća i mogu se uočiti uključci različitih veličina. Udaljavanjem se širina smanjuje i uključci postaju sve sitniji.

Na slici 9 prikazana je mikrostruktura materijala vijka u nagriženom stanju.

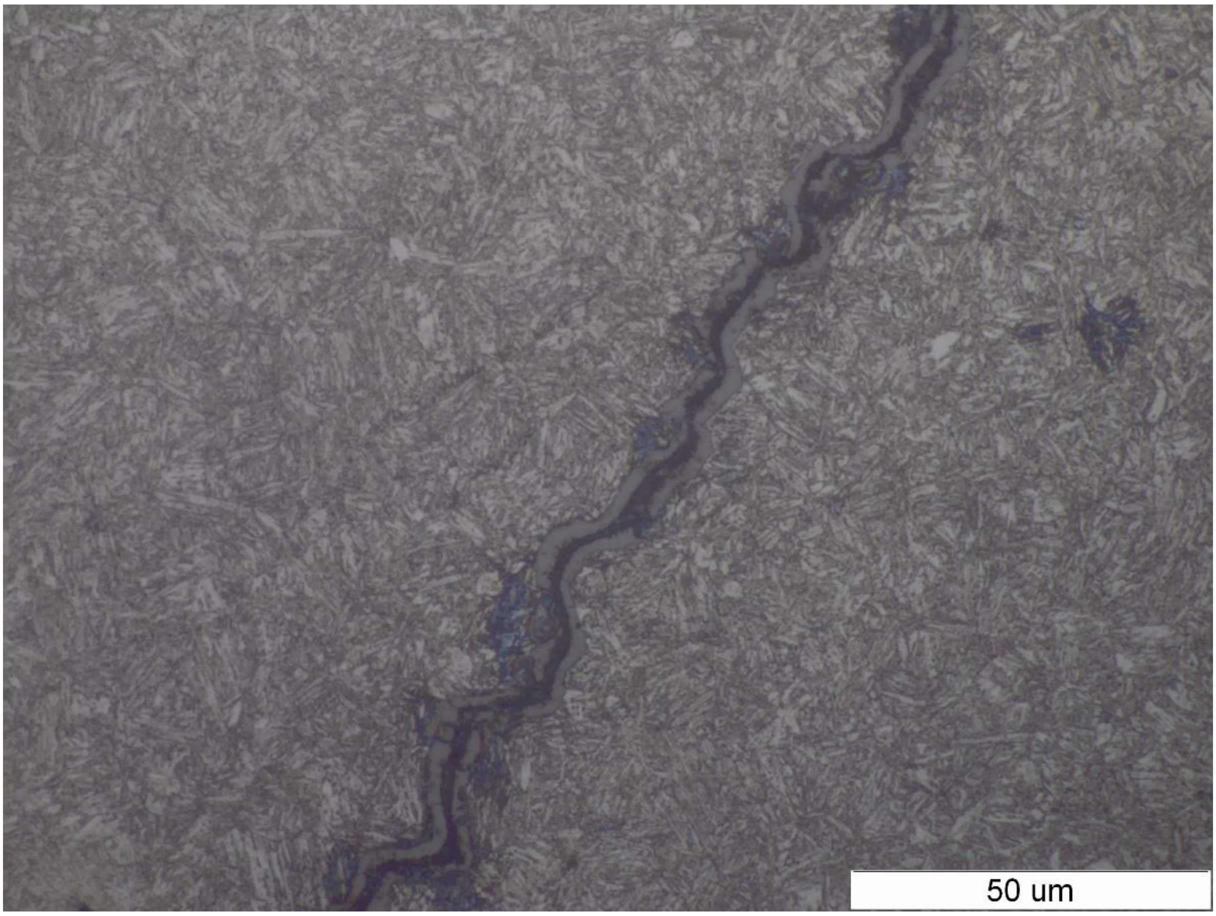

Slika 9. Pukotina – svjetlosni mikroskop, uvećanje: 1000:1

4.2 Analiza elektronskim mikroskopom

Nakon analize uzorka na svjetlosnom mikroskopu, uzorak se promatrao i na SEM-u (skenirajući elektronski mikroskop) Tescan Vega 5136 MM. Elektronski mikroskop je uređaj kojim se pomoću snopa elektrona dobiva uvid u mikrostrukturu materijala uzorka. Snop elektrona skenira po uzorku i na taj način izaziva niz reakcija s atomima na površini uzorka. Signal putuje do procesora koji ih analizira i generira sliku. [2]

Analiza na elektronskom mikroskopu koji je precizniji od svjetlosnog potvrdila nam je ono što smo prethodno zaključili. Ovdje je posebno promatran rub same pukotine pod većim povećanjem koji je imao zaobljen izgled, iz čega se daju naslutiti uzroci pukotine.

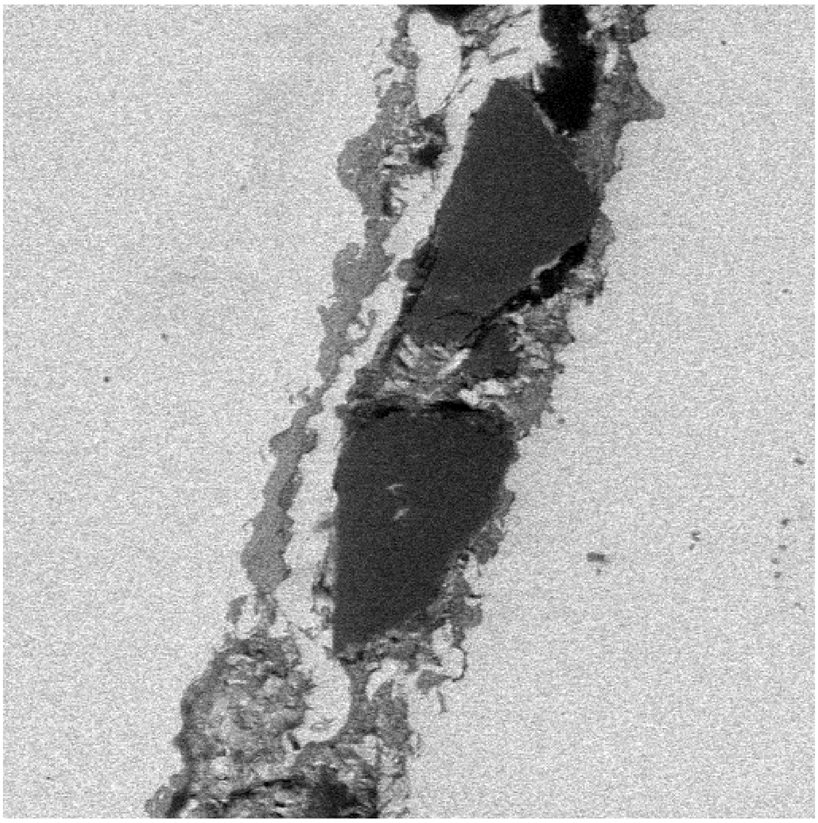

Slika 10. Uključci u pukotini – SEM, uvećanje: 300:1

4.3. Mjerenje mikrotvrdoće

Tvrdoća je otpornost materijala prema prodiranju drugog, znatno tvrđeg tijela. Mikrotvrdoća određena je Vickersovom metodom na tvrodmjeru PMT-3Y42. Indentor je četverostrana dijamantna piramida s vršnim kutom od 136° koja se utiskuje u uzorak pomoću vrle sile 2N, u trajanju od 10-ak sekundi (HV0,2 tvrdoća). Mjerenje je provedeno na lijevom i desnom vrhu uzoraka sa i bez pukotine. Provedena su tri mjerenja u svakom vrhu zbog preciznijeg utvrđivanja tvrdoće uzorka. Prema danoj formuli izračunate su vrijednosti za svako mjerenje, pomoću kojih je iz tablice za određivanje tvrdoće isčitana vrijednost. [4]

Formula za račun: $(X_2 - X_1) * 0,302$

Tablica 1. Tvrdoća uzorka bez pukotine

Mjerenje	**Lijevi vrh (X_1)**	**Desni vrh (X_2)**	**Tvrdoća**
1.	347	449	391
2.	342	453	330
3.	339	456	298

Prosječna vrijednost tvrdoće: (391+330+298)/3 = 339.6 HV0,2

Tablica 2. Tvrdoća uzorka s pukotinom

Mjerenje	**Lijevi vrh (X_1)**	**Desni vrh (X_2)**	**Tvrdoća**
1.	348	458	336
2.	344	450	362
3.	342	453	330

Prosječna vrijednost tvrdoće: (336+362+330)/3 = 342,6 HV0,2

5. ZAKLJUČAK

Analizom rezultata provedenih istraživanja može se zaključiti slijedeće:

- usporedbom mikrostruktura svih analiziranih uzoraka pomoću svjetlosnog mikroskopa nema razlike u osnovnom materijalu vijka bez pukotine i vijka s pukotinom.
- analiza mjerene mikrotvrdoće potkrepljuje gore navedenu tezu jer razlike u vrijednostima nisu značajne.
- detaljnijom analizom mikrostrukture pomoću SEMa vidljive su nemetalne uključine unutar pukotina.
- Na temelju tih podataka može se pretpostaviti da su pukotinu uzrokovale nemetalne uključine u samom materijalu. Te uključine predstavljaju slabo mjesto u materijalu i uslijed naprezanja tijekom toplinske obrade mogu uzrokovati pojavu i propagaciju pukotine.

LITERATURA:

[1] T. Filetin, F. Kovačiček, J. Indof: Svojstva i primjena materijala – Sveučilište u Zagrebu – FSB, 2007.

[2] https://hr.wikipedia.org/wiki/Glavna_stranica

[3] M. Stupnišek, F. Cajner: Osnove toplinske obrade metala – Sveučilište u Zagreb – FSB, 2001.

[4] V. Ivušić, M. Franz, Đ. Španiček, L. Ćurković: Materijali 1 – Sveučilište u Zagrebu – FSB, 2011.

EKSPERIMENTALNO IZUČAVANJE INDENTACIJSKE LOMNE ŽILAVOSTI U NANOSTRUKTURIRANIM TVRDIM METALIMA

EXPERIMENTAL STUDY OF INDENTATION FRACTURE TOUGHNESS IN NANOSTRUCTURED CEMENTED CARBIDES

Matija Sakoman[1], Danko Ćorić [1], Božo Renić[1]

[1]Faculty of Mechanical Engineering and Naval Architecture, Ivana Lučića 5, Croatia

Abstract

In this paper the hardness and Vickers indentation fracture toughness values for nanostructured cemented carbides was tested and analysed. The experimental part included the testing of three samples: WC with 5% cobalt (WC-5Co), WC with 10% cobalt (WC-10Co) and WC with 15% cobalt (WC-15Co). Hardness was tested by Vickers method (HV30) according to HRN EN ISO 6507-1: 2005. Fracture toughness was determined and compaired by different indentation methods such as Palmqvist, Shetty, Niihara, Antis etc. These methods use the length of cracks that propagate from the tip of the Vickers pyramid imprint to determine fracture toughness. The results show that by increasing the amount of Cobalt in cemented carbides hardness values drop, and the fracture toughness increases. They also indicate a difference in results using various mathematical models. By sintering nanostructured cemented carbide, higher hardness values with a small decrease in fracture toughness can be achieved.

***Keywords**: nanostructured cemented carbides, hardness, fracture toughness.*

Sažetak

U ovom radu ispitivane su i analizirane vrijednosti tvrdoće i lomne žilavosti nanostrukturiranih tvrdih metala. Eksperimentalni dio uključivao je provođenje ispitivanja na tri uzorka: s 5% kobalta (WC-5Co), 10% kobalta (WC-10Co) odnosno 15% kobalta (WC-15Co). Tvrdoća je ispitana metodom po Vickersu (HV30) sukladno normi HRN EN ISO 6507-1:2005. Lomna žilavost ispitivana je različitim metodama kao što su Palmqvist, Shetty, Niihara, Antis i druge. Za izračun lomne žilavosti u ovim metodama koriste se duljine pukotina koje propagiraju iz vrhova otiska. Rezultati pokazuju da se s povećanjem udjela kobalta u tvrdom metalu smanjuje tvrdoća, a lomna žilavost povećava. Rezultati također pokazuju razlike u vrijednostima lomne žilavosti po pojedinim metodama. Primjenom nanostrukturiranih tvrdih metala, može se ostavriti viša tvrdoća uz tek neznatno smanjenje lomne žilavosti.

***Ključne riječi**: nanostrukturirani tvrdi metali, tvrdoća, lomna žilavost.*

INTRODUCTION

As a material for cutting tools hardmetals, also known as cemented carbides have proven to be an optimal material comparing the price and tool lifetime. Improvements in hardness, fracture toughness and consequently, service life of hardmetal tools are nowadays achieved with a decrease of a grain size, and for that reason the development of ultrafine (0.2 - 0.5 μm) and nanostructured (<0.2 μm) cemented carbides has took place in a wide scale, Figure 1.

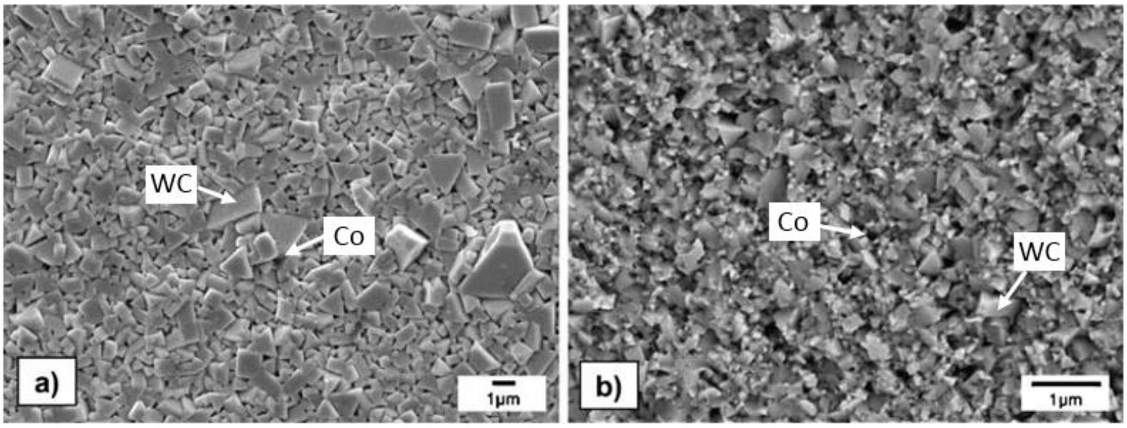

**Figure 1. SEM images of WC-Co cemented carbides:
(a) submicron and (b) nano-grained WC-Co cemented carbide [2]**

The microstructure of cemented carbides consists of a higher portion of tungsten carbide (WC) and possibly smaller portions of titanium and tantalum carbides, mutually linked to a binder phase that is cobalt (Co). The cobalt matrix provides toughness, and carbides are here to provide high tribological properties, mainly connected to high hardness values. These materials are most commonly used for the production of cutting tools for metal and stone processing, and tools for the oil and gas drilling industry. Cutting tools made from cemented carbides generally have better properties than high-speed steel ones [1].

Grain size plays an important role in cemented carbide properties, and a range of hardness and fracture toughness values can be achieved by adjusting that grain size. Those powders are nowadays be consolidated into homogeneous microstructures of extremely high strength, hardness and satisfactory fracture toughness, Figure 2.

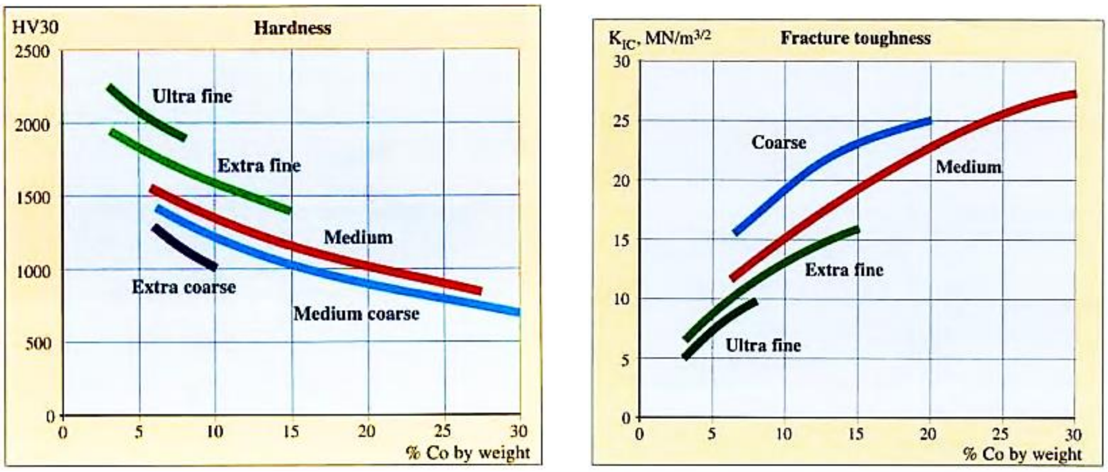

a) b)

Figure 2. (a) Hardness and (b) fracture toughness (Palmquist) as a function of the Co content for various WC grain sizes [3]

This allows a longer service life of a cutting tool, application at higher cutting speeds and less tolerances of a machined part [4, 5]. Fracture toughness (K_{IC}) is a property that describes the ability of the material to endure the occurrence and spreading of a crack [6]. The properties of these metals are also largely determined by the amount of Co-binder, peculiarly when it comes to mechanical properties such as hardness and fracture toughness.

MATERIALS AND METHODS

Three samples with 5% Co (WC-5Co), 10% Co (WC-10Co) and 15% Co (WC-15Co) were consolidated by sinter / HIP process as shown in Figure 3. The pre-compacted mixture of cobalt and tungsten carbide powders was sintered in vacuum and pressed by hot isostatic pressing in a protective atmosphere of inert gas (argon).

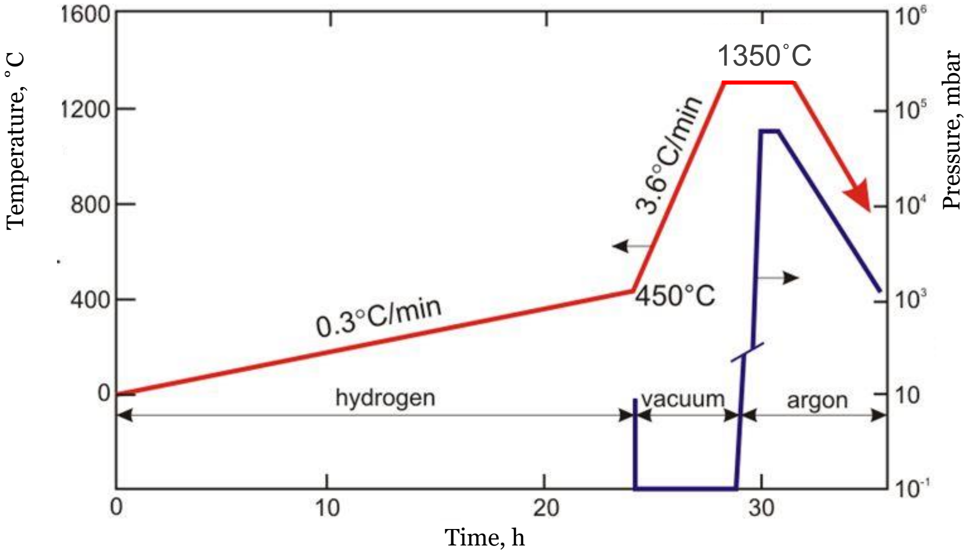

Figure 3. Sinter/HIP cycle

Metallographic preparation of the samples through several grinding and polishing stages was conducted in order to minimise the effect of residual stresses, and surface roughness affecting the results [7, 8] as follows:

1. grinding with diamond-abrasive MD-Piano 120 with water cooling,
2. fine grinding with MD-Allegro with a 9 µm granular diamond paste with coolant lubricant (alcohol and water),
3. fine grinding with MD-Largo with 3 µm granular diamond paste with cooling with lubricant,
4. polishing with MD-Dac 3-micron granulated diamond paste with coolant lubricant,
5. final polishing with MD-Chem tile with colloidal paint.

After the preparation of the surface hardness and fracture toughness tests were performed on metallographically polished samples shown in Figure 4.

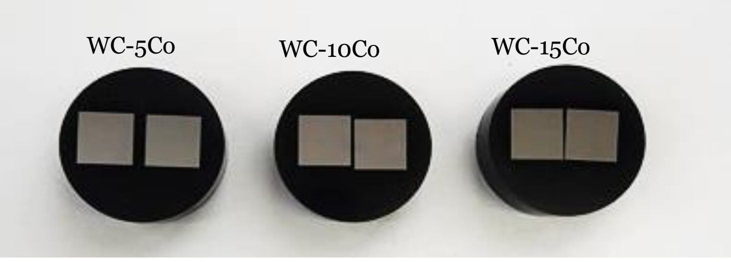

Figure 4. Samples of cemented carbides

Hardness was measured by Vickers method at reference hardness tester (manufactured by Indentec, United Kingdom, type: 5030 TKV) with a load of 294,20 N (HV30), according to recommendations for this type of material. On each sample, a total of 15 measurements were made. The hardness values for Vickers methods were calculated by the following equation:

$$HV = 0{,}1891 \cdot \frac{F}{d_{sr}^2} \tag{1}$$

where are:

d_{sr} – mean value of the indentation imprint diagonal, $d_{sr} = \frac{d_1+d_2}{2}$ [mm],
F – indentation force [N].

Fracture toughness was determined by various indentation methods in order to determine the differences in results and applicability of various mathematical models for this type of material.

Compared to classical test methods, indentation technique has a number of advantages such as simple and fast measurement that does not require sophisticated measurements of cracks, small sample dimensions, and minimum sample preparation at a low price [9, 10]. Nowadays, various mathematical models that describe Vickers indentation fracture toughness, such as the Anstis, Niihara, Casellas, Shetty, Palmqvist, Evans and Charles, Tanaka, NMH (Niihara, Morena and Hasselman) and Lankford models [11] are known.

This paper uses various methods for calculating fracture toughness which in the calculation includes the values of hardness, indentation force and the length of the cracks originating from the tip of the Vickers imprint, Figure 5.

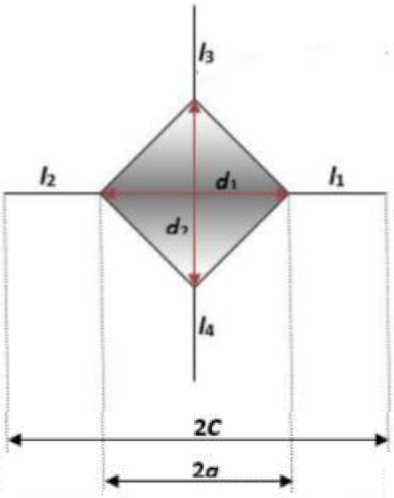

Figure 5. Vickers indentation and cracks occurring in cemented carbide materials

The crack lengths l_1, l_2, l_3, l_4, were measured using a metallographic inverted Olympus GX51F-5 microscope with an integrated DP25 digital camera and an associated image analysis program. Equations of models for calculating fracture toughness are as follows [12]:

Palmqvist:

$$K_{Ic} = 0.0028 \cdot HV^{1/2} \cdot \left(\frac{F}{T}\right)^{1/2} \tag{2}$$

Anstis:

$$K_{Ic} = 0.016 \cdot \frac{F}{c^{3/2}} \cdot \left(\frac{E}{HV}\right)^{1/2} \tag{3}$$

Casellas:

$$K_{Ic} = 0.024 \cdot \frac{F}{c^{3/2}} \cdot \left(\frac{E}{HV}\right)^{1/2} \tag{4}$$

Shetty et al.:

$$K_{Ic} = 0.0319 \cdot \frac{F}{a \cdot l^{1/2}} \tag{5}$$

Niihara et al.:

$$K_{Ic} = 0.0089 \cdot \left(\frac{E}{HV}\right)^{2/5} \cdot \frac{F}{a \cdot l^{1/2}} \tag{6}$$

Evans and Carles:

$$K_{Ic} = 0.0752 \cdot \frac{F}{c^{3/2}} \tag{7}$$

Tanaka:

$$K_{Ic} = 0.0725 \cdot \frac{F}{c^{3/2}} \tag{8}$$

Lankford:

$$K_{Ic} = 0.0782 \cdot \left(HV \cdot a^{1/2}\right) \cdot \left(\frac{E}{HV}\right)^{2/5} \cdot \left(\frac{c}{a}\right)^{-1.56} \tag{9}$$

Niihara, Morena and Hasselman:

$$K_{Ic} = 0.0309 \cdot \left(\frac{E}{HV}\right)^{2/5} \cdot \frac{F}{c^{3/2}} \tag{10}$$

where:

F [N] – applied load during Vickers test,
l [m] – the average crack length measured from vertices of the indentation to the crack tip,
T [m] – the total crack length; $T = l_1 + l_2 + l_3 + l_4$,
a [m] – a half of the indentation diagonal,
c [m] – the crack length from the centre of the indentation to the crack tip,
E [GPa] – Young's modulus, (E = 600 GPa)
HV [GPa] –Vickers hardness.

RESULTS AND DISCUSSION

Figure 6 shows the optical micrograph images of the Vickers pyramid imprints embedded in the surface of the nanostructured cemented carbide WC-5Co, WC-10Co and WC-15Co after testing. Yellow colour shows the Vickers pyramid diagonals, and the red colour shows the length of the cracks that originate from the tip of the imprint.

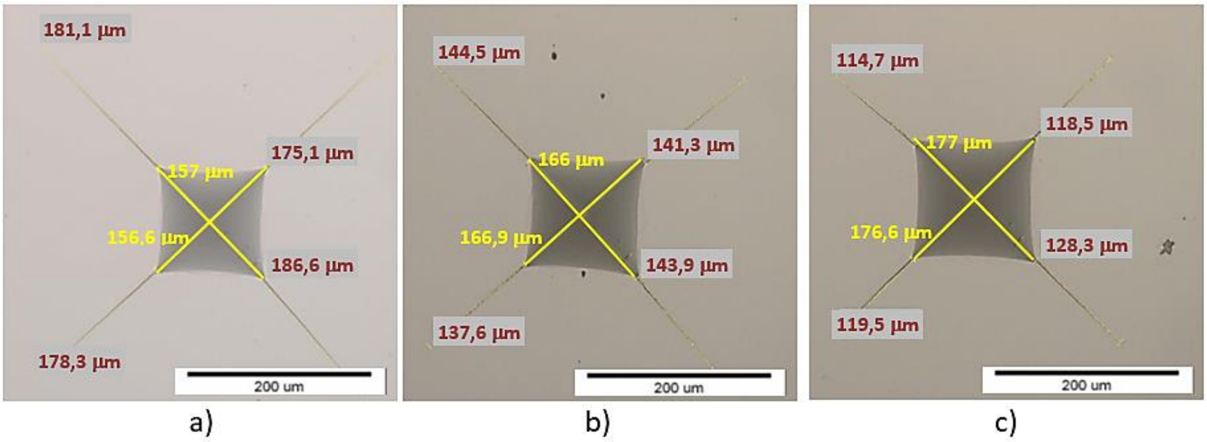

Figure 6. The Optical micrograph of the Vickers indentation and cracks on the sample: (a) WC-5Co, (b) WC-10Co, (c) WC-15Co

Table 1 shows the mean hardness values from 15 measurements together with the measurement uncertainty and standard deviation for each of the tested samples. The measurement uncertainty is expressed as the half of the maximum and minimum deviation range.

Table 1. Hardness measurement results

Sample	Hardness mean value, HV	Measurement uncertainty, HV	Standard deviation, HV
WC-5Co	2263	28,0	15,2
WC-10Co	2014	25,6	12,3
WC-15Co	1779	12,6	6,0

From the results it visible that the hardness values are significantly decrease with the increase in Cobalt content. The difference in hardness values for the sample with the 5 % and the sample with the 15 % Co is around 500 HV. Standard deviation of the hardness measurement results is very small which indicates a homogeneous microstructure for all tested samples.

When comparing the results in Table 1 to the ones shown in Figure 2a, it is visible that the investigated samples are harder than the extra-fine and ultra-fine cemented carbides, which goes in favour of the results carried out earlier that indicate a nanostructured material.

Table 2 contains the mean values of the fracture toughness for all three samples measured by different models.

Table 2. Fracture toughness measurement results with standard deviation

Models	**WC-5Co**	**WC-10Co**	**WC-15Co**
Pamlqvist [$\mathrm{MPa\cdot m^{1/2}}$]	8,39 ± 0,10	9,03 ± 0,07	9,35 ± 0,09
Anstis [$\mathrm{MPa\cdot m^{1/2}}$]	5,84 ± 0,16	7,81 ± 0,13	9,51 ± 0,15
Casellas [$\mathrm{MPa\cdot m^{1/2}}$]	8,76 ± 0,24	11,71 ± 0,19	14,26 ± 0,23
Shettey et al.[$\mathrm{MPa\cdot m^{1/2}}$]	8,88 ± 0,11	9,56 ± 0,08	9,89 ± 0,09
Niihari et al. [$\mathrm{MPa\cdot m^{1/2}}$]	9,27 ± 0,12	10,45 ± 0,09	11,36 ± 0,11
Evans and Charles[$\mathrm{MPa\cdot m^{1/2}}$]	5,28 ± 0,14	6,66 ± 0,10	7,62 ± 0,12
Tanaka [$\mathrm{MPa\cdot m^{1/2}}$]	5,09 ± 0,14	6,42 ± 0,10	7,34 ± 0,12
Lankford [$\mathrm{MPa\cdot m^{1/2}}$]	8,85 ± 0,25	11,85 ± 0,20	14,38 ± 0,24
Niihara, Morena, Hasselman [$\mathrm{MPa\cdot m^{1/2}}$]	8,11 ± 0,22	10,72 ± 0,17	12,89 ± 0,20

From Table 2 it is visible that the fracture toughness results increase with increasing Cobalt content. The difference in fracture toughness values indicated that not all methods are applicable for determination of fracture toughness of nanostructured cemented carbides. While Tanaka shows generally lowest fracture toughness results around 5,09 $\mathrm{MPa\cdot m^{1/2}}$ for a cemented carbide with 5% Co, the values using Niiharis equasions amout arround 9,27 $\mathrm{MPa\cdot m^{1/2}}$. The similar behaviour occurs for 10% and 15% Co amount. This indicates that a more detailed investigation on the crack types prior to using the mathematical equations should be conducted. Comparing the most commonly used, and recommended method for determining fracture toughness, Palmquist it is visible that it has large similarities in the results calculated by Shettey method. Opposed to that Tanaka, Evans and Charles show largest nonconformity with the Palmquist results.

The fracture toughness values determined by different models are illustrated in Figure 7.

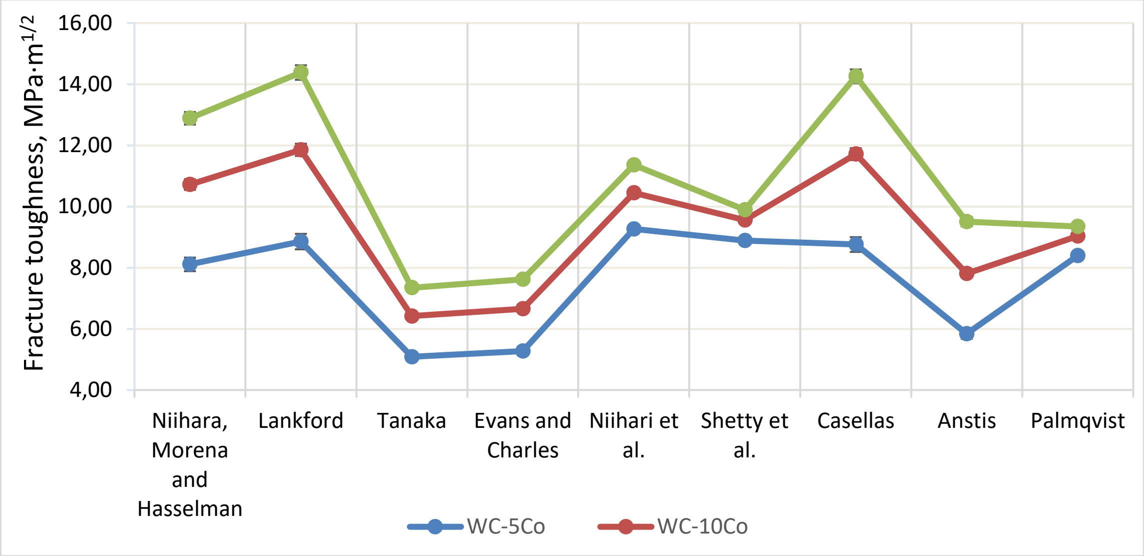

Figure 7. Fracture toughness results measured by different models

Additionally when comparing the Palmquist fracture toughness of extra-fine and ultra-fine cemented carbides with the same Co content (see Figure 2b), the existence of extremely small nano-sized grain is confirmed.

CONCLUSION

Cemented carbide consolidated by sinter / HIP process have shown to be homogenous and have exceptional mechanical properties. Thanks to the application of high pressure at high temperature at the same time, sintered cemented carbides have significantly better performance than those obtained from classic compacting and subsequent sintering processes.

All the results obtained on the composite WC-Co system indicate the importance of the Co binder, which means that the matrix share significantly influences the hardness and fracture toughness of the WC-Co material.

The test results showed that the hardness of the test material was significantly reduced by the increase in cobalt content. With 1 % of cobalt percentage reduction, the reduction in hardness is approximately 50 HV.

The fracture toughness results indicate that the values calculated from different mathematical models are notably different and are non-consistent. While Tanaka shows generally lowest fracture toughness results around 5,09 MPa·m$^{1/2}$ for a cemented carbide with 5% Co, the values using Niiharis equations amout arround 9,27 MPa·m$^{1/2}$. For further analysis a more detailed analysis of the types of cracks prior to using specific equations should be conducted. For future research it is also recommended to conduct an experimental procedure for determining the real elasticity modulus of a specific sample using nanoindentation technique.

Since cemented carbide cutting tools often require high hardness and high fraction toughness which are contradictory properties, it is necessary to find a compromise between the appropriate cobalt content that provides the optimal combination of toughness and hardness for a particular application.

REFERENCES

[1] D. Ćorić, Special Metallic Materials - Part III, textbook, Faculty of mechanical engineering and naval architecture University of Zagreb, Zagreb, 2017.

[2] M. Brieseck, W. Lengauer, B. Gneiß, K. Wagner, S. Wagner, A straightforward method for analysing the grain-size distribution in tungsten carbide - cobalt hardmetals, Microchimica Acta 2010, 168 (3-4), 309-316.

[3] Sandvik Hard Materials, Understanding Cemented Carbide, Available online: http://allaboutmetallurgy.com/wp/wp-content/uploads/2016/12/UnderstandCementedCarbide.pdf (Downloaded 12.03. 2018.)

[4] V. Bonache, M.D.Salvador, D. Busquets, P. Burguete, E. Martinez, F. Sapina, E. Sanchez, Synthesis and processing of nanocrystalline tungsten carbide: Toward cemented carbides with optimal mechanical properties, Int. J. Refract. Met. Hard Mater. 2011, 29, 78–84.

[5] T. Aleksandrov Fabijanić, Ž. Alar, D. Ćorić, Influence of consolidation process and sintering temperature on microstructure and mechanical properties of near-nano and nanostructured WC-Co Cemented Carbides, Int. J. Refract. Met. Hard Mater. 2015, 54, 82–89.

[6] D. Ćorić, Ž. Alar, Selected chapters from the mechanical properties of the material, textbook, Faculty of mechanical engineering and naval architecture University of Zagreb, Zagreb, 2016.

[7] D.K. Shetty, I.G. Wright, P.N. Mincer, A.H. Clauer, Indentation fracture toughness of WC-Co cermets, J. Mater. Sci. 1985, 20, 1873–1882.

[8] M.W. Barsoum, Series in Material Science and Engineering Fundamentals of Ceramics, Taylor & Francis: Abingdon, UK, 2003.

[9] F. Sergejev, M. Antonov, Comparative study on indentation fracture toughness measurements on cemented carbides, Proc. Estonian Acad., Sci. Eng. 2006, 12, 388–398.

[10] S. Sheikh, R. M’Saoubi, P. Flasar, M. Schwind, T. Persson, J. Yang, L. Llanes, Fracture toughness of cemented carbides: Testing method and microstructural effect, Int. J. Refract. Met. Hard Mater. 2015, 49, 153–160.

[11] G.D. Quinn, Fracture toughness of ceramics by the Vickers indentation crack lenght method: A critical review, National Institute of Standards and Technology, Gaithersburg, 2006.

[12] Aleksandrov Fabijanić Tamara Ćorić Danko, Šnajdar Musa Mateja Sakoman Matija, Vickers indentation fracture toughness of near- nano and nanostructured WC-Co cemented carbides, Metals (2075-4701) 7 (2017), 143; 143-1-143-16

DUPLEKS SUSTAV ZAŠTITE PREVLAKAMA

DUPLEX COATING SYSTEM FOR CORROSION PROTECTION

Debora Briševac[1],**Ivan Stojanović**[1]

[1]Sveučilište u Zagrebu, Fakultet strojarstva i brodogradnje, Ivana Lučića 5, Zagreb, Hrvatska

Sažetak

Cink je jedan od glavnih metala koji se koristi za zaštitu od korozije u obliku prevlake, zbog njegove sposobnosti da galvanski štiti čelik. U vodi, cink ima dobru otpornost na koroziju samo u relativno uskom rasponu pH vrijednosti od 6 do 11, zbog čega se za određene uvjete dodatno zaštićuje pokrivnom organskom prevlakom. Takav sustav prevlaka naziva se dupleks sustav. U radu je detaljno opisan dupleks sustav zaštite prevlakama te njihovo područje primjene. Eksperimentalni dio rada sastoji se od mjerenja debljine dupleks sustava prevlaka pomoću dvije nerazorne metode – magnetske metode i metode vrtložnih struja. Rezultati nerazornih ispitivanja potom su uspoređeni s rezultatima dobivenim primjenom mikroskopa.

Ključne riječi: *pocinčani čelik, organska prevlaka, dupleks sustav prevlaka, debljina prevlake, mjerenja*

Abstract

Zinc is a metal commonly used for coating and corrosion protection since it has the ability to galvanically protect steel. It provides good corrosion resistance in water, but only within a relatively narrow pH range from 6 to 11. Thus, in certain environments zinc is further protected by organic coatings. This coating system is called duplex system. The paper presents the duplex system for corrosion protection and the areas of its application. In the experimental part of the study the thickness of the duplex coating system was measured using two non-destructive methods- a magnetic method and an eddy-current method. The obtained results were then compared to the results of the measurement carried out using a microscope.

Keywords: *galvanized steel, organic coating, duplex coating system, film thickness, measurements*

1. UVOD

Vruće cinčanje pripada skupini prevlaka koje se nanose na metale procesom uranjanja. Postupak vrućeg cinčanja sastoji se od četiri koraka. Prvo je potrebno pripremiti površinu čišćenjem svih nečistoća (masti, ulja, ostataka boje, šljake od zavarivanja,...) te naknadnog ispiranja vodom i kiselinom da bi se uklonila zaostala hrđa, ljuskanje i ostale organske komponente. Po potrebi, površina se još čisti pjeskarenjem ili sličnim postupcima. Drugi korak je uklanjanje oksida s površine, koji su se stvorili tijekom procesa čišćenja ili samog stajanja dijela na zraku. Nakon toga slijedi uranjanje dijela u kupku rastaljenog cinka. Proces traje dok se ne stvori legirni sloj cinka i metala s površine, najčešće 30 s do 2 min, ovisno o veličini elementa. Temperatura kupke uglavnom varira između 450 do 475°C. Posljednji korak je sušenje i, prema potrebi, obrada površine. Vruće cinčane proizvode karakterizira siva metalna površina, koja pod mikroskopom ima vidljive slojeve – zeta, delta i gama te površinski slobodni cink – eta sloj.

Prednosti vrućeg cinčanja [1]:

- izvrsna trajnost sloja pri pH vrijednostima od 5 do 10
- izvrsna zaštita geometrijski kompliciranih dijelova
- unutarnja i vanjska zaštita dijelova
- dijelovi su spremni za korištenje odmah nakon pocinčavanja.

Nedostaci vrućeg cinčanja [1]:

- dimenzije dijelova koji se pocinčavaju ovise o veličini kade za cinčanje
- pri pH vrijednostima ispod 5 ili iznad 10, površine se moraju dodatno zaštititi premazima
- nanošenjem premaza može doći do bubrenja i stvaranja mjehurića, ako se prethodno ne zatvore sve poroznosti na površini
- pocinčavanje, općenito, nije pogodno kao zaštita za uronjene konstrukcije.

Kada vruće pocinčane površine ne pružaju dovoljnu zaštitu od korozije ili ne zadovoljavaju zahtjeve, potrebno je na njih nanijeti premaz. Kombinacija premazivanja i vrućeg cinčanja naziva se dupleks sustav zaštite površina. Tim se postupkom mogu dobiti antikorozivna svojstva kakva nema niti samo premaz, niti samo cinčanje.

Dakle, neki od razloga premazivanja vruće cinčanog čelika su [2]:

1. poboljšana zaštita od korozije
2. ekonomičnost
3. sinergijski efekt
4. jednostavnost naknadnog bojanja
5. estetičnost
6. označavanje bojama – npr. za signalizaciju ili maskiranje
7. produljenje trajanja prethodno pocinčanog čelika
8. popravak pocinčanog sloja.

Nedostatak dupleks sustava zaštite je priprema površine. Ako se površina ne pripremi pravilno, gotovo uvijek dolazi do problema s adhezijom između premaza i pocinčane površine. Cink ima specifično vrijeme pasivacije. Nakon pocinčavanja, na površini se stvara sloj cinkovih oksida. Unutar par sati, pa i dana, cinkovi oksidi prelaze u cinkove hidrokside. Tek nakon par tjedana i mjeseci, na površini se stvara gusti sloj cinkovih karbonata iz kojeg nastaje cinkova patina. Ako se boja nanosi za vrijeme prvih 24 do 48 sati, kada je na površini stvoren sloj cinkovih oksida ili nakon stvaranja cinkove patine, priprema površine ne predstavlja veliki problem. Tada je potrebno samo lagano prebrusiti površinu kako bi se uklonila ulja, masti i nečistoće. No, problem se javlja pri premazivanju konstrukcija u kritičnom vremenu, nakon 48 sati i prije stvaranja patine (otprilike godinu dana nakon pocinčavanja – ovisno o atmosferskim uvjetima), što se najčešće događa u industriji. U tom kritičnom razdoblju, potrebno je potpuno ukloniti cinkove okside i hidrokside s površine kako bi se osigurala kvalitetna adhezija. Priprema površine tada se sastoji od brušenja, površinskog pjeskarenja te čišćenja blagom kiselinom.

Dakle, kod dupleks sustava zaštite, čelik prvo štiti cinkova prevlaka koja djeluje kao barijera i katodno štiti podlogu, dok naknadno bojanje usporava korodiranje samog cinka te djeluje kao barijera [2]. Taj efekt naziva se sinergijski. Upravo zbog toga, konstrukcija zaštićena dupleks prevlakom, imat će 1,5 do 2,3 puta dulji radni vijek od konstrukcije zaštićene ili cinkom ili bojom u istim uvjetima [3].

Boja koja se nanosila na pocinčani čelik u ovom radu je vodorazrjedivi akrilni premaz. Prednosti vodorazrjedivih akrilnih premaza je jednostavnost nanošenja (npr. kistom, valjkom ili naštrcavanjem), relativno su cjenovno pristupačni, imaju zadovoljavajuću boju i sjaj, fleksibilni su te vrlo dobro prianjaju na galvanizirane površine. Nedostaci koji se javljaju kod istih su teško nanošenje pri niskim temperaturama i vlažnoj atmosferi te lošije kvašenje površine [1].

Dupleks sustavi imaju sve veću primjenu za konstrukcije kao što su: radio tornjevi, dalekovodi, prometni znakovi, znakovi signalizacije, mostovi, čelične konstrukcije, stupovi za električne vodove za tramvaje i vlakove, transformatorski kotlovi, okviri na izlozima te u automobilskoj industriji [4].

2. METODE MJERENJA DEBLJINE ZAŠTITNIH PREVLAKA

Određivanje debljine premaza daje brojne informacije o stanju zaštite neke površine. Važno je da premazi na proizvodima koji se štite ne budu niti previše tanki, čime se smanjuje njihova antikorozivna zadaća, ali niti previše debeli, zbog čega se povećavaju proizvodni troškovi, vrijeme sušenja te brojni drugi defekti na premazu. Debljina premaza ovisi o brojnim faktorima, npr. tehnici nanošenja, ljudskom faktoru, vrsti premaza, uvjetima pri kojemu se nanosi premaz, stanju površine prije premazivanja, itd.

Prema normi HRN EN ISO 2808:2008 debljina se može mjeriti na mokrom (DMF) ili suhom filmu (DSF) [5].

Metode mjerenja debljine suhog filma prevlaka dijele se na [5]:

- razorne (destruktivne) metode te
- nerazorne (nedestruktivne) metode.

Destruktivne metode karakterizira razaranje uzorka nekom od tehnika, npr. rezanje, bušenje, glodanje te promatranje pod mikroskopom. Takav postupak je dugotrajan i skup, zbog potrebe za kvalificiranim osobljem te opremom. No, upravo ta mjerenja su referentna i prijeko potrebna u mnogim situacijama.

Nedestruktivne metode su puno brže, jednostavnije i češće korištene. Njima se uzorci mogu ispitivati i u laboratorijima, ali i na terenu. Svaka od nedestruktivnih metoda, zasniva se na različitim fizikalnim principima zbog čega svaka ima prednosti ili nedostatke u usporedbi s drugom [4].

U ovom radu, uspoređuju se mjerenja debljine prevlaka dviju nedestruktivnih metoda – metoda magnetske indukcije i metoda vrtložnih struja, s referentnom destruktivnom metodom pomoću mikroskopa.

Na rezultate mjerenja debljine suhog filma premaza mogu utjecati [5]:

- geometrija dijela (dimenzije, debljina)
- svojstva materijala (permeabilnost, provodljivost)
- površinska hrapavost
- magnetska polja (zaostali magnetizam, magnetska polja u blizini).

2.1. Metoda magnetske indukcije

Uređaji koji služe za mjerenje debljine prevlaka metodom magnetske indukcije rade na principu privlačnih sila koje se javljaju između permanentnog magneta i feromagnetne metalne podloge. Uređaj u sebi sadrži elektromagnet koji stvara promjenu u magnetnom polju u blizini feromagnetne podloge (slika 1). Generirane privlačne sile proporcionalne su s udaljenosti magneta i podloge, čime se lako očitava debljina prevlaka s uređaja. Metoda se primjenjuje samo na magnetičnim metalima [5,6].

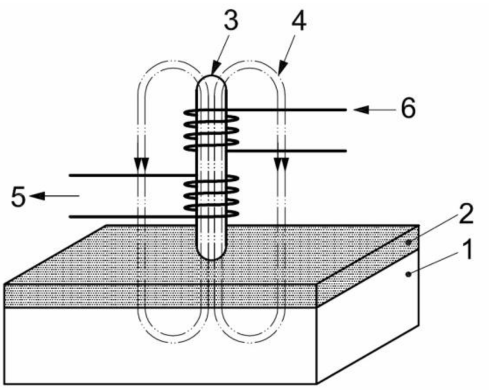

Sl. 1: Shematski prikaz mjerenja debljina zaštitnih premaza metodom magnetske indukcije: 1 – osnovni metal, 2 – prevlaka, 3 – feromagnetična jezgra, 4 – promjenjivo magnetsko polje (NF), 5 – izmjereni signal, 6 – struja [4,6]

2.2. Metoda vrtložnih struja

Za razliku od magnetske metode, metoda vrtložnih struja je primjenjiva za mjerenje debljina premaza na nemagnetičnim metalnim podlogama. Metoda se temelji na razlici u električnoj vodljivosti premaza i nemagnetične podloge. Dakle, sonda generira visokofrekventno izmjenično magnetsko polje, čime dolazi do stvaranja vrtložnih struja (slika 2). Važno je da podloga na koju je nanesen premaz ima dovoljnu debljinu, kako se ne bi ponašala kao beskonačno debela ploča. Preciznost i točnost mjerenja osigurava se optimalnom frekvencijom pri kojoj radi uređaj, kako bi dubina prodiranja vrtložnih struja u podlogu bila što manja [5,6].

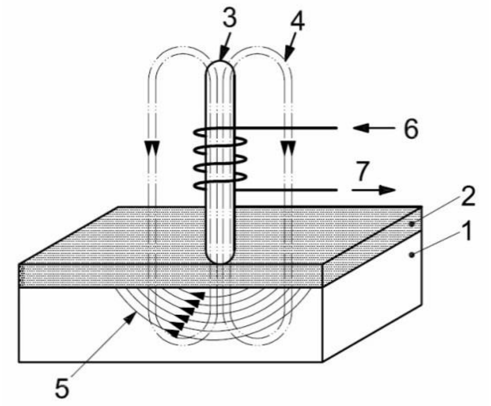

Sl. 2: Shematski prikaz mjerenja debljina zaštitnih premaza metodom vrtložnih struja: 1 – osnovni metal, 2 – prevlaka, 3 – željezna jezgra, 4 – promjenjivo magnetsko polje (VF), 5 – vrtložne struje, 6 – struja, 7 - izmjereni signal [4,6]

3. EKSPERIMENTALNI RAD

Vruće cinčanje čelika provelo se u tvrtki Cinčaona Helena. Ispitivanje je provedeno na četiri uzorka (slika 3). Postupak započinje različitim pripremama površina te mjerenjem debljine cinkove prevlake. Na uzorke se potom nanosi akrilna boja na bazi vode. Nakon sušenja boje, ispituje se debljina dupleks prevlake, prionjivost prevlake te korozijska postojanost u slanoj komori. Dio se jednog od uzorka (uzorak 4) izrezuje te se debljina prevlaka ispituje na svjetlosnom mikroskopu u cilju usporedbe rezultata s nerazornim metodama. Sva ispitivanja provedena su u Laboratoriju za zaštitu materijala i Laboratoriju za materijalografiju FSB-a.

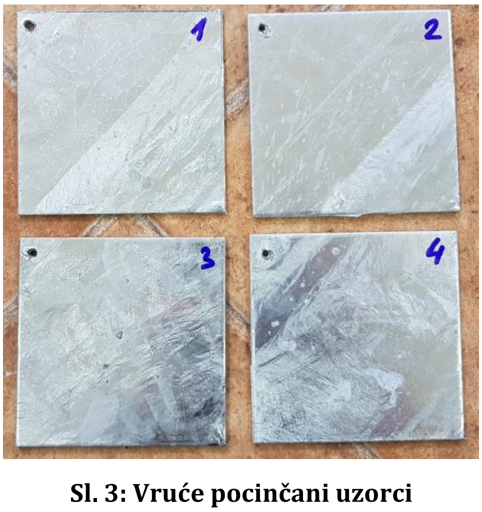

Sl. 3: Vruće pocinčani uzorci

3.1. Priprema uzoraka

Ispitani uzorci su pocinčane čelične pločice dimenzija 100 x 100 mm, debljine 5 mm. Svi uzorci su novo pocinčani (prije < 48 sati). Površina uzoraka 2 i 4 pripremljena je pomoću brusnog papira P120. Uzorak 3 pripremljen je brusnom krpicom Scotch-Brite 7448, a površina uzorka 1 nije pripremljena. Na uzorke se potom nanosi akrilni premaz CORTEC VpCl 386 White u više slojeva (slika 4).

Sl. 4: Uzorci zaštićeni premazom CORTEC VpCl 386 White

3.2. Ispitivanje fizikalno-kemijskih svojstava prevlaka

Mjerenje debljine prevlake

a) Nerazorna metoda

Mjerenje debljine prevlake provedeno je u Laboratoriju za zaštitu materijala, FSB, u Zagrebu. Debljina premaza odredila se na svim uzorcima uređajem DeFelsko PosiTector 6000 koji radi na principu metode vrtložnih struja i magnetske metode sukladno normi HRN EN ISO 2808:2008 (slika 5). Uređaj je umjeren na vlastitom etalonu u dvije točke. Prednost ovakvog uređaja je istovremeno mjerenje debljine i cinkove prevlake i boje (slika 4). Na svakom uzorku provedeno je 10 mjerenja, a izračunata je minimalna, maksimalna debljina te aritmetička sredina debljine premaza. Rezultati ispitivanja nerazornim metodama prikazani su u tablici 1.

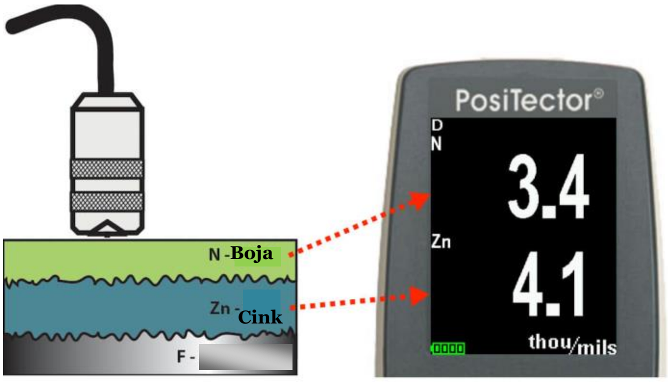

Sl. 5: Princip rada uređaja DeFelsko PosiTector 6000 [6]

b) Razorna metoda

Mjerenje debljine prevlake referentnom metodom, tj. pomoću mikroskopa, prikazano je na slici 6. Da bi se uzorak mogao ispitati na mikroskopu, prvo ga je potrebno pripremiti. Priprema uzorka sastojala se od ulijevanja uzorka u polimernu masu te brušenja sa šest različitih brusnih ploča (sve manjih hrapavosti) i poliranja s dvije ploče uz pomoć dijamantne paste. Ispitivanje se sastojalo od šest mjerenja na svakom mjestu (ukupno tri mjesta, dakle 18 mjerenja) pri povećanju od 100x (slika 7). Rezultati mjerenja na uzorku 4 prikazani su u tablici 2.

Sl. 6: Svjetlosni mikroskop Olympus GX51 (lijevo) te ispitni uzorak (desno)

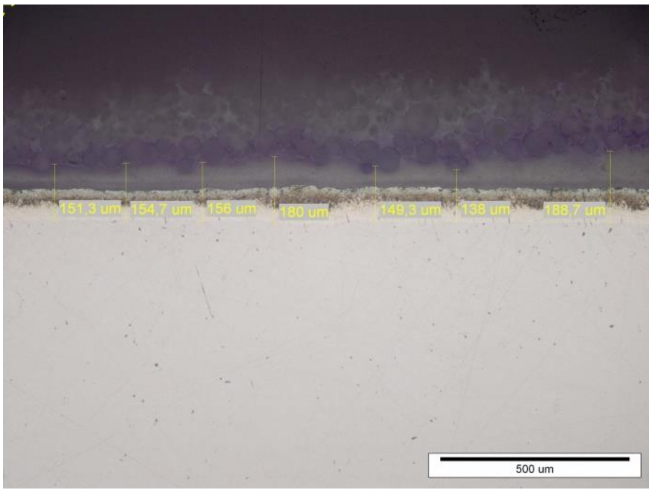

Sl. 7: Debljina dupleks sustava prevlaka na uzorku 4

Ispitivanja otpornosti na morsku atmosferu

Prije stavljanja u slanu komoru, na uzorcima se zarezala linija. Ispitivanje je provedeno u 5%-tnoj otopini NaCl sukladno normi ISO 9227, u trajanju od 168 sati, u komori Ascott S450. Cilj ispitivanja je određivanje otpornosti prevlake na morski okoliš. Slika 8 prikazuje uzorke 1, 2 i 3 nakon ispitivanja u slanoj komori te etalonski uzorak 4 koji nije bio korozijski ispitan.

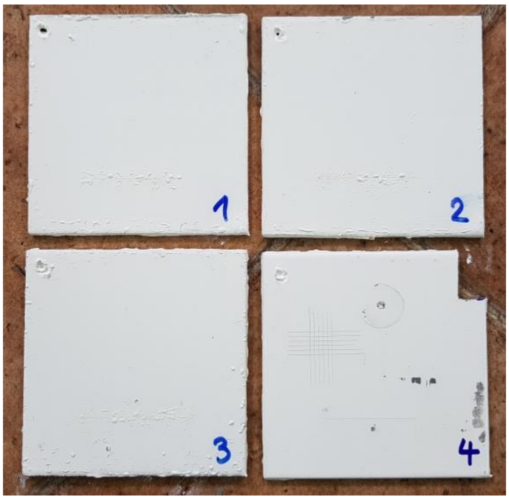

Sl. 8: Uzorci nakon ispitivanja u slanoj komori Ascott S450

Ispitivanje prionjivosti prevlake

Ispitivanje prionjivosti provedeno je pomoću dvije metode – cross-cut i pull-off metode. Cross-cut test proveo se urezivanjem mrežice sukladno normi HRN EN ISO 2409:2013, dok se pull-off test proveo sukladno standardu ASTM D4541. Ispitivanja su provedena na uzorku 4 (etalonu) prije stavljanja u slanu komoru, dok su se na ostala tri uzorka (1, 2, 3) provela nakon završetka ispitivanja u slanoj komori (slika 9).

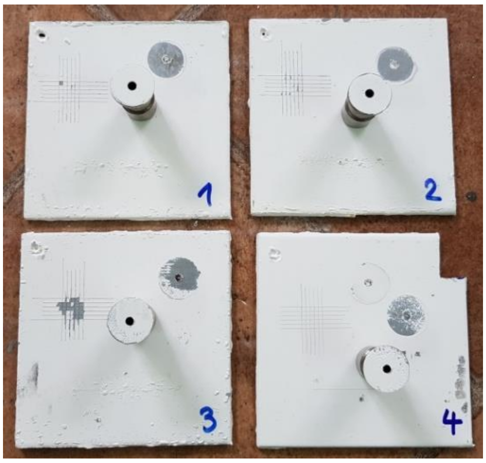

Sl. 9: Uzorci nakon ispitivanja cross-cut i pull-off metodom

4. REZULTATI

U tablici 1 prikazani su rezultati mjerenja debljine metodom vrtložnih struja i magnetskom metodom na uređaju DeFelsko PosiTector 6000. Iz tablice se može zaključiti kako je prevlaka na uzorku četiri nanijeta nešto deblje te da je debljina prevlake na uzorku dva nešto tanja od ostalih uzoraka. Razlike u debljini javljaju se zbog nanošenja prevlake pomoću kista, što je vrlo jednostavna i brza metoda, ali se njome ne može dobiti jednoličan sloj.

Tab. 1: Rezultati mjerenja debljine cinka i prevlake u μm uređajem DeFelsko PosiTector 6000

	Aritmetička sredina, $\bar{x}$	Maksimum	Minimum	Standardno odstupanje
Uzorak 1	163,4	170	155	4,54
Uzorak 2	141,1	155	128	7,23
Uzorak 3	154,9	170	144	6,52
Uzorak 4	178,6	184	174	3,04

U tablici 2 nalaze se podaci o debljini prevlake cinka i prevlake zasebno.

Tab. 2: Rezultati mjerenja debljine cinka i prevlake u μm uređajem DeFelsko PosiTector 6000 za uzorak 4

	Aritmetička sredina, $\bar{x}$		Maksimum		Minimum		Standardno odstupanje	
	Cink	Prevlaka	Cink	Prevlaka	Cink	Prevlaka	Cink	Prevlaka
Uzorak 4	75,6	103	78	107	74	100	1,11	2,32

Tablica 3 sadrži podatke mjerenja pomoću mikroskopa.

Tab. 3: Rezultati mjerenja debljine cinka i prevlake u μm mikroskopskom metodom

	Aritmetička sredina, $\bar{x}$	Maksimum	Minimum	Standardno odstupanje
Uzorak 4	146,3	188,7	117,3	17,42

Rezultati mjerenja prionjivosti nalaze se u tablici 4. Iz priloženog se može zaključiti kako najlošiju prionjivost ima uzorak 3, koji je pripremljen brusnom krpicom. Za uzorak 4 bitno je naglasiti kako je mjerenje metodom cross-cut provedeno prije stavljanja u slanu komoru, a svi ostali uzorci ispitani su nakon vađenja iz slane komore. Najveću prionjivost cross-cut metodom imaju uzorak 1 (nepripremljeni) te uzorak 2 (pripremljen brusnim papirom). Najveću prionjivost pull-off metodom imaju uzorci pripremljeni brusnim papirom (2 i 4).

Tab. 4: Rezultati mjerenja prionjivosti

Ispitivanje prionjivosti	Uzorak			
	1	**2**	**3**	**4**
Cross-cut	1	1	4	0
Pull-off, MPa	4,27	7,40	7,09	7,80

4.1. Usporedba rezultata referentne metode i nedestruktivnih metoda

Prema normi HRN EN ISO 2808:2008, stvarna debljina sloja može se izračunati preko jednakosti:

$D = \bar{x} \pm C$, gdje je (1)

D – debljina zaštitnog premaza,

x̄ – srednja vrijednost debljine te

C – nepouzdanost srednje vrijednosti.

Nepouzdanost srednje vrijednosti računa se prema formuli:

$C = t \cdot s/\sqrt{n}$, za (2)

n – broj ponovljenih mjerenja,

t – factor Studentove razdiobe i

s – procjena standardne devijacije niza mjerenja.

Za ispitivanje na mikroskopu, rezultati mjerenja obrađeni su za n=18 ponovljenih mjerenja, uz statističku vjerojatnost P=95 % te pripadni faktor Studentove razdiobe t=2,101, dok su kod ispitivanja nerazornim metodama, rezultati obrađeni za n=10 ponovljenih mjerenja, statističku vjerojatnost P=95% te pripadni faktor Studentove razdiobe t=2,228.

Nepouzdanost srednje vrijednosti kao najbolje procjene niza ponovljenih mjerenja izjednačava se s mjernom nesigurnošću tj. C= ±U(D), gdje je ±U(D) mjerna nesigurnost ponovljenog niza mjerenja [4].

U tablici 5 uspoređeni su rezultati mjerenja nerazornim metodama pomoću uređaja DeFelsko PosiTector 6000 i mjerenja debljine prevlake na svjetlosnom mikroskopu Olympus GX51. Rezultati koji se uspoređuju, odnose se za uzorak 4.

Tab. 5: Usporedba rezultata mjerenja nerazornim metodama i mikroskopskom metodom

Nazivna minimalna debljina d_0 [µm] / Vrsta prevlake	Rezultati metalografske metode [µm]		Rezultati nerazornih metoda [µm]		Metalografska metoda / nerazorne metode [µm]	
	Odstupanje $d_{MM} - d_0$	Mjerna nesigurnost $\pm C_{MM}$ P = 95 %	Odstupanje $D_{NM} - d_0$	Mjerna nesigurnost $\pm C_{NM}$ P = 95 %	Dopuštena maksimalna razlika ±C	Utvrđena razlika
130 / premaz + Zn	+ 16,3	± 8,87	+ 48,6	± 2,25	11,12	32,3

5. ZAKLJUČAK

Dupleks sustavi prevlaka produžuju vijek trajanja konstrukcija i osiguravaju njen estetski izgled.

Ispitivanjima u slanoj komori utvrđeno je da najbolju prionjivost ostvaruje premaz nanesen na površinu cinka koji je prethodno pripremljen brusnim papirom gradacije P120.

Mjerenjem debljine dupleks prevlake metodom magnetske indukcije/vrtložnih struja utvrđeno je da takva metoda odstupa od mjerenja debljine mikroskopom za 22%. Kod minimalne vrijednosti ta je razlika veća, dok kod maksimalne izmjerene debljine prevlake nema veće razlike između magnetske indukcije/vrtložnih struja i metalografske metode.

LITERATURA

[1] Vincent Louis D., "The Protective Coating User's Handbook", 2nd edition, 2010, NACE International.

[2] Janke T., Langill T., Painting hot dip galvanized steel, American Galvanizers Association, 3-1, pp. 1-6, (1999).

[3] Duplex System: Painting Over Hot-Dip Galvanized Steel, American Galvanizers Association, 2012.

[4] Stojanović I., Juraj D. (2017) Točnost i pouzdanost mjerenja debljine zaštitnih premaza nedestruktivnim metodama na vruće pocinčanim čeličnim podlogama, In: MATRIB 2017, Kovačević, S. (ur.), Zagreb: Hrvatsko društvo za materijale i tribologiju, pp. 303-312

[5] Juraga I., Alar V., Stojanović I., "Korozija i zaštita premazima", 2014, FSB.

[6] Norma HRN EN ISO 2808:2008, Boje i lakovi - Određivanje debljine filma (ISO 2808:2007; EN ISO 2808:2007).

[7] https://www.defelsko.com/p6000-probe-details, pristupljeno 01.06.2018.

DOPIRANI NANOSTRUKTURIRANI TiO_2 ZA FOTONAPONSKU PRIMJENU

DOPED NANOSTRUCTURED TiO_2 FOR PHOTOVOLTAIC APPLICATION

Ivana Panžić[1], Juraj Hanžek[2], Marija Ivezić[3], Milivoj Plodinec[1,4], Krunoslav Juraić[1], Domagoj Belić[1], Andreja Gajović[1]

[1]Ruđer Bošković Institute, Bijenička 54, 10000 Zagreb, Croatia
[2]student at University of Zagreb, Faculty of Science, Department of Physics, Zagreb, Croatia
[3]student at University of Zagreb, Faculty of chemical engineering and technology, Zagreb, Croatia
[4]Fritz-Haber-Institute der Max-Planck-Gesellschaft, Faradayweg 4-6, D-14195 Berlin, Germany

Abstract

Nanostructured TiO_2 is known as a material with excellent physical and chemical properties, as high specific surface area, high photo-activity and environmental stability. It was studied for application in solar energy, primarily as electron transporting layer in perovskite and dye sensitized solar cells. In this work we studied the TiO_2 doped with samarium with the aim to improve TiO_2 optical properties and photovoltaic performances. The influence of doping to TiO_2 morphology and structure were correlated to photovoltaic performances. Pure TiO_2 and doped with 1% Sm samples were prepared by sol-gel syntheses. The structure, morphology and inbuilt of samarium was studied using high and atomic resolution transmission electron microscopy and compared with Raman spectroscopy measurements. For photovoltaic use the thin layers of doped TiO_2 were applied at the conducting glass by blade casting. The morphology of the layers was observed by FEG-SEM, while the optical properties were studied by UV-vis spectroscopy. The dye sensitized solar cells were assembled, I-V characteristic and quantum efficiency were measured. Their performances will be discussed in the view of structure and crystallite sizes of the TiO_2 powder with and without doping as well as in the view of the morphology of the obtained electron conducting layers.

Keywords*: nanostructured TiO_2, doping, structure, optical properties, electrical properties.*

Sažetak

Nanostrukturirani TiO_2 poznat je kao materijal s odličnim fizičkim i kemijskim svojstvima, kao što je visoka specifična površina, visoka fotoaktivnost i stabilnost. Proučavan je za fotonaponsku primjenu, prvenstveno kao sloj za transport elektrona u perovskitnim i bojom senzitiziranim solarnim ćelijama. U ovom radu proučavamo TiO_2 dopiran sa samarijem s ciljem poboljšanja optičkih svojstava TiO_2 i fotonaponskih performansi. Utjecaj dopiranja na TiO_2 morfologiju i strukturu bio je koreliran s fotonaponskim performansama. Uzorci čistog TiO_2 i dopiranog s 1% Sm su pripremljeni sol-gel sintezom. Struktura, morfologija i ugradnja samarija proučavana je pomoću transmisijske elektronske mikroskopije visokog razlučivanja i rezultat je uspoređen s Raman spektroskopijom. Za fotonaponsku upotrebu tanki slojevi dopiranog TiO_2 naneseni su na vodljivo staklo rakel nožem. Morfologija slojeva istraživana je pomoću FEG-SEM, dok su optička svojstva proučavana pomoću UV-vis spektroskopije. Bojom senzitizirane solarne ćelije su sastavljne i mjerena je I-V karakteristika i kvantna učinkovitost. Njihova svojstva će se raspravljati uzimajući u obzir strukturu, veličine kristalita TiO_2 sa i bez dopranja, kao i morfologiju dobivenih slojeva za vođenje elektrona.

Ključne riječi: *nanostrukturirani TiO_2, dopiranje, struktura, optička svojstva, električna svojstva.*

UTJECAJ TEKUĆINE ZA OPLEMENJIVANJE NA REALIZACIJU AKROMATSKIH TONOVA

INFLUENCE OF LIQUIDE PRIMER ON IMPLEMENTATION ACROMATIC TONE VALUE

Dino Priselac[1], Igor Majnarić[1], Marko Morić[2]

[1]Sveučilište u Zagrebu, Grafički fakultet, Getaldićeva 2, 10 000 Zagreb, Hrvatska

[2]Sveučilište Sjever, Jurja Križanića 31b, 42 000 Varaždin, Hrvatska

Sažetak

Cilj ovoga rada je ispitati da li će nanošenjem premaza (primera) doći do povećanja kvalitete crnih otisaka. Uzorci za ispitivanje su otisnuti na papiru za umjetnički tisak pomoću HP Indigo WS6800 te su podvrgnuti postupku prajmiranja na HP Indigo In-Line Primeru. Ukupno su otisnuta tri uzorka: jedan bez primera, jedan s niskim nanosom primera (0,5 g/m^2) te jedan s visokim nanosom primera (1 g/m^2). Na otiscima je provedeno određivanje L*a*b* vrijednosti iz kojih je potom napravljen njihov prikaz u 3D L*a*b* prostoru te je određena kolorimetrijska razlika u odnosu na referentni FOGRA 51 uzorak. Također je izmjeren sjaj ispitanih uzoraka.

Ključne riječi: *Primer, tonska vrijednost, kolorimetrijska razlika DE*

Abstract

The aim of this paper is to examine whether will applying the coating (primer) increase the quality of black prints. The samples are printed on coated by HP Indigo WS6800 and were exposed to priming process on HP Indigo In-Lime Primer. Three samples were printed: one without primer, one with low primer deposit (0,5 g/m^2) and one with high primer deposit (1 g/m^2). The L*a*b* values were determined on the prints from which was made their representation in 3D L*a*b* space and colorimetric difference was determined in regard to reference FOGRA51 sample. Gloss of the tested samples was measured as well in this paper.

Keywords: *Primer, Tone value, colorimetric difference DE*

1. UVOD

Zahtjevne tiskovne podloge poput polimera i metala zahtjevaju dodatno obrađivanje kako bi se mogla postići što veća kvaliteta otiska. Tako se tiskovne podloge mogu podvrgnut premazivanju odnosno nanošenju primera kako bi došlo do bolje apsorpcije bojila na tiskovnu podlogu. Polimerne tiskovne podloge podvrgavaju se tretmanu korone, a metalne podloge plazma tretmanu. Korona tretman je tehnika modificiranja površine kod koje se pri niskim temperaturama odvija koronalno pražnjenje plazme kako bi se postigla promjena u površinskom svojstvu te kako bi se povećala trajnost otiska. Plazma tretman koristi se kako bi se promijenila površinska svojstva polimera bez promjene glavnih svojstava tog polimera. Glavni nedostatak plazma tretmana jest što površinska promjena na materijalu nije trajna. [1]

Neke od metode nanosa primera su: primiranje na bazi bakrotiska, primiranje na bazi fleksotiska, primiranje pomoću Meyerove šipke, primiranje pomoću obrnutog valjka, primiranje na bazi sitotiska. [2]

1.1. Primiranje na bazi bakrotiska

Kod nanošenja primera na podlogu tehnikom bakrotiska količina premaza prenesenog na tiskovnu podlogu ovisi o veličini ćelije i uzorka na bakrotiskarskom valjku. Gravirani valjak rotira i grabi premaz iz spremnika. Rakel skida višak premaza s površine valjka i prenosi premaz unutar ćelija na tiskovnu podlogu koja se nalazi između temeljnog i tiskovnog cilindra. (Slika 1) Važno je da kvaliteta rakela bude dovoljno velika da se minimizira habanje jer se višak premaza prenosi na aplicirajući valjak. Također je važno uočiti da je udio volumena ćelije transferiranog na tiskovnu podlogu određen omjerom brzine role, viskoznosti premaza i geometrijom ćelija na bakrotiskarskoj tiskovnoj formi. Tanji sloj premaza s povećanom glatkoćom i ujednačenosti može se nanijeti na površinu tiskovne podloge korištenjem temeljnog cilindra malog promjera (20-50 mm) i djelomično korištenjem četvrekotune geometrije ćelija te procesom obrnutog bakrotiska. Smanjenjem promjera cilindra smanjuje se površina područja doticanja s površinom podloge. Nanosi premaza debljine od 0.010 do 40 mikrona mogu se koristit na podlogama gdje je potrebna mala tolerancija poput elektroničkih komponenti. [2]

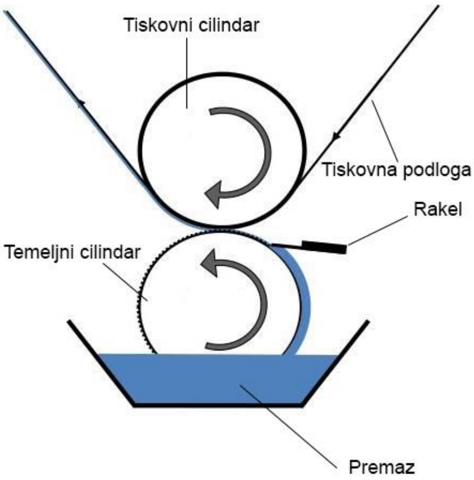

Slika 20: Prikaz primiranja na bazi bakrotiska

1.2. Primiranje na bazi fleksotiska

Fleksografski postupak nanošenja premaza na tiskovnu podlogu karakteriziran je korištenjem gumene ili fotopolimerne forme za prijenos premaza. Koriste se premazi na bazi otapala, UV-a ili premazi na bazi vode. Premazi na bazi vode čine većinu, a koriste se uglavnom u ambalažnoj industriji. Takvi premazi mogu pružati otpor na abraziju, toplinu i lužine. Mogu se primijeniti direktno preko većina bojila koja se koriste u fleksografskom tisku. Pomoću sustava komornog rakela određuje se količina premaza koji će aniloks valjak prenijeti na tiskovnu formu iz koje se premaz nanosi na tiskovnu podlogu. (Slika 2) Tiskari moraju često podešavati nanos premaza kako bi se postigla željena debljina nanosa. Fleksografski premazi eliminiraju probleme poput izvlačenja premaza i uvelike smanjuju varijaciju u debljini nanosa promjenom brzine nanošenja. Debljina premaza je inherentno definirana fleksografskim procesom. Između 19 i 24% sadržaja ćelije biva nanešeno na tiskovnu podlogu. [2]

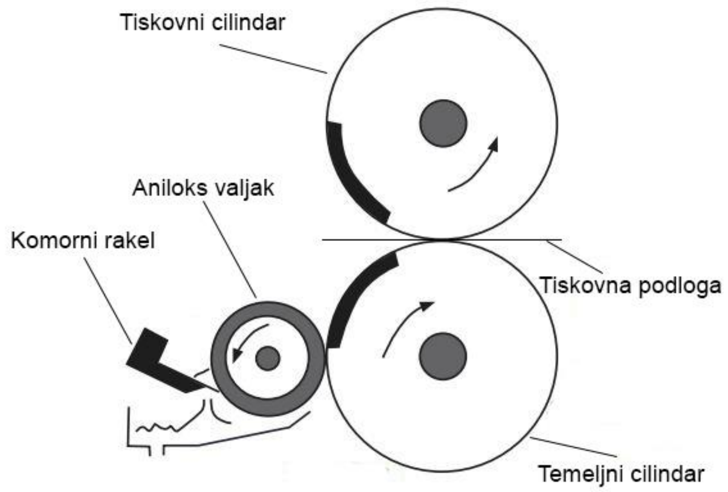

Slika 21: Prikaz primiranja na bazi fleksotiska

1.3. Meyerova šipka

Premazivanje Meyerovom šipkom (Slika 3) primjenjuje se i kod tiska iz role i kod tiska iz arka. Primijenjuje se kod premaza na bazi emulzija s niskom viskoznošću pri otiskivanju na osjetljivim tiskovnim podlogama kao što su papirnate etikete. Sastoji se od šipke načinjene od nehrđajućeg čelika na koju je namotana žica također od nehrđajućeg čelika određenog promjera. Promjer žice određuje količinu premaza koji će se prenijeti na tiskovnu podlogu neovisno o tome da li se šipkom prijeđe po papiru ili se papirom prijeđe po šipci. Šipke su dostupne u raznim veličinama kako bi se mogle nanijeti različite količine premaza. [2] [3]

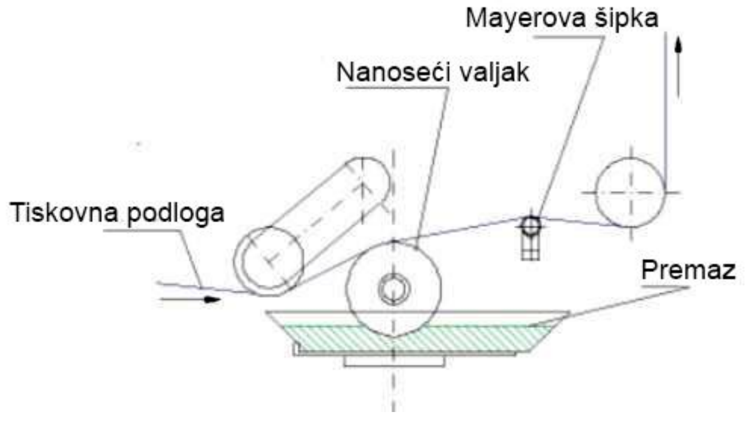

Slika 22: Prikaz primiranja pomoću Meyerove šipke

2. EKSPERIMENTALNI DIO

U eksperimentalnom dijelu ovoga rada standardni FOGRA uzorci su otisnuti na papir gramature 90 g/m^2 pomoću HP Indigo WS6800 [4]. RIP je napravljen na HPE ProLiant ML350 Gen9 serveru [5]. Na pojedinim uzorcima je proveden postupak prajmiranja pomoću HP Indigo In-line primer jedinice. Količina primera na uzorku s niskim nanosom iznosi 0,5 g/m^2, a korišteni primer je Michem In-line primer 030 koji je posebno napravljen za korištenje u HP Indigo In-line primer jedinici [6] (Slika 5 i 6).

Nakon ispisa uzorci su bili podvrgnuti mjerenju. Prvo se pomoću uređaja X-Rite DTP41 i softvera Monaco Profiler odredio gamut reprodukcije uzoraka, a zatim su se pomoću uređaja X-Rite eXact izmjerile Lab vrijednosti te su pomoću programa Origin 8.5. napravljeni grafovi koji prikazuju ovisnost kolorimetrijske razlike o rastertonskoj vrijednosti i 3D Lab prostor.

Također je pomoću glosmetra X-Rite Elcometer određen sjaj otisaka. Tiskovna podloga korištena u ovome radu jest premazani bezdrvni papir Condat Digital Gloss RL. Sastoji se od 50% celuloze, 40% kalcijeva karbonata, 4.5% vode, a ostatak (5.5%) čine dodaci [7] (Slika 4).

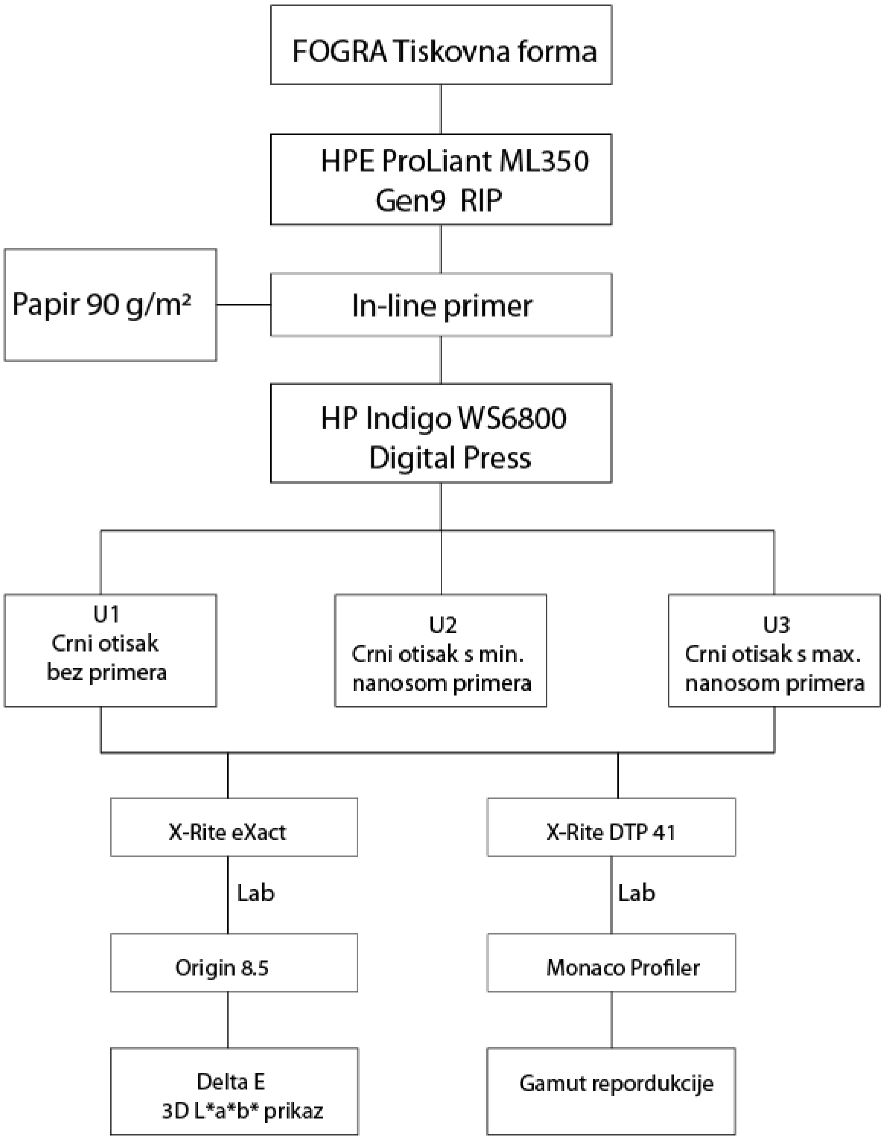

Slika 23: Tijek eksperimentalnog dijela rada

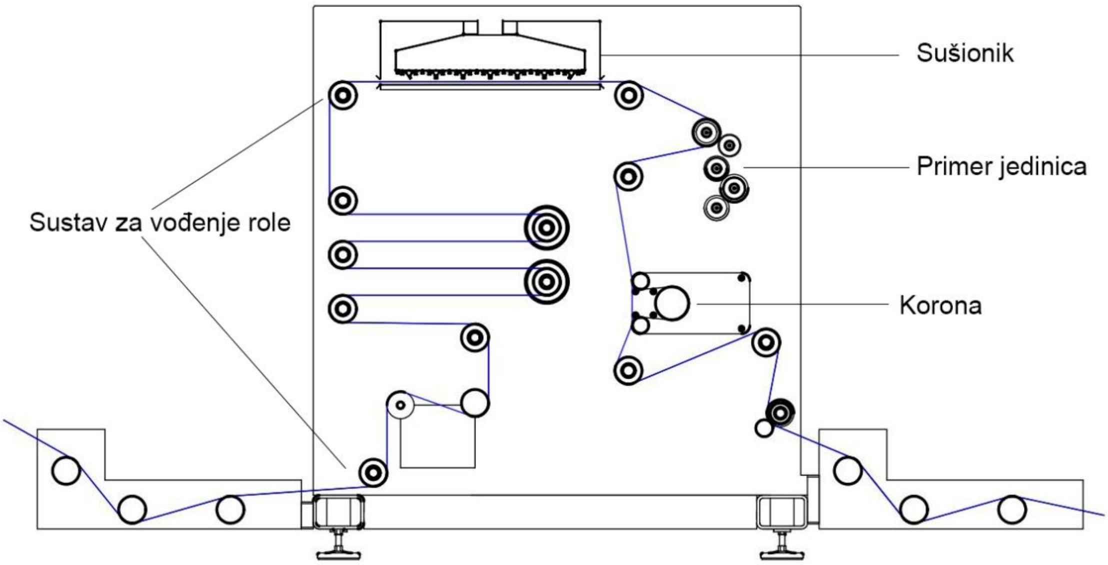

Slika 24: Prikaz HP Indigo In-Line Primera

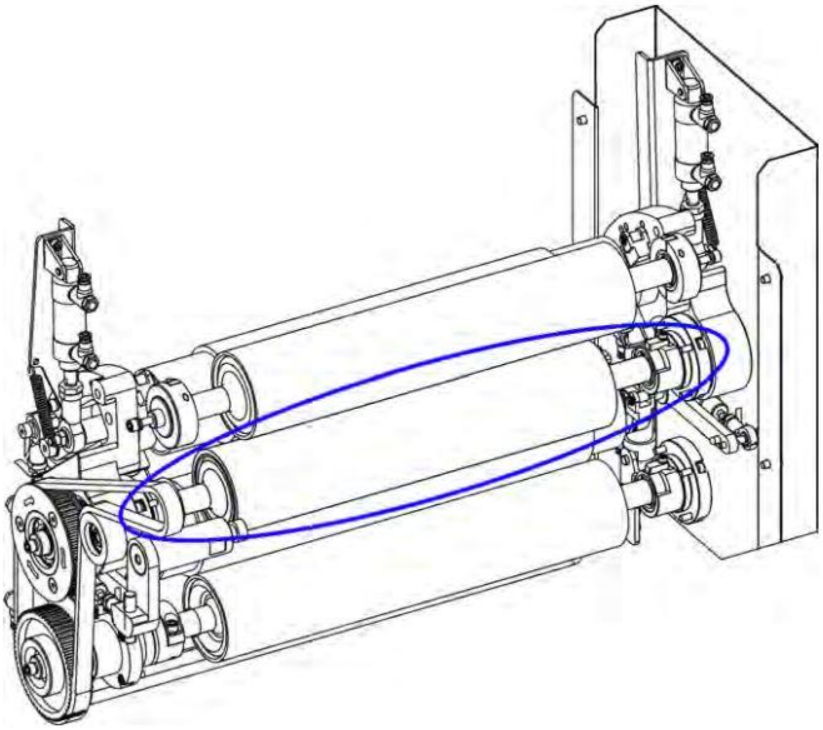

Slika 25: Prikaz jedinice za primiranje u HP Indigo In-Line Primeru

Tablica 10: Popis i karakteristike korištenih uređaja i materijala

Naziv uređaja	**Karakteristike**
X-Rite DTP41 Colorimeter & Densitometer	• Raspon valnih duljina: 400-700 nm • Raspon mjerenja: 0 – 160 % Reflektancija; 0D – 2.5D Gustoća zacrnjenja; • Denzitometrijski standardi: Status T, E, I, & A • Geometrija 45°/0° • Standardni promatrač: 2°/10° • Standardni izvori svjetla: A, C, D50, D65, D75, F2, F7,F11, & F12 • RS232
X-Rite eXact	• Raspon valnih duljina: 400-700 nm • Raspon mjerenja: 0 – 200% Reflektancija; • Brzina mjerenja: 2 s • Optička razlučivost: 10 nm • Geometrija 45°/0° • Standardni promatrač: 2°/10° • Mjerna površina: Ø1.5, Ø2, Ø4 i Ø6 mm • Standard: ISO 13655:2009
X-Rite Elcometer 407 Statistical Glossmeter	• Kut mjerenja: 20°, 60° i 85° • Automatski statistička obrada (max, min, std) • Standardi: AS/NZS 1580.602.2, ASTM C 584, ASTM D 1455, ASTM D 2457, ASTM D 4039, ASTM D 523, DIN 67530, ECCA T2, EN 12373-11, EN 13523-2, ISO 2813, ISO 7668, JIS K 5600-4-7, JIS Z 8741, TAPPI T 653.
HP Indigo WS6800	• Brzina ispisa: do 30 m/min prilikom ispisa 4 boja • Rezolucija slike: 812 dpi; 2438x2438 dpi HDI Linijatura: 175,180,196, 210 lpi Maks. format slike: 320 x 980 mm
HP Indigo In-Line Primer Unit	• Dimnezija: 1470 x 1772 x 1311 mm • Max. širina tiskovne podloge: 350 mm • Debljina tiskovne podloge: 12 do 450 mikrona • Brzina valjaka (74 mm): Niska: 46 RPM; Srednja: 69 RPM; Visoka: 92 RPM • Korona: 400-1000 W (default: 800 W)
Michem In-line primer	• Pojavnost: bijela, transparentna tekućina; • pH vrijednost: 8-10; • viskoznost (cps): <100;

Condat Digital Gloss RL	• Gramatura: 90 g/m^2; • Debljina: 70 µm; • Opacitet: 89%; • Bijelina D65/10°: 118.7%; • Sjaj: 70%; • Glatkoća po Bekku: 1400 s; • Vlažnost: 40%;

3. REZULTATI I RASPRAVA

3.1. 3D L*a*b* prostor i kolorimetrijska razlika

Na slici 7 a) koja prikazuje 3D L*a*b* prostor može se uočiti da se oba uzorka s primerom poklapaju s referentim FOGRA 51 uzorkom, dok kod uzorka bez primera postoje odstupanja kod svih rastertonskih vrijednosti. Povećanjem rastertonske vrijednosti na osi a*(zelena-magenta) dolazi do promjene kod svih uzoraka iz vrijednosti oko 0,85 za 20% RTV-a na vrijednost oko -0,05 za 100% RTV-a, što znači da se uzorci kreću od magente prema zelenoj. Na osi b* (plava-žuta) ta je promjena puno više izraženija. Uzorci za 20% RTV-a imaju vrijednost oko -4,5, a za 100% RTV-a vrijednost na osi b* iznosi oko -1, to jest, uzorci se pomiču od plave prema žutoj.

Na slici 7 b) prikazane su kolorimetrijske razlike triju ispitanih uzoraka. Najveću kolorimetrijsku razliku za 20% RTV-a ima uzorak s niskim nanosom primera, a najmanju ima uzorak bez primera. Kod 60% RTV-a najveću razliku ima uzorak bez primera, a najmanja je i dalje za uzorak bez primera. Za vrijednost 100% RTV-a sva tri uzorka se nalaze unutar narančastog područja što znači da je kolorimetrijska razlika uočljiva. Najveću kolorimentrijsku razliku ima uzorak s visokim nanosom primera, a najmanju uzorak s niskim nanosom primera.

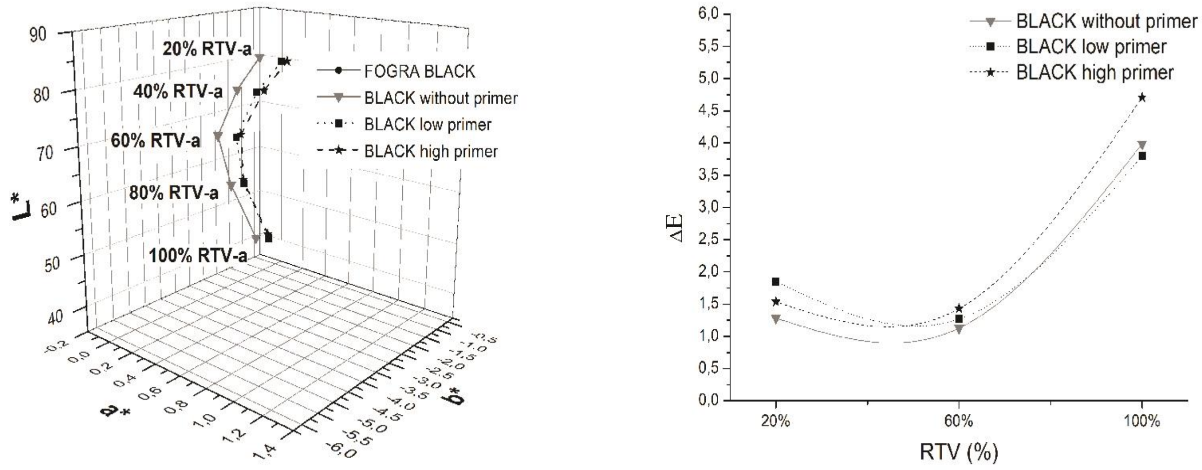

a) b)

Slika 26: a) Prikaz 3D L*a*b* prostora ispitanih uzorka; b) Prikaz kolorimetrijske razlike ispitanih uzoraka

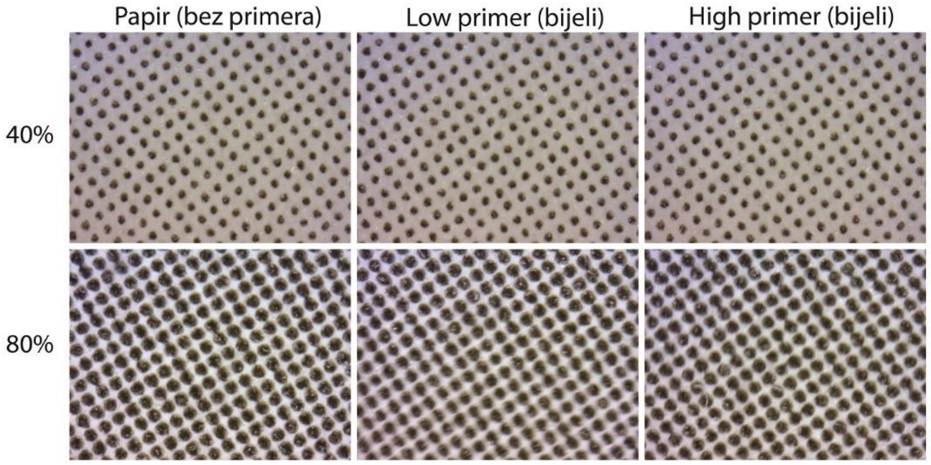

Slika 27: Mikroskopska snimka uzoraka za 40 i 80% RTV-a

3.2. Sjaj otisaka

Na slici 9 je prikazana raspodjela rezultata dobivena za mjerenje sjaja uzoraka. Najveću vrijednost sjaja ima uzorak Paper, a najmanju vrijednost sjaja poprima uzorak Paper + low primer. Može se primijetiti da dodatkom primera dolazi do opadanja vrijednosti sjaja ispitanih uzoraka.

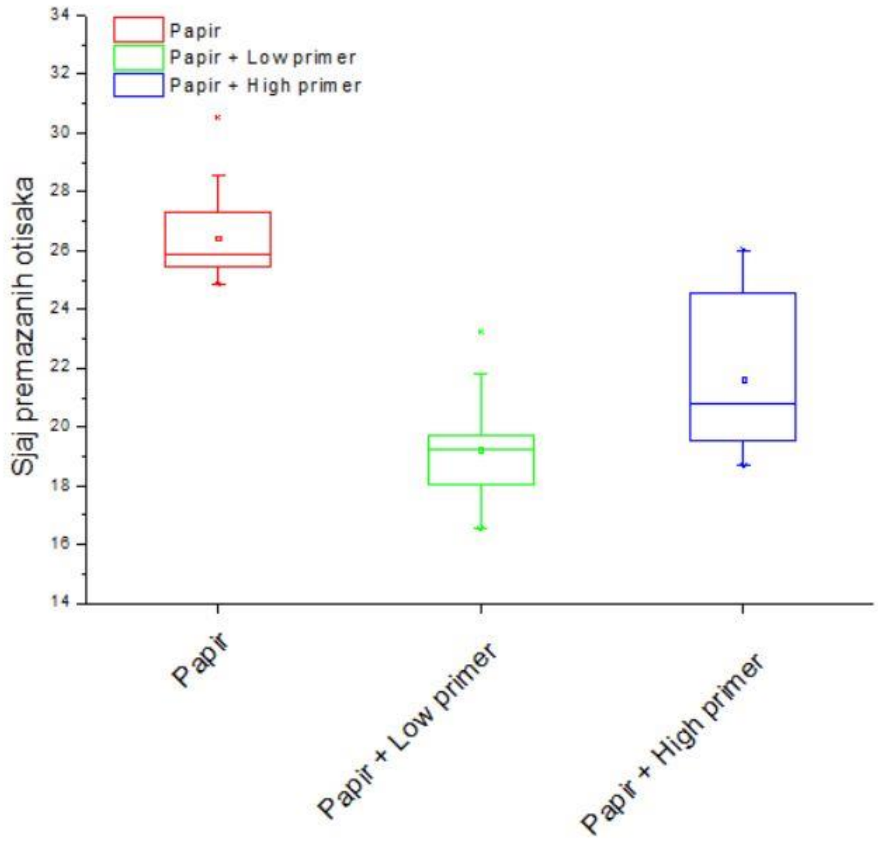

Slika 28: Sjaj ispitanih uzoraka

4. ZAKLJUČAK

Većom brzinom okretaja valjka u jedinici za nanošenje primera moguće je nanijeti veću količinu premaza. S obzirom da je količina nanesenog primera određena gravimetrijskom metodom, za bolje rezultate potrebno je napraviti mjerenje profila nanosa. Nanošenjem primera na ispitane uzorke nije došlo do povećanja kvalitete otiska u odnosu na uzorak na koji nije nanešen primer. Razlog tome je taj što je kao tiskovna podloga korišten papir koji se koristi za umjetnički tisak, a on već sadrži određene premaze te iz tog razloga kod ovakvih tiskovnih podloga nije potrebno primjenjivati postupak prajmiranja kako bi došlo do povećanja kvalitete otiska.

LITERATURA

[1] M. Niaounakis, “Surface Treatment,” *Biopolym. Process. Prod.*, pp. 303–326, 2015.

[2] R. A. Wolf, *Plastic Surface Modification*. München: Carl Hanser Verlag GmbH & Co. KG, 2010.

[3] www.holoeast.com/machines/coating/adhesive-coating-Meyer-Bar.html. (14.5.2018.)

[4] http://h20195.www2.hp.com/v2/GetPDF.aspx/4aa5-3064enw.pdf.(13.5.2018.)

[5] https://h20195.www2.hpe.com/v2/getpdf.aspx/c04375628.pdf.(22.5.2018.)

[6] https://www.michelman.com/Michem-In_Line-Primer/Michem(r)-In_Line-Primer-030/.(27.5.2018.)

[7] https://cmspro.lecta.com/digital/LectaProductCertificates/SafetyDataSheet_Condat.pdf.(23.5.2018.)

Vela Luka, Croatia
International Conference
MATRIB 2018
MATERIALS, TRIBOLOGY, RECYCLING

A NEW GENERATION OF X-RAY COMPUTED TOMOGRAPHY DEVICES FOR QUALITY INSURANCE AND METROLOGY INSPECTION IN THE FIELD OF ADDITIVE MANUFACTURING AND OTHER SCIENCES

Christopher Zepp[*1], Philip Sperling[†2]

[1]YXLON International GmbH, Essener Bogen 15, 22419 Hamburg, Germany

Keywords: Radiographic testing (RT), Computed Tomography, Metrology, Additive Manufacturing

Summary: The YXLON FF35 CT system, see Fig. 1(a), is designed to achieve extremely precise X-ray inspection results for a wide range of applications while at the same time it offers user friendliness at highest level by a new intuitive touch interface control concept and further smart functionalities. Available in a single or dual tube configuration, it is perfect for very small to medium size parts inspection in the automotive, electronics, aerospace and material science industries and research [1].

1. INTRODUCTION

Computed tomography goes light years beyond regular 2-D X-ray technology to deliver accurate three-dimensional images of scanned objects, including their voids and areas of differing density. It has become one of the most important and powerful non-destructive testing (NDT) methods - an achievement resulting from the continuous improvement of CT scanning and reconstruction methods, the enabling of increased precision and resolution, the manufacturing of cheaper and more compact devices and finally innovative concepts allowing for highest user friendliness to simplify the execution of successful CT experiments with high quality results.

Today´s range of NDT applications is applied to nearly every industry, i.e. automotive, electronics, aerospace and material science. Here, CT is used for research and development, failure analysis, process and quality control, small series inspection, combined DR-CT inspection, defect and material analysis, assembly checks and, becoming more and more important, metrology, i.e. dimensional measurements. To comply with such a variety of demands, YXLON has developed the powerful FF35 CT with an optional dual-tube-configuration (nano-focus transmission tube and high power micro-focus tube), which makes the FF35 CT extremely versatile. With a simple touch of a button, each tube can be adjusted independently. Intuitive system control is accomplished via two touchscreens displaying easy-to-understand graphics, see Fig. 1(b). Intelligent functionality supports the user: As an example, "IntelliGuard" avoids collision with X-ray tube and detector by automatically determining the outer-shape of the inspection item during a 360° rotation. CT trajectories such as “HeliExtend” (Helical CT scan and reconstruction method) provide consistently good image quality from top to bottom, and capture elongated specimen with a high magnification scan. The ability to select a custom centre of scan rotation using ‘virtual axis rotation’ (“FlexCenter”) offers considerable comfort and saves time. The inspected item does not need to be repositioned if regions of interest fall outside the physical centre of rotation. A system health monitor provides information on various parameters, see Fig. 1(c). Results are consolidated and displayed in a ‘traffic light’ representation. Additionally, one can access this health-state of the system and the progress of the CT (and reconstruction) from everywhere through remote monitoring software.

2. EXPERIMENTAL METHOD

Experiments are performed by choosing one out of two different x-ray sources mounted side-by-side in the high

---

* e-mail: christopher.zepp@hbg.yxlon.com

precision laboratory CT system FF35. The nano-focus transmission x-ray tube with a maximum photon energy of 190 kV and a maximum output power of 15 W enables highest resolution by accessing sub-micron length scales. The more powerful directional x-ray source performs up to 225 kV and a maximum target power of 280 W. The FF35 CT is equipped with a 300 mm x 250 mm (w x h) flat panel detector with a pixel size of 139 μm and various scintillator materials. A granite base enables precise manipulation of the inspection part which can weight up to 30 kg. By using the horizontal scan field extension or the helical CT option for vertical scan field extension the maximum scan field can be 300 mm in diameter or 500 mm in height. The additional detector axis for movements along the beam direction (focus to detector distance (FDD)) allows for the optimal combination of magnification (up to factor 200 and more) and collected photons for highly resolved CT results with an optimal signal-to-noise ratio. Reconstruction of the CT volumes is carried out by a filtered back projection algorithm. Data quality can be improved by applying a numerous variety of correction filters for beam-hardening, ring-artefacts, noise, bad pixels, focal spot drift, and more.

3. RESULTS

Results of representative applications, e.g. from additive manufacturing, carbon fibre composites and metrology will be highlighted during the presentation to demonstrate the performance of today´s laboratory CT devices, such as the YXLON FF35 CT.

References

[1] Internet: http://www.yxlon.com/products/x-ray-and-ct-inspection-systems/yxlon-ff35-ct

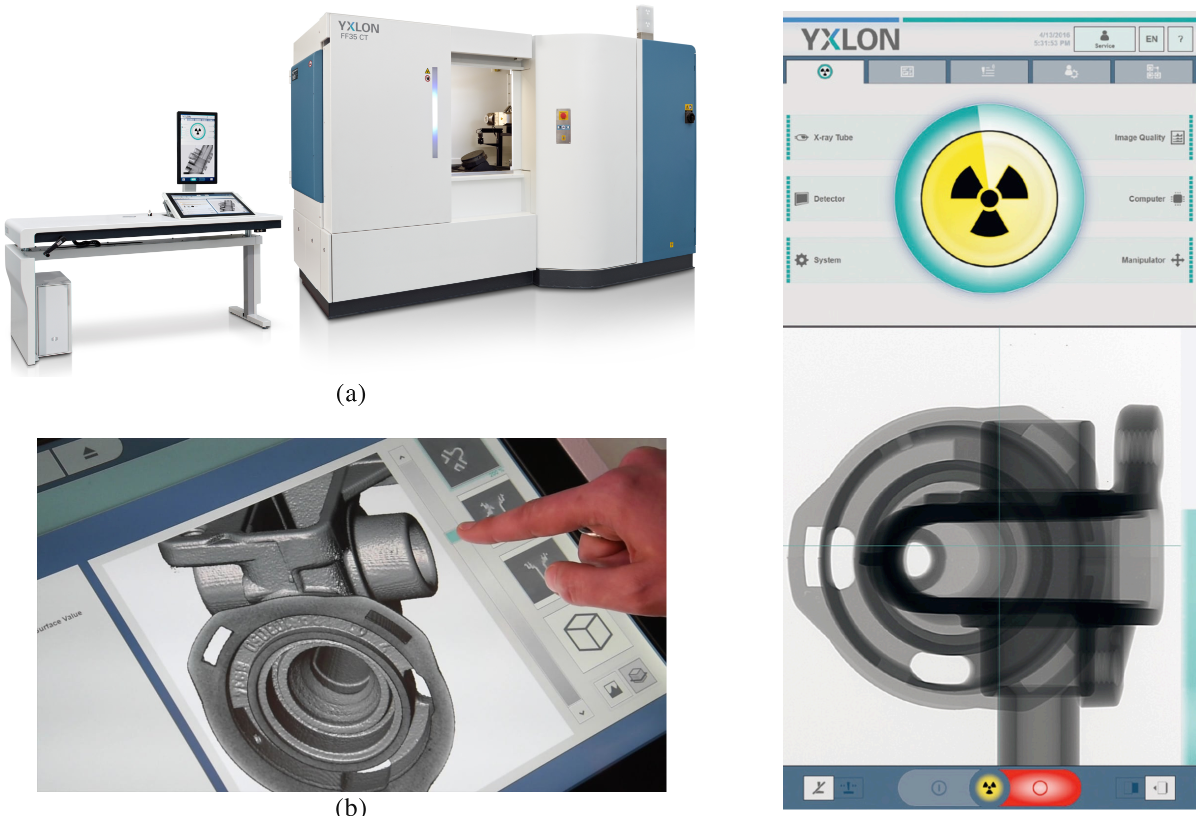

(a)

(b)

(c)

Figure 1: (a) The YXLON FF35 CT represents a new generation of high resolution and precision CT inspection devices and it features an innovative and highly intuitive touch screen control concept (b). (c) System parameter and status are shown in the health monitor while the radioscopic image is displayed below.

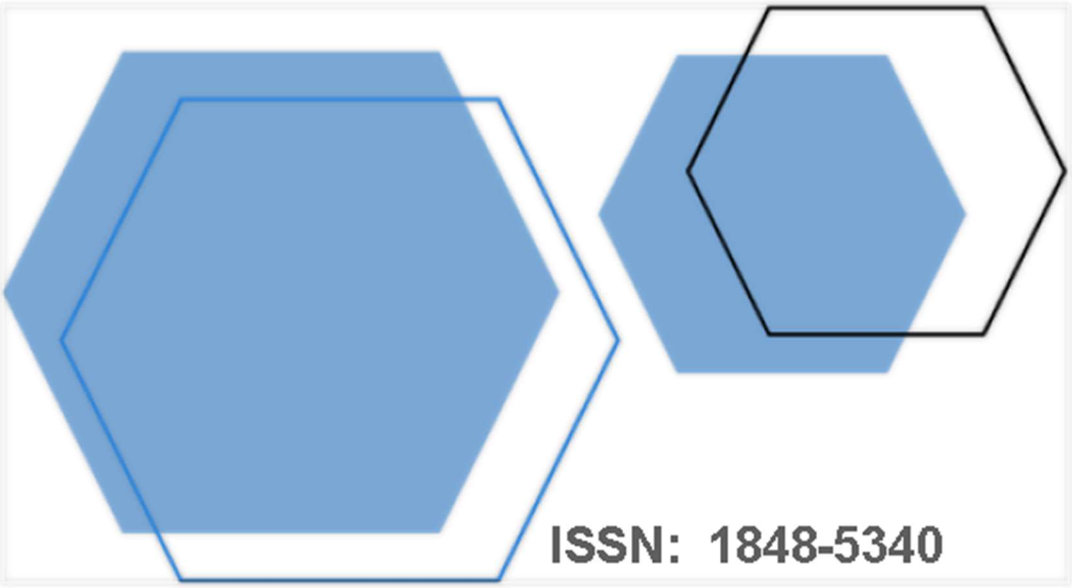

ISSN: 1848-5340